Studies of Polycyclic Aromatic Hydrocarbon-Based Organic Materials for Optoelectronic Applications

by

© Maryam Faghih Abdollahi

A thesis submitted to the School of Graduate Studies in partial fulfilment of the requirements for the degree of

Ph.D.

Department of Chemistry

Memorial University of Newfoundland

April 2023

St. John's Newfoundland

Abstract

π-Conjugated polycyclic aromatic hydrocarbons (PAHs) have found increasing applications in the fields of organic photonics and optoelectronics owing to their highly tunable photophysical properties, redox activity, and supramolecular self-assembling behavior. This PhD thesis mainly focuses on the studies of four classes of PAH-based organic materials, namely diphenyl dibenzofulvenes (DP-DBFs), pentacenetetraone-derived π-extended tetrathiafulvalene analogues (TTFAQ-AQ), donor/acceptor (D/A)-functionalized phenanthroimidazoles (PIs), and bis(diarylmethylene)dihydroanthracenes (Ar_4-DHAs).

DP-DBFs have been known to show intriguing crystallization-induced emission enhancement (CIEE) and aggregation-induced emission (AIE) properties; however, the molecular origins for them to exhibit such unique photophysical properties have not yet been clearly reported in the literature. In the first project of this thesis work, we designed and prepared a series of DP-DBFs with various substituents. With the aid of solution and solid-state fluorescence spectroscopic analysis, the AIE and CIEE properties of DP-DBFs were investigated. Our studies confirmed that the twist angle around the C=C bond in the DP-DBF is a key factor to control its fluorescence behavior.

In the second study, the structure-property relationship of TTFAQ-AQs were systematically examined. Analyses of their redox properties and electronic band gaps suggested that they could be promising organic semiconducting materials. Moreover, the synthesized TTFAQ-AQs featured double curved π-surfaces that contain both electron-deficient and electron-rich segments. In this way, they can serve as versatile

supramolecular partners to interact with 3-dimensional π-conjugated host molecules such as fullerenes. A benzo-fused TTFAQ-AQ derivative was observed to form organized organic co-crystals with electron deficient C_{70} fullerene through concave-convex shape complementarity and strong donor-acceptor interactions. The results point to promising application in redox-active organic electronic materials.

The third project embarked on the design of novel PI-derived organic chromophores and fluorophores. PI derivatives containing electron-donating dithiafulvenyl (DTF) groups and electron-accepting aldehyde groups were synthesized and characterized in terms of their fluorescence and electrochemical properties. The DTF-functionalized PI derivatives were found to show fluorescence sensitivity to singlet oxygen through a chemiluminescent mechanism. Moreover, the chemical oxidative dimerization of DTF end groups led to the construction of a new type of TTFV-PI macrocycles, which showed interesting fluorescence turn-on/off behavior when they interacted with C_{60} and C_{70} fullerenes at different ratios. These features make the synthesized PI materials interesting candidates in the fabrication of efficient fluorescence sensors for singlet oxygen and fullerenes.

The last project focuses on the synthesis, characterization, and mechanistic analyses on the photocyclization of a series of Ar_4-DHAs. We have made three different derivatives functionalized with methoxy groups at various positions of the phenyl ring, a tethered Ar_4-DHA derivative as a rigid model compound, and their photocyclized products. Although the cyclodehydrogenation reaction of this class of PAHs through the Scholl reaction has been well studied, photocyclization reaction still lacks sufficient understanding and evidence to support detailed mechanisms. In our work, it has been observed that the photocyclization only happens on one side of

Ar_4-DHA through a two-fold Mallory reaction. To better understand the mechanisms involved and the molecular reasons behind the two-fold Mallory reaction, we have utilized experimental and theoretical approaches including X-ray crystallographic analyses and density functional theory (DFT) calculations. The frontier molecular orbital (FMO) analyses offered convincing explanation for the regioselectivity of the two-fold Mallory reaction on a Ar_4-DHA. In addition, the importance of the position of the methoxy substituent on the mechanism of photocyclization has been revealed; in particular, when the methoxy groups are at the *ortho* positions, cyclodemethoxylation occurred instead of cyclodehydrogenation. Collectively, the work in Chapter 5 offers in-depth understanding of the photochemical properties of Ar_4-DHAs as well as valuable guidance for future work on the synthesis of π-extended PAHs and nanographenes from readilly accessbile Ar_4-DHA precursors.

Acknowledgements

Firstly, I would like to express my deepest gratitude to my supervisor Prof. Yuming Zhao for his invaluable knowledge and patience. Indeed, he has been the guiding light throughout my PhD journey. Thank you Dr. Zhao for all the positive encouragements you have provided which not only enabled me to discover my abilities, but also helped me shape my confidence and perspective. Under your supervision, my PhD has been an absolutely adventurous learning experience and, undoubtedly, you will always be a great role model to me.

Special thanks to my committee members - Dr. Huck Grover and Dr. Karen Hattenhauer for their valuable time and insightful feedback during committee meetings. I would also like to extend my sincere thanks to Dr. Flinn for his help and guidance throughout my program.

Many thanks to C-CART members, Dr. Jian-Bin Lin, Dr. Celine Schneider and Dr. Stefana Egli, for the help, insights, and time they have devoted during my research.

I would like to thank Dr. Christina Bottaro, Deputy Head of Research and Graduate Studies, for being ever so kind and encouraging. You have been always so supportive and helped me and my family adjust to our big life changes. Thank you Dr. Bottaro for every thing!

My thanks also go to the administrative staff, Ms. Mary Flinn, Ms. Rosalind Collins and Ms. Debbie Hickey in the Chemistry department for their timely assistance. To the teaching lab demonstrators, Mr. Cliff McCarthy and Ms. Anne Sheppard, I would like to express my gratitude. They are amazing colleagues and so

supportive.

To my amazing friends and lab members, Mohammadreza Khadem, Zahra Ahmadian, Farshid Shahrokhi, Fatemeh Salami, Azadeh Afzali, Ramin Eradeh, and Monther Zreid, words are not enough to express how pleasant and unforgettable you have made these years to me. It could not have been better!

To my soulmate, Reza! Whenever I look back at the joys and sorrows throughout these years, I thank my God for having you by my side. You have been my strength, emotional support, and mentor in every experience I have had. You are the biggest reason for my accomplishments in life. To my sweetheart, Rita! You are a blessing in my life! It is not easy to have a student mom honey but thank you for wanting me and for showing me it's okay to sometimes just be a mom. Thank you for arriving right on time and helping me be the best version of myself!

Finally, I am so thankful to my loving family and to my in-laws. Your unconditional love always makes me feel connected to you, even when we cannot share in person. I know that you are as proud of me as I am of you .

Last but not the least, I would also like to express my appreciation to all the faculty members and staff of the Department of Chemistry and Memorial University for the great environment they create for the students. I would also like to sincerely thank Memorial University, NSERC, and Dr. Linqin Chen for research funding and scholarship supports. There is no doubt that the supports they provided during these years have enabled us to tackle the problems more easily and grasp more opportunities to reach a brighter future.

Contents

List of Figures

List of Schemes

List of Tables

List of Abbreviations and Symbols

ACQ	aggregation-caused quenching
AIE	aggregation-induced emission
APPI	atmospheric pressure photo ionization
Ar_4-DHAs	bis(diarylmethylene)dihydroanthracenes
aq	aqueous
calcd	calculated
cm	centimeter(s)
ca.	circa
CI	conical intersection
CIEE	crystallization-induced emission enhancement
CV	cyclic voltammetry
DFT	density functional theory
d	doublet

DTF	dithiafulvene or dithiafulvenyl
DP-DBFs	diphenyl dibenzofulvenes
Et	ethyl
exTTF	π-extended tetrathiafulvalene
S_1	first excited state
FTIR	fourier transform infrared
FMO	frontier molecular orbital
g	gram(s)
S_0	ground state
HOMO	highest occupied molecular orbital
h	hour(s)
HRMS	high resolution mass spectrometry
Hz	hertz
IR	infrared
ISE	isomerization stabilization energy
J	coupling constant
LUMO	lowest unoccupied molecular orbital

m	multiplet
m/z	mass to charge ratio
MALDI-TOF	matrix assisted laser desorption ionization/time of flight
Me	methyl
mg	milligram(s)
MHz	megahertz
MMFF	Merck Molecular Force Field
min	minute(s)
mL	milliliter(s)
mmol	millimole(s)
mol	mole(s)
m.p.	melting point
MS	mass spectrometry
mV	millivolt(s)
mW	milliwatt(s)
MECP	minimum energy crossing point
nm	nanometer(s)

NMR	nuclear magnetic resonance
NICS	nucleus-independent chemical shift
ORTEP	oak ridge thermal ellipsoid plot
ppm	parts per million
PES	potential energy surface(s)
PXRD	powder X-ray diffraction
S_2	second excited state
s	singlet
TBC	tetrabenzocoronene
TD-DFT	time-dependent density functional theory
t	triplet
THF	tetrahydrofuran
TLC	thin-layer chromatography
DMF	dimethylformamide
SEM	scanning electron microscope
DLS	dynamic light scattering
TTF	tetrathiafulvalene

TTFAQ	anthraquinone-type π-extended tetrathiafulvalene
TTFV	tetrathiafulvalene vinylogue
UV-Vis	ultraviolet-visible
V	volt(s)
XRD	X-ray diffraction
δ	chemical shift
ϵ	molar attenuation coefficient
λ_{max}	maximum absorption wavelength

Chapter 1

Introduction

1.1 Organic Fluorogenic Materials

1.1.1 Introduction to Fluorescence

During the history of humankind, light has been an essential element of life. In modern society, the importance of light in technological innovation and discoveries is undeniable. The development of light emitting materials or luminescent compounds has attracted significant attention in the field of advanced photonics and optoelectronics. In particular, organic light-emitting diodes (OLEDs)[1,2] and organic field-effect transistors (OFETs)[3] are critically required functional luminophores that operate in the forms of crystals and thin solid films. In biomedical research, fluorescent molecular probes have been widely used to detect biologically imporant events taking place in aqueous media and cellular environments.[4] The vibrant advancement in this area was highlighted by Nobel Prize in Chemistry for 2008, which was awarded to Osamu Shimomura, Martin Chalfie, and Roger Y. Tsien for their discovery and

development of the green fluorescent protein (GFP) as a valuable tool to gain insights into biological pathways.

Generally speaking, when a beam of light shines upon a material, several possible events would occur, including absorption, transmission, and scattering. The light absorbed in the visible or ultraviolet region of the spectrum may have sufficient energy to induce molecular excitation from the ground electronic state to excited electronic states. Such excited states may then return to the ground state through rotational and vibrational relaxation or undergo some photochemical pathways to form other products. Deactivation of an excited state in these ways is called non-radiative decay. The excess energy of an excited state can also be released by a light-emitting process (i.e., radiative decay), which is well known as photoluminescence. The mechanism that describes the processes of light absorption, emission, and the electronic states associated with them can be clearly illustrated by the Jablonski diagram (Figure 1.1). Depending on the frequency of the light, the molecule can be excited to a vibrational level of higher excited electronic states, followed by rapid dropping back to the lowest vibrational level of that excited state, called vibrational relaxation, as a non-radiative transition. From here, other transitions including non-radiative internal conversion (IC) and intersystem crossing (ISC) to a triplet excited state, or radiative transitions such as fluorescence and phosphorescence are possible.[5,6]

The fluorescence quantum yield (Φ) is used to measure the efficiency of fluorescence emission.The fluorescence quantum yield is 100% if all excited molecules return to ground state by emitting fluorescence. In reality, a portion of the excited molecules may undergo other processes such as conversion to the triplet state, collision with solvent molecules or with molecules of another solute in solution state, and

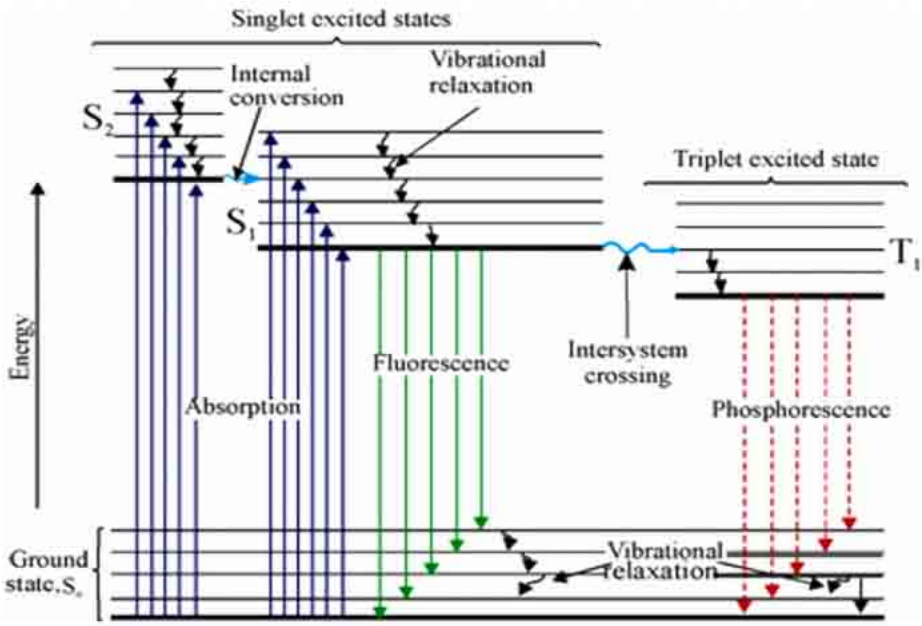

Figure 1.1: The Jablonski diagram illustrating various photophysical pathways (adopted from https://qr.ae/pr1aiq).

photochemical conversions. The occurrence of these processes reduces the fluorescence efficiency or even can completely quench the fluorescence. In typical fluorescence spectroscopic analyses, it is preferred to have the solution of a fluorescent compound in a sufficiently dilute concentration with only one fluorescent solute present, in order to avoid significant fluorescence quenching.[6]

1.1.2 Aggregation-Caused Quenching (ACQ)

Fluorescent compounds (or luminophores) in aggregate states may show different behavior than that in a dilute solution, depending on their molecular structures. Typical organic luminophores, upon aggregation, would show partial or complete fluorescence quenching, a phenomenon known as aggregation-caused quenching

(ACQ).[7,8] There have been extensive studies on the mechanism and photophysical processes related to ACQ. Birks' classic book entitled *Photophysics of Aromatic Molecules* is a well-known reference which provides a good understanding of ACQ. Birk explained that many conventional aromatic luminophores experience ACQ when they are in aggregate states, while as isolated molecules (e.g., in dilute solution) they are highly luminescent.[9] In general, such luminophores are planar aromatic systems or take large discotic plate-like molecular shapes (e.g., perylene) with extended π-conjugation. When these molecules are in close contact through aggregation, significant intermolecular π-π stacking occurs among them, which in turn favors the formation of excimers after photoexcitation. The formation of excimers then facilitates non-radiative decays and causes fluorescence quenching.[10–12] Figure 1.2 represents a good example of the ACQ effect. As can be seen, a dilute solution of *N*,*N*-dicyclohexyl-1,7-dibromo-3,4,9,10-perylenetetracarboxylic diimide (DDPD) in THF shows strong fluorescence. Addition of water, as a nonsolvent, to this solution induced aggregation of DDPD. It was observed that increase in the water fraction reduced the luminescence and eventually quenched it. When the water fraction was higher than 60 vol%, the solvating power or THF/water ratio decreases dramatically and DDPD precipiated out of the solution, causing ACQ. In the aggregate states, the perylene core of DDPD experiences significant π–π stacking and leads to excimer formation, which is the key reason for the observed fluorescene quenching.[13]

Fluorescent compounds have extensive applications in sensing and bioimaging. In particular, luminophores that can detect biological molecules in physiological buffers or environmental water have attractd growing attention.[14–16] However, these applications face challenges; for example, most of organic fluorescent compounds do

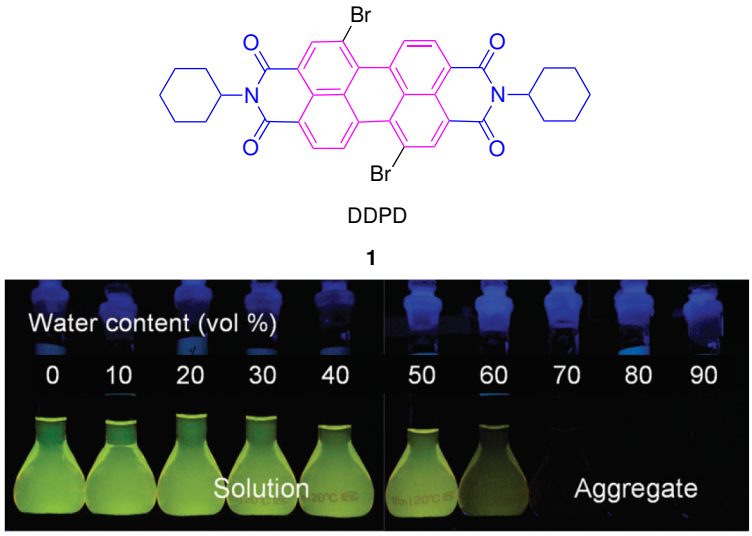

Figure 1.2: Fluorescence photographs of solutions/suspensions of DDPD (10 mM) in THF/water mixtures with different water contents (reproduced from reference with permission from the Royal Society of Chemistry).[13]

not show sufficient water solubility. Functionalization of these Luminophores with polar hydrophilic groups can improve their miscibility in water. However, when these compounds are dispersed in water, another issue arises, which is the formation of aggregates. Aggregation of typical organic fluorophores leads to fluorescence quenching, which reduces or destroys their fluorescence sensing performance. For solid-state fluorescence application, the problems caused by aggreation are also significant. For example, in organic light-emitting diodes (OLEDs), luminophores are prepared as thin solid films or in crystalline states to achieve luminescent function. In such states, luminophores are at their highest concentration in a non-solvent environment and hence show significant aggregation degrees. These effects in turn induce quenched fluorescence.[13,17] Typical organic fluorophores that show ACQ effects are unsuitable for the above mentioned applications. On the other

hand, certain types of organic fluorophores that can retain sufficient emission efficient or even gain enhanced fluorescence when they are in the solid and/or aggregated states provide ideal solutions to these challenges. Novel organic fluorophores and luminogens featuring aggregation-induced emission and crystallization-induced emission enhancement properties have been discovered and developed the past few decades.

1.1.3 Aggregation-Induced Emission (AIE) and Crystallization-Induced Emission Enhancement (CIEE)

In 2001, an unusual phenomenon of certain aggregated luminophores was reported by Tang and co-workers, which was later termed aggregation-induced emission (AIE). The seminal work on AIE quickly attracted considerable attention in the following years, since it offered an effective approach to tackle the problem of ACQ.[18–21] In Tang's studies, 1-methyl-1,2,3,4,5-pentaphenylsilole (**2**), which was non-emissive in its dilute ethanol solution, turned into a strong emitter upon addition of water (higher than 50 vol%) and also in film casting (Figure 1.3). Figure 1.3B shows the changes in the quantum yield of **2** upon addition of water. In 2007, Tang *et al.* introduced another unique photophysical phenomenon termed crystallization-induced emission enhancement (CIEE). For CIEE, a compound in an amorphous state shows weakly emissive or non-emissive properties, but in the crystalline form it turns into a strong emitter.[22] Based on their observations, crystallization of a dye, namely BpPDBF (**3**) (Figure 1.4), resulted in a fluorescence quantum yield enhanced by 180- and 32-folds in comparison with those measured in solution state

and amorphous powder, respectively. Traditionally, it is believed that intermolecular π-π interactions in crystal packing would cause an organic luminogen to show quenched fluorescence as a result of enhanced nonradiative decay in the crystalline state. However, structural and molecular examination of the class of CIEE-active luminogens such as 1,1,2,3,4,5-hexaphenylsilole (HPS),[22] 1,2-diphenyl-3,4-bis-(diphenylmethylene)-1-cyclobutene (HPDMCb),[23] and tetraphenylethene (TPE)[24,25] derivatives has revealed that their sterically hindered and twisted structures prevent the molecules from adopting a co-planar conformation. As a result, the intermolecular π-π interactions among these molecules in the solid state are limited. Moreover, in the crystal lattice, intermolecular forces such as C–H$\cdots\pi$ and C–H$\cdots$X (X = N, O, F, Cl) interactions can further disrupt the non-radiative decay pathway, resulting in enhanced fluorescence emission.[26]

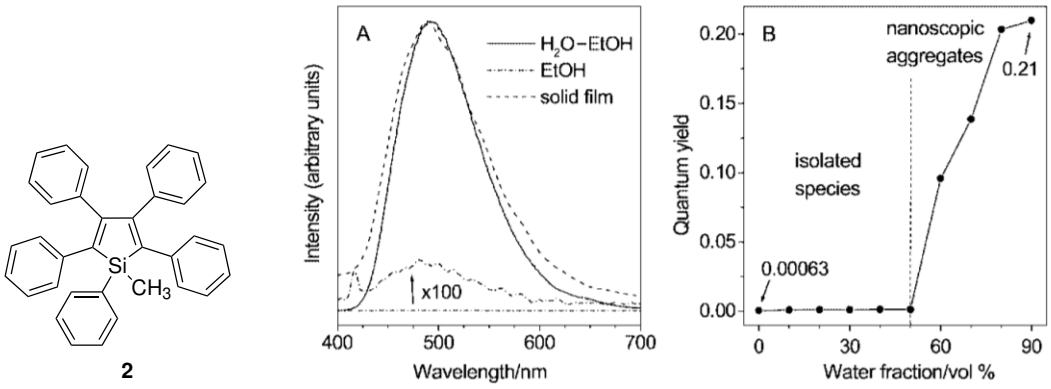

Figure 1.3: (A) PL spectra of **2** in water/ethanol mixture (90/10 vol%), ethanol, and solid film;(**2**: 10 μM); excitation wavelength (nm): 381 (for solutions), 325 (for film). (B) Quantum yield of **2** vs. solvent composition of the water/ethanol mixture (reproduced from reference with permission from the Royal Society of Chemistry).[18]

In contrast to the disc-like planar perylene derivatives, compounds such as silole **2** and hexaphenylsilole (HPS) adopt a non-planar propeller molecular shape.[18] In a solvent with high solubility, the molecules of non-planar compounds take twisted conformations and experience dynamic intramolecular rotations, which hinders their radiative property. However, in aggregate and crystalline forms, co-planarization of these molecules occur to some extent, resulting in better conjugation between the peripheries and the core unit, hence, enhances the emission properties. It is worth mentioning that although in the aggregated states the intramolecular rotation is somewhat restricted, π-π stacking does not occur significantly between the propeller-shaped molecules. In particular, the perfect co-facial alignment of the molecules is prohibited. As a result, the formation of excimers is limited and the ACQ effect is thus attenuated.[26]

Intramolecular rotational and vibrational motions allow an excited state to effectively dissipate its energy in a non-radiative manner. As such, they play a key role in fluorescence quenching. To rationalize their observed AIE effects, Tang *et al.* proposed a mechanism of restricted intramolecular motions (RIM).[27] For instance, the intramolecular rotational motions of propeller-like tetraphenyl ethylene (TPE), and the vibrational motions of 10,10′,11,11′-tetrahydro-5,5′-bidibenzo[a,d][7]annulenylidene (THBDBA), and butterfly-like bis(diarylmethylene)-dihydroanthracenes (Ar_4-DHA) in the solution state would effectively consume the energies of their excited states via non-radiative relaxation channels (Figure 1.4). When these luminophores are in the aggregated states, their intramolecular motions become restricted and the non-radiative decay pathways are subsequently blocked to increase the efficiency of emission.[28,29]

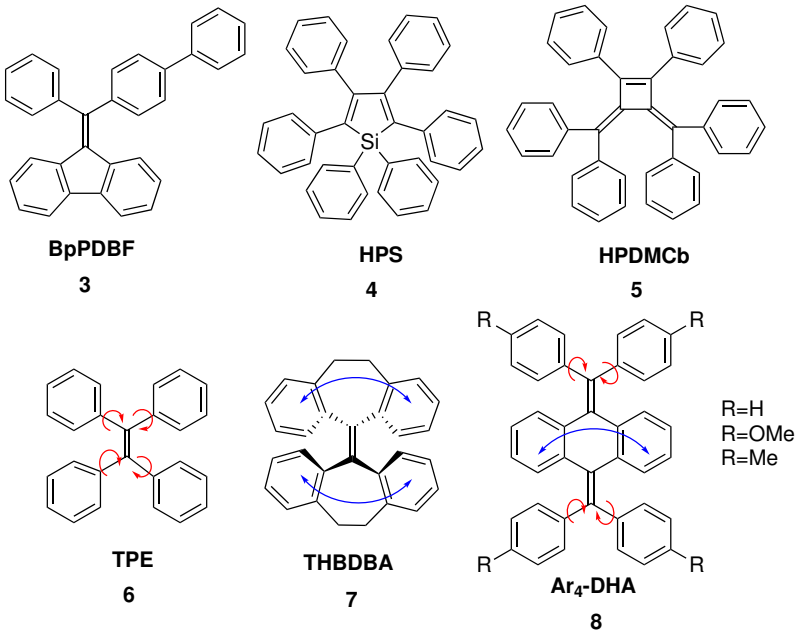

Figure 1.4: The structures of compounds BpPDBF, HPS, and HPDMCb and intramolecular rotational and vibrational motions (red and blue arrows respectively) in TPE, THBDBA, and Ar_4-DHA.

The RIM mechanism represents a milestone in the studies of AIE luminophores, not only allowing for in-depth understanding to be established but offering useful theoretical guidance for the design and synthesis of a large variety of AIE luminophores. In recent years, the rapid expansion of the family of AIE luminophores has greatly accelerated in their application in organic optoelectronic devices. Moreover, with growing experimental and theoretical studies, more sophisticated theoretical models have been established in addition to the RIM mechanism to rationalize the AIE effects in detail and with high accuracy.

1.1.3.1 AIE- and CIEE-Active Luminogens

Recently, it has been demonstrated that the way molecules are packed in the crystalline state or through aggregation is an important factor influencing their emission behaviour. In 2012, Zhang and co-workers reported that a series of diphenyl-dibenzofulvene (DP-DBF) substituted with alkoxy groups of different lengths showed varying solid-state emission properties (see Figure 1.5).[30] Among these derivatives, the fluorescence of compound **9** showed polymorphism dependence. Two of its crystalline forms (**9a** and **9b**) exhibited enhanced blue and yellow-green emission. In an amorphous solid state, they yielded weak orange luminescence. The fluorescence enhancement by crystallization was rationalized based on inhibited internal rotations as a result of strong intermolecular interactions in the crystalline state. The differences in the emission wavelengths of **9a** and **9b** were attributed to conformational changes. According to crystallographic analysis, the torsion angles of **9a** and **9b** are 74.40°/57.95° and 65.43°/44.83°, respectively. As a result, the benzene rings of **9b** are more co-planar with respect to the fluorene ring and a better π-electron conjugation was proposed as the reason for the observed fluorescence color changes. Moreover, the emission of these compounds could be tuned via heating, cooling, and grinding, making them appealing stimuli-responsive fluorophores.

In another study, Zheng and co-workers reported the emission properties of an imidazolium macrocycle based on bridged tetraphenylethylene (TPE) **23** in both non-aggregated and aggregated states.[31] Scheme 1.1 describes the detailed synthetic route to this macrocycle. Compound **23** was emissive when it was well dissolved (without aggregation) in a solvent, such as $CHCl_3$ containing 2% DMSO. Fluorescence spectral

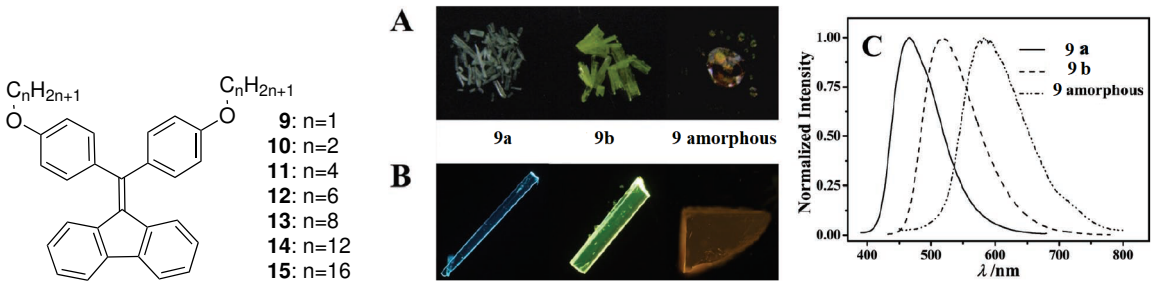

Figure 1.5: The structures of DP-DBF derivatives (on the left), A,B) ambient light photos (A) and CLSM images (B) of **9**: blue emission crystal (**9a**), yellow-green emission crystal (**9b**) and amorphous solid (**9** amorphous). C) The fluorescence spectra of **9a** , **9b** , and **9** amorphous (Copyright 2012 Wiley. Used with permission).[30]

analysis revealed that **23** gave an emission band in the solution phase. When the solution was continuously mixed with hexane, as a poor solvent, this emission band decreased and a new aggregation-induced emission band emerged at a much longer wavelength (bathochromic shift). Further, this macrocycle was found to form a 2:1 host-guest complex with C_{60} fullerene, and the complexation caused the fluorescence of **23** to be quenched.

In a study on *ortho*-substituted DP-DBF **24a**–**c** (Figure 1.6), the relationship between the type of substituent and photoluminescence (PL) properties was investigated.[32] It was revealed that both **24a** and **24b** are AIE-active and their emission efficiencies and wavelengths are dependent on the morphology of aggregates. However, **24c**, which contains a trifluoroacetylamino group, is neither AIE-active nor fluorescent in dilute solution. Such properties could be attributed to the photoinduced electron-transfer resulting from the strong electron-withdrawing effect of the trifluoroacetyl group that leads to PL quenching. In 2019, Nguyen and co-

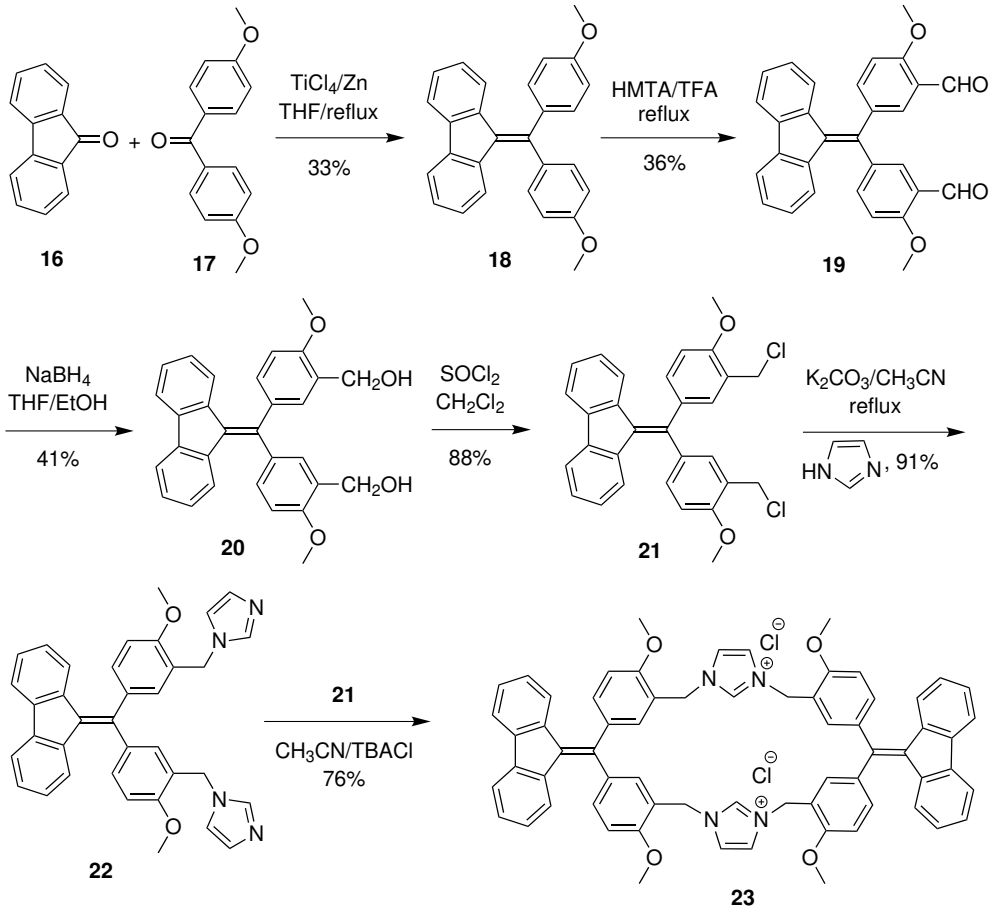

Scheme 1.1: Synthetic route to an imidazolium macrocycle **23** that contains bridged TPE units.

workers introduced a tethered DP-DBF system, with a conjugated vinyl bridge at the *ortho* positions (see **25**, Figure 1.6).[33] The incorporation of a vinyl group not only increases the degree of π-conjugation in the DP-DBF system, but restricts the internal rotation of the phenyl rings. As such, its solid-state fluorescence efficiency is significantly higher than that of the solution phase. X-ray crystallographic analysis indicated that the molecules are orderly packed in the crystalline state to show some interlocking effects, which can be correlated with the much greater quantum yield measured in the crystalline state (Φ_{cryst}=34.7%) in comparison to the aggregates in

the solution phase (Φ_{AIE}=43.2%) and thin films (Φ_{tf}=20.2%) .

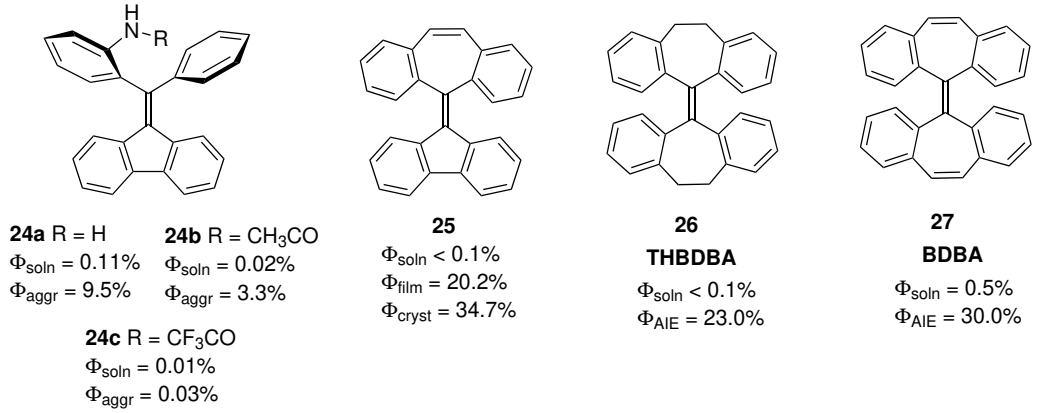

Figure 1.6: The structures and fluorescence quantum yields of selected fluorene–TPE derivatives.

This study can be compared with some related systems, such as [7,7]fulvalene 10,10′,11,11′-tetrahydro-5,5′-bidibenzo[a,d][7]-annulenylidene (THBDBA, Figure 1.6, **26**) and a fully conjugated analogue (BDBA, Figure 1.6, **27**).[28] Regarding THBDBA **26**, restricted intramolecular vibration (RIV) was regarded as a mechanism accounting for its AIE activity. The detailed rationale is described as follows. In the solution phase, the structure of **26** still shows conformational flexiblility to a certain degree, despite the tethered phenyl rings. In particular, the molecule of **26** can rapidly interchange between the boat and chair conformations. As such, the excited state of **26** in solution deactivates mainly through a path of vibrational relaxation (non-radiative decay), showing quenched fluorescence. In the aggregated states, the intramolecular vibrations of **26** are significantly hindered due to intermolecular stacking effects. On the other hand, the radiative (fluorescence) path is enhanced and the fluorescence becomes more efficient in the aggregated states. This rationale is

further corroborated by the AIE properties of BDBA **27** (Figure 1.6). In the molecular structure of BDBA, there are two vinyl groups bridging the phenyl rings. Unlike the case of **26**, the conformation of **27** cannot undergo boat-to-chair interconversion. As a result, BDBA **27** shows a much higher Φ_{AIE} than that of THNDBA **26**. Overall, compound **25** shows the highest fluorescence efficiency upon aggregation and even in the crystalline state among the analogues systems in Figure 1.6.

In 2015, Zhang and co-workers introduced a series of pyridinium-substituted tetraphenylethylene salts (**28a**–**g**) with tunable solid state emission.[34] As can be seen from Figure 1.7, various counter anions were utilized in preparation of these derivatives. Depending on crystal structures and packing motifs, the emission of these compounds in crystalline state shows colors varying from green to yellow with high efficiency. The emission of amorphous solids, however, shows red color. The red-shift of emission was explained based on an argument of loose packing and a more planar conformation of the molecules in amorphous state compared with a better packing of cations and the respective anions in crystalline state. Interestingly, the red fluorescence color of amorphous solids could turn into the respective green- to yellow-color emission in crystalline state after exposure to the vapors of methanol. Moreover, this color switching process was reversible; upon exposure to the vapor of CH_2Cl_2 or grinding, crystalline solids could be changed back into amorphous solids to give red-color emission (Figure 1.7).

In another study of TPE derivatives, a carbazole substituted tetraphenylethylene (Figure 1.8, **29**), with typical CIEE activity, was reported.[35] The luminescence color of its crystals was tuneable and dependent on the type of the solvent used for crystal growth. By co-crystallization of **29** with four different solvents, including

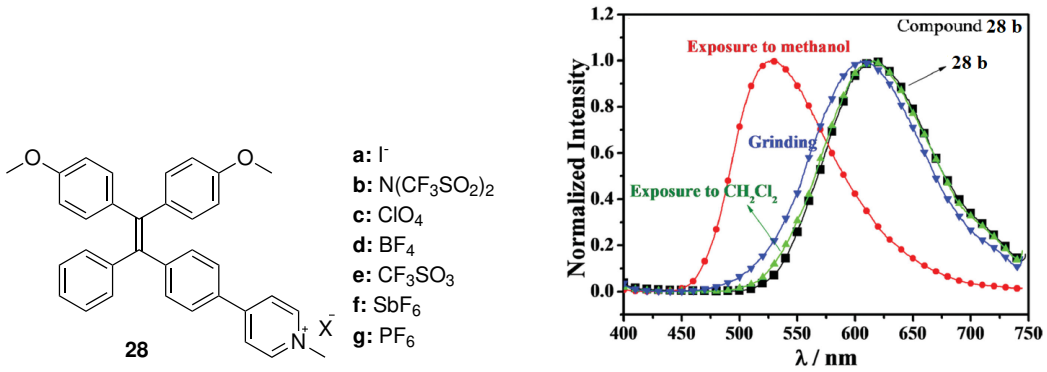

Figure 1.7: The structures of pyridinium-substituted tetraphenylethylene salts (on the left) and fluorescence spectra of **28b** after exposure to vapors of solvents and grinding (on the right) (Copyright 2015 Wiley. Used with permission)[34].

N,*N*-dimethylformamide (DMF), chloroform ($CHCl_3$), tetrahydrofuran (THF), and dichloromethane (CH_2Cl_2), four different crystal structures were obtained and they showed different emission colors, ranging from blue to green. The amorphous solids of this compound showed yellow-color emission. In addition, these crystals were found to be sensitive to grinding and exposure to various solvent vapors. As such the amorphous and crystalline states could be interconverted. In 2017, Chi and co-workers introduced an unusual mechanoluminescent material based on nitro substituted TPE (**30**, Figure 1.8).[36] Its crystals show porous structures and are non-emissive. However, the emission could be turned on by grinding, leading to an increase of the quantum yield from less than 0.1% for the crystals to 20.8% after grinding, and even to 82.5% in the amorphous state.

With respect to further studies in the field of stimuli-responsive materials, the synthesis and photophysical characterization of acridonyl-tetraphenylethene (AD-TPE) (**31**) by Tian is also worth mentioning.[37] AD-TPE **31** (Figure 1.8) showed turn-on and color tunable luminescence responses towards mechanical grinding and

hydrostatic compression. This compound is composed of donor and acceptor moieties, including TPE and AD, respectively. In its crystal structure, the orthogonal conformation between TPE and AD restricts the intramolecular charge transfer (ICT) process, causing emission from the locally excited (LE) state. Nevertheless, this twisted conformation could be changed upon force perturbation under mechanical stimuli, which resulted in a better overlap of frontier molecular orbitals between the donor and acceptor groups and hence facilitated the formation of an ICT state. As shown in Figure 1.9, application of mechanical pressure effectively led to a luminescence switching from an almost non-emissive solid to a bright cyan-color emitting state of compound **31**.

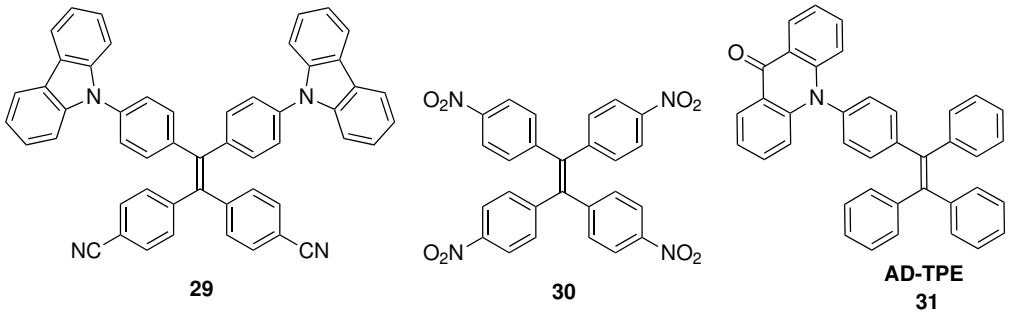

Figure 1.8: Chemical structures of compounds **29**- **31**.

In 2015, Tian and co-workers reported the synthesis of a series of saddle-shaped *N*,*N*′-disubstituted-dihydrodibenzo[a,c]phenazines (**32** and **33**) and their unique luminescence properties.[38] As shown in Figure 1.10, the emission colors of these derivatives can be tuned in the range of red to deep blue and even to white. This behaviour is temperature-viscosity dependent. For the fluorescence of FIPAC, decrease in temperature from 233 K to 133 K was accompanied with a lowering of the intensity of the red emission band and the hypsochromic shift of the blue-

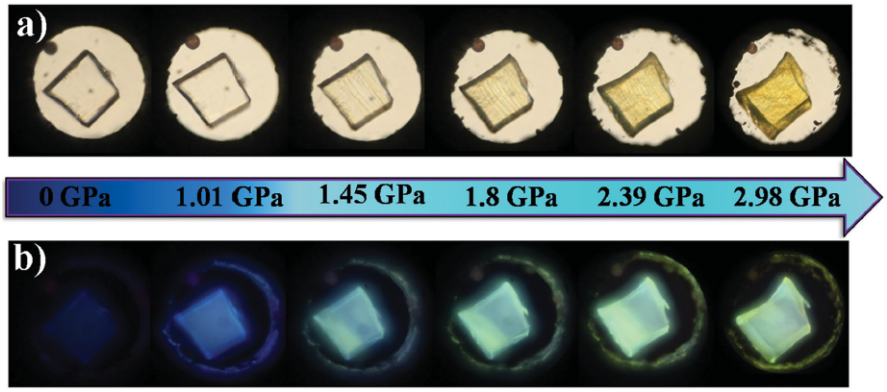

Figure 1.9: a) Visible and, b)fluorescence images of a single crystal of AD-TPE (**31**) under different hydrostatic pressures (Copyright 2015 Wiley. Used with permission).[37]

green emission (at almost 233 and 173 K). Based on this steady-state approach, planarization may couple with other electronic and structural relaxation processes to account for the observed multiple emissions that represent different degrees of temperature dependence.

1.2 Redox-Active Organic Materials

1.2.1 Introduction to TTF- and DTF-Functionalized Organic Materials

sulfur heterocycles have found extensive applications in modern synthetic, materials, biological, and medicinal chemistry. Among the vast number of sulfur-based heterocycles, tetrathiafulvalene (TTF, see Scheme 1.2A) stands out as the most well-known and thoroughly investigated system in the literature.[39–45] Ever since the seminal work by Wudl and co-workers on TTF in the early 1970s,[46,47] enormous

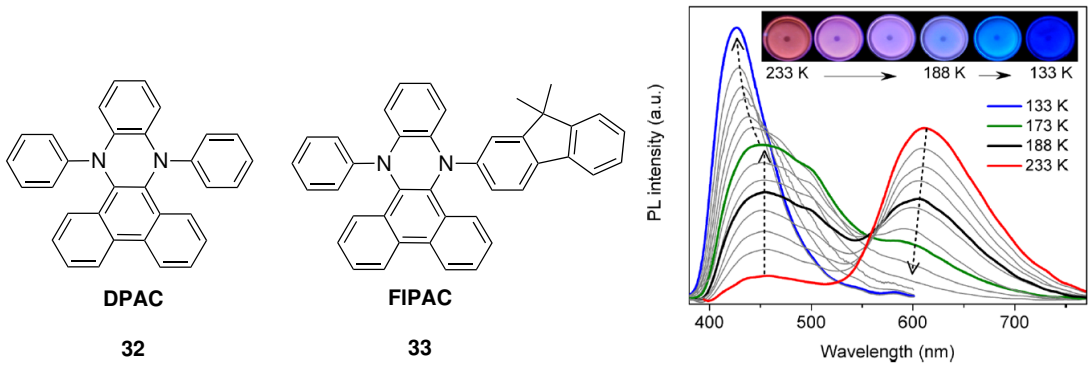

Figure 1.10: The structures of DPAC and FIPAC and temperature-dependent fluorescence spectra of FIPAC (**33**) in *n*-butanol from 233 to 133 K with various viscosities. The arrows indicate the direction of fluorescence response upon reducing the temperature. Inset: represented photographs under 365 nm UV light (Copyright 2015 American Chemical Society. Adopted with permission)[38].

research efforts have been dedicated to the subject of TTF-based functional π-conjugated materials and molecular devices. TTF contains two non-aromatic 1,3-dithiole rings which can be sequentially transformed into aromatic dithiolium rings upon oxidation. Due to this property, TTF shows excellent electron-donating ability and has been widely used as a π-electron donor in many redox-active π-conjugated materials and molecular electronic devices.

The half structure of TTF, namely 1,4-dithiafulvene (DTF, Scheme 1.2B), is also a very interesting organic functional group. The unsubstituted parent DTF molecule is 2-methylene-1,3-dithiole, which was only theoretically investigated in the early literature in terms of its structural and thermochemical properties.[48,49] Based on nucleus-independent chemical shift (NICS) and isomerization stabilization energy (ISE) calculations, Nielsen and Sauer proposed that the 1,3-dithiole ring in unsubstituted DTF behaves in a similar way to that in TTF, which renders DTF

a good organic π-electron donor as well.[50] Much research has been conducted on DTF derivatives, with the 1,3-dithiole unit linked to other functional groups through π-conjugation. The π-extension in various DTF derivatives not only improves their stability, but also enriches their synthetic accessibility, electronic properties, and redox activities. For these reasons, functionalized DTFs, like TTF and its derivatives, have also been widely used as molecular building blocks in organic conjugated materials.

Conceptually, the DTF group can be integrated in π-conjugated molecular systems through three main connection motifs as illustrated in Scheme 1.2B. In motifs I and II, the DTF group is directly connected to a π-conjugated unit via covalent linkages (e.g., C–C bond) at the vinylidene position, while in motif III π-extension is achieved through fusion of the 1,3-dithiole ring with other conjugated structures. When multiple DTF groups are connected to a π-unit in a conjugated manner, the resulting systems, in many cases, can be viewed as π-extended analogues of TTF (often referred to as ex-TTFs), which have attracted enormous attention in the field of TTF chemistry. Likewise, as represented in Scheme 1.2C, TTF moiety can also be integrated in conjugated systems as motifs I and II through covalent linkages, and motif III via extension from 1,3-dithiole rings.

1.2.2 Synthetic Methods for TTF-/DTF-Functionalization

The first synthesis of DTF was reported by Kirmse and Horner in 1958.[51] Photolysis of 4-phenyl-1,2,3-thiadiazole (**34**) led to thiokene **36** through a Wolff rearrangement, and the combination of **36** with biradical intermediate **35**, subsequently yielded diphenyl-substituted DTF **37** (Scheme 1.3A). However, this method was not suitable

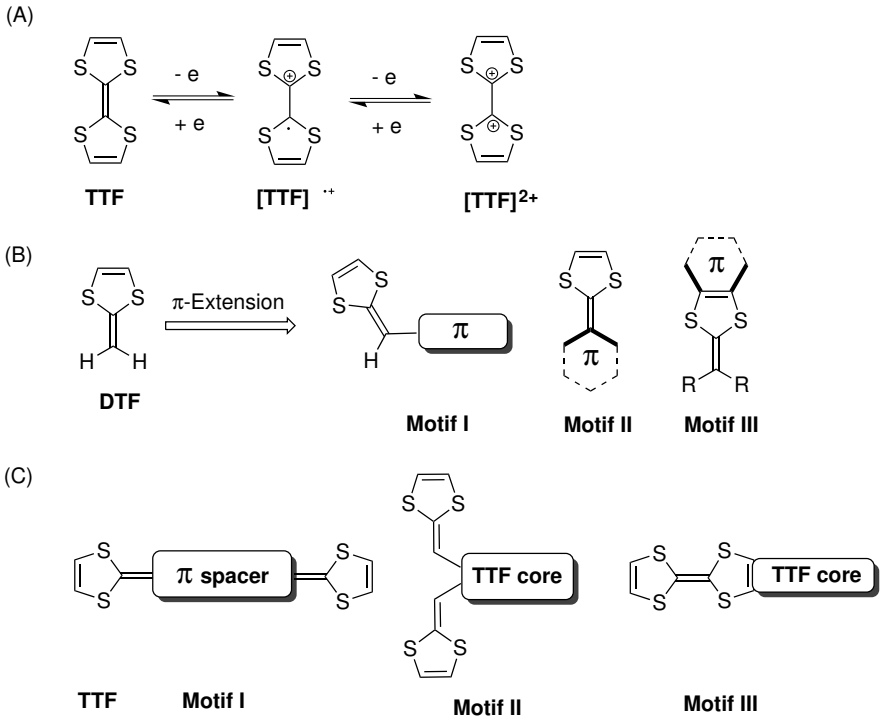

Scheme 1.2: (A) Stepwise single-electron transfer reactions of TTF. (B) General strategies for integrating the DTF, and (C) TTF units into π-conjugated systems.

for DTF-functionalization due to low yield and lack of control over stereoselectivity. More practically useful synthetic methods were later developed based on Wittig-type olefination reactions. In 1971, Hartzler reported a one-pot synthetic method for 2-benzylidene-1,3-dithioles (i.e., phenyl-substituted DTFs).[52] The reaction involved two steps: (i) cycloaddition of an aliphatic phosphine-CS_2 complex with acetylene to form a phosphorane intermediate, and (ii) a Wittig reaction with a benzaldehyde counterpart. Later, Cava and co-workers[53] devised a modified approach to conveniently prepare 1,3-dithiol-2-yl phosphonium salts (e.g., **41** in Scheme 1.3B) by protonation of the phosphorane intermediates with HBF_4. These phosphonium salts can be readily converted into Wittig reagents under basic conditions, allowing

olefination to occur with various aldehydes and ketones of choice. A plethora of similar types of phosphonium salts and phosphonate reagents were thereafter prepared, making Wittig-type olefination a dominant synthetic methodology for DTF-functionalization on π-conjugated systems. In 2007, Bryce and co-workers[54] reported a phosphite-promoted olefination method, in which a 1,3-dithiole-2-thione (e.g., **43**) was directly reacted with a ketone or aldehyde substrate in the presence of $P(OMe)_3$ or $P(OEt)_3$ to achieve DTF-functionalization (Scheme 1.3C). There are several advantages for this method: (i) The method is one-step and quite straightforward to execute. (ii) There are a vast number of π-conjugated ketones and aldehydes available, which greatly benefits the structural design and modifications of DTF-functionalized π-systems. (iii) The 1,3-dithiole-2-thione precursors can be readily synthesized and easily tailored. For these reasons, the phosphite-promoted olefination reactions have become a highly popular DTF-functionalization strategy in recent years. Indeed, most of the examples of DTF-functionalized systems highlighted in chapter were prepared through this efficient synthetic method. Moreover, a double S-vinylation approach can be useful for post-olefination functionalization.[55–57] This method uses 1,2-benzenedithiol to react with a *gem*-dihalovinyl system (e.g., Scheme 1.3D). With the DTF product featuring a π-extended benzo[*d*][1,3]dithiole structure. Recently, the groups of Morin and Nielsen respectively demonstrated that this reaction could achieve highly efficient DFT-functionalization on large polycyclic aromatic hydrocarbon (PAH) cores, such as anthanthrene and tetraceno[2,1,12,11-*opqra*]tetracene, under very mild conditions.[58,59] It was noted that the reaction could be used to handle some challenging DTF synthesis where Wittig-type and phosphite-promoted olefination methods failed.

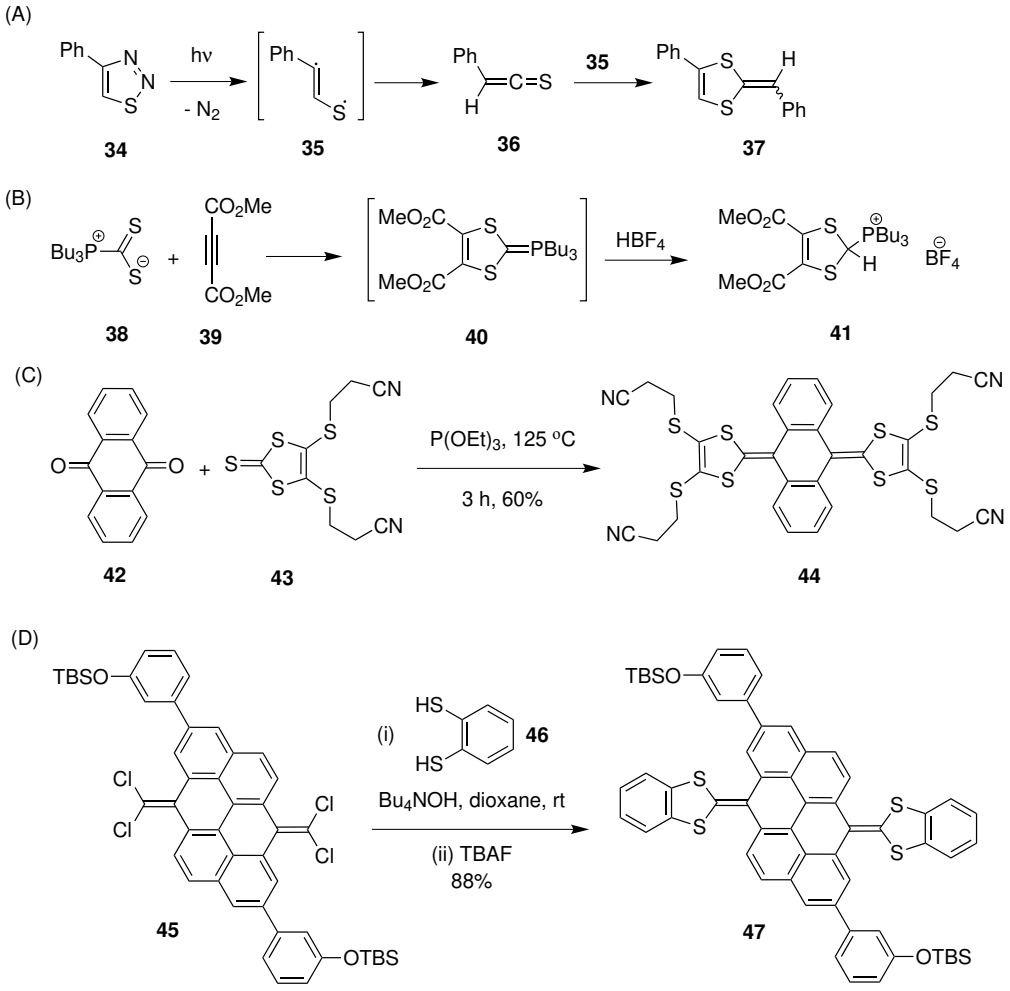

Scheme 1.3: (A) Formation of DTF through photolysis of 1,2,3-thiadiazole. (B) Synthesis of 1,3-dithiol-2-yl phosphonium. (C) A phosphite-promoted olefination reaction. (D) Post-olefination functionalization through double S-vinylation.

1.2.3 Properties and Reactivities

Tetrathiafulvalenes and 1,4-dithiafulvenes have long been known as electron-rich heterocycles which can readily release an electron upon oxidation. In 1974 Mayer and Kröber[60] examined the oxidation of a series of diaryl-substituted DTFs (**48a**–**d**, Scheme 1.4) and elucidated the structures of oxidized products as **49a**–**d**, based on elemental and UV-Vis absorption analyses. A detailed mechanism was proposed therein, suggesting the oxidation of DTF first generates a radical cation which subsequently dimerizes to form a stable dication salt. The aryl group attached to the vinyl position of DTF is believed to facilitate the electron transfer to form the radical cation intermediate, while the presence of a vinyl proton is essential for the elimination step to yield a stable dication product. Mayer and Kröber[60] also pointed out that this dimerization reaction has "preparative interest and allows access to electron-rich butadienes and novel heterocycles."

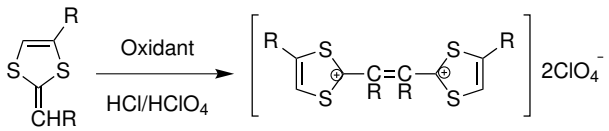

48 a-d **49 a-d**

(**a**) R= Ph, (**b**) R= *p*-tol, (**c**) R= *p*-Cl-C_6H_4, (**d**) R= *p*-OMe-C_6H_4
Oxidant: benzoquinone, 2,6-dimethoxy-*p*-benzoquinone, or chloranil

Scheme 1.4: Oxidative dimerization of DTFs.

The oxidative dimerization of DTF can be induced by a variety of oxidants such as $(BrC_6H_4)_3SbCl_6$,[61,62] I_2,[63,64] Br_2,[65,66] and $AgBF_4$.[67–69] Electrochemical conditions were also found to promote DTF dimerization reactions, affording TTF vinologues (TTFV) as products.[70–73] In 1996 Hapiot *et al.*[74] investigated the mechanism of DTF

oxidative dimerization by means of cyclic voltammetric (CV) analysis. Their studies showed that a fast single-electron transfer first generates a radical cation species, which rapidly forms a protonated dimer (see Scheme 1.5A). This protonated dication then slowly deprotonates into TTFV, which is quickly oxidized into a stable TTFV dication at a potential lower than that for the starting DTF. Figure 1.11 illustrates the cyclic voltammogram of a *para*-CN substituted phenyl-DTF (DTF-CN) measured at a low scan rate (0.2 V/s). On the first anodic scan, an irreversible peak appears at +0.74 V due to the oxidation of DTF. After the first reverse cathodic scan, a new reversible wave pair emerges at much lower potentials, which corresponds to the TTFV product resulting from oxidative dimerization.[74] Indeed, the oxidative dimerization has turned out to be the most useful reactivity of DTF for synthetic purposes. Over the past few decades, a large variety of π-extended TTF analogues and related conductive polymers have been prepared through this facile oxidative C–C bond forming approach.[75,76]

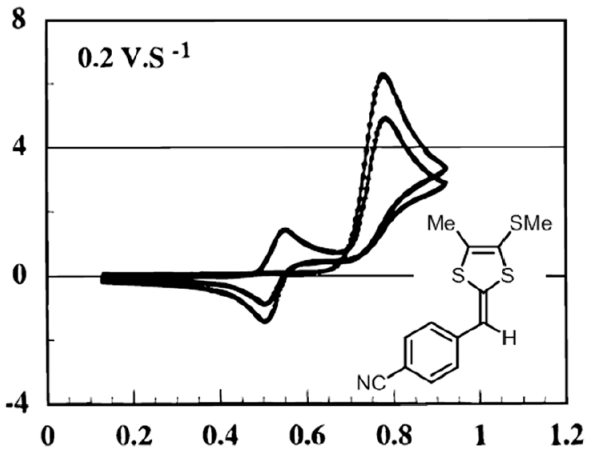

Figure 1.11: Cyclic voltammogram of DTF-CN measured in acetonitrile. Reproduced with permission from reference.[74] Copyright 1996 American Chemical Society.

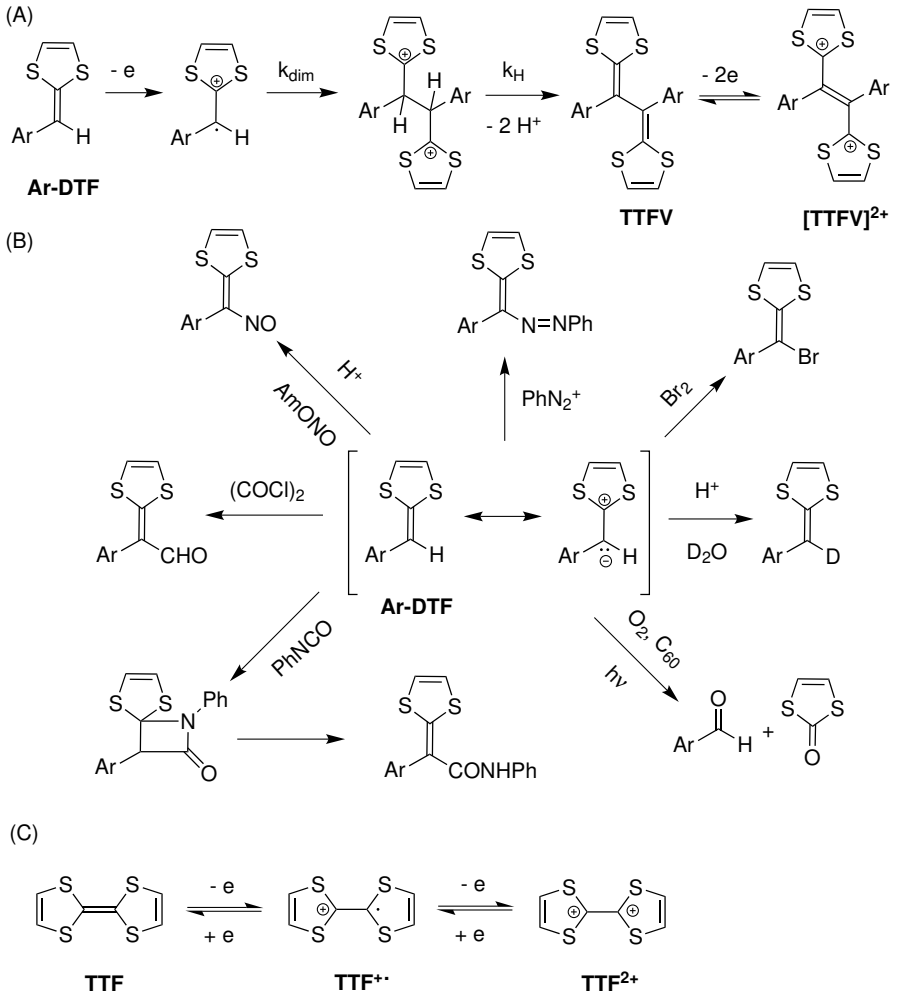

Scheme 1.5: (A) Oxidative dimerization of DTF. (B) Summary of the reactivities of DTFs with electrophiles. (C) Redox activity of a representative TTF in three states.

Other reactivities of DTF have also been reported in the literature, a summary of which is outlined in Scheme 1.5B. In most of these reactions, the vinylidene proton of DTF is displaced by various electrophilic groups. Hartzler in his 1971 paper[52] considered benzylidenedithioles (i.e., phenyl-DTFs) as quasi aromatic systems, which can be described by the resonance scheme shown in Scheme 1.5B. As such, the exo-ring C=C bond can act as a nucleophile susceptible to various substitution

reactions, including bromination,[77] addition to a diazonium salt,[78] nitrosylation,[78] and formylation with oxalyl chloride.[79] DTF can also be readily protonated by a strong acid. For instance, our group recently observed facile H/D exchange when DTFs were treated with trifluoroacetic acid (TFA) in the presence of excess D_2O.[80] The activated C=C bond of DTF can also undergo cycloaddition reactions. For example, the reaction between DTF and phenyl isocyanate (PhNCO) first led to a β-lactam intermediate, which was then transformed into an amide-functionalized DTF product.[81] DTF was found to undergo a photo-oxidative cleavage reaction in the presence of C_{60} fullerene and air.[58,82] In this reaction, the photo-excitation of C_{60} first induced the formation of singlet oxygen, which then reacted with the C=C bond to cleave DTF into the corresponding aldehyde and 1,3-dithiol-2-one. As noted previously, TTF and its derivatives are strong π-donor species and this feature has been widely utilized in producing redox responsive ligands and sensors. Scheme 1.5C represents three reversible redox states of a simple TTF moiety, in which the first step is oxidation to $TTF^{+\cdot}$, followed by another oxidation to TTF^{2+}. As a result, TTF meets the required factors for switchable processes, including the ease of oxidation (low ${E^1}_{1/2}$ and ${E^2}_{1/2}$ values), the possibility of performing oxidation steps either chemically or electrochemically via the ability to control the produced oxidized compounds as well as the adjustable electron donating feature of TTF, and, more importantly, reversible oxidation steps, accounting for stable produced charged species. It should be mentioned that the last point is of great importance in designing switchable devices.

Recently some unique reactivities have been discovered. Bouzan *et al.* observed that when a phenyl-DTF carrying an *ortho*-substituent (e.g., CH_3 or Br) was

subjected to iodine-promoted oxidative coupling conditions, the resulting product afforded an unusual dispiro-tricyclic structure such as compounds **51a/b** shown in Scheme 1.6A.[83,84] It was proposed that the presence of an *ortho*-substituent hinders the deprotonation step in the oxidative dimerization mechanism, hence allowing $Na_2S_2O_3$ to react with the protonated dication intermediate during the workup step. It was also found that the DTF group directly linked to a π-extended aryl group, such as anthracene[84] and pyrene,[85] may become inert to oxidative dimerization due to the strong resonance effect that stabilizes the radical cation intermediate. Such properties are in line with a new type of iodine-mediated vinylic sulfenylation reactions recently disclosed by Fu and co-workers.[86] As shown in Scheme 1.6B, 1-naphthyl and 9-anthryl-substituted DTFs **52** were first oxidized by iodine and the resulting radical cations, instead of undergoing oxidative dimerization, reacted with 1,3,4-thiadiazole-2-thiols **53** to form thiadiazolyl-substituted products **54** in good yields.

Our group recently discovered by serendipity that the DTF group can undergo an intramolecular alkyne-dithiolium cycloaddition reaction. As shown in Scheme 1.6C, bis-DTF **55** was originally intended to generate polymers through iodine-promoted DTF oxidative coupling. To our surprise, the reaction ended up with the formation of bis(indenothiophene) **56** as the major product.[87] A control reaction of **55** under the treatment of TFA yielded a cyclized product **57**, indicating that protonation of the vinylic carbon of DTF is a key step in the cyclization reaction. Density functional theory (DFT) mechanistic studies revealed that protonation of the DTF group leads to a dithiolium cation which favors reaction with the *ortho*-alkynyl group to form an intramolecular cycloaddition product.[88]

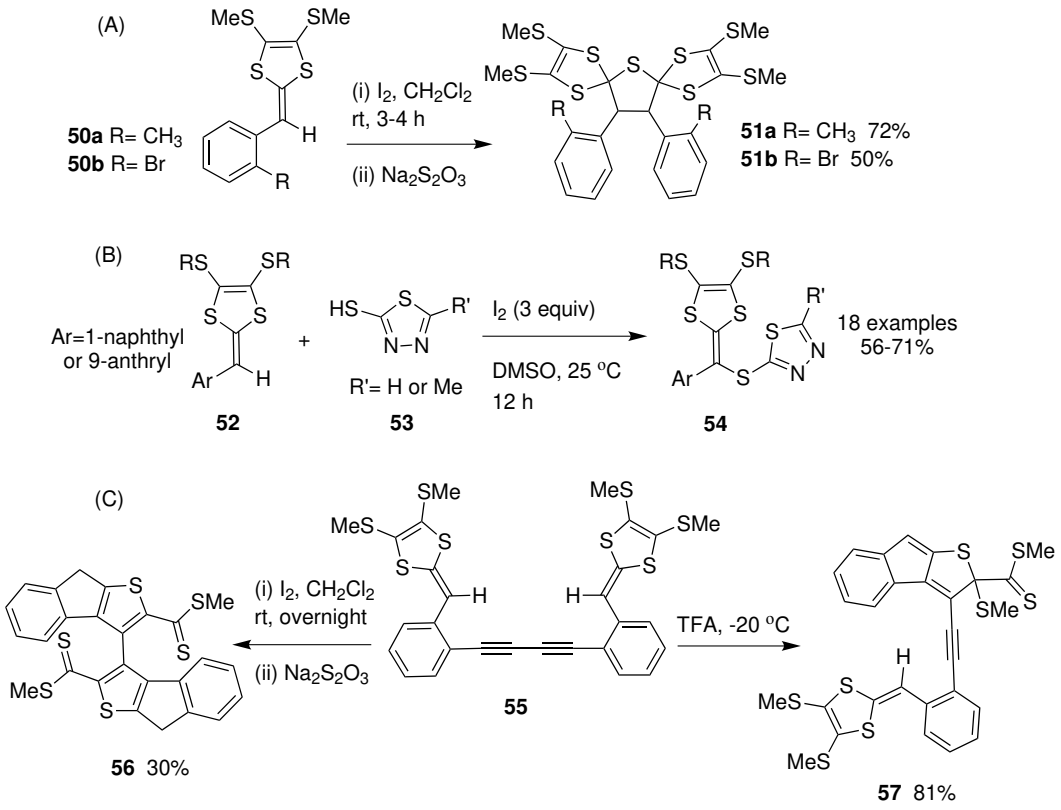

Scheme 1.6: (A) Unique oxidative dimerization of *ortho*-substituted phenyl-DTFs. (B) Oxidative vinylic C–H sulfenylation. (C) Alkynyl-dithiolium cycloadditions.

1.2.4 Recent Advances in DTF and TTF-Functionalized Organic Materials

The DTF and TTF groups can be applied as an active electron-donating group in various π-conjugated systems to bring about enhanced optoelectronic performance. In 2008, Leriche and co-workers[89] synthesized a group of DTF-functionalized triphenylamines (TPAs) (**58a/b**, Figure 1.12). These compounds were tested as organic semiconductors in organic field effect transistors (OFETs) and photovoltaic (PV) devices. Compound **58b** was found to show a hole mobility (3.2×10^{-4} cm^2 V^{-1} s^{-1}) which is about one order of magnitude higher than that of **58a** due to stronger

π-stacking in the solid state. Compound **58b** was also paired with C_{60} fullerene (electron acceptor) to form a bilayer heterojunction solar cell. The solar cell gave a power conversion efficiency (η) of 0.11%, but the stability of the device was poor. In 2013, Wan *et al.*[90] developed a bis(DTF)-substituted TPA **59a**, which features simple preparation and high molar absorptivity. Under AM 1.5G irradiation (100 mW cm^{-2}), the dye-sensitized solar cell (DSSC) based on **59a** gave a maximum power conversion efficiency of 4.41%. Compared with a simple TPA dye, DTF-functionalized TPA **59a** attained a 79% increase in η. Analogous DTF-TPA dyes **59b** and **59c** were also prepared and used for DSSCs. The devices afforded power conversion efficiencies of 3.78% and 4.09%, respectively.[91]

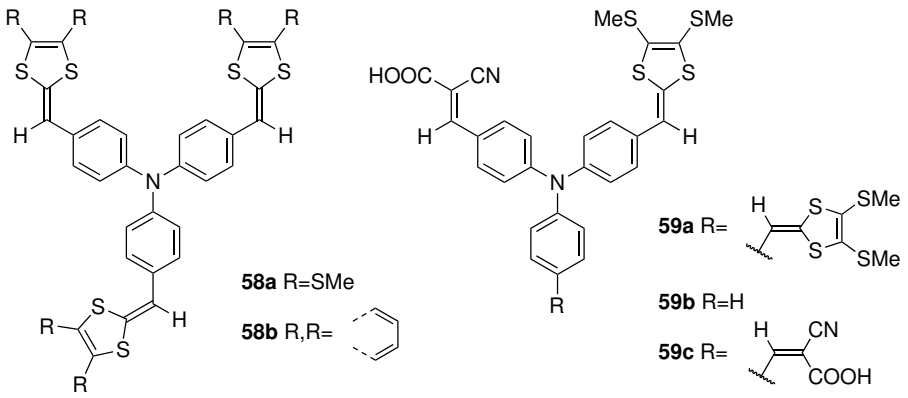

Figure 1.12: DTF-functionalized conjugated molecules utilized for solar cell devices.

In 2017, Zhan and co-workers, taking advantage of the hole-transporting property of TTF, prepared efficient perovskite solar cell (PSC).[92] They synthesized carboxylic acid- functionalized TTF (TTA, Figure 1.13) and applied it at the interface of ITO glass/$CH_3NH_3PbI_3$ in PSCs device as the hole-transporting material (HTM). The use of TTA HTM resulted in high η of 16.7% and a better device performance. SEM

measurements confirmed a high-quality surface without cracks. Furthermore, this substrate avoided the need of dopants for PSCs application and led to a better fill factor (FF) and short-circuit current density (J_{sc}) by modulating conductivity.

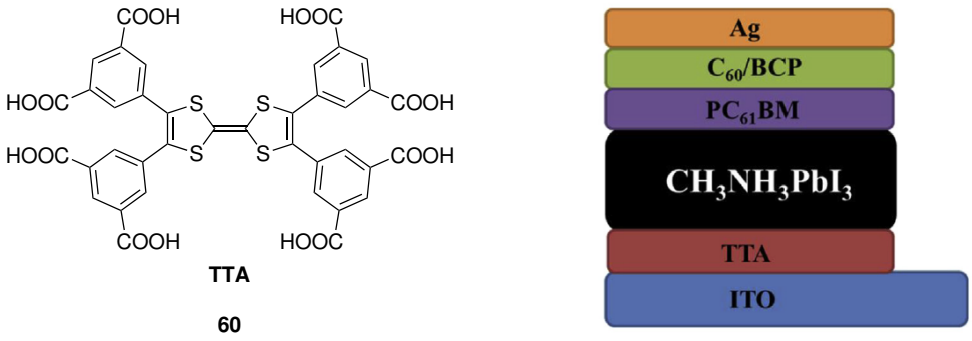

Figure 1.13: Chemical structures of TTA (on the right) and the schematic device structure of the PSCs with TTA as HTM and Ag layer as the top cathode (Copyright 2017 Elsevier. Reproduced with permission from with permission)[92].

Our group in 2016 synthesized a TTFV-pyrene macrocycle **62** through direct oxidative coupling of a bis(DTF)-pyrene precursor **61**.[85] As shown in Scheme 1.7, the synthetic procedures involved two important steps. In the first step, bis(DTF)-pyrene **61** was subjected to a partial oxidative dimerization (iodine as oxidant) in the solution phase for a limited period of time, forming a mixture of dimer and unreacted monomer. Without purification, the mixture was then subjected to grinding in the presence of iodine and silica gel to afford macrocycle **62** in an overall yield of 37%. A molecular modeling study suggested that the presence of DTF groups facilitates the binding of macrocycle **62** with electron-deficient aromatics such as nitrobenzene. UV-Vis titration experiments further confirmed that **62** could act as a supramolecular host for nitrobenzene with an association constant of 3644.6 $\pm$ 0.4 M^{-1}.

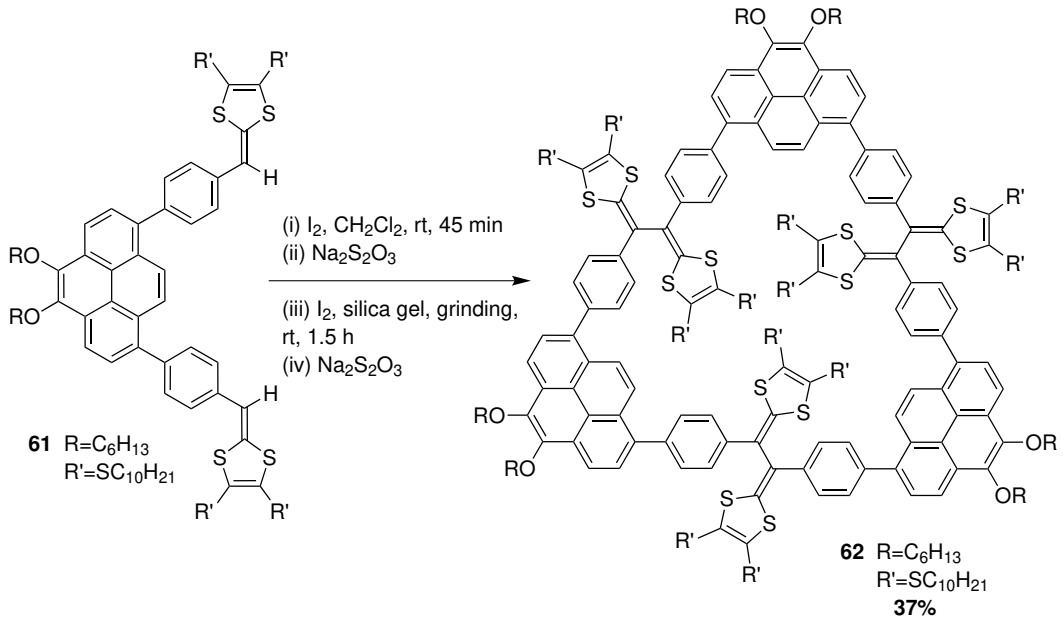

Scheme 1.7: Synthesis of a pyrene-TTFV macrocycle **62**.

Inspired by these findings, we designed a series of multivalent DTF-functionalized polyarenes **63**–**64** (Figure 1.14) as building blocks for the construction of redox-active polymer thin film sensors for nitrobenzene explosives.[93,94] Octa(DTF) **63** was found to form a microporous cross-linked polymer thin film on a glassy carbon electrode upon multi-cycle cyclic voltammetric scans. The thin film showed sensitive electrochemical responses to nitrobenzene at sub-mM concentrations.[93] To improve the durability of the cross-linked polymer thin film, a double-layer strategy was recently devised by our group.[94] Tetra(DTF) **64** was electropolymerized on a robust TTFV polymer film pre-deposited on a glassy carbon electrode, and the two layers of polymers were covalently bound. The double-layer polymer thin film exhibited very high sensitivity and selectivity for 2,4,6-trinitrobenzene (TNT) among other nitrobenzene derivatives, and hence can be used as a TNT sensor with excellent durability and re-usability.

Regarding metal cation sensing properties, Sallé and co-workers designed and

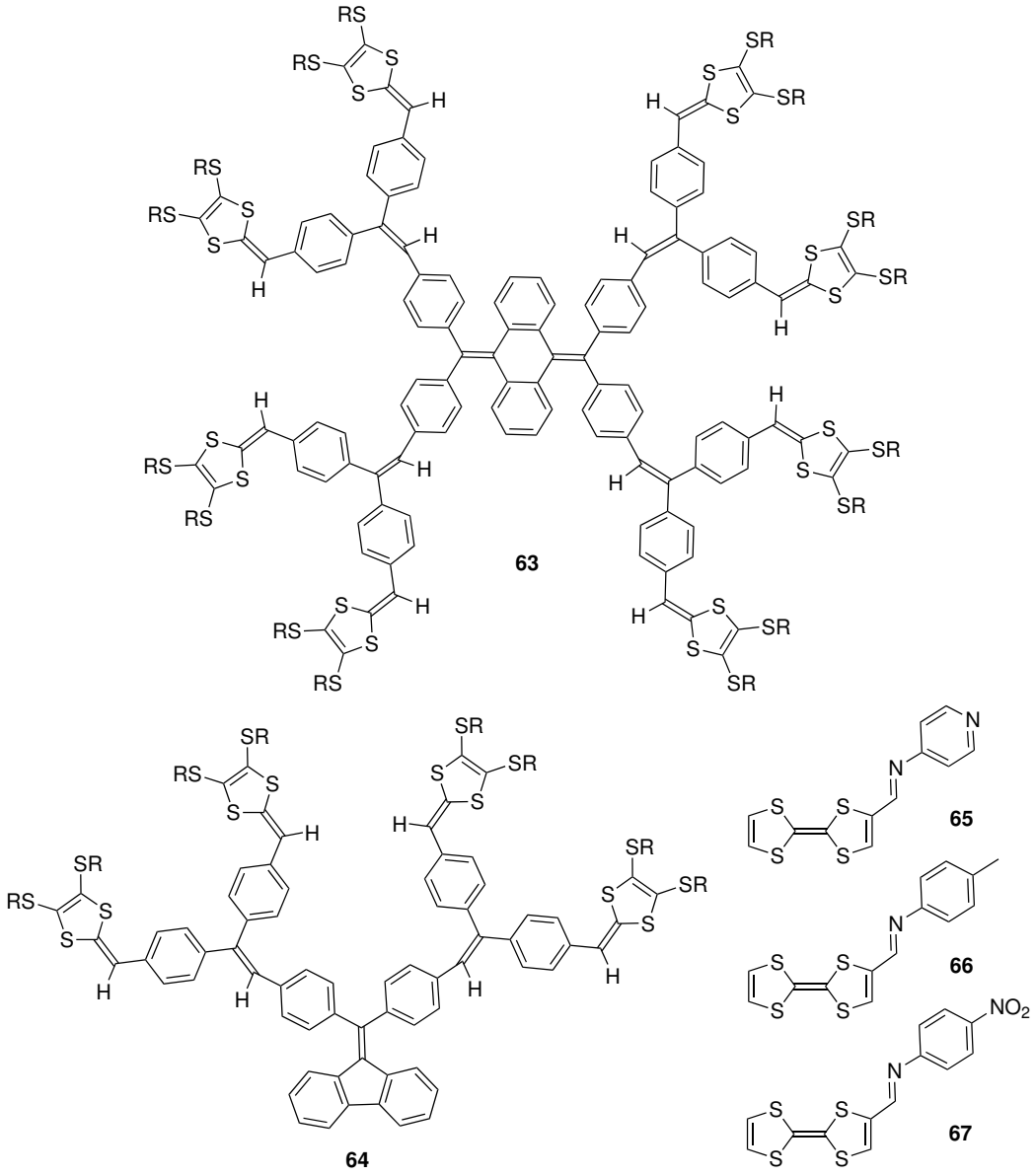

Figure 1.14: Multivalent DTF building blocks for redox-active polymers.

synthesized a series of donor-π-acceptor TTF derivatives incorporated with an imine conjugated linker (see **65**–**66**, Figure 1.14).[95,96] The pyridyl-substituted systems (**65**) showed significant binding affinity as well as good selectivity for Pb^{2+} (log K = 3.5 in CH_2Cl_2/CH_3CN). This binding property was examined and confirmed by UV/Vis analysis, ^1H NMR titrations, cyclic voltammetry, and significant colorimetric responses. Interestingly, upon addition of Pb^{2+}, the yellow-orange color of free ligand solution turned into deep purple-deep blue. These changes were explained based on the modification of ICT from HOMO of the donor TTF moiety to the acceptor pyridyl unit through metal coordination.

As excellent organic electron donors, TTF and DTF have been widely used in the design and synthesis of functional organic π-conjugated materials for decades. Indeed, there is a vast body of literature related to this topic and its size is still growing rapidly in various fields such as organic solar cells, Molecular wires, redox-active polymer sensors, dispersants for single-walled carbon nanotubes and so forth. It can be envisioned that studies dealing with these fundamental issues will be of great value for future design and application of TTF-/DTF-based organic conjugated materials.

1.3 Supramolecular Chemistry

Jean-Marie Lehn, who is well known as the father of supramolecular chemistry and the Nobel Prize winner for his work in this area in 1987, defined supramolecular chemistry as "chemistry beyond the molecule." According to his definition, the goal of supramolecular chemistry is to design systems in which molecules are held together

through non-covalent interactions rather than covalent forces. Commonly seen non-covalent interactions include ionic bonding, hydrogen bonding, dipole-dipole and ion-dipole interactions, π-stacking, metal coordination, and van der Waals forces.[97,98] Although the non-covalent interactions are weaker than covalent forces, numerous of them combined together can still effectively dictate the shapes and properties of supramolecular assemblies.

1.3.1 Host-Guest Chemistry and Supramolecular Self-Assemblies

Supramolecular chemistry encompasses the non-covalent binding of host and guest molecules, where the host-guest complexes are in thermodynamically controlled equilibrium with the host and guest species. Generally speaking, a host molecule is designed to contain specific functional groups (binding sites) and molecular shape (cavity) to encapsulate a guest molecule(s) through non-covalent forces or shape complementarity. As such, the complexation of a host and a guest molecule(s) is an exergonic process, which affords measurable binding energy or association constant(s).[98,99]

Besides host-guest chemistry, supramolecular chemistry also deals with the association of multiple molecular buidling blocks via spontaneous non-covalent interactions to form large-scale supramolecular assemblies (generally referred to as self-assembly). The well-known double-strained helix of DNA represents a biologically important example of supramolecular self-assemblies and self-organization, in which two individual strands of DNA are organized through hydrogen bonding and

π-stacking interactions to yield a double helical structure.[99] Self-assembly has been developed as a very useful synthetic approach to generate novel organized supramolecular structures with controllable responsiveness to ambient conditions, including pH, light, electricity, redox potential, and magnetic field.[100] The study by Ghadiri et al. is another remarkable example of supramolecular self-assembly systems.[101] In 1999, they reported the preparation of photoswitchable self-assemblies of azobenzene derivative **68**, which contains two tethered cyclic octapeptides (Figure 1.15). When the azo group of **68** takes the *trans* configuration, the molecule shows a linear shape. In the solution phase, the molecules of *trans*-**68** form linear long-range assemblies through intermolecular hydrogen-bonding interactions between the cyclic octapeptides. Upon UV irradiation, the *trans*-azo group can be switched into the *cis* isomer. As a result, the molecule takes a non-linear shape that favors intramolecular hydrogen-bonding interactions. The long-range self-assembly falls apart and each molecule of **68** forms a closed structure, in which the two cyclic octapeptide units are engaged through intramolecular hydrogen bonds. Actually, the intramolecular hydrogen-bonding interactions are so significant that the closed *cis*-isomer is resistant to photoinduced *cis*-to-*trans* isomerization.

1.3.2 π-Extended Derivatives as Fullerene Receptors

C_{60} fullerenes, a cage-like allotrope of carbon, was first reported by Robert Curl, Richard Smalley, and Harold Kroto as one of the most remarkable discoveries in chemistry in 1985. It was followed by discovery of other types of fullerenes such as fullerenes with 70, 72, 76, 84 and even up to 100 carbon atoms in the following

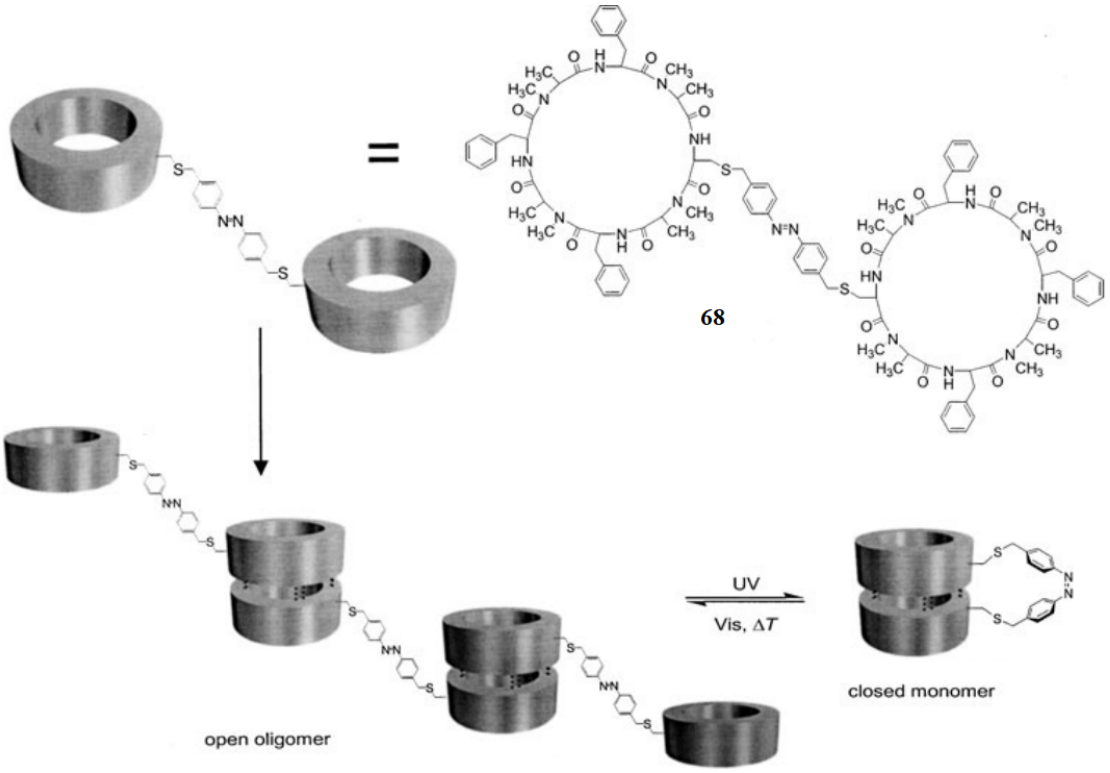

Figure 1.15: Photoswitchable self-assemblies of azobenzene-cyclic octapeptides **68** (Copyright 1999 Wiley. Used with permission)[101].

years.[102,103] C_{60} fullerene resembles the shape of a soccer ball and contains 12 pentagons and 20 hexagons in its structure. C_{70} fullerene, on the other hand, has the shape of a rugby ball, consisting of 25 hexagons and 12 pentagons in its structure. The C–C bond angles of these buckyballs show a considerable strain due to deviation from an ideal sp^2-hybridized bond angle (120°). Therefore, relief of this strain is a key driving force for their reactivity.

It is worth mentioning that both C_{60} and C_{70} fullerenes are very good electron acceptors, owning to a triply degenerated LUMO (t_{1u}) which is low-lying in energy.[104] Besides covalent functionalization,[105,106] owning to their electronic properties and geometrical features, fullerenes could act as appealing supramolecular partners for

PAHs. This could happen through their electron donating properties and shape and size complementary relationship with PAHs through non-covalent interactions. In terms of the types of the fullerene molecular receptors in host-guest assemblies reported to date, they can be generally categorized as macrocyclic scaffolds,[107–109] receptors with flat-convex surfaces including porphyrins,[110] concave receptors such as corannulene-based receptors,[111,112] carbon nanorings,[111,113] and concave π-extended tetrathiafulvalene derivatives.[114–116] Each type of receptor shows advantages and limitations. Their application and importance in advanced sensing, electronic, and optoelectronic devices have been continuously developed. In addition to the formation of supramolecular assemblies, some studies successfully measured and reported the association constants of fullerene-receptor assemblies through absorption, fluorescence, and NMR titration analyses. These association constants provided quantitative assessment of binding interactions as well as the performance of some receptors for chemical sensing of fullerenes.[115,117–119]

In 2013, Mulla et al. reported the design and synthesis of a series of tweezer-like and macrocyclic tetrathiafulvalene vinylogues (TTFVs) through a click reaction (Figure 1.16).[115] Among these derivatives, tweezer **69b**–**c** and macrocycle **70b**, consisting of anthracene and pyrene units, showed significant fluorescence enhancement in response to the interactions with C_{70}. For C_{60} fullerene, however, they showed little fluorescence response. Control over the binding and release of fullerene was achieved through titration of a solution of **70b** with trifluoroacetic acid (TFA). This was ascribed to a mechanism, where the TTFV units undergo protonation/deprotonation to give drastic conformational changes. Upon increasing the amount of TFA, UV-vis spectroscopic analysis confirmed the release of C_{60} from

its host **70b**. This experiment supported the reversible complexation process.

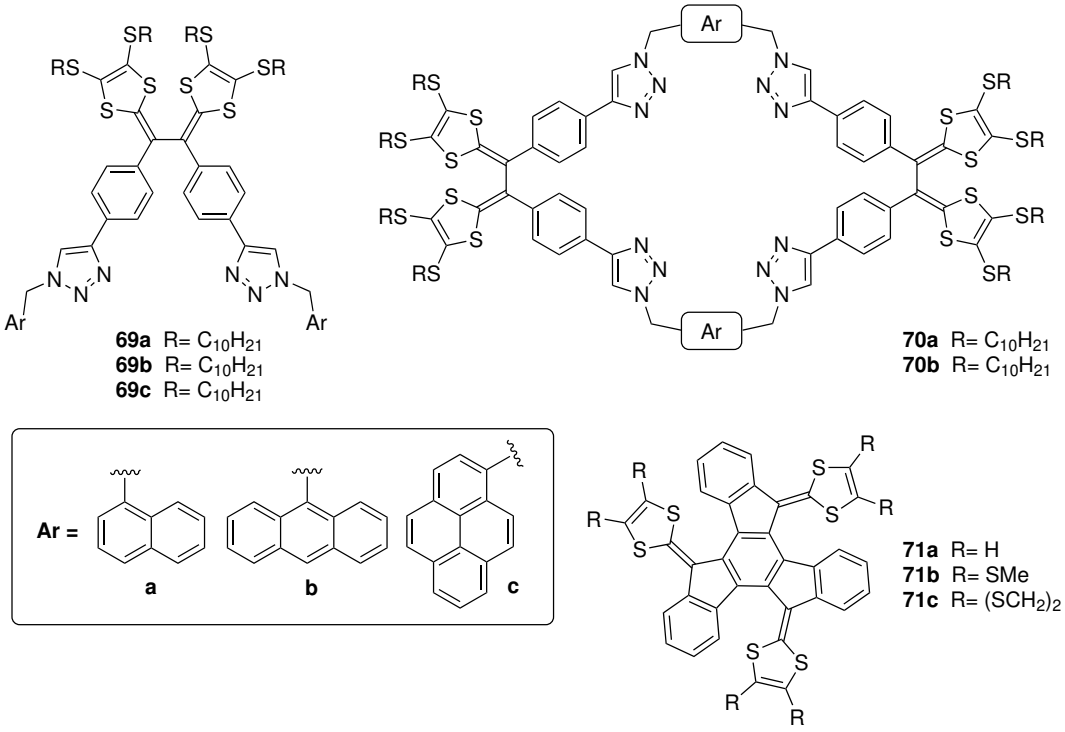

Figure 1.16: TTFV-based tweezers, macrocycles, and truxene-TTFs.

In 2007, Martin and co-workers studied the binding between the concave extended π-surface of truxene-TTFs (**71a**–**c**, Figure 1.16) with C_{60} and C_{70} fullerenes.[118] In the ^{1}H NMR titrations of a solution of **71a** with C_{60} and C_{70}, respectively, they observed the shielding of aromatic protons and slight deshielding of the dithiole signals. With the titration data, a 1:1 binding isotherm was established and with binding due to charge transfer interactions. It was also disclosed that the aromatic face of truxene-TTFs is the main site of interaction, while binding constants of $(1.2 \pm 0.3) \times 10^3$ M^{-1} and $(0.8 \pm 1.5) \times 10^3$ M^{-1} were reported for C_{60} and C_{70}, respectively.

Besides many examples in this field,[117,119,120] the studies representing the supramolecular interactions of fullerenes and host molecules through X-ray

crystallographic analysis are worth mentioning. In 2020, Gao et al. reported the synthesis of a buckybowl and succeeded to grow the co-crystal of C_{70} and this buckybowl.[121] Solution-phase UV-vis analysis was not helpful to confirm the host-guest interactions; however, ^{1}H NMR analysis offered evidence for the occurrence of buckybowl–C_{70} binding, and the binding stoichiometry was determined to be 1:1 and 2:1. The first and second binding constants (K_a) of buckybowl with C_{70} in toluene-d_8 at 298 K were estimated to be 1575 $\pm$ 17 M^{-1} and 1463 $\pm$ 51 M^{-1}, respectively. To gain insight into the complexation mechanism, a co-crystal was grown by slow evaporation of *n*-butyl acetate solution. This analysis reveals a 2:1 ratio for the binding of buckybowl and C_{70}. The buckybowl molecules acted as hosts to encapsulate C_{70} through their electron donor character with several concave-convex interactions. As can be seen in Figure 1.17, they formed two-dimensional sheets with the C_{70} arranged linearly, which exhibited ambipolar transport features with electron and hole mobilities up to 0.40 and 0.07 $cm^2V^{-1}s^{-1}$. This study for the first time showed the application of functionalized C_{70} fragment.

1.4 Imidazole-Based π-Conjugated Materials

Compared to other heterocycles, imidazoles are small five-membered heterocycles that contain two distinct nitrogen atoms. The N1 and N3 resemble the electron-rich pyrrole nitrogen and electron-deficient pyridine properties, respectively. Moreover, an imidazole ring consists of six π electrons, which according to the Hückel's rule give aromatic character.[122,123] It can undergo tautomerization, in which the acidic proton can be rapidly exchanged between two nitrogens, as well as bearing both

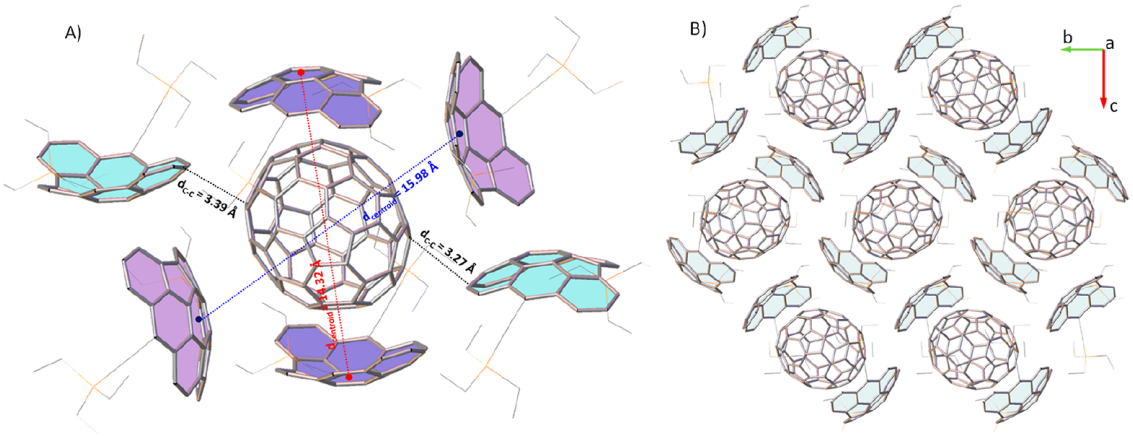

Figure 1.17: (A) Selected intermolecular distances in buckybowl–C_{70} co-crystals and (B) crystal packing of the complex (Copyright 2020 American Chemical Society. Reproduced with permission)[121].

acidic and basic sites and showing amphoteric character. Owning to its unique electronic and biological features, imidazoles have attracted attention in different fields including OLEDs, light-emitting electrochemical cells, optical sensors,[124–126] as well as medicinal chemistry as anti-aging agents, anti-coagulants, anti-inflammatory, anti-bacterial, anti-fungal, and so forth.[127–129] To further modify the properties of imidazoles, such as rigidity, planarity, thermal, and photophysical properties, various aromatic systems could be fused to C4 and C5. Figure 1.18 represents a few examples of basic imidazole derivatives including (1*H*-benzo[*d*]imidazole (BI), 3*H*-naphtho[1,2-*d*]imidazole (NI-1), 1*H*-naphtho[1,2-*d*]imidazole (NI-2), 1*H*-phenanthro[9,10-*d*]imidazole (PI), and 9*H*-pyreno[4,5-*d*]imidazole (PyI)). Tailoring the HOMO and LUMO energy levels and gaps for application in different fields is highly important, which could be achieved successfully by altering the aromatic motifs (Figure 1.18).[122]

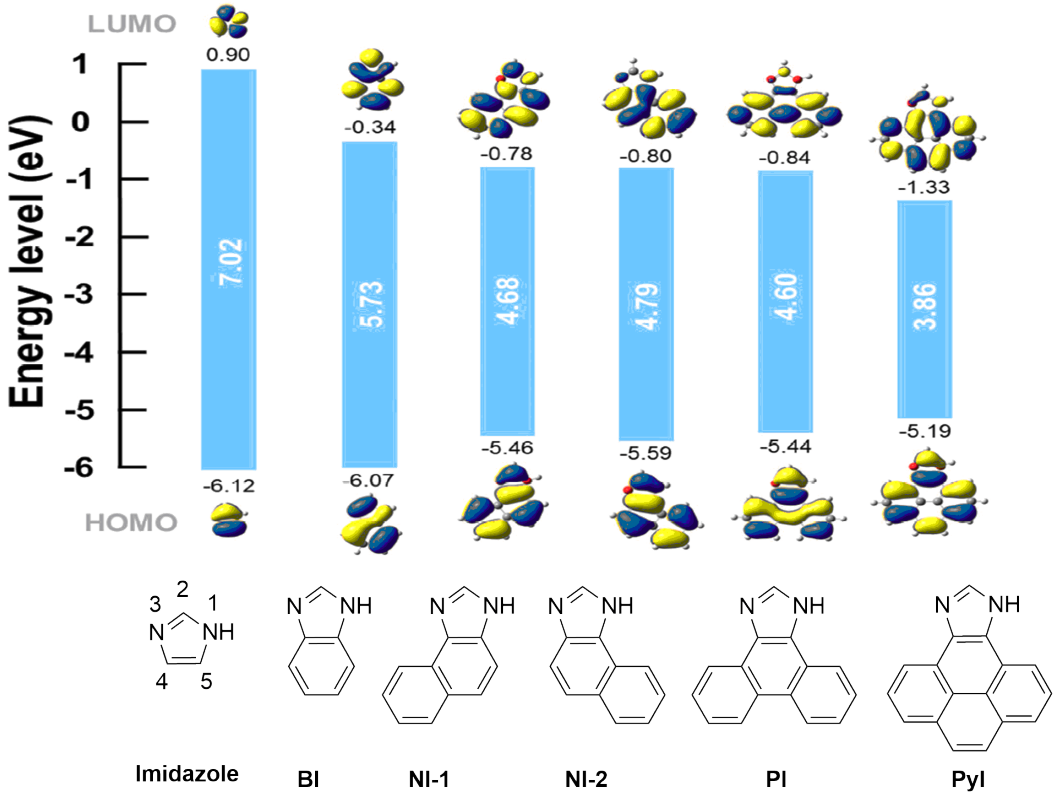

Figure 1.18: Representative examples of imidazole derivatives and electronic distributions (Copyright 2018 Wiley. Used with permission)[122].

1.4.1 General Synthetic Methods

Imidazoles were first introduced by Debus from a condensation reaction between glyoxal and ammonia in 1858 as shown in Figure 1.19A. Later in 1882, Radiszewski reported another approach of condensing 1,2-dicarbonyls such as glyoxal, α-keto aldehyde or α-diketones with an aldehyde in the presence of ammonia (Figure 1.19B). Following this method, Knapp and co-workers reported the use of a milder reagent, barium manganate, to convert imidazolines to imidazole, which was known as dehydrogenation of imidazole (Figure 1.19C). Other methods worth mentioning include Wallach synthesis (Figure 1.19D), from α-halo ketones (Figure 1.19E),

Marckwald synthesis (Figure 1.19F), and from aminonitrile and aldehyde (Figure 1.19G).[130]

The most commonly used strategy to generate imidazole is through the Debus-Radziszewski reaction (Figure 1.20). Known for almost one century, this method is still widely used today. The reaction occurs through a multi-component condensation mechanism involving a dicarbonyl, an aldehyde, and ammonia. When a 1,2-diketone undergoes the Debus-Radziszewski reaction, a 2,4,5-trisubstituted imidazole core is formed. Such reaction needs to be run at relatively high temperature. Moreover, altering the reaction conditions by use of AcOH, EtOH, thermal or microwave heating, or in the presence of various acidic catalysts, can result in better yields and easier purification of products.[131,132]

1.4.2 Phenanthroimidazole (PI) and Recent Progress in PI Based Materials

Amongst various imidazole derivatives, PIs have attracted enormous attention, due to their rigidity and conjugated aromatic structures which afford considerable thermal stability, bipolar transporting properties, prolonged fluorescence lifetimes, and high quantum yields.[133] In the structure of PI, the phenanthrene unit acts as an electron donor and the imidazole moiety acts as an electron acceptor, providing intramolecular charge transfer (ICT) properties. The above-mentioned properties make PIs show appealing application in many fields, such as electroluminescence, chemical sensing, bioimaging, and medicinal chemistry.[124,133,134] Tian et al. in 2013, reported the synthesis of 23 multi-aryl imidazole motifs and investigated their

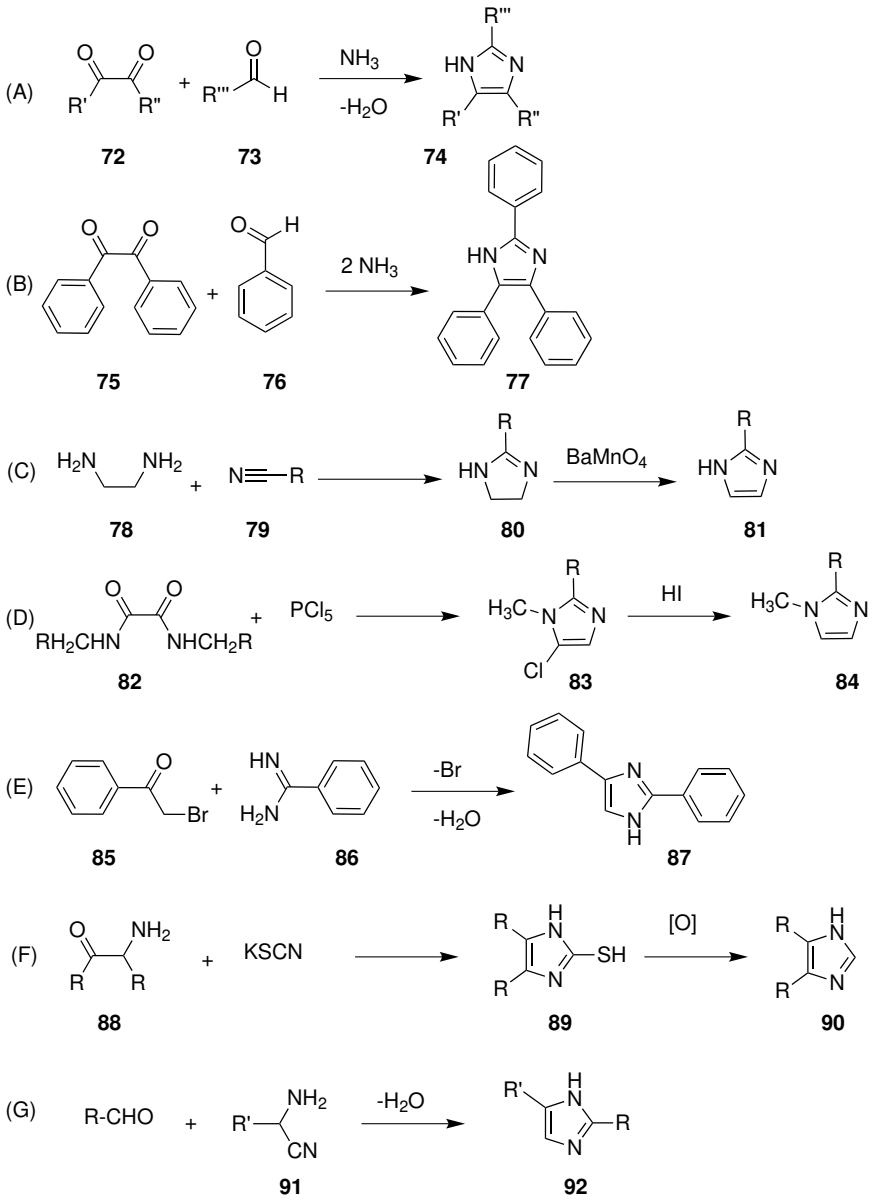

Figure 1.19: General synthetic approaches for imidazole derivatives.

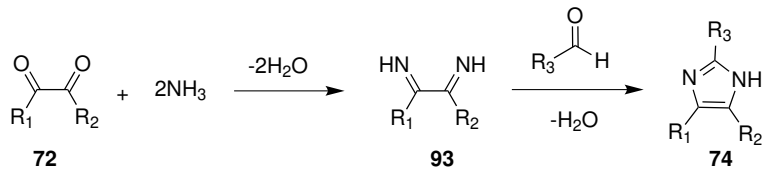

Figure 1.20: General scheme of the Debus-Radziszewski synthesis.

structure–fluorescence property relationships. This study assessed the influence of the imidazole group, the electron withdrawing substituent, and the increase in the planarity through C–C bond formation between adjacent phenyl rings. It was observed that the fluorescence quantum yields of **96**–**98** (Figure 1.21) with two imidazole groups and the ones bearing strong electron withdrawing groups CHO and NO_2 (**94d**–**e** and **95d**–**e**) almost doubled. Moreover, PI derivatives **95**–**97** exhibit high fluorescence quantum yields above 0.8, which is the result of higher planarity, rigidity, and better π-conjugation.

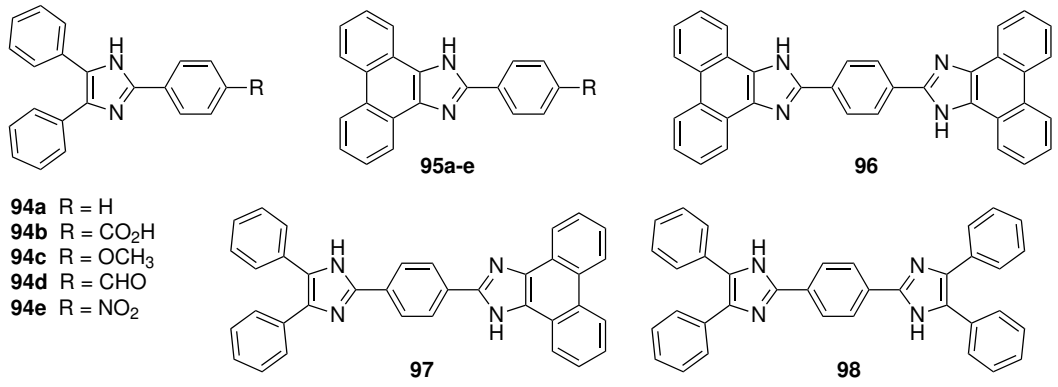

Figure 1.21: Selected examples of various imidazole motifs.

In another study, Wang et al. reported the design and synthesis of a series of PIs (Figure 1.22), which feature linear and branched PI structures, 1,2-diphenyl-phenanthro[9,10-*d*]imidazole (**PPI**), 4,4'-bis-(1-phenyl-phenanthro[9,10-*d*]imidazol-2-

yl)biphenyl (**BPPI**) and 4,4',4"-tris(1-phenyl-phenanthro[9,10-*d*]imidazol-2-yl)-1,3,5-triphenylbenzene (**TPPI**).[135] **BPPI** showed significant thermal stability, excellent fluorescence quantum yield (Figure 1.22), blue fluorescence emission, and balanced carrier injection. To evaluate the electroluminescence (EL) properties of these PIs, a double-layered and a multi-layered device were fabricated. The former device based on **BPPI** exhibited a higher maximum emission (468 nm) and a lower turn-on voltage (2.8 V) than the latter one with an independent electron injection layer, suggesting that the PI unit is an efficient building block to tune both the carrier injection features and blue emission.

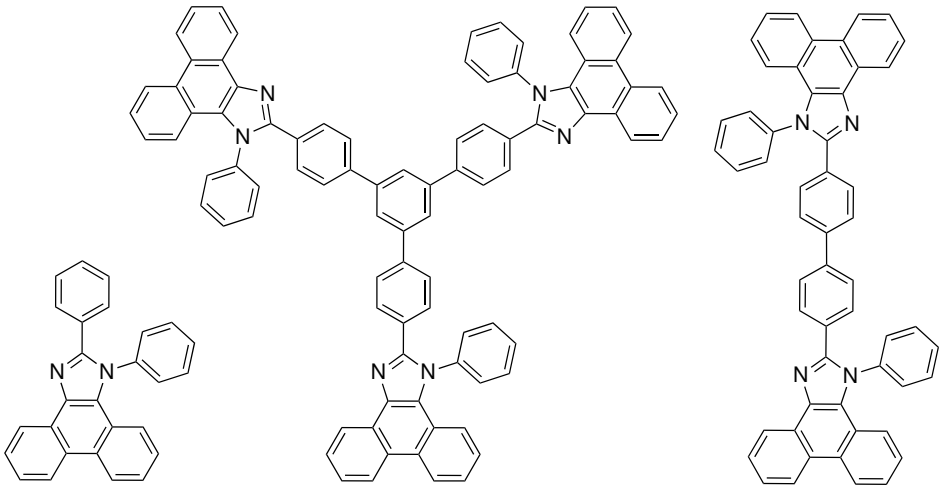

Figure 1.22: Structure and fluorescence quantum yields of **PPI**, **BPPI**, and **TPPI** motifs.

Although calix[4]arenes have been widely used for selective binding to cations, anions, and neutral molecules, their relatively small cavity resulted in limited binding features. Extended calixarenes, with enlarged cavity size and flexibility, afford

sizable holes but poor pre-organization of the guest molecules and collapse.[136] In this regard, Botana et al. reported the synthesis of compound **102** from the reaction of tetra-*p*-formyltetra-*O*-propylcalix[4]arene with phenanthrenequinone in the presence of NH_4OAc.[137] The resulting calixarene afforded an expanded cavity, stabilized by hydrogen-bonded bridges and/or ion pairing, which prevented collapse into fully stacked pinched cone conformations as expected. According to X-ray analysis (Figure 1.23), the phenanthroimidazole units are protonated and bridged through hydrogen binding with TFA and methanol molecules to stabilize the cavity, making it suitable for encapsulation of sizable guests.

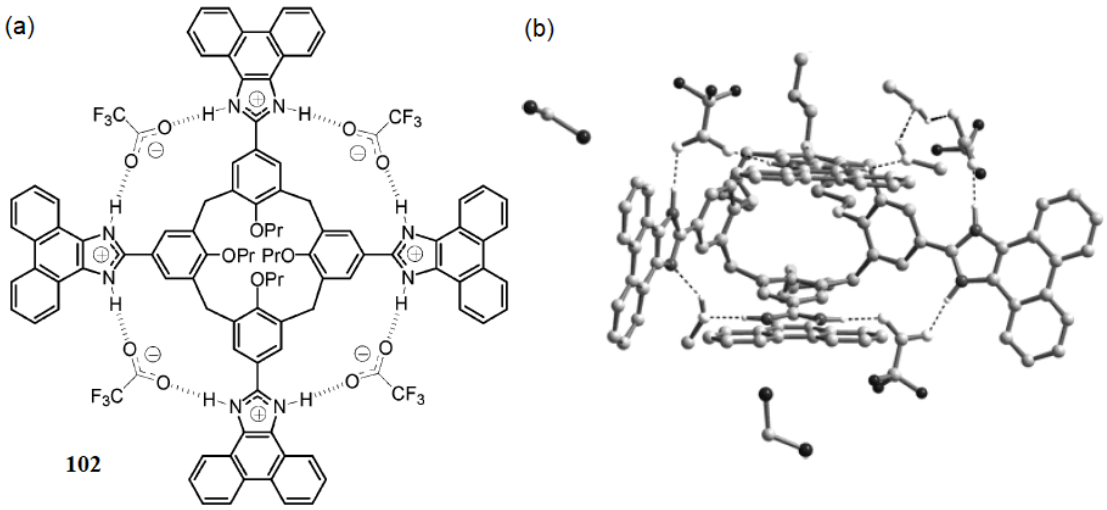

Figure 1.23: (A) Chemical structure and (B) X-ray structure of **PI** based calixarene **102** (Copyright 2003 American Chemical Society. Reproduced with permission)[137].

1.5 Outline of This Thesis

This PhD thesis has accomplished five major projects, which are mainly focused on the synthesis and characterization of functionalized π-conjugated oligomers, PAHs, DTF- and imidazole-based molecular materials. Suzuki-Miyaura cross-coupling, olefination, oxidative coupling, condensation, and photocyclization reactions have been utilized in the synthetic work. Furthermore, instrumental analytical techniques such as NMR, mass spectrometry, IR, UV-Vis absorption spectroscopy, fluorescence, X-ray single crystallography, and cyclic voltammetry (CV) have been performed to characterize the newly developed structures. The detailed research results are outlined in Chapters 2 to 5.

In Chapter 2, the synthesis and molecular properties of various diphenyl-dibenzofulvene (DP-DBF) derivatives are reported. The synthetic strategies involve Ramirez dibromoolefination and Suzuki-Miyaura cross-coupling as the key steps. The photophysical properties of theses derivatives in both liquid and solid state were investigated by UV-Vis absorption and fluorescence spectroscopic analyses. Moreover, the crystal structures of the developed DP-DBFs have been analyzed via X-ray single crystallography. According to this structure–property study, the crystallization-induced emission enhancement (CIEE) was found to show a clear correlation with the twist angle around the C=C bond of the DP-DBF structure and their solid-state fluorescence quantum yield increased as the twist angle decreased. Amongst these derivatives, although *para*-substituted DP-DBFs showed a significant CIEE feature, they did not follow the linear correlation. The results of this project point out an effective molecular approach to design various related AIE and CIEE luminogens and

tune their solid state fluorescence properties.

Chapter 3 describes the synthesis and characterization of saddle-shaped donor–acceptor-substituted TTFAQ-AQs, containing an anthraquinodimethane extended tetrathiafulvalene (TTFAQ) and an anthraquinone (AQ) unit. The target TTFAQ-AQs have been synthesized through regioselective Ramirez gem-dibromoolefination and double *S*-vinylation reactions. The structural and electronic properties were investigated via UV–vis absorption, cyclic voltammetric, and X-ray single crystallography analyses. TTFAQ-AQs show noticeable intramolecular charge-transfer feature, resulting in amphoteric redox behavior and narrow electronic energy band gaps. In addition, the supramolecular interactions of TTFAQ-AQs with C_{60} and C_{70} fullerenes were examined in both solution and solid phases as well as theoretically through density functional theory (DFT) calculations. Based on X-ray analyses and computational modeling studies, the deep cavity of a benzo-TTFAQ-AQ derivative was found to show stronger interaction energies and better shape complementarity with C_{70} rather than C_{60}, enhancing the selectivity toward C_{70} fullerene. As the first example of ordered supramolecular assemblies constructed by fullerene and a redox-active donor-acceptor partner, this study paves the way to approach more fullerene-based crystalline materials with redox activity and charge-transfer properties.

Chapter 4 deals with the synthesis and investigation of donor-acceptor phenanthroimidazole (PI)-based fluorophores and macrocycles. The synthesis of the fluorophores have been approached through condensation, Suzuki-Miyaura cross-coupling, and phosphite-promoted olefination reactions. The structural, photophysical ,and redox properties were evaluated using X-ray diffraction, UV-Vis absorption, fluorescence spectroscopy, and cyclic voltammetric analyses. In

addition the effect of donor and acceptor functional groups on properties of the PI derivatives were thoroughly investigated. The DTF-functionalized PI was confirmed to be responsive to singlet oxygen through singlet oxygen induced oxidative cleavage of DTF C=C bond, examined through time dependent ^{1}H NMR analyses as well as fluorescence spectroscopy. Moreover, TTFV-PI macrocycle was found to result in interesting fluorescence turn-on/off behaviour in response to titration with C_{60} and C_{70} fullerenes. This supramolecular interaction has been discussed based on the photoinduced electron transfer between the electron donor TTFV moiety to the electron deficient fullerenes leading to turn on emission followed by the interaction between fullerene and central PI which resulted in a fluorescence quenching effect. Based on the findings of this study, developing advanced singlet-oxygen biosensors and optical sensors is promising for future work.

Chapter 5 represents the synthesis and detailed characterization of bis(diarylmethylene)dihydroanthracenes, referred to as Ar_4-DHAs. The synthetic approaches involved Ramirez dibromoolefination and Suzuki-Miyaura cross-coupling as the main steps to reach three different methoxy-substituted derivatives of Ar_4-DHAs, which then underwent photocyclization or photocyclization/Scholl reaction to afford cyclized products. A demethylation reaction followed by an etherification reaction were also performed to form tethered model compound. X-ray single crystallography, UV-Vis, and fluorescence spectroscopic analyses have been utilized to reveal the structural and photophysical properties of these materials. DFT calculations have also been conducted to provide theoretical insights. It is noteworthy that the cyclized products are considerably more fluorescent compared to their precursors, which is the result of enhanced π-conjugation and a better electron delocalization.

Moreover, the photoclization only occurs in a manner of two-fold Mallory reaction with specific regioselectivity. The observed regioselectivity is consistent with the LUMO distribution on the intermediate species. Overall, this study has not only gathered valuable experimental results for the photocyclization reactions occurring on various Ar_4-DHA systems, but provided insightful theoretical explanations for the detailed reactivity and selectivity of each photocyclization step involved.

Chapter 2

Molecular Tuning of the Crystallization-Induced Emission Enhancement of Diphenyl-Dibenzofulvene Luminogens

The contents of this chapter were published as a communication paper in *Chem. Commun.*, **2021**, *57*, 484. Contributions of authors are described below: Maryam F. Abdollahi is the first author, who conducted the synthesis of all the diphenyl-dibenzofulvene compounds, growth of all the single crystals, and relevant spectroscopic characterizations. She also contributed to the manuscript preparation and editing.

Mr. Jian You and Prof. Tao Wang are collaborators of this project (Beijing University of Chemical Technology), who performed the solid-state photophysical analyses including fluorescence emission spectral, lifetime, and quantum yield characterizations.

Prof. Yuming Zhao is the supervisor of M. F. Abdollahi, who helped develop the concepts and design of this project. Prof. Zhao is the corresponding author of this paper.

Note that compound numbering in this chapter differs from Chapter 1. In this chapter, the compounds are numbered in the same way as those in the publication.

2.1 Introduction

Organic luminogens that show aggregation-induced emission (AIE) and crystallization-induced emission enhancement (CIEE) properties[22,27,138] have received considerable attention in recent years, owing to their appealing applications in fluorescent chemical sensors,[139] biological probes,[140–142] organic field-effect transistors (OFETs),[143] and organic light emitting devices (OLEDs).[144,145] Such luminogens are generally non-emissive in dilute solution, but exhibit moderate-to-high degrees of fluorescence in their aggregated states such as amorphous solid or crystalline forms. Many reported AIE and CIEE luminogens are designed to contain structurally hindered π-conjugated backbones, so that upon aggregation their fluorescence can be enhanced due to restricted intramolecular motions (RIM).[28,146,147] Diphenyl-dibenzofulvene (**DP-DBF**) derivatives constitute an intriguing class of AIE and CIEE luminogens, featuring relatively simple molecular structures and easy synthesis. Since the first study by

Tang and co-workers in 2006,[32] numerous **DP-DBF**-based luminogens have been reported in the literature, some of which show very interesting polymorphism-dependent emission, strong CIEE effects, and thermochromic and mechanochromic fluorescence properties.[22,30,33,148–150]

It is noteworthy that the emission efficiencies of various literature reported **DP-DBFs** show a substantial degree of variations (see the summary in Figure 2.1). By analyzing these data, one would reasonably expect to find some correlations between the fluorescence properties of **DP-DBFs** with their molecular parameters (e.g., molecular geometry and substitution effects).

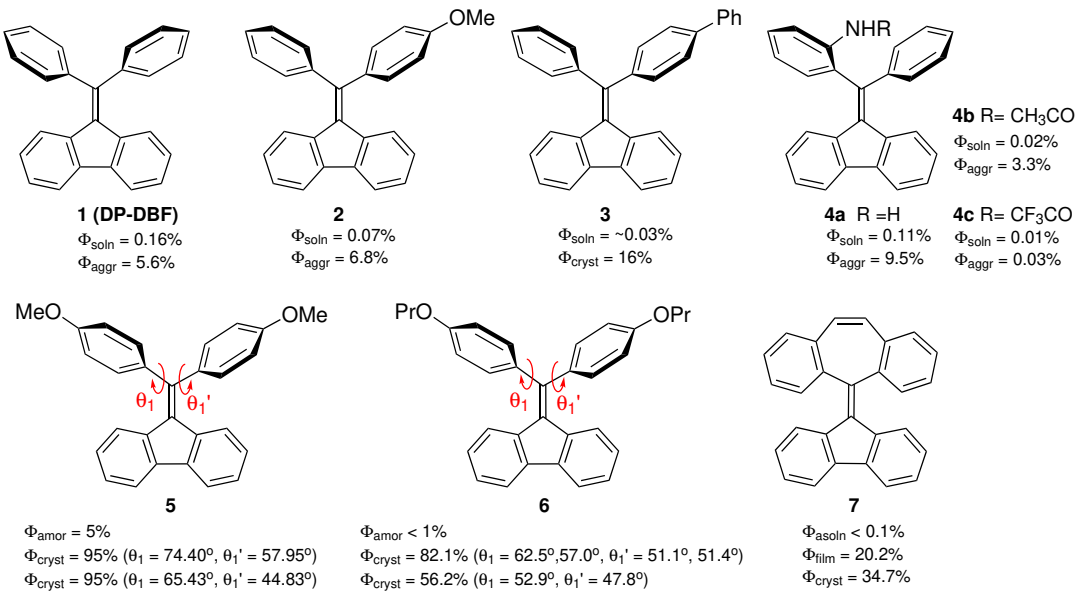

Figure 2.1: Literature reported **DP-DBF** derivatives and their fluorescence quantum yields (Φ_f) in the solution phase (soln), aggregated (aggr), amorphous solid (amor), thin film (film), and crystalline (cryst) states.

Previously, Tang[148,149] and Zhang[30] attributed the fluorescence enhancement and emission wavelength shifts of **DP-DBF** luminogens **5** and **6** in the aggregated and

crystalline states to the twist angle (θ_1) between the phenyl and vinyl units in the structure of **DP-DBF**. However, such rationalization was not strongly supported by theoretical analysis and experimental evidence. Shuai and co-workers in 2012 performed a molecular dynamics study to show that both the bond stretching in the **DBF** unit and the twisting around the C=C bond play essential roles in the electronic non-adiabatic transition of **DP-DBF**.[151] Recently, it has been reported that restriction of the twisting around the C=C bond plays a crucial role in the AIE of various π-conjugated systems.[152] In 2013, Li and Blancafort developed a conical intersection (CI) model to explain the AIE properties of **DP-DBF**.[153] According to their model, the first excited state (S_1) of **DP-DBF** can be deactivated to the ground state (S_0) through an S_1/S_0 CI seam. As illustrated in Figure 2.2, **DP-DBF** in the solution phase can readily reach an energetically accessible region of the CI seam, where molecular geometries show a high twist angle ($\theta_2 > 50°$) about the C=C bond of **DP-DBF**. This non-radiative decay pathway quenches the fluorescence of **DP-DBF** in the solution phase. In the solid state, however, the twist around the C=C bond is restricted and there is only a high-energy region of CI seam existing on the potential energy surface (PES), which in turn results in enhanced solid-state fluorescence. This modelling study thus motivated us to propose that the twist angle about the C=C bond of **DP-DBF** (θ_2) in the minimum energy structure of the ground state is a key factor controlling its fluorescence behavior, especially the fluorescence quantum yield in the aggregated state. Upon aggregation, restricted intramolecular motion should significantly influence the internal conversion of the first excited state (S_1) to the CI seam on the PES. If θ_2 is relatively large, the amount of energy required for the S_1 state to reach the CI seam should be small and the fluorescence is thus

well quenched. If θ_2 is small, the non-radiative decay pathway through the CI seam becomes difficult to access.

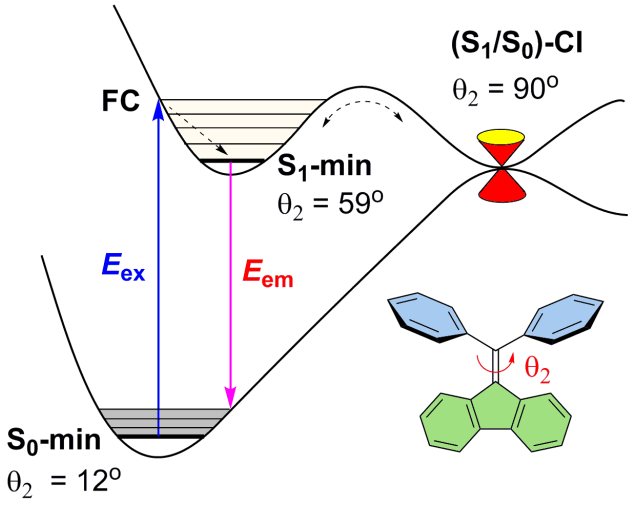

Figure 2.2: Potential energy surfaces of **DP-DBF** in the solution phase with a conical intersection (CI) seam.

Validation of the above hypothesis requires systematic examination of **DP-DBFs** with varied θ_2 values. To do so, we chose the approach of attaching functional groups to different positions of the two phenyl rings in **DP-DBF** to finely tune the twist angle θ_2 by steric effects. A series of **DP-DBFs** derivatives functionalized with methoxy (OMe) or benzyloxy (OBn) substituents was thus designed and prepared in this work. Scheme 2.1 outlines our synthetic methods. Additionally, compound **9** was prepared as a special **DP-DBF** model where the rotations of the phenyl groups are completely restricted.

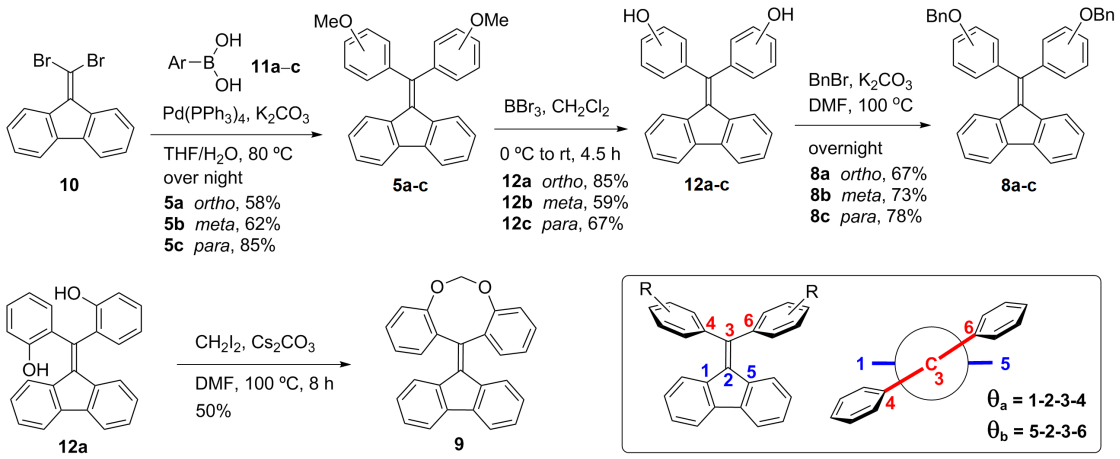

Scheme 2.1: Synthesis of substituted **DP-DBFs 5a–c**, **8a–c**, and **9**. Inset: Definition of dihedral angles θ_a and θ_b in the structure of **DP-DBF**.

2.2 Results and discussion

With these substituted **DP-DBFs** in hand as models, we then carried out comparative analyses focusing on their structural, electronic, and fluorescence properties. Figure 2.3 shows the electronic absorption spectra of **DP-DBFs 5a–c**, **8a–c**, and **9** measured in the solution phase. *ortho*-OMe substituted **5a** gives three distinct $\pi \rightarrow \pi^*$ absorption peaks at 316, 302, and 282 nm. In addition, there is a broad absorption shoulder ranging from ca. 330 to 420 nm. Comparatively, the spectrum of *ortho*-tethered **9** shows $\pi \rightarrow \pi^*$ absorption peaks at similar wavelengths; however, its long-wavelength shoulder band at 329 nm appears to be much steeper and narrower. The different spectral patterns can be attributed to the different rotational modes between **5a** and **9**; the phenyl groups of **5a** can rotate to form various conformers in the solution phase, but the tethered phenyl rings of **9** are inhibited from such rotational modes. The spectrum of *meta*-OMe substituted **5b** shows two absorption peaks at 320 and 287 nm, along with a very broad absorption shoulder in

the region of 330 to 440 nm. The edge of the long-wavelength absorption shoulder of **5b** is significantly red-shifted relative to that of **5a**, suggesting a higher degree of π-conjugation in **5b**. For the spectrum of *para*-OMe substituted **5c**, a broad absorption band at 369 nm can be seen and its absorption edge is the most red-shifted among the **DP-DBFs**. The spectra of OBn-substituted **DP-DBFs** show similar features to those of their OMe-substituted analogues, indicating little contribution of the benzyl groups to the electronic absorption features. To determine the $S_0 \rightarrow S_1$ vertical transition energies for the **DP-DBFs**, the half-height wavelength of the lowest-energy maximum absorption band ($\lambda_{1/2}^{abs}$) in each absorption spectrum was considered. The experimental values show good agreement with time-dependent density functional theory (TD-DFT) calculated $S_0 \rightarrow S_1$ energies (see Table S2, Appendix I). For both groups of OMe and OBn-substituted **DP-DBFs**, a red-shift trend in $\lambda_{1/2}^{abs}$ *can* be clearly observed as: *ortho* < *meta* < *para*. It is worth mentioning that the solid-state UV-Vis absorption spectra of the **DP-DBFs** were also measured, showing very small variations in comparison with the solution-phase spectra (see Fig. S23, Appendix I).

The single crystals of **DP-DBFs 5a**–**c**, **8a**–**c**, and **9** were grown and their molecular structures were elucidated by single crystal X-ray diffraction (XRD) analysis (Figure 2.4). In the crystal structure of *ortho*-OMe substituted **5a**, the two OMe groups take two different orientations (*cis* and *trans*) with respect to the fluorene plane. These two conformations exist in a ratio of ca. 1 : 1, and they show similarly large twist angles around the C=C bond. In contrast to **5a**, the crystal structure of *ortho*-OBn-substituted **8a** only shows the *trans* conformation with a small twist angle around the C=C bond. Both *meta*-substituted **5b** and **8b** adopt a *trans* conformation in terms of the relative orientation of the OMe or OBn substituents, while the benzyl

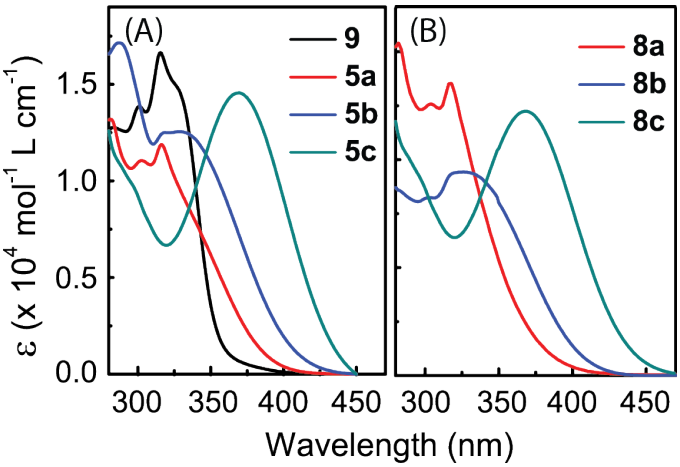

Figure 2.3: UV-Vis absorption spectra of (A) **5a**–**c** and **9**, and (B) **8a**–**c** measured in chloroform.

groups in the structure of **8b** show a certain degree of rotational disorder. It is also worth mentioning that there was another crystalline form of **5b** obtained during the crystallization process. Such crystals were formed in a relatively small quantity, and the molecular structure adopts a *cis* conformation (see Fig. S25A, Appendix I). Two distinct crystal structures of *para*-OMe-substituted **5c** were previously reported by Zhang and co-workers.[150] One is colorless with blue emission, and the other is yellow in color with green emission. In our experiment, we obtained the single crystal of **5c** that is similar to the first type of the crystal reported in Zhang's study, colorless with blue emission. The molecular structure of *para*-OBn-substituted **8c** shows a similar **DP-DBF** conformation to that of **5c**, but the twist angle about the C=C bond appears to be smaller. In the crystal structure of **9**, the two oxygen groups are in a *cis* conformation and the C=C bond shows a moderate degree of twisting. Overall, the twist angles around the C=C bonds in the crystal structures of **5a**–**c**, **8a**–**c**, and **9** show a wide range of variation as expected. To quantitatively assess the

degree of twisting, the sum of two dihedral angles (θ_a and θ_b, see the inset of Scheme 2.1 for definition) about the C=C bond were measured and compiled in Table 2.1.

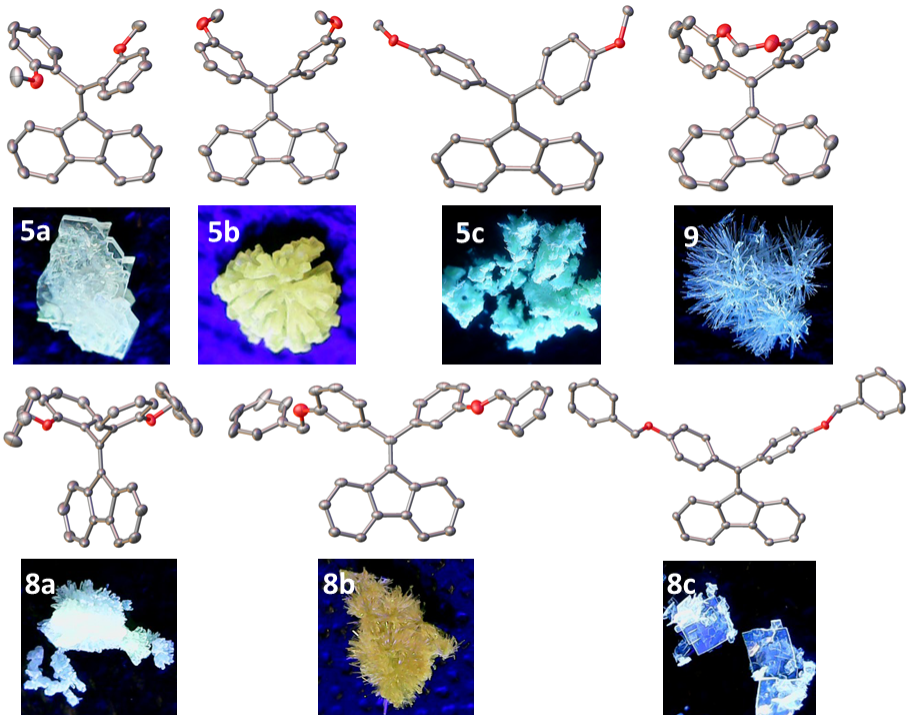

Figure 2.4: Selected molecular structures of **5a**–**c**, **8a**–**c**, and **9** determined from their single crystals, and photographic images of the crystals of these compounds under UV-light irradiation.

All the **DP-DBF** derivatives **5a**–**c**, **8a**–**c**, and **9** show insignificant fluorescence in the solution phase; however, their crystals exhibit luminescence with various intensities and colors under UV-light irradiation (see Figure 2.4). *para*-Substituted **DP-DBFs 5c** and **8c** give strong bright blue emission, while *ortho*-substituted **DP-DBFs 5a** and **8a** exhibit moderate blue emission in the crystalline state. *meta*-Substituted **DP-DBFs 5b** and **8b** afford moderate-to-weak luminescence in yellowish green color, which is very different from the other **DP-DBFs**. Solid-state fluorescence

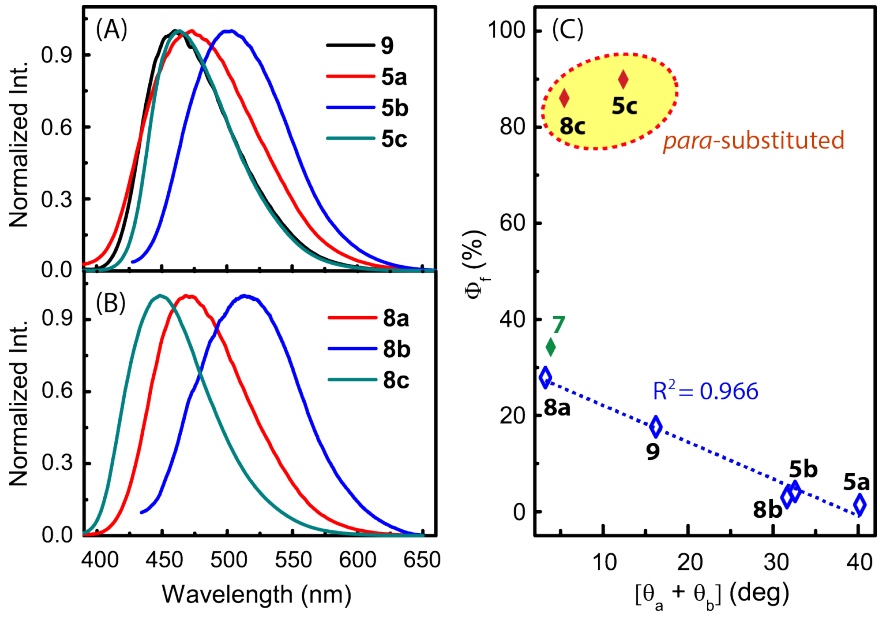

Figure 2.5: Fluorescence spectra of (A) **5a**–**c** and **9**, and (B) **8a**–**c** measured in the crystalline state. (C) Correlation between the twist angle ($[\theta_a + \theta_b]$) around the C=C bond of **DP-DBF** and fluorescence quantum yield (Φ_f) in the crystalline state.

spectra of the **DP-DBF** crystals were measured (Figure 2.5), and detailed emission properties are provided in Table 2.1. All the **DP-DBF** crystals give a relatively broad emission band without distinctive vibronic features. Both the OMe and OBn-substituted series show a trend of increasing maximum emission wavelength (λ_{em}) as follows: *para* < *ortho* < *meta*. The trend is different from the shift of λ_{abs} observed in the UV-Vis analysis. The much longer emission wavelengths of *meta*-substituted **5b** and **8b** relative to the other **DP-DBFs** are consistent with their yellowish green-colored luminescence in the solid state. Stokes shifts ($\Delta\nu$) were calculated according to the difference between λ_{abs} and λ_{em} in the solid state (see Table 2.1). It is noteworthy that the Stokes shifts of *para*-substituted **5c** and **8c** are considerably smaller than those of *ortho* and *meta*-substituted **DP-DBFs**, suggesting that para-

substituted DP-DBFs undergo a much smaller degree of structural variations during the $S_0 \rightarrow S_1$ excitation in the crystallin state.

Table 2.1: Summary of twist angles and photophysical properties for **DP-DBF** derivatives in the solid state.

entry	$[\theta_a + \theta_b]$ (°)	λ_{abs} (nm)	λ_{em} (nm)	Φ_f (%)	$\Delta\nu$ (cm^{-1})
5a	40.2	319	473	1.44	10206
5b	32.6	333	497	4.22	10306
5c	12.4	376	468	89.81	4904
8a	3.2	319	454	27.89	10117
8b	31.6	332	515	2.95	10665
8c	5.4	379	449	86.01	4113
9	16.2	319	457	17.63	9561

Figure 2.5C illustrates the correlations of the fluorescence quantum yields (Φ_f) of **DP-DBF** crystals with the degree of twisting about the C=C bond ($[\theta_a + \theta_b]$). In line with our hypothesis, the experimental results show clear correlations between the twisting of C=C bond and the fluorescence efficiency in the crystalline state. The Φ_f values of **DP-DBF** crystals show an increasing trend with decreasing twist angle about the C=C bond. In particular, *meta* and *ortho*-substituted **DP-DBFs** give an excellent linear relationship between Φ_f and $[\theta_a + \theta_b]$. This result supports the theory that restricted torsional vibration about the C=C bond is the origin of the AIE and CIEE properties of **DP-DBF**. Given that *ortho*-tethered **9** also clearly follows the same linear correlation, rotational modes of the phenyl groups can be ruled out as a significant factor to the fluorescence efficiency in the solid state. It is also remarkable

to note that the literature reported **DP-DBF7**, the structure of which contains an ethylene bridge linking the *ortho* positions of the two phenyl rings, also follows the same linear trend.[151] In contrast to *meta* and *ortho*-substituted **DP-DBFs**, *para*-substituted **5c** and **8c** do not follow the linear trend of fluorescence quantum yields. Actually, both compounds exhibit very high Φ_f values in the crystalline state, and these values are comparable with those of the *para*-substituted **DP-DBFs** reported in the literature.[30,150] Their high CIEE performances can be attributed to enhanced π-delocalization arising from *para*-alkoxy substitution. Finally, it is worth noting that **5a** and **9** are not CIEE luminogens, since their powders give greater Φ_f values than their crystals (see Table S1, Appendix I).

2.3 Conclusions

In conclusion, with the access to a range of substituted **DP-DBF** single crystals, we have unambiguously confirmed that the twist angle around the C=C bond is a key molecular factor controlling their solid-state fluorescence properties. For non-*para*-substituted **DP-DBFs**, their fluorescence quantum yields in the crystalline state can be predicted by a linear correlation with the twist angle. *Para*-Substituted **DP-DBFs**, on the other hand, show very strong CIEE performances but do not follow the linear correlation. Our structure–property studies not only provide in-depth understanding of the physical origin of the AIE and CIEE performances of **DP-DBFs**-based luminogens, but disclose an effective molecular approach to rationally design and finely tune the fluorescence properties of various related AIE and CIEE luminogens.

2.4 Experimental

2.4.1 Materials and Methods

Chemicals were purchased from commercial suppliers and used directly without purification. Evaporation and concentration were performed using a rotary evaporator. Flash column chromatography was carried out through 240-400 mesh silica gel and thin-layer chromatography (TLC) via silica gel F254 covered on plastic sheets, which was visualized under UV irradiation. Melting points (m.p.) were measured using an SRS OptiMelt melting point apparatus. ^{1}H and ^{13}C NMR spectra were measured on a Bruker Avance III 300 MHz multinuclear spectrometer. Chemical shifts (δ) are reported in ppm downfield relative to the signals of the internal reference $SiMe_4$ or residual solvent (CH_2Cl_2: δ_H = 5.32 ppm, δ_C = 54.0 ppm; $CHCl_3$: δ_H = 7.24 ppm, δ_C = 77.0 ppm; acetone–*d6*: δ_H = 2.05 ppm, δ_C = 29.9, 206.7 ppm). Coupling constants (J) are given in Hz. Infrared spectra (IR) were recorded on a Bruker Alfa spectrometer. High-resolution APPI-TOF MS analysis was performed using a GCT premier Micromass Technologies instrument. UV-Vis absorption spectra were analyzed through a Cary 6000i spectrophotometer. Solid-state fluorescence spectra of **5a-c**, **8a-c**, and **9** were recorded on the FLS980 series of fluorescence spectrometer (Edinburgh Instruments, EI) at room temperature. The samples were measured in both the crystalline and grounded powdery forms. Luminescence lifetimes of the crystals of **5a-c** and **9** were also measured with the FLS980 series of fluorescence spectrometer. The measured emission decays were fit to a multi-exponential function using the standard convolute-and-compare nonlinear least-squares procedure. Emission absolute quantum yields (Φ_F) in the solid state

were determined at room temperature.

Single-crystal X-ray diffraction (SCXRD) data was collected at 100(2) K on an XtaLAB Synergy-S, Dualflex, HyPix-6000HE diffractometer using Cu K_α radiation (λ = 1.5406 Å). The crystal was mounted on nylon CryoLoops with Paraton-N. The data collection and reduction were processed within CrysAlisPro (Rigaku OD, 2019). A multi-scan absorption correction was applied to the collected reflections. Using OLEX2,[154] structures were solved with the SHELXT structure solution program[155] using intrinsic phasing and refined with the SHELXL refinement package[156] using Least Squares minimization. All non-hydrogen atoms were refined anisotropically and the organic hydrogen atoms were generated geometrically.

Molecular geometries of **DP-DBFs 5a-c**, **8a-c**, and **9** were optimized at the M06-2X/Def2SVP level of theory using the Gaussian 16 software package.[157] The optimized geometries were subjected to TD-DFT calculations at the TD-B3LYP/6-311+G(d,p) level to compute the vertical electronic transition energies (only singlet-to-singlet transitions were considered, nstates = 20).

General procedure A

Synthesis of 5a–c

9-(Dibromomethylene)-9*H*-fluorene (10) was prepared according to the literature method. To a solution of 10 (2.00 g, 5.95 mmol) and an arylboronic acid (2.25 g, 14.9 mmol) in THF (40 mL) and deionized water (14 mL) was added K_2CO_3 (4.00 g, 29.8 mmol). The reaction mixture was bubbled with N_2 flow for 10 min, and $Pd(PPh_3)_4$ (0.270 g, 0.238 mmol) was added. Under N_2 protection, the mixture was

stirred and heated at 80 °C for 12 h. The formation of desired product was monitored by TLC analysis. After completion of the reaction, the mixture was cooled to rt and poured to a separatory funnel including water, and extracted with CH_2Cl_2 (3×20 mL) three times. The combined organic layers were dried over $MgSO_4$, filtered and concentrated under reduced pressure. The resulting residue was purified by silica gel column chromatography using CH_2Cl_2/hexanes as eluent.

9-(Bis(2-methoxyphenyl)methylene)-9*H*-fluorene (5a)

Compound **5a** was prepared according to the general Suzuki-Miyaura cross coupling procedure **A** and purified by silica gel column chromatography (CH_2Cl_2/hexanes, 40:60) as a colorless solid (1.35 g, 3.45 mmol, 58%). m.p.: 197.2-201.4 °C; IR (neat): 3051, 2923, 2852, 1621, 1578, 1500, 1444, 1179, 1117, 1024, 779, 750 cm^{-1}; ^1H NMR (300 MHz, $CDCl_3$): δ 7.68–7.65 (m, 2H), 7.53 (dd, J = 7.5, 1.8 Hz, 2H), 7.39-7.35 (m, 2H), 7.21 (td, J = 7.5, 1.2 Hz, 2H), 7.05-6.89 (m, 7H), 6.41 (d, J = 7.9 Hz, 2H), 3.72 (s, 6H) ppm; ^{13}C NMR (75 MHz, $CDCl_3$): δ 156.35, 140.38, 139.03, 138.66, 135.25, 131.06, 130.56, 128.98, 127.38, 126.70. 124.57, 121.08, 119.04, 111.53, 55.65 ppm; HRMS (APPI-TOF, positive mode): m/z calcd for $C_{44}H_{36}O_4$ $[M]^+$ 390.16198, found 390.16365.

9-(Bis(3-methoxyphenyl)methylene)-9*H*-fluorene (5b)

Compound **5b** was prepared according to the general Suzuki-Miyaura cross coupling procedure **A** and purified by silica gel column chromatography (CH_2Cl_2/hexanes, 35:65) as a yellow solid (1.45 g, 3.71 mmol, 62%). m.p.: 159-162 °C; IR (neat): 3047, 2963, 2834, 1585, 1483, 1289, 1193, 1126, 1083, 856, 777, 704 cm^{-1}; ^1H NMR (300

MHz, $CDCl_3$): δ 7.68 (d, J = 6.9 Hz, 2H), 7.3 (dd, J = 8.4, 7.5 Hz, 2H), 7.26–7.21 (m, 2H), 7.00-6.92 (m, 8H), 6.68 (d, J = 8.1 Hz, 2H), 3.77 (s, 6H) ppm; ^{13}C NMR (75 MHz, $CDCl_3$): δ 159.94, 144.90, 144.08, 140.50, 138.54, 134.12, 129.93, 127.70, 126.51, 125.11, 121.84, 119.20, 114.66, 113.97, 55.34 ppm; HRMS (APPI-TOF, positive mode): m/z calcd for $C_{28}H_{22}O_2$ $[M]^+$ 390.1619, found 390.1622.

9-(Bis(4-methoxyphenyl)methylene)-9*H*-fluorene (5c)

Compound **5c** was prepared according to the general Suzuki-Miyaura cross coupling procedure **A** and purified by silica gel column chromatography (CH_2Cl_2/hexanes, 35:65) as a yellow solid (1.97 g, 5.04 mmol, 85%). m.p.: 130-149 °C; IR (neat): 3048, 2997, 2834, 1600, 1503, 1455, 1274, 1170, 783, 750, 735, 694 cm^{-1}; ^{1}H NMR (300 MHz, $CDCl_3$): δ 7.71 (d, J = 7.5 Hz, 2H), 7.30–7.20 (m, 6H), 6.90–6.98 (m, 6H), 6.8 (d, J = 7.8 Hz, 2H), 3.87 (s, 6H) ppm; ^{13}C NMR (75 MHz, $CDCl_3$): δ 159.91, 145.55, 140.19, 139.19, 135.60, 133.26, 131.93, 127.12, 126.23, 124.56, 119.20, 114.03, 55.33 ppm; HRMS (APPI-TOF, positive mode): m/z calcd for $C_{28}H_{22}O_2$ $[M + H]^+$ 391.1692, found 391.1689.

General procedure B

Synthesis of 12a–c

To an ice-cooled solution of **DP-DBF** derivative (**5a-c**) (1.00 g, 2.56 mmol) in dry CH_2Cl_2 (25 mL), a fresh solution of BBr_3 (2.67 mL, 25.2 mmol) in dry CH_2Cl_2 (5 mL) was added dropwise. The resulting reaction mixture was stirred at 0 °C for ca. 3 h and then the ice bath was removed. The reaction was continued at rt for

another 1 h. The progress of the reaction was monitored by TLC analysis. Upon completion, the reaction was quenched very carefully with water. The resulting mixture was then diluted with brine and extracted with CH_2Cl_2 (3×20 mL) three times. The combined organic layers were dried over $MgSO_4$, filtered, and concentrated under reduced pressure, resulting in demethylated products (**12a**–*c*) without further purification.

2,2′-((9*H*-fluoren-9-ylidene)methylene)diphenol (12a)

Compound **12a** was prepared according to the general demethylation procedure **B** as a brownish creamy solid (0.790 g, 2.18 mmol, 85%). m.p.: > 215.6 °C (decomp). IR (neat): 3475, 3374, 3054,1575, 1486, 1445, 1339, 1271, 1211, 1179, 1100, 1033, 876, 855, 759, 734 cm^{-1}; ^1H NMR (300 MHz, acetone-d_6): δ 8.64 (s, 1H), 7.88-7.75 (m, 2H), 7.55–7.23 (m, 6H), 7.08–6.93 (m, 6H), 6.50 (d, J = 7.8 Hz, 2H) ppm; ^{13}C NMR (75 MHz, acetone-d_6): δ 152.95, 140.60, 137.92, 137.62, 129.50, 129.26, 128.96, 128.27, 126.93, 126.67, 124.66, 121.18, 119.29, 116.31 ppm; HRMS (ESI-TOF, negative mode): *m/z* calcd for $C_{26}H_{18}O_2$ $[M]^-$ 362.1307, found 362.1299.

3,3'-((9*H*-fluoren-9-ylidene)methylene)diphenol (12b)

Compound **12b** was prepared according to the general demethylation procedure **B** as a creamy solid (0.550 g, 1.52 mmol, 59%). m.p.: > 207.4 °C (decomp). IR (neat): 3263, 3.054, 2922, 1580, 1489, 1443, 1353, 1263, 1244, 1196, 1180, 1124, 931, 776, 747, 729 cm^{-1}; ^1H NMR (300 MHz, acetone-d_6): δ 8.44 (s, 1H), 7.79 (d, J = 7.5 Hz, 2H), 7.34–7.24 (m, 4H), 6.99-6.87 (m, 8H), 6.73 (d, J = 8.1 Hz, 2H), 5.61 (s, 1H) ppm; ^{13}C NMR (75 MHz, acetone-d_6): δ 157.82, 145.58, 144.27, 140.40, 138.43,

130.06, 127.83, 126.45, 125.03, 119.87, 119.26, 115.66, 115.05 ppm; HRMS (ESI-TOF, negative mode): *m/z* calcd for $C_{26}H_{18}O_2$ $[M]^-$ 362.1307, found 362.1297.

4,4′-((9*H*-fluoren-9-ylidene)methylene)diphenol (12c)

Compound **12c** was prepared according to the general demethylation procedure **B** as an orange solid (0.620 g, 1.71 mmol, 67%). m.p.: > 261 °C (decomp). IR (neat): 3333, 3053, 2921, 1687, 1602, 1585, 1505, 1429, 1367, 1218,1132, 1106, 968, 835, 777 cm^{-1}; ^1H NMR (300 MHz, acetone-d_6): δ 7.78 (d, J = 7.5 Hz, 2H), 7.26–7.18 (m, 6H), 6.99–6.92 (m, 6H), 6.83 (d, J = 7.8 Hz, 2H) ppm; ^{13}C NMR (75 MHz, acetone-d_6): δ 152.92, 146.73, 140.04, 139.21, 134.49, 132.49, 131.66, 127.34, 127.11, 126.17, 124.44, 119.16, 115.46 ppm; HRMS (APPI-TOF, negative mode): *m/z* calcd for $C_{26}H_{18}O_2$ $[M]^-$ 362.13068, found 362.13232.

General procedure C

Synthesis of 8a–c

To the solution of a hydroxylated **DP-DBF** (**12a**–**c**) (0.500 g, 1.38 mmol) in DMF (15 mL) K_2CO_3 (0.570 g, 4.14 mmol) was added. The resulting mixture was stirred at rt for 15 min, and benzyl bromide (0.410 mL, 3.44 mmol) was then added dropwise. The reaction was further heated to 100 °C for 12 h, and was monitored by TLC analysis. Upon completion, the reaction was quenched with water and extracted with ethyl acetate (3 × 20 mL). The combined organic layers were washed with water, brine, dried over $MgSO_4$, and concentrated under reduced pressure. The residue was subjected to silica gel column chromatography using CH_2Cl_2/hexanes as eluent,

affording pure compounds **8a**–*c*, respectively.

9-(Bis(2-(benzyloxy)phenyl)methylene)-9*H*-fluorene (8a)

Compound **8a** was obtained according to the general benzylation procedure **C** as a creamy white solid (0.50 g, 0.92 mmol, 67%). m.p.: 165.3-170.5 °C. IR (neat): 3056, 3030, 2928, 2915, 2873, 1591, 1484, 1443, 1288, 1234, 1160, 1115, 1080, 998, 780 cm^{-1}; ^1H NMR (300 MHz, $CDCl_3$): δ 7.68 (d, J = 7.2 Hz, 2H), 7.46 (dd, J = 7.5, 1.5 Hz, 2H), 7.32–7.08 (m,15H), 6.97-6.88 (m, 6H), 6.44 (d, J = 7.8 Hz, 2H), 5.01 (s, 4H) ppm; ^{13}C NMR (75 MHz, $CDCl_3$): δ ppm 156.54, 155.49, 140.39, 139.61, 138.77, 137.03, 131.90, 130.94, 128.94, 128.26, 127.93, 127.54, 127.35, 126.59, 124.85, 121.13, 119.02, 113.09, 112.74, 70.14, 69.81 ppm; HRMS (APPI-TOF, positive mode): *m/z* calcd for $C_{40}H_{30}O_2$ $[M]^+$ 542.2246, found 542.2236.

9-(Bis(3-(benzyloxy)phenyl)methylene)-9*H*-fluorene (8b)

Compound **8b** was obtained according to the general benzylation procedure **C** as a yellow solid (0.54 g, 1.0 mmol, 73%). m.p.: 163.6-167.2 °C. IR (neat): 3057, 3029, 2925, 2859, 1582, 1481, 1431, 1377, 1315, 1285, 1213, 1155, 1027, 1003, 776 cm^{-1}; ^1H NMR (300 MHz, $CDCl_3$): δ 7.69 (d, J = 7.5 Hz, 2H), 7.41–7.21 (m, 16H), 7.03–6.91 (m, 8H), 6.68 (d, J = 8.1 Hz, 2H), 5.02 (d, J = 2.8 Hz, 4H) ppm; ^{13}C NMR (75 MHz, $CDCl_3$): δ 159.18, 144.72, 144.07, 140.50, 138.50, 136.78, 134.16, 129.97, 128.54, 127.97, 127.70, 127.58, 126.53, 125.12, 122.12, 119.20, 115.64, 114.94, 70.06 ppm; HRMS (APPI-TOF, positive mode): *m/z* calcd for $C_{40}H_{30}O_2$ $[M]^+$ 542.2246, found 542.2244.

9-(Bis(4-(benzyloxy)phenyl)methylene)-9*H*-fluorene (8c)

Compound **8c** was obtained according to the general benzylation procedure **C** as a yellow solid (0.580 g, 1.06 mmol, 78%). m.p.: 192.2–194.0 °C. IR (neat): 3090, 3028, 2920, 2869, 1600, 1502, 1465, 1448, 1379, 1287, 1233, 1171, 1108, 1003, 969, 860, 824, 790 cm^{-1}; ^1H NMR (300 MHz, $CDCl_3$): δ 7.71 (d, J = 7.5 Hz, 2H), 7.49-7.20 (m, 17H), 7.02–6.93 (m, 6H), 6.79 (d, J = 8.7 Hz, 2H), 5.12 (s, 4H) ppm; ^{13}C NMR (75 MHz, $CDCl_3$): δ 159.14, 145.45, 140.20, 139.14, 136.78, 135.82, 133.41, 131.86, 128.59, 128.12, 127.64, 127.15, 126.24, 124.58, 119.12, 114.96, 70.12 ppm; HRMS (APPI-TOF, positive mode): m/z calcd for $C_{40}H_{30}O_2$ $[M]^+$ 542.2246, found 542.2242.

12-(9*H*-fluoren-9-ylidene)-12*H*-dibenzo[*d*,*g*][1,3]dioxocine (9)

A suspension of compound **12a** (0.30 g, 0.83 mmol) and Cs_2CO_3 (0.220 g, 2.48 mmol) in DMF (10 mL) was stirred at rt for 15 min. To this mixture was added CH_2I_2 (0.10 mL, 1.2 mmol) dropwise. The reaction mixture was then heated to 100 °C for 8 h. The reaction was monitored by TLC analysis. Upon completion, the reaction was quenched with water and extracted with ethyl acetate (3 × 15 mL). The organic layers were combined, washed with water and brine, dried over $MgSO_4$, and concentrated under reduced pressure. The resulting residue was purified by silica gel column chromatography (CH_2Cl_2/hexanes, 50:50) to give pure compound **9** as a creamy white solid (0.15 g, 0.40 mmol, 50%). m.p.: 227.4–235.1 °C. IR (neat): 3053, 2999, 2955, 2852, 1619, 1597, 1571, 1483, 1435, 1273, 1235, 1182, 1143, 1046, 1000, 964, 877, 852, 781 cm^{-1}; ^1H NMR (300 MHz, CD_2Cl_2): δ 7.63–7.61 (m, 2H),

7.30–7.24 (m, 4H), 7.20 (td, J = 7.5, 0.9 Hz, 2H), 7.09-7.04 (m, 4H), 6.88 (td, J = 7.5, 1.4 Hz, 2H), 6.52 (d, J = 8.1 Hz, 2H), 6.27 (d, J = 7.5 Hz, 1H), 5.36 (d, J = 7.5 Hz, 1H) ppm; ^{13}C NMR (75 MHz, CD_2Cl_2): δ 153.63, 140.70, 137.51, 136.09, 129.97, 129.50, 128.30, 126.89, 124.98, 123.88, 120.98, 119.38, 93.74 ppm; HRMS (APPI-TOF, positive mode): m/z calcd for $C_{27}H_{18}O_2$ $[M]^+$ 374.13068, found 374.13128.

Chapter 3

Structural Tuning of Curved TTFAQ-AQ as a Redox-active Supramolecular Partner for C_{70} Fullerene

The contents of this chapter were published as a full paper in *J. Org. Chem.*, **2021**, *86*, 14855–14865. Contributions of authors are described below: Maryam F. Abdollahi is the first author, who conducted the synthesis of anthraquinodimethane extended tetrathiafulvalene (TTFAQ) compounds, growth of the single crystals and cocrystal, and relevant spectroscopic characterizations. She also contributed to the manuscript preparation and editing.

Prof. Yuming Zhao is the supervisor of M. F. Abdollahi, who helped develop the concepts and design of this project. Prof. Zhao is the corresponding author of this

paper.

Note that compound numbering in this chapter differs from the previous chapters. In this chapter, the compounds are numbered in the same way as those in the publication.

3.1 Introduction

Tetrathiafulvalene (TTF) is a fascinating small organic π-conjugated molecule that has been extensively used as a redox-active building block in a wide range of organic electronic materials and supramolecular systems.[46,158–168] Extension of the π-conjugated backbone of TTF gives rise to intriguing π-extended TTFs (exTTFs) that exhibit structural and electronic properties very different from those of pristine TTF.[43,161,168–174] The class of exTTFs built upon an anthraquinoid (AQ) π-spacer, generally referred to as TTFAQ (Figure 3.1), has captured long-lasting research interest owing to its unique structural and electronic properties.[163,171,175–184] The molecular structure of TTFAQ generally favors a saddle shape in its neutral state. Upon oxidation, TTFAQ can readily release two electrons to form a stable dication with a dramatic conformational change and increased aromaticity. Taking advantage of the electron-donating properties of TTFAQ, various charge-transfer (CT) systems and redox-controllable supramolecular assemblies have been developed over the past decades.[174,182,185–192]

It is worth remarking that the saddle shape of neutral TTFAQ creates two concave π-surfaces that can engage with carbon nanomaterials, ranging from two-dimensional graphene sheets,[193,194] cylindrical-shaped carbon nanotubes[191,195–199] to 3-dimensional

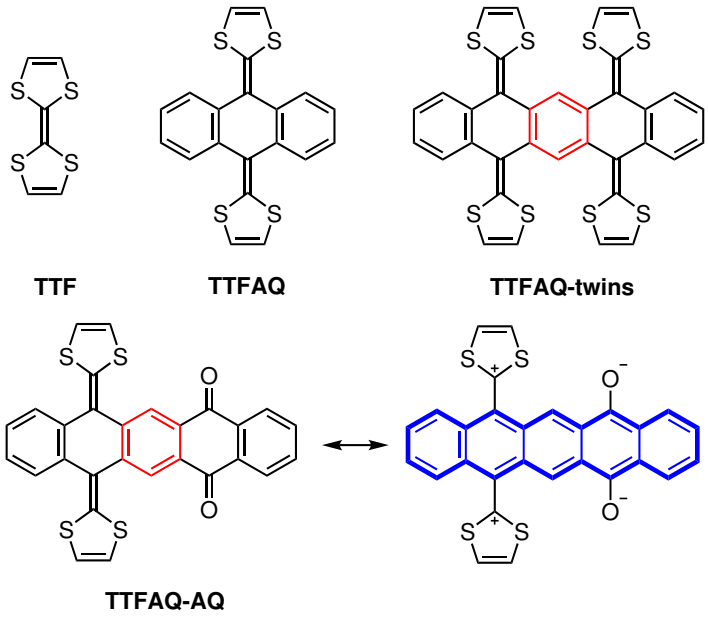

Figure 3.1: Structures of TTF, TTFAQ, TTFAQ-twins, and TTFAQ-AQ.

fullerenes[114,117,120,200–202] and carbon nanodots,[203] through attractive π–π interactions.[170,204] Based on a notion of "concave-convex complementarity",[111,116,205] Martín and others successfully devised various TTFAQ-based fullerene receptors that are applicable in selectively separating fullerenes and forming multifunctional supramolecular materials.[114,117,120,200–202] Experimental and theoretical studies have pointed out that TTFAQ plays a vital role in binding with fullerenes, owing to its electron-donating nature and curved π-surfaces (shape complementarity).[111,205–207] It is thus reasonable to envision that more intriguing redox-active systems and supramolecular hosts/partners for fullerenes would be found from new TTFAQ derivatives that feature elongated π-frameworks.

Our group previously reported a class of π-extended TTFAQs derived from pentacene-5,7,12,14-tetraone (TTFAQ-twins, Figure 3.1), which structurally can be viewed as conjoined twins of TTFAQ.[208] Extension of the π-conjugation of TTFAQ

in this way enables significant electronic communication, bringing about enhanced electron-donating ability and multi-stage redox activity. It is worth noting that oxidation of TTFAQ-twins results in a tetracation with a pentacene central π-unit. Such properties motivated us to pursue new pentacene-5,7,12,14-tetraone derived TTFAQ analogues. In this work, a donor-acceptor system, termed TTFAQ-AQ, was designed and synthesized. TTFAQ-AQ is an ensemble of TTFAQ (donor) and AQ (acceptor) units, which are π-fused together through sharing of a central benzene ring (Figure 3.1). Intramolecular charge transfer (ICT) through the resonance effect can be anticipated in TTFAQ-AQ (see the scheme in Figure 3.1), which would render its central π-unit a certain degree of pentacene-like character. Such a π-electron "push–pull" feature should give rise to interesting redox activity and photophysical properties. Moreover, the elongated central pentacene unit of TTFAQ-AQ is conducive to enhancing supramolecular interactions with various carbon nanomaterials such as fullerenes.

3.2 Results and Discussion

3.2.1 Synthesis of TTFAQ-AQs

At the outset of our studies, double-olefination on pentacene-5,7,12,14-tetraone (**1**) (Scheme 3.1) was conceived as a synthetic strategy for TTFAQ-AQs. The search for a regioselective reaction allowing only the 5 and 14 positions of pentacene-5,7,12,14-tetraone to be functionalized is key to the success of this synthetic approach. In our previous studies,[208] a phosphite-promoted olefination of pentacenetetraone with

1,3-dithiol-2-thione was investigated and the results showed that trisubstitution at the 5, 7, and 12 positions dominated. Other olefination methods were therefore utilized. In this work, we found that high regioselectivity of 5,14-disubstitution could be attained through the Ramirez *gem*-dibromoolefination reaction.[209,210] As shown in Scheme 3.1, the reaction of pentacenetetraone (**1**) with CBr_4/Ph_3P in refluxing toluene led to the formation of 7,12-bis(dibromomethylene)-7,12-dihydropentacene-5,14-dione (**2**) in a good yield. The molecular structure of **2** was unambiguously confirmed by single-crystal X-ray diffraction (SCXRD) analysis (see the inset in Scheme 1). With compound **2** in hand, double *S*-vinylation reactions of the vinylidene dibromide moieties of **2** with suitable 1,2-dithiols were conducted to accomplish the assembly of TTFAQ-AQ structure. In our synthesis, two double *S*-vinylation approaches were explored. The first approach utilized 1,2-dithiols *in situ* generated from the hydrolysis of 1,3-dithiol-2-thiones **3a**/**b** by tetrabutylammonium hydroxide in isopropanol.[211] The reactions afforded two TTFAQ-AQs **4a** and **4b** in reasonably good yields. In the second approach, 1,2-benzenedithiol (**5**) was reacted with **2** in the presence of tetrabutylammonium hydroxide,[212] affording benzoannulated TTFAQ-AQ **6** in a good yield.

3.2.2 Molecular Structural and π–π Stacking Properties of TTFAQ-AQs

The molecular structures and purity of TTFAQ-AQs **4a**/**b** and **6** were characterized and confirmed by NMR, IR, and MS analyses. Single crystals of **4a** and **6** were successfully grown by slow recrystallization from CH_2Cl_2 at 4 °C, and they were

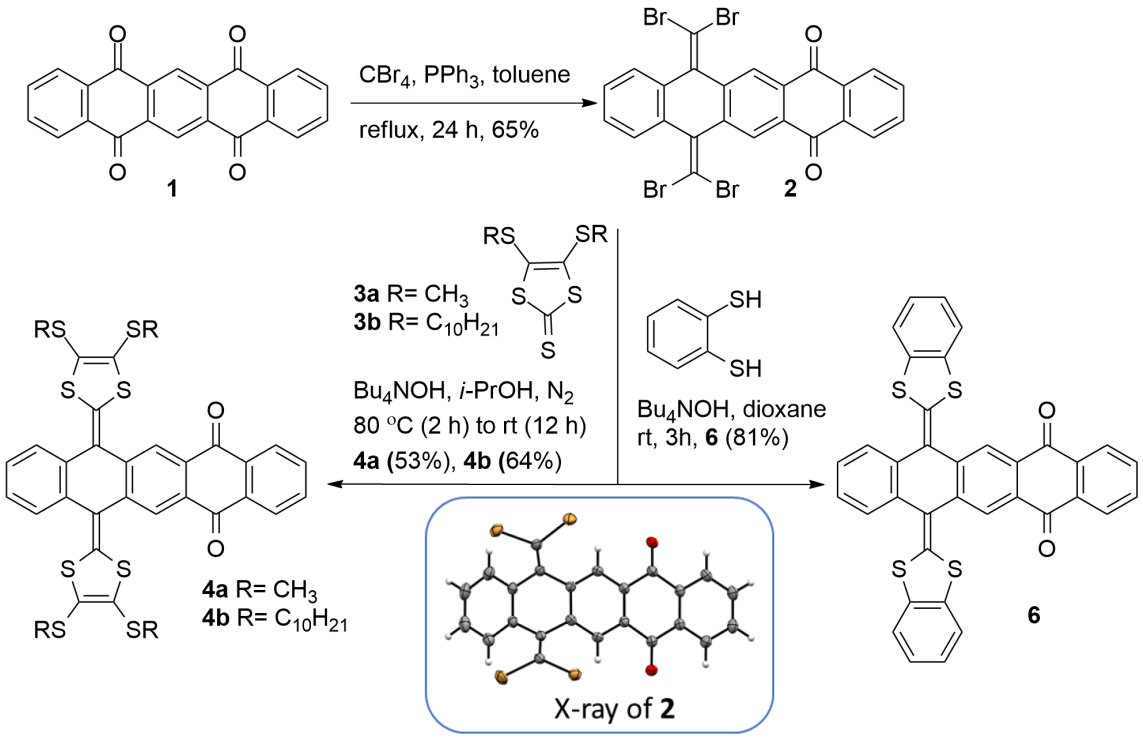

Scheme 3.1: Synthesis of TTFAQ-AQs **4a**/**b** and **6**. Inset: X-ray structure of **2** (CCDC 2068078).

subjected to SCXRD analysis to elucidate detailed molecular structural and solid-state packing properties. As can be seen from Figure 3.2, both **4a** and **6** show a saddle-like conformation consisting of two orthogonally oriented π-segments, referred to as *S*- and *C*-faces. The *S*-face arises from the curved TTFAQ moiety, which exhibits a much deeper concavity than the *C*-face; especially, the *S*-face of benzo-fused TTFAQ-AQ **6** shows a nearly semicircular shape (Figure 3.2B) with a depth of 4.58 Å. Such a molecular shape resembles that of the "buckycatcher" devised by Sygula *et al.*,[112] boding well for its ability to act as an efficient concave receptor for fullerenes. The central pentacene segments of **4a** and **6** (*C*-face) adopt the shape of a "kinked board" as shown in Figure 3.2. It is noteworthy that the AQ moieties in

the molecular structures of **4a** and **6** still retains planarity, while the *C*-face of **4a** appears to be more kinked than that of **6**.

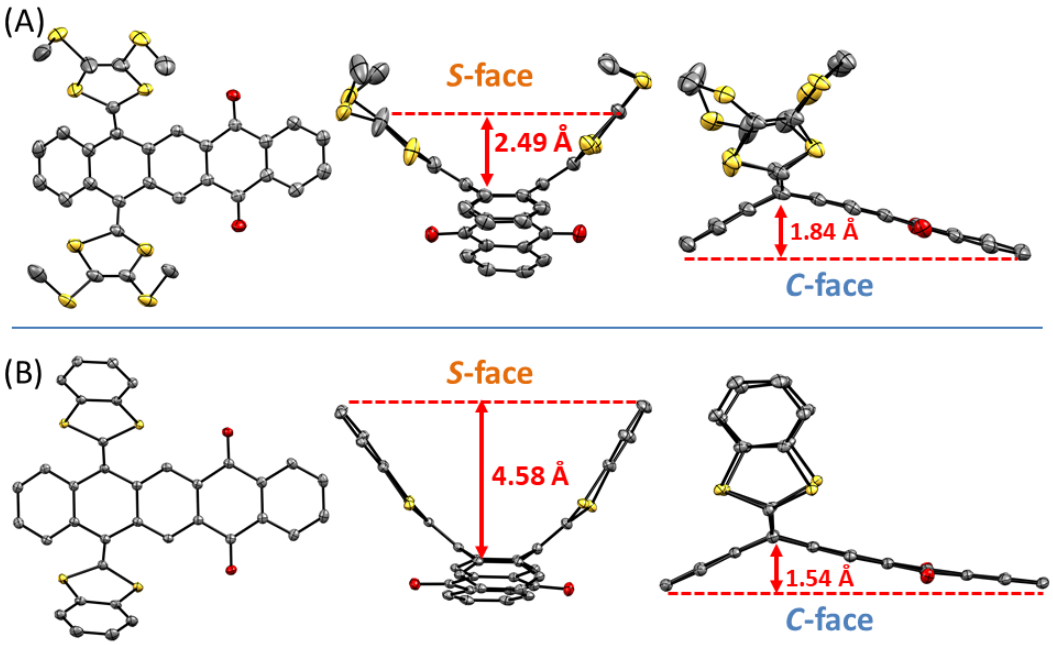

Figure 3.2: ORTEP drawings with 30% ellipsoid probability for non-hydrogen atoms for (A) **4a** (CCDC 2087913) and (B) **6** (CCDC 2036902). Structures are viewed from front (left), edge of *S*-face (middle), and edge of *C*-face (right).

Intimate intermolecular π–π stacking exists in the crystal structures of **4a** and **6**. In the crystal of **4a**, face-on stacking takes place between electron-donating dithiole and electron-withdrawing AQ groups, respectively (Figure 3.3A). The intercentroid distances between closely stacked arene rings are 4.05 Å for dithiole$\cdots$dithiole stacking and 3.63 Å for AQ$\cdots$AQ stacking. The tighter stacking between AQ groups can be rationalized by their more planar and extended π-surface. No stacking occurs between dithiole and AQ moieties in the crystal structure of **4a**, even though the two groups show complementary electronic nature and have the potential to stack

via intermolecular donor–acceptor interactions. In the crystal structure of **6**, the packing modes appear to be different (Figure 3.3B). Intermolecular dithiole$\cdots$AQ face-on stacking becomes a dominant feature in the crystal packing of **6**. Herein, the intercentroid distance for the dithiole$\cdots$AQ stacking is 3.67 Å, which is much shorter than the dithiole$\cdots$dithiole distance in the packing of **4a**. In contrast to the SMe-substitution in **4a**, the benzo-fused dithiole group of **6** gives a more extended and delocalized π-surface, which facilitates the pairing of it with the AQ group through complementary donor–acceptor interactions. On the other hand, close AQ$\cdots$AQ face-on stacking can be found in the crystal structure of **6**, and the packing geometry is similar to that observed in **4a**. The π–π stacking modes disclosed by X-ray analysis indicate that benzo-fused dithiole, owing to its larger π-face, serves as a much better packing partner for electron-deficient arenes than the relatively small SMe-substituted dithiole group. On the other hand, the planar AQ group has been proven capable of packing with an extended π-partner in the solid state regardless of its electronic nature (donor or acceptor). DFT calculations disclose that the intermolecular AQ$\cdots$AQ stacking can bring about a stabilization energy similar to that arising from intermolecular dithiole$\cdots$AQ stacking (see Figures S-32 and S-33, Appendix II).

3.2.3 Molecular Orbital and Electronic Properties

The frontier molecular orbital (FMO) properties of TTFAQ-AQs **4a**/**b** and **6** were investigated by DFT calculations. As shown in Figure 3.4, the electron-donating TTFAQ moiety is the main contributor to occupied MOs (i.e., HOMO and HOMO

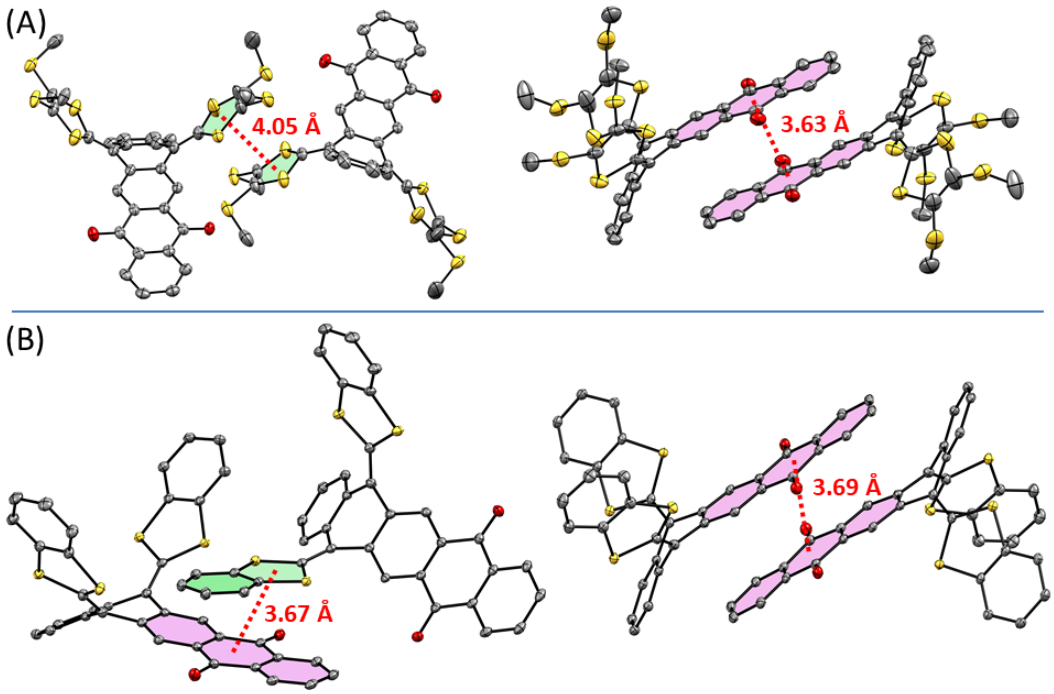

Figure 3.3: Intermolecular π–π stacking modes in the crystal structures of (A) **4a** and (B) **6**.

− 1), while the unoccupied MOs (LUMO and LUMO + 1) are dominated by the electron-withdrawing AQ unit. SMe and $SC_{10}H_{21}$-substituted TTFAQ-AQs show similar HOMO–LUMO gaps (4.061 eV for **4a** and 4.086 eV for **4b**), indicating that alkyl groups exert insignificant effects on the π-electronic properties of TTFAQ-AQ. For compound **6**, the benzo groups make more significant contributions to HOMO − 1 than HOMO. The LUMO and LUMO + 1 of **6** show similar contour distributions to those of **4a**/**b**. It is noteworthy that the HOMO–LUMO gap of **6** is wider than those of **4a**/**b**, even though **6** possesses a more extended π-framework due to benzoannulation.

The calculated FMO properties agree with the experimental results of cyclic voltammetric (CV) and UV-Vis absorption analyses. As shown in Figure 3.5A, the

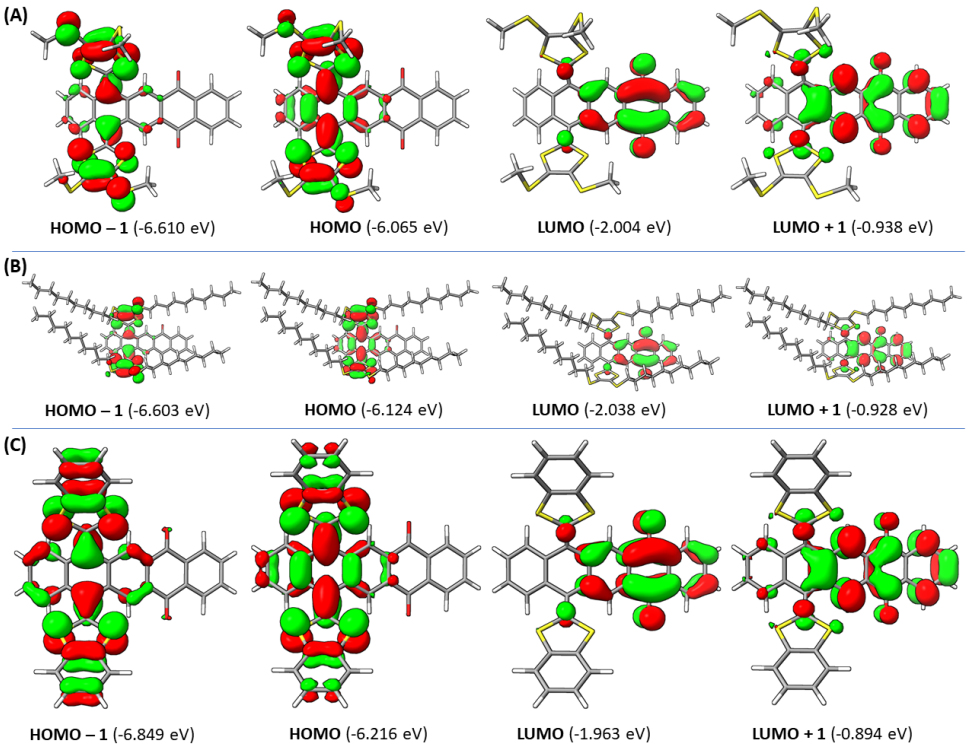

Figure 3.4: Isocontours (at 0.03 a.u.) and eigenvalues of the frontier molecular orbital of TTFAQ-AQs calculated at the M06-2X/Def2-SVP level of theory. (A) **4a**, (B) **4b**, and (C) **6**.

voltammograms of TTFAQ-AQs **4a**/**b** and **6** exhibit similar amphoteric behavior. In the positive potential window, a quasi-reversible redox wave pair can be observed, which is due to the simultaneous two-electron transfer process on the TTFAQ (donor) moiety. In the negative potential window, two quasi-reversible redox wave pairs are present, corresponding to stepwise single-electron transfers on the electron-accepting AQ (acceptor) unit. The CV data confirmed that the TTFAQ-AQ system retains the redox activity of the TTFAQ and AQ groups. Compared with typical TTFAQs,[175,179,188] the oxidation potentials of **4a**/**b** and **6** are significantly shifted to more positive values as a result of ICT interactions with the neighboring electron-

withdrawing AQ unit through π-conjugation. The degrees of ICT in the TTFAQ-AQs are further reflected by their relatively narrow electronic bandgaps (E_g). As summarized in Table 3.1, two methods were utilized to determine the E_g. The first method is based on the difference between the half-wave potentials of the first oxidation and first reduction processes in the cyclic voltammogram, and the second is based on the difference between the onset potentials of the first oxidation and the first reduction processes. The results show that benzo-fused TTFAQ-AQ **6** has a slightly larger bandgap than those of **4a/b**, which is consistent with the trend of their DFT calculated HOMO–LUMO gaps. It is worth mentioning that all the TTFAQ-AQs show relatively small bandgaps, which point to potential application in small-molecule organic semiconductors.[213,214]

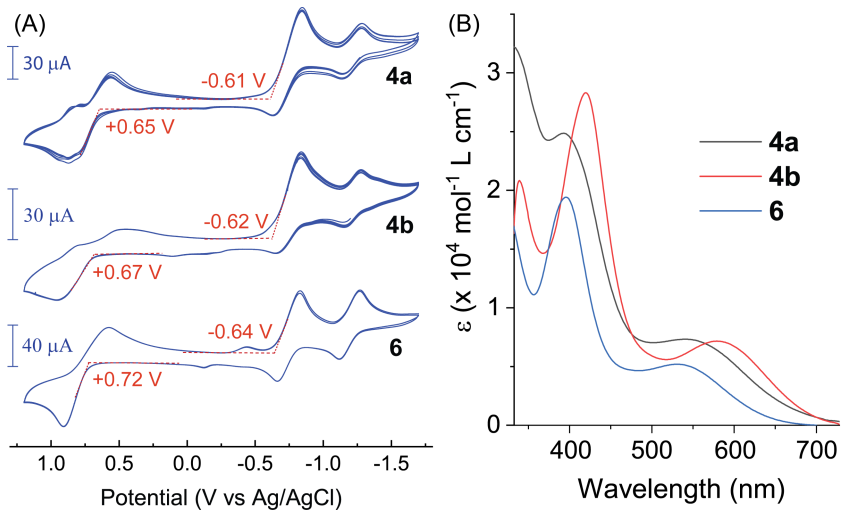

Figure 3.5: (A) Cyclic voltammograms of **4a/b** and **6** measured in CH_2Cl_2 in the presence of Bu_4NPF_6 (0.10 M). Working electrode: glassy carbon, counter electrode: Pt wire, reference electrode: Ag/AgCl, scan rate: 0.10 V s^{-1}. Onset potentials for oxidation and reduction are indicated. (B) UV-Vis spectra of **4a/b** and **6** measured in CH_2Cl_2 at room temperature.

Table 3.1: Summary of CV properties of TTFAQ-AQs **4a/b** and **6**

Entry	$E_{1/2}^{ox}$ (V)[a]	E_{ox}^{onset} (V)[b]	$E_{1/2}^{red1}$ (V)[c]	$E_{1/2}^{red2}$ (V)[d]	E_{red}^{onset} (V)[e]	E_g^{CV1} (V)[f]	E_g^{CV2} (V)[g]
4a	+0.71	+0.65	-0.75	-1.22	-0.61	1.46	1.26
4b	+0.72	+0.67	-0.75	-1.22	-0.62	1.47	1.29
6	+0.75	+0.72	-0.75	-1.20	-0.64	1.50	1.36

[a] Half-wave potential of first oxidation process. [b] Onset potential of first oxidation process.

[c] Half-wave potential of first reduction process. [d] Half-wave potential of second reduction process.

[e] Onset potential of first reduction process. [f] $E_g^{CV1} = E_{ox}^{onset} - E_{red}^{onset}$; [g] $E_g^{CV2} = E_{1/2}^{ox} - E_{1/2}^{red1}$.

The UV-Vis absorption spectra of TTFAQ-AQs **4a/b** and **6** in CH_2Cl_2 are compared in Figure 3.5B. The three compounds give similar spectral profiles, featuring two significant $\pi \rightarrow \pi^*$ bands in the low-energy region. The long-wavelength band appears as a broad peak with moderate intensity, which can be assigned to the HOMO $\rightarrow$ LUMO transition according to time-dependent density functional (TD-DFT) analysis (see Tables S-8 to S-10, Appendix II). The short-wavelength peak is sharper in shape and more intense, which is mainly due to the HOMO $\rightarrow$ LUMO + 1 transition. It is noteworthy that the absorption peaks of decyl-substituted TFAQ-AQ **4b** are more red-shifted than those of **4a** and **6**. It is possible that the long alkyl chains in **4b** facilitate intermolecular aggregation in a way similar to the stacking of discotic liquid crystals, while the enhanced aggregation results in more pronouncedly red-shifted absorption. TTFAQ-AQs also show solvatochromic properties (Figures S-28 to S-30, Appendix II). Take **6** as an example, the lowest-energy absorption band appears at 561 nm in $CHCl_3$, and it is significantly blue-shifted to 526 nm in DMF and 516 nm in THF. Such a trend of solvent effects contradicts the ICT argument which would predict the absorption to be more red-shifted as the solvent polarity increases. An explanation based on intermolecular donor–acceptor interactions concurs with the experimental observation, which is reasoned that the solvation of **6** in non-polar or

weakly polar solvents is poor due to the polar nature of **6**. As such, the degree of intermolecular π–π stacking (e.g., dithiole$\cdots$AQ stacking) would be more significant in less polar solvents, leading to enhanced intermolecular charge-transfer interactions and hence red-shifted UV-Vis absorption. The optical bandgap (E_g^{opt}) of TTFAQ-AQs could be obtained from their cutoff absorption wavelengths (686 nm for **4a**, 696 nm for **4b**, and 642 nm for **6**) in the UV-Vis spectra. The results show a trend of 1.78 eV (**4b**), 1.81 eV (**4a**), and 1.93 eV (**6**). Different from the trend of CV determined bandgaps, the E_g^{opt} of **4b** is slightly narrower than that of **4a**. This can be explained by the more pronounced aggregation effects induced by the long alkyl chains in the structure **4b**.

3.2.4 Supramolecular Interactions with Fullerenes

The extended π-surface and saddle-like molecular shape of TTFAQ-AQ render it an appealing supramolecular partner for concave-convex interactions with fullerenes. To further explore this aspect, TTFAQ-AQ **6** was subjected to co-crystallization with C_{60} and C_{70} fullerenes, respectively, in view of the very deep cavity generated by its π-extended *S*-face. In our experiments, slow evaporation of a solution of **6** and C_{70} in chlorobenzene/*n*-hexane (10:1, v/v) at room temperature afforded black rod-like co-crystals of **6**/C_{70} that allowed for single crystallographic analysis to elucidate detailed supramolecular self-assembling properties. In the co-crystal structure, molecules of **6** and C_{70} are orderly packed to form a grid-like 3-dimensional network (Figure 3.6A). Close examination of the superstructure of **6**/C_{70} reveals intimate π–π stacking among the molecules of **6** and C_{70}, while the void space within the **6**/C_{70} network is filled with

solvent molecules (chlorobenzene and *n*-hexane). The interacting geometry of **6** and C_{70} in the crystal packing is particularly noteworthy. The molecule of **6** interacts with C_{70} via both its *S*- and *C*-faces. On the *S*-face, the two benzodithiole units (highlighted by blue-color shade in Figure 3.6B) show intimate π–π interactions with the surface of C_{70}, affording a tweezer-type binding mode. Similarly, the *C*-face of **6** is bound to another C_{70} molecule through π–π interactions with the benzene and benzoquinone moieties (highlighted by purple-color shade in Figure 3.6B).

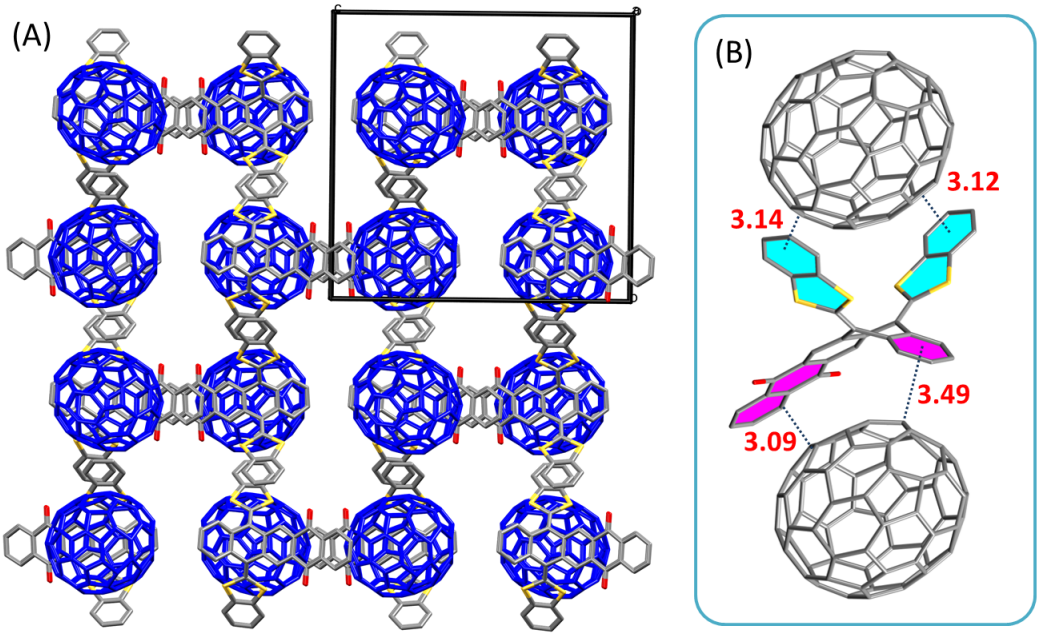

Figure 3.6: (A) Packing diagram of the co-crystal of **6** and C_{70} viewed along the *a*-axis of the unit cell. (B) Packing geometry of **6** and C_{70} with close intermolecular distances highlighted in Å. Hydrogen atoms and solvate molecules are omitted for clarity. CCDC 2036905

In addition to π–π interactions between the concave surfaces of **6** and convex surface C_{70}, π–π stacking also occurs on other sides of the π-surfaces of **6** in the

co-crystal. As highlighted in Figure 3.7A, face-to-face stacking is formed between adjacent benzodithiole units with a certain degree of slippage. It is worth noting that benzodithiole$\cdots$benzodithiole stacking does not occur in the single crystal of **6**. Figure 3.7B highlights the intermolecular AQ$\cdots$AQ stacking, which is similar to that observed in the single crystal structure of **6**. Eventually, the π-surfaces of TTFAQ-AQ **6** are all engaged in π–π stacking. Viewing along the perspective shown in Figure 3.7C, one can see a highly efficient complementary packing motif, in which a π-dimer of **6** provides two *S*-faces and two *C*-faces to interact with four molecules of C_{70}.

The co-crystallization of **6** with C_{60} fullerene, nevertheless, was unsuccessful despite numerous attempts under various crystallization conditions. In most of the cases, separate single crystals of **6** and C_{60} fullerene precipitates were formed. The failure in co-crystallization of **6** with C_{60} fullerene can be attributed to the relatively low degree of complementarity between the spherical shape of C_{60} fullerene and the unsymmetrical shape of **6** according to DFT modeling studies (*vide infra*). We have also attempted to co-crystallize TTFAQ-AQs **4a/b** with C_{60} and C_{70} fullerenes, respectively, but no co-crystals could be obtained after numerous trials. In view of their relatively small *S*-faces and the presence of hindered alkyl groups attached to the dithiole rings, it is not surprising that TTFAQ-AQs **4a/b** did not form co-crystals with fullerenes. The outcomes of our co-crystallization investigations eventually point out that sufficiently π-extended *S*-face in TTFAQ-AQ and an oblong molecular shape of fullerene are two essential requirements for them to form organized supramolecular assemblies in the crystalline lattice.

To examine the supramolecular interactions of TTFAQ-AQ with fullerenes in the solution phase, UV-Vis and ^{1}H NMR titrations of **6** with C_{60} and C_{70} fullerenes were

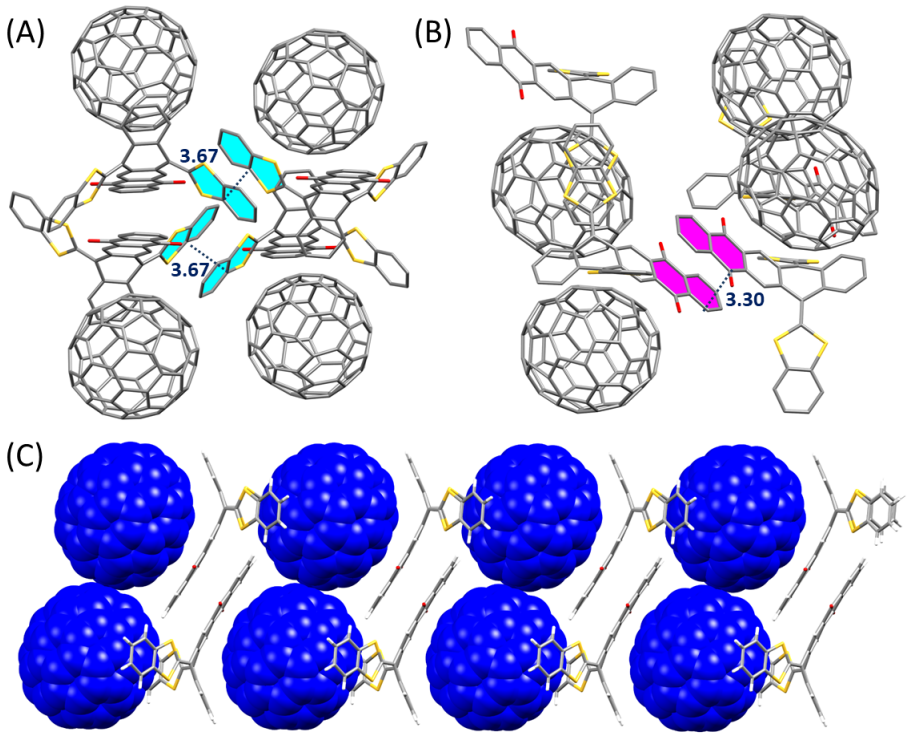

Figure 3.7: Packing geometries of **6** and C_{70} with (A) intermolecular benzodithiole–benzodithiole stacking and (B) intermolecular AQ$\cdots$AQ stacking highlighted (dashed lines showing interatomic distances in Å). (C) Supramolecular structures assembled by complementary π–π stacking among the π-surfaces of **6** and C_{70}. Hydrogen atoms and solvate molecules are omitted for clarity. CCDC 2036905

performed. In highly diluted solutions (10^{-6} to 10^{-5} M), compound **6** did not show any significant binding behavior with C_{60} and C_{70} fullerenes. This is evidenced by both UV-Vis absorption and ^{1}H NMR titration results (see Appendix II). Even at mM concentrations, the ^{1}H NMR titration of **6** with C_{60} fullerene still pointed to negligible binding (Figure S-11, Appendix II). Upon addition of C_{70} to the solution of **6** at 8.0 mM, the proton signals of **6** were found to gradually weaken in intensity and broaden in line shape (Figure 3.8). The chemical shifts of most of the proton signals

of **6**, however, remained nearly unchanged throughout the titration, except that the singlet at 8.83 ppm, which is due to the protons of the central benzene ring shared by TTFAQ and AQ moieties, moved slightly to downfield. The titration results suggest that the binding of **6** and C_{70} leads to complex supramolecular assemblies rather than simple 1:1 and/or 1:2 guest-host complexes. According to the X-ray packing motif of **6**/C_{70}, the protons of **6** should be subject to shielding effects when both the *S*- and *C*-faces of **6** interact with C_{70}. So, if the supramolecular assemblies of **6** and C_{70} in the solution phase were organized in a fashion similar to that in the co-crystal structure, the proton signals of **6** would be significantly shifted upfield. The emergence of multiple new signals in the relatively upfield aromatic region (6.86 to 7.09 ppm) at the end stage of the titration agrees with this argument. After addition of more than 7 equivalents of C_{70}, the NMR spectra show distinct signals due to both free **6** and bound complexes of **6** and C_{70}, indicating that a slow-exchange equilibrium dictates the binding mechanism.

3.2.5 Computational Modeling of Noncovalent Interactions between TTFAQ-AQ and Fullerenes

DFT calculations were undertaken to quantitatively evaluate the energetics of noncovalent interactions between **6** and C_{60}/C_{70} fullerenes. Our modeling studies examined two types of 1:1 binding complexes, where a fullerene molecule (C_{60} or C_{70}) interacts with the *S*- and *C*-faces of TTFAQ-AQ **6**, respectively. Detailed interaction energies are summarized in Table 3.2. The results indicate that both the *S*- and *C*-faces of **6** are attractive towards fullerenes. It is worth noting that the interaction

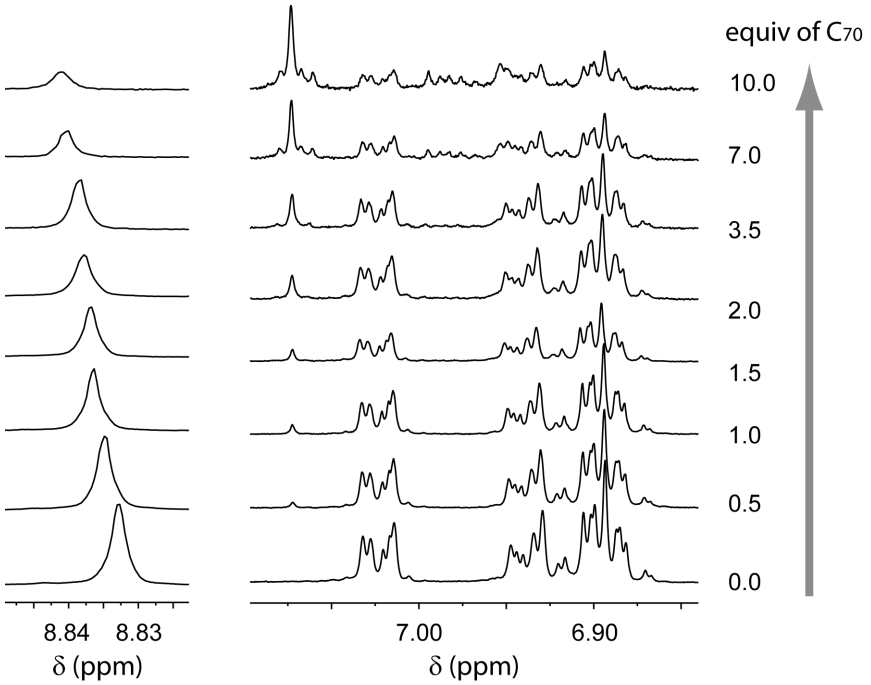

Figure 3.8: Expanded ^{1}H NMR spectra monitoring the titration of TTFAQ-AQ **6** (8.0 mM in 1:1 benzene-d_6/CS_2) with C_{70} fullerene (from 0.0 to 10.0 molar equiv).

energies (ΔE_{int}) of **6** with C_{60} and C_{70} via the *S*-face are 2–4 kcal/mol stronger than that of corannulene with C_{60} or C_{70} fullerene (ca. -17 kcal/mol) reported by Josa *et al.*[206] The *C*-face binding of **6** with fullerenes is about 5 kcal/mol weaker than the *S*-face. Interaction Gibbs free energies (ΔG_{int}) also corroborate that the *S*-face of **6** is a more thermodynamically favored binding site for fullerenes than the *C*-face. For each π-surface, its binding with C_{70} is about 1–2 kcal/mol more stable than with C_{60}.

To further understand the shape complementarity effect, noncovalent interactions in these complexes were investigated using the methods based on reduced density gradient analysis (RDG)[215] and quantum theory of atoms in molecules (QTAIM).[216] For the two complexes where C_{60} and C_{70} fullerenes are respectively bound to the *S*-face of TTFAQ-AQ **6**, the molecular conformations of **6** do not differ too much

Table 3.2: Interaction energies (in kcal/mol) of 1:1 complexes of **6** with C_{60} and C_{70} fullerenes calculated at the M06-2X/Def2-SVP level of theory

Entry	ΔE_{int} [a]	ΔH_{int} [b]	ΔE_{int} [c]
6/C_{60} (*S*-face)	-19.49	-18.90	-4.68
6/C_{60} (*C*-face)	-14.71	-13.84	-2.21
6/C_{70} (*S*-face)	-21.13	-20.55	-6.43
6/C_{70} (*C*-face)	-16.43	-15.60	-3.76

[a] ΔE_{int} = E(complex) – E(fullerene) – E(**6**), where E is the total electronic energy with zero-point energy (ZPE) corrections. [b] ΔH_{int} = H(complex) – H(fullerene) – H(**6**), where H is the enthalpy with ZPE corrections. [c] ΔE_{int} = G(complex) – G(fullerene) – G(**6**), where G is the Gibbs free energy with ZPE corrections.

(see Figure 3.9A and C). The RDG isosurfaces of these two complexes reveal that the interactions of **6** with C_{60} and C_{70} fullerenes have the entire π-surface of the benzo-TTFAQ segment engaged in the binding. QTAIM analysis revealed four (3,-1) bond critical points between C_{60} the dithiole groups of **6** and hence confirmed that the dithiole rings, particularly the sulfur atoms, are the major contributors to the *S*-face/C_{60} binding. In the *S*-face/C_{70} binding mode, eight bond critical points are involved and the active binding units in **6** encompass both dithiole and benzo groups. This result clearly illustrates the reason for **6** to bind with C_{70} more strongly than C_{60}; that is, the relatively deep cavity of *S*-face matches well the oblong shape of C_{70} and hence allows for more intimate concave-convex interactions.

The binding modes of **6** with fullerenes via the *C*-face, however, show more noticeable differences in the molecular shape of **6**. As can be seen in Figure 3.9B and D, the central pentacene unit adopts a greater degree of curvature in binding with C_{60}

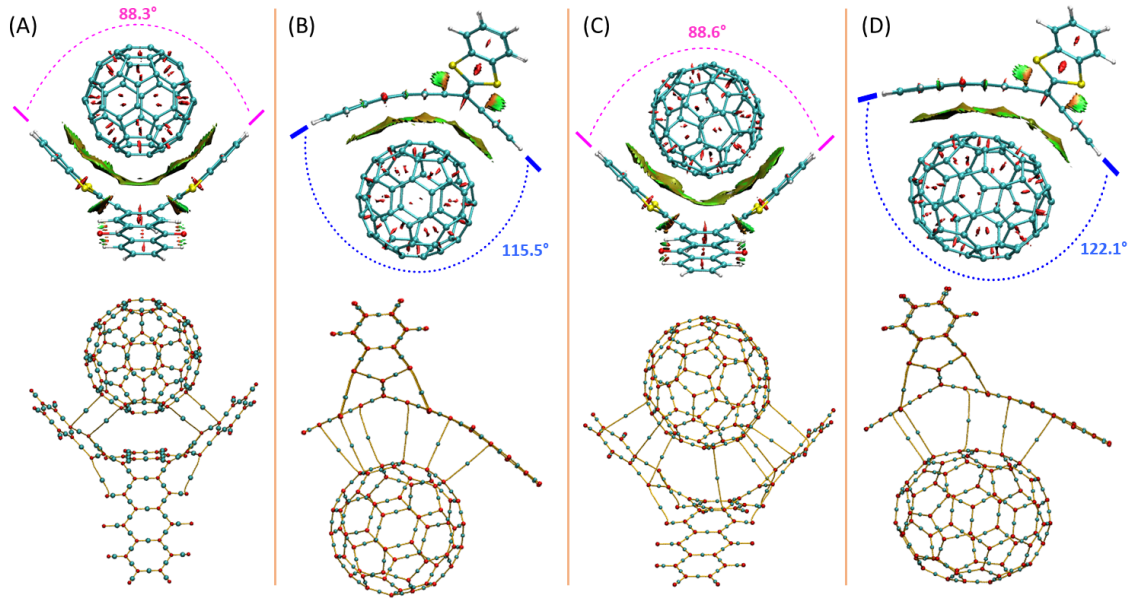

Figure 3.9: Optimized 1:1 complexes of TTFAQ-AQ **6** with (A) C_{60} via *S*-face, (B) C_{60} via *C*-face, (C) C_{70} via *S*-face, and (D) C_{70} via *C*-face. The top row shows molecular structures with RDG isosurfaces at 0.50 au and interplanar angles between terminal phenyl rings of the *S* and *C*-faces.The bottom row depicts molecular graphs with bond paths (orange-color lines) and (3,1) bond critical points (cyan-color dots). Calculations were performed at the M06-2X/Def2SVP level of theory.

via the *C*-face, indicating that the kinked *C*-face of **6** matches the oblong shape of C_{70} in a much better degree than the spherical shape of C_{60}. The RDG isosurface analysis indicates that the majority of the π-surface of the kinked anthracene is involved in intimate π–π stacking with fullerene. QTAIM analysis shows that the *C*-face binds with C_{60} and C_{70} in a similar way. Overall, the *S*-face of TTFAQ-AQ **6** is more selective for C_{70} fullerene, while the *C*-face shows similar affinity for C_{60} and C_{70} fullerenes.

3.3 Conclusions

In summary, we report herein the synthesis of a new class of donor-acceptor systems based on a π-fused TTFAQ-AQ framework. The molecular structural, electronic, and electrochemical redox properties of three TTFAQ-AQ derivatives were characterized. Featuring a double curved conformation with two extended concave π-surfaces, benzoannulated TTFAQ-AQ **6** showed the ability to co-crystallize with oblong-shaped C_{70} fullerene, forming highly organized 3-dimensional supramolecular networks in the solid state. Regardless of their opposite electronic nature, the two π-surfaces of **6** both interact attractively with C_{70} through intimate concave-convex interactions. Computational modeling studies confirmed that TTFAQ-AQ **6** affords stronger interaction energies and better shape complementarity with C_{70} than C_{60} fullerene. In particular, the deep cavity of *S*-face in **6** is more discriminatory in binding with C_{70} fullerene, rendering **6** a selective supramolecular partner for C_{70} fullerene. To our knowledge, the co-crystal of **6**/C_{70} presents the first example of ordered supramolecular assemblies constructed by fullerene and a redox-active donor-acceptor partner. Our designed TTFAQ-AQs offer the access to more fullerene-based crystalline materials with redox activity and charge-transfer properties. We anticipate TTFAQ-AQ/fullerene hydrid materials will find application in advanced electronic and optoelectronic devices.

3.4 Experimental

3.4.1 Materials and Methods

Chemicals and reagents were procured from commercial suppliers and used directly without purification. All reactions were conducted in standard, dry glassware. Evaporation and concentration were carried out with a rotary evaporator. Flash column chromatography was performed with 240-400 mesh silica gel, and thin-layer chromatography (TLC) was carried out with silica gel F254 covered on plastic sheets and visualized by UV light. Melting points (m.p.) were measured using an SRS OptiMelt melting point apparatus and are uncorrected. ^{1}H and ^{13}C NMR spectra were measured on a Bruker Avance III 300 MHz multinuclear spectrometer. Chemical shifts (δ) are reported in ppm downfield relative to the signals of the internal reference $SiMe_4$ or residual solvent (CH_2Cl_2: δ_H = 5.32 ppm, δ_C = 54.0 ppm; $CHCl_3$: δ_H = 7.24 ppm, δ_C = 77.0 ppm). Coupling constants (J) are given in Hz. Infrared spectra (IR) were recorded on a Bruker Alfa spectrometer. High-resolution APPI-TOF MS analysis was done on a GCT premier Micromass Technologies instrument. UV-Vis absorption spectra were measured on a Cary 6000i spectrophotometer. Cyclic voltammetric (CV) analysis was carried out in a standard three-electrode setup, where a glassy carbon electrode was used as the working electrode, a Pt wire as the counter electrode, and Ag/AgCl as the reference. The experiments were controlled by a BASi Epsilon potentiostat.

Single-crystal X-ray diffraction (SCXRD) data was collected at 100(2) K on an XtaLAB Synergy-S, Dualflex, HyPix-6000HE diffractometer using Cu K_α radiation (λ = 1.5406 Å). The crystal was mounted on nylon CryoLoops with Paraton-N. The

data collection and reduction were processed within CrysAlisPro (Rigaku OD, 2019). A multi-scan absorption correction was applied to the collected reflections. Using OLEX2,[154] structures were solved with the SHELXT structure solution program[155] using intrinsic phasing and refined with the SHELXL refinement package[156] using Least Squares minimization. All non-hydrogen atoms were refined anisotropically and the organic hydrogen atoms were generated geometrically.

DFT computational modeling were performed using the Gaussian 16 software package.[157] Molecular geometries of TTFAQ-AQs **4a**, **4b**, and **6** and supramolecular complexes of **6** and C_{60}/C_{70} fullerenes were optimized in the gas phase at the M06-2X/Def2-SVP level of theory. The optimized geometries were subjected to frequency calculations at the same level to validate they are energy minima (without imaginary frequencies) as well as to obtain thermodynamic energies. TD-DFT calculations of TTFAQ-AQs **4a**, **4b**, and **6** were performed on its optimized geometries at the CAM-B3LYP/6-311+G(2d,p) level of theory. Molecular structures and frontier molecular orbitals were visualized by the ChimeraX software package.[217] Analysis of noncovalent interactions based on reduced density gradient (RDG) isosurfaces and QTAIM theory were computed using the Multiwfn program[218] and the results were visualized by the VMD software package.[219]

3.4.2 Synthesis and Characterization

Synthesis of 7,12-bis(dibromomethylene)pentacene-5,14(7*H*,12*H*)-dione (2)

Triphenylphosphine (7.73 g, 29.5 mmol) and carbon tetrabromide (4.89 g, 14.8 mmol) were dissolved in toluene (30 mL). The mixture was stirred at rt under an atmosphere of N_2 for 20 min. Then pentacene-5,7,12,14-tetraone (**1**) (1.00 g, 2.95 mmol) was added and the resulting mixture was heated with an oil bath at reflux for 24 h. The progress of the reaction was monitored via TLC analysis to ensure starting material **1** to be completely consumed. Upon completion, the reaction solution was subjected to vacuum filtration. The filtrate was concentrated *in vacuo* and the residue was subjected to silica flash column chromatography (CH_2Cl_2/hexanes, 1:1 v/v) to afford compound **2** as a yellow solid (1.25 g, 1.92 mmol, 65%). mp: 205–215 °C. IR (neat): 3065, 1670, 1582, 1332, 951, 690 cm^{-1}. ^1H NMR (300 MHz, CD_2Cl_2): δ 8.77 (s, 2H), 8.30 (dd, J = 5.7, 3.3 Hz, 2H), 7.91 (dd, J = 6.0, 3.3 Hz, 2H), 7.84 (dd, J = 5.7, 3.3 Hz, 2H), 7.38 (dd, J = 6.0, 3.3 Hz, 2H). $^{13}C\{^1H\}$ NMR (75 MHz, CD_2Cl_2): δ 182.2, 141.1, 138.5, 135.1, 134.4, 133.5, 131.5, 127.9, 127.7, 127.2, 126.6, 93.2, 53.8. HRMS (APPI, positive mode): m/z calcd for $C_{24}H_{11}{}^{79}Br_4O_2$ $[M + H]^+$: 650.7452, found: 650.7451. X-Ray (CCDC 2068078).

Synthesis of 7,12-bis(4,5-bis(methylthio)-1,3-dithiol-2-ylidene)pentacene-5,14(7*H*,12*H*)-dione (4a)

A solution of compound **2** (0.100 g, 0.153 mmol) and 4,5-bis(methylthio)-1,3-dithiole-2-thione **3a** (0.0940 g, 0.415 mmol) in isopropanol (15 mL) was bubbled with N_2 under

constant stirring. After 10 min tetrabutylammonium hydroxide (1 M in MeOH, 1.52 mL, 1.52 mmol) was added in one portion, resulting in the formation of a green solution which turned to black gradually. The resulting solution was heated with an oil bath at 80 °C for 2 h and the reaction was continued overnight at rt. Dark brown solid precipitate was formed which was collected by suction filtration and purified using column chromatography (ethyl acetate/hexanes, 1:4 v/v), which resulted in pure compound **4a** (0.056 g, 0.081 mmol, 53%) as a dark brown solid. mp: > 205 °C (decomp). IR (neat): 3056, 2960, 2921, 2848, 1674, 1581, 1477, 1450, 1416, 1260, 1080, 1024 cm^{-1}. ^1H NMR (300 MHz, $CDCl_3$): δ 8.46 (s, 2H), 8.33 (dd, J = 5.8, 3.3 Hz, 2H), 7.81 (dd, J = 5.8, 3.3 Hz, 2H), 7.62 (dd, J = 5.9, 3.3 Hz, 2H), 7.36 (dd, J = 5.8, 3.3 Hz, 2H), 2.41 (s, 6H), 2.40 (s, 6H). $^{13}C\{^1H\}$ NMR (75 MHz, $CDCl_3$): δ 182.6, 139.7, 136.2, 134.1, 134.0, 133.7, 130.9, 127.2, 126.9, 126.4, 126.4, 125.5, 123.9, 122.2, 19.2. HRMS (APPI, positive mode): m/z calcd for $C_{32}H_{22}O_2S_8$ $[M]^+$: 693.9385, found: 693.9368. X-Ray (CCDC 2087913).

Synthesis of 7,12-bis(4,5-bis(decylthio)-1,3-dithiol-2-ylidene)pentacene-5,14(7*H*,12*H*)-dione (4b)

A solution of compound **2** (0.100 g, 0.153 mmol) and 4,5-bis(decylthio)-1,3-dithiole-2-thione **3b** (0.219 g, 0.459 mmol) in isopropanol (15 mL) was bubbled with N_2 under stirring. After 10 min tetrabutylammonium hydroxide (1 M in MeOH, 1.52 mL, 1.52 mmol) was added in one portion. A dramatic color change from yellow to green and then black was observed. The reaction mixture was heated with an oil bath at 80 °C for 2 h and then cooled to rt. The mixture was kept stirring at rt until TLC analysis showed the consumption of starting material **2**. The reaction solution

was concentrated *in vacuo* and the residue was subjected to column chromatography (ethyl acetate/hexanes, 1:5 v/v) to afford pure compound **4b** (0.118 g, 0.0980 mmol, 64%) as a dark brown semi-solid. IR (neat): 3045, 2980, 2950, 1678, 1570, 1465, 1450, 1420, 1250, 1075, 1020 cm^{-1}. ^1H NMR (300 MHz, $CDCl_3$): δ 8.50 (s, 2H), 8.34 (dd, J = 5.9, 3.3 Hz, 2H), 7.80 (dd, J = 5.9, 3.4 Hz, 2H), 7.65 (dd, J = 5.8, 3.3 Hz, 2H), 7.34 (dd, J = 5.8, 3.3 Hz, 2H), 2.84–2.80 (m, 8H), 1.66–1.61 (m, 7H), 1.26–1.23 (m, 54H), 0.87–0.83 (m, 15H). $^{13}C\{^1H\}$ NMR (75 MHz, $CDCl_3$): δ 181.5, 138.9, 135.5, 133.1, 133.0, 132.7, 129.8, 126.1, 126.0, 125.7, 125.6, 124.4, 122.9, 120.5, 35.4, 30.9, 28.6, 28.53, 28.50, 28.3, 28.1, 27.5, 21.7, 13.1. HRMS (APPI, positive mode): m/z calcd for $C_{68}H_{94}O_2S_8$ $[M]^+$: 1198.5019, found: 1198.4985.

Synthesis of 7,12-bis(benzo[*d*][1,3]dithiol-2-ylidene)pentacene-5,14(7*H*,12*H*)-dione (6)

A solution of compound **2** (0.100 g, 0.153 mmol) in 1,4-dioxane (4 mL) was bubbled with N_2 for 10 min to remove oxygen. Under stirring and N_2 protection, 1,2-dithiobenzene **5** (0.0660 g, 0.470 mmol) was slowly added to the solution. After stirring for 5 min, tetrabutylammonium hydroxide (1 M in MeOH, 0.918 mL, 0.918 mmol) was added in one portion, resulting in the formation of a dark purple solution. This mixture was stirred at rt for another 3 h, and then diluted with methanol (50 mL). The diluted solution was quickly heated with an oil bath at reflux for 5 min, and then cooled down to rt. Brownish purple solid precipitate was formed, which was collected by suction filtration and purified via silica flash column chromatography (ethyl acetate/hexanes, 1:4 v/v) to afford pure compound **6** (0.0760 g, 0.123 mmol, 81%) as a dark purple solid. mp: $>$ 235 °C (decomp). IR (neat): 3056, 1670, 1568,

1520, 1453, 1332, 1284, 1162, 1042, 955, 713 cm^{-1}. ^{1}H NMR (300 MHz, CD_2Cl_2): δ 8.55 (s, 2H), 8.25 (dd, $J = 5.7$, 3.3 Hz, 2H), 7.78–7.73 (m, 4H), 7.35 (dd, $J = 5.7$, 3.3 Hz, 2H), 7.25–7.20 (m, 4H), 7.09–7.06 (m, 4H). $^{13}C\{^{1}H\}$ NMR (75 MHz, CD_2Cl_2): δ 182.5, 140.3, 136.9, 134.7, 134.6, 134.1, 133.8, 131.0, 127.0, 126.9, 126.2, 125.8, 124.1, 122.2, 121.4, 121.2. HRMS (APPI, positive mode): m/z calcd for $C_{36}H_{19}O_2S_4$ $[M + H]^+$: 611.0262, found: 611.0257. X-Ray (CCDC 2036902).

Chapter 4

Donor–Acceptor Fluorophores and Macrocycles Built Upon Wedge-Shaped π–Extended Phenanthroimidazoles

The contents of this chapter were published as a full paper in *J. Org. Chem.*, **2023**, *88*, 3451–3465. Contributions of authors are described below: Maryam F. Abdollahi is the first author, who carried out synthesis of phenanthroimidazole derivatives, growth of the single crystals and co-crystal, and relevant spectroscopic characterizations. She also contributed to the manuscript preparation and editing.

Prof. Yuming Zhao is the supervisor of M. F. Abdollahi, who helped develop the concepts and design of this project. Prof. Zhao is the corresponding author of this paper.

Note that compound numbering in this chapter differs from previous chapters. In this chapter, the compounds are numbered in the same way as those in the publication.

4.1 Introduction

Small-molecule organic fluorophores, owing to their ease of synthesis, tunable photophysical properties, and good thermal stability, have found extensive applications in electroluminescence, chemical sensing, and bioimaging.[12,17,220–228] Among the vast array of organic fluorophores reported in the literature, phenanthrene-based molecular systems have attracted considerable attention in recent years, because of their appealing luminescent properties, such as versatile liquid and solid-state fluorescence, long emission lifetimes, and high quantum yields.[133,229–232] 1*H*-phenanthro[9,10-*d*]imidazole (herein referred to as **PI**, Figure 4.1) is a heterocyclic derivative of phenanthrene, in which a 1,3-imidazole ring is fused with the 9,10 C–C bond of phenanthrene. As such, the **PI** molecule possesses a planar $\pi-$delocalized framework that gives rise to rich (opto)electronic activities.

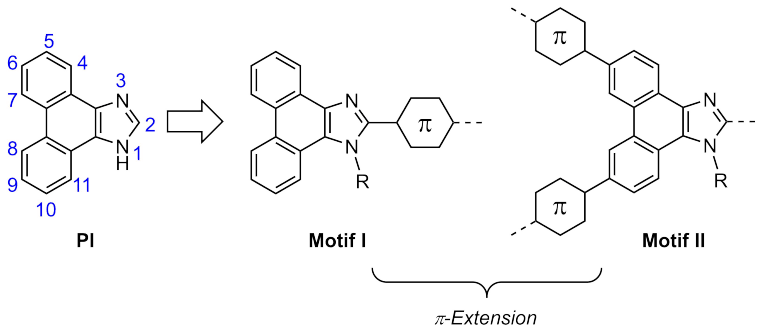

Figure 4.1: Structures of phenanthroimidazole (**PI**) and two of its $\pi-$extended motifs.

Synthetically, the **PI** core can be prepared through the condensation reaction

of phenanthrene-9,10-dione with an aldehyde and an amine partner under acidic conditions.[124,233] This condensation approach has led to a large number of π-extended **PI** derivatives, in which the imidazolyl moiety is functionalized with various aryl groups at the 2 position (motif I, in Figure 4.1). Moreover, the imidazolyl N–H group can be readily substituted with an alkyl or aryl group to further modify solubility and intermolecular aggregation behavior.[233,234] **PI**-containing functional materials so far reported in the literature are predominantly derivatives based on motif I, many of which have found applications in fluorescent and phosphorescent organic light emitting diodes (OLEDs), ratiometric fluorescent probes, fluorescent photo-switches, and medicines.[124,134,235–239] On the other hand, the **PI** group contains active sites on the phenanthrene side, through which $\pi-$extensions can also be made. Of particular interest is the aryl-functionalization at the 6 and 9 positions (motif II, Figure 4.1). For example, Lee and co-workers in 2016 prepared 6,9-diphenanthryl and 6,9-dipyrenyl substituted **PI** derivatives as high-performance OLED materials.[124] In 2018, Kothavale *et al.* reported that 6,9-diphenyl substitution on **PI** resulted in red-shifted emission and enhanced fluorescence quantum yields.[133] Clearly, the 6,9-functionalization is an appealing approach for generating novel electroluminescent **PI** materials; however, **PI** derivatives of this type are scant. To address this deficiency, we have recently carried out a synthetic study aiming at generating 6,9-functionalized $\pi-$extended **PI** derivatives as functional molecular building blocks for fluorescent and redox-active $\pi-$conjugated materials. We were particularly intrigued by the wedge-shaped conformation arising from the 6,9-functionalization pattern, which could conceivably lead to more complex molecular architectures, such as molecular tweezers, coiled $\pi-$conjugated oligo-/polymers, and shape-persistent macrocycles. It

is noteworthy that the **PI** system shows charge transfer (CT) behavior, where the phenanthrene and imidazole units play the roles of electron donor (D) and acceptor (A), respectively.[133,240,241] Covalent attachment of other D/A groups to the backbone of **PI** can create multiple D/A fluorophores that show tunable CT emissions useful for electroluminescence applications.[133,242] Moreover, the redox properties of **PI** derivatives have allowed efficient redox mediators to be developed for electrochemical reactions.[243–245]

Based on the aforementioned considerations, we set up to investigate a new class of D/A-substituted **PI** derivatives through the 6,9-functionalization approach (i.e., motif II type) in order to develop new **PI**-based molecular materials for luminescence and electrochemical applications. Our molecular design has been mainly focused on the use of 1,3-dithiafulvenes (DTFs) as redox-active end groups to functionalize the **PI** unit (see Scheme 4.1A). DTF is a five-membered heterocycle showing excellent electron-donating properties and redox activity.[246–248] Over the past decade, DTF has been extensively used as a molecular building block in the development of stimuli-responsive polymers,[249] molecular switches and wires,[250,251] shape-persistent macrocycles,[252] and chemical sensors.[246,252,253] In addition to redox properties, DTF exhibits a facile reactivity towards oxidative dimerization,[254,255] rendering it a versatile synthetic handle for C–C bond forming and corresponding $\pi-$elongation. As illustrated in Scheme 4.1B, an aryl-substituted DTF can undergo a single electron transfer under oxidative conditions to yield a DTF radical cation. Dimerization of two DTF radical cations followed by a double deprotonation step leads to the formation of a tetrathiafulvalene vinylogue (TTFV) product. It is worth mentioning that TTFV is a $\pi-$extended analogue of the well-known organic electronic

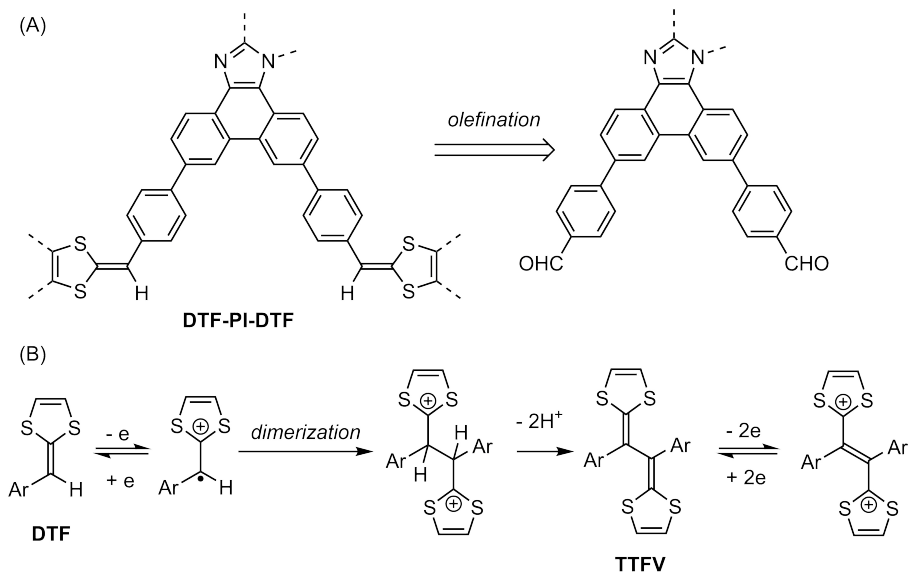

Scheme 4.1: (A) Our designed bis(DTF)-functionalized **PI** and its immediate precursor via retrosynthetic analysis. (B) Reaction mechanism for the oxidative dimerization of an aryl-substituted DTF.

material, tetrathiafulvalene (TTF).[168] The increased $\pi-$units in TTFV makes it a better electron donor than DTF. As such, TTFV can be reversibly oxidized at a lower oxidation potential relative to that of DTF.[80,115]

In this thesis, we have carried out studies on the class of DTF-functionalized **PI** derivatives as illustrated in Scheme 4.1A. Synthetically, these compounds can be directly obtained from olefination reactions of corresponding aldehyde precursors, which are also of interest to us, since they represent **PI**s substituted with electron-withdrawing (aldehyde) groups. Comparative analysis of both types of **PI** derivatives should lead to better understanding of the substitution effects on electronic, redox, and photophysical properties. The reactivity of DTF end groups was expected to yield $\pi-$extended oligomeric and macrocyclic products, which contain TTFV units in their molecular backbones. Previous studies have demonstrated that TTFV-based

molecular tweezers and macrocycles can act as supramolecular hosts for binding electron-deficient arenes and fullerenes.[115] In this context, the synthesis of TTFV-**PI** hybrids was also targeted using the DTF-functionalized **PI**s as building blocks, in order to explore their applications in supramolecular chemistry. Our detailed synthetic and characterization results are described in the following sections.

4.2 Results and discussion

4.2.1 Synthesis

Our initial synthetic attempt towards the wedge-shaped DTF-functionalized **PI** is illustrated in Schemes 4.2. At first, 3,6-dibromophenanthrene-9,10-dione (**2**) was prepared through the reaction of phenanthrene-9,10-dione (**1**) with bromine at an elevated temperature in the presence of dibenzoyl peroxide.[256] Compound **2** was then subjected to the condensation reaction with benzaldehyde (**3**) and ammonium acetate in acetic acid to give imidazole product **4** in a good yield. Suzuki-Miyaura cross-coupling of compound **4** and *p*-formylphenylboronic acid pinacol ester (**5**) was subsequently carried out, leading to dialdehyde-substituted **PI 6** in 69% yield. With **6** in hand, it was expected that a phosphite-promoted olefination reaction[181] with 1,3-dithiole-2-thiones (**7**)[257,258] would give the bis(DTF)-substituted **PI 8**. Nevertheless, the olefination performed in the presence of $P(OMe)_3$ at 130 °C did not afford the desired product **8**. Instead, the reaction yielded a significant amount of yellow-colored precipitates, the chemical structure(s) of which could not be clearly elucidated due to insolubility.

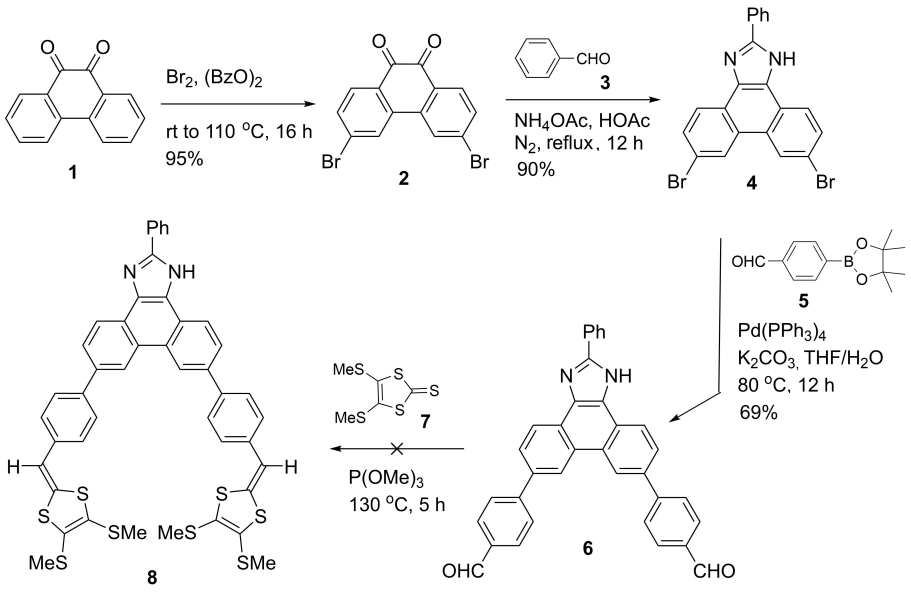

Scheme 4.2: Synthetic efforts towards bis(DTF)-functionalized **PI 8**.

The imidazolyl N–H is known to show acidity ($pK_a \approx 14$),[259] which was assumed to be the main reason for the failed synthesis of bis(DTF)-substituted **PI 8**. Based on this reasoning, we then envisioned that blockage of the free imidazolyl N–H site with an alkyl or aryl substituent would circumvent the problems encountered in the synthesis of **8**. To achieve this, a modified synthetic approach was adopted as illustrated in Scheme 4.3. In the first step of this synthesis, aniline was introduced to the condensation reaction with phenanthrenedione **2**, benzaldehyde, and ammonium acetate in acetic acid. The condensation reaction gave *N*-phenylated **PI 10** in 69% yield. Compound **10** underwent double Suzuki-Miyaura cross coupling reactions with phenylboronic acid or boronate **5**, respectively, to yield compounds **11** and **12** in good yields. Compound **12** contains two benzaldehyde groups, which were subsequently converted into two DTF substituents through a phosphite-promoted olefination reaction. As shown in Scheme 4.3, the olefination reaction was conducted

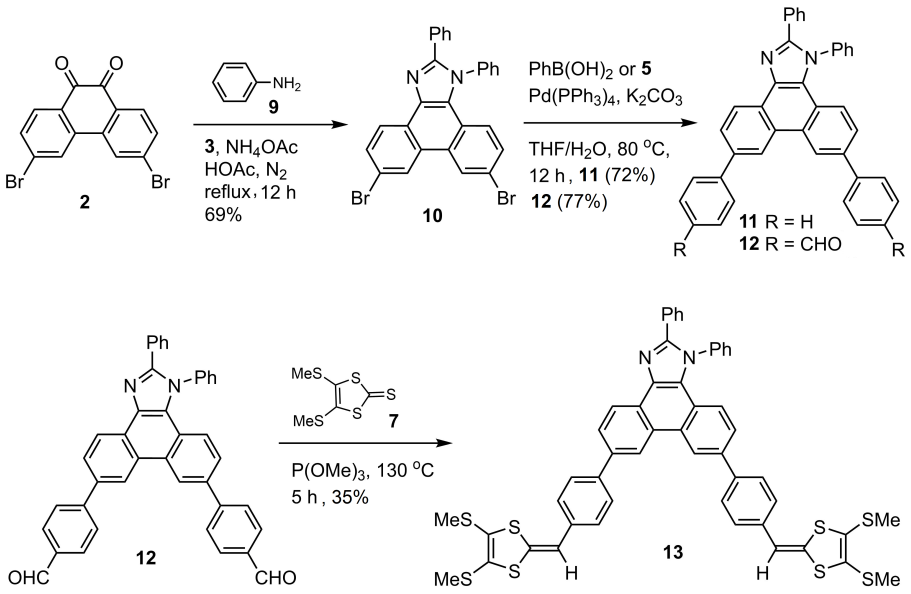

Scheme 4.3: Synthesis of bis(DTF)-functionalized **PI 13**.

in $P(OMe_3)$ at 130 °C for 5 h, giving the bis(DTF)-substituted **PI 13** in 35% yield. The yield of **13** was moderate because significant side reactions occurred along with the olefination reaction, likely due to phosphite-mediated couplings of aldehydes.[260] The acquisition of diphenyl-substituted **PI 11**, on the other hand, offered a model **PI** system for comparative analyses in subsequent characterization studies.

Bis(DTF)-substituted **PI 13** was then subjected to an iodine-induced oxidative coupling reaction[252] in order to achieve further π-extended derivatives. In principle, the oxidative coupling of **13** may result in two different types of products, acyclic oligo-/polymers and macrocycles. In view of the macrocyclization of other wedge-shaped bis(DTF)-substituted arenes observed in our previous studies,[252] the formation of macrocyclic products in the oxidative coupling of **13** was anticipated to be favored. As shown in Scheme 4.4, the oxidative coupling of **13** was conducted by adding **13** to an iodine solution in CH_2Cl_2 at room temperature under stirring.

The reaction mixture immediately turned into a dark green color. After a period of 15 min, the reaction was quenched by addition of an aqueous $Na_2S_2O_3$ solution. MALDI-TOF MS analysis of the reaction mixture showed the formation of oligomeric products ranging from dimer to tetramer. It was also observed that a certain amount of insoluble substances were formed, which are possibly due to higher oligomers or polymers. Thin-layer chromatographic (TLC) analysis revealed that a significant product of this reaction was a soluble yellow-color compound **14**, which was subsequently isolated from the reaction mixture by silica column chromatography. ^{1}H NMR analysis of **14** showed that the two vinylic proton signals of **13** at 6.53 and 6.49 ppm were absent after the reaction. A range of proton signals similar to those aromatic signals of **13** were observed in the ^{1}H NMR spectrum of **14**, but their line shapes were considerably broadened. MALDI-TOF MS analysis of **14** confirmed that it is a cyclic dimer resulting from a two-fold DTF oxidative coupling reaction **13**. Statistically, the cyclodimerization of **13** could end up with two regioisomers **14a-b** as shown in Scheme 4.4. These two isomers formed an inseparable mixture in a total yield of 38%.

4.2.2 Crystal Structural Properties of PI 12

Single crystals of **PI 12** were carefully grown through slow evaporation of a solution of pure **12** in ethyl acetate at room temperature, allowing the elucidation of its molecular structure and solid-state packing properties by X-ray diffraction (XRD) analysis. Figure 4.2A illustrates the molecular structure of **12** measured from its single crystal. Herein, the central **PI** moiety is nearly planar, while the two benzaldehyde units at

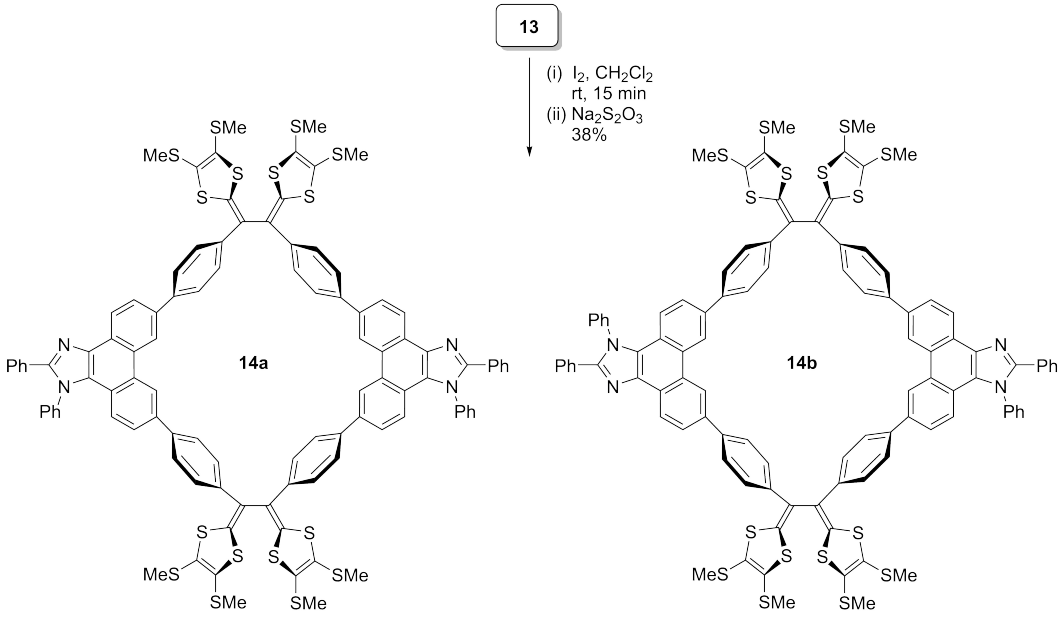

Scheme 4.4: Preparation of TTFV-**PI** macrocycles **14** through oxidative coupling of bis(DTF)-**PI 13**.

the 6 and 9-positions show moderate torsional angles (14.0° and 35.7°) with respect to the **PI** unit. The two phenyl groups linked to the N1 and C2 positions of the imidazole unit show much greater torsion angles (41.3° and 79.2°) to the central **PI** group to minimize steric clashing. Such conformational features suggest that phenyl substitution at the 6 and 9 positions of the **PI** unit can readily bring about flat extended π-frameworks, hence resulting in enhanced resonance effects. Wedge-shaped molecules of **12** are packed in a triclinic P-1 space group in the single crystalline state. As can be seen in Figure 4.2B, the packing diagram of **12** shows an organized motif in which the slipped stacking mode plays a dominant role. The detailed slip-stacked geometry for **12** is depicted in Figure 4.3A and B. This stacking mode is predominantly dictated by the interactions between benzaldehyde groups and phenanthryl moieties. It is also noteworthy that the two adjacent molecules

of **12** in this packing motif adopt an anti-parallel orientation with an interplanar distance of 3.69 Å, which is slightly longer than the van der Waals diameter of carbon. Imidazolyl N atoms do not contribute significantly to intermolecular interactions in the crystal packing of **12**. However, it is conceivable that the unsubstituted N atom in the imidazolyl unit shows basicity, allowing it to be readily protonated by an acid to form imidazolium ion. In the field of crystal engineering, imidazolium moieties have been frequently paired with dicarboxylic acids to form various supramolecular networks assembled through hydrogen bonding interactions.[261] To shed light on this aspect, we grew a co-crystal of **12** with oxalic acid through vapor diffusion of methanol into an ethyl acetate solution of **12** with oxalic acid (at ca. 1:1 mole ratio) at room temperature. X-ray structural analysis of the co-crystal of **12** and oxalic acid shows that the imidazolyl C=N site is protonated to form an imidazolium ion, which in turn attracts an oxalate dianion through an N–H$\cdots$O hydrogen bond. The H$\cdots$O distance is 1.98 Å and the N–H$\cdots$O bond angle is 161.6°. Apart from this hydrogen bonding interaction, the oxalate dianion also forms hydrogen bonds with nearby neutral oxalic acid molecules. As shown in Figure 4.3C and D, the slipped stacking mode of protonated **12** in the co-crystal is considerably different from that observed in the single crystal of **12**. Herein, the two adjacent molecules of **12**, although still retaining an anti-parallel orientation, are brought closer as a result of the formation of hydrogen bonds with oxalate dianion. Viewing from the top of the π-stack, one can see a zig-zag shaped supramolecular scaffold (see Figure 4.3C). The cavities created by the assembly of protonated **12** in the co-crystal allow oxalate ions and oxalic acid molecules to assemble into linear hydrogen bonded supramolecular wires as illustrated in Figure 4.4. Overall, our crystallographic results indicate that wedge-

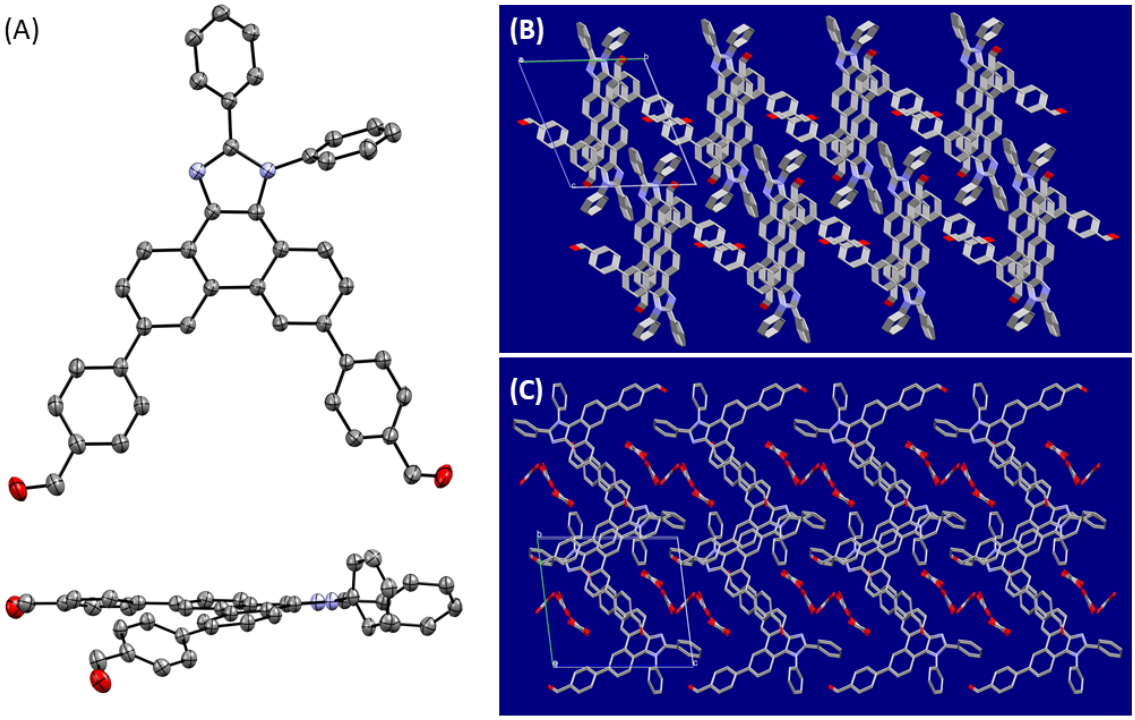

Figure 4.2: (A) ORTEP drawings (50% of probability ellipsoids) **12** viewed from different perspectives (CCDC 2210552). (B) Packing diagram of the single crystal of **12** viewed along the *b* axis of the unit cell. (C) Packing diagram of the co-crystal of **12** and oxalic acid viewed from the *b* axis of the unit cell (CCDC 2210553). Hydrogen atoms are omitted for clarity.

shaped **PI** molecules with aryl-extension at the 6,9-positions can serve as shape-persistent building blocks for preparing organic (co)crystals using hydrogen bonding as a key driving force.

4.2.3 Electrochemical Redox Activities

The electrochemical redox properties of bis(DTF)-substituted **PI 13** and related TTFV-**PI** macrocycles **14** were investigated by cyclic voltammetry. As shown in

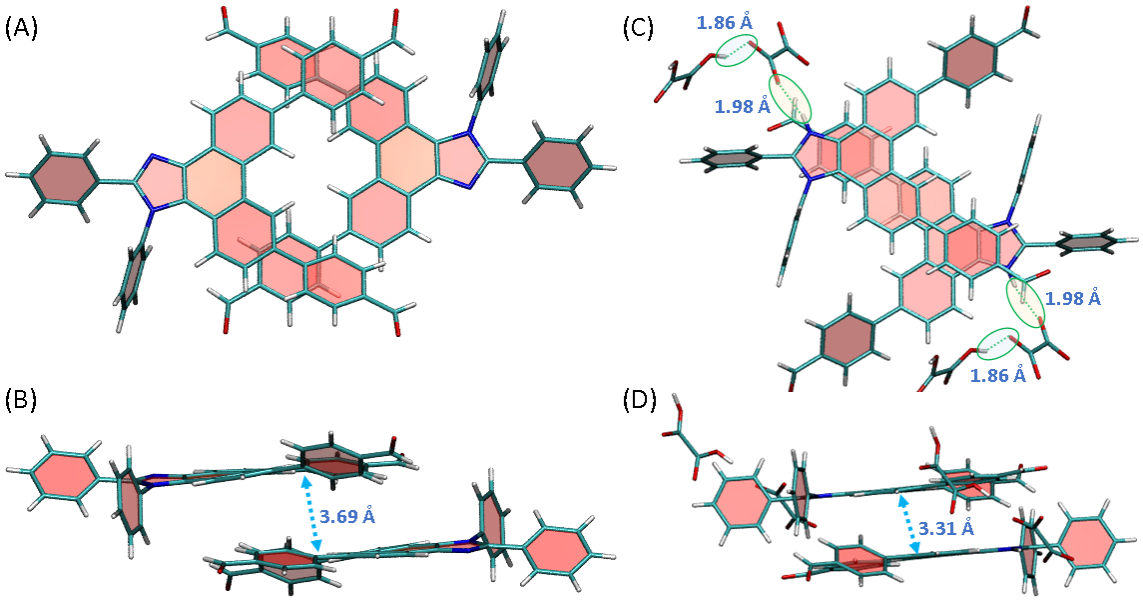

Figure 4.3: (A) and (B): Intermolecular $\pi - \pi$ stacking mode in the single crystal of **12** viewed from different perspectives. (C) and (D): Intermolecular $\pi - \pi$ stacking mode in the co-crystal of **12** and oxalic acid viewed from different perspectives.

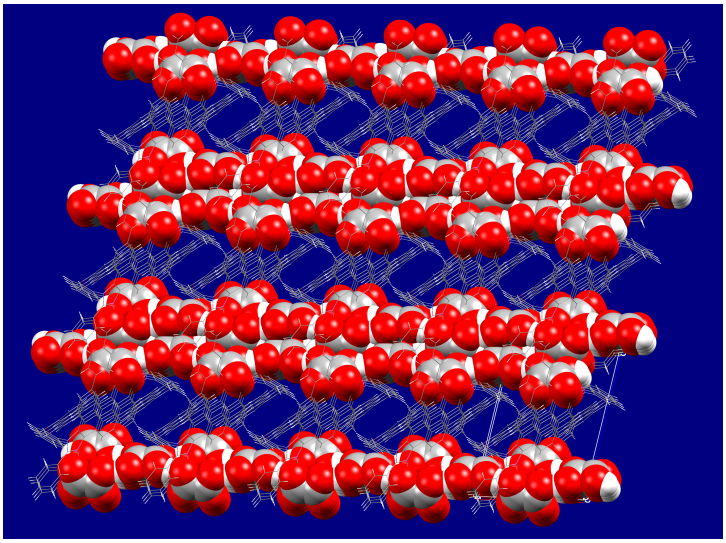

Figure 4.4: Packing diagram of the co-crystal of **12** and oxalic acid viewed along the *c*-axis of the unit cell. The molecules of **12** are depicted by the framework model and oxalic acids are represented by the space-filling model.

Figure 4.5, the cyclic voltammogram of **13** shows an anodic peak at +0.85 V in the forward scan of the first cycle. The oxidation potential is consistent with those measured for mono-DTF-substituted arenes,[248,254] indicating that the two DTF groups in **13** undergo simultaneous single-electron transfers at the same potential, resulting in the formation of two DTF radical cations. In the first reverse scan, a cathodic peak rises at +0.49 V. The potential of this peak is much lower than the reduction potential of a typical DTF radical cation.[248] Given the facile reactivity of DTF cations toward oxidative dimerization, it is reasonable to propose that bis(DTF)-**PI 13** upon electrochemical oxidation quickly forms dicationic TTFV products on the working electrode surface through oxidative coupling reactions. In the following cycles of CV scans, the DTF oxidation peak is gradually attenuated and somewhat shifted to lower voltages. The cathodic peak due to TTFV shows only a slight shift in potential, but its intensity increases significantly. Along with these changes, a new anodic peak emerges at +0.63 V, which is consistent with the oxidation potentials of typical TTFV compounds.[254,262] After multiple cycles of CV scans, a polymer thin film was observed to be deposited on the surface of the working electrode. The thin film may contain products resulting from various oxidative coupling reactions of bis(DTF)-**PI 13**, such as TTFV-containing macrocyclic oligomers and acyclic oligo-/polymers. The film was then subjected to exhaustive rinsing with CH_2Cl_2 to remove soluble oligomers and macrocyclic products. After this treatment, the remaining film was constituted by only insoluble polymeric products (herein denoted as poly-[**13**]). CV scans of the thin film of poly-**13** in CH_2Cl_2 in the presence of Bu_4NBF_6 revealed a reversible redox wave pair at E_{pa} = +0.66 V and E_{pc} = +0.62 V, respectively. It is interesting to note that the CV profile of TTFV-**PI** macrocycles **14** measured

under the same experimental conditions shows a quasi-reversible redox wave pair (E_{pa} = +0.70 V and E_{pc} = +0.50 V). The different CV patterns between poly-**13** and macrocycles **14** corroborate that the thin film of poly-**13** contains polymeric products rather than macrocycles. The results also indicate that compound **13** would show different reactivities when subjected to chemical and electrochemical oxidative conditions, respectively.

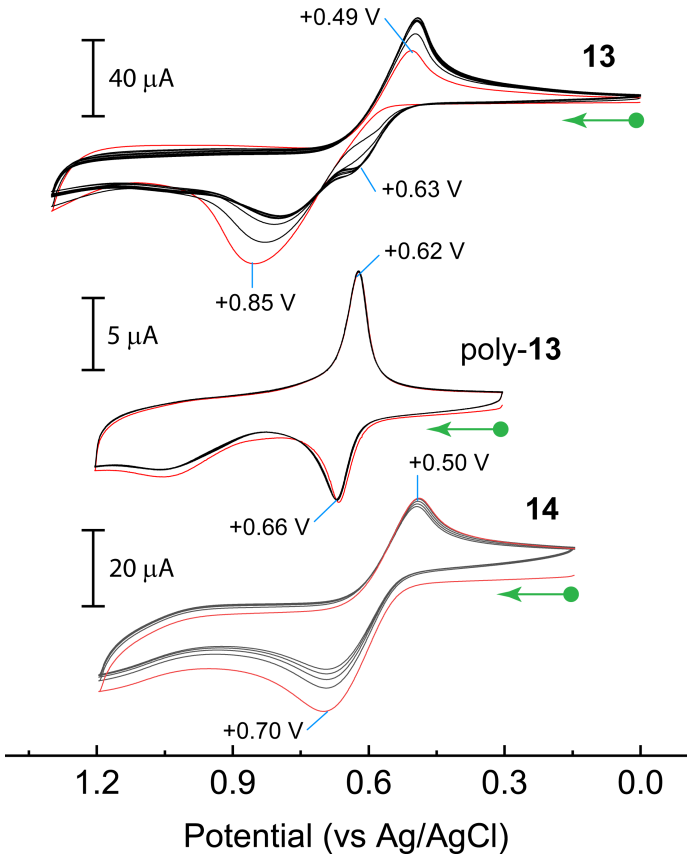

Figure 4.5: Cyclic voltammograms of (A) **13**, (B) thin film of poly-**13**, and (C) **14** measured in CH_2Cl_2 with Bu_4NBF_6 (0.1 M) added as electrolyte. Working electrode: glassy carbon; counter electrode: Pt wire; reference electrode: Ag/AgCl; scan rate: 0.10 V/s. The arrows indicate the starting points and directions of CV scans. The first cycle of CV scans is highlighted by red color.

4.2.4 Electronic Absorption and Emission Properties

The electronic absorption properties of **PI** derivatives **11**–**14** were examined by UV-Vis spectroscopy (see Figure 4.6). The absorption spectrum of diphenyl-substituted **PI 11** shows two significant $\pi \rightarrow \pi^*$ bands at 276 and 329 nm, respectively. In addition to these bands, a relatively weak long-wavelength absorption shoulder is seen at 376 nm, the origin of which can be assigned to HOMO $\rightarrow$ LUMO and HOMO $\rightarrow$ L + 1 transitions according to TD-DFT calculations (see Table S-3, Appendix III for details). The absorption spectrum of dibenzaldehyde-substituted **PI 12** shows a number of peaks at 261, 288, 304, 343, and 378 nm. The lowest-energy peak of **12** at 378 nm is similar to that of **11**; however, the lowest-energy band edge of **12** is notably red-shifted relative to that of **11**. This shift can be attributed to the electron-withdrawing effect of the two aldehyde groups in **12**. Bis(DTF)-substituted **PI 13** exhibits two absorption bands at 280 and 382 nm, and its lowest-energy band edge is more red-shifted than that of **12**. The observed trend of spectral shift indicates that the electron-donating DTF group has a stronger effect on lowering electronic transition energy than the electron-withdrawing aldehyde group does. The lowest-energy absorption band of TTFV-**PI** macrocycles **14** is similar to that of DTF-substituted **13**, suggesting that the TTFV unit makes little contribution to the π-electron delocalization on the macrocyclic structure. Previous studies have shown that TTFV favors a twisted nonplanar conformation[115,263] which inhibits efficient orbital overlap across its entire π-framework.

PI derivatives **11** and **12** show strong fluorescence with quantum yields (Φ_F) of 24% for **11** and 32% for **12** determined in CH_2Cl_2. The fluorescence spectra of

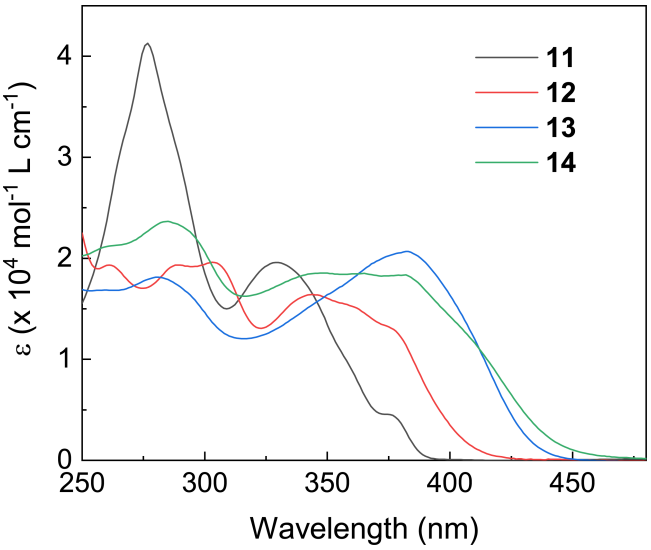

Figure 4.6: UV-Vis absorption spectra of **11**–**14** measured in CH_2Cl_2 at room temperature.

PI 11 measured in various organic solvents reveal insignificant solvatofluorochromic effects (Figure 4.7A). For example, the maximum emission wavelength (λ_{em}) of **11** is slightly shifted from 398 to 412 nm when the solvent is changed from nonpolar hexane to strongly polar DMSO. For dibenzaldehyde-substituted **PI 12**, the solvatofluorochromic effects are quite significant (see Figure 4.7B and 4.8B). In nonpolar aromatic solvents such as benzene and *p*-xylene, compound **12** gives a maximum emission wavelength (λ_{em}) at 438 nm. In polar organic solvents, the values of λ_{em} are shifted to much longer wavelengths (e.g., 490 nm in acetone and 511 nm in DMSO).

The solvatofluorochromic effects exhibited by **12** were then examined using the Lippert-Mataga plot (Figure 4.8A), in which the Stokes shifts ($\Delta\nu$) of **12** measured in different solvents are plotted against solvent orientation polarizability (Δf). The Lippert-Mataga equation[264,265] describes the relationship between the observed $\Delta\nu$

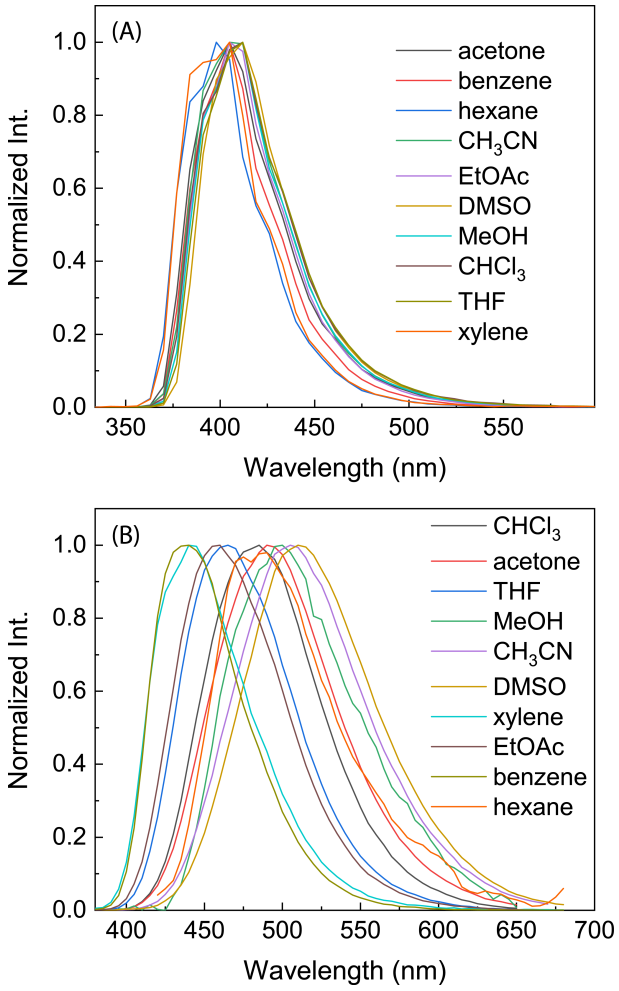

Figure 4.7: Normalized fluorescence spectra of (A) **11** and (B) **12** measured in various organic solvents at room temperature.

of a fluorophore in different solvents as follows,

$$\Delta\nu = \frac{2(\mu_e - \mu_g)^2}{hca^3} \times [(\frac{\epsilon_r - 1}{2\epsilon_r + 1}) - (\frac{n^2 - 1}{2n^2 + 1})] + C \tag{4.1}$$

where μ_e and μ_g are the dipole moments in the excited and ground states, respectively, h is the Planck's constant, c is the speed of light, a is the Onsager radius, ϵ and n are the relative permittivity and refractive index of the solvent, respectively, and C is the observed Stokes shift of the fluorophore in a non-solvatochromic environment. In the Lippert-Mataga equation, the following term denotes the solvent orientation polarizability (Δf).

$$\Delta f = (\frac{\epsilon_r - 1}{2\epsilon_r + 1}) - (\frac{n^2 - 1}{2n^2 + 1}) \tag{4.2}$$

As can be seen in Figure 4.8A, the plot of $\Delta\nu$ versus Δf for **12** shows a trend generally agreeing with the Lippert-Mataga equation; however, the linearity of this plot is poor. It has also been noted that the emission of **12** in hexane appears to be aberrant. Hexane as a nonpolar solvent should induce an emission wavelength similar to those observed from other nonpolar solvents. To our surprise, the emission spectrum of **12** in hexane resembles those measured in relatively polar solvents such as $CHCl_3$ and acetone, with a maximum emission wavelength at 484 nm. It was also observed that the solubility of **12** in hexane was very low, hence leading us to speculate that aggregation in hexane may occur significantly to cause such red-shifted emission. To study the aggregation properties, we analyzed a solution of **12** in hexane by dynamic light scattering (DLS) experiments. The DLS results clearly show that nano- and micro-scale particles are suspended in the solution of **12** in hexane. The

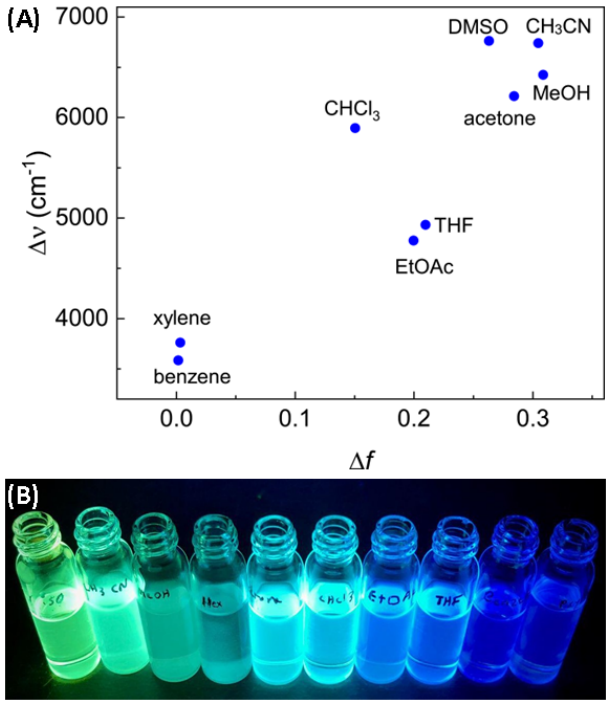

Figure 4.8: (A) Plot of Stokes shift ($\Delta\nu$) against solvent orientation polarizability (Δf) for compound **12**. (B) Photographic image of **12** in various solvents under the irradiation of a UV lamp. Solvent from left to right are: DMSO, CH_3CN, MeOH, hexane, acetone, $CHCl_3$, EtOAc, THF, benzene, *p*-xylene.

sizes of these particles follow two major distributions, with average diameters of 868 nm and 17.0 micron, respectively (see Figure S-19, Appendix III).

4.2.5 Chemiluminescent Response of 13 to Singlet Oxygen

In contrast to **PI** derivatives **11** and **12**, bis(DTF)-substituted **PI 13** shows very weak fluorescence in organic solvents (e.g., $\Phi_F = 4.6\%$ in CH_2Cl_2). The substantially quenched fluorescence of **13** can be attributed to the electron-donating effects of the DTF groups in **13**, which facilitate a non-radiative photoinduced electron transfer (PET) process once the compound is photoexcited. Previous studies have shown

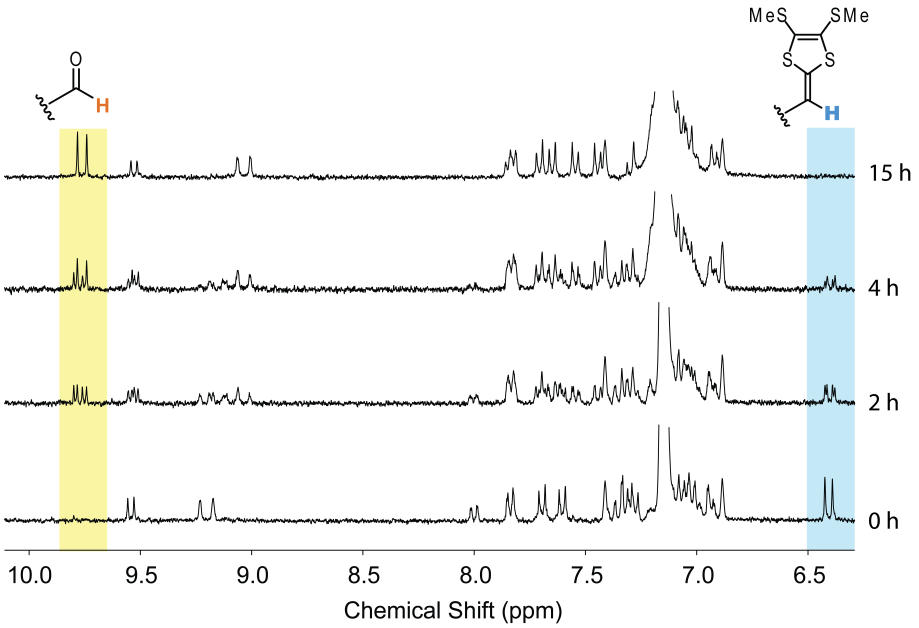

Figure 4.9: Partial ^{1}H NMR spectra (300 MHz, C_6D_6) monitoring the mixture of **13** (1.06×10^{-3} M) and C_{60} fullerene (2.50×10^{-3} M) at varied times.

that when a DTF is linked to an arene, the electron-rich vinyl bridge is susceptible to oxidative C=C bond cleavage by singlet oxygen (Scheme 4.5B).[177,212] Singlet oxygen can be generated by photosensitizers such as C_{60} and C_{70} fullerenes, since fullerenes can be readily excited to stable triplet states under visible light, which in turn photosensitize triplet oxygen into singlet oxygen.[212,266] In our experiments, a mixture of compound **13** and C_{60} fullerene in C_6D_6 was prepared and let exposed to air and ambient light. The composition of this solution was examined by ^{1}H NMR analysis at varied times (see Figure 4.9). Within a few hours, the NMR spectral patterns of **13** had already shown dramatic changes. It is noteworthy that the two vinyl protons of **13** give rise to two singlets at 6.42 and 6.39 ppm, respectively. Their intensities were observed to gradually reduce with increasing time after mixing with fullerene. On the other hand, a group of signals at 9.80, 9.79, 9.76, and 9.74 ppm

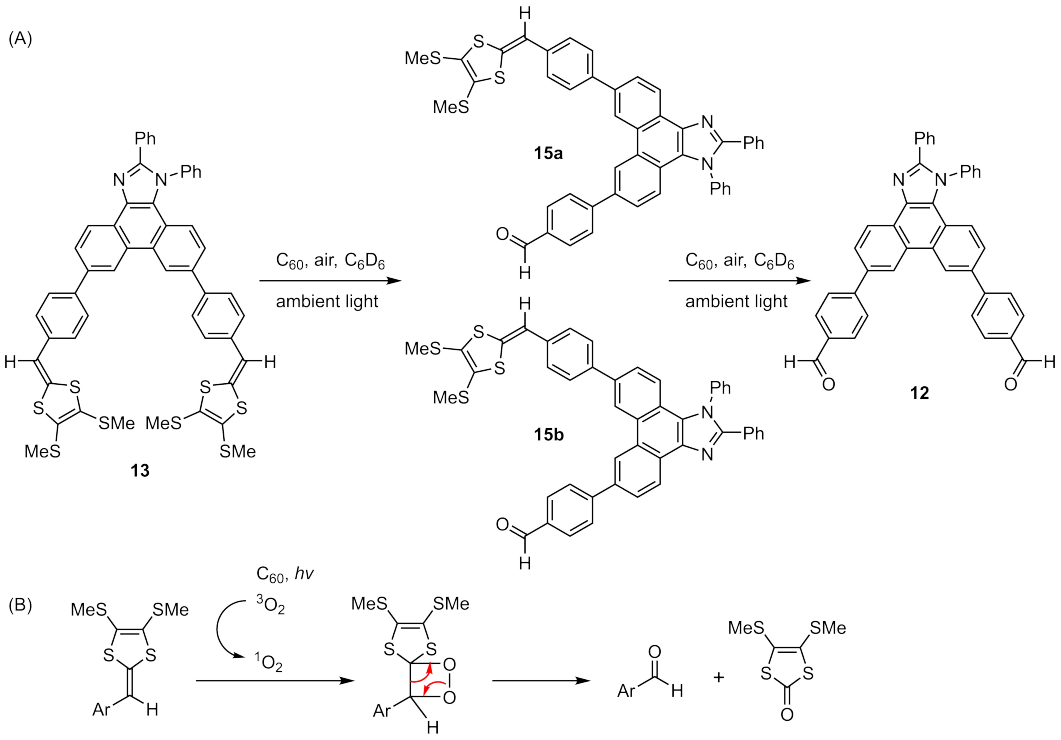

Scheme 4.5: (A) Oxidative cleavage reactions of the C=C bonds in **13**. (B) Mechanism for the oxidative cleavage reaction of an aryl-DTF with singlet oxygen promoted by photosensitization of C_{60} fullerene.

emerged. When the time reached 15 hours and longer, the vinyl proton signals of **13** completely disappeared and two new sharp singlets at 9.78 and 9.74 ppm were clearly seen. The final ^{1}H NMR spectral patterns match those of **12**, indicating a complete transformation from **13** to **12** via the singlet oxygen-induced C=C bond cleavage reactions illustrated in Scheme 4.5A. During the first few hours, there were actually four different aldehyde proton signals (9.80–9.74 ppm) observed, indicating that the oxidative cleavages of the two DTF groups in **13** took place in a stepwise manner; that is, two intermediates **15a** and **15b** were formed first and then both were converted into the final product **12**.

The formation of **12** through oxidative C=C cleavage of **13** could also be detected by fluorescence analysis. A substantial increase in fluorescence was observed when the mixture of **13** and C_{60} in benzene was let stand under air and ambient light for a certain period of time. This outcome can be rationalized by a chemiluminescent mechanism, in which the oxidative C=C cleavage converts non-fluorescent **13** into highly fluorescent **12**. To examine the detailed fluorescence changes associated with this process, fluorescence spectra were measured at varied times to monitor the solutions of **13** in benzene in the presence of C_{60} and C_{70} fullerenes, respectively. As shown in Figure 4.10A and C, the observed fluorescence intensity increases strongly with increasing time. The growing emission band shows a maximum peak at 437 nm. Given that the increased fluorescence is mainly due to the formation of compound **12**, the observed fluorescence enhancement can be treated as linearly proportional to the concentration of **12**. As such, kinetic curves for the photosensitized oxidative cleavage reactions can be established by plotting the fluorescence enhancement against the time (see Figure 4.10B and D). The resulting kinetic data could be well fitted with the first-order kinetic equation given below,

$$F - F_0 = Ae^{kt} + C$$

where F and F_0 are fluorescence intensities at the maximum emission wavelength (λ_{em} = 437 nm) determined at a time and the initial point, respectively, while k is the rate constant (h^{-1}), t is the time (h), A and C are constants. The kinetic curve fitting analysis yields rate constants of 0.228 ± 0.011 h^{-1} (with C_{60}) and 0.348 ± 0.015 h^{-1} (with C_{70}). It is reasonable to consider that the first-order kinetic behavior is

because the generation of singlet oxygen in the solution phase is much faster than the oxidative cleavage steps. As such, the measured overall rate constant (k) equals the rate of the rate-limiting step, which is the oxidative cleavage reaction of the C=C bond. Considering that the quickly generated singlet oxygen would remain at a constant concentration throughout the reaction, the reaction rate is only linearly proportional to the concentration of the DTF reactant and hence exhibits an apparent first-order behavior. Since C_{70} fullerene shows stronger absorption in the visible region of the spectrum than C_{60} fullerene, it is reasonable to observe that C_{70} acted as a more effective photosensitizer than C_{60} under ambient light irradiation. Overall, the results of our fluorescence analysis demonstrate that bis(DTF)-**PI 13** is highly reactive to singlet oxygen. The chemiluminescent properties exhibited by **13** could lead to potential application in fluorescence sensing and imaging of singlet oxygen as well as other reactive oxidative species (ROS).[266]

4.2.6 Fluorescence Turn-On/Off Responses of TTFV-PI Macrocycles 14 to Fullerenes

TTFV-**PI** macrocycles **14** were observed to be weakly fluorescent in organic solvents ($\Phi_F = 3.3\%$ in CH_2Cl_2). Similar to the case of bis(DTF)-**PI 13**, the electron-donating TTFV moieties embedded in the macrocycle cause strong fluorescence quenching through photoinduced electron transfer from TTFV to **PI**. Unlike **PI 13**, however, the TTFV units in **14** do not exhibit significant reactivity towards singlet oxygen, which is evidenced by the observation that the mixture of **14** with C_{60} or C_{70} fullerene showed no changes in ^{1}H NMR spectral patterns after being exposed to air and

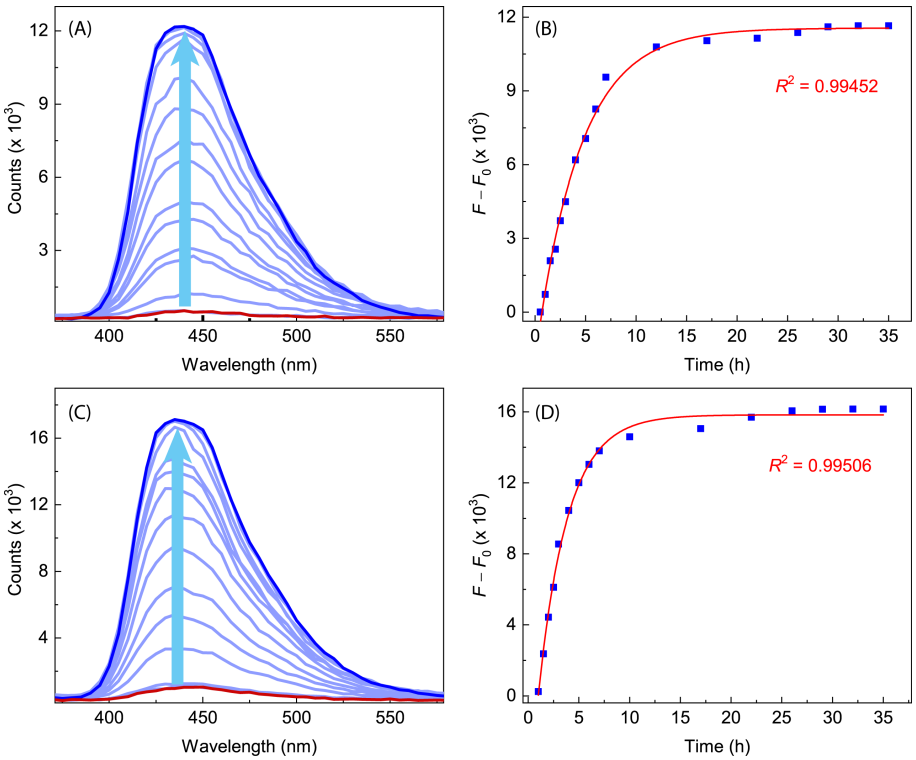

Figure 4.10: Fluorescence spectra monitoring solutions of **13** and fullerenes in benzene under air and ambient light conditions. (A) **13** (5.12×10^{-5} M) and C_{60} (7.20×10^{-5} M), (C) **13** (5.52×10^{-5} M) and C_{70} (8.40×10^{-5} M). The arrows indicate the trend of fluorescence change with increasing time. Plots of fluorescence enhancement ($F - F_0$) as a function of time for (B) the mixture of **13** and C_{60} and (D) the mixture of **13** and C_{70}. Data are fitted with a first-order kinetic equation (red traces).

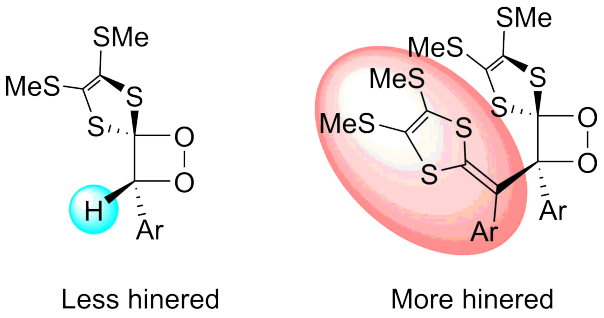

Figure 4.11: Comparison of the steric effects between proposed transition states for DTF and TTFV oxidative cleavage reactions.

ambient light for a sufficiently long period of time (see Figure S-14, Appendix III). The lack of oxidative C=C cleavage reactivity on **14** can be rationalized by the large steric hindrance around the vinyl groups in TTFV, which prohibits the C=C bonds of TTFV from effectively interacting with singlet oxygen; for example, if the oxidative cleavage undergoes a 1,2-dioxetane like transition state as proposed in Scheme 4.5B, one can envision that the association of TTFV with singlet oxygen would have to overcome a considerable amount of steric clashing (see Figure 4.11) to form such a transition state.

The mixing of TTFV-**PI** macrocycles **14** with fullerenes in the solution phase was found to result in interesting fluorescence turn-on/off properties. As shown in Figure 4.12A and C, titration of the solution of **14** in chlorobenzene with 0.95 molar equiv of C_{60} led to about 2.9-fold fluorescence increase at the maximum emission wavelength (459 nm), while addition of 2.65 molar equiv of C_{70} caused 2.7-fold fluorescence enhancement. The increased fluorescence can be rationalized by the non-covalent interactions between **14** with electron-deficient fullerene molecules. Molecular modelling studies suggest that **14** can offer a suitable π-cavity to host a

fullerene molecule through concave-convex $\pi-\pi$ interactions. As illustrated in Figure 4.13, such supramolecular interactions would make fullerene stay in close proximity to the TTFV moieties of **14**, hence facilitating photoinduced electron transfer from TTFV to fullerene.[115] In this way, the fluorescence quenching of the **PI** unit by TTFV is attenuated.

It is worth mentioning that the fluorescence turn-on behavior of **14** was observed only when fullerene was added in a relatively small amount. When the amount of fullerene surpassed a certain threshold (about 1.0 equiv for C_{60} or 2.6 equiv for C_{70}), the fluorescence change of **14** showed a decreasing trend with increasing addition of fullerene. To further understand this phenomenon, fluorescence titrations of **PI 11** with C_{60} and C_{70} were carried out. As shown in Figure 4.14, addition of fullerenes resulted in steady fluorescence quenching for **PI 11**. The amount of C_{60} (ca. 70.3 molar equiv) needed to completely quench the fluorescence of **11** is far greater than that of C_{70} fullerene (ca. 26.6 molar equiv), indicating that C_{70} is a stronger quencher than C_{60} for **PI 11**. Since the molecular structure of **11** resembles the fluorogenic **PI** moieties in macrocycles **14**, it is reasonable to propose that fullerenes can exert two opposite effects on the fluorescence properties of **14**. When the amount of fullerene is relatively small, photoinduced electron transfer from TTFV to fullerene plays a dominant role in the photophysics of **14**–fullerene supramolecular complexes, resulting in enhanced fluorescence with increasing addition of fullerene (i.e., fluorescence turn-on). When the amount of fullerene becomes relatively large, however, the quenching effect of fullerene on the fluorogenic **PI** units of **14** becomes dominant. As a result, the turn-off effect outweighs the turn-on effect, reverting the fluorescence of **14** to a decreasing trend with increasing addition of fullerene.

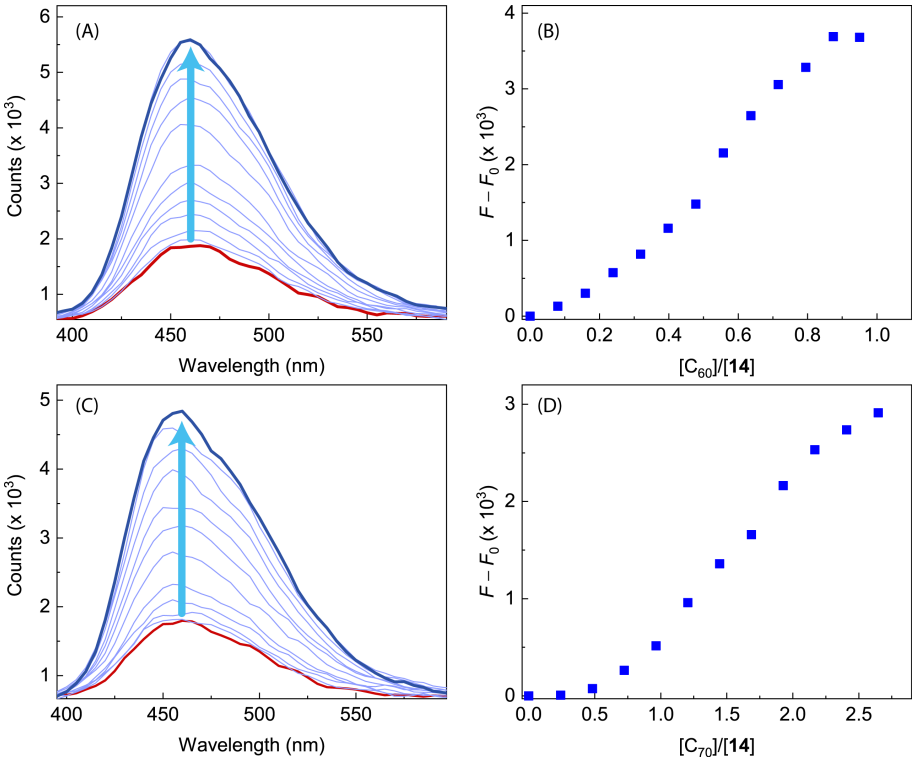

Figure 4.12: Fluorescence spectra of TTFV-**PI** macrocycles **14** monitoring the addition of (A) C_{60} fullerene (from 0.00 to 0.95 molar equiv) and (C) C_{70} fullerene (from 0.00 to 2.65 molar equiv) in chlorobenzene. The arrows indicate the trend of fluorescence change with increasing fullerene titration. Correlations of the fluorescence enhancement ($F - F_0$) of **14** with increasing addition of (B) C_{60} fullerene and (D) C_{70} fullerene.

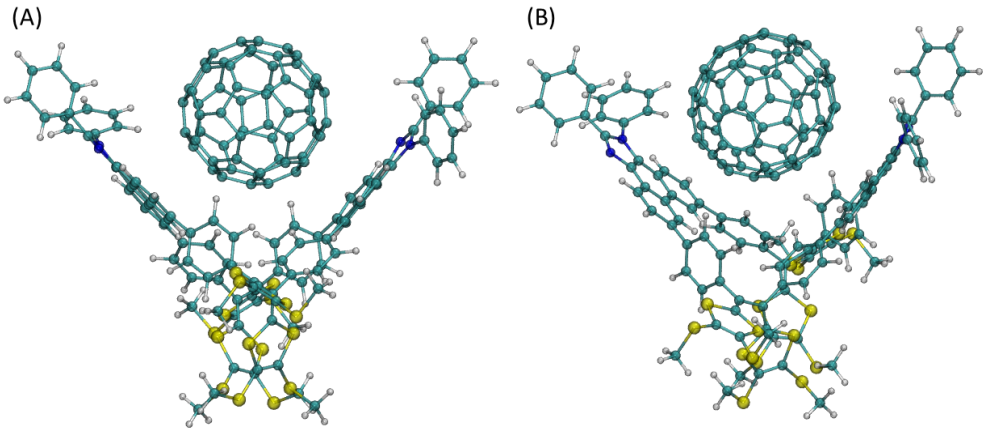

Figure 4.13: 1:1 Complexes of (A) **14b** and C_{60} fullerene and (B) **14b** and C_{70} fullerene. Structures were optimized by molecular mechanics calculations using the *MMFF* force field.

4.3 Conclusions

In conclusion, we have synthesized a new class of wedge-shaped **PI** derivatives through π-extension at the 6,9-positions of the **PI** core. The molecular structural and electronic properties of these **PI** derivatives have been systematically investigated by X-ray single crystal diffraction, cyclic voltammetric, UV-Vis absorption, and fluorescence spectroscopic analyses. Attachment of D/A groups at the ends of these molecules can effectively bring about versatile photophysical properties and electrochemical reactivities. The aldedye-functionalzed **PI** system exhibits strong solvatofluorochromic effects, making such type of fluorophore useful for fluorescence applications where large Stokes shifts are desired. On the other hand, the **PI** derivative with redox-active DTF end groups undergoes facile oxidative C=C cleavage when interacting with singlet oxygen. This reactivity points to potential applications in fluorescence sensing and imaging of singlet oxygen. We have also

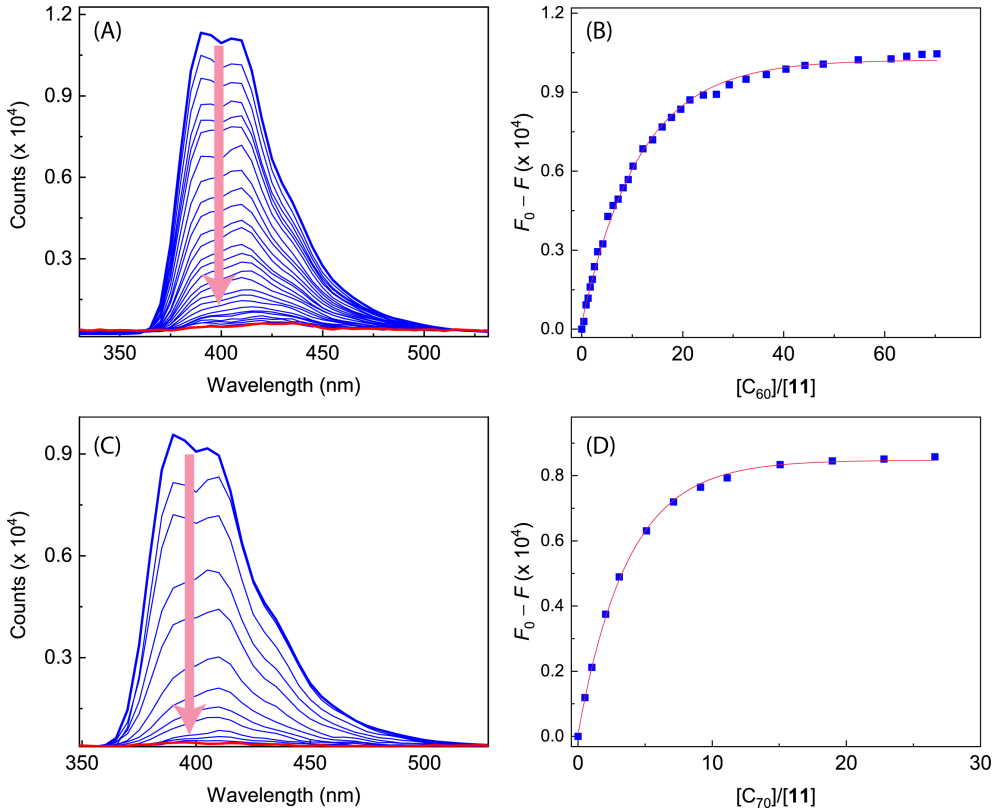

Figure 4.14: Fluorescence spectra of **PI 11** monitoring the addition with (A) C_{60} fullerene (from 0.00 to 70.3 molar equiv) and (C) C_{70} fullerene (from 0.00 to 26.6 molar equiv) in chlorobenzene. The arrows indicate the trend of fluorescence change with increasing fullerene titration. Correlations of the fluorescence quenching ($F_0 - F$) of **11** with increasing addition of (B) C_{60} fullerene and (D) C_{70} fullerene.

demonstrated the wedge-shaped **PI** group can be further extended through DTF oxidative coupling reactions to form macrocyclic products. In the case of TTFV-**PI 14**, fluorescence turn-on behavior was observed upon interacting with a certain amount of fullerenes. Detailed photophysical mechanisms related to this phenomenon awaits further investigation. Nonetheless, our current results suggest a molecular approach to regulate photoinduced electron/energy transfer processes taking place on the supramolecular assemblies of fullerene and TTFV-**PI** macrocycles. Further studies along this direction should yield valuable knowledge to advance the progress in organic photovoltaic and fluorescence sensing technologies.

4.4 Experimental

4.4.1 Materials and Methods

Chemicals were purchased from commercial suppliers and used directly without purification. Compounds **2** and **7** was prepared according to the methods previously reported.[256–258] Evaporation and concentration were performed using a rotary evaporator. Flash column chromatography was carried out through 240-400 mesh silica gel and thin-layer chromatography (TLC) via silica gel F254 covered on plastic sheets, which was visualized under UV irradiation. Melting points (m.p.) were measured using an SRS OptiMelt melting point apparatus. ^{1}H and ^{13}C NMR spectra were measured on a Bruker Avance III 300 MHz multinuclear spectrometer. Chemical shifts (δ) are reported in ppm downfield relative to the signals of the internal reference $SiMe_4$ or residual solvent (CH_2Cl_2: δ_H = 5.32 ppm, δ_C = 54.0 ppm; $CHCl_3$: δ_H =

7.24 ppm, δ_C = 77.0 ppm; C_6D_6: δ_H = 7.16 ppm, δ_C = 128.4 ppm; DMSO–*d6*: δ_H = 2.50 ppm, δ_C = 39.5 ppm; acetone–*d6*: δ_H = 2.05 ppm, δ_C = 29.9, 206.7 ppm). Coupling constants (J) are given in Hz. Infrared spectra (IR) were recorded on a Bruker Alfa spectrometer. MALDI-TOF MS analysis was performed on an ultraflex TOF/TOF instrumnet using 2-[(2*E*)-3-(4-*tert*-butylphenyl)-2-methylprop-2-enylidene]malononitrile (DCTB) as the matrix. High-resolution APPI-TOF MS analysis was performed using a GCT premier Micromass Technologies instrument. UV-Vis absorption spectra were analyzed through a Cary 6000i spectrophotometer.

Cyclic voltammetric (CV) analysis was carried out in a standard three-electrode setup, using a glassy carbon electrode as the working electrode (round shape, surface area = 7.609 mm^2), a Pt wire as the counter electrode, and Ag/AgCl as the reference electrode. The experiments were with a BASi Epsilon electrochemical workstation. The working electrode was polished with 1.0 micron alumina slurry on a polishing pad prior to use. Before CV scans, the sample solution was gently bubbled with argon flow for ca. 1 min to be deoxygenated. All CV scans were conducted at room temperature.

Solution-phase fluorescence spectra were measured on a Photon Technology International (PTI) QuantaMaster spectrofluorometer. Relative fluorescence quantum yields were determined by the following equation,

$$\Phi_F = \Phi_s \times \frac{I_s}{I_r} \times \frac{A_r}{A_s} \times \frac{n_s^2}{n_r^2} \tag{4.3}$$

where Φ_F is the fluorescence quantum yield, I is the integrated area under the emission profile, A is the absorbance at a particular excitation wavelength, n is the

refractive index of the medium. The subscripts s and r denote sample and reference, respectively. Quinine sulfate ($\Phi_F = 54.6\%$) was used as the reference.

Single-crystal X-ray diffraction (SCXRD) data was collected at 100(2) K on an XtaLAB Synergy-S, Dualflex, HyPix-6000HE diffractometer using Cu K_α radiation ($\lambda = 1.5406$ Å). The crystal was mounted on nylon CryoLoops with Paraton-N. The data collection and reduction were processed within CrysAlisPro (Rigaku OD, 2019). A multi-scan absorption correction was applied to the collected reflections. Using OLEX2,[154] structures were solved with the SHELXT structure solution program[155] using intrinsic phasing and refined with the SHELXL refinement package[156] using Least Squares minimization. All non-hydrogen atoms were refined anisotropically and the organic hydrogen atoms were generated geometrically.

DFT and TD-DFT computational analyses were performed using the Gaussian 16 software package.[157] Molecular geometries of **PI** derivatives **11**, **12**, and **13** were optimized at the M06-2X/Def2-SVP level of theory using the polarizable continuum model (PCM) taking the solvent (CH_2Cl_2) effects into account. The optimized geometries were subjected to frequency calculations at the same level to validate they are energy minima (without imaginary frequencies) as well as to obtain thermodynamic energies. TD-DFT calculations of **PI 11**, **12**, and **13** were performed at the PCM(CH_2Cl_2)//TD-M06-2X/6-311+G(2d,p) level of theory using their PCM(CH_2Cl_2)//M06-2X/Def2-SVP optimized geometries. Supramolecular assemblies of **14** with C_{60} and C_{70} fullerenes were optimized by molecular mechanics calculations implemented in Spartan'18 software (Wavefunction, Inc., Irvine, CA) using the *MMFF* force field.

4.4.2 Synthesis and Characterization

6,9-Dibromo-2-phenyl-1*H*-phenanthro[9,10-*d*]imidazole (4)

3,6-Dibromophenanthrene-9,10-dione (**2**) (1.50 g, 4.09 mmol), benzaldehyde (**3**) (0.652 g, 6.15 mmol), and ammonium acetate (3.90 g, 50.7 mmol) were dissolved in glacial acetic acid (25 mL). The reaction mixture was heated with an oil bath at reflux for 12 h under a N_2 atmosphere and then cooled down to rt. The resulting pale brown mixture was poured into methanol (50 mL) under stirring, yielding a crude product of **4** as brownish precipitates. Crude **4** was collected by vacuum filtration and then subjected to silica flash column chromatography (ethyl acetate/hexanes, 30:70 v/v) to afford pure compound **4** (1.67 g, 3.69 mmol, 90%) as a brown solid. mp: $>$ 315 °C (decomp). IR (neat): 3634, 3203, 3069, 2925, 2857, 1826, 1570, 1481, 1450, 1401, 1355, 1270, 1100, 1073, 1019, 961 cm^{-1}. ^1H NMR (300 MHz, DMSO-*d6*): δ 13.60 (s, 1H), 9.14 (s, 2H), 8.50 (d, J = 8.9 Hz, 2H), 8.29 (d, J = 7.2 Hz, 2H), 7.93 (s, 1H), 7.64–7.49 (m, 4H).$^{13}C\{^1H\}$ NMR (75 MHz, CD_2Cl_2): δ 150.3 (2 $\times$), 131.2, 130.5, 130.0, 129.5, 128.8, 128.0, 127.5, 127.2, 126.7, 126.4, 124.5, 121.9, 119.5, 119.4 (two carbon signals are missing due to coincidental overlaps). HRMS (APPI$^+$/TOF): *m/z*: $[M + H]^+$ calcd for $C_{21}H_{13}{}^{79}Br_2N_2$ 452.9425; found, 452.9444.

4,4′-(2-Phenyl-1*H*-phenanthro[9,10-*d*]imidazole-6,9-diyl)dibenzaldehyde (6)

To a solution of **4** (0.196 g, 0.433 mmol), and 4-(4,4,5,5-tetramethyl-1,3,2-dioxaborolan-2-yl)benzaldehyde (**5**) (0.300 g, 1.30 mmol) in THF (20 mL) and deionized water (7 mL) was added K_2CO_3 (0.240 g, 1.73 mmol). The reaction mixture was bubbled with N_2 flow for 10 min, and then $Pd(PPh_3)_4$ (0.025 g, 0.022

mmol) was added under stirring. The reaction mixture was heated with an oil bath at 80 °C for 12 h under a N_2 atmosphere. Upon completion, the reaction mixture was cooled down to rt and poured into brine (20 mL). The resulting mixture was extracted twice with CH_2Cl_2 (30 mL). The organic layers were combined, dried over $MgSO_4$, and evaporated under vacuum. The residue was subjected to silica column chromatography (ethyl acetate/hexanes 50:50 v/v) to give pure compound **6** (0.150 g, 0.298 mmol, 69%) as a light green powder. mp: 334–341 °C. IR (neat): 3612, 3301, 3052, 2820, 2718, 2052-1806, 1686, 1593, 1450, 1394, 1307, 1209, 1168, 1112, 1065, 950 cm^{-1}. ^1H NMR (300 MHz, DMSO-*d6*): δ 13.62 (s, 1H), 10.13 (s, 2H), 9.41 (d, J = 8.8 Hz, 2H), 8.74–8.70 (m, 2H), 8.36–8.08 (m, 12H), 7.66–7.51 (m, 3H). Due to poor solubility, $^{13}C\{^1H\}$ NMR of **6** could not be obtained. HRMS (APPI$^+$/TOF): *m/z*: $[M + H]^+$ calcd for $C_{35}H_{23}N_2O_2$, 503.1760; found, 503.1777.

6,9-Dibromo-1,2-diphenyl-1*H*-phenanthro[9,10-*d*]imidazole (10)

3,6-Dibromophenanthrene-9,10-dione (**2**) (1.00 g, 2.73 mmol), benzaldehyde (**3**) (0.652 g, 4.09 mmol), aniline (**9**) (0.373 mL, 4.09 mmol), and ammonium acetate (2.63 g, 34.1 mmol) were dissolved in glacial acetic acid (20 mL). The mixture was heated with an oil bath at reflux for 12 h under a N_2 atmosphere. The reaction mixture was cooled down to rt and then poured into methanol (60 mL), yielding crude product **10** as a brownish precipitates. Crude **10** was collected by vacuum filtration and then subjected to silica flash column chromatography (ethyl acetate/hexanes, 20:80 v/v) to afford pure compound **10** as a brown solid (1.00 g, 1.89 mmol, 69%). mp: > 220 °C (decomp). IR (neat): 3050, 2937, 1647, 1597, 1562, 1496, 1441, 1403, 1368, 1283, 1148, 1020, 945 cm^{-1}. ^1H NMR (300 MHz, acetone-*d6*): δ 9.09 (dd, J = 9.9, 2.0 Hz,

2H), 8.71 (d, J = 8.5 Hz, 1H), 7.94 (dd, J = 8.5, 1.8 Hz, 1H), 7.74–7.71 (m, 4H), 7.64 (dd, J = 7.2, 1.4 Hz, 2H), 7.50 (dd, J = 8.9, 1.9 Hz, 1H), 7.39–7.31 (m, 3H), 7.10 (d, J = 8.9 Hz, 1H). $^{13}C\{^1H\}$ NMR (75 MHz, acetone-*d6*): δ 138.4, 136.9, 130.9, 130.4, 130.2, 130.0, 129.3, 129.2, 129.0, 128.1, 127.2, 126.4, 124.4, 122.4, 122.0, 119.4, 119.0 (six carbon signals are missing due to coincidental overlaps). HRMS ($APPI^+$/TOF): *m/z*: $[M]^{+\cdot}$ calcd for $C_{27}H_{16}{}^{79}Br_2N_2$, 525.9680; found, 525.9681.

1,2,6,9-Tetraphenyl-1*H*-phenanthro[9,10-*d*]imidazole (11)

To a solution of **10** (0.400 g, 0.757 mmol) and phenylboronic acid (0.276 g, 2.271 mmol) in THF (40 mL) and deionized water (13 mL) was added K_2CO_3 (0.418 g, 3.028 mmol). After 10 min and under N_2 protection, $Pd(PPh_3)_4$ (0.044 g, 0.038 mmol) was added. The reaction mixture was stirred and heated with an oil bath at 80 °C for 12 h and then cooled down to rt. The reaction mixture was into brine (40 mL) and extracted twice with CH_2Cl_2 (50 mL). The organic layers were combined, dried over $MgSO_4$, and evaporated under vacuum. The residue was subjected to silica column chromatography (ethyl acetate/hexanes 20:80 v/v) to give pure compound **11** (0.285 g, 0.545 mmol, 72%) as a pale brown powder. mp: 265–272 °C. IR (neat): 3055, 2967, 1960- 1769, 1603, 1490, 1469, 1454, 1407, 1384, 1331, 1264, 1155, 1072 cm^{-1}. ^1H NMR (300 MHz, CD_2Cl_2): δ 8.98 (d, J = 1.9 Hz, 1H), 8.93 (d, J = 1.7 Hz, 1H), 8.79 (d, J = 8.4 Hz, 1H), 7.94 (dd, J = 8.3, 1.7, 1H), 7.80–7.76 (m, 2 H), 7.68–7.66 (m, 2H), 7.60–7.17 (m, 18H). $^{13}C\{^1H\}$ NMR (75 MHz, CD_2Cl_2): δ 151.1, 141.6, 141.0, 138.7, 138.3, 137.5, 137.2, 130.6, 130.2, 129.9, 129.4, 129.3, 129.1, 128.9, 128.8, 128.5, 128.3, 128.1, 127.5, 127.4, 127.3, 127.2, 126.7, 126.6, 125.6, 123.1, 122.4, 122.3, 121.7, 121.4 (one carbon signal is missing due to coincidental overlaps). HRMS

(APPI$^+$/TOF) m/z: $[M]^{+\cdot}$ calcd for $C_{39}H_{26}N_2$, 522.2096; found, 522.2095.

4,4′-(1,2-Diphenyl-1*H*-phenanthro[9,10-*d*]imidazole-6,9-diyl)dibenzaldehyde (12)

Compound **10** (0.800 g, 1.51 mmol), 4-(4,4,5,5-tetramethyl-1,3,2-dioxaborolan-2-yl) benzaldehyde (**5**) (1.05 g, 4.54 mmol), K_2CO_3 (0.840 g, 6.04 mmol), and $Pd(PPh_3)_4$ (0.087 g, 0.075 mmol) were reacted following the same procedures described in the synthesis of compound **11** to yield pure compound **12** (0.680 g, 1.17 mmol, 77%) as a greenish yellow powder. mp: 280–289 °C. IR (neat): 3060, 2951, 2823, 2734, 1741, 1692, 1593, 1563, 1493, 1450, 1308, 1213, 1170, 1071 cm^{-1}. ^1H NMR (300 MHz, $CDCl_3$): δ 10.12 (s, 1H), 10.09 (s, 1H), 9.06–8.98 (m, 3H), 8.07–8.00 (m, 7H), 7.91–7.88 (m, 2H), 7.66–7.56 (m, 8H), 7.34–7.29 (m, 4H). $^{13}C\{^1H\}$ NMR (75 MHz, $CDCl_3$): δ 191.9, 191.8, 151.7, 147.7, 147.0, 138.4, 137.7, 137.1, 136.2, 135.28, 135.20, 130.4, 130.3, 130.2, 130.0, 129.5, 129.4, 129.1, 129.0, 128.5, 128.3, 128.1, 127.9, 127.4, 126.9, 125.8, 123.8, 123.1, 122.9, 122.1, 121.7 (two carbon signals are missing due to coincidental overlaps). HRMS (APPI$^+$/TOF) m/z: $[M]^{+\cdot}$ calcd for $C_{41}H_{26}N_2O_2$, 578.1994; found, 578.1975.

6,9-Bis(4-((4,5-bis(methylthio)-1,3-dithiol-2-ylidene)methyl)phenyl)-1,2-diphenyl-1*H*-phenanthro[9,10-*d*]imidazole (13)

Dibenzaldehyde (**12**) (0.100 g, 0.173 mmol) and compound (**7**) (0.117 g, 0.518 mmol) were dissolved in $P(OMe)_3$ (6 mL) in a 25 mL round-bottom flask. The reaction mixture was heated with an oil bath to 130 °C for 5 h. Unreacted $P(OMe)_3$ was then removed through vacuum distillation, and the residue was subjected to silica flash

column chromatography (ethyl acetate/hexanes 25:75 v/v) to give pure compound **13** (0.056 g, 0.060 mmol, 35%) as a yellow powder. mp: > 160 °C (decomp). IR (neat): 3005, 2912, 1654, 1632, 1545, 1503, 1454, 1392, 1257, 1158 1014 cm^{-1}. ^1H NMR (300 MHz, $CDCl_3$): δ 9.01 (d, J = 1.3 Hz, 1H), 8.95 (d, J = 0.75 Hz, 1H), 8.78 (d, J = 8.3 Hz, 1H), 7.96 (dd, J = 8.6, 1.4 Hz, 1H), 7.81 (d, J = 8.2 Hz, 2H), 7.69 (d, J = 8.3 Hz, 2H), 7.59–7.47 (m, 8H), 7.35–7.17 (m, 8H), 6.53 (s, 1H), 6.49 (s, 1H), 2.39 (s, 3 H), 2.38 (s, 3H), 2.37 (s, 3H), 2.36 (s, 3H). $^{13}C\{^1H\}$ NMR (75 MHz, $CDCl_3$): δ 135.7, 130.2, 129.9, 129.3, 129.1, 128.4, 128.1 (2 ×), 127.4 (2 ×), 127.2, 124.7, 123.2, 18.86. HRMS ($APPI^+$/TOF) m/z: $[M + H]^+$ calcd for $C_{51}H_{39}N_2S_8$, 935.0879; found, 935.0892.

TTFV-PI macrocycles 14

To a solution of compound **13** (0.080 g, 0.085 mmol) in CH_2Cl_2 (30 mL) were added iodine chips (0.054 g, 0.213 mmol). The resulting dark green solution was stirred at rt for 15 min. An aqueous solution of satd $Na_2S_2O_3$ (90 mL) was then added and the resulting mixture was stirred at rt for another 15 min. A color change from dark green to yellow was observed during this process. The reaction mixture was extracted twice with CH_2Cl_2 (40 mL). The combined organic layers were dried over $MgSO_4$ and then concentrated under reduced pressure. The residue was subjected to silica flash column chromatography (CH_2Cl_2/hexanes 80:20 v/v) to yield macrocycles **14** as a yellow powder (0.031 g, 38%). mp: 255–293 °C. ^1H NMR (300 MHz, CD_2Cl_2): δ 8.93–8.75 (m, 9H), 7.95–7.92 (m, 3H), 7.78–7.49 (m, 47 H), 7.25–7.16 (m, 13H), 2.41–2.15 (m, 36 H). $^{13}C\{^1H\}$ NMR (75 MHz, CD_2Cl_2): δ 151.1, 138.5, 135.9, 130.2, 129.9, 129.3, 129.1, 128.1, 127.7, 127.4, 127.0, 126.5, 123.2, 122.1, 121.5, 18.79, 18.72,

18.5. HRMS (MALDI$^+$/TOF) *m/z*: $[M]^{+\cdot}$ calcd for $C_{102}H_{72}N_4S_{16}$, 1865.1322; found, 1865.1303.

Chapter 5

On the Photocyclization of Ar_4-DHA Derivatives

Note that compound numbering in this chapter differs from previous chapters.

5.1 Introduction

In 2004, Geim and Novoselov for the first time experimentally demonstrated the existence of graphene, a single layer of graphite.[267] This discovery soon sparked enormous interest in exploring this novel carbon allotrope as advanced electronic and photonic materials. However, in the organic synthetic community, even prior to the emergence of graphene, studies with focus on the precise synthesis of highly extended structures of graphene were already undertaken. These PAHs represent the segments of infinite graphene layers, commonly referred to as nanographenes or graphene nanoribbons (GNRs) depending on their sizes and shapes. Nanographenes can be constructed through the bottom-up approach (e.g., stepwise synthesis), which ensures

their structures to be monodisperse and defect free. On the other hand, the synthesis of nanographenes requires the use of highly efficient cycloaromatization reactions as the key methodologies for assembling their highly π-extended conjugate frameworks. In this field, Müllen and others have extensively investigated various synthetic methods, ranging from oxidative cyclodehydrogenation (e.g., Scholl reaction) and cyclohalogenation to transition metal-catalyzed C–H arylation and others.[224]

Bis(diarylmethylene)dihydroanthracenes, hereafter referred to as R-DHAs, are polyarene compounds that can be rapidly synthesized from abundantly available 9-10-anthraquinone and various areneboronic acids or ester derivatives. This class of compounds show highly twisted molecular structures as a result of the significant steric clashing between the aryl substitutents and the central anthracene moiety (see examples in Figure 5.1). As such, they give rise to intriguing supramolecular packing and unusual photo-physical properties in the solid and aggregated states.[29,268–272]

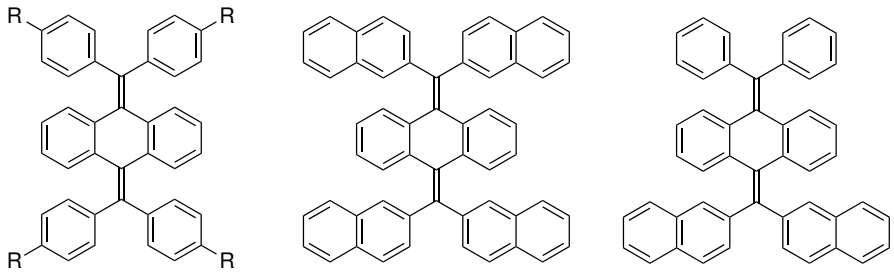

Figure 5.1: Derivatives of Ar_4-DHAs reported in the literature.

Synthetically, R-DHAs can be used as direct precursors for the construction of a class of highly π-extended PAHs, namely, tetrabenzocoronene (TBC) and related derivatives such as tetranaphthobenzo-, tetranaphthodibenzo-, and tetrafluorenodibenzocoronene (TNBC, TNDBCs, and Et-TFDBC). These structures

(see Fig 5.2) belong to the family of contorted nanographenes and therefore have attracted considerable attention in the development of nanographene-based molecular electronic materials and devices.[271]

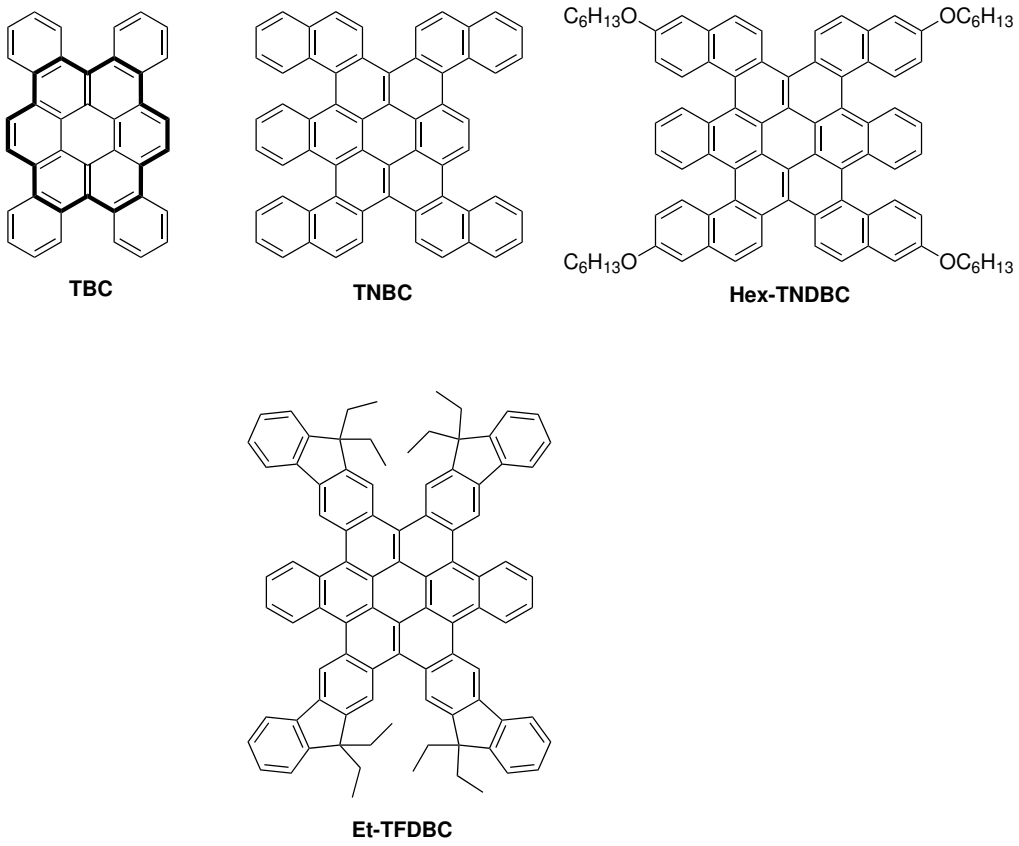

Figure 5.2: Structures of tetrabenzocoronene, tetranaphthobenzo-, tetranaphthodibenzo-, and tetrafluorenodibenzocoronenes (TBC, TNBC, TND-BCs, and Et-TFDBC). The bonds shown in bold in TBC indicate the coronene core.

TBC itself has a coronene core (Figure 5.2) with four benzo groups fused on its edges, creating two Fjord regions and hence making its structure slightly twisted. TBC and its derivatives have been investigated as organic semiconductors and the

results are very promising for future application.[270,273] The preparation of TBC can be done through a four-fold cycloaromatization reaction on R-DHA (R = phenyl). The four steps of intramolecuar cycloaromatization can be induced through different methodologies, while the commonly used ones are the well-known Scholl reaction and photo-induced cyclization reaction (e.g., the Mallory photocycylization).[270,274]

The Scholl reaction was first reported by Ronald Scholl in 1910, whose pioneering work has been extensively used in oxidative aryl-aryl coupling.[275] As highlighted in a review by Müllen and co-workers, this methodology has enabled the synthesis of well-defined graphene nanoribbons with the formation of hundreds of C–C bonds.[276] However with respect to the reaction conditions, the Scholl reaction usually needs high temperature and the presence of a strong acid, often a Lewis acid, together with an oxidant. Such harsh conditions are not friendly to many organic functional groups, thus limiting the synthetic scope of this reaction. Moreover, the reagents used in the Scholl reaction have changed significantly overtime. The early studies utilized excess neat $AlCl_3$ in the presence of air at high temperature.[275] Later on, oxidizing Lewis acid such as $CuCl_2$ or $Cu(OTf)_2$ were introduced to the reaction conditions, which lowered the temperature to room temperature.[277] Recently, reagents such as $FeCl_3/CH_3NO_2/CH_2Cl_2$,[278], $MoCl_5$,[279,280], phenyliodine bis(trifluoroacetate) (PIFA)-boron trifluoride etherate ($BF_3{\cdot}OEt_2$),[281,282]have been widely employed. In recent years, the use of 2,3-dichloro-5,6-dicyano-1,4-benzoquinone (DDQ) with a Brønsted acid such as CH_3SO_3H, triflic acid, and CF_3CO_2H, or a Lewis acid (e.g., $AlCl_3$, $BF_3{\cdot}OEt_2$, or $Sc(OTf)_3$), has become more and more popular in various Scholl reactions reported in the literature.[283,284] Nevertheless, the use of harsh acidic and oxidative reagents has not been completely excluded from the Scholl reaction

conditions. On the other hand, these conditions can induce the rearrangements of the polycyclic aromatic skeletons and consequently lead to the formation of various byproducts.[285] Moreover, the Scholl reaction suffers from a limited scope of reaction starting materials. In particular, substrates functionalized with oxidizable substituents cannot avoid significant side reactions, which in turn affect the structural integrity and purity of the desired Scholl products.[286]

To avoid the challenges associated with the use of the Scholl reaction in synthesis, the search for other cyclization methods for efficient aromatization has been undertaken. It has been demonstrated that some photocyclization reactions can proceed smoothly and cleanly without the use of strong acids, oxidants, as well as complex metal catalysts. As such, these reactions can produce the target cyclized products in high yields without forming significant amounts of by-products. On top of these, many organic functional groups are tolerant to photoirradiation conditions, which allow for a wider scope of starting materials. These are the advantages of photocyclization reaction which makes it a great alternative cycloaromatization strategy to the reactions that involve harsh conditions (e.g., the Scholl reaction).[287,288]

A pioneering work on photocyclization reactions was first introduced by Mallory in 1962, who investigated the cyclodehydrogenation of stilbene under UV irradiation with I_2 being used as an oxidant.[289] Later on, this type of reaction was recognized as the Mallory photocyclization or Mallory reaction. Although iodine helps to improve the yield of the Mallory reaction by accelerating the dehydrogenation step, it yields hydrogen iodide as a byproduct, which often induces significant side-reactions and lowers the yield as a result of its high acidity. To avoid this problem, Katz *et al.* modified the Mallory reaction conditions by adding propylene oxide (PPO) to quench

the undesired hydrogen iodide, which has been known as the Katz's modification.[290] Nowadays, both the Scholl and the Mallory reaction are useful aromization methods for the construction of challenging extended PAH structures (e.g., nanographenes). However, in many synthetic cases, these cyclization reactions have been observed to yield mixtures of partially and fully cyclized products. In fact, the choice of an effective aromatization method is dependent on the specific synthetic target. For example, Wu's group recently demonstrated that a synthetic route involving sequential Mallory and Scholl reactions could produce TBC-based PAHs in much better overall yields than using the Mallory or Scholl reaction only (Scheme 5.1).[270] However, Tao's synthetic pathway started with oxidative dehydrogenation which gave a mixture of half-cyclized products. The mixture was then converted to fully cyclized products using either $FeCl_3$ or $Cu(OTf)_2$ and $AlCl_3$ as the catalyst, which were optimized based on the precursors and the yield of the final product (Scheme 5.1).[272]

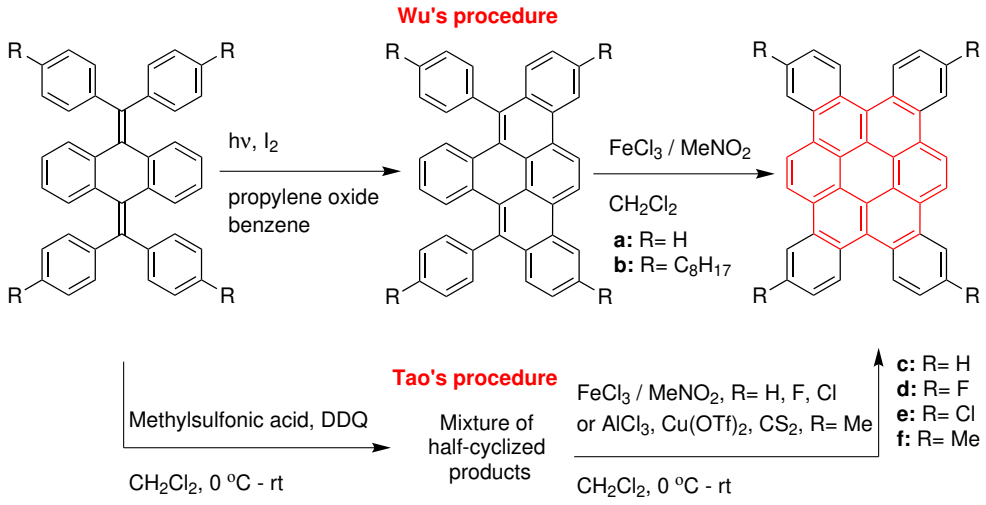

Scheme 5.1: Synthesis of TBC derivatives through stepwise Scholl reactions or sequential Mallory–Scholl reactions.

It is noteworthy that, in the early studies of photocyclization reactions on precursors functionalized with substituents such as *ortho*-methoxy groups, eliminative photocyclization was reported as a problem of the original I_2/O_2 conditions.[291] To overcome this drawback, precursors functionalized with two *ortho*-methoxy groups were used so that one of methoxy groups would still remain after the elimination.[292] However, the elimination of the leaving group was later utilized to control the selectivity of photocyclization sites. In 1989 Mallory developed a method of using a catalytic amount of sulfuric acid to promote the elimination of methanol.[293] Although showing some selectivity, the reaction shows a very low yield and took a prolonged reaction time. Later in 2016, Morin and co-workers reported the regioselective synthesis of nanographenes through a type of photochemical cyclodehydrochlorination (CDHC) reaction. According to their studies, CDHC can serve as a more efficient and substrate-tolerant approach for producing nanographenes and analogous extended PAHs with both electron-rich and electron-deficient substituents and even sterically hindered and contorted PAHs.[287] In the same year, photochemical cyclodehydrofluorination was also reported for the synthesis of triphenylene and phenanthrene derivatives. However, only the cyclization reactions of polyfluorinated precursors resulted in high yields.[294]

With respect to the mechanism involved in the photocyclodehydrogenation reaction forming TBC derivatives, Tao et al. proposed a step-wise radical cation forming mechanism in 2018.[271] They mentioned the stability of the involved radical cation and the formation of the less sterically hindered products as the key factors dictating the selectivity and the reaction outcome. In spite of many research in this topic, there is still no concrete experimental evidence for the mechanism of

the photocyclization reaction. The work of this chapter is aimed at addressing this knowledge deficiency. To reach our goal, we performed mechanistic investigations on the photocyclization reactions of a series of bis(diarylmethylene)dihydroanthracenes, hereafter referred to as Ar_4-DHAs. At the outset of this study, we planned to have the four aryl groups (i.e., Ar) in our target Ar_4-DHAs be the same, so that their syntheses could be reasonably carried out in a concise manner without facing the daunting challenges of regioselectivity. The following sections describe the results of our synthesis, characterization, and mechanistic analyses.

5.2 Results and discussion

5.2.1 Synthesis of Ar_4-DHAs via Suzuki Coupling Reactions

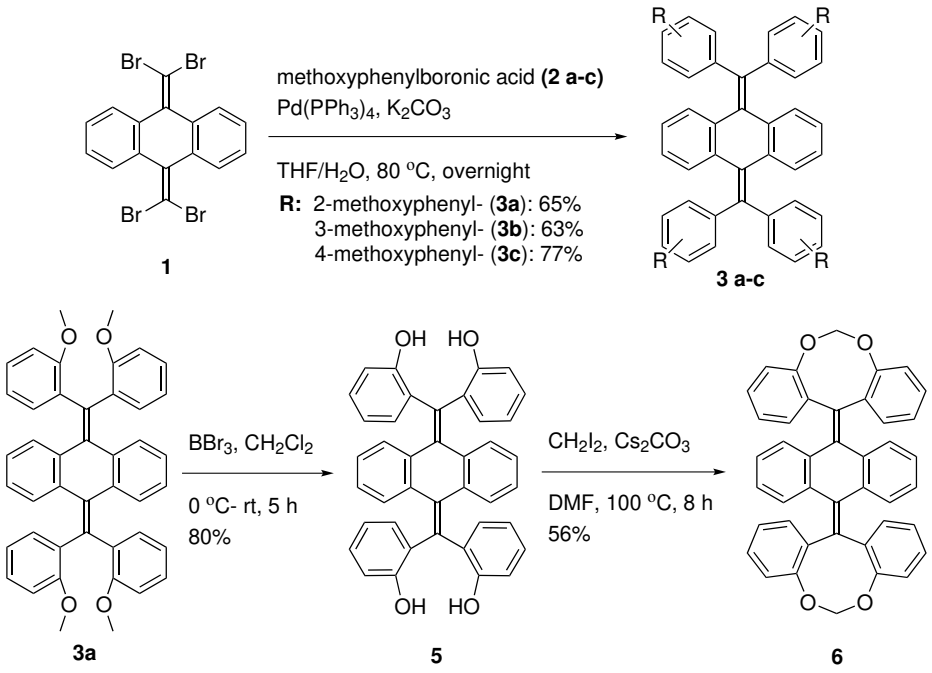

Scheme 5.2: Synthesis of Ar_4-DHAs derivatives **3a**–**c**, **5**, **6**.

Scheme 5.2 shows the synthetic approaches to Ar_4-DHA derivatives **3a**–**c**, which were developed based on literature procedures[272] with suitable modifications. To begin with, we chose bis(dibromomethylene)-substituted DHA **1** as the starting material, taking advantage of its reactivity to various areneboronic acids/esters under the Suzuki-Miyaura cross coupling conditions. Three coupling reactions were conducted on **1**, using 2-methoxyphenylboronic acid (**2a**), 3-methoxyphenylboronic acid (**2b**), and 4-methoxyphenylboronic acid (**2c**)[29] as the cross-coupling partners, respectively. The cross coupling reactions afforded Ar_4-DHAs **3a**–**c** in good yields (63%–77%). With Ar_4-DHA **3a**, a demethylation reaction was performed using boron tribromide (BBr_3) and at relatively low temperature (from 0 °C to rt in 5 h), which resulted in a yield of 80% of compound **5**. The resulting hydroxylated Ar_4-DHA **5** was then subjected to an etherification reaction with diiodomethane (CH_2I_2) in the presence of Cs_2CO_3. Through this reaction, the two adjacent oxygen atoms on each side of the molecule were tethered via a methylene unit. Compared with Ar_4-DHA **3a**–**c**, the structure of **6** is more rigid and constrained. It was expected that with the four phenyl groups restricted from free rotation, this compound would serve as a model to understand specific structural and conformational effects on photocyclization reactivity.

5.2.2 Structural characterizations of Ar_4-DHAs

The synthesized Ar_4-DHA derivatives **3a**–**c**, **5**, and **6** were characterized by NMR, FT-IR, and MS analyses to confirm their molecular structures and purity. Moreover, single crystals of **3a**, **3b**, **3c**, and **6** were successfully grown and then subjected to

single crystal X-ray diffraction (XRD) analysis. Detailed molecular structures of these compounds determined by X-ray analysis are discussed below.

It was found that molecules of **3a** are packed in a monoclinic $P2_1/c$ group in the crystalline state, and the unit cell contains 20 molecules of **3a** and the void space is filled with numerous solvent ($CHCl_3$) molecules (Figure 5.3). Solving the diffraction data resulted in five similar molecular structures in the crystal, one of which is shown in Figures 5.4. Similar to the X-ray structures of Ar_4-DHA compounds reported in the literature,[29,270] the π-framework of **3a** features a highly twisted conformation due to the significant steric crowding between the phenyl groups and the central anthracene unit. The *ortho*-methoxy groups on each pair of adjacent phenyl groups are positioned in an "anti" orientation to alleviate the steric clashing, while the central anthracene moiety can be seen to take a kinked shape. There are no significant intermolecular π-stacking or C–H$\cdots\pi$ interactions involved in the crystal packing due to significant steric crowding.

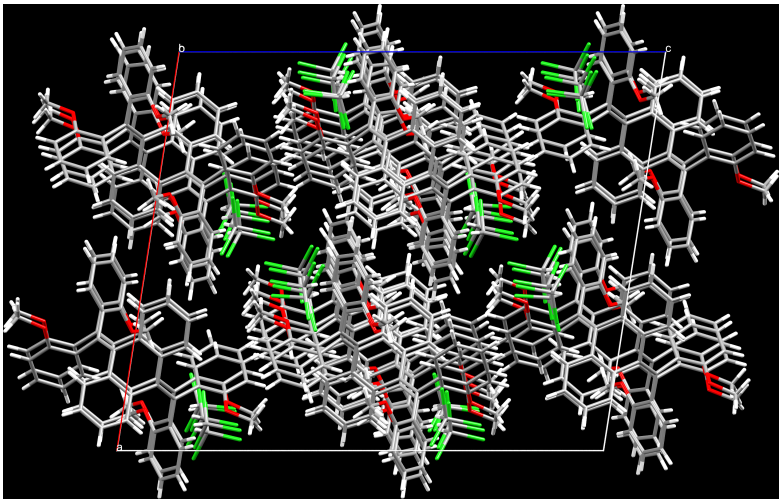

Figure 5.3: Diagram of molecules **3a** and $CHCl_3$ packed in the unit cell (viewed along the b-axis) (CCDC 1980235).

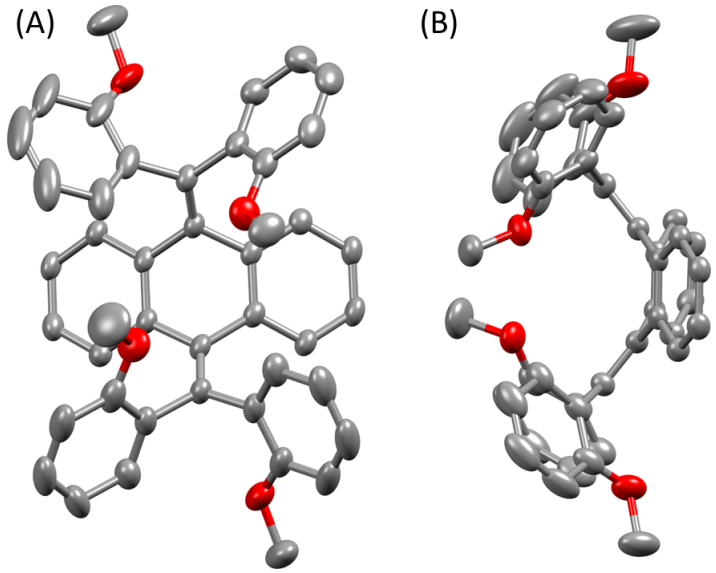

Figure 5.4: ORTEP drawings (50% ellipsoid probability) for one of the molecular structures determined from the single crystal XRD analysis of **3a**. (A) Front view, (B) side view. Hydrogen atoms are not shown for clarity.

The X-ray structure of **3b** is shown in Figure 5.5. Similar to **3a**, the π-conjugated framework of **3b** also shows a contorted conformation. Relative to the central anthracene unit, three of the four *meta*-substituted methoxy groups are positioned inwardly, while the fourth methoxy group points outside the π-skeleton of DHA.

The crystal structure of **3b** is in a triclinic system and takes the $P\bar{1}$(No. 2) space group. There are two identical molecules in the unit cell (Figure 5.6A). Between the two molecules, two intermolecular C–H$\cdots\pi$ contacts occur between the methoxy and phenyl groups, and another two C–H$\cdots\pi$ contacts are due to edge-to-edge interactions with adjacent phenyl rings. Unlike the case of **3a**, the packing of **3b** in the crystalline state is more efficient (see Figure 5.6B), leaving no void space for any solvent molecules to occupy.

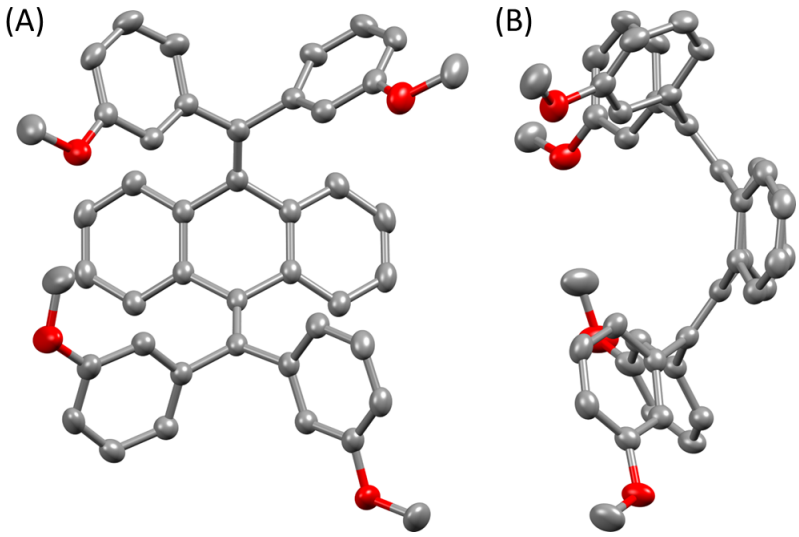

Figure 5.5: ORTEP drawings (50% ellipsoid probability) of **3b** viewed from (A) front and (B) side. Hydrogen atoms are not shown for clarity (CCDC 1980237).

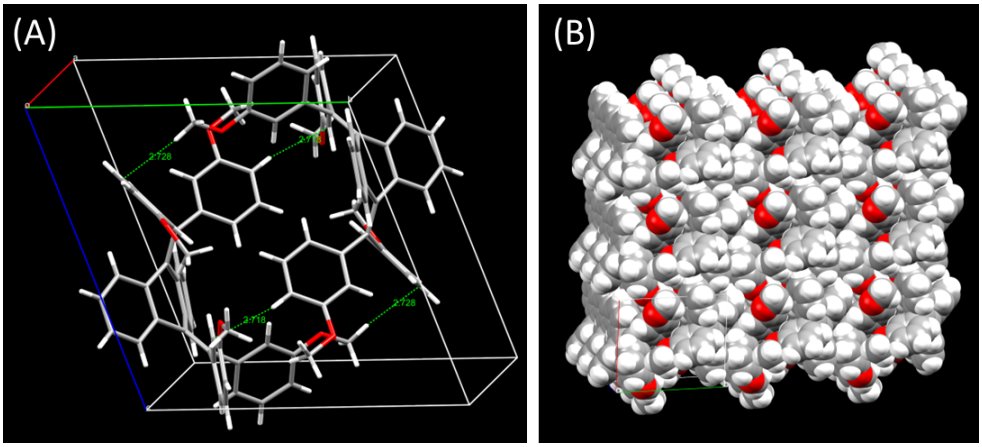

Figure 5.6: (A) Drawing of the two molecules in the unit cell of **3b**. (B) Crystal packing diagram of **3b** viewed along the *c*-axis.

Previously, the single crystal structure of **3c** was measured and reported by Tang and co-workers.[29] In our work, we have also determined the X-ray structure of **3c** and our measured structure is slightly different from the published one in terms of the orientation of the phenyl groups. As shown in Figure 5.7, one of the phenyl rings

(highlighted by a dashed circle) shows a dihedral angle (with respect to the C=C unit) that is considerably larger than the other phenyl groups. In the unit cell, there are two identical molecules of **3c** packed in the unit cell, which is a triclinic sytem and a $P\bar{1}$(No. 2) space group (Figure 5.9A).

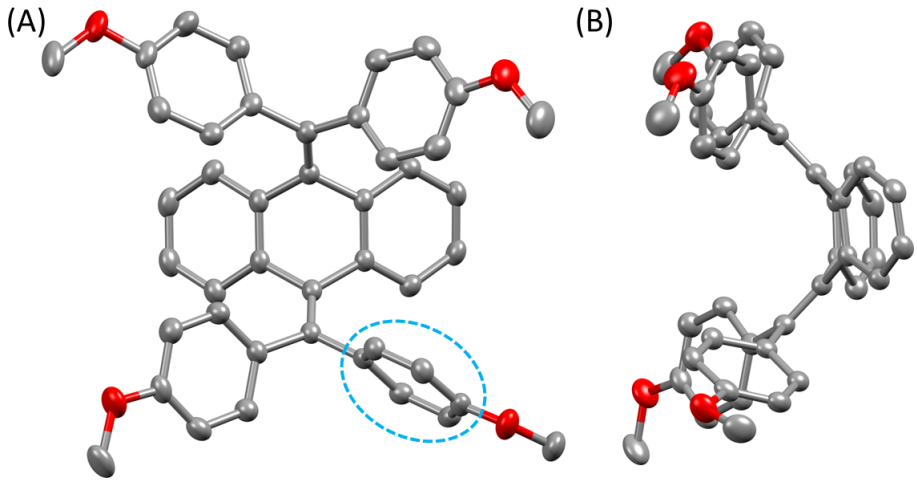

Figure 5.7: ORTEP drawings (50% ellipsoid probability) for one of the molecular structures determined from the single crystal XRD analysis of **3c**. (A) Front view, (B) side view. Hydrogen atoms are not shown for clarity (CCDC 2255457).

The single crystal structure of **6** also shows a $P\bar{1}$(No. 2) space group, with two identical molecules occupying the unit cell. Figure 5.8 shows the molecular structure of **6** determined by X-ray analysis, in which two OCH_2O groups tether each pair of adjacent phenyl rings, forming two eight-membered rings. The solid-state packing of **6** does not show intermolecular interactions as significant as that of **3b**, leaving some void space to be occupied by solvent molecules ($CHCl_3$) (see Figure 5.9B). Overall, the four Ar_4-DHAs **3a**–**3c** and **6** show similar shapes in terms of their π-conjugated skeletons; however, the positions of alkoxy substituents exert important influence on

intermolecular interactions and hence dictate the efficiency and motif of solid-state packing.

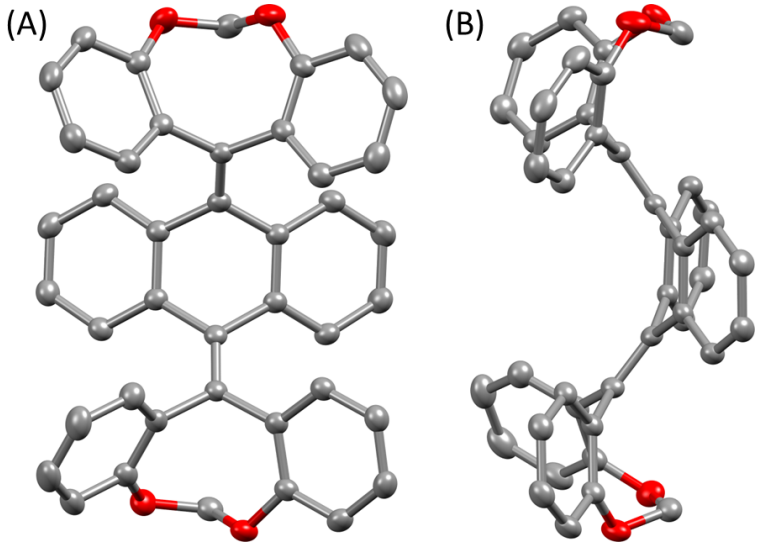

Figure 5.8: ORTEP drawings (50% ellipsoid probability) of **6** viewed from (A) front and (B) side. Hydrogen atoms are not shown for clarity (CCDC 1980238).

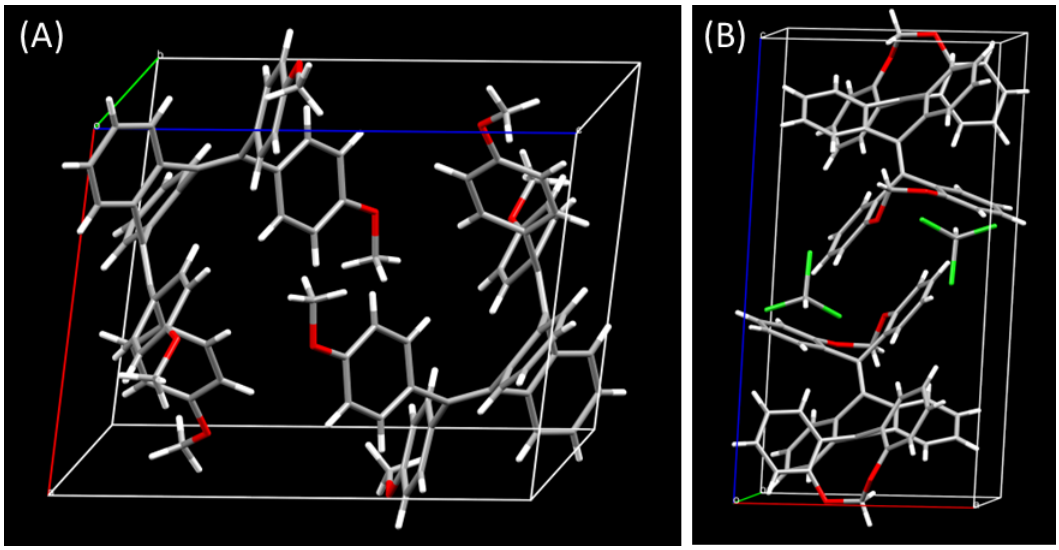

Figure 5.9: Packing diagrams of (A) **3c** and (B) **6** in the unit cells.

5.2.3 Photocyclization of Ar_4-DHAs

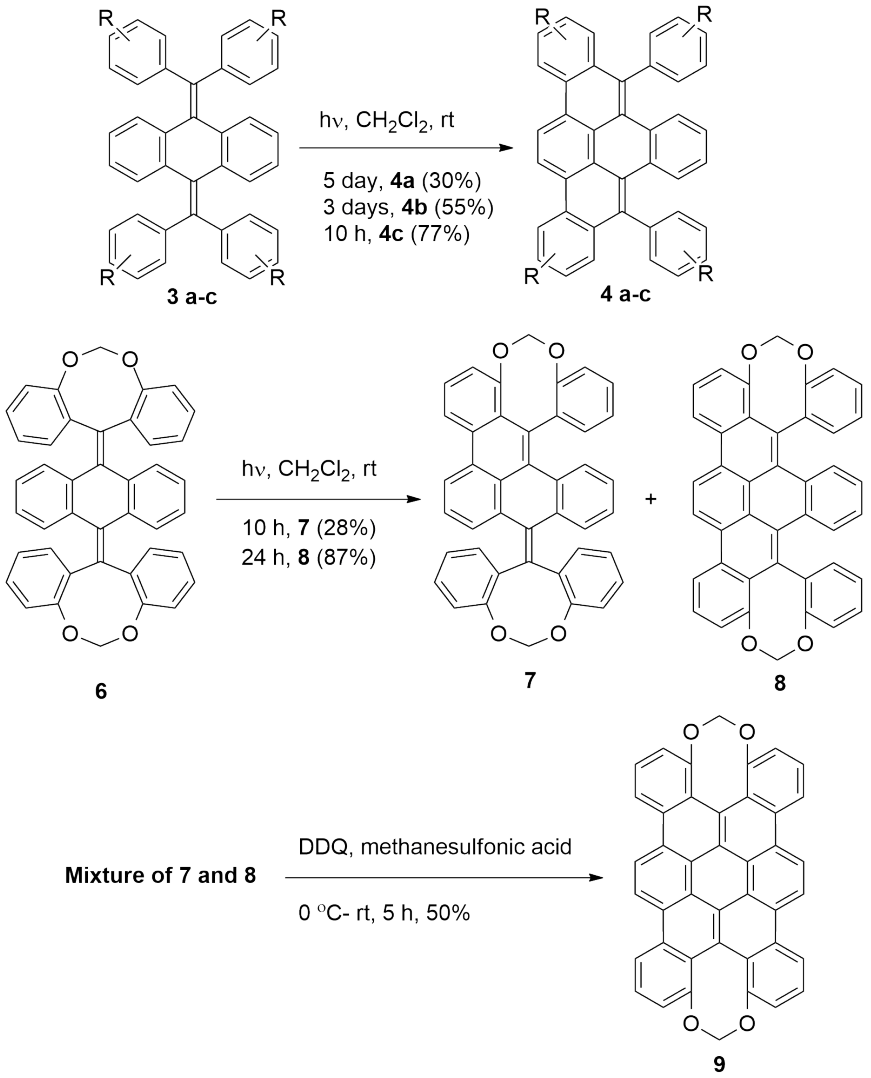

Scheme 5.3: Synthesis of cyclized Ar_4-DHAs, compounds **4a**–**c**, **7**, **8**, **9**.

As can be seen in Scheme 5.3, to prepare the cyclized products, solutions of Ar_4-DHA derivatives **3a**–**3c** and **6** in dichloromethane were subjected to UV irradiation. Ideally, if all the four stilbene subunits in an Ar_4-DHA molecule undergo photocyclodehydrogenation (i.e., Mallory) reactions, a tetrabenzocoronene

(TBC) product will be formed. However, it has been reported that such a scenario is unlikely to happen. Rather, the formation of partially cyclized products was consistently observed in the photocyclization of various Ar_4-DHA substrates.[270,271,274] These facts led us to ponder whether the photocyclization of Ar_4-DHAs would show any regioselectivity, if the reaction proceeds through a stepwise manner. Scheme 5.4 illustrates the four steps of stilbene cyclization on a tetraphenyl-substituted DHA (Ar_4-DHA) to form a TBC product. In the second step, there are three possibilities for the formation of regioisomers (**12**, **13**, **14**). Among them, two have the phenanthrene moieties (highlighted by colored bold bonds) joined together to form "fused" π-systems (**12**, **14**), while another shows the two phenanthrene subunits in a "disjoint" motif (**13**). To facilitate further discussion, we name these partially cyclized intermediates anit-fuse (**12**), anti-disj (**13**), and syn-fuse (**14**), respectively. Herein, syn and anti refer to the relative positions of the two phenanthrene subunits with respect to the central anthracene group. The terms, fuse and disj, are used to describe the connectivity between the two phenanthrene groups.

In our experiments, we first tested the photocyclizability of **3a** in CD_2Cl_2 using a photoreactor equipped with a UV light source (λ = 302–312 nm, 64 W). The reaction was checked by ^{1}H NMR analysis at varied times of reaction. As can be seen from Figure 5.10, the NMR spectrum of pure **3a** shows a number of relatively broad signals in the aromatic region (6.5–8.0 ppm). The broad shapes of these peaks can be attributed to the high degree of steric crowding caused by the *ortho*-methoxy-substituted phenyl rings, which significantly hinders their rotation at room temperature. Upon UV light irradiation, a multitude of new peaks grew slowly as the reaction time increased. These peaks reflect the formation of various cyclized

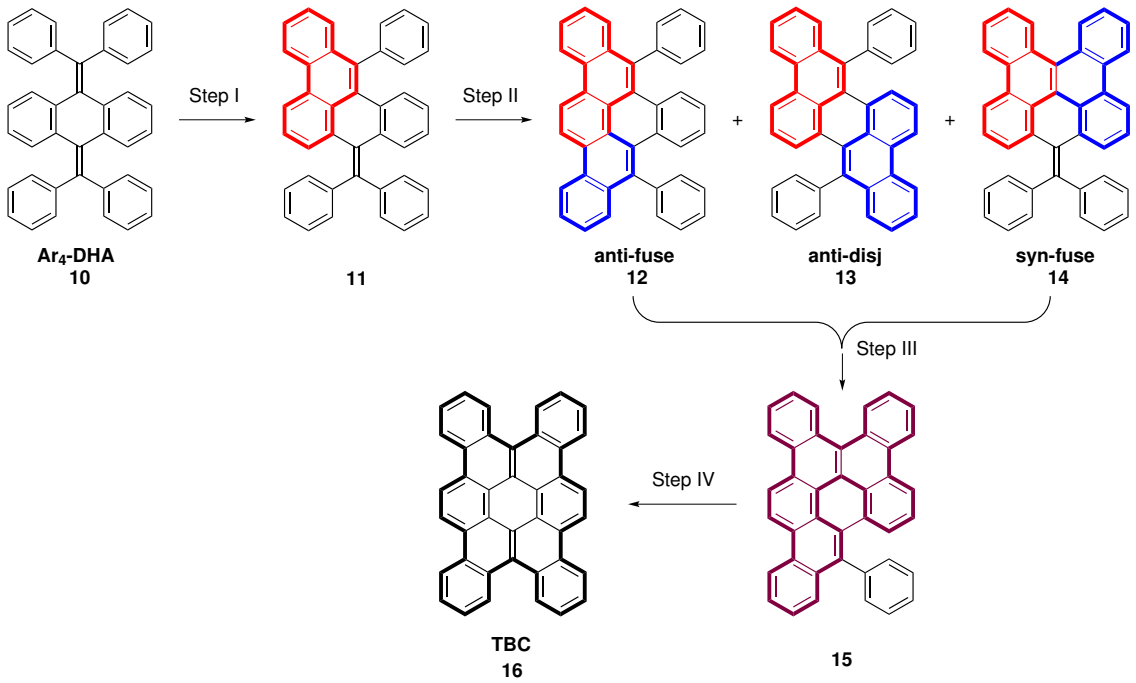

Scheme 5.4: Stepwise photocyclization of a Ar_4-DHA substrate. Fused polycyclic aromatic rings are highlighted by colored bonded bonds.

intermediates and final products. The NMR spectra kept changing for about 100 hours and then remained unchanged, indicating that the overall reaction is slow. It is worth noting that at the final stage, the NMR spectrum pattern appeared to be very complex in the region of 6.5–8.0 ppm, making the detailed spectral assignment and interpretation very difficult. In the downfield region, four sharp signals show up at 9.09, 9.08, 8.96, and 8.93 ppm, which can be assigned to the major product of the photocyclization. During the reaction, a group of weak signals, appearing as two sets of doublet of doublets, were also observed (see the signals highlighted by cyan-colored dashed box in Figure 5.10). These peaks vanished at the final stage of reaction, suggesting that they are very likely due to some intermediary cyclized species. Nevertheless, the highly complex spectral patterns of the photocyclization

product(s) of **3a** make it difficult to establish their molecular structures.

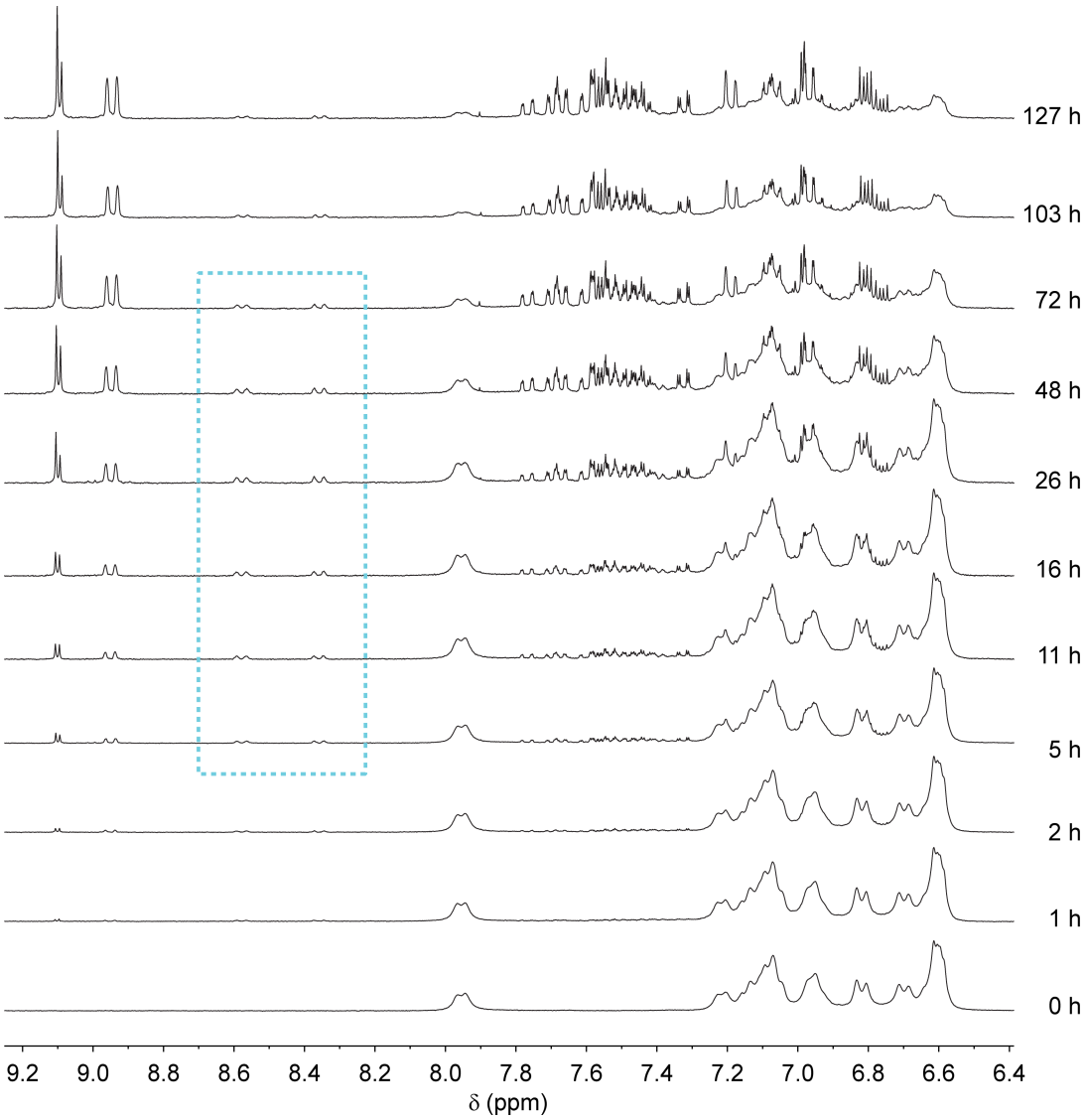

Figure 5.10: ^{1}H NMR spectra monitoring the photocyclization of **3a** (9.6 mM) in CD_2Cl_2.

A relatively large-scale photocyclization reaction of **3a** was next performed in CH_2Cl_2 under irradiation with the same UV source. After 5 days of reaction time, the reaction mixture was purified through silica column chromatography, resulting

in a pure compound which was identified as the anti-fuse product **4a** (30% isolated yield) by NMR, MS, and X-ray crystallographic analyses.

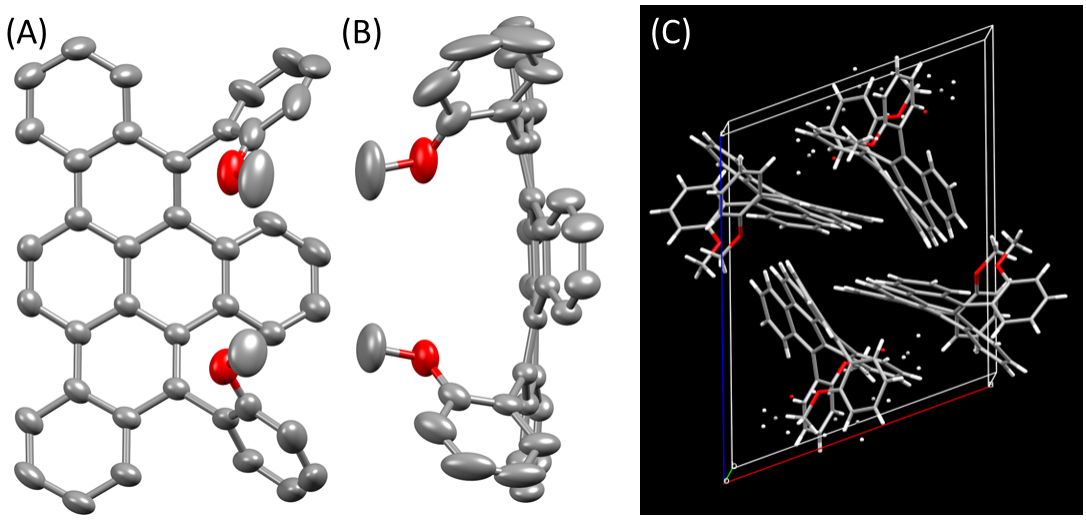

Figure 5.11: (A) and (B) ORTEP drawings (50% ellipsoid probability) of one of the molecular structures of **4a** determined from XRD analysis viewed from front and side. (B) Packing diagram showing four molecules of **4a** in the unit cell (CCDC 1980465).

According to the MS and X-ray analyses, the photocyclization of **3a** actually underwent a cyclodemethoxylation pathway rather than cyclodehydrogenation. As can be seen from Figure 5.11, two methoxy groups were eliminated after the photocyclization, resulting in an anti-fuse product **4a**. The π-conjugated framework of **4a** is planar and delocalized in comparison with its precursor **3a**. As such, compound **4a** was found to show significantly red-shifted electronic absorption and strongly enhanced fluorescence (vide infra). It is also interesting to observe that the crystal structure of **4a** contains two different conformers, in which the two unreacted phenyl rings have their *ortho*-methoxy groups oriented in the same and opposite directions, respectively (see Figure 5.11C). The two-fold demethoxylation reaction

under photochemical conditions is not a surprising outcome. As illustrated by the exemplar photocyclizations in Scheme 5.5, the photocyclodehydrogenation needs to undergo a challenging *trans* oxidative elimination of two hydrogen atoms (**18**). For the demethoxylation reaction, however, the hydrogen and methoxy group to be eliminated are in a *trans* configuration (**21**), which is well predisposed for an E2 mechanism without the need for any oxidants. Moreover, the elimination of methoxy can significantly reduce steric hindrance and hence make the cyclized product more stable. Overall, the photocyclodemethoxylation pathway is more favored both kinetically and thermodynamically over the cyclodehydrogenation reaction.

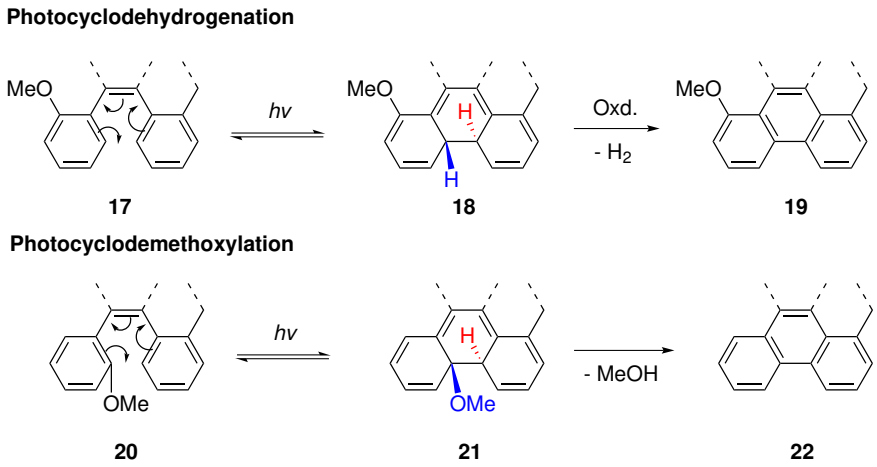

Scheme 5.5: Comparison of the mechanisms for photocyclodehydrogenation and photocyclodemethoxylation pathways.

The photocyclization of *meta*-methoxy-substituted Ar_4-DHA **3b** was investigated by ^{1}H NMR analysis under the same photochemical conditions used for **3a**. Figure 5.12 shows the detailed NMR spectral changes in association with the progress of the photocyclization. Unlike **3a**, the NMR signals in the spectrum of pure **3b** are sharp

and well-resolved, indicating easy free rotation of the phenyl groups in the structure. Clearly, moving the methoxy groups from *ortho* to *meta* position significantly reduces the steric crowding and hence enable the phenyl groups to undergo free rotation at room temperature.

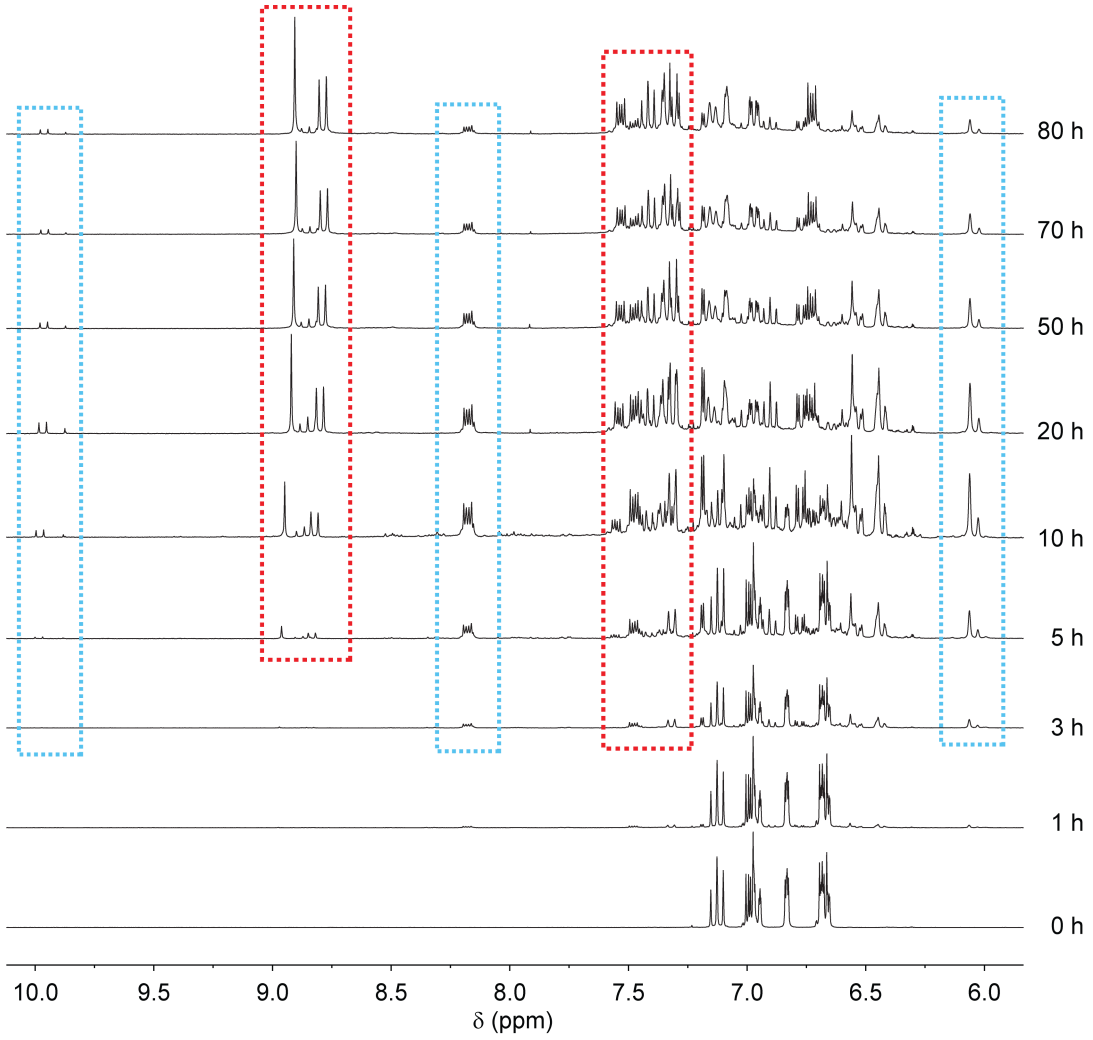

Figure 5.12: ^{1}H NMR spectra monitoring the photocyclization of **3b** (9.0 mM) in CD_2Cl_2.

The NMR monitoring experiments indicate that a major product was gradually

formed during the reaction, and its key NMR signals are highlighted by red-colored dashed boxes in Figure 5.12. Besides this product, some characteristic signals emerged as well (highlighted by cyan-colored dashed boxes) at the middle stage of the reaction, but they became insignificant at the final stage. This observation suggests that these signals are likely due to the intermediate resulting from the first step of cyclization on **3b**. In view of the photocyclization outcome of **3a**, it is likely that the major product of the photocyclization of **3b** results from two steps of cyclization. To further characterize its structure, a relatively large-scale reaction was carried out in CH_2Cl_2 under UV irradiation. After 3 days of reaction, silica column purification was conducted and the isolated major product was subjected to NMR and MS analyses. The spectroscopic data suggest that it is the anti-fuse **4b** (structure shown in Scheme 5.3) through two steps of photocyclization. Attempts to grow single crystals of **4b** for X-ray analysis did not meet success. As such, the structural elucidation of **4b** at this juncture cannot be considered as being conclusive.

We further monitored the photocyclization of *para*-methoxy-substituted Ar_4-DHA **3c** by ^{1}H NMR analysis (see Figure 5.13). The *para*-substitutions in the structure **3c** lead to NMR spectral patterns much simpler than those of **3a** and **3b**, which in turn make spectral assignments and interpretation much easier. In contrast to the cases of **3a** and **3b**, the photocyclization of **3c** proceeded at a much faster rate and the NMR monitoring data show a very clean transformation from **3c** to a single final product **4c** after 10 hours. A large-scale reaction was then conducted, allowing column purified **4c** to be acquired for NMR and MS analyses. Our spectroscopic analysis point out that **4c** results from a two-fold photocyclodehydrogenation and the structure takes the anti-fuse motif.

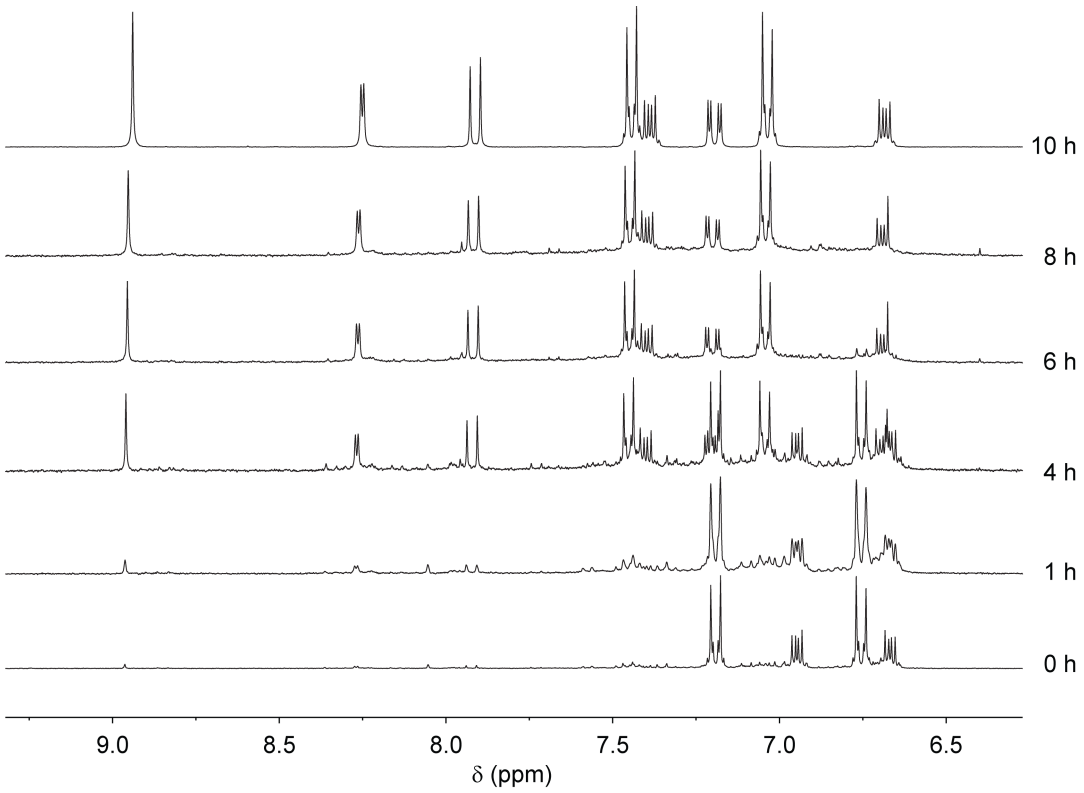

Figure 5.13: ^{1}H NMR spectra monitoring the photocyclization of **3c** (10.1 mM) in CD_2Cl_2.

According to the results of the photocyclization reactions on **3a**–**3c**, several conclusions can be made at this point. First, steric hindrance has an important influence on the reaction rate of the photocyclization of Ar_4-DHA, which is evidenced by the observation that the photocyclization became faster and faster when the substituents are changed from *ortho*, *meta*, to *para* positions. Second, the photocyclization generally favors two steps of cyclization, and the product shows a selectivity for the anti-fuse structure. This conclusion is substantiated by the X-ray data of **4a** as well as the results reported on the photocyclization of similar Ar_4-DHAs.[270,271] Third, when a leaving group is attached to the *ortho* position of the phenyl ring, elimination of the leaving group is much favored over the dehydrogenation process. Finally, the first step of cyclization on an Ar_4-DHA appears to be significantly faster than the second step of cyclization. This conclusion is drawn from the NMR monitoring data, which show that signals of intermediary species remained quite insignificant throughout the entire reaction.

Finally, we investigated the photocyclization of tethered Ar_4-DHA **6** employing the same conditions used for compounds **3a**–**3b**. Structurally, compound **6** is significantly more rigid and the four phenyl rings are restricted from free rotation due to the presence of OCH_2O tether groups. The structural rigidity of **6** is evidenced by the observation that the two protons on each OCH_2O group are diastereotopic. As can be seen from Figure 5.14, the ^{1}H NMR spectrum of **6**, one of the methylene protons appears as a doublet at 5.69 ppm (J = 7.5 Hz), while another proton is significantly deshielded and its signal overlaps with other aromatic proton signals in the region of 6.70–7.00 ppm. According to the X-ray structural analysis, the methylene groups of **6** constitute two eight-membered rings that take a boat-like conformation (see Figure

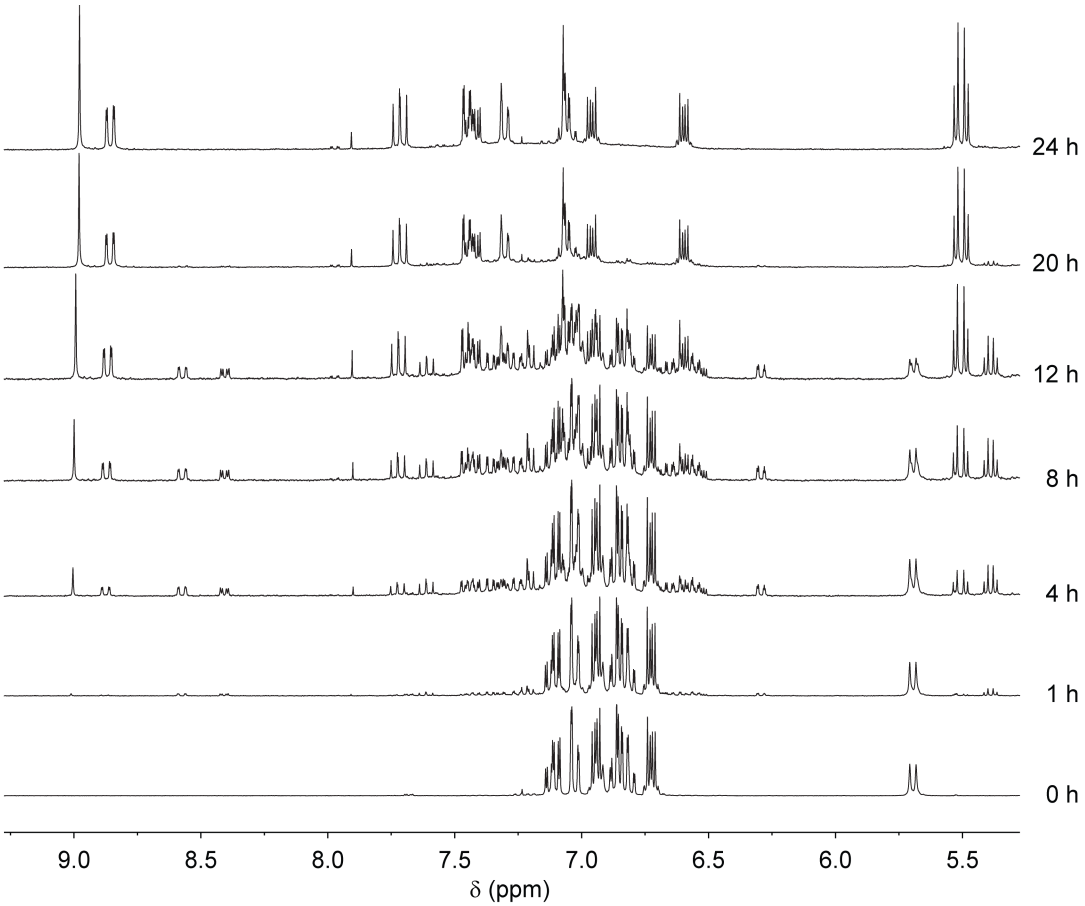

Figure 5.14: ^{1}H NMR spectra monitoring the photocyclization of **6** (10.6 mM) in CD_2Cl_2.

5.15). In each of the methylene groups, one hydrogen atom is pointing towards the edge of the central anthracene moiety, which is a strongly deshielding zone. The other proton points away from the central anthracene unit and therefore does not experience significant magnetic anisotropic effects.

During the photocyclization process, the ^{1}H NMR spectral patterns in the aromatic region show dramatic changes at varied times (see Figure 5.14). In about four hours, a multitude of new peaks can be clearly observed. Among them, three signals in the downfield are characteristic, which appear at 9.01 (s), 8.87 (dd, J =

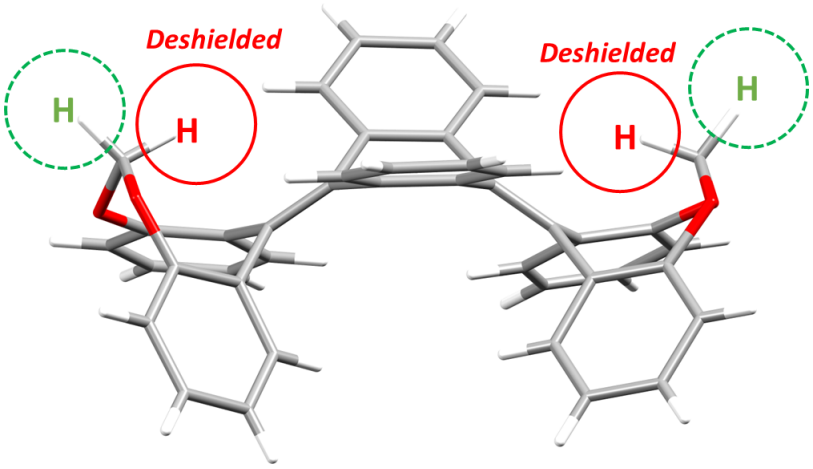

Figure 5.15: Different deshielding effects on the two types of diastereotopic methylene hydrogens in **6**.

8.5, 1.3 Hz), 8.57 (dd, J = 7.0, 2.3 Hz), and 8.41 (dd, J = 7.0, 2.4 Hz) ppm. The two signals at 8.57 and 8.41 ppm can be observed for up to 12 hours of reaction time and then disappear, while the other two signals at 9.01 and 8.87 ppm continue to grow. These results indicate the formation of a significant amount of intermediate, most likely that results from the cyclization of one stilbene unit in the molecule of **6**. Similar spectral features are clearly observable in the upfield region, which shows a number of new peaks at 5.3–5.5 ppm from 4 to 12 hours. After 20 hours of reaction, the doublet (at 5.70 pm) that is due to one of the methylene hydrogen of **6** completely disappears, and only two doublets remain around 5.46–5.54 ppm. The results suggest the occurrence of two steps of photocyclization, and the final product of this process is an anti-fuse product. The cyclization reactions make the molecule more planar and hence move the methylene hydrogens away from the deshielding zone of the central anthrancene unit.

In a relatively large-scale photocyclization reaction of **6** in CH_2Cl_2, the irradiation

time was set at 10 hours. After that, the reaction products were subjected to silica column chromatography. To our satisfaction, mono-cyclized intermediate **7** (see Scheme 5.3 for structure) was isolated in 28% yield and then fully characterized by spectroscopic and X-ray crystallographic analyses. Figure 5.16 shows the detailed molecular and crystal packing structure of **7**. It is particularly noteworthy that in the structure of **7**, the two methylene hydrogens on the cyclized stilbene side are further away from the central anthracene unit, while the methylene group on the opposite side remain a geometry similar to its precursor **6** (see Figure 5.18). Such structural features are in line with the ^{1}H NMR data for purified **7**, where four distinct signals for the methylene hydrogens can be clearly seen at 6.30, 5.68, 5.40, and 5.37 ppm (Figure 5.17). According to the molecular structure revealed by X-ray analysis, the pseudo doublet at 6.30 ppm can be assigned to the proton located in the deshielding zone (labelled by a red-color circle in Figure 5.18). When the reaction time of photocyclization of **6** was prolonged to 24 hours, a major product was obtained in 87% after column chromatographic separation. NMR and MS analyses indicate that this product is compound **8**, which resulted from a two-fold Mallory cyclization on **6** and takes an anti-fuse π-conjugated motif (See Scheme 5.3). Compound **8** was stable under UV irradation and would not undergo further cyclization, even though there are still two stilbene moieties remaining in its structure. To convert it into a TBC product, however, required the use of a Scholl reaction. In our work, we first prepared a mixture of **7** and **8** through photocyclization of **6** for 24 hours. The mixture was then treated with methanesulfonic acid (CH_3SO_3H) and DDQ in CH_2Cl_2 at 0 °C to afford TBC **9** in 50% yield.

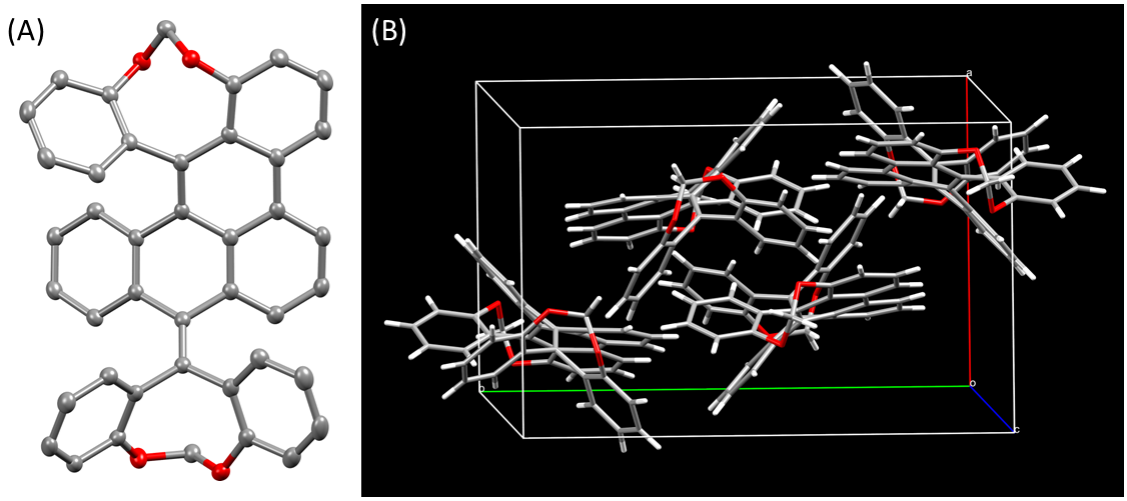

Figure 5.16: (A) ORTEP drawing (50% ellipsoid probability) of compound **7** (hydrogen atoms removed for clarity). (B) Packing diagram of **7** viewing along the *c*-axis of the unit cell (CCDC 1980466).

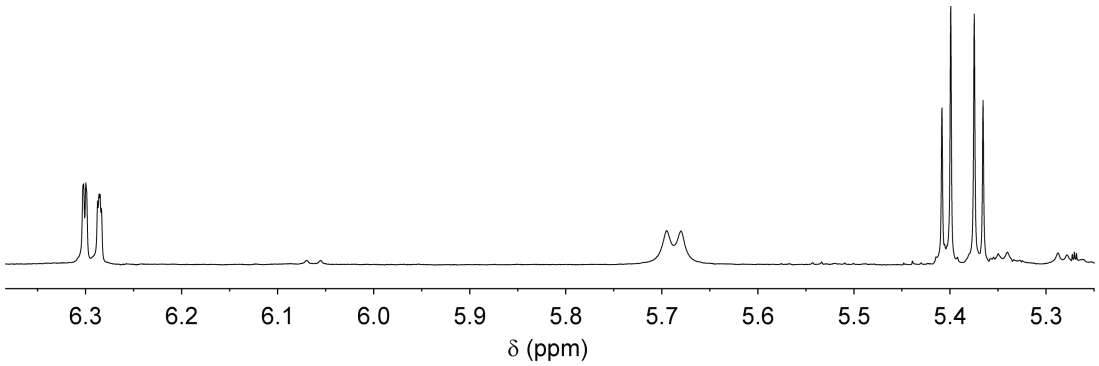

Figure 5.17: Expanded ^{1}H NMR spectrum of **7** show four methylene hydrogen signals in the region of 5.3–6.3 ppm.

5.2.4 Electronic Absorption and Emission Properties of Ar_4-DHA Derivatives

The electronic absorption and emission properties of Ar_4-DHA **3a-c**, **4a-c**, **6**, **8**, and **9**, were investigated by UV-Vis and fluorescence analysis. As shown in Figure 5.19, the spectrum of *ortho*-methoxy-substituted Ar_4-DHA **3a** shows a distinct $\pi \rightarrow \pi^*$

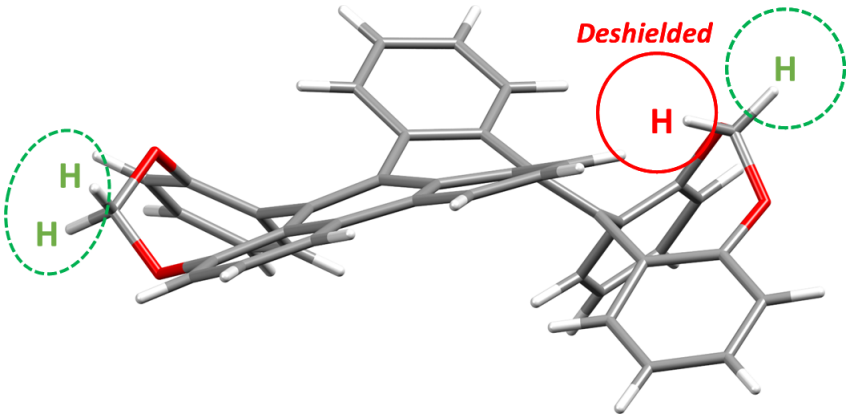

Figure 5.18: X-ray crystal structure of compound **7** showng different deshielding effects on the bridging methylene protons.

absorption peak at 284 nm and a broad absorption shoulder ranging from ca. 300 to 367 nm. Comparatively, the *meta*-methoxy-substituted derivative, **3b**, shows an absorption peak at 285 nm along with a much broader and red-shifted shoulder band from 310 to 375 nm. The UV-Vis spectrum of *para*-methoxy-substituted **3c** exhibits a broad absorption spectral profile, in which the edge of the long-wavelength absorption shoulder is significantly red-shifted to 400 nm. The absorption spectrum of **6** also shows broad absorption bands at 276 nm and 313 nm. The low-energy absorption edge matches that of *meta*-methoxy-substituted **3b**, although compound **6** contains alkoxy substituents at the *ortho* positions.

Figure 5.20 shows the UV-Vis spectra of the compounds resulting from photocyclization of various Ar_4-DHAs. The increased π-conjugation in compounds **4a-c**, **8**, and **9** makes the absorption bands, particularly the low-energy ones, substantially red-shifted in comparison with their precursors. Moreover, the spectra exhibit a greater number of absorption bands due to more allowed $\pi \rightarrow \pi^*$ transitions. To understand their electronic origins, time-dependent density functional theory (TD-

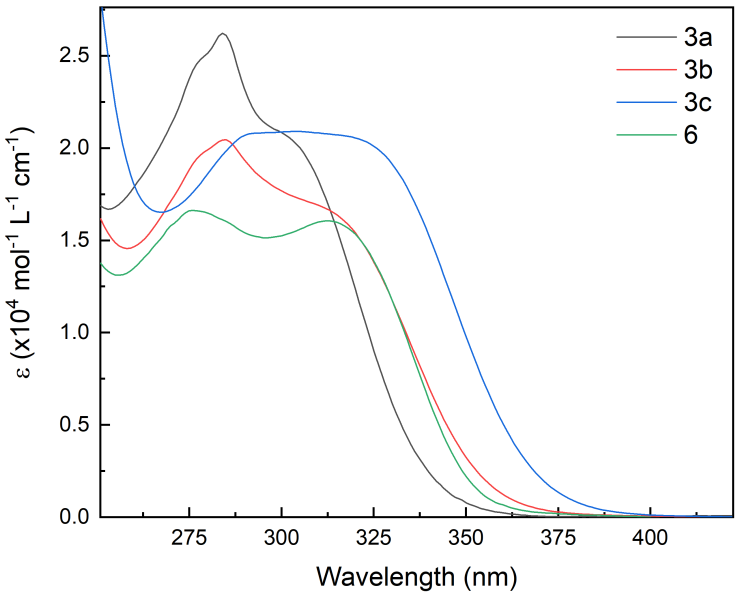

Figure 5.19: UV-Vis spectra of **3a-c**, and **6** measured in CH_2Cl_2 at room temperature.

DFT) calculations were performed on compound **4c** (see Figure S-20 and Table S-7, Appendix IV). The results indicate that the long-wavelength band that appears as a broad peak in its spectrum can be assigned to the HOMO → LUMO transition. In terms of the substitution effects, the long-wavelength absorption bands of Ar_4-DHA show a red-shifting trend in their maximum absorption wavelengths, which is *ortho* < *metha* < *para* for compounds **4a**–**4c**. For tethered compound **8** and fully-cyclized TBC **9** the absorptions are further red-shifted due to their higher dgrees of π-conjugation.

It is worth noting that Ar_4-DHAs **3a**–**3c** are non-emissive in the solution phase. These outcomes can be attributed to their photoreactive stilbene moieties, which allow the photoexcited states of these compounds to undergo rapid cyclization reactions (non-radiative) instead of fluorescence (radiative) processes. In contrast,

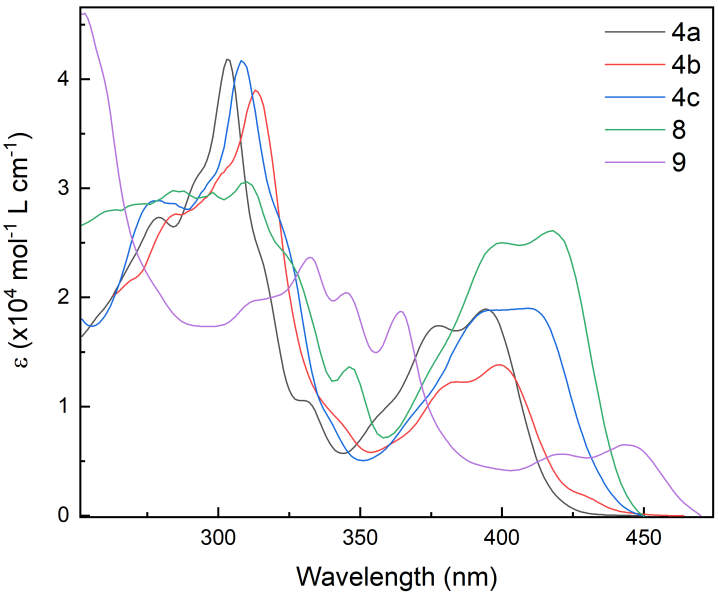

Figure 5.20: UV-Vis spectra of **4a-c**, **8**, and **9** measured in CH_2Cl_2 at room temperature.

the photocyclized products, **4a**–**4c** and **8**, show significant fluorescence and their fluorescence spectra are shown in Figure 5.21. It is worth mentioning that among the photocyclized products, tethered compound **8** shows the highest quantum yield value (44%). The second highest fluorescence quantum yield is that of **4a** (42%), while the fluorescence quantum yields of **4b** and **4c** are 13% and 9.0%, respectively. These data together point out that restricted intermolecular rotation plays a key role in the photophysical and photochemical mechanisms, since both the tethered compound **8** and *ortho*-substituted **4a** show lowered rotational freedom due to tethering and steric crowding effects. Indeed, unlike the untethered Ar_4-DHAs **3a**–**3c**, tethered Ar_4-DHA **6** is fluorescent and its spectrum gives an emission band at 440 nm with a quantum yield of 11%, which further corroborates the effects of tethering groups on fluorescence

enhancement. In terms of substitution effects, *para*-methoxy-substituted **4c** shows the most red-shifted maximum emission wavelength (at 481 nm). This observation is in line with the UV-Vis absorption data, indicating that *para*-methoxy-substitution results in the highest degree of π-conjugation.

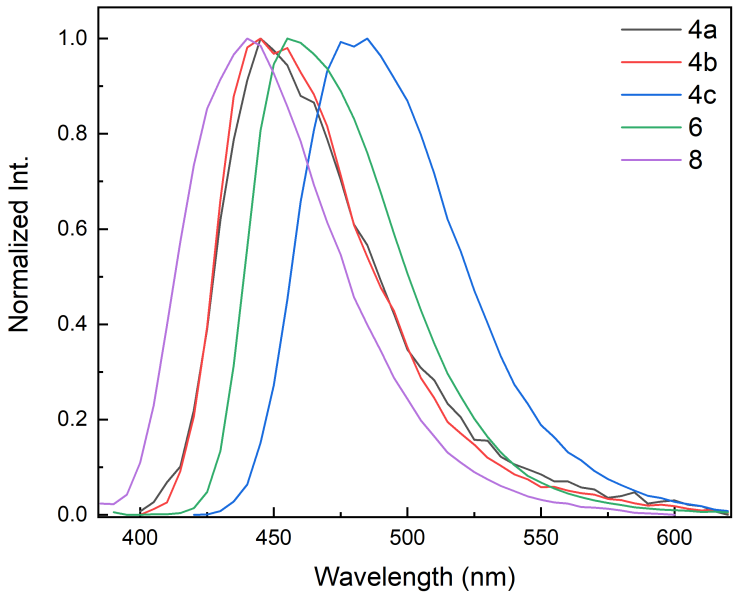

Figure 5.21: Fluorescence spectra of **4a-c**, **6**, and **8** measured in CH_2Cl_2 at room temperature.

5.2.5 On the Photocyclization Mechanisms of Ar_4-DHAs

Experimental evidence based on our spectroscopic and crystallographic analyses has pointed to the scenario that when an Ar_4-DHAs is subjected to photoirradiation, only two of the stilbene moieties can achieve cyclization, whereas the other two remain unreactive. Moreover, the selectivity of the two-fold Mallory photocyclization favors

the anti-fuse isomer as illustrated in Scheme 5.4. In our experiments, none of the anti-disj and syn-fuse isomers has been observed. According to the experimental results, two fundamentally important questions arise with regard to the mechanisms for the photocyclization processes taking place on an Ar_4-DHA system. Detailed discussions and rationalizations are made below.

The first question is: why does the photocyclization only achieve the ring closure on two stilbene units, rather than all the four of them? To address this question, we herein make discussion based on a theoretical model recently established by Salazar and Faraji[295], who used spin-flip TD-DFT to investigate the photo-interconversion between cyclotriene and hexatriene. According to this model, we propose that photoexcitation of a Ar_4-DHA leads to a vertical electronic transition from the ground state to the first excited state (see the $S_0 \rightarrow S_1$ transition in Figure 5.22A). The potential energy surfaces (PES) of S_1 and S_2 (the second excited state) show minimum energy crossing point (MECP) seams, which allow the crossing of S_1 and S_2 to occur readily. The PES of S_2 has a conical interaction (CI) seam with S_1 , through which the excited state undergoes the photocyclization process to arrive at the cyclized product. In this mechanism, the radiative decay pathway (i.e., fluorescence) is insignificant, which accounts for the observed non-emissive behavior of typical Ar_4-DHAs (**3a**–**3c**).

After the photoreaction proceeds through two steps of Mallory cyclization, the more rigid and π-delocalized structure of the cyclized product make the PES of S_1 and S_2 to change greatly. It is reasonable to conceive that the increased π-extension make the S_1 more stabilized and lower-lying in energy, which in turn causes the MECP seams between S_1 and S_2 to vanish. In this scenario, the S_1 cannot undergo the photocyclization efficiently. Instead, it favors a deactivation pathway by emission

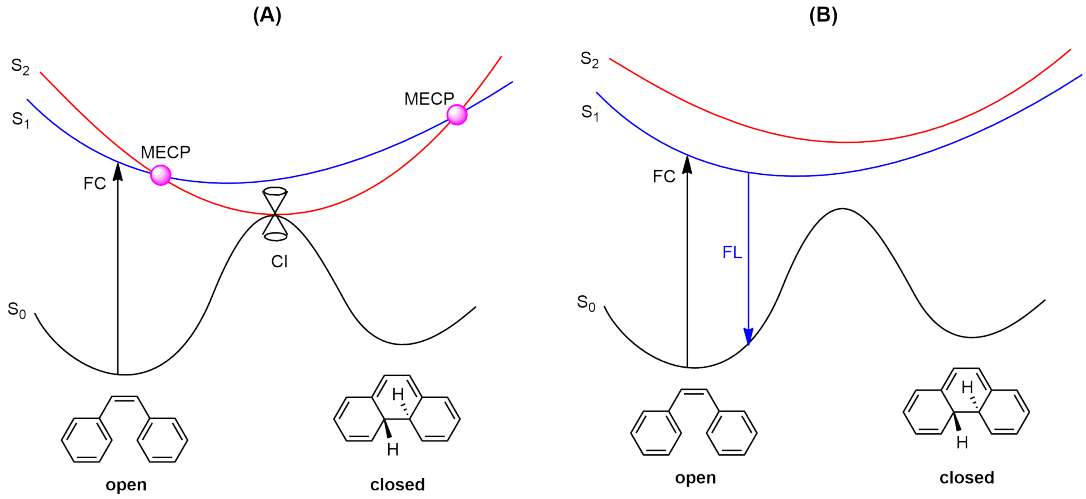

Figure 5.22: Proposed mechanisms for (A) the photocyclization of a stilbene moiety in a Ar_4-DHA system, and (B) radiative pathway for the final photocyclized product of a Ar_4-DHA. S_0: ground electronic state; S_1: first electronic excited state; S_2: second electronic excited state; FC: Franck-Condon state; FL: fluorescence; MECP: minimum energy crossing point; CI: conical intersection.

of photonic energy to yield fluorescence. This rationalization is consistent with the relatively strong fluorescence observed for cyclized products **4a**–**4c** and **8**.

Now, let's deal with the second question: why does the two-fold Mallory cyclization favor an anti-fuse selectivity? The exact answer to this question needs a comprehensive analysis of the excited-state properties of the intermediate resulting from the mono-cyclization of an Ar_4-DHA. Nevertheless, a simplified model based on frontier molecular orbital (FMO) theory can provide sufficient insight at this stage. As commonly known that the pericyclic reaction on a hexatriene system is dictated by FMO properties; under thermal conditions (ground state), the HOMO of the triene dictates the reactivity, while under photochemical conditions (excited state), the LUMO plays a key role. Based on this argument, we propose that the

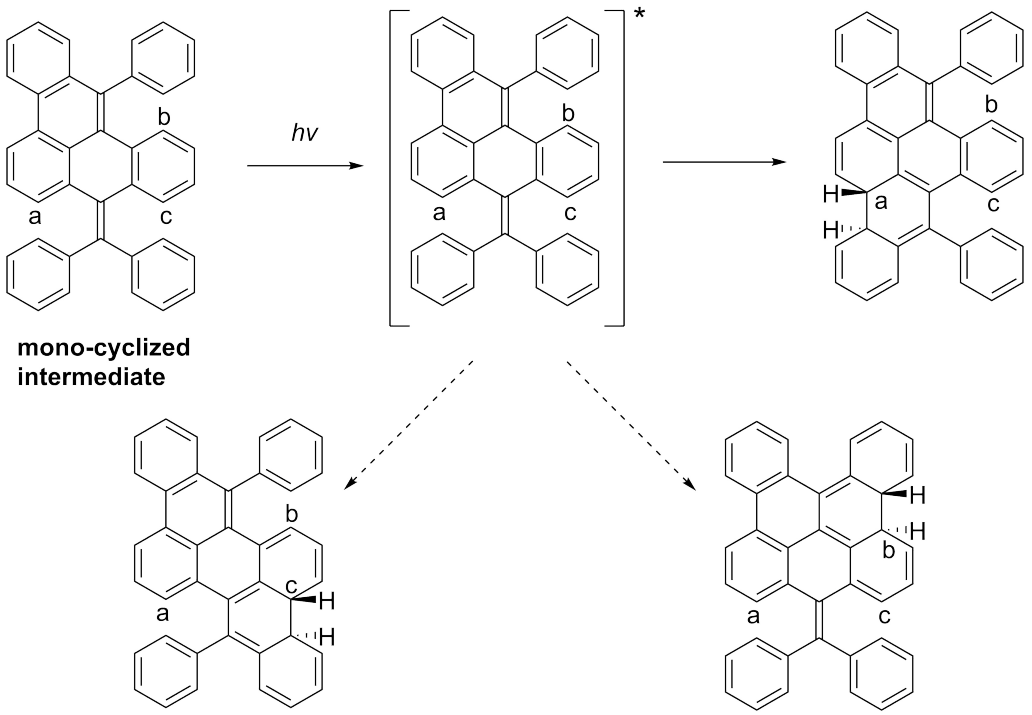

Scheme 5.6: Reaction scheme showing the regioselective pathway for the second Mallory cyclization on an Ar_4-DHA system.

photoreactivity of the mono-cyclized intermediate of an Ar_4-DHA can be correlated to the orbital coefficients of the LUMO, since photoexcitation predominantly leads to the HOMO $\rightarrow$ LUMO transition. As labelled in Scheme 5.6, there are three active sites (a–c) on the central anthracene unit of a mono-cyclized intermediate, which can possibly undergo further cyclization. If the following cyclization occurs on site a, the resulting Mallory cyclization yields an anti-fuse product. Photocyclizations on sites b and c, on the other hand, should lead to anti-disj and syn-fuse products, respectively. For any of these reactive sites, if the orbital coefficient in the LUMO is large, the probability of percyclic reaction taking place on this site is high, and vice versa.

Figure 5.23 shows the FMO properties of compound **7**, which contains a mono-cyclized structure. It can be seen that the antibonding orbitals, especially the LUMO,

show orbital coefficient distributions favor the scenario for the anti-fuse selectivity. The molecular segments that are responsible for the formation of anti-disj and syn-fuse isomers, however, either show a very small orbital co-efficient or a node in the LUMO. Therefore, the selectivity of the second step of Mallory photocyclization is toward the anti-fuse product.

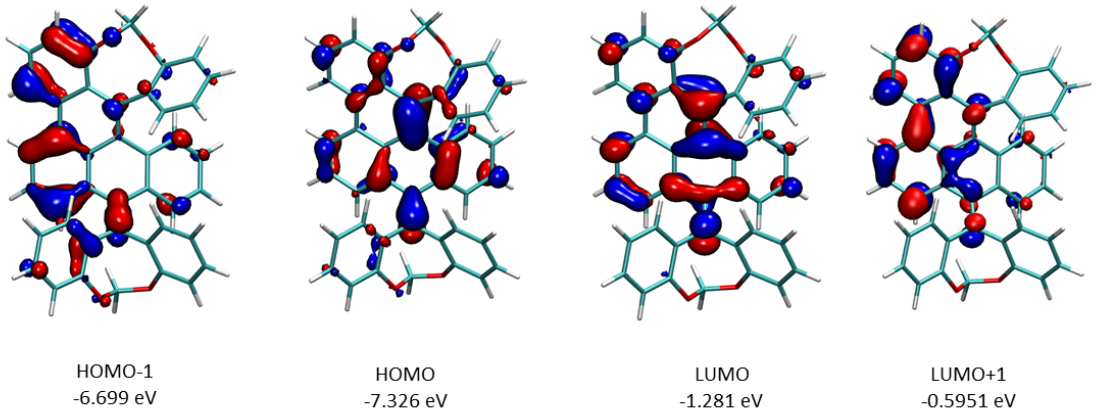

Figure 5.23: Plots (isovalue = 0.04 au) and energies of the frontier molecular orbitals of compound **7** calculated at the M06-2X/Def2-SVP level of theory.

5.3 Conclusions

In this chapter, a series of Ar_4-DHA compounds has been successfully synthesized and characterized by spectroscopic and X-ray crystallographic analyses. These compounds serve as ideal models for investigating the cycloaromatization strategies for the synthesis of exotic π-extended PAHs and nanographenes. Our results have shown that the Mallory photocyclization reaction presents an approach to cyclize Ar_4-DHA with better tolerance to electron-donating substituents (e.g., methoxy) than the Scholl

reaction. However, the setback of the Mallory reaction is that the photocyclization only achieves two steps of cyclization. It is interesting to note that the two-fold Mallory photocyclization on an Ar_4-DHA system shows regioselectivity favoring the formation of the anti-fuse isomer only. When the *ortho*-positions of an Ar_4-DHA are substituted with methoxy groups, the photocyclization follows the de-methoxylation pathway (i.e., elimination of methanol) instead of dehydrogenation. Overall, the synthetic and spectroscopic studies described in this chapter offer valuable insight into the future synthetic work on nanographenes and related nanocarbon materials. Careful considerations of the excited-state properties, particularly those of the cyclization intermediates, must be taken if photochemical approaches are involved in the synthesis. It is anticipated that continued efforts on studying the detailed excited-state dynamics will lead to the discovery of more efficient and wider-scope cycloaromatization methods for the bottom-up synthesis of nanographene-related nanocarbon materials.

5.4 Experimental

5.4.1 Materials and Methods

Chemicals were purchased from commercial suppliers and used directly without purification. Photocyclization reactions were performed in a quartz NMR tube or custom-made a quartz glass tube according to the scale of reaction. The reactions were conducted under the irradiation of a halogen lamp (100 W) or in a Rayonet photochemical reactor equipped with eight UV lamps (64 W in total). Flash

column chromatography was performed with silica gel 60 (240-400 mesh). Thin-layer chromatography (TLC) was done with silica gel F254 coated on plastic sheets and visualized by UV light. Melting points were measured on an MPA100 melting point apparatus (Stanford Research Systems). ^{1}H and ^{13}C NMR spectra were measured on a Bruker Avance III 300 MHz multinuclear spectrometer. Chemical shifts (δ) are reported in ppm downfield relative to the signal of either the internal reference $SiMe_4$ (0 ppm) or residual solvent ($CHCl_3$: $\delta_H = 7.24$ ppm, $\delta_C = 77.2$ ppm; CH_2Cl_2: $\delta_H = 5.32$ ppm, $\delta_C = 54.0$ ppm, C_3H_6O; $\delta_H = 2.05$ ppm, $\delta_C = 206.68, 29.92$ ppm). Coupling constants (J) are given in Hz. Infrared spectra (IR) were recorded on a Bruker Alfa spectrometer. HRMS analyses were performed on an Agilent 6230 TOF LC/MS instrument using an APPI ionizer and a QSTAR XL hybrid quadrupole/TOF mass spectrometer equipped with an o-MALDI ion source. UV-Vis-NIR absorption spectra were measured on a Cary 6000i spectrophotometer. Single-crystal X-ray diffraction data was collected at 100(2) K on a XtaLAB Synergy-S, Dualflex, HyPix-6000HE diffractometer using Cu-Kα radiation ($\lambda = 1.5406$ Å). The crystal was mounted on nylon CryoLoops with Paraton-N. The data collection and reduction were processed within CrysAlisPro (Rigaku OD, 2019). A multi-scan absorption correction was applied to the collected reflections. Using Olex,[154] the structure was solved with the ShelXT[155] structure solution program using Intrinsic Phasing and refined with the ShelXL[156] refinement package using Least Squares minimization. All non-hydrogen atoms were refined anisotropically. All hydrogen atoms were located in difference Fourier maps.

Molecular modeling studies were carried out using the Gaussian 16 software.[157] Visualization of the calculated molecular structures and orbitals were done by

VMD.[219]

5.4.2 Synthesis and Characterization

Compounds **2a-i** were purchased from Combi-Blocks, Inc. (San Diego, USA). Compounds **1**[296] and **3c**[29] were prepared according to the literature procedures.

General procedure A

Synthesis of 3a and 3b

To a solution of **1** (1.00 g, 1.92 mmol) and methoxyphenylboronic acid (**2a**–**c**) (1.31 g, 8.64 mmol) in 30 mL of THF and 10 mL of deionized water was added K_2CO_3 (1.33 g, 9.60 mmol). The reaction mixture was bubbled with N_2 flow for 15 min, and $Pd(PPh_3)_4$ (0.110 g, 0.0960 mmol) was added and heated to 80 °C. It was stirred overnight under N_2. The reaction was monitored with TLC (CH_2Cl_2/hexanes). Upon completion, the mixture was cooled to room temperature and poured into a separatory funnel including water and extracted three times with CH_2Cl_2. The combined organic layers were dried over $MgSO_4$, filtered and concentrated under reduced pressure. The resulting residue was purified by silica gel column chromatography using appropriate portions of CH_2Cl_2/hexanes as eluent.

9,10-bis(bis(2-methoxyphenyl)methylene)-9,10-dihydroanthracene (3a)

Compound **3a** was prepared based on general procedure **a** and was purified using silica gel column chromatography (CH_2Cl_2/hexanes, 35:65) as a light pink solid (0.790 g, 1.25 mmol, 65%). m.p.: 310.0–315.4 °C; IR (neat): 3062, 2922, 2041, 1886, 1711,

1594, 1578, 1485, 1293, 1255, 1021, 974 cm^{-1}; ^1H NMR (300 MHz, $CDCl_3$): δ 8.03 (s, 2H), 7.30–6.64 (m, 22H), 3.97 (s, 6H), 3.71 (s, 6H) ppm; ^{13}C NMR (75 MHz, $CDCl_3$): δ 158.26, 155.77, 137.39, 133.30, 132.76, 132.76, 132.15, 130.33, 127.84, 127.29, 126.32, 124.87, 120.01, 119.15, 110.23, 55.23 ppm; HRMS (APPI-TOF, positive mode): m/z calcd for $C_{44}H_{36}O_4$ $[M]^+$ 628.26136, found 628.26213.

9,10-bis(Bis(3-methoxyphenyl)methylene)-9,10-dihydroanthracene (3b)

Compound **3b** was prepared based on general procedure **A** and was purified using silica gel column chromatography (CH_2Cl_2/hexanes, 50:50) as a light brown solid (0.760, 1.20 mmol, 63% g). m.p.: 170.0–185.5 °C; IR (neat): 3057, 3021, 2934, 1594, 1572, 1483, 1459, 1426, 1311, 1283, 1252, 1206, 1174, 1121, 1089, 1045 cm^{-1}; ^1H NMR (300 MHz, $CDCl_3$): δ 7.21 (s, 1H), 7.18 (s, 2H), 7.16 (s, 1H), 7.06–7.03 (m, 8H), 6.90 (dd, J = 2.4, 1.5 Hz, 4H), 6.76–6.72 (m, 8H), 3.69 (s, 12H) ppm; ^{13}C NMR (75 MHz, $CDCl_3$): δ 159.48, 143.56, 139.44, 137.43, 135.34, 129.16, 127.87, 125.27, 122.33, 115.49, 112.41, 55.27 ppm; HRMS (APPI-TOF, positive mode): m/z calcd for $C_4H_{36}O_4$ $[M]^{\cdot+}$ 628.26136, found 628.25622.

2,2′,2″,2‴-(Anthracene-9,10-diylidenebis(methanediylylidene))tetraphenol (5)

To an ice-cooled solution of compounds **3a** (1.00 g, 1.59 mmol) in 25 mL dry CH_2Cl_2, a fresh solution of BBr_3 (3.01 mL, 31.80 mmol) in 5 mL dry CH_2Cl_2 was added dropwise. The resulting reaction mixture was stirred at 0 °C for 4 h and then ice bath was removed and the reaction was continued at room temperature for another 1 h. The reaction was monitored with TLC (ethyl acetate/hexanes; 30:70) and was finally

quenched with water. The reaction mixture was diluted with brine and extracted with CH_2Cl_2 three times. The combined organic layers were dried over $MgSO_4$, filtered and concentrated under reduced pressure. Compound **5** was isolated as a light brown solid (0.730 g, 1.27 mmol, 80%), used for next step without further purification. m.p.: 241.8–294.8 °C; IR (neat): 3301–3060, 3028, 2922, 1697, 1577, 1485, 1444, 1343, 1186, 1103 cm^{-1}; ^1H NMR (300 MHz, acetone-d_6): δ 9.40 (s, 2H), 8.33 (s, 1H), 7.84 (d, J = 6.9 Hz, 1H), 7.35–6.63 (m, 24H) ppm; ^{13}C NMR (75 MHz, acetone-d_6): δ 154.77, 154.65, 152.02, 137.32, 136.73, 131.19, 130.66, 129.29, 128.49, 128.30, 128.23, 126.94, 126.55, 126.14, 125.70, 125.25, 120.84, 120.76, 119.79, 115.96, 115.49, 115.36 ppm; HRMS (APPI-TOF, negative mode): m/z calcd for $C_{40}H_{28}O_4$ $[M]^+$ 572.19876, found 572.20151.

9,10-Bis(12*H*-dibenzo[*d*,*g*][1,3]dioxocin-12-ylidene)-9,10-dihydroanthracene (6)

A suspension of compound 5 (0.500 g, 0.870 mmol) and Cs_2CO_3 (1.70 g, 5.22 mmol) in DMF was stirred for 20 min, and then was treated with CH_2I_2 (0.17 mL, 2.18 mmol) dropwise. The temperature was increased to 100 °C. The reaction was monitored with TLC and after 8 h was quenched with water and extracted with ethyl acetate (3 × 20 mL). The organic layers were combined, washed with water and brine, and were dried over $MgSO_4$, followed by concentrating under reduced pressure. The residue was purified using silica gel column chromatography (CH_2Cl_2/hexanes; 50:50). Compound **6** was obtained as a light yellow solid (0.290 g, 0.486 mmol, 56%). m.p.: 325.8–380.4 °C. IR (neat): 3064, 2921, 2852, 1725, 1665, 1628, 1573, 1483, 1459, 1298, 1233, 1145, 1102, 1089 cm^{-1}. ^1H NMR (300 MHz, CD_2Cl_2): δ 7.14–7.08 (m, 4H), 7.04

(d, J = 0.9 Hz, 2H), 7.01 (d, J = 0.9 Hz, 2H), 6.96–6.92 (m, 6H), 6.89–6.79 (m, 8H), 6.72 (dd, J = 5.7, 3.3 Hz, 4H), 5.69 (d, J = 7.5 Hz, 2H) ppm; ^{13}C NMR (75 MHz, CD_2Cl_2): δ 155.57, 137.12, 136.13, 134.46, 131.28, 129.32, 128.88, 127. 38, 125.78, 123.22, 120.01, 93.0 ppm; HRMS (APPI-TOF, positive mode): m/z calcd for $C_{42}H_{24}O_4$ $[M]^+$ 592.16746, found 592.16632.

General procedure B

Synthesis of 4a–c, 7 and 8 from 3a–3c, and 6

9,10-Bis(diarylmethylene)-9,10-dihydroanthracene (0.500 mmol) was dissolved in 50 mL of dry CH_2Cl_2. The solution was placed into a quartz tube and was sealed. The solution was irradiated under UV light (302–312 nm) in a photochemical reactor. The progress of the reaction was monitored through TLC (ethyl acetate/hexanes) and stopped upon completion. The reaction mixture was concentrated under reduced pressure and the residue was subjected to silica gel column chromatography (ethyl acetate/hexanes or DCM/hexanes) to afford purified product.

5,10-Bis(2-methoxyphenyl)dibenzo[h,rst]pentaphene (4a)

After 5 days of reaction, compound **4a** was synthesized from compound **3a** based on general procedure **b** and was purified using silica gel column chromatography (ethyl acetate/hexanes, 10:90) as a yellow solid (0.0840 g, 0.149 mmol, 30%). NMR and single crystal X-ray analyses confirmed that the product contains a mixture of isomers. m.p.: 286.0–291.2 °C; IR (neat): 3060, 3023, 2994, 1595, 1575, 1489, 1475, 1453, 1376, 1289, 1178, 1158, 1112 cm^{-1}. ^{1}H NMR (300 MHz, CD_2Cl_2): δ 9.09 (s,

1H), 9.08 (s, 1H) , 8.93 (d, J = 8.1 Hz, 2H), 7.76 (dd, J = 8.4, 0.9 Hz, 1H), 7.70–7.41 (m, 9H), 7.32 (dd, J = 7.8, 1.8 Hz, 1H), 7.2 (m, 1H), 7.09–6.92 (m, 4H), 6.83–6.74 (m, 2H), 3.83 (s, 4H), 3.55 (s, 2H) ppm; ^{13}C NMR (75 MHz, CD_2Cl_2): δ 158.87, 133.39, 133.35, 132.09, 132.04, 131.44, 131.10, 129.72, 129.52, 129.43, 129.02, 128.96, 128.11, 127.67, 127.36, 126.95, 126.44, 126.16, 126.08, 125.97, 122.86, 122.80, 121.73, 121.64, 121.15, 111.94, 110.76, 55.53 ppm; HRMS (APPI-TOF, positive) m/z calculated for $C_{42}H_{28}O_2$ $[M]^+$ 564.20893, found 564.20885.

3,12-Dimethoxy-5,10-bis(3-methoxyphenyl)dibenzo[*h,rst*]pentaphene (4b)

After 3 days of photocyclization reaction of **3b** and based on general procedure **b**, compound **4b** was purified using silica gel column chromatography (ethyl acetate/hexanes, 20:80) as a yellow solid (0.172 g, 0.275 mmol, 55%). NMR analysis confirmed that the product contains a mixture of isomers that cannot be interpreted properly. m.p.: 245.0–256.0 °; IR (neat): 3059, 2994, 2929, 2831, 1614, 1600, 1575, 1455, 1285, 1246, 1226, 1197, 1144, 1120, 1092, 1044 cm^{-1}C. ^{1}H NMR (300 MHz, CD_2Cl_2): δ 8.9 (s, 2H), 8.78 (d, J = 9 Hz, 2H), 7.53 (dd, J = 6.0, 3.3 Hz, 2H), 7.42 (t, J = 7.8 Hz, 2H), 7.36–7.28 (m, 4H), 7.19–7.13 (m, 2H), 7.09–7.08 (m, 2H), 6.98 (dd, J = 2.7, 0.9 Hz, 1H), 6.96 (dd, J = 2.7, 0.9 Hz, 1H), 6.73 (dd, J = 6.3, 3.3 Hz, 2H), 3.70 (s, 1H), 3.75–3.72 (2s, 10H), 3.49 (s, 1H) ppm; ^{13}C NMR (75 MHz, $CDCl_3$): δ 159.47, 157.98, 143.33, 142.07, 141.32, 133.79, 133.63, 133.08, 132.89, 130.77, 130.39, 129.07, 125.66, 124.60, 124.48, 123.98, 121.54, 120.44, 117.17, 115.21, 114.79, 111.12, 110.63, 107.49, 55.50, 55.01 ppm; HRMS (APPI-TOF, positive) m/z calculated for $C_{44}H_{32}O_4$ $[M+H]^+$ 625.2379, found 625.2356.

2,13-Dimethoxy-5,10-bis(4-methoxyphenyl)dibenzo[*h,rst*]pentaphene (4c)

The photocyclization reaction of **3c** was carried out for 10 h and based on general procedure **b**, resulting in compound **4c** as a white powder (0.240 g, 0.384 mmol, 77%) after silica column chromatographic purification (ethyl acetate/hexanes, 15:85). m.p.: 303.2–305.0 °C; IR (neat): 3065, 3019, 2921, 2852, 1587, 1560, 1471, 1450, 1406, 1275, 1263, 1246, 1218, 1078, 991 cm^{-1}. ^1H NMR (300 MHz, CD_2Cl_2): δ 8.94 (s, 2H), 8.25 (d, J = 2.4 Hz, 2H), 7.91 (d, J = 9.3 Hz, 2H), 7.44 (m, 4H), 7.39 (dd, J = 6.3, 3.6 Hz, 2H), 7.19 (dd, J = 9.3, 2.4 Hz, 2H), 7.04 (m, J = 8.7, 2.7 Hz, 4H), 6.68 (dd, J = 6.3, 3.6 Hz, 2H), 4.03 (s, 6H), 3.84 (s, 6H) ppm; ^{13}C NMR (75 MHz, CD_2Cl_2): δ 159.32, 158.25, 134.20, 133.87, 133.73, 133.37, 130.90, 130.41, 129.24, 127.11, 126.36, 126.01, 125.88, 124.93, 121.23, 117.31, 114.33, 103.30, 55.55, 55.34 ppm; HRMS (ESI-TOF, positive) m/z calculated for $C_{44}H_{32}O_4$ $[M+H]^+$ 625.2379, found 625.2366.

5-(12*H*-dibenzo[*d,g*][1,3]dioxocin-12-ylidene)-5H-benzo[*g*]benzo[6,7]tetrapheno[11,12-*de*][1,3]dioxocine (7)

The photocyclization reaction of compound **6** was carried out for 10 h and based on general procedure **B**, resulting in compound **7** as a yellow solid (0.0830 g, 0.139 mmol, 28%) after silica column chromatographic purification (CH_2Cl_2/hexanes, 45:55). m.p.: 350–365 °C; IR (neat): 3064, 2955, 2920, 2851, 1598, 1572, 1484, 1441, 1403, 1302, 1272, 1236, 1218, 1203, 1179, 1123, 1099, 1044, 1007 cm^{-1}. ^1H NMR (300 MHz, CD_2Cl_2): δ 8.57 (dd, J = 5.4, 0.9 Hz, 1H), 8.40 (dd, J = 4.5, 0.9 Hz, 1H), 7.61 (dd, J = 4.8, 4.5 Hz, 1H), 7.43 (m, 1H), 7.36 (dd, J = 4.5, 0.6 Hz, 1H), 7.32 (dd, J = 4.5, 0.9 Hz, 1H), 7.25 (dd, J = 4.8, 0.6 Hz, 1H), 7.23–7.18 (m, 2H), 7.11-

7.00 (m, 7H), 6.82–6.81 (m, 2H), 6.68–6.60 (m, 2H), 6.56–6.52 (m, 2H), 6.30–6.28 (m, 1H), 5.69 (d, J = 4.5 Hz, 1H), 5.40 (d, J = 2.7 Hz, 1H), 5.37 (d, J = 2.7 Hz, 1H) ppm; ^{13}C NMR (75 MHz, CD_2Cl_2): δ 156.08, 155.63, 154.04, 139.11, 136.32, 135.74, 135.11, 135.05, 133.59, 132.22, 132.01, 131.22, 130.65, 130.49, 130.31, 129.54, 129.25, 129.12, 128.62, 128.59, 128.41, 127.74, 127.54, 126.76, 126.08, 125.74, 125.48, 125.39, 123.32, 123.24, 122.37, 121.63, 121.48, 120.71, 120.02, 101.08, 92.96 ppm; HRMS (APPI-TOF, positive) m/z calculated for $C_{42}H_{26}O_4$ $[M]^+$ 594.18311, found 594.18283.

Compound 8

Compound **6** was subjected to photocyclization for 24 h following the general procedure **B** described above. Upon completion, compound **8** was obtained and purified through silica column chromatography (CH_2Cl_2/hexanes, 30:70) as a yellow solid (0.257 g, 0.433 mmol, 87%). m.p.: > 400 °C (decomp); IR (neat): 3095, 3071, 2960, 2907, 1610, 1596, 1572, 1552, 1477, 1439, 1282, 1238, 1199, 1181, 1150, 1130, 1100, 1047 cm^{-1}. ^{1}H NMR (300 MHz, CD_2Cl_2): δ 9.05 (s, 2H), 8.92 (dd, J = 8.4, 1.2 Hz, 2H), 7.77 (dd, J = 8.4, 7.5 Hz, 2H), 7.51 (dd, J = 7.2, 1.2 Hz, 2H), 7.48–7.45 (m, 2H), 7.38 (d, 1.2 Hz, 1H), 7.35 (d, 1.2 Hz, 1H), 7.17–7.04 (m, 6H), 6.68 (dd, J = 6.3, 3.3 Hz, 2H), 5.63 (d, J = 4.5 Hz, 2H), 5.59 (d, J = 4.5 Hz, 2H) ppm; ^{13}C NMR (75 MHz, $CDCl_3$): δ 155.31, 153.90, 145.10, 139.87, 135.42, 134.51, 133.15, 131.42, 130.59, 130.37, 129.08, 128.42, 127.03, 126.84, 126.20, 125.62, 122.74, 122.08, 121.33, 121.18, 100.73 ppm; HRMS (APPI-TOF, positive) m/z calculated for $C_{42}H_{24}O_4$ $[M]^+$ 592.16746, found 592.16638.

Compound 9

To a mixture of partially cyclized derivatives **7** and **8** (0.090 g, 0.15 mmol) dissolved in CH_2Cl_2 (75 mL) was added methanesulfonic acid (2.5 mL) at 0 °C. This mixture was treated with a solution of DDQ (0.205 g, 0.905 mmol) as in 10 mL CH_2Cl_2. It was followed by a very sharp color change from yellow to dark brown. The reaction was continued for 5 h and reached room temperature gradually, which was finally quenched by addition of a saturated aqueous solution of $NaHCO_3$ (100 mL). Then the CH_2Cl_2 layer was separated and washed with water and brine solution three times (100 mL) and dried over $MgSO_4$ and filtered. The solution was concentrated under vacuum and was dispersed in methanol (100 mL) to form product **9** as precipitates. The product was collected by vacuum filtration as a black powder (0.044 g, 0.074 mmol, 50%). m.p.: $>$ 420 °C (decomp). IR (neat): 3102, 3085, 2952, 2900, 1600, 1560, 1550, 1466, 1230, 1200, 1181, 1150, 1100 cm^{-1}. ^1H NMR (300 MHz, CD_2Cl_2): δ 9.22 (s, 4H), 8.88 (dd, J = 7.9, 1.1 Hz, 4H), 7.83 (t, J = 8.1 Hz, 4H), 7.49 (dd, J = 7.3, 0.93, 4H), 5.85 (s, 4H) ppm; ^{13}C NMR could not be obtained due to the poor solubility; HRMS (APPI-TOF, positive) m/z calculated for $C_{42}H_{20}O_4$ $[M]^+$ 588.13616, found 588.13379.

Chapter 6

Conclusions and Future Work

In this PhD thesis, four research projects have been successfully accomplished and published (Chapters 2–4). The project described in Chapter 5 is also complete and will be sent out for peer-reviewed publication shortly. The underlying theme running across these diversified projects is the synthesis and characterization of novel PAH-based functional molecular materials. Specifically, four classes of π-conjugated molecular systems have been investigated, namely diphenyl dibenzofulvenes (DP-DBFs), pentacenetetraone-derived π-extended tetrathiafulvalene analogues (TTFAQ-AQs), donor/acceptor (D/A)-functionalized phenanthroimidazoles (PIs), and bis(diarylmethylene)dihydroanthracenes (Ar_4-DHAs). These compounds were analyzed and characterized using spectroscopic techniques, single-crystal X-ray diffraction, and electrochemical analyses, shedding light on their structure-property relationships and paving the way to rationally design advanced PAH-based functional molecular materials.

In the first project, we have focused on finding the origin of the observed AIE

and CIEE properties of DP-DBFs and their correlation with the twist around the C=C double bond. The DP-DBF derivatives we investigated contain methoxy and benzyloxy functional groups at different positions of phenyl ring as well as a tethered DP-DBF, and their synthesis was done through mainly Suzuki-Miyaura cross-coupling and nucleophilic substitution reactions, while the resulting DP-DBFs provided a wide range of twist angles about the double bond. Single crystals of all these derivatives were successfully grown and characterized by X-ray analysis, based on which a systematic study of molecular structure–fluorescence property correlations became possible. With the aid of absorption and emission spectroscopic analyses, we have revealed a clear linear correlation between the twist angle of the double bond in DP-DBF and the AIE/CIEE properties. Our experimental results concur with a conical intersection seam model previously published, proving that an increase in the C=C twist angle leads to decreased fluorescence efficiency (quantum yield) in the crystalline state, and vice versa. Our results have effectively provided fundamental understanding of the origin of the AIE/CIEE behaviour of DP-DBF–based luminogens. For the future work, high-level computational analyses of DP-BDFs in terms of their excited-state potential energy surfaces are conceived. Without a doubt, these studies require the use of expensive configuration interaction theories and/or time-dependent density functional theory (TD-DFT) approaches. Nevertheless, successful implentation of these analyses will deepen the understanding of AIE/CIEE-active fluorophores and guide our future design of more efficient and task-specific organic fluorophores that work in the aggregated and solid states.

In the second research project, three derivatives of TTFAQ-AQs were designed and synthesized as redox-active π-extended tetrathiafulvalene analogues. Their

synthesis was efficiently achieved through a regioselective double-olefination reaction, involving Ramirez geminal-dibromoolefination reaction followed by a double *S*-vinylation reaction. The target TTFAQ-AQs show a double curved conformation with two concave π-surfaces, which are electron-donating and electron-accepting, respectively. Based on X-ray diffraction analysis, a benzoannulated TTFAQ-AQ was found to contain a deeper π-extended cavity that facilitate its co-crystallization with oblong C_{70} fullerene. It is remarkable that the co-crystal contains organized three-dimensional supramolecular networks in the solid state. However, based on ^{1}H NMR titration analysis in the solution phase, the binding with C_{70} is beyond simple 1:1 and/or 1:2 guest-host interactions. Instead, the results point to complex supramolecular assemblies. Moreover, these observations are in good agreement with computational modeling, which confirmed a better shape complementarity between C_{70} and benzo-fused TTFAQ-AQ as well as stronger interactions. Furthermore, cyclic voltammetric analysis of these compounds revealed narrow HOMO–LUMO gaps, which are consistent with optical band gaps and theoretically calculated HOMO–LUMO energies. It is noteworthy that this study suggests promisingapplication in advanced electronic and optoelectronic devices. However, for the future study, novel TTFAQ-AQ derivatives with highly extended π-surfaces must be pursued, so that a better supramolecular interaction and more stable supramolecular assemblies in the liquid state can be realized. The challenges can be addressed through the rational molecular design and well-defined structure-property relationships.

The third project was centered on the design, synthesis, and characterization of a new class of donor-acceptor wedge-shaped phenanthroimidazole (PI) derivatives through π-extension at the 6,9-positions of the PI core to yield aldehyde-, DTF-

, and TTFV-functionalized PIs. These materials have been systematically studied using X-ray single crystal diffraction, cyclic voltammetric, UV-Vis absorption, and fluorescence spectroscopic analyses. It was observed that the PI bearing aldehyde moieties as the electron-accepting functional groups, shows significant fluorescence efficiency as well as a wide range of Stokes shifts in different organic solvents. In contrast, DTF and TTFV-substitution resulted in negligible fluorescence emission (i.e., fluorescence quenching). Based on ^{1}H NMR and fluorescence analyses, we discovered that the redox-active DTF-substituted PI undergoes singlet oxygen-induced C=C cleavage, which provides a chemiluminescent mechanism to yield fluorescence turn-on responsiveness. The formation of highly emissive aldehyde-substituted PI from non-emissive DTF-PI makes this method stand out amongst other singlet oxygen sensing approaches. Moreover, the oxidative coupling reaction of DTF end groups led to the formation of TTFV-PI macrocycles. Although macrocyclic system was not responsive to singlet oxygen, the fluorescence titration analyses of them in interaction with C_{60} or C_{70} fullerene revealed intriguing fluorescence turn-on/off behavior. These results suggest the electron/energy transfer from electron donating units, DTF and TTFV, to the electron accepting PI core, which ends up with the quenching of the fluorescence. However, under certain conditions, disruption of this electron transfer property leads to fluorescence turn-on behavior. All in all, this study presents a novel approach to adjust the electrochemical and photophysical features of PI-based materials, making them versatile candidates for the application in organic photovoltaic and fluorescence sensory devices. It is noteworthy that **PI 8** possesses the potential of further functionalization on imidazolyl N–H to reach a wide range of structure-property relationships. However, due to time limitation, the

investigation of further synthetic pathways to reach this derivative was not achieved in this study and is of great interest as future research direction.

The forth project describes the synthesis and characterization of bis(diarylmethylene)dihydroanthracenes, referred to as Ar_4-DHAs. Ramirez dibromoolefination and Suzuki-Miyaura cross-coupling were performed to obtain three different methoxy-substituted derivatives of Ar_4-DHAs, which then underwent photocyclization or photocyclization/Scholl reactions to afford cycloaromatized products. To form a tethered model compound, a demethylation reaction followed by an etherification reaction was also performed. The structure and properties of Ar_4-DHAs precursors and cyclized products have been studied thoroughly through X-ray single crystallography, UV-Vis spectroscopy, fluorescence spectroscopy, and DFT theoretical analysis. According to the data obtained from photophysical analysis, we have found that upon cyclization, the Ar_4-DHAs cyclized products reach remarkable fluorescence enhancement and show a red-shifted maximum absorption band. This observation is due to a higher degree of π-conjugation as a result of cyclization reaction. It is worth mentioning that photocyclization reaction led to the formation of half-cyclized products and, interestingly, it only ended up with the formation of an "anti-fuse" isomer. To explain the two-fold Mallory reaction, we made discussion based on the theoretical study by Salazar and Faraji, which deals with the PES of S_1 and S_2 before and after photocyclization. Prior to photocyclization, the PES show MECP seams, allowing the crossing of S_1 and S_2 to occur. This step leads to two-fold Mallory photocyclization, but the fluorescence pathway is insignificantly involved. After two steps of photocyclization, a dramatic change occurs on the PES of S_1 and S_2, which suppresses the next step of photocyclization. Instead, it revives a highly efficient

radiative decay pathway, yielding a highly emissive cyclized product and annihilating further photocyclizability. The observed reactivities could be rationalized by FMO analyses, showing that the anti-fuse isomer formation is favored, since LUMO orbital coefficient distributions are much larger at the positions which result in anti-fuse selectivity. To sum up, this chapter has successfully shed light on the mechanisms of photocyclization processes taling place on Ar_4-DHAs and clarified the existing questions in this field. Future studies are suggested to focus on more systematic experimental analyses and theoretical modeling of the excited-state dynamics to find out possible approaches to further enhance the photcyclization reactivities of Ar_4-DHA systems. If successful, some electron-rich functionalized nanographenes can be accessed through photochemical synthesis without the use of the highly oxidative Scholl conditions.

Bibliography

[1] Uoyama, H.; Goushi, K.; Shizu, K.; Nomura, H.; Adachi, C. Highly efficient organic light-emitting diodes from delayed fluorescence. *Nature* **2012**, *492*, 234–238.

[2] Zhang, Q.; Li, J.; Shizu, K.; Huang, S.; Hirata, S.; Miyazaki, H.; Adachi, C. Design of efficient thermally activated delayed fluorescence materials for pure blue organic light emitting diodes. *J. Am. Chem. Soc.* **2012**, *134*, 14706–14709.

[3] Zhao, J.; Li, Q.; Huang, Y.; Li, S.; Tang, W.; Peng, S.; Chen, S.; Liu, W.; Guo, X. Manufactured-on-demand steep subthreshold organic field effect transistor for low power and high sensitivity ion and fluorescence sensing. 2017 IEEE International Electron Devices Meeting (IEDM). 2017; pp 8–3.

[4] Sun, C.; Li, R.; Song, Y.; Jiang, X.; Zhang, C.; Cheng, S.; Hu, W. Ultrasensitive and reliable organic field-effect transistor-based biosensors in early liver cancer diagnosis. *J. Anal. Chem.* **2021**, *93*, 6188–6194.

[5] Qi, J.; Chen, C.; Zhang, X.; Hu, X.; Ji, S.; Kwok, R. T.; Lam, J. W.; Ding, D.; Tang, B. Z. Light-driven transformable optical agent with adaptive functions for boosting cancer surgery outcomes. *Nat. Commun.* **2018**, *9*, 1–12.

[6] Parker, C.; Rees, W. Fluorescence spectrometry. A review. *Analyst* **1962**, *87*, 83–111.

[7] Huang, M.; Yu, R.; Xu, K.; Ye, S.; Kuang, S.; Zhu, X.; Wan, Y. An arch-bridge-type fluorophore for bridging the gap between aggregation-caused quenching (ACQ) and aggregation-induced emission (AIE). *Chem. Sci.* **2016**, *7*, 4485–4491.

[8] Ma, X.; Sun, R.; Cheng, J.; Liu, J.; Gou, F.; Xiang, H.; Zhou, X. Fluorescence aggregation-caused quenching versus aggregation-induced emission: a visual teaching technology for undergraduate chemistry students. *J Chem Educ.* **2016**, *93*, 345–350.

[9] Birks, J. B. *Aromatic Molecules*; Wiley, New York, 1970; Vol. 704.

[10] Bakalova, R.; Zhelev, Z.; Aoki, I.; Ohba, H.; Imai, Y.; Kanno, I. Silica-shelled single quantum dot micelles as imaging probes with dual or multimodality. *J. Anal. Chem.* **2006**, *78*, 5925–5932.

[11] Zhelev, Z.; Ohba, H.; Bakalova, R. Single quantum dot-micelles coated with silica shell as potentially non-cytotoxic fluorescent cell tracers. *J. Am. Chem. Soc.* **2006**, *128*, 6324–6325.

[12] Mei, J.; Leung, N. L.; Kwok, R. T.; Lam, J. W.; Tang, B. Z. Aggregation-induced emission: together we shine, united we soar! *Chem. Rev.* **2015**, *115*, 11718–11940.

[13] Hong, Y.; Lam, J. W.; Tang, B. Z. Aggregation-induced emission. *Chem. Soc. Rev.* **2011**, *40*, 5361–5388.

[14] Thompson, R. B. *Fluorescence sensors and biosensors*; CRC Press, 2005.

[15] Geddes, C. D.; Lakowicz, J. R. *Advanced concepts in fluorescence sensing: Part A: Small molecule sensing*; Springer Science & Business Media, 2007; Vol. 9.

[16] Jares-Erijman, E. A.; Jovin, T. M. FRET imaging. *Nat. Biotechnol.* **2003**, *21*, 1387–1395.

[17] Tang, C. W.; VanSlyke, S. A. Organic electroluminescent diodes. *Appl. Phys. Lett.* **1987**, *51*, 913–915.

[18] Luo, J.; Xie, Z.; Lam, J. W.; Cheng, L.; Chen, H.; Qiu, C.; Kwok, H. S.; Zhan, X.; Liu, Y.; Zhu, D., et al. Aggregation-induced emission of 1-methyl-1,2,3,4,5-pentaphenylsilole. *Chem. Commun.* **2001**, 1740–1741.

[19] Chen, Z.; Zhang, J.; Song, M.; Yin, J.; Yu, G.-A.; Liu, S. H. A novel fluorene-based aggregation-induced emission (AIE)-active gold (I) complex with crystallization-induced emission enhancement (CIEE) and reversible mechanochromism characteristics. *Chem. Commun.* **2015**, *51*, 326–329.

[20] Chen, T.; Yang, S.; Chai, J.; Song, Y.; Fan, J.; Rao, B.; Sheng, H.; Yu, H.; Zhu, M. Crystallization-induced emission enhancement: A novel fluorescent Au-Ag bimetallic nanocluster with precise atomic structure. *Sci. Adv.* **2017**, *3*, e1700956.

[21] Yang, L.; Koo, D.; Wu, J.; Wong, J. M.; Day, T.; Zhang, R.; Kolongoda, H.; Liu, K.; Wang, J.; Ding, Z., et al. Benzosiloles with crystallization-induced emission enhancement of electrochemiluminescence: synthesis, electrochemistry, and crystallography. *Chem. Eur. J.* **2020**, *26*, 11715–11721.

[22] Dong, Y.; Lam, J. W.; Qin, A.; Li, Z.; Sun, J.; Sung, H. H.-Y.; Williams, I. D.; Tang, B. Z. Switching the light emission of (4-biphenylyl) phenyldibenzofulvene by morphological modulation: crystallization-induced emission enhancement. *Chem. Commun.* **2007**, 40–42.

[23] Dong, Y.; Lam, J. W.; Qin, A.; Sun, J.; Liu, J.; Li, Z.; Sun, J.; Sung, H. H.; Williams, I. D.; Kwok, H. S., et al. Aggregation-induced and crystallization-enhanced emissions of 1,2-diphenyl-3,4-bis (diphenylmethylene)-1-cyclobutene. *Chem. Commun.* **2007**, 3255–3257.

[24] Zhao, N.; Yang, Z.; Lam, J. W.; Sung, H. H.; Xie, N.; Chen, S.; Su, H.; Gao, M.; Williams, I. D.; Wong, K. S., et al. Benzothiazolium-functionalized tetraphenylethene: an AIE luminogen with tunable solid-state emission. *Chem. Commun.* **2012**, *48*, 8637–8639.

[25] Yuan, W. Z.; Gong, Y.; Chen, S.; Shen, X. Y.; Lam, J. W.; Lu, P.; Lu, Y.; Wang, Z.; Hu, R.; Xie, N., et al. Efficient solid emitters with aggregation-induced emission and intramolecular charge transfer characteristics: molecular design, synthesis, photophysical behaviors, and OLED application. *Chem. Mater.* **2012**, *24*, 1518–1528.

[26] Tong, J.; Wang, Y. J.; Wang, Z.; Sun, J. Z.; Tang, B. Z. Crystallization-induced emission enhancement of a simple tolane-based mesogenic luminogen. *J. Phys. Chem. C* **2015**, *119*, 21875–21881.

[27] Mei, J.; Hong, Y.; Lam, J. W.; Qin, A.; Tang, Y.; Tang, B. Z. Aggregation-induced emission: the whole is more brilliant than the parts. *J. Adv. Mater.* **2014**, *26*, 5429–5479.

[28] Leung, N. L.; Xie, N.; Yuan, W.; Liu, Y.; Wu, Q.; Peng, Q.; Miao, Q.; Lam, J. W.; Tang, B. Z. Restriction of intramolecular motions: the general mechanism behind aggregation-induced emission. *Chem. Eur. J.* **2014**, *20*, 15349–15353.

[29] He, Z.; Zhang, L.; Mei, J.; Zhang, T.; Lam, J. W.; Shuai, Z.; Dong, Y. Q.; Tang, B. Z. Polymorphism-dependent and switchable emission of butterfly-like bis(diarylmethylene)dihydroanthracenes. *Chem. Mater.* **2015**, *27*, 6601–6607.

[30] Gu, X.; Yao, J.; Zhang, G.; Yan, Y.; Zhang, C.; Peng, Q.; Liao, Q.; Wu, Y.; Xu, Z.; Zhao, Y., et al. Polymorphism-Dependent Emission for Di(p-methoxylphenyl)dibenzofulvene and Analogues: Optical Waveguide/Amplified Spontaneous Emission Behaviors. *Adv. Funct. Mater.* **2012**, *22*, 4862–4872.

[31] Wang, J.-H.; Feng, H.-T.; Luo, J.; Zheng, Y.-S. Monomer emission and aggregate emission of an imidazolium macrocycle based on bridged tetraphenylethylene and their quenching by C_{60}. *J. Org. Chem.* **2014**, *79*, 5746–5751.

[32] Tong, H.; Dong, Y.; Häußler, M.; Lam, J. W.; Sung, H. H.-Y.; Williams, I. D.; Sun, J.; Tang, B. Z. Tunable aggregation-induced emission of diphenyldibenzofulvenes. *Chem. Commun.* **2006**, 1133–1135.

[33] Crocker, R. D.; Zhang, B.; Pace, D. P.; Wong, W. W.; Nguyen, T. V. Tetrabenzo [5.7] fulvalene: a forgotten aggregation induced-emission luminogen. *Chem. Commun.* **2019**, *55*, 11591–11594.

[34] Hu, F.; Zhang, G.; Zhan, C.; Zhang, W.; Yan, Y.; Zhao, Y.; Fu, H.; Zhang, D. Highly Solid-State Emissive Pyridinium-Substituted Tetraphenylethylene Salts: Emission Color-Tuning with Counter Anions and Application for Optical Waveguides. *Small* **2015**, *11*, 1335–1344.

[35] Wang, Y.; Zhang, G.; Zhang, W.; Wang, X.; Wu, Y.; Liang, T.; Hao, X.; Fu, H.; Zhao, Y.; Zhang, D. Tuning the Solid State Emission of the Carbazole and Cyano-Substituted Tetraphenylethylene by Co-Crystallization with Solvents. *Small* **2016**, *12*, 6554–6561.

[36] Yu, T.; Ou, D.; Yang, Z.; Huang, Q.; Mao, Z.; Chen, J.; Zhang, Y.; Liu, S.; Xu, J.; Bryce, M. R., et al. The HOF structures of nitrotetraphenylethene derivatives provide new insights into the nature of AIE and a way to design mechanoluminescent materials. *Chem. Sci.* **2017**, *8*, 1163–1168.

[37] Qi, Q.; Qian, J.; Tan, X.; Zhang, J.; Wang, L.; Xu, B.; Zou, B.; Tian, W. Remarkable turn-on and color-tuned piezochromic luminescence: mechanically switching intramolecular charge transfer in molecular crystals. *Adv. Funct. Mater.* **2015**, *25*, 4005–4010.

[38] Zhang, Z.; Wu, Y.-S.; Tang, K.-C.; Chen, C.-L.; Ho, J.-W.; Su, J.; Tian, H.; Chou, P.-T. Excited-state conformational/electronic responses of saddle-shaped N, N-disubstituted-dihydrodibenzo [a, c] phenazines: wide-tuning emission from red to deep blue and white light combination. *J. Am. Chem. Soc.* **2015**, *137*, 8509–8520.

[39] Bryce, M. R.; Murphy, L. C. Organic metals. *Nature* **1984**, *309*, 119.

[40] Jørgensen, T.; Hansen, T. K.; Becher, J. Tetrathiafulvalenes as building-blocks in supramolecular chemistry. *Chem. Soc. Rev.* **1994**, *23*, 41–51.

[41] Nielsen, M. B.; Lomholt, C.; Becher, J. Tetrathiafulvalenes as building blocks in supramolecular chemistry II. *Chem. Soc. Rev.* **2000**, *29*, 153–164.

[42] Bryce, M. R. Functionalised tetrathiafulvalenes: New applications as versatile π-electron systems in materials chemistry. *J. Mater. Chem.* **2000**, *10*, 589–598.

[43] Iyoda, M.; Hasegawa, M.; Miyake, Y. Bi-TTF, bis-TTF, and related TTF oligomers. *Chem. Rev.* **2004**, *104*, 5085–5114.

[44] Perez, E. M.; Illescas, B. M.; Herranz, M. Á.; Martin, N. Supramolecular chemistry of π-extended analogues of TTF and carbon nanostructures. *New J. Chem.* **2009**, *33*, 228–234.

[45] Martín, N. Tetrathiafulvalene: the advent of organic metals. *Chem. Commun.* **2013**, *49*, 7025–7027.

[46] Wudl, F.; Smith, G. M.; Hufnagel, E. J., Bis-1,3-dithiolium chloride: an unusually stable organic radical cation. *J. Chem. Soc. D* **1970, 1453–1454**,

[47] Coffen, D. L.; Chambers, J. Q.; Williams, D. R.; Garrett, P.; Canfield, N. Tetrathioethylenes. *J. Am. Chem. Soc.* **1971**, *93*, 2258–2268.

[48] Kao, J.; Eyermann, C.; Southwick, E.; Leister, D. A systematic approach to calculate molecular properties of organosulfur compounds containing the carbon-sulfur (Csp2-S) bond. *J. Am. Chem. Soc.* **1985**, *107*, 5323–5332.

[49] Benassi, R.; Taddei, F. Ground-state molecular stabilization of substituted ethylenes. A theoretical mo ab-initio thermochemical study. *J. Mol. Struct. THEOCHEM* **2001**, *572*, 169–183.

[50] Nielsen, M. B.; Sauer, S. P. On the aromaticity of tetrathiafulvalene cations. *Chem. Phys. Lett.* **2008**, *453*, 136–139.

[51] Kirmse, W.; Horner, L. Über Lichtreaktionen VIII. Photolyse von 1.2. 3-Thiodiazolen. *Justus Liebigs Ann. Chem.* **1958**, *614*, 4–18.

[52] Hartzler, H. D. 2-Benzylidene-1,3-dithioles. Remarkably rapid Wittig reaction. *J. Am. Chem. Soc.* **1971**, *93*, 4961–4962.

[53] Sato, M.; Gonnella, N. C.; Cava, M. P. Synthesis and reactions of (4,5-dicarbomethoxy-1, 3-dithiolyl) tributylphosphonium tetrafluoroborate. *J. Org. Chem.* **1979**, *44*, 930–934.

[54] Christensen, C. A.; Batsanov, A. S.; Bryce, M. R. Thiolated π-extended tetrathiafulvalenes: Versatile multifunctional π-systems. *J. Org. Chem.* **2007**, *72*, 1301–1308.

[55] Hurtley, W. R. H.; Smiles, S. CCXCIX.—2: 2-Bis-1: 3-benzdithiolene. *J. Chem. Soc.* **1926**, *129*, 2263–2270.

[56] Mizuno, M.; Cava, M. P. Organic metals. A study of the Hurtley-Smiles tetrathiafulvalene synthesis. *J. Org. Chem.* **1978**, *43*, 416–418.

[57] Gimbert, Y.; Moradpour, A.; Dive, G.; Dehareng, D.; Lahlil, K. A variable mechanism for the nucleophilic vinylic substitutions in a series of gem-dihalogenated alkenes by a bidentate sulfur nucleophile: an experimental and AM1 theoretical study. *J. Org. Chem.* **1993**, *58*, 4685–4690.

[58] Giguere, J.-B.; Morin, J.-F. Super extended Tetrathiafulvalene: synthesis, Optoelectronic Properties, Fullerenes Complexation, and Photooxidation Study. *J. Org. Chem.* **2015**, *80*, 6767–6775.

[59] Broman, S. L.; Andersen, C. L.; Jousselin-Oba, T.; Mansø, M.; Hammerich, O.; Frigoli, M.; Nielsen, M. B. Tetraceno [2,1,12,11-opqra] tetracene-extended tetrathiafulvalene–redox-controlled generation of a large PAH core. *Org. Biomol. Chem.* **2017**, *15*, 807–811.

[60] Mayer, R.; Kröber, H. Oxydative Dimerisierung von 1,4-Dithiafulvenen (2-Methylen-1,3-dithiolen). *J. Prakt. Chem.* **1974**, *316*, 907–912.

[61] Ohta, A.; Yamashita, Y. Oxidative intramolecular cyclization of 2,2-bis (1,4-dithiafulven-6-yl)-3,3-bithienyls affording novel bis (1,3-dithiole) electron donors. *J. Chem. Soc., Chem. Commun.* **1995**, 1761–1762.

[62] Yamashita, Y.; Tomura, M.; Zaman, M. B. synthesis and properties of novel tetrathiafulvalene vinylogues. *Chem. Commun.* **1998**, 1657–1658.

[63] Müller, H.; Salhi, F.; Divisia-Blohorn, B. Bis-substituted tetrathiapentalenes—Novel building blocks for extended tetrathiafulvalenes and conducting polymers. *Tetrahedron Lett.* **1997**, *38*, 3215–3218.

[64] Massue, J.; Bellec, N.; Guerro, M.; Bergamini, J.-F.; Hapiot, P.; Lorcy, D. Crown ether vinylogous tetrathiafulvalene receptors: Complexation interference on the molecular movements triggered by electron transfer. *J. Org. Chem.* **2007**, *72*, 4655–4662.

[65] Lakshmikantham, M.; Cava, M. P.; Carroll, P. J. Novel oxidative rearrangement of o-xylene-. alpha.,. alpha.'-diylidenebis (4, 5-dicarbomethoxy-1,3-dithiole). *J. Org. Chem.* **1984**, *49*, 726–728.

[66] Frère, P.; Gorgues, A.; Jubault, M.; Riou, A.; Gouriou, Y.; Roncali, J. Electrochemically induced intramolecular cyclization of 1, 2-bis (1, 4-dithiafulven-6-yl) benzenes. *Tetrahedron Lett.* **1994**, *35*, 1991–1994.

[67] Guerro, M.; Roisnel, T.; Pellon, P.; Lorcy, D. Redox-active dithiafulvenyldiphenylphosphine as a mono-or bidentate ligand: Intramolecular coupling reaction in the coordination sphere of a metal carbonyl fragment. *Inorg. Chem.* **2005**, *44*, 3347–3355.

[68] Guerro, M.; Pham, N. H.; Massue, J.; Bellec, N.; Lorcy, D. New redox active ligands involving a tetrathiafulvalene vinylogue backbone. *Tetrahedron* **2008**, *64*, 5285–5290.

[69] Gontier, E.; Bellec, N.; Brignou, P.; Gohier, A.; Guerro, M.; Roisnel, T.; Lorcy, D. Pyridyldithiafulvenes as Precursors of Coordination-Driven Self-Assembled Redox Active Macrocycle. *Org. Lett.* **2010**, *12*, 2386–2389.

[70] Frère, P.; Gorgues, A.; Jubault, M.; Riou, A.; Gouriou, Y.; Roncali, J. Electrochemically induced intramolecular cyclization of 1, 2-bis (1, 4-dithiafulven-6-yl) benzenes. *Tetrahedron Lett.* **1994**, *35*, 1991–1994.

[71] Benahmed-Gasmi, A.; Frère, P.; Roncali, J.; Elandaloussi, E.; Orduna, J.; Garin, J.; Jubault, M.; Gorgues, A. Oxidative dimerization of 2-(1,4-dithiafulven-6-yl) thiophenes: an alternative route towards extensively π-conjugated tetrathiafulvalene analogs. *Tetrahedron lett.* **1995**, *36*, 2983–2986.

[72] Lorcy, D.; Carlier, R.; Robert, A.; Tallec, A.; Le Maguerès, P.; Ouahab, L. Electrochemical synthesis of extended TTF. *J. Org. Chem.* **1995**, *60*, 2443–2447.

[73] Hascoat, P.; Lorcy, D.; Robert, A.; Carlier, R.; Tallec, A.; Boubekeur, K.; Batail, P. Formation of Attractive π-Redox Cyclophanes. *J. Org. Chem.* **1997**, *62*, 6086–6089.

[74] Hapiot, P.; Lorcy, D.; Tallec, A.; Carlier, R.; Robert, A. Mechanism of dimerization of 1,4-dithiafulvenes into TTF vinylogues. *J. Phys. Chem.* **1996**, *100*, 14823–14827.

[75] Inagi, S.; Naka, K.; Chujo, Y. Functional polymers based on electron-donating TTF and derivatives. *J. Mater. Chem.* **2007**, *17*, 4122–4135.

[76] Zhao, Y.; Chen, G.; Mulla, K.; Mahmud, I.; Liang, S.; Dongare, P.; Thompson, D. W.; Dawe, L. N.; Bouzan, S. Tetrathiafulvalene vinylogues as versatile building blocks for new organic materials. *Pure Appl. Chem.* **2012**, *84*, 1005–1025.

[77] Guerro, M.; Lorcy, D. A simple route to novel functionalized tetrathiafulvalene vinylogues. *Tetrahedron Lett.* **2005**, *46*, 5499–5502.

[78] Lakshmikantham, M.; Cava, M. P. Some novel transformations of 1,4-dithiafulvenes. *J. Org. Chem.* **1981**, *46*, 3246–3249.

[79] Sarhan, A. A.; Bolm, C. Light-Induced synthesis of π-Extended Tetrathiafulvalenes Incorporating Ferrocenes: An Efficient Route for the synthesis of Electron-Donor Materials. *Synthesis* **2009**, 1000–1006.

[80] Shahrokhi, F.; Abdollahi, M. F.; Zhao, Y. A comparative study of redox-active dithiafulvenyl-functionalized 1,3,6,8-tetraphenylpyrene derivatives. *J. Org. Chem.* **2021**, *86*, 12723–12736.

[81] Spies, H.; Gewald, K.; Mayer, R. Zur Reaktion von Natriumphenylacetylid mit Schwefel oder Selen und Heterokumulenen. *J. Prakt. Chem.* **1971**, *313*, 804–810.

[82] Mulla, K.; Zhao, Y. When dithiafulvenyl functionalized π-conjugated oligomers meet fullerenes and single-walled carbon nanotubes. *J. Mater. Chem. C* **2013**, *1*, 5116–5127.

[83] Bouzan, S.; Dawe, L. N.; Zhao, Y. Bromophenyl substituted dithiafulvenes and

tetrathiafulvalene vinylogues: synthesis, structure, and electronic properties. *Tetrahedron Lett.* **2013**, *54*, 4666–4669.

[84] Woolridge, K.; Goncalves, L. C.; Bouzan, S.; Chen, G.; Zhao, Y. Aryl-substituted dithiafulvenes: synthesis, electronic properties, and redox reactivity. *Tetrahedron Lett.* **2014**, *55*, 6362–6366.

[85] Khadem, M.; Walsh, J. C.; Bodwell, G. J.; Zhao, Y. A Macrocyclization of 1,8-Bis(dithiafulvenyl)pyrenes. *Org. Lett.* **2016**, *18*, 2403–2406.

[86] Fu, H.; Zhao, B.; Zhu, W. Elemental iodine mediated synthesis of thiadiazole-based dithiafulvalene donors via C (SP2)–S formation. *Tetrahedron Lett.* **2019**, *60*, 124–128.

[87] Wang, Y.; Zhao, Y. Dithiafulvenyl-substituted phenylacetylene derivatives: synthesis and structure–property–reactivity relationships. *Org. Biomol. Chem.* **2015**, *13*, 9575–9579.

[88] Wang, C.; Flinn, C.; Zhao, Y. Intramolecular alkyne–dithiolium cycloaddition: a joint experimental and DFT mechanistic study. *RSC Adv.* **2017**, *7*, 36623–36631.

[89] Alévêque, O.; Leriche, P.; Cocherel, N.; Frère, P.; Cravino, A.; Roncali, J. Star-shaped conjugated systems derived from dithiafulvenyl-derivatized triphenylamines as active materials for organic solar cells. *Sol. Energy Mater. Sol. Cells* **2008**, *92*, 1170–1174.

[90] Wan, Z.; Jia, C.; Duan, Y.; Chen, X.; Lin, Y.; Shi, Y. Novel organic dye

employing dithiafulvenyl-substituted arylamine hybrid donor unit for dye-sensitized solar cells. *Org. Electron.* **2013**, *14*, 2132–2138.

[91] Wan, Z.; Jia, C.; Duan, Y.; Chen, X.; Li, Z.; Lin, Y. Novel organic sensitizers containing dithiafulvenyl units as additional donors for efficient dye-sensitized solar cells. *RSC Adv.* **2014**, *4*, 34896–34903.

[92] Chen, Q.; Li, X.; Jiu, T.; Ma, S.; Li, J.; Xiao, X.; Zhang, W. Tetrathiafulvalene derivative as a new hole-transporting material for highly efficient perovskite solar cell. *Dyes Pigm.* **2017**, *147*, 113–119.

[93] Khadem, M.; Zhao, Y. Multivalent dithiafulvenyl functionalization of dendritic oligo (phenylene vinylene)s with an anthraquinodimethane core. *Chem. Commun.* **2017**, *53*, 1821–1824.

[94] Shahrokhi, F.; Zhao, Y. A tetrathiafulvalene vinylogue-based double-layer polymer thin film as a highly sensitive and selective TNT sensor. *New J. Chem.* **2019**, *43*, 5277–5281.

[95] Balandier, J.-Y.; Belyasmine, A.; Sallé, M. Tetrathiafulvalene–Imine–Pyridine Assemblies for Pb2+ Recognition. *EurJOC* **2008**, *2008*, 269–276.

[96] Balandier, J.-Y.; Chas, M.; Dron, P. I.; Goeb, S.; Canevet, D.; Belyasmine, A.; Allain, M.; Sallé, M. N-aryl pyrrolo-tetrathiafulvalene based ligands: synthesis and metal coordination. *J. Org. Chem.* **2010**, *75*, 1589–1599.

[97] Lehn, J.-M. Supramolecular chemistry. *Science* **1993**, *260*, 1762–1763.

[98] Steed, J. W.; Atwood, J. L. *Supramolecular chemistry*; John Wiley & Sons, 2022.

[99] Lehn, J.-M. Supramolecular chemistry: from molecular information towards self-organization and complex matter. *Rep. Prog. Phys.* **2004**, *67*, 249.

[100] Ballardini, R.; Balzani, V.; Credi, A.; Gandolfi, M. T.; Venturi, M. Artificial molecular-level machines: which energy to make them work? *Acc. Chem. Res.* **2001**, *34*, 445–455.

[101] Vollmer, M. S.; Clark, T. D.; Steinem, C.; Ghadiri, M. R. Photoswitchable hydrogen-bonding in self-organized cylindrical peptide systems. *Angew. Chem. Int. Ed.* **1999**, *38*, 1598–1601.

[102] Smalley, R. E. Discovering the fullerenes. *Rev. Mod. Phys.* **1997**, *69*, 723.

[103] Kroto, H. W.; Heath, J. R.; O'Brien, S. C.; Curl, R. F.; Smalley, R. E. C60: Buckminsterfullerene. *Nature* **1985**, *318*, 162–163.

[104] Illescas, B. M.; Martin, N. [60] Fullerene-based electron acceptors. *C. R. Chim.* **2006**, *9*, 1038–1050.

[105] Yu, G.; Gao, J.; Hummelen, J. C.; Wudl, F.; Heeger, A. J. Polymer photovoltaic cells: enhanced efficiencies via a network of internal donor-acceptor heterojunctions. *Science* **1995**, *270*, 1789–1791.

[106] Neti, V. S. P. K.; Cerón, M. R.; Duarte-Ruiz, A.; Olmstead, M. M.; Balch, A. L.; Echegoyen, L. High-yield, regiospecific bis-functionalization of C_{70} using a

Diels–Alder reaction in molten anthracene. *Chem. Commun.* **2014**, *50*, 10584–10587.

[107] Effing, J.; Jonas, U.; Jullien, L.; Plesnivy, T.; Ringsdorf, H.; Diederich, F.; Thilgen, C.; Weinstein, D. C_{60} and C_{70} in a Basket?–Investigations of Mono- and Multilayers from Azacrown Compounds and Fullerenes. *Angew. Chem., Int. Ed. Engl.* **1992**, *31*, 1599–1602.

[108] Andersson, T.; Nilsson, K.; Sundahl, M.; Westman, G.; Wennerström, O. C_{60} embedded in γ-cyclodextrin: a water-soluble fullerene. *J. Chem. Soc., Chem. Commun.* **1992**, 604–606.

[109] Atwood, J. L.; Koutsantonis, G. A.; Raston, C. L. Purification of C_{60} and C_{70} by selective complexation with calixarenes. *Nature* **1994**, *368*, 229–231.

[110] Boyd, P. D.; Reed, C. A. Fullerene- porphyrin constructs. *Acc. Chem. Res.* **2005**, *38*, 235–242.

[111] Kawase, T.; Kurata, H. Ball-, bowl-, and belt-shaped conjugated systems and their complexing abilities: exploration of the concave-convex π-π interaction. *Chem. Rev.* **2006**, *106*, 5250–5273.

[112] Sygula, A.; Fronczek, F. R.; Sygula, R.; Rabideau, P. W.; Olmstead, M. M. A double concave hydrocarbon buckycatcher. *J. Am. Chem. Soc.* **2007**, *129*, 3842–3843.

[113] Nielsen, M. B.; Diederich, F. Conjugated oligoenynes based on the diethynylethene unit. *Chem. Rev.* **2005**, *105*, 1837–1868.

[114] Pérez, E. M.; Sánchez, L.; Fernández, G.; Martín, N. exTTF as a building block for fullerene receptors. Unexpected solvent-dependent positive homotropic cooperativity. *J. Am. Chem. Soc.* **2006**, *128*, 7172–7173.

[115] Mulla, K.; Shaik, H.; Thompson, D. W.; Zhao, Y. TTFV-based molecular tweezers and macrocycles as receptors for fullerenes. *Org. Lett.* **2013**, *15*, 4532–4535.

[116] Perez, E. M.; Martin, N. Curves ahead: molecular receptors for fullerenes based on concave–convex complementarity. *Chem. Soc. Rev.* **2008**, *37*, 1512–1519.

[117] Grimm, B.; Santos, J.; Illescas, B. M.; Munoz, A.; Guldi, D. M.; Martin, N. A new exTTF-crown ether platform to associate fullerenes: Cooperative n-π and π-π effects. *J. Am. Chem. Soc.* **2010**, *132*, 17387–17389.

[118] Pérez, E. M.; Sierra, M.; Sánchez, L.; Torres, M. R.; Viruela, R.; Viruela, P. M.; Ortí, E.; Martín, N. Concave tetrathiafulvalene-type donors as supramolecular partners for fullerenes. *Angew. Chem. Int. Ed.* **2007**, *46*, 1847–1851.

[119] Gayathri, S. S.; Wielopolski, M.; Perez, E. M.; Fernandez, G.; Sanchez, L.; Viruela, R.; Ortí, E.; Guldi, D. M.; Martín, N. Discrete supramolecular donor–acceptor complexes. *Angew. Chem. Int. Ed.* **2009**, *48*, 815–819.

[120] Isla, H.; Gallego, M.; Pérez, E. M.; Viruela, R.; Orti, E.; Martin, N. A bis-exTTF macrocyclic receptor that associates C60 with micromolar affinity. *J. Am. Chem. Soc.* **2010**, *132*, 1772–1773.

[121] Gao, G.; Chen, M.; Roberts, J.; Feng, M.; Xiao, C.; Zhang, G.; Parkin, S.;

Risko, C.; Zhang, L. Rational functionalization of a C70 buckybowl to enable a C70: Buckybowl cocrystal for organic semiconductor applications. *J. Am. Chem. Soc.* **2020**, *142*, 2460–2470.

[122] Chen, W.-C.; Zhu, Z.-L.; Lee, C.-S. Organic light-emitting diodes based on imidazole semiconductors. *Adv. Opt. Mater.* **2018**, *6*, 1800258.

[123] Hofmann, K. *Imidazole and Its Derivatives, Volume 6, Part 1*; John Wiley & Sons, 2009.

[124] Liu, B.; Yuan, Y.; He, D.; Huang, D.-Y.; Luo, C.-Y.; Zhu, Z.-L.; Lu, F.; Tong, Q.-X.; Lee, C.-S. High-Performance Blue OLEDs Based on Phenanthroimidazole Emitters via Substitutions at the C6-and C9-Positions for Improving Exciton Utilization. *Chem. Eur. J.* **2016**, *22*, 12130–12137.

[125] Subeesh, M. S.; Shanmugasundaram, K.; Sunesh, C. D.; Won, Y. S.; Choe, Y. Utilization of a phenanthroimidazole based fluorophore in light-emitting electrochemical cells. *J. Mater. Chem. C* **2015**, *3*, 4683–4687.

[126] Zhang, Y.; Yang, R.; Liu, F.; Li, K. luorescent sensor for imidazole derivatives based on monomer- dimer equilibrium of a zinc porphyrin complex in a polymeric film. *J. Anal. Chem.* **2004**, *76*, 7336–7345.

[127] Han, M. S.; Kim, D. H. Effect of zinc ion on the inhibition of carboxypeptidase A by imidazole-bearing substrate analogues. *Bioorg. Med. Chem.* **2001**, *11*, 1425–1427.

[128] Shalini, K.; Sharma, P. K.; Kumar, N. Imidazole and its biological activities: A review. *Der Chemica Sinica* **2010**, *1*, 36–47.

[129] Congiu, C.; Cocco, M. T.; Onnis, V. Design, synthesis, and in vitro antitumor activity of new 1, 4-diarylimidazole-2-ones and their 2-thione analogues. *Bioorg. Med. Chem.* **2008**, *18*, 989–993.

[130] Bhatnagar, A.; Sharma, P.; Kumar, N., et al. A review on "Imidazoles": Their chemistry and pharmacological potentials. *Int. J. PharmTech Res.* **2011**, *3*, 268–282.

[131] Gallagher, T. F.; Fier-Thompson, S. M.; Garigipati, R. S.; Sorenson, M. E.; Smietana, J. M.; Lee, D.; Bender, P. E.; Lee, J. C.; Laydon, J. T.; Griswold, D. E., et al. 2, 4, 5-Triarylimidazole inhibitors of IL-1 biosynthesis. *Bioorganic Med. Chem. Lett.* **1995**, *5*, 1171–1176.

[132] Saxer, S.; Marestin, C.; Mercier, R.; Dupuy, J. The multicomponent Debus–Radziszewski reaction in macromolecular chemistry. *Polym. Chem.* **2018**, *9*, 1927–1933.

[133] Kothavale, S.; Bhalekar, S.; Sekar, N. Highly fluorescent blue-green emitting phenanthroimidazole derivatives: Detail experimental and DFT study of structural and donating group effects on fluorescence properties. *Dyes Pigm.* **2018**, *159*, 209–221.

[134] Wang, S.; Li, H.; Chen, C.; Zhang, J.; Li, S.; Qin, X.; Li, X.; Wang, K. Cytotoxicity and DNA binding property of phenanthrene imidazole with polyglycol side chains. *Bioorg. Med. Chem.* **2012**, *22*, 6347–6351.

[135] Wang, Z.; Lu, P.; Chen, S.; Gao, Z.; Shen, F.; Zhang, W.; Xu, Y.; Kwok, H. S.; Ma, Y. Phenanthro [9, 10-d] imidazole as a new building block for blue light emitting materials. *J. Mater. Chem.* **2011**, *21*, 5451–5456.

[136] Consoli, G. M.; Cunsolo, F.; Geraci, C.; Gavuzzo, E.; Neri, P. Atropisomerism in 1, 5-bridged calix [8] arenes. *Org. Lett.* **2002**, *4*, 2649–2652.

[137] Botana, E.; Naettinen, K.; Prados, P.; Rissanen, K.; de Mendoza, J. p-(1 H-Phenanthro [9, 10-d] imidazol-2-yl)-Substituted Calix [4] arene, a Deep Cavity for Guest Inclusion. *Org. Lett.* **2004**, *6*, 1091–1094.

[138] Xu, B.; Zhang, J.; Tian, W. Aggregation-Induced Emission of 9, 10-Distyrylanthracene Derivatives and Their Applications. *Aggregation-Induced Emission: Fundamentals and Applications, Volumes 1 and 2* **2013**, 61–82.

[139] Hong, Y. Aggregation-induced emission—fluorophores and applications. *Methods Appl. Fluoresc.* **2016**, *4*, 022003.

[140] Yuan, W. Z.; Yu, Z.-Q.; Lu, P.; Deng, C.; Lam, J. W.; Wang, Z.; Chen, E.-Q.; Ma, Y.; Tang, B. Z. High efficiency luminescent liquid crystal: aggregation-induced emission strategy and biaxially oriented mesomorphic structure. *J. Mater. Chem.* **2012**, *22*, 3323–3326.

[141] Kwok, R. T.; Leung, C. W.; Lam, J. W.; Tang, B. Z. Biosensing by luminogens with aggregation-induced emission characteristics. *Chem. Soc. Rev.* **2015**, *44*, 4228–4238.

[142] Wang, Y.-F.; Zhang, T.; Liang, X.-J. Aggregation-Induced Emission: Lighting up Cells, Revealing Life! *Small* **2016**, *12*, 6451–6477.

[143] Aldred, M. P.; Zhang, G.-F.; Li, C.; Chen, G.; Chen, T.; Zhu, M.-Q. Optical properties and red to near infrared piezo-responsive fluorescence of a tetraphenylethene–perylenebisimide–tetraphenylethene triad. *J. Mater. Chem. C* **2013**, *1*, 6709–6718.

[144] Ning, Z.; Chen, Z.; Zhang, Q.; Yan, Y.; Qian, S.; Cao, Y.; Tian, H. Aggregation-induced emission (AIE)-active starburst triarylamine fluorophores as potential non-doped red emitters for organic light-emitting diodes and Cl_2 gas chemodosimeter. *Adv. Funct. Mater.* **2007**, *17*, 3799–3807.

[145] Qin, W.; Yang, Z.; Jiang, Y.; Lam, J. W.; Liang, G.; Kwok, H. S.; Tang, B. Z. Construction of efficient deep blue aggregation-induced emission luminogen from triphenylethene for nondoped organic light-emitting diodes. *Chem. Mater.* **2015**, *27*, 3892–3901.

[146] Ren, Y.; Lam, J. W.; Dong, Y.; Tang, B. Z.; Wong, K. S. Enhanced emission efficiency and excited state lifetime due to restricted intramolecular motion in silole aggregates. *J. Phys. Chem. B* **2005**, *109*, 1135–1140.

[147] He, J.; Xu, B.; Chen, F.; Xia, H.; Li, K.; Ye, L.; Tian, W. Aggregation-induced emission in the crystals of 9,10-distyrylanthracene derivatives: the essential role of restricted intramolecular torsion. *J. Phys. Chem. C* **2009**, *113*, 9892–9899.

[148] Tong, H.; Dong, Y.; Hong, Y.; Häussler, M.; Lam, J. W.; Sung, H. H.-Y.; Yu, X.; Sun, J.; Williams, I. D.; Kwok, H. S., et al. Aggregation-induced emission:

effects of molecular structure, solid-state conformation, and morphological packing arrangement on light-emitting behaviors of diphenyldibenzofulvene derivatives. *J. Phys. Chem. C* **2007**, *111*, 2287–2294.

[149] Luo, X.; Li, J.; Li, C.; Heng, L.; Dong, Y. Q.; Liu, Z.; Bo, Z.; Tang, B. Z. Reversible switching of the emission of diphenyldibenzofulvenes by thermal and mechanical stimuli. *J. Adv. Mater.* **2011**, *23*, 3261–3265.

[150] Lin, Y.; Li, C.; Song, G.; He, C.; Dong, Y. Q.; Wang, H. Freezing-induced multi-colour emissions of AIE luminogen di(4-propoxyphenyl)dibenzofulvene. *J. Mater. Chem. C* **2015**, *3*, 2677–2685.

[151] Gao, X.; Peng, Q.; Niu, Y.; Wang, D.; Shuai, Z. Theoretical insight into the aggregation induced emission phenomena of diphenyldibenzofulvene: a nonadiabatic molecular dynamics study. *Phys. Chem. Chem. Phys.* **2012**, *14*, 14207–14216.

[152] Kokado, K.; Sada, K. Consideration of molecular structure in the excited state to design new luminogens with aggregation-induced emission. *Angew. Chem.* **2019**, *131*, 8724–8731.

[153] Li, Q.; Blancafort, L. A conical intersection model to explain aggregation induced emission in diphenyl dibenzofulvene. *Chem. Commun.* **2013**, *49*, 5966–5968.

[154] Dolomanov, O. V.; Bourhis, L. J.; Gildea, R. J.; Howard, J. A.; Puschmann, H. OLEX2: A Complete Structure Solution, Refinement and Analysis Program. *J. Appl. Crystallogr.* **2009**, *42*, 339–341.

[155] Sheldrick, G. M. SHELXT–Integrated Space-Group and Crystal-Dtructure Determination. *Acta Crystallogr. A* **2015**, *71*, 3–8.

[156] Sheldrick, G. M. Crystal Structure Refinement with SHELXL. *Acta Crystallogr. C* **2015**, *71*, 3–8.

[157] Frisch, M. J. et al. Gaussian 16 Revision C.01. Gaussian Inc., Wallingford CT, 2016.

[158] Jørgensen, T.; Hansen, T. K.; Becher, J. Tetrathiafulvalenes as Building-Blocks in Supramolecular Chemistry. *Chem. Soc. Rev.* **1994**, *23*, 41–51.

[159] Bryce, M. R. Functionalised Tetrathiafulvalenes: New Applications as Versatile π-Electron Systems in Materials Chemistry. *J. Mater. Chem.* **2000**, *10*, 589–598.

[160] Jérome, D. Organic Conductors: From Charge Density Wave TTF–TCNQ to Superconducting $(TMTSF)_2PF_6$. *Chem. Rev.* **2004**, *104*, 5565–5592.

[161] Bendikov, M.; Wudl, F.; Perepichka, D. F. Tetrathiafulvalenes, Oligoacenenes, and Their Buckminsterfullerene Derivatives: The Brick and Mortar of Organic Electronics. *Chem. Rev.* **2004**, *104*, 4891–4946.

[162] Nielsen, M. B.; Lomholt, C.; Becher, J. Tetrathiafulvalenes as Building Blocks in Supramolecular Chemistry II. *Chem. Soc. Rev.* **2000**, *29*, 153–164.

[163] Martín, N.; Sánchez, L.; Herranz, M. A.; Illescas, B.; Guldi, D. M. Electronic Communication in Tetrathiafulvalene (TTF)/C_{60} Systems: toward Molecular Solar Energy Conversion Materials? *Acc. Chem. Res.* **2007**, *40*, 1015–1024.

[164] Segura, J. L.; Martín, N. New Concepts in Tetrathiafulvalene Chemistry. *Angew. Chem. Int. Ed.* **2001**, *40*, 1372–1409.

[165] Hasegawa, M.; Iyoda, M. Conducting Supramolecular Nanofibers and Nanorods. *Chem. Soc. Rev.* **2010**, *39*, 2420–2427.

[166] Martín, N. Tetrathiafulvalene: the Advent of Organic Metals. *Chem. Commun.* **2013**, *49*, 7025–7027.

[167] Azov, V. A. Recent Advances in Molecular Recognition with Tetrathiafulvalene-based Receptors. *Tetrahedron Lett.* **2016**, *57*, 5416–5425.

[168] Jana, A.; Bähring, S.; Ishida, M.; Goeb, S.; Canevet, D.; Sallé, M.; Jeppesen, J. O.; Sessler, J. L. Functionalised Tetrathiafulvalene-(TTF-) Macrocycles: Recent Trends in Applied Supramolecular Chemistry. *Chem. Soc. Rev.* **2018**, *47*, 5614–5645.

[169] Gorgues, A.; Hudhomme, P.; Sallé, M. Highly Functionalized Tetrathiafulvalenes: Riding along the Synthetic Trail from Electrophilic Alkynes. *Chem. Rev.* **2004**, *104*, 5151–5184.

[170] Pérez, E. M.; Illescas, B. M.; Herranz, M. Á.; Martín, N. Supramolecular Chemistry of π-Extended Analogues of TTF and Carbon Nanostructures. *New J. Chem.* **2009**, *33*, 228–234.

[171] Brunetti, F. G.; López, J. L.; Atienza, C.; Martín, N. π-Extended TTF: a Versatile Molecule for Organic Electronics. *J. Mater. Chem.* **2012**, *22*, 4188–4205.

[172] Zhao, Y.; Chen, G.; Mulla, K.; Mahmud, I.; Liang, S.; Dongare, P.; Thompson, D. W.; Dawe, L. N.; Bouzan, S. Tetrathiafulvalene Vinylogues as Versatile Building Blocks for New Organic Materials. *Pure Appl. Chem.* **2012**, *84*, 1005–1025.

[173] Bergkamp, J. J.; Decurtins, S.; Liu, S.-X. Current Advances in Fused Tetrathiafulvalene Donor–Acceptor Systems. *Chem. Soc. Rev.* **2015**, *44*, 863–874.

[174] Hammerich, O.; Nielsen, M. B. Extended Tetrathiafulvalenes with Polycyclic Aromatic Cores. *J. Mater. Chem. C* **2019**, *7*, 2809–2822.

[175] Bryce, M. R.; Moore, A. J. A New Highly-conjugated TTF Analogue: synthesis, Electrochemistry and a Conducting TCNQ Complex of 9,10-Anthracenediylidene-2,2'-bis(4,5-dimethyl-1,3-dithiole). *Synth. Met.* **1988**, *25*, 203–205.

[176] Bryce, M. R.; Moore, A. J.; Hasan, M.; Ashwell, G. J.; Fraser, A. T.; Clegg, W.; Hursthouse, M. B.; Karaulov, A. Electrical and Magnetic Properties and X-Ray Structure of a Highly Conductive 4:1 Complex of Tetracyanoquinodimethane and a Tetrathiafulvalene Derivative. *Angew. Chem. Int. Ed. Engl.* **1990**, *29*, 1450–1452.

[177] Jones, A. E.; Christensen, C. A.; Perepichka, D. F.; Batsanov, A. S.; Beeby, A.; Low, P. J.; Bryce, M. R.; Parker, A. W. Photochemistry of the π-Extended 9,10-Bis(1,3-dithiol-2-ylidene)-9,10-dihydroanthracene System: Generation and

Characterisation of the Radical Cation, Dication, and Derived Products. *Chem. Eur. J.* **2001**, *7*, 973–978.

[178] Christensen, C. A.; Bryce, M. R.; Batsanov, A. S.; Becher, J. New Strategies and Building Blocks for Functionalised 9,10-Bis(1,3-dithiol-2-ylidene)-9,10-dihydroanthracene Derivatives, including Pyrrolo-annelated Derivatives and π-Extended Systems with Intramolecular Charge-Transfer. *Org. Biomol. Chem.* **2003**, *1*, 511–522.

[179] Chen, G.; Zhao, Y. synthesis and Electronic Properties of Alkyne–TTFAQ based Molecular Wires. *Tetrahedron lett.* **2006**, *47*, 5069–5073.

[180] Christensen, C. A.; Batsanov, A. S.; Bryce, M. R. Extreme Conformational Constraints in π-Extended Tetrathiafulvalenes: Unusual Topologies and Redox Behavior of Doubly and Triply Bridged Cyclophanes. *J. Am. Chem. Soc.* **2006**, *128*, 10484–10490.

[181] Christensen, C. A.; Batsanov, A. S.; Bryce, M. R. Thiolated π-Extended Tetrathiafulvalenes: Versatile Multifunctional π-Systems. *J. Org. Chem.* **2007**, *72*, 1301–1308.

[182] García, R.; Herranz, M. A.; Torres, M. R.; Bouit, P.-A.; Delgado, J. L.; Calbo, J.; Viruela, P. M.; Ortí, E.; Martín, N. Tuning the Electronic Properties of Nonplanar exTTF-based Push–Pull Chromophores by Aryl Substitution. *J. Org. Chem.* **2012**, *77*, 10707–10717.

[183] Ogi, D.; Fujita, Y.; Mori, S.; Shirahata, T.; Misaki, Y. Bis-and Tris-fused

Tetrathiafulvalenes Extended with Anthracene-9,10-diylidene. *Org. Lett.* **2016**, *18*, 5868–5871.

[184] Kato, M.; Fujita, Y.; Yamauchi, T.; Mori, S.; Shirahata, T.; Misaki, Y. Redox-Switchable Bis-fused Tetrathiafulvalene Analogue: Observation and Control of Two Different Reduction Processes from Dication to Neutral State. *Org. lett.* **2018**, *20*, 5121–5125.

[185] Díaz, M. C.; Herranz, M. A.; Illescas, B. M.; Martín, N.; Godbert, N.; Bryce, M. R.; Luo, C.; Swartz, A.; Anderson, G.; Guldi, D. M. Probing Charge Separation in Structurally Different C_{60}/exTTF Ensembles. *J. Org. Chem.* **2003**, *68*, 7711–7721.

[186] Herranz, M. Á.; Martín, N.; Campidelli, S.; Prato, M.; Brehm, G.; Guldi, D. M. Control over Electron Transfer in Tetrathiafulvalene-modified Single-walled Carbon Nanotubes. *Angew. Chem. Int. Ed.* **2006**, *45*, 4478–4482.

[187] Fernández, G.; Pérez, E. M.; Sánchez, L.; Martín, N. Self-Organization of Electroactive Materials: A Head-to-Tail Donor–Acceptor Supramolecular Polymer. *Angew. Chem. Int. Ed.* **2008**, *47*, 1094–1097.

[188] Shao, M.; Zhao, Y. TTFAQ-cored D/A Ensembles: synthesis, Electronic Properties, and Redox Responses to Transition Metal Ions. *Tetrahedron Lett.* **2010**, *51*, 2892–2895.

[189] Takano, Y.; Herranz, M. A.; Martín, N.; Radhakrishnan, S. G.; Guldi, D. M.; Tsuchiya, T.; Nagase, S.; Akasaka, T. Donor–Acceptor Conjugates of

Lanthanum Endohedral Metallofullerene and π-Extended Tetrathiafulvalene. *J. Am. Chem. Soc.* **2010**, *132*, 8048–8055.

[190] Shao, M.; Dongare, P.; Dawe, L. N.; Thompson, D. W.; Zhao, Y. Biscrown-annulated TTFAQ–Dianthracene Hybrid: synthesis, Structure, and Metal Ion Sensing. *Org. Lett.* **2010**, *12*, 3050–3053.

[191] Romero-Nieto, C.; Garcia, R.; Herranz, M. A.; Ehli, C.; Ruppert, M.; Hirsch, A.; Guldi, D. M.; Martin, N. Tetrathiafulvalene-based Nanotweezers–Noncovalent Binding of Carbon Nanotubes in Aqueous Media with Charge Transfer Implications. *J. Am. Chem. Soc.* **2012**, *134*, 9183–9192.

[192] Scharl, T.; Ferrer-Ruiz, A.; Saura-Sanmartín, A.; Rodríguez-Pérez, L.; Herranz, M. Á.; Martín, N.; Guldi, D. M. Charge Transfer in Graphene Quantum Dots Coupled with Tetrathiafulvalenes. *Chem. Commun.* **2019**, *55*, 3223–3226.

[193] Brunetti, F. G.; Isla, H.; Aragó, J.; Ortí, E.; Pérez, E. M.; Martín, N. Exploiting Multivalent Nanoparticles for the Supramolecular Functionalization of Graphene with a Nonplanar Recognition Motif. *Chem. Eur. J.* **2013**, *19*, 9843–9848.

[194] Muñoz, A.; Rodrìguez-Pérez, L.; Casado, S.; Illescas, B. M.; Martín, N. Multivalent Fullerene/π-Extended TTF Electroactive Molecules – Non-covalent Interaction with Graphene and Charge Transfer Implications. *J. Mater. Chem. C* **2019**, *7*, 8962–8968.

[195] Brunetti, F. G.; Romero-Nieto, C.; López-Andarias, J.; Atienza, C.; López, J. L.; Guldi, D. M.; Martín, N. Self-Ordering Electron Donor–Acceptor Nanohybrids Based on Single-walled Carbon Nanotubes Across Different Scales. *Angew. Chem. Int. Ed.* **2013**, *52*, 2180–2184.

[196] de Juan, A.; Pouillon, Y.; Ruiz-González, L.; Torres-Pardo, A.; Casado, S.; Martín, N.; Rubio, Á.; Pérez, E. M. Mechanically Interlocked Single-Wall Carbon Nanotubes. *Angew. Chem. Int. Ed.* **2014**, *53*, 5394–5400.

[197] Liang, S.; Subrahmanyam, A. V.; Khadem, M.; Zhao, Y.; Adronov, A. Selective Dispersion of Single-walled Carbon Nanotubes with Electron-rich Fluorene-based Copolymers. *RSC Adv.* **2016**, *6*, 25733–25740.

[198] Martínez-Periñán, E.; de Juan, A.; Pouillon, Y.; Schierl, C.; Strauss, V.; Martín, N.; Rubio, Á.; Guldi, D. M.; Lorenzo, E.; Pérez, E. M. The Mechanical Bond on Carbon Nanotubes: Diameter-selective Functionalization and Effects on Physical Properties. *Nanoscale* **2016**, *8*, 9254–9264.

[199] Balakrishna, B.; Menon, A.; Cao, K.; Gsänger, S.; Beil, S. B.; Villalva, J.; Shyshov, O.; Martin, O.; Hirsch, A.; Meyer, B.; Kaiser, U.; Guldi, D. M.; von Delius, M. Dynamic Covalent Formation of Concave Disulfide Macrocycles Mechanically Interlocked with Single-walled Carbon Nanotubes. *Angew. Chem. Int. Ed.* **2020**, *59*, 18774–18785.

[200] Fernandez, G.; Sánchez, L.; Pérez, E. M.; Martin, N. Large exTTF-based dendrimers. Self-assembly and peripheral cooperative multiencapsulation of C60. *J. Am. Chem. Soc.* **2008**, *130*, 10674–10683.

[201] Huerta, E.; Isla, H.; Pérez, E. M.; Bo, C.; Martín, N.; Mendoza, J. d. Tripodal exTTF-CTV Hosts for Fullerenes. *J. Am. Chem. Soc.* **2010**, *132*, 5351–5353.

[202] Canevet, D.; Gallego, M.; Isla, H.; de Juan, A.; Pérez, E. M.; Martín, N. Macrocyclic Hosts for Fullerenes: Extreme Changes in Binding Abilities with Small Structural Variations. *J. Am. Chem. Soc.* **2011**, *133*, 3184–3190.

[203] Ferrer-Ruiz, A.; Scharl, T.; Haines, P.; Rodríguez-Pérez, L.; Cadranel, A.; Herranz, M. Á.; Guldi, D. M.; Martín, N. Exploring Tetrathiafulvalene–Carbon Nanodot Conjugates in Charge Transfer Reactions. *Angew. Chem. Int. Ed.* **2018**, *57*, 1001–1005.

[204] Pérez, E. M.; Martín, N. π–π Interactions in Carbon Nanostructures. *Chem. Soc. Rev.* **2015**, *44*, 6425–6433.

[205] Pérez, E. M.; Capodilupo, A. L.; Fernandez, G.; Sánchez, L.; Viruela, P. M.; Viruela, R.; Ortí, E.; Bietti, M.; Martín, N. Weighting Non-covalent Forces in the Molecular Recognition of C_{60}. Relevance of Concave–Convex Complementarity. *Chem. Commun.* **2008**, 4567–4569.

[206] Josa, D.; Rodríguez-Otero, J.; Cabaleiro-Lago, E. M.; Santos, L. A.; Ramalho, T. C. Substituted Corannulenes and Sumanenes as Fullerene Receptors. A Dispersion-corrected Density Functional Theory Study. *J. Phys. Chem. A* **2014**, *118*, 9521–9528.

[207] Calbo, J.; de Juan, A.; Aragó, J.; Villalva, J.; Martín, N.; Pérez, E. M.; Ortí, E. Understanding the Affinity of Bis-exTTF Macrocyclic Receptors

towards Fullerene Recognition. *Phys. Chem. Chem. Phys.* **2019**, *21*, 11670–11675.

[208] Younes, E. A.; Zhao, Y. Highly π-Extended Tetrathiafulvalene Analogues Derived from Pentacene-5,7,12,14-tetraone. *RSC Adv.* **2015**, *5*, 88821–88825.

[209] Desai, N.; McKelvie, N.; Ramirez, F. A New synthesis of 1,1-Dibromoolefins via Phosphine-Dibromomethylenes. The Reaction of Triphenylphosphine with Carbon Tetrabromide. *J. Am. Chem. Soc.* **1962**, *84*, 1745–1747.

[210] Corey, E.; Fuchs, P. A Synthetic Method for Formyl → Ethynyl Conversion (RCHO → RC≡CH or RC≡CR'). *Tetrahedron Lett.* **1972**, *13*, 3769–3772.

[211] Shahrokhi, F.; Estabragh, R. F.; Zhao, Y. Synthesis and Comparative Studies of K-Region Functionalized Pyrene Derivatives. *New J. Chem.* **2020**, *44*, 16786–16794.

[212] Giguere, J.-B.; Morin, J.-F. Superextended Tetrathiafulvalene: synthesis, Optoelectronic Properties, Fullerenes Complexation, and Photooxidation Study. *J. Org. Chem.* **2015**, *80*, 6767–6775.

[213] Mishra, A.; Bäuerle, P. Small Molecule Organic Semiconductors on the Move: Promises for Future Solar Energy Technology. *Angew. Chem. Int. Ed.* **2012**, *51*, 2020–2067.

[214] Lin, Y.; Li, Y.; Zhan, X. Small Molecule Semiconductors for High-Efficiency Organic Photovoltaics. *Chem. Soc. Rev.* **2012**, *41*, 4245–4272.

[215] Johnson, E. R.; Keinan, S.; Mori-Sánchez, P.; Contreras-García, J.; Cohen, A. J.; Yang, W. Revealing Noncovalent Interactions. *J. Am. Chem. Soc.* **2010**, *132*, 6498–6506.

[216] Bader, R. F. Atoms in Molecules. *Acc. Chem. Res.* **1985**, *18*, 9–15.

[217] Goddard, T. D.; Huang, C. C.; Meng, E. C.; Pettersen, E. F.; Couch, G. S.; Morris, J. H.; Ferrin, T. E. UCSF ChimeraX: Meeting Modern Challenges in Visualization and Analysis. *Protein Sci.* **2018**, *27*, 14–25.

[218] Lu, T.; Chen, F. Multiwfn: A Multifunctional Wavefunction Analyzer. *J. Comput. Chem.* **2012**, *33*, 580–592.

[219] Humphrey, W.; Dalke, A.; Schulten, K. VMD: Visual Molecular Dynamics. *J. Mol. Graph.* **1996**, *14*, 33–38.

[220] Wysocki, L. M.; Lavis, L. D. Advances in the chemistry of small molecule fluorescent probes. *Curr. Opin. Chem. Biol.* **2011**, *15*, 752–759.

[221] Chan, J.; Dodani, S. C.; Chang, C. J. Reaction-based small-molecule fluorescent probes for chemoselective bioimaging. *Nat. Chem.* **2012**, *4*, 973–984.

[222] Yu, T.; Liu, L.; Xie, Z.; Ma, Y. Progress in small-molecule luminescent materials for organic light-emitting diodes. *Sci. Chin. Chem.* **2015**, *58*, 907–915.

[223] Kim, H. M.; Cho, B. R. Small-molecule two-photon probes for bioimaging applications. *Chem. Rev.* **2015**, *115*, 5014–5055.

[224] Narita, A.; Wang, X.-Y.; Feng, X.; Müllen, K. New advances in nanographene chemistry. *Chem. Soc. Rev.* **2015**, *44*, 6616–6643.

[225] Li, Y.; Liu, J.-Y.; Zhao, Y.-D.; Cao, Y.-C. Recent advancements of high efficient donor–acceptor type blue small molecule applied for OLEDs. *Mater. Today* **2017**, *20*, 258–266.

[226] Wei, Q.; Fei, N.; Islam, A.; Lei, T.; Hong, L.; Peng, R.; Fan, X.; Chen, L.; Gao, P.; Ge, Z. Small-molecule emitters with high quantum efficiency: mechanisms, structures, and applications in OLED devices. *Adv. Opt. Mater.* **2018**, *6*, 1800512.

[227] Shen, Q.; Wang, S.; Yang, N.-D.; Zhang, C.; Wu, Q.; Yu, C. Recent development of small-molecule organic fluorophores for multifunctional bioimaging in the second near-infrared window. *J. Lumin.* **2020**, *225*, 117338.

[228] Qin, Y.; Li, G.; Qi, T.; Huang, H. Aromatic imide/amide-based organic small-molecule emitters for organic light-emitting diodes. *Mater. Chem. Front.* **2020**, *4*, 1554–1568.

[229] Zhu, Z.-L.; Chen, W.-C.; Zhang, L.-D.; Liu, X.-L.; Tong, Q.-X.; Wong, F.-L.; Lu, F.; Lee, C.-S. A pyridine based meta-linking deep-blue emitter with high conjugation extent and electroluminescence efficiencies. *J. Mater. Chem. C* **2016**, *4*, 6249–6255.

[230] Liu, H.; Bai, Q.; Yao, L.; Zhang, H.; Xu, H.; Zhang, S.; Li, W.; Gao, Y.; Li, J.; Lu, P., et al. Highly efficient near ultraviolet organic light-emitting diode based on a meta-linked donor–acceptor molecule. *Chem. Sci.* **2015**, *6*, 3797–3804.

[231] Chen, W.-C.; Tong, Q.-X.; Lee, C.-S. The development of phenanthroimidazole

derivatives in blue-emitting organic electroluminescence. *Sci. Adv. Mater.* **2015**, *7*, 2193–2205.

[232] Tang, X.; Bai, Q.; Peng, Q.; Gao, Y.; Li, J.; Liu, Y.; Yao, L.; Lu, P.; Yang, B.; Ma, Y. Efficient deep blue electroluminescence with an external quantum efficiency of 6.8% and $CIE_y < 0.08$ based on a phenanthroimidazole–sulfone hybrid donor–acceptor molecule. *Chem. Mater.* **2015**, *27*, 7050–7057.

[233] Sonalin, S.; Mishra, A.; Sahu, A. K.; Mishra, A. K.; Imran, P. M.; Bhuvanesh, N. S.; Nagarajan, S. Aggregation behavior and high charge-carrier OFET-mobility of functionalized phenanthro[9,10-*d*]imidazoles. *J. Phys. Chem. C* **2020**, *124*, 13053–13062.

[234] Sonalin, S.; Kurlekar, K.; Anjali, A.; Imran, P. M.; Nagarajan, S. synthesis of phenanthro[9,10-*d*]imidazoles and their potential applications in solution processable bottom-gated OFETs. *Asian J. Org. Chem.* **2020**, *9*, 939–946.

[235] Lin, W.; Long, L.; Yuan, L.; Cao, Z.; Chen, B.; Tan, W. A ratiometric fluorescent probe for cysteine and homocysteine displaying a large emission shift. *Org. Lett.* **2008**, *10*, 5577–5580.

[236] Lin, W.; Yuan, L.; Tan, W.; Feng, J.; Long, L. Construction of fluorescent probes via protection/deprotection of functional groups: a ratiometric fluorescent probe for Cu^{2+}. *Chem. Eur. J.* **2009**, *15*, 1030–1035.

[237] Idris, M.; Coburn, C.; Fleetham, T.; Milam-Guerrero, J.; Djurovich, P. I.; Forrest, S. R.; Thompson, M. E. Phenanthro[9,10-*d*]triazole and imidazole

derivatives: high triplet energy host materials for blue phosphorescent organic light emitting devices. *Mater. Horiz.* **2019**, *6*, 1179–1186.

[238] Côté, B.; Boulet, L.; Brideau, C.; Claveau, D.; Ethier, D.; Frenette, R.; Gagnon, M.; Giroux, A.; Guay, J.; Guiral, S., et al. Substituted phenanthrene imidazoles as potent, selective, and orally active mPGES-1 inhibitors. *Bioorg. Med. Chem. Lett.* **2007**, *17*, 6816–6820.

[239] Kundu, A.; Karthikeyan, S.; Sagara, Y.; Moon, D.; Anthony, S. P. Unusual fluorescent photoswitching of imidazole derivatives: the role of molecular conformation and twist angle controlled organic solid state fluorescence. *Phys. Chem. Chem. Phys.* **2018**, *20*, 27385–27393.

[240] Eseola, A. O.; Adepitan, O.; Görls, H.; Plass, W. Electronic/substituents influence on imidazole ring donor–acceptor capacities using 1*H*-imidazo[4,5-*f*][1,10]phenanthroline frameworks. *New J. Chem.* **2012**, *36*, 891–902.

[241] Chen, W.-C.; Yuan, Y.; Ni, S.-F.; Zhu, Z.-L.; Zhang, J.; Jiang, Z.-Q.; Liao, L.-S.; Wong, F.-L.; Lee, C.-S. Highly efficient deep-blue electroluminescence from a charge-transfer emitter with stable donor skeleton. *ACS Appl. Mater. Interf.* **2017**, *9*, 7331–7338.

[242] Tian, M.; Wang, C.; Wang, L.; Luo, K.; Zhao, A.; Guo, C. Study on the synthesis and structure–effect relationship of multi-aryl imidazoles with their fluorescence properties. *J. Lumin.* **2014**, *29*, 540–548.

[243] Jang, J. H.; Ahn, S.; Park, S. E.; Kim, S.; Byon, H. R.; Joo, J. M. synthesis

of redox-active phenanthrene-fused heteroarenes by palladium-catalyzed C–H annulation. *Org. Lett.* **2020**, *22*, 1280–1285.

[244] Francke, R.; Little, R. D. Optimizing electron transfer mediators based on arylimidazoles by ring fusion: synthesis, electrochemistry, and computational analysis of 2-aryl-1-methylphenanthro [9,10-*d*]imidazoles. *J. Am. Chem. Soc.* **2014**, *136*, 427–435.

[245] Johnson, B. M.; Francke, R.; Little, R. D.; Berben, L. A. High turnover in electro-oxidation of alcohols and ethers with a glassy carbon-supported phenanthroimidazole mediator. *Chem. Sci.* **2017**, *8*, 6493–6498.

[246] Abdollahi, M. F.; Zhao, Y. Recent advances in dithiafulvenyl-functionalized organic conjugated materials. *New J. Chem.* **2020**, *44*, 4681–4693.

[247] Keshri, S. K.; Asthana, D.; Chorol, S.; Kumar, Y.; Mukhopadhyay, P. Appending diverse π-extended acceptors with tetrathiafulvalene/dithiafulvalene donors: multistate redox properties, radical ion generation, and mid-IR-absorbing mixed-valence states. *Chem. Eur. J.* **2018**, *24*, 1821–1832.

[248] Woolridge, K.; Goncalves, L. C.; Bouzan, S.; Chen, G.; Zhao, Y. Aryl-substituted dithiafulvenes: synthesis, electronic properties, and redox reactivity. *Tetrahedron Lett.* **2014**, *55*, 6362–6366.

[249] Liang, S.; Chen, G.; Peddle, J.; Zhao, Y. Reversible dispersion and releasing of single-walled carbon nanotubes by a stimuli-responsive TTFV-phenylacetylene polymer. *Chem. Commun.* **2012**, *48*, 3100–3102.

[250] Lissau, H.; Frisenda, R.; Olsen, S. T.; Jevric, M.; Parker, C. R.; Kadziola, A.; Hansen, T.; Van Der Zant, H. S.; Nielsen, M. B.; Mikkelsen, K. V. Tracking molecular resonance forms of donor–acceptor push–pull molecules by single-molecule conductance experiments. *Nat. Commun.* **2015**, *6*, 1–8.

[251] Vestergaard, M.; Jennum, K.; Sørensen, J. K.; Kilså, K.; Nielsen, M. B. synthesis and characterization of cruciform-conjugated molecules based on tetrathiafulvalene. *J. Org. Chem.* **2008**, *73*, 3175–3183.

[252] Khadem, M.; Walsh, J. C.; Bodwell, G. J.; Zhao, Y. A macrocyclization of 1,8-bis(dithiafulvenyl)pyrenes. *Org. Lett.* **2016**, *18*, 2403–2406.

[253] Khadem, M.; Zhao, Y. Multivalent dithiafulvenyl functionalization of dendritic oligo(phenylene vinylene)s with an anthraquinodimethane core. *Chem. Commun.* **2017**, *53*, 1821–1824.

[254] Hapiot, P.; Lorcy, D.; Tallec, A.; Carlier, R.; Robert, A. Mechanism of dimerization of 1,4-dithiafulvenes into TTF vinylogues. *J. Phys. Chem.* **1996**, *100*, 14823–14827.

[255] Heinze, J.; Frontana-Uribe, B. A.; Ludwigs, S. Electrochemistry of conducting polymers–persistent models and new Concepts. *Chem. Rev.* **2010**, *110*, 4724–4771.

[256] Brunner, K.; van Dijken, A.; Börner, H.; Bastiaansen, J. J.; Kiggen, N. M.; Langeveld, B. M. Carbazole compounds as host materials for triplet emitters in organic light-emitting diodes: tuning the HOMO level without influencing the triplet energy in small molecules. *J. Am. Chem. Soc.* **2004**, *126*, 6035–6042.

[257] Svenstrup, N.; Becher, J. The organic chemistry of 1,3-dithiole-2-thione-4,5-dithiolate (DMIT). *Synthesis* **1995**, *1995*, 215–235.

[258] Parg, R. P.; Kilburn, J. D.; Ryan, T. G. A one-step synthesis of 1,3-dithiol-2-ylphosphonate esters from 1,3-dithiole-2-thiones. *Synthesis* **1994**, *1994*, 195–198.

[259] Grimmett, M. Advances in imidazole chemistry. *Adv. Heterocycl. Chem.* **1970**, *12*, 103–183.

[260] Schou, S. S.; Parker, C. R.; Lincke, K.; Jennum, K.; Vibenholt, J.; Kadziola, A.; Nielsen, M. B. On the phosphite-mediated synthesis of dithiafulvenes and π-extended tetrathiafulvalenes. *Synlett* **2013**, *24*, 231–235.

[261] Trivedi, D. R.; Ballabh, A.; Dastidar, P. Supramolecular assemblies in salts and co-crystals of imidazoles with dicarboxylic acids. *CrystEngComm* **2003**, *5*, 358–367.

[262] Bellec, N.; Boubekeur, K.; Carlier, R.; Hapiot, P.; Lorcy, D.; Tallec, A. Controlling the conformation changes associated to electron transfer steps through chemical substitution: intriguing redox behavior of substituted vinylogous TTF. *J. Phys. Chem. A* **2000**, *104*, 9750–9759.

[263] Afzali, A.; Abdollahi, M. F.; Zhang, B.; Zhao, Y. Donor/acceptor substituted dithiafulvenes and tetrathiafulvalene vinylogues: electronic absorption, crystallographic, and computational analyses. *New J. Chem.* **2021**, *45*, 11918–11926.

[264] Mataga, N.; Kaifu, Y.; Koizumi, M. The solvent effect on fluorescence spectrum, change of solute-solvent interaction during the lifetime of excited solute molecule. *Bull. Chem. Soc. Jpn.* **1955**, *28*, 690–691.

[265] Lippert, E. Dipolmoment und elektronenstruktur von angeregten molekülen. *Z. Naturforsch. A–Astrophys. Phys. Phys. Chem.* **1955**, *10*, 541–545.

[266] Mroz, P.; Tegos, G. P.; Gali, H.; Wharton, T.; Sarna, T.; Hamblin, M. R. Photodynamic therapy with fullerenes. *Photochem. Photobiol. Sci.* **2007**, *6*, 1139–1149.

[267] Novoselov, K. S.; Geim, A. K.; Morozov, S. V.; Jiang, D.; Zhang, Y.; Dubonos, S. V.; Grigorieva, I. V.; Firsov, A. A. Electric field effect in atomically thin carbon films. *Science* **2004**, *306*, 666–669.

[268] Jacky, W.; Herman, H.; ZhongáTang, B., et al. Aggregation-induced emission and aggregation-promoted photochromism of bis(diphenylmethylene)dihydroacenes. *Chem. Sci* **2015**, *6*, 3538–3543.

[269] Davy, N. C.; Man, G.; Kerner, R. A.; Fusella, M. A.; Purdum, G. E.; Sezen, M.; Rand, B. P.; Kahn, A.; Loo, Y.-L. Contorted hexabenzocoronenes with extended heterocyclic moieties improve visible-light absorption and performance in organic solar cells. *Chem. Mater.* **2016**, *28*, 673–681.

[270] Zhang, X.; Jiang, X.; Zhang, K.; Mao, L.; Luo, J.; Chi, C.; Chan, H. S. O.; Wu, J. synthesis, self-assembly, and charge transporting property of contorted tetrabenzocoronenes. *J. Org. Chem.* **2010**, *75*, 8069–8077.

[271] Kumar, S.; Tao, Y.-T. Contorted Naphtho-and Fluorenocoronenes: Syntheses and Properties of Polycyclic Aromatics beyond Benzo-and Thiophenocoronenes. *Org. Lett.* **2018**, *20*, 2320–2323.

[272] Pola, S.; Kuo, C.-H.; Peng, W.-T.; Islam, M. M.; Chao, I.; Tao, Y.-T. Contorted tetrabenzocoronene derivatives for single crystal field effect transistors: correlation between packing and mobility. *Chem. Mater.* **2012**, *24*, 2566–2571.

[273] Watson, M. D.; Fechtenkötter, A.; Müllen, K. Big is beautiful-"aromaticity" revisited from the viewpoint of macromolecular and supramolecular benzene chemistry. *Chem. Rev.* **2001**, *101*, 1267–1300.

[274] Wu, J.; Pisula, W.; Müllen, K. Graphenes as potential material for electronics. *Chem. Rev.* **2007**, *107*, 718–747.

[275] Scholl, R.; Mansfeld, J., meso-Benzdianthron (Helianthron), meso-Naphthodianthron, und ein neuer Weg zum Flavanthren. *Ber. Dtsch. Chem. Ges.* **1910, *43*, 1734–1746**,

[276] Narita, A.; Feng, X.; Hernandez, Y.; Jensen, S. A.; Bonn, M.; Yang, H.; Verzhbitskiy, I. A.; Casiraghi, C.; Hansen, M. R.; Koch, A. H., et al. synthesis of structurally well-defined and liquid-phase-processable graphene nanoribbons. *Nat. Chem.* **2014**, *6*, 126–132.

[277] Kovacic, P.; Kyriakis, A., Polymerization of benzene to p-polyphenyl by aluminum chloride-cupric chloride. *J. Am. Chem. Soc.* **1963, *85*, 454–458**,

[278] Kovacic, P.; Kyriakis, A. Polymerization of benzene to p-polyphenyl. *Tetrahedron Lett.* **1962**, *3*, 467–469.

[279] Kramer, B.; Fröhlich, R.; Waldvogel, S. R., Oxidative Coupling Reactions Mediated by $MoCl_5$ Leading to 2, 2-Cyclolignans: The Specific Role of HCl. *Eur. J. Org. Chem.* **2003, *2003*, 3549–3554**,

[280] Schubert, M.; Franzmann, P.; Wünsche von Leupoldt, A.; Koszinowski, K.; Heinze, K.; Waldvogel, S. R. Over-Oxidation as the Key Step in the Mechanism of the $MoCl_5$-Mediated Dehydrogenative Coupling of Arenes. *Angew. Chem. Int. Ed.* **2016**, *55*, 1156–1159.

[281] Takada, T.; Arisawa, M.; Gyoten, M.; Hamada, R.; Tohma, H.; Kita, Y., Oxidative biaryl coupling reaction of phenol ether derivatives using a hypervalent iodine (III) reagent. *J. Org. Chem* **1998, *63*, 7698–7706**,

[282] Moreno, I.; Tellitu, I.; Domínguez, E.; SanMartín, R. A Simple Route to New Phenanthro-and Phenanthroid-Fused Thiazoles by a PIFA-Mediated (Hetero) biaryl Coupling Reaction. *Eur. J. Org. Chem.* **2002**, *2002*, 2126–2135.

[283] Kamo, M.; Tsuda, A.; Nakamura, Y.; Aratani, N.; Furukawa, K.; Kato, T.; Osuka, A. Metal-dependent regioselective oxidative coupling of 5,10,15-triarylporphyrins with DDQ-Sc (OTf) 3 and formation of an oxo-quinoidal porphyrin. *Org. Lett.* **2003**, *5*, 2079–2082.

[284] Zhai, L.; Shukla, R.; Rathore, R. Oxidative C- C bond formation (Scholl reaction) with DDQ as an efficient and easily recyclable oxidant. *Org. Lett.* **2009**, *11*, 3474–3477.

[285] Zhang, Y.; Pun, S. H.; Miao, Q. The Scholl Reaction as a Powerful Tool for synthesis of Curved Polycyclic Aromatics. *Chem. Rev.* **2022**, *122*, 14554–14593.

[286] Grzybowski, M.; Skonieczny, K.; Butenschoen, H.; Gryko, D. T. Comparison of oxidative aromatic coupling and the Scholl reaction. *Angew. Chem. Int. Ed.* **2013**, *52*, 9900–9930.

[287] Daigle, M.; Picard-Lafond, A.; Soligo, E.; Morin, J.-F. Regioselective synthesis of nanographenes by photochemical cyclodehydrochlorination. *Angew. Chem.* **2016**, *128*, 2082–2087.

[288] He, J.; Mathew, S.; Kinney, Z. J.; Warrell, R. M.; Molina, J. S.; Hartley, C. S. Tetrabenzanthanthrenes by mitigation of rearrangements in the planarization of ortho-phenylene hexamers. *Chem. Commun.* **2015**, *51*, 7245–7248.

[289] Mallory, F. B.; Wood, C. S.; Gordon, J. T.; Lindquist, L. C.; Savitz, M. L. Photochemistry of Stilbenes. I. *J. Am. Chem. Soc.* **1962**, *84*, 4361–4362.

[290] Liu, L.; Yang, B.; Katz, T. J.; Poindexter, M. K. Improved methodology for photocyclization reactions. *J. Org. Chem.* **1991**, *56*, 3769–3775.

[291] Duclos Jr, R. I.; Tung, J. S.; Rapoport, H. A high-yield modification of the Pschorr phenanthrene synthesis. *J. Org. Chem.* **1984**, *49*, 5243–5246.

[292] Finnie, A. A.; Hill, R. The synthesis of 1, 5, 7, 10-tetraoxygenated 3-methylphenanthrenes. *J. Chem. Res. Synop.* **1987**, 78–79.

[293] Mallory, F. B.; Rudolph, M. J.; Oh, S. M. Photochemistry of stilbenes. 8.

Eliminative photocyclization of o-methoxystilbenes. *J. Org. Chem.* **1989**, *54*, 4619–4626.

[294] Li, Z.; Twieg, R. J. Photocyclodehydrofluorination. *Chem. Eur. J.* **2015**, *21*, 15534–15539.

[295] Salazar, E.; Faraji, S. Theoretical study of cyclohexadiene/hexatriene photochemical interconversion using spin-flip time-dependent density functional theory. *Mol. Phys.* **2020**, *118*, e1764120.

[296] Chen, Z.-Q.; Chen, T.; Liu, J.-X.; Zhang, G.-F.; Li, C.; Gong, W.-L.; Xiong, Z.-J.; Xie, N.-H.; Tang, B. Z.; Zhu, M.-Q. Geminal cross-coupling of 1,1-dibromoolefins facilitating multiple topological π-conjugated tetraarylethenes. *Macromolecules* **2015**, *48*, 7823–7835.

Appendix I

Supplementary Information for Chapter 2

Molecular tuning of the crystallization-induced emission enhancement of diphenyl-dibenzofulvene luminogens

https://doi.org/10.1039/D0CC07013K

Table of Content

1. NMR Spectra for New Compounds

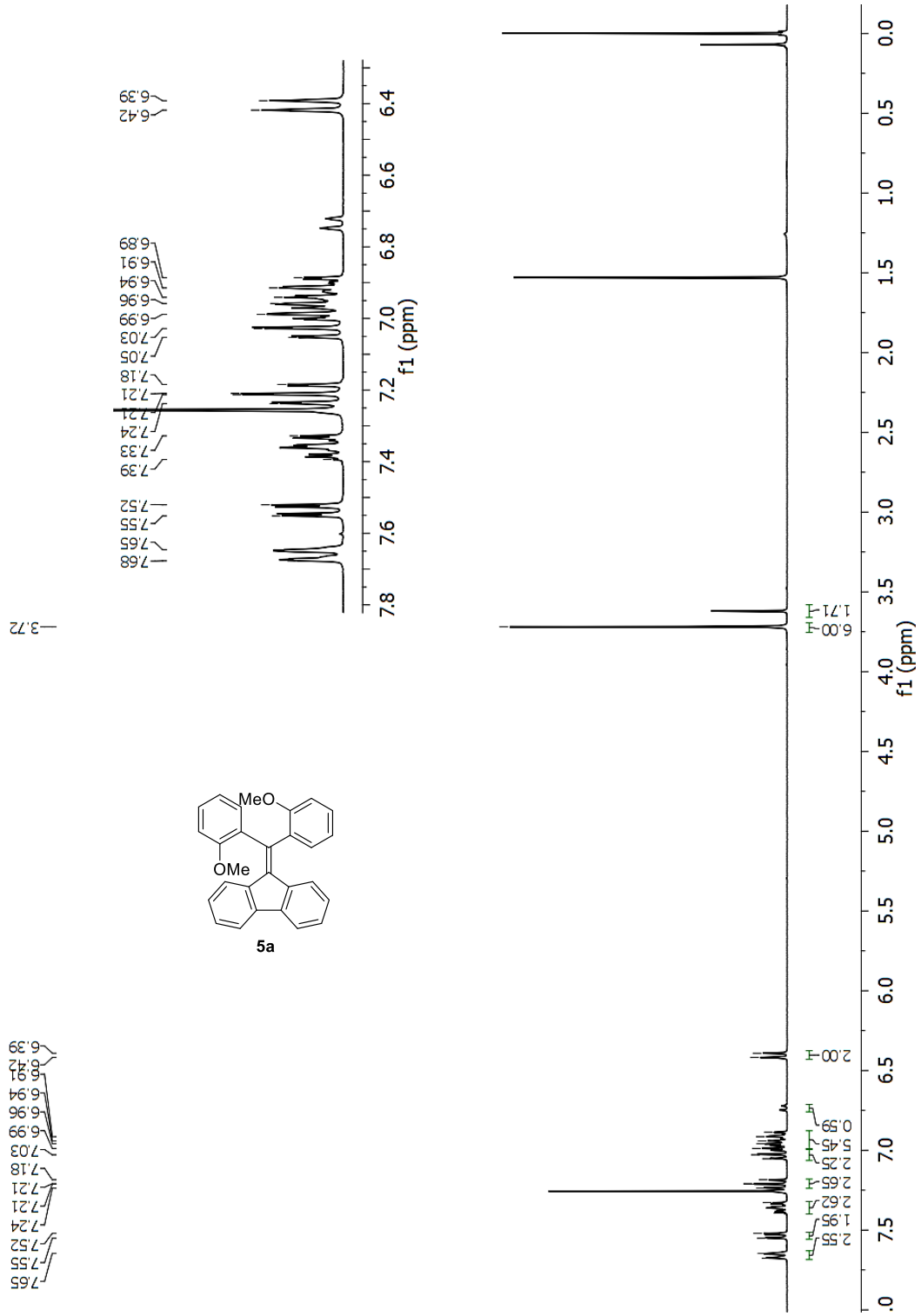

Fig. S-1 ^{1}HNMR (300 MHz, $CDCl_3$) of compound **5a.**

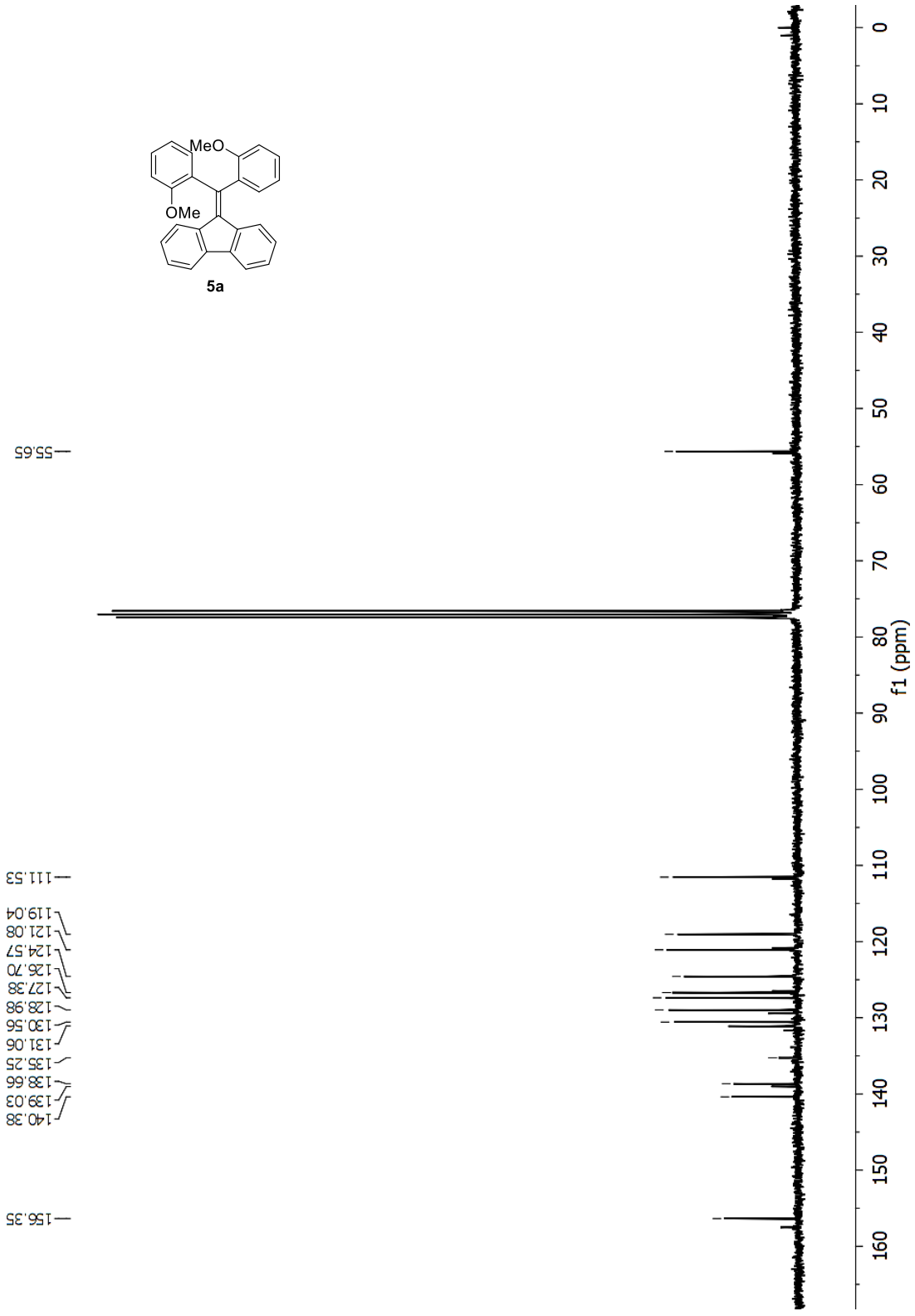

Fig. S-2 ^{13}CNMR (75 MHz, $CDCl_3$) of compound **5a.**

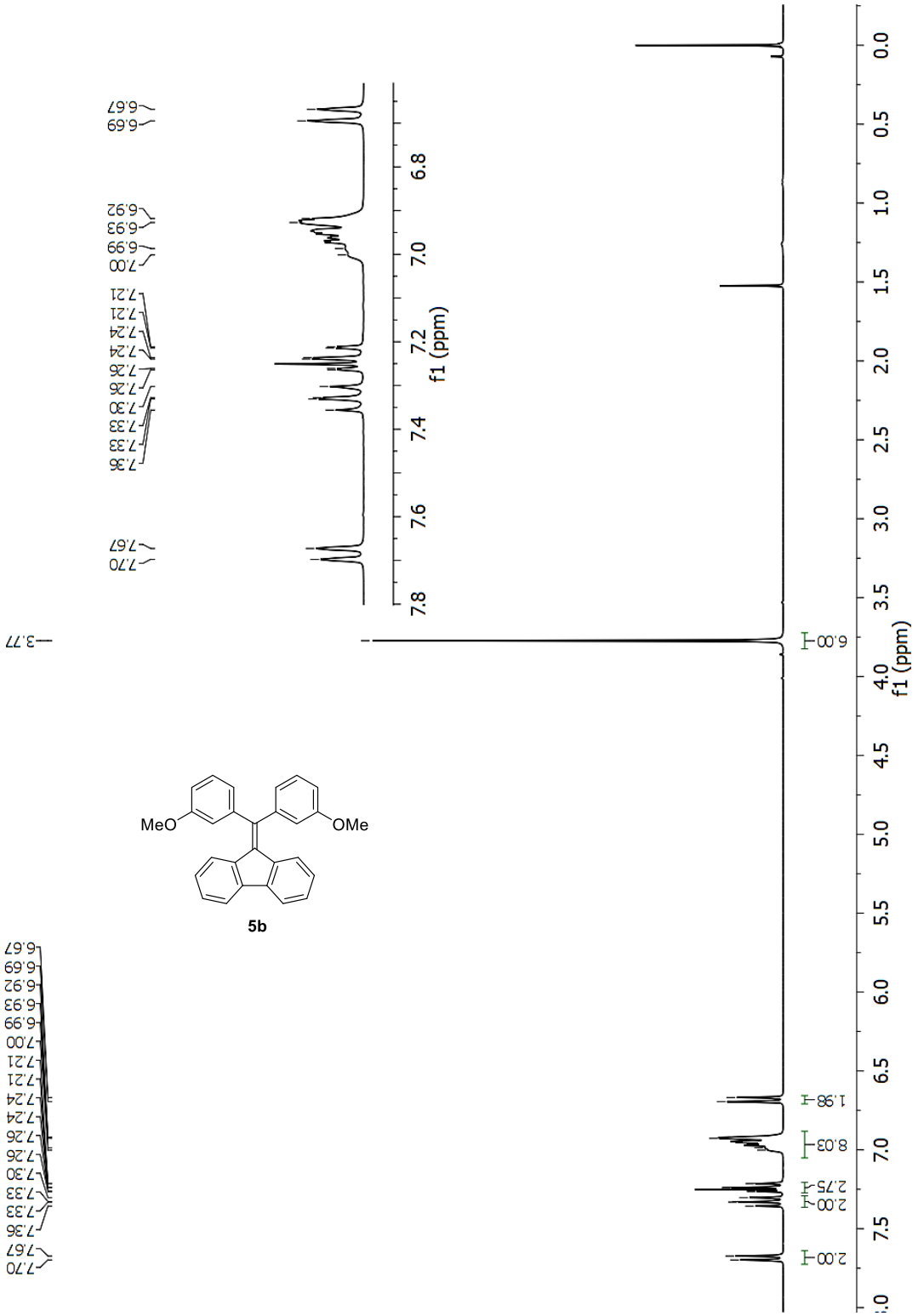

Fig. S-3 ^{1}HNMR (300 MHz, $CDCl_3$) of compound **5b.**

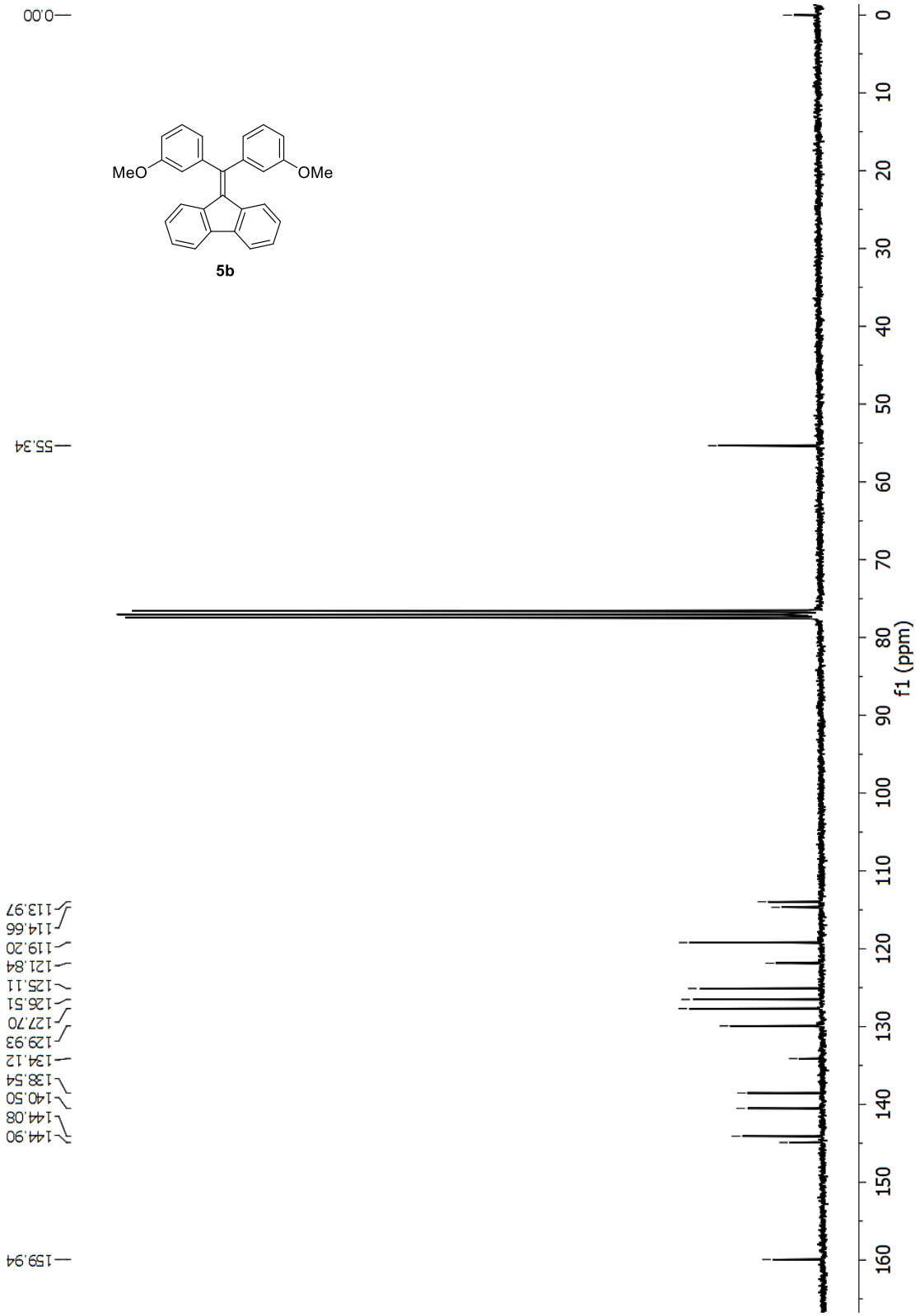

Fig. S-4 ^{13}CNMR (75 MHz, $CDCl_3$) of compound **5b.**

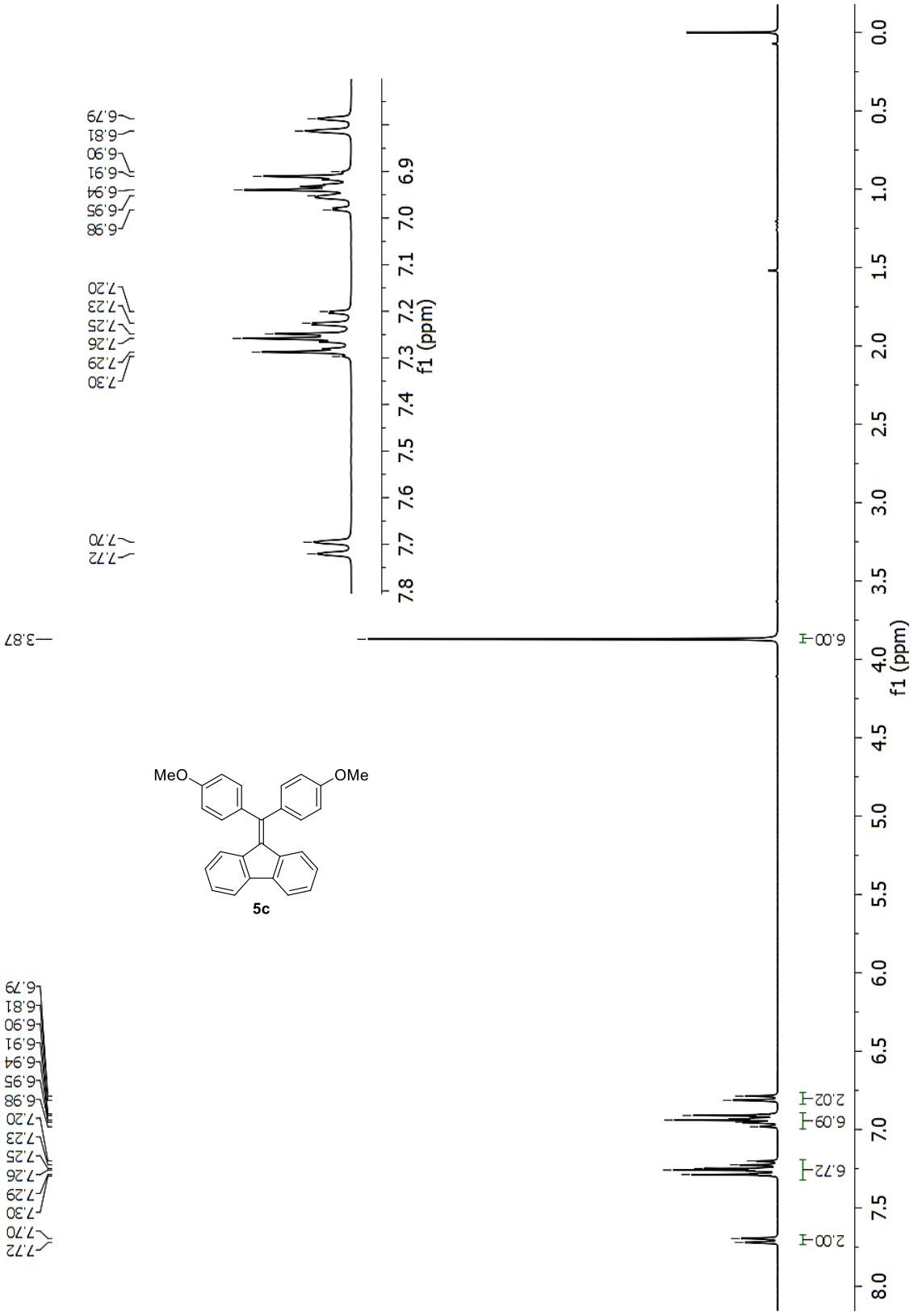

Fig. S-5 ^{1}HNMR (300 MHz, $CDCl_3$) of compound **5c.**

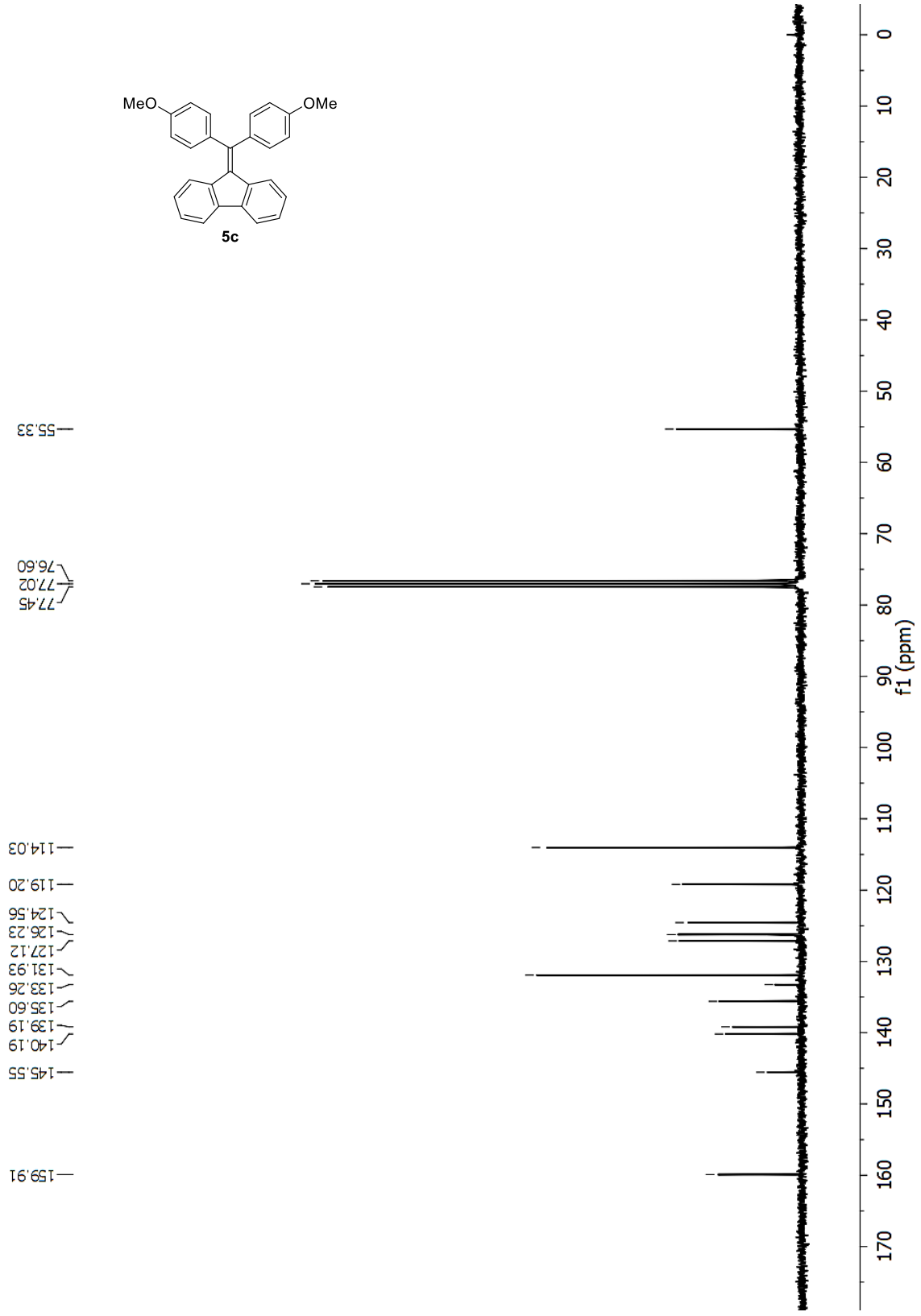

Fig. S-6 ^{13}CNMR (75 MHz, $CDCl_3$) of compound **5c.**

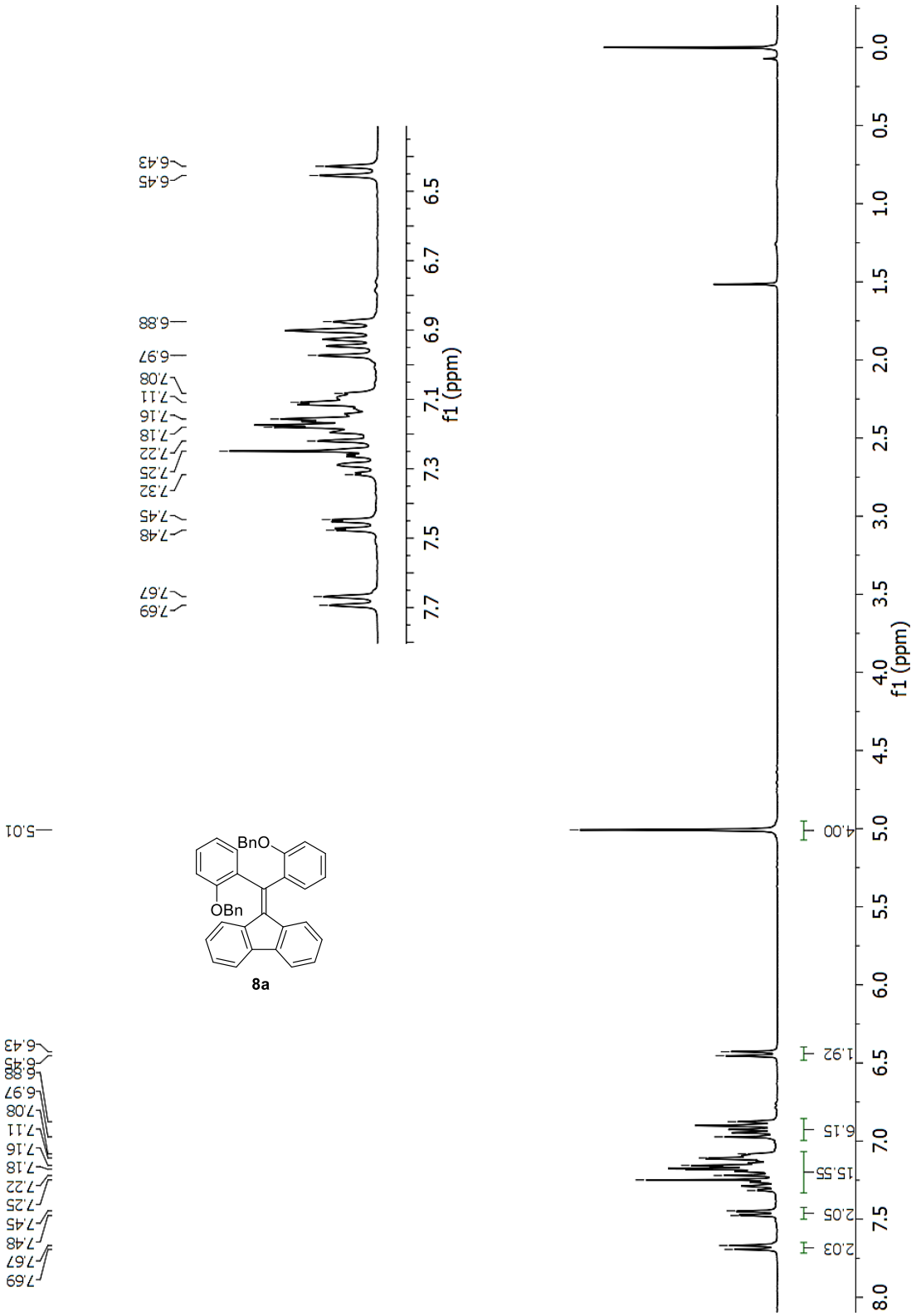

Fig. S-7 ^{1}HNMR (300 MHz, $CDCl_3$) of compound **8a.**

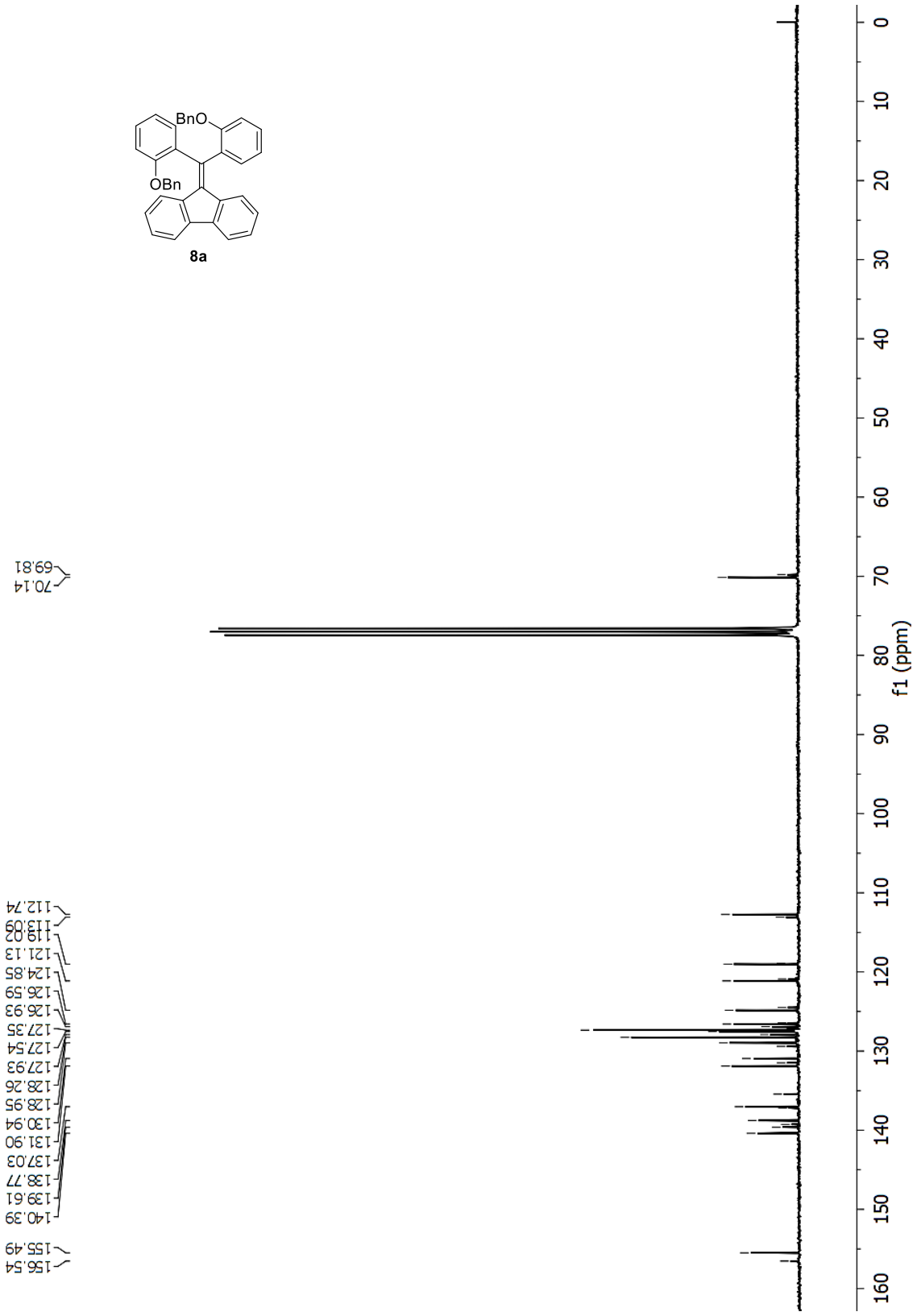

Fig. S-8 ^{13}CNMR (75 MHz, $CDCl_3$) of compound **8a.**

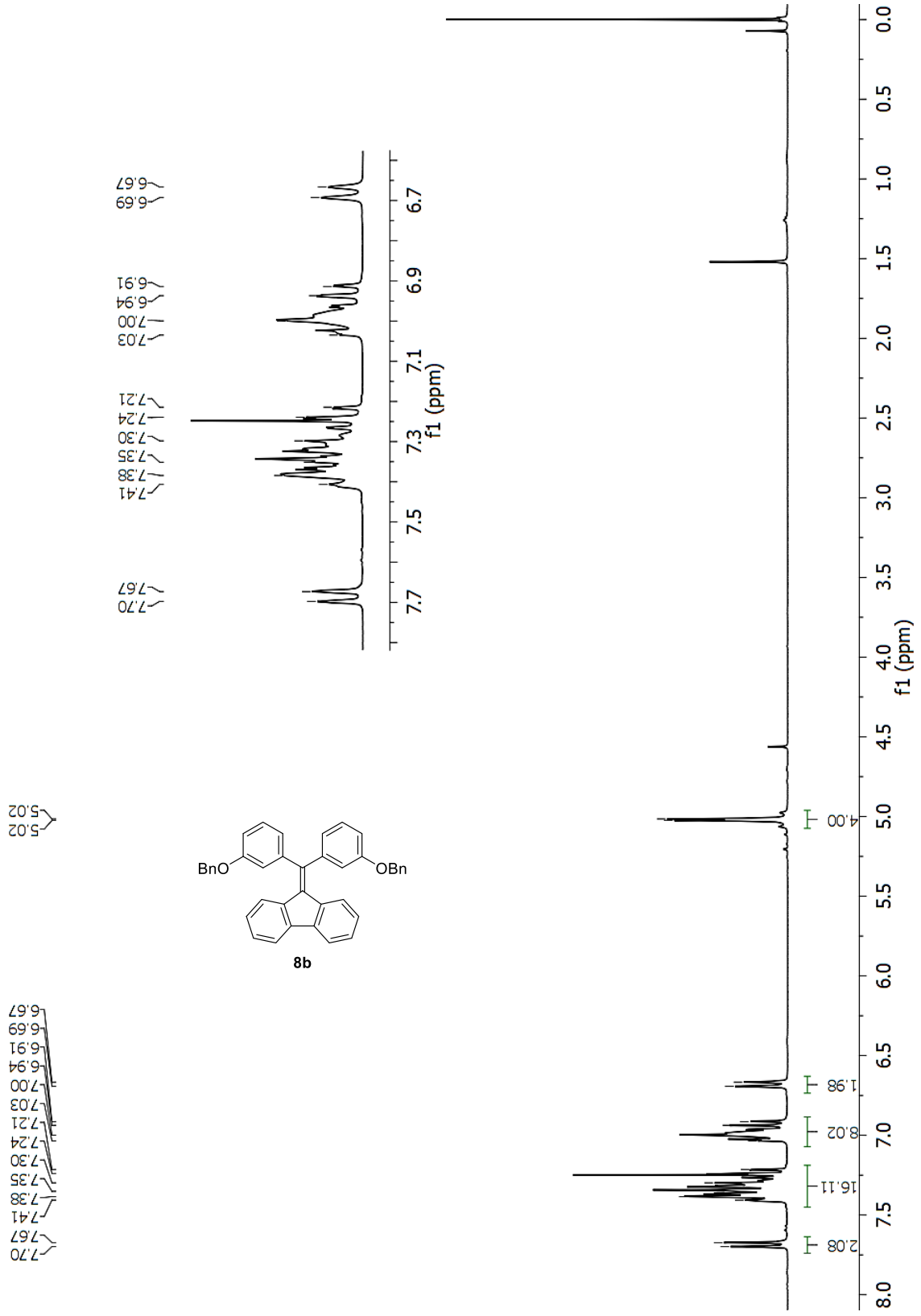

Fig. S-9 ^{1}HNMR (300 MHz, $CDCl_3$) of compound **8b.**

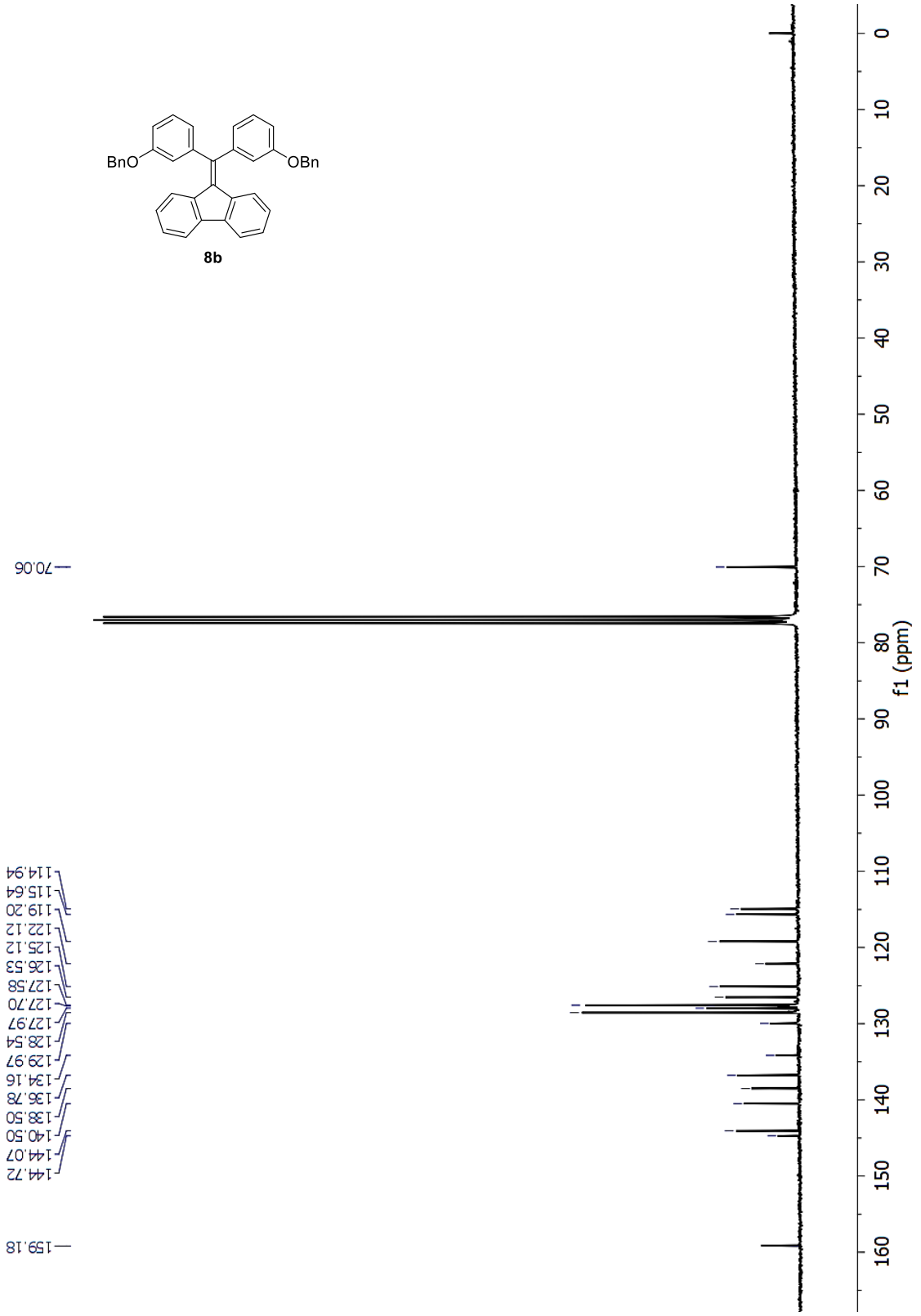

Fig. S-10 ^{13}CNMR (75 MHz, $CDCl_3$) of compound **8b.**

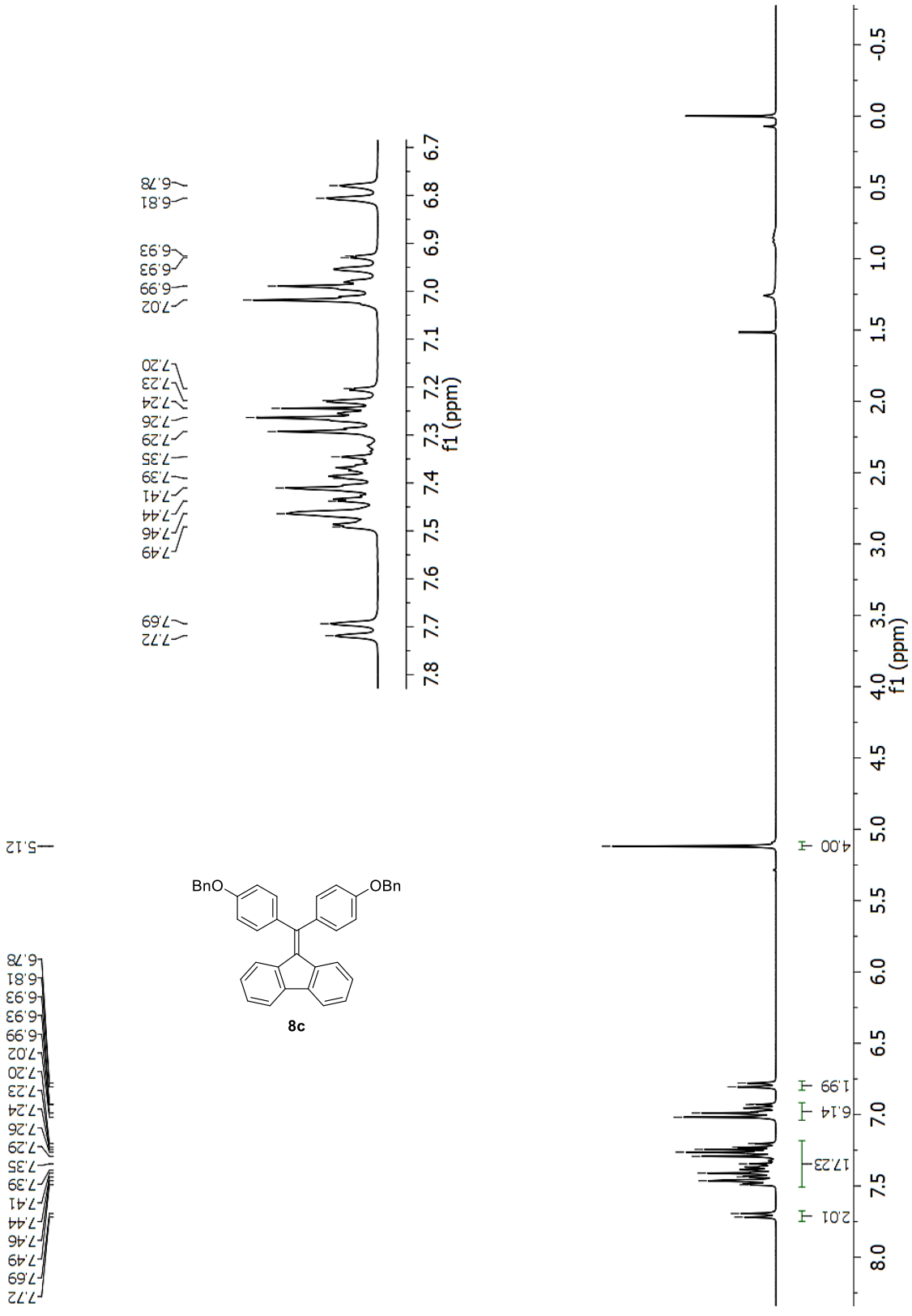

Fig. S-11 ^{1}HNMR (300 MHz, $CDCl_3$) of compound **8c.**

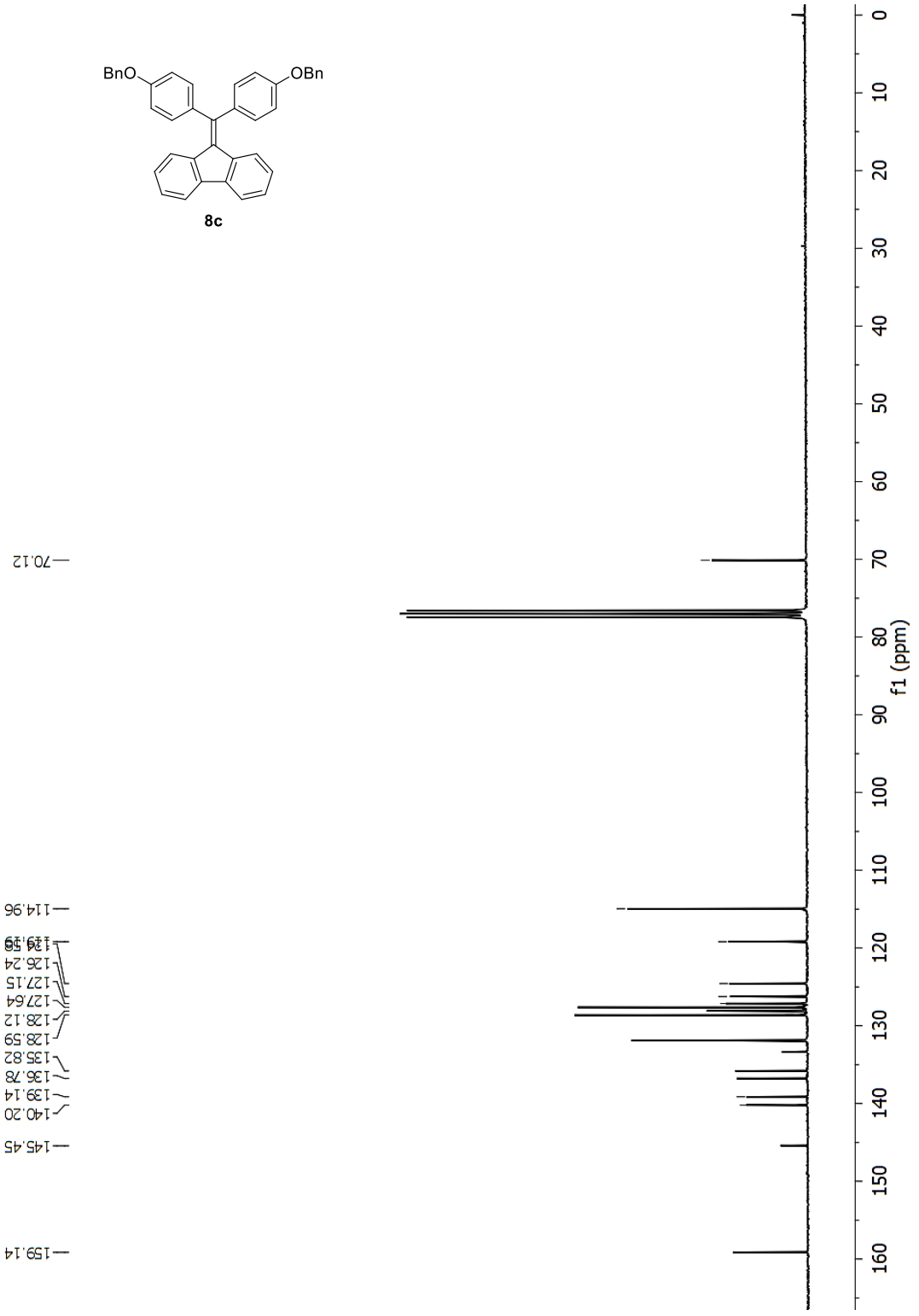

Fig. S-12 ^{13}CNMR (75 MHz, $CDCl_3$) of compound **8c.**

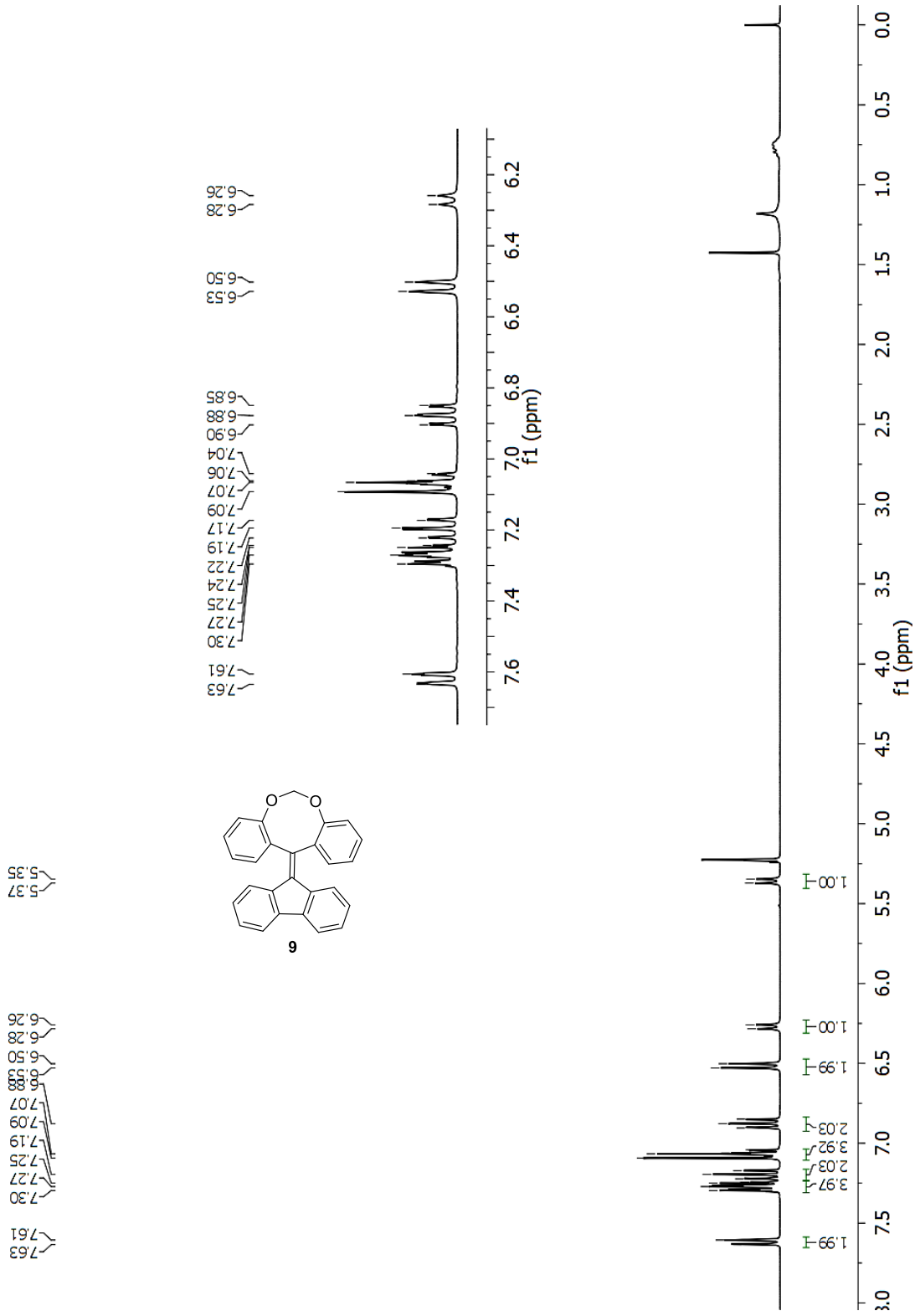

Fig. S-13 ^{1}HNMR (300 MHz, CD_2Cl_2) of compound **9.**

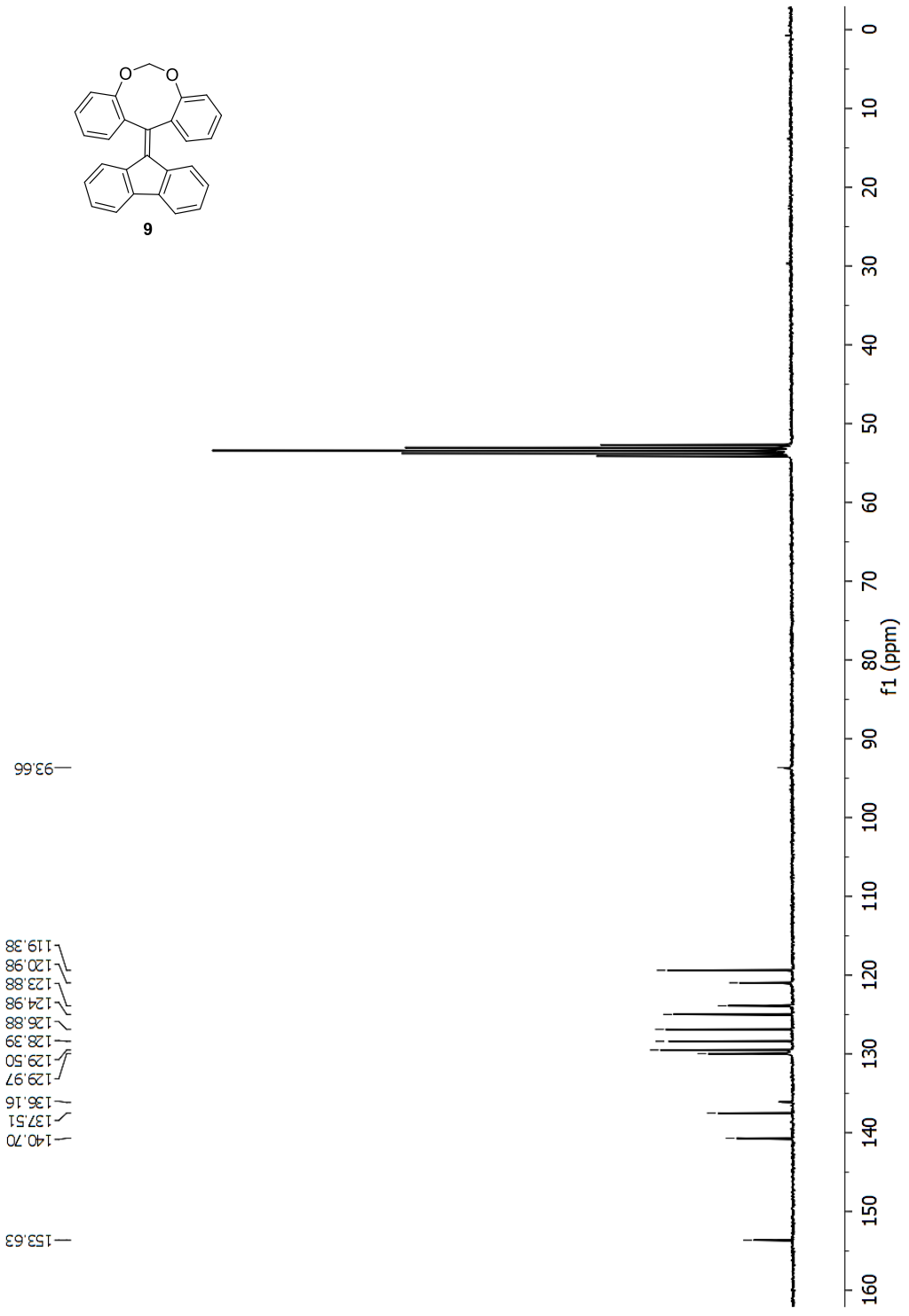

Fig. S-14 ^{13}CNMR (75 MHz, CD_2Cl_2) of compound **9.**

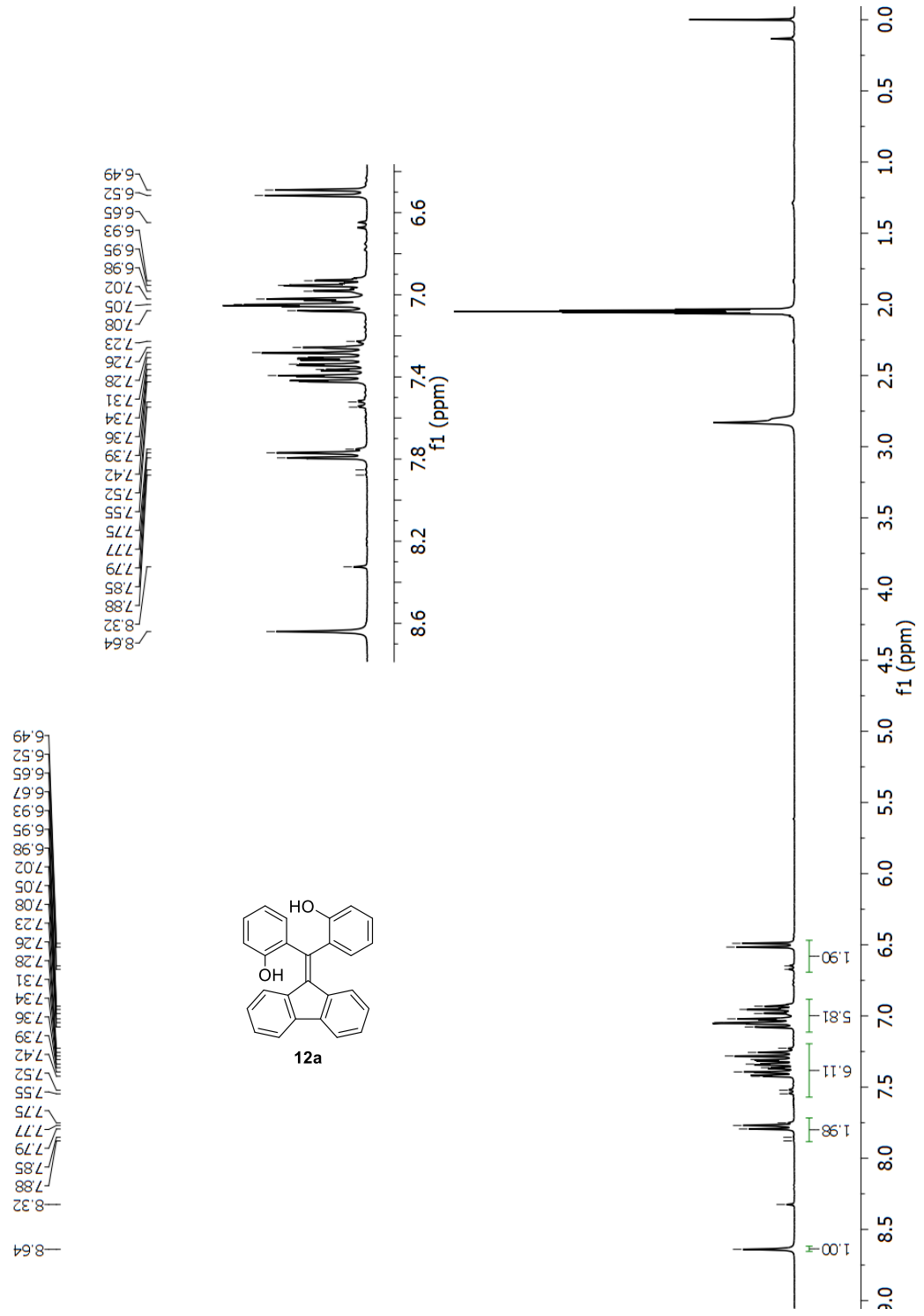

Fig. S-15 [1]HNMR (300 MHz, acetone-d_6) of compound **12a.**

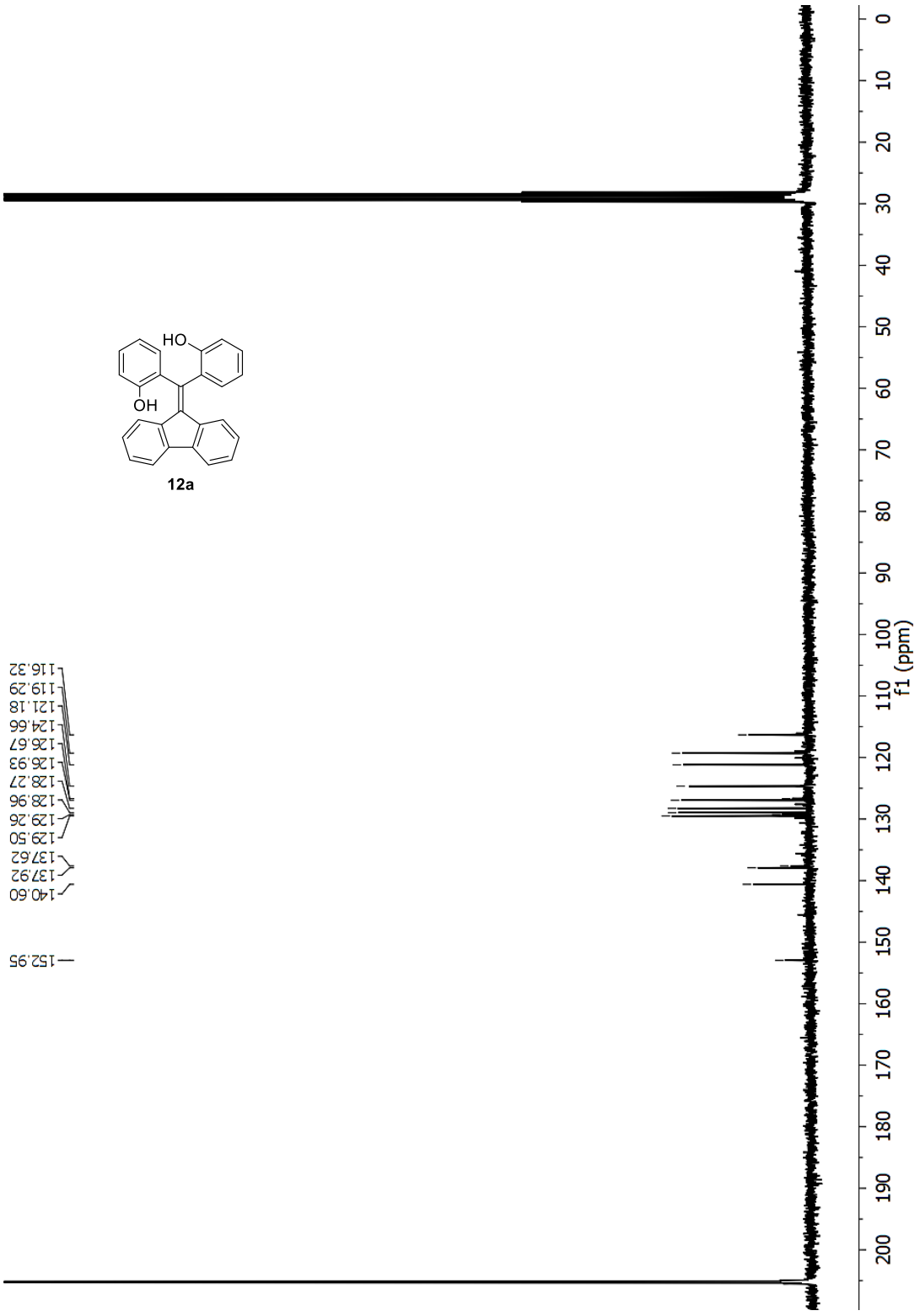

Fig. S-16 ^{13}CNMR (75 MHz, acetone-d_6) of compound **12a.**

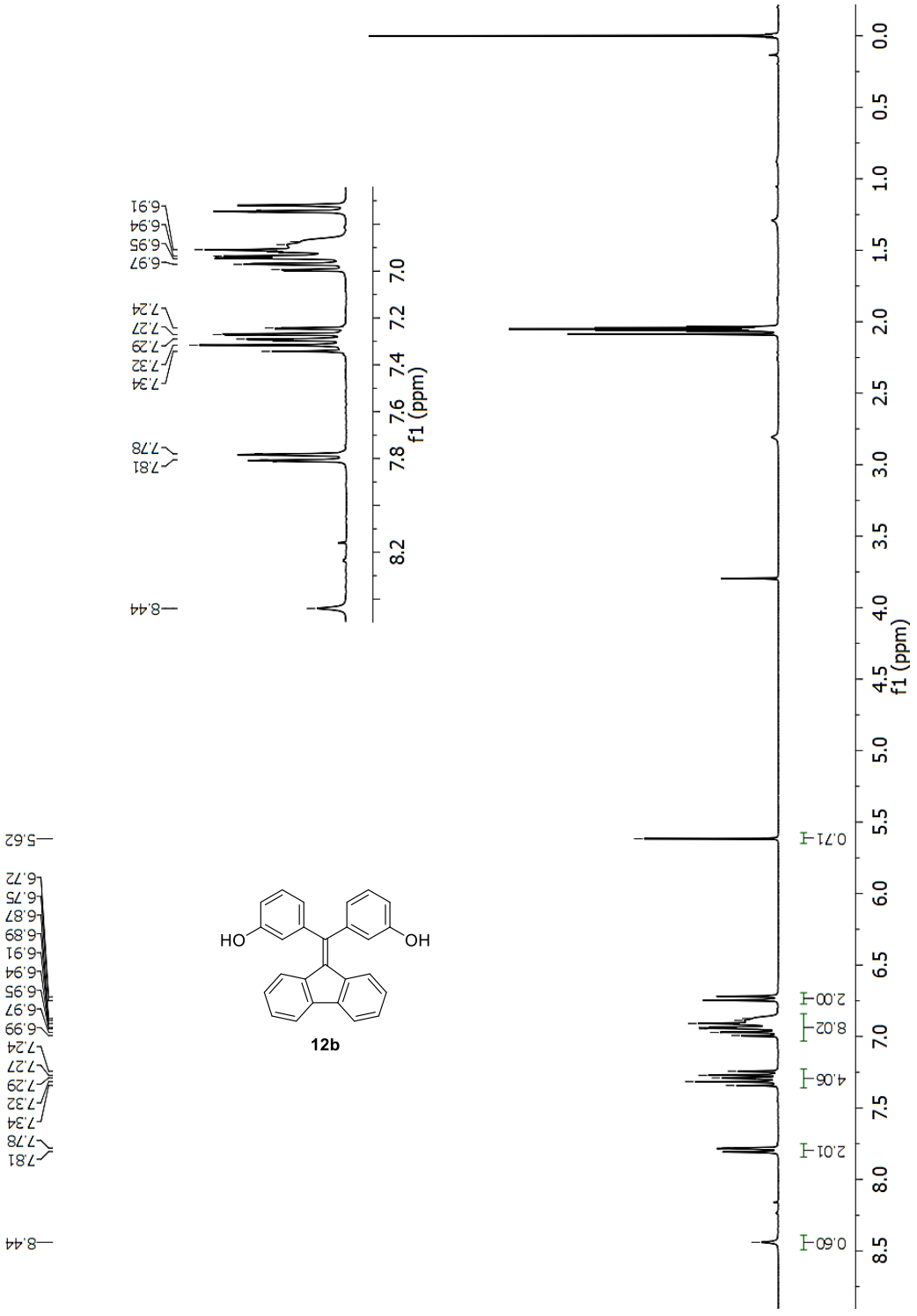

Fig. S-17 [1]HNMR (300 MHz, acetone-d_6) of compound **12b.**

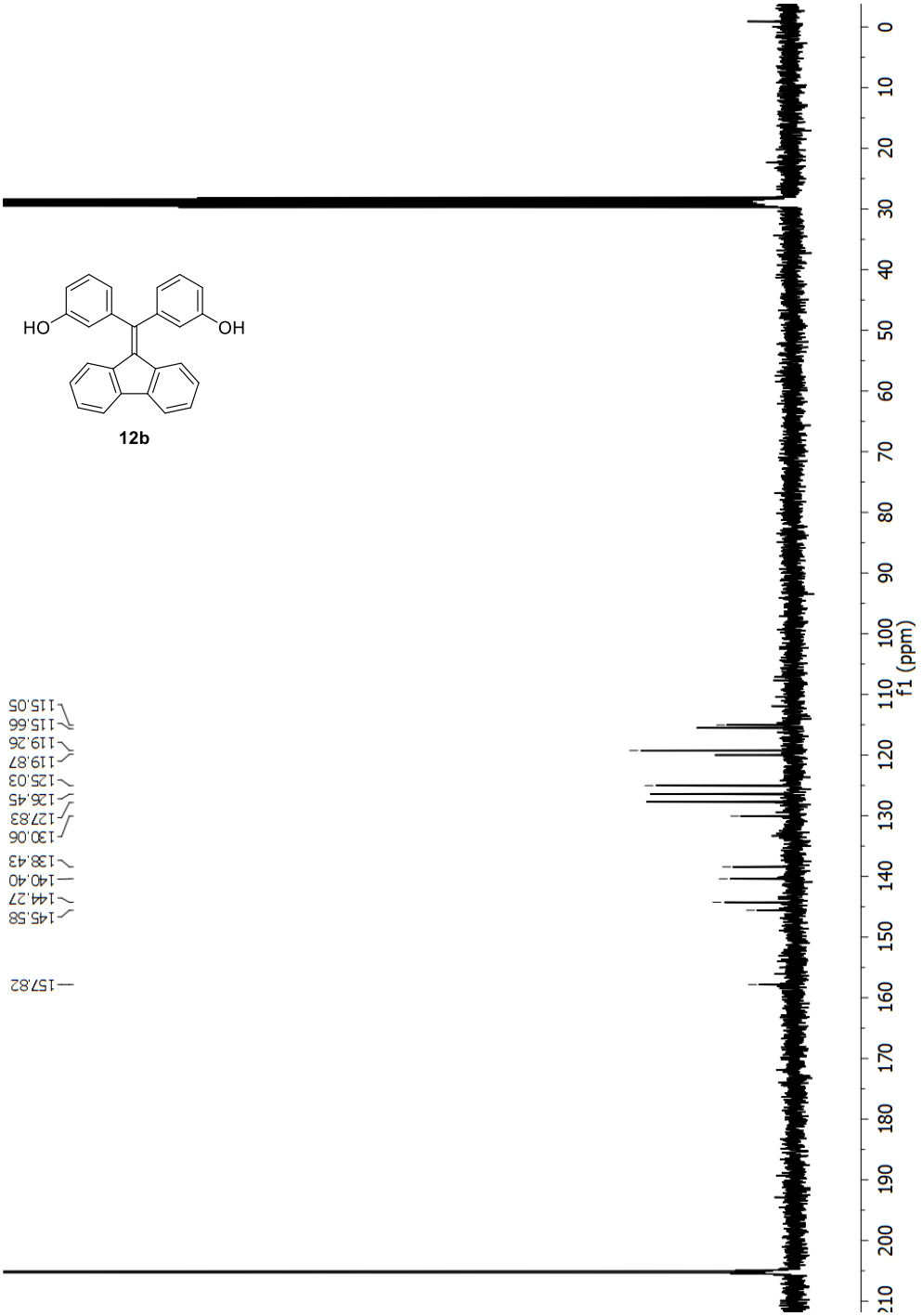

Fig. S-18 ^{13}CNMR (75 MHz, acetone-d_6) of compound **12b.**

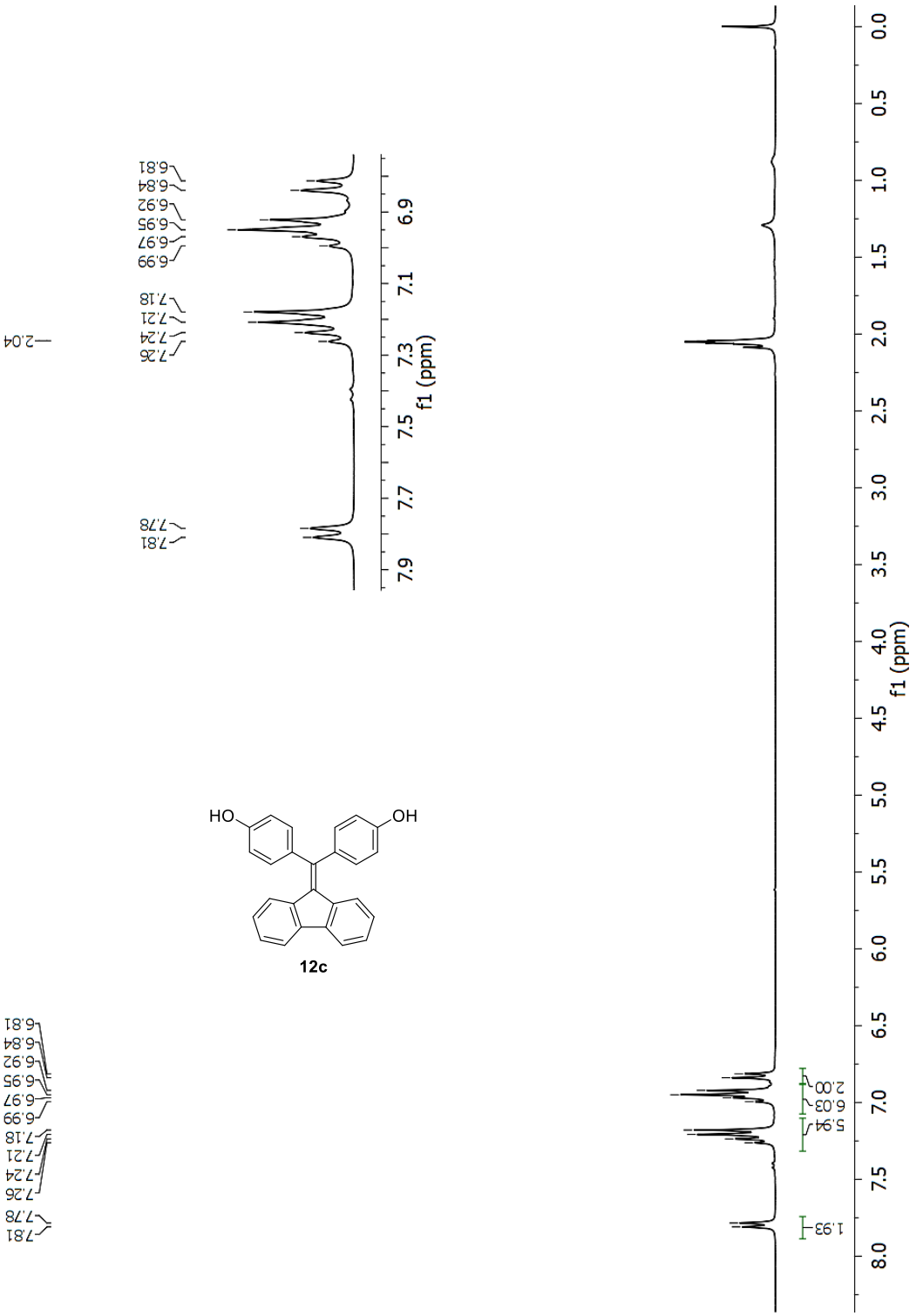

Fig. S-19 ^{1}HNMR (300 MHz, acetone-d_6) of compound **12c.**

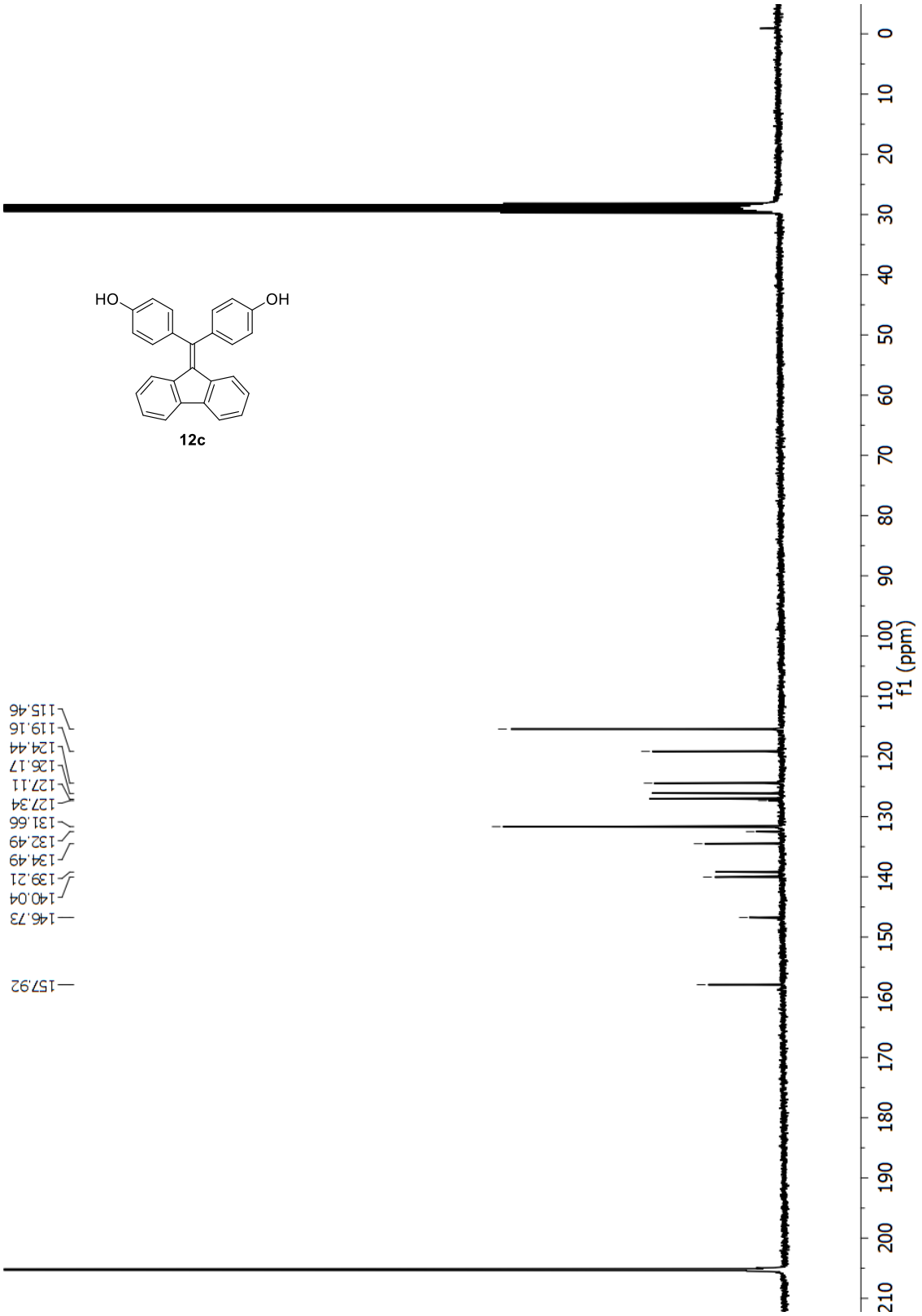

Fig. S-20 ^{13}CNMR (75 MHz, acetone-d_6) of compound **12c.**

2. Solid-State UV-Vis and Fluorescence Spectral Analysis

2.1 Experimental conditions

Solid-state UV-Vis absorption spectra of **5a-c**, **8a-c**, and **9** were measured from their solid thin films prepared by drop-casting on their CH_2Cl_2 solutions on a quartz substrate. Solid-state fluorescence spectra of **5a-c**, **8a-c**, and **9** were recorded on the FLS980 series of fluorescence spectrometer (Edinburgh Instruments, EI) at room temperature. B. The samples were measured in both the crystalline and grounded powdery forms. Luminescence lifetimes (τ) of the crystals of **5a-c** and **9** were also measured with the FLS980 series of fluorescence spectrometer. The measured emission decays were fit to a multi-exponential function using the standard convolute-and-compare nonlinear least-squares procedure. Emission absolute quantum yields (Φ_f) in the solid state were determined at room temperature.

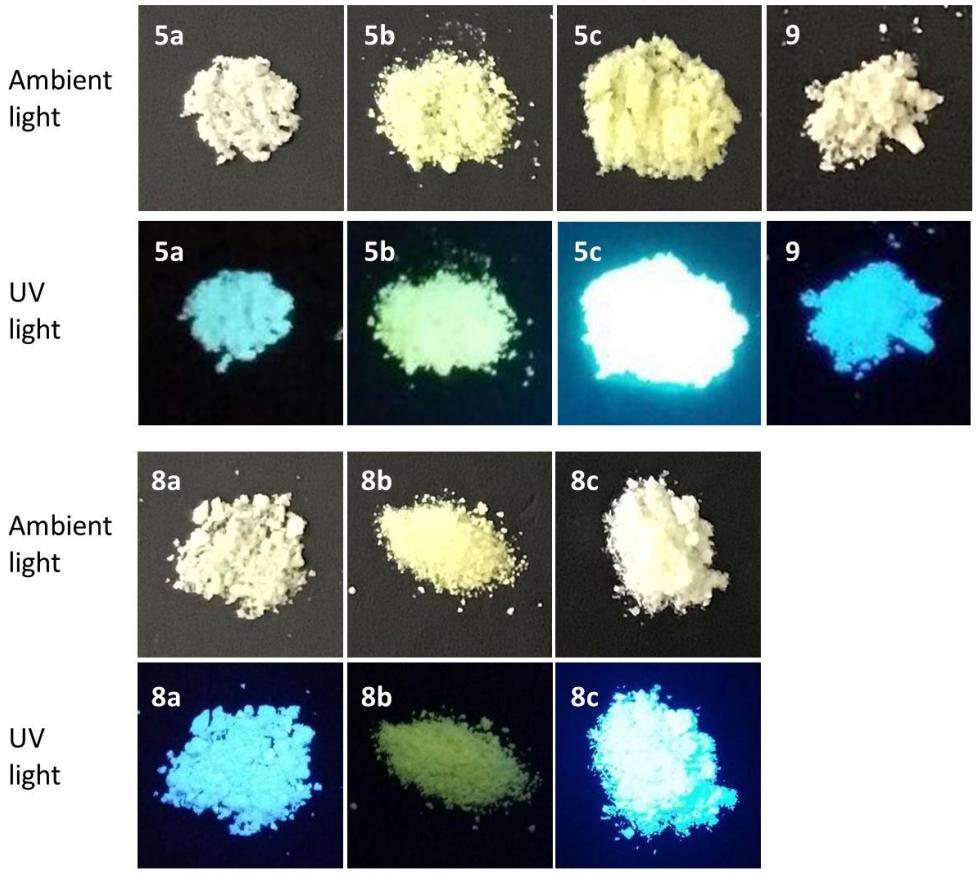

Fig. S-21 Photographic images of the grounded powders of **5a-c**, **8a-c**, and **9** under ambient light and UV light irradiation**.**

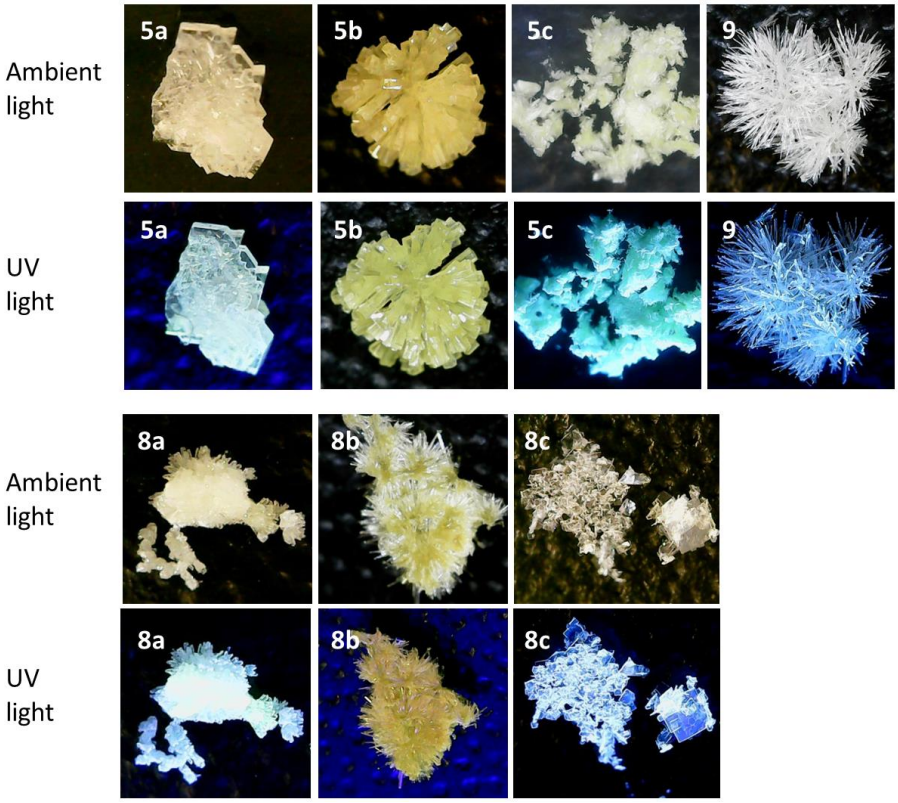

Fig. S-22 Photographic images of the crystals of **5a-c**, **8a-c**, and **9** under ambient light and UV light irradiation**.**

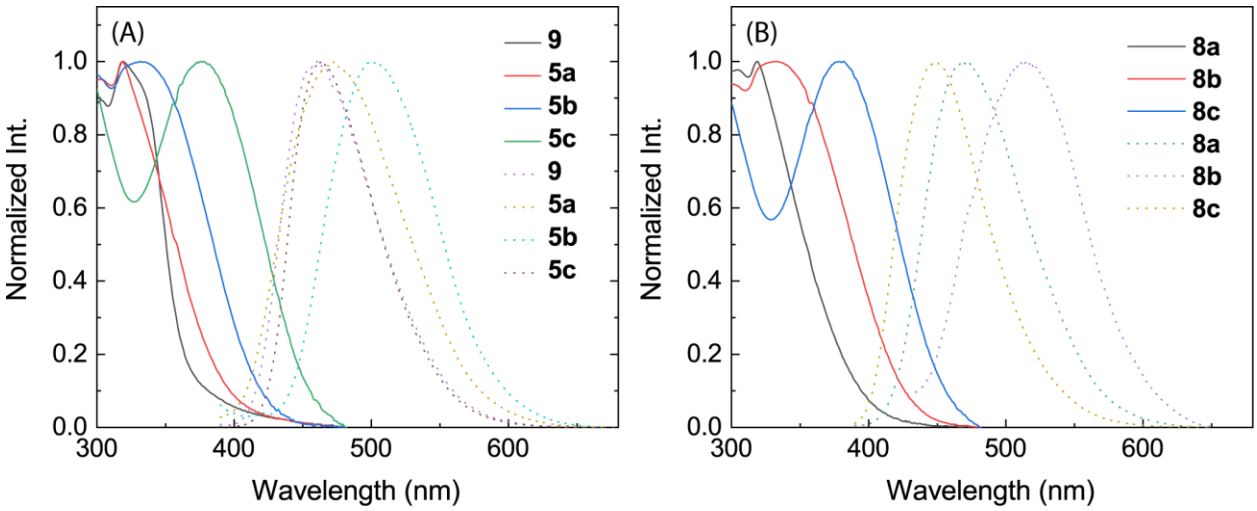

Fig. S-23 Solid-state UV-Vis absorption spectra (solid lines, measured from solid thin films cast on a quartz substrate) and fluorescence spectra (dotted lines, measured in the crystalline state) for the compounds **5a-c**, **8a-c**, and **9.**

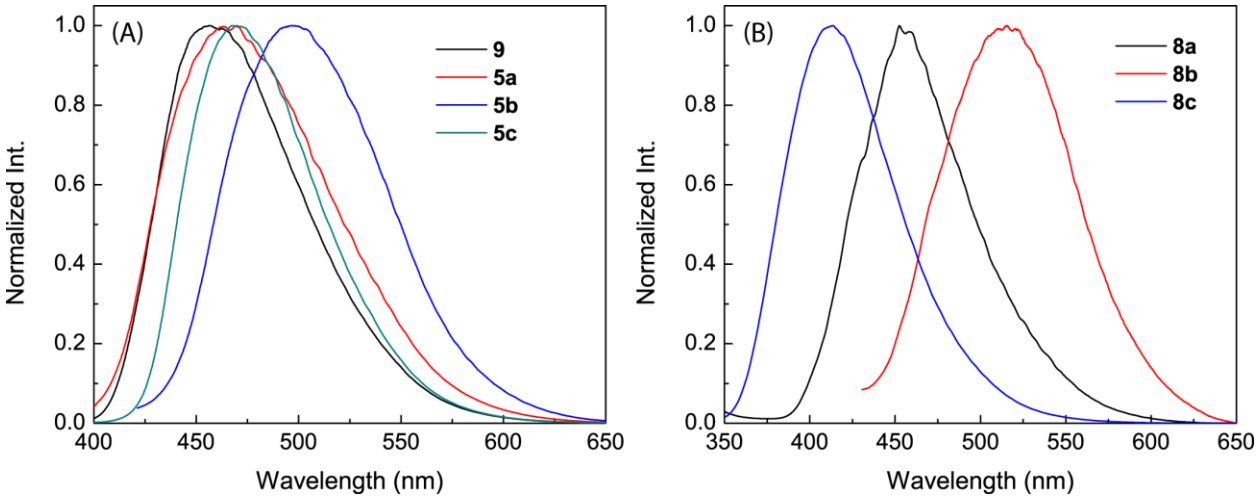

Fig. S-24 Solid-state fluorescence spectra for the grounded powders of **5a-c**, **8a-c**, and **9.**

Table S-1 Summary of solid-state fluorescence properties of **5a-c**, **8a-c**, and **9**

Entry		λ_{em} (nm)	Lifetime (ns)	Φ_f (%)
5a	powder	466	-	16.21
	crystal	473	5.988 14.42	1.44
5b	powder	497	-	1.8
	crystal	507	3.539 14.47	4.22
5c	powder	468	-	66.59
	crystal	461	12.62	89.81
9	powder	457	-	23.51
	crystal	459	11.40 27.20	17.63
8a	powder	454	-	10.94
	crystal	471	-	27.89
8b	powder	515	-	1.59
	crystal	514	-	2.95
8c	powder	413	-	74.26
	crystal	449	-	86.01

3. Electronic Absorption Properties

3.1 Experimental conditions

UV-Vis absorption spectra were measured on a Cary 6000i spectrophotometer. Samples were dissolved in chloroform and measured at room temperature.

3.2 Time-dependent density functional theory (TD-DFT) calculations

Molecular geometries of **DP-DBF**s **5a-c**, **8a-c**, and **9** were optimized at the M06-2X/Def2SVP level of theory using the *Gaussian 16* software package.[1] The optimized geometries were subjected to TD-DFT calculations at the TD-B3LYP/6-311+G(d,p) level to compute the vertical electronic transition energies (only singlet-to-singlet transitions were considered, nstates = 20).

Table S-2 Summary of electronic absorption properties of **DP-DBF**s **5a-c**, **8a-c**, and **9**

Entry	$\lambda_{S0\rightarrow S1}$ (cald) (nm)	$\lambda^{abs}_{1/2}$ (exp) (nm)	λ_{max} (exp) (nm)	*f*
5a	378 (*cis*) 355 (*trans*)	351	316	0.0783 (*cis*) 0.0063 (*trans*)
5b	384 (*cis*) 384 (*trans*)	374	331	0.0028 (*cis*) 0.0024 (*trans*)
5c	399	407	368	0.4097
8a	360	343	316	0.0135
8b	390	373	328	0.0027
8c	397	407	368	0.4775
9	371	343	315	0.0048

$\lambda_{S0\rightarrow S1}$ is the wavelength corresponding to the vertical transition from the ground state (S_0) to the first-excited state (S_1) calculated at the TD-B3LYP/6-311+G(d,p) level.
$\lambda^{abs}_{1/2}$ is the half-height wavelength of the lowest-energy absorption band.
f is calculated oscillator strength.

[1]Gaussian 16, Revision B.01, M. J. Frisch, G. W. Trucks, H. B. Schlegel, G. E. Scuseria, M. A. Robb, J. R. Cheeseman, G. Scalmani, V. Barone, G. A. Petersson, H. Nakatsuji, X. Li, M. Caricato, A. V. Marenich, J. Bloino, B. G. Janesko, R. Gomperts, B. Mennucci, H. P. Hratchian, J. V. Ortiz, A. F. Izmaylov, J. L. Sonnenberg, D. Williams-Young, F. Ding, F. Lipparini, F. Egidi, J. Goings, B. Peng, A. Petrone, T. Henderson, D. Ranasinghe, V. G. Zakrzewski, J. Gao, N. Rega, G. Zheng, W. Liang, M. Hada, M. Ehara, K. Toyota, R. Fukuda, J. Hasegawa, M. Ishida, T. Nakajima, Y. Honda, O. Kitao, H. Nakai, T. Vreven, K. Throssell, J. A. Montgomery, Jr., J. E. Peralta, F. Ogliaro, M. J. Bearpark, J. J. Heyd, E. N. Brothers, K. N. Kudin, V. N. Staroverov, T. A. Keith, R. Kobayashi, J. Normand, K. Raghavachari, A. P. Rendell, J. C. Burant, S. S. Iyengar, J. Tomasi, M. Cossi, J. M. Millam, M. Klene, C. Adamo, R. Cammi, J. W. Ochterski, R. L. Martin, K. Morokuma, O. Farkas, J. B. Foresman, and D. J. Fox, Gaussian, Inc., Wallingford CT, 2016.

4. Crystallographic Analysis

Single crystals of compounds **5a-c**, **8a-c**, and **9** suitable for X-ray diffraction analysis were grown by slow diffusion of hexane into their chloroform solutions at room temperature. Single-crystal X-ray diffraction data was collected at 100(2) K on a XtaLAB Synergy-S, Dualflex, HyPix-6000HE diffractometer using Cu *K*α radiation (λ = 1.5406 Å). Crystal was mounted on nylon CryoLoops with Paraton-N. The data collection and reduction were processed within *CrysAlisPro* (Rigaku OD, 2019). A Gaussian absorption correction was applied to the collected reflections. Using Olex[2,٢] the structure was solved with the ShelXT[٣] structure solution program using Intrinsic Phasing and refined with the ShelXL[٤] refinement package using Least Squares minimization. All non-hydrogen atoms were refined anisotropically. The organic hydrogen atoms were generated geometrically.

For *ortho*-OMe substituted **5a**, two different conformations, namely *cis* and *trans*, were grown as a single crystal at ratio of 49:51. Molecular structures of the two conformers are depicted in Fig. S-25.

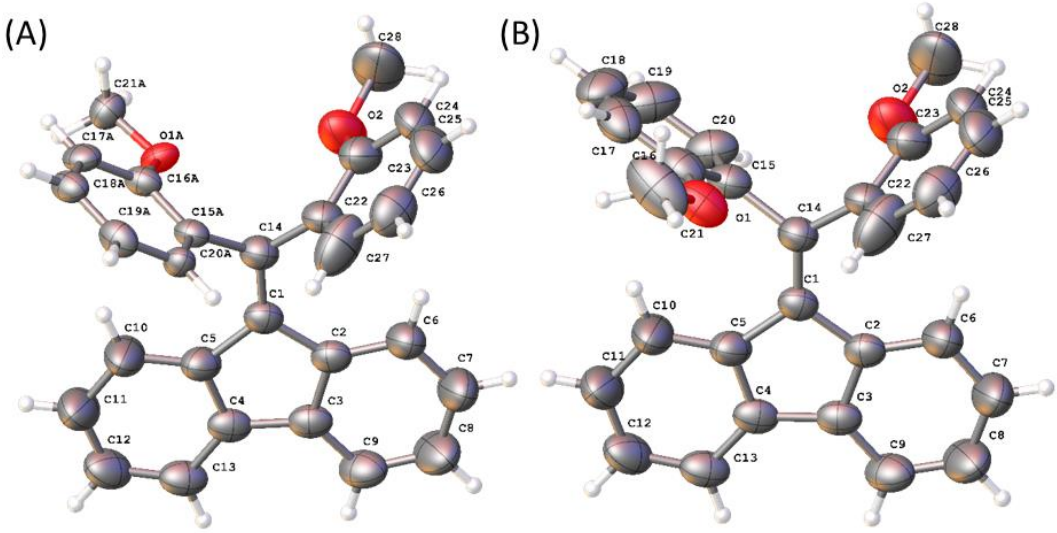

Fig. S-25 ORTEP drawings (50% probability level) of two different conformations, (A) *cis* and (B) *trans*, showed in the same single crystal of **5a** (CCDC 1980233).

[٢]Dolomanov, O.V., Bourhis, L.J., Gildea, R.J, Howard, J.A.K. & Puschmann, H. (2009), *J. Appl. Cryst*. 42, 339-341.

[٣]Sheldrick, G.M. (2015). *Acta Cryst*. A71, 3-8.

[4] Sheldrick, G.M. (2015). *Acta Cryst*. C71, 3-8.

For *meta*-OMe substituted **5b**, two types of single crystals were obtained during the crystallization process. As shown in Fig. S-26A. the *cis* single crystal structure shows two OMe groups on the same side with respect to the fluorene plane, and this crystal is a minor product (ca. 20%). The *trans* single crystal (Figure S-26B) is the major product (ca. 80%).

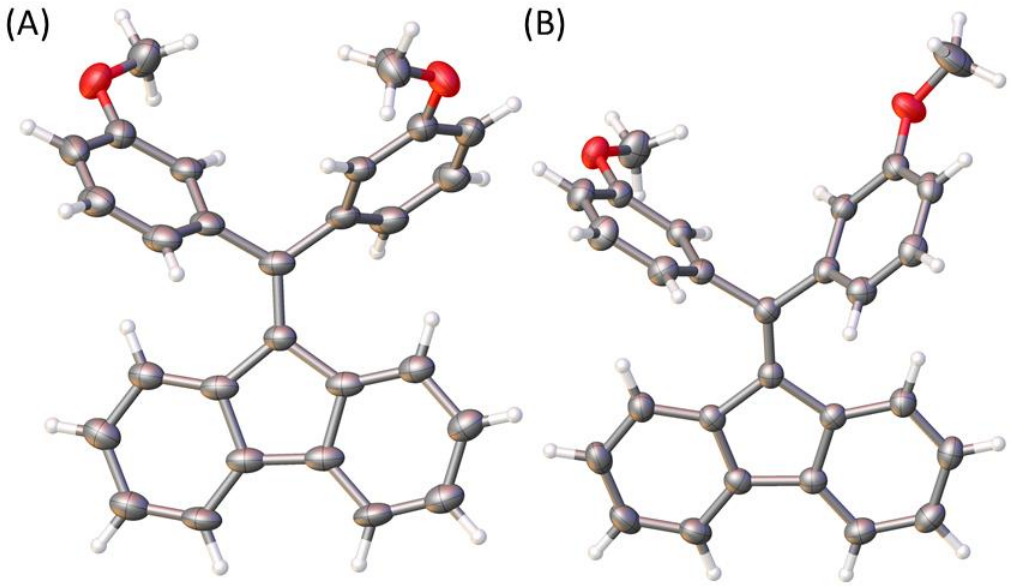

Fig. S-26 ORTEP drawings (50% probability level) of two single crystal structures, (A) *cis* (CCDC 2017099) and (B) *trans* (CCDC 2016939), of **5b**.

Crystallographic data for the **DP-DBP** derivatives reported in this work have been deposited with the Cambridge Crystallographic Data Centre (CCDC). CCDC numbers: 1980233 (**5a**), 2016939 (**5b** *trans*), 2017099 (**5b** *cis*), 2016946 (**5c**), 2016948 (**8a**), 2016952 (**8b**), 2016953 (**8c**), 2016933 (**9**).

Appendix II

Supplementary Information for Chapter 3

Structural Tuning of Curved TTFAQ-AQ as a Redox-active Supramolecular Partner for C_{70} Fullerene

https://doi.org/10.1021/acs.joc.1c01633

Table of Contents

1. NMR Spectra for New Compounds

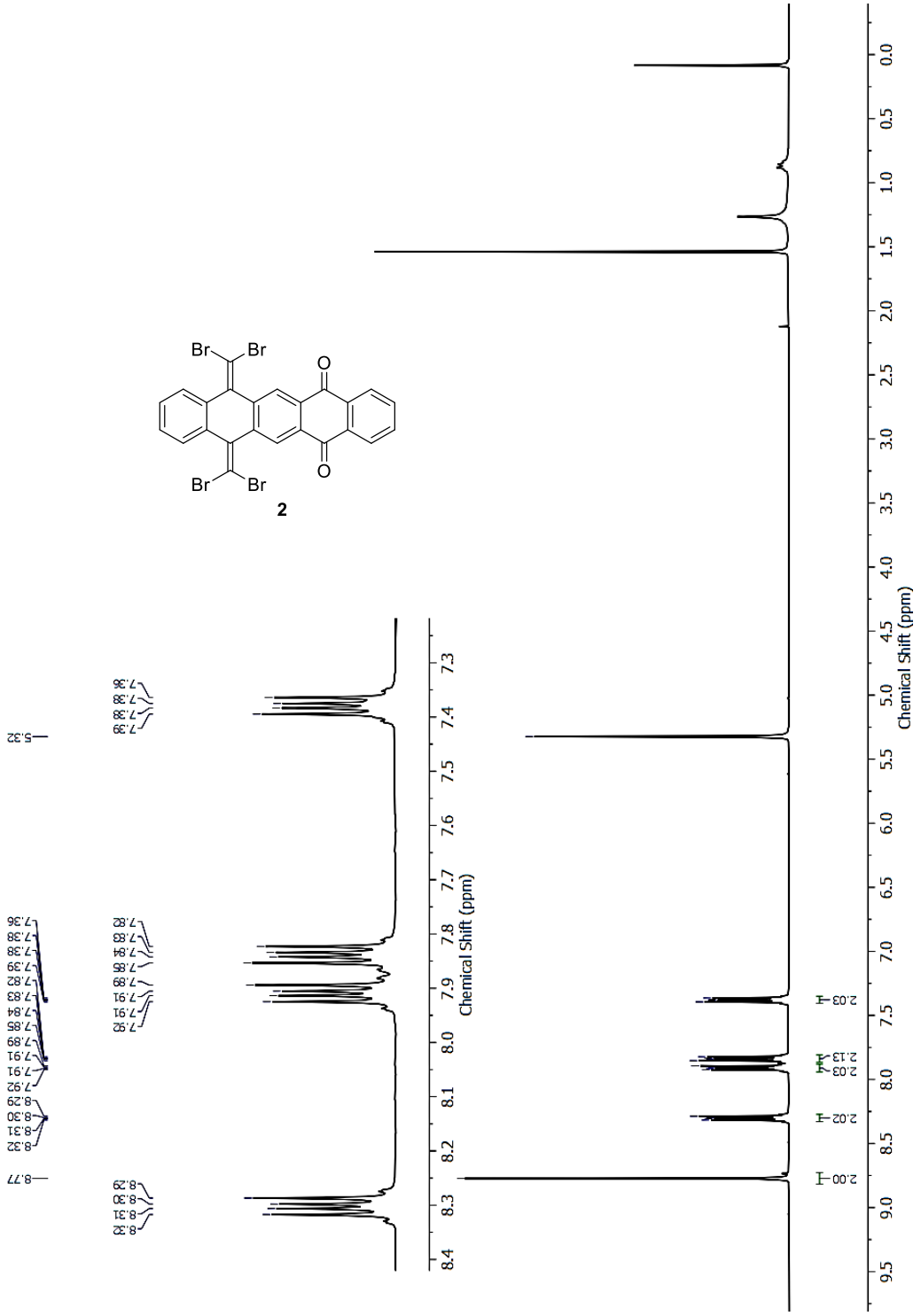

Fig. S-1 ^{1}H NMR (300 MHz, CD_2Cl_2) of compound **2**.

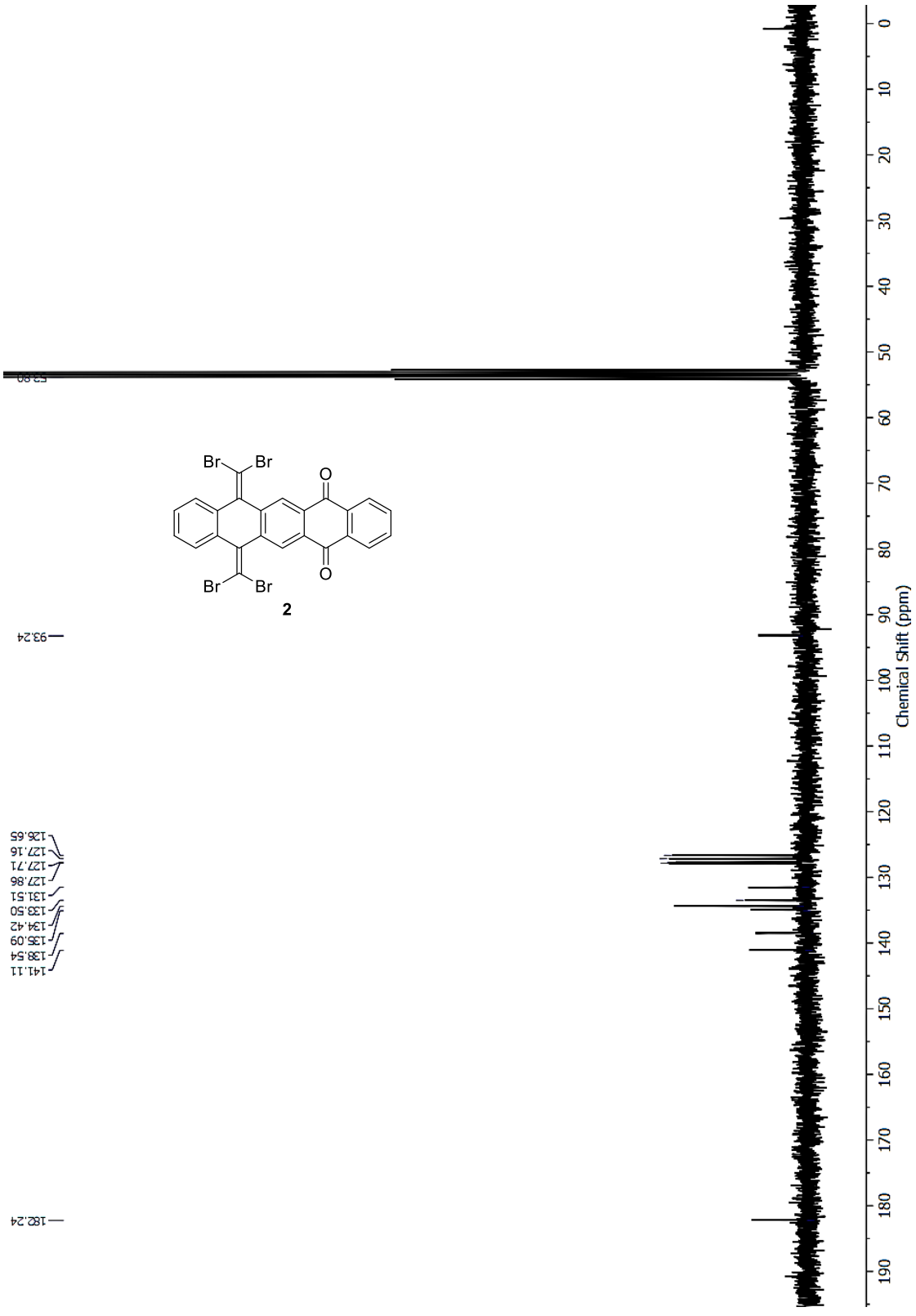

Fig. S-2 $^{13}C\{^{1}H\}$ NMR (75 MHz, CD_2Cl_2) of compound **2.**

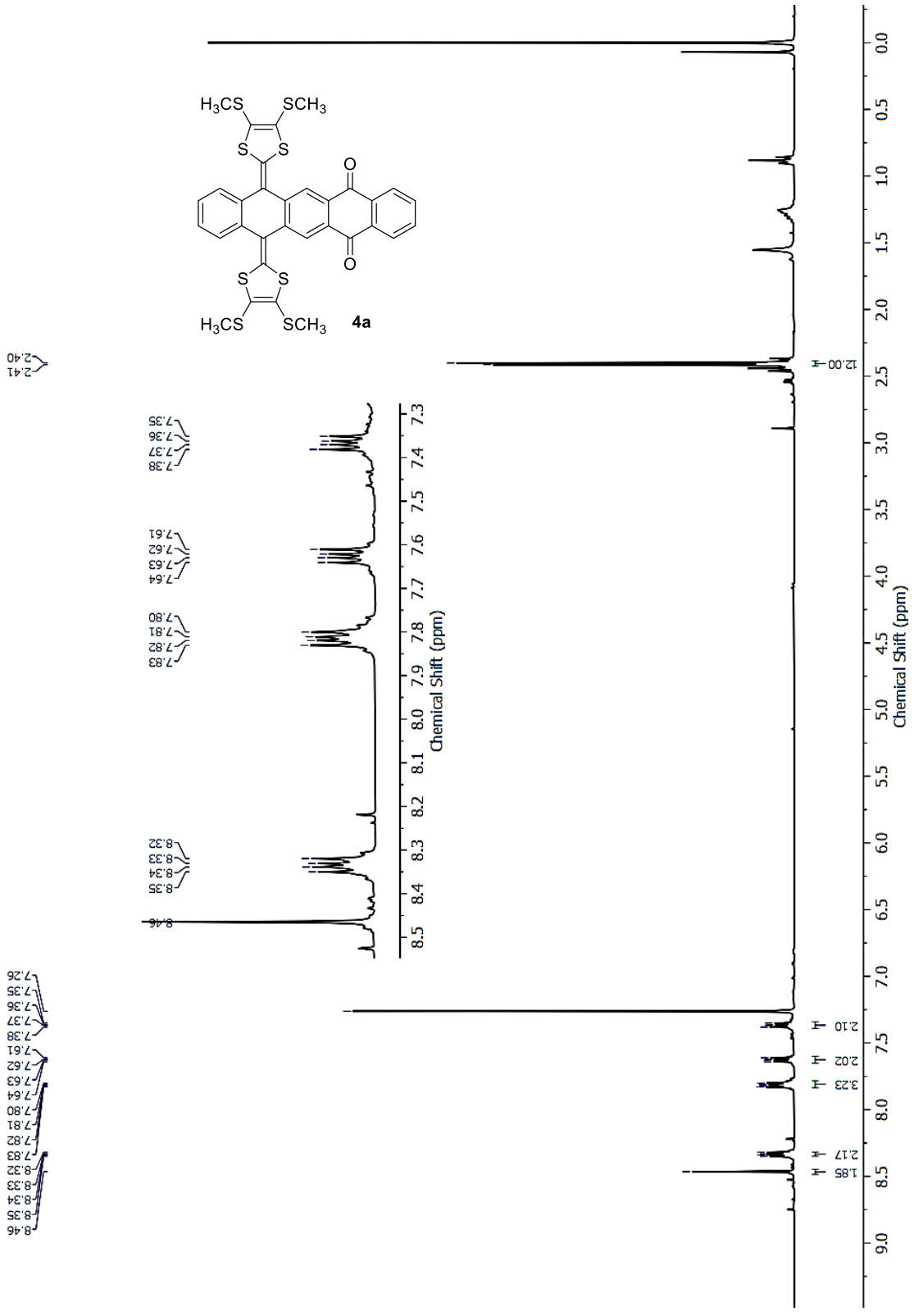

Fig. S-3 ^{1}H NMR (300 MHz, $CDCl_3$) of compound **4a**.

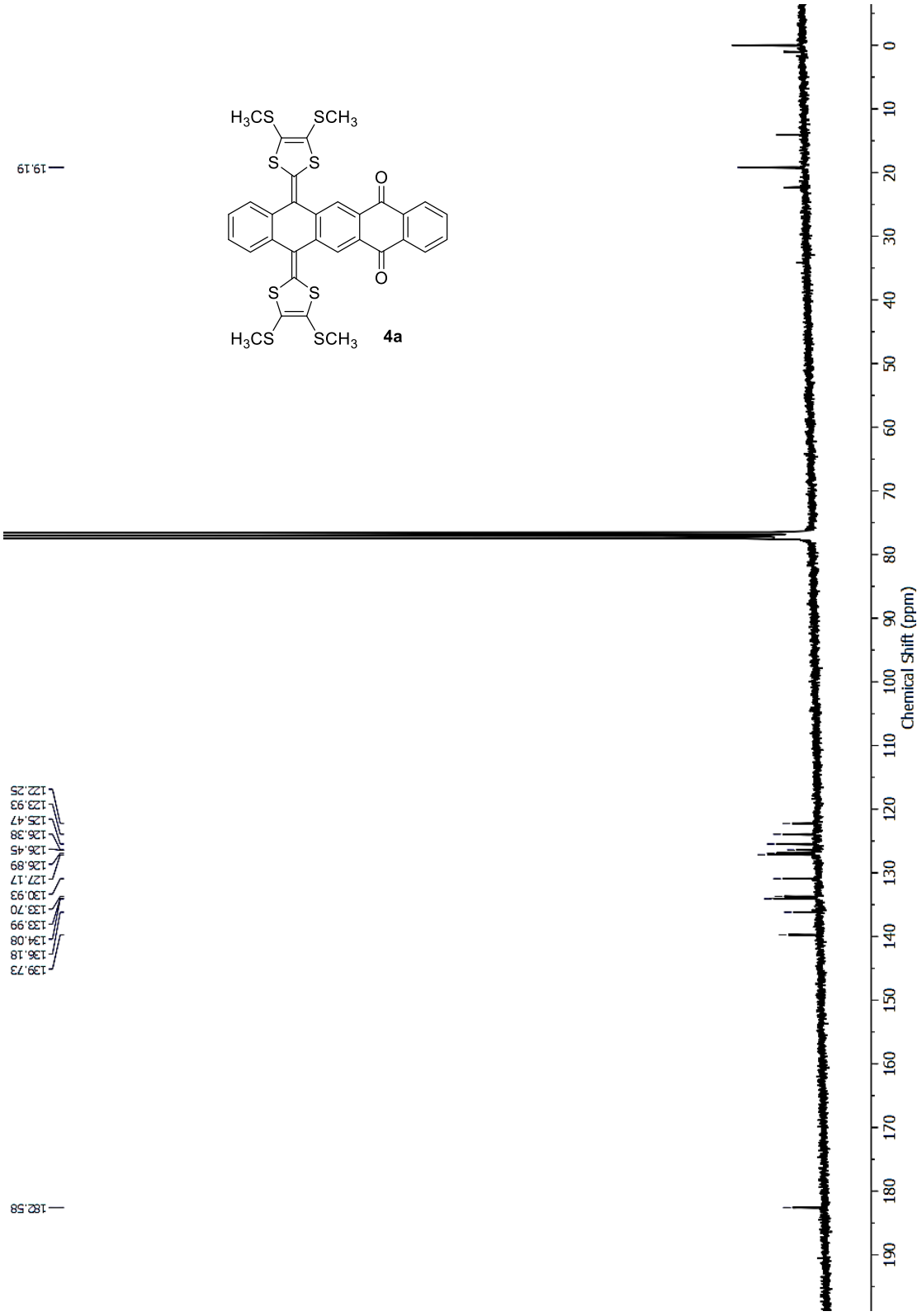

Fig. S-4 $^{13}C\{^{1}H\}$ NMR (75 MHz, $CDCl_3$) of compound **4a**.

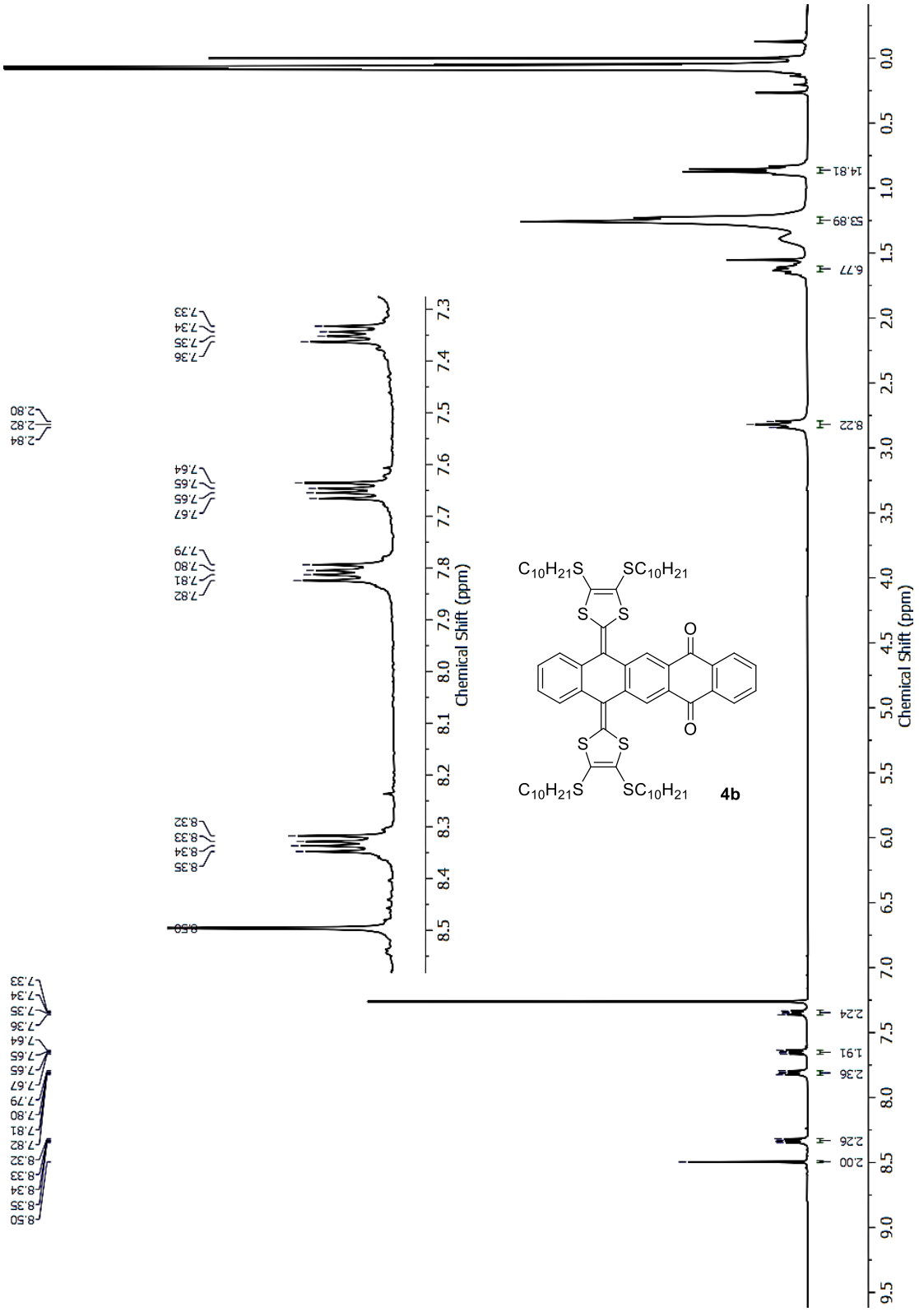

Fig. S-5 ^{1}H NMR (300 MHz, $CDCl_3$) of compound **4b**.

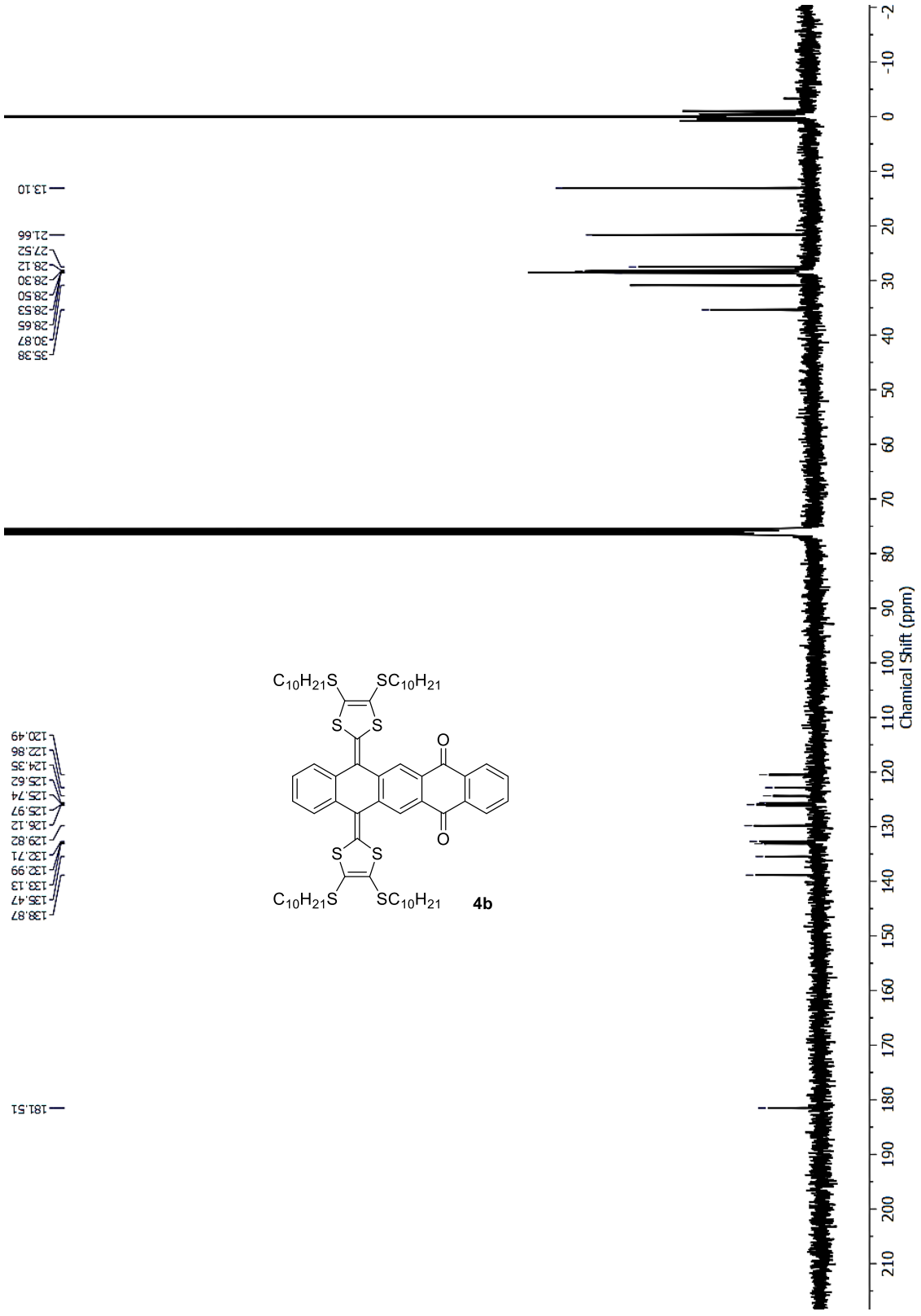

Fig. S-6 $^{13}C\{^{1}H\}$ NMR (75 MHz, $CDCl_3$) of compound **4b**.

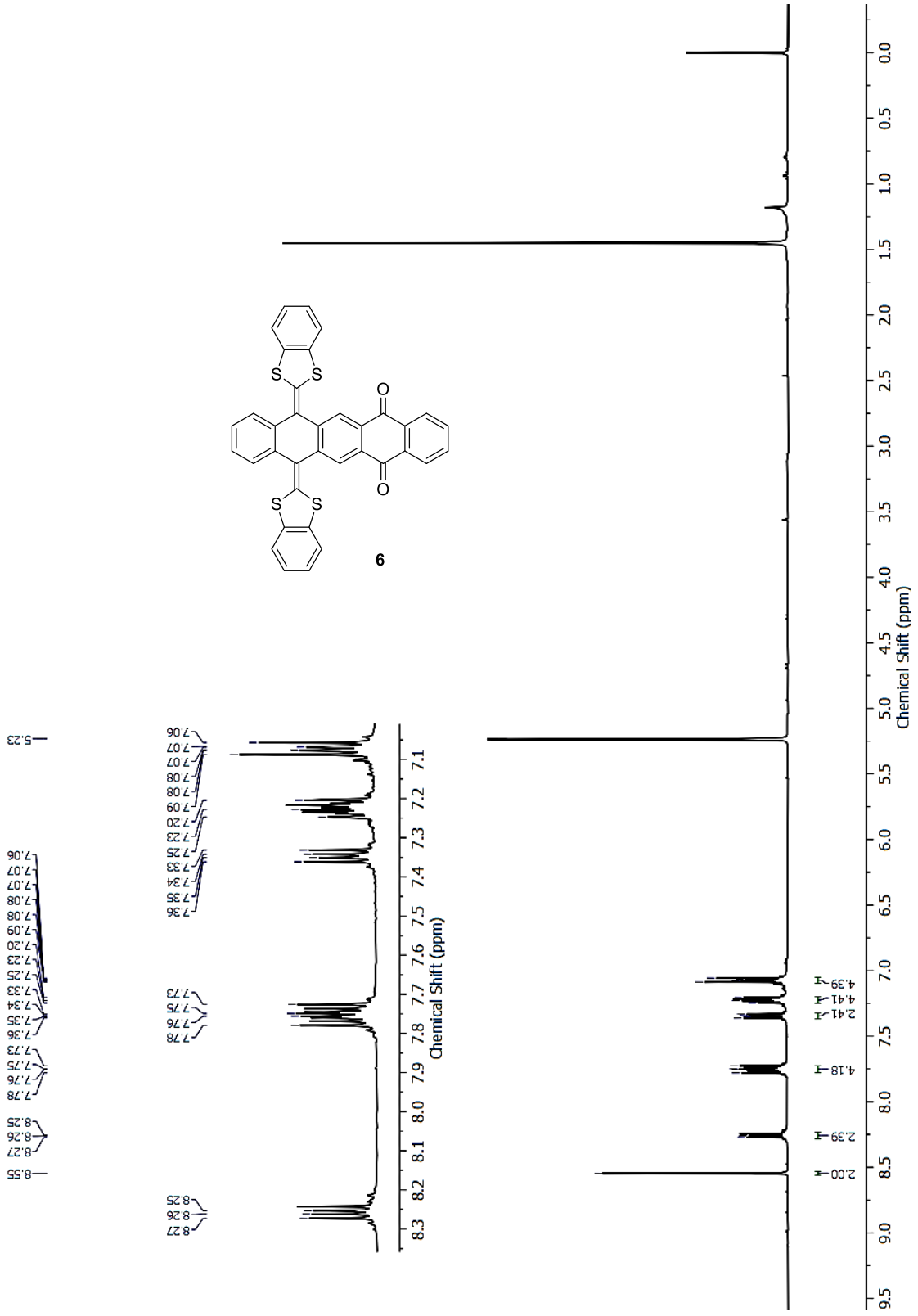

Fig. S-7 ^{1}H NMR (300 MHz, CD_2Cl_2) of compound **6**.

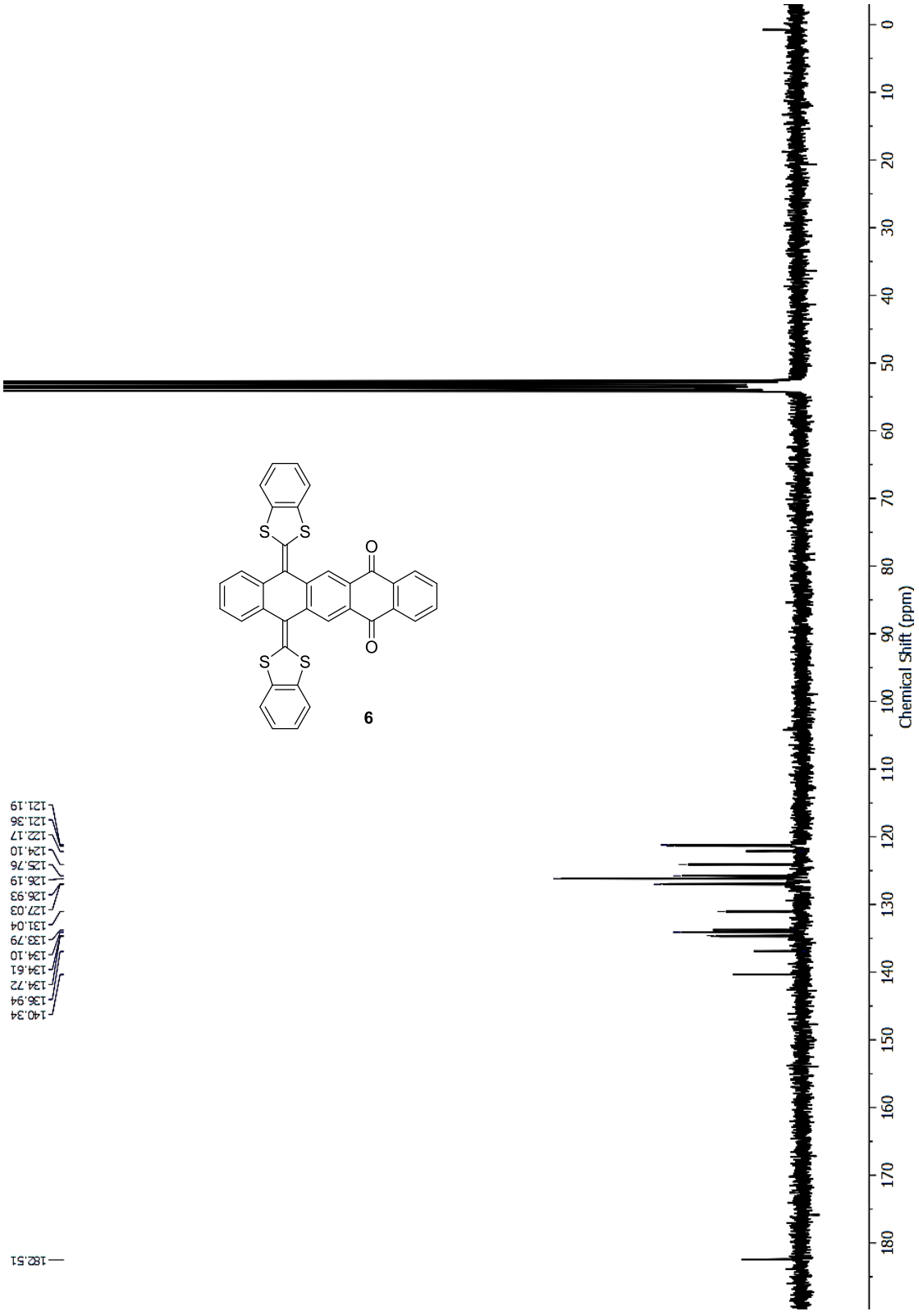

Fig. S-8 $^{13}C\{^{1}H\}$ NMR (75 MHz, CD_2Cl_2) of compound **6**.

2. ^{1}H NMR Titrations of Compounds 4a, 4b, and 6 with C_{70} and C_{60} Fullerenes

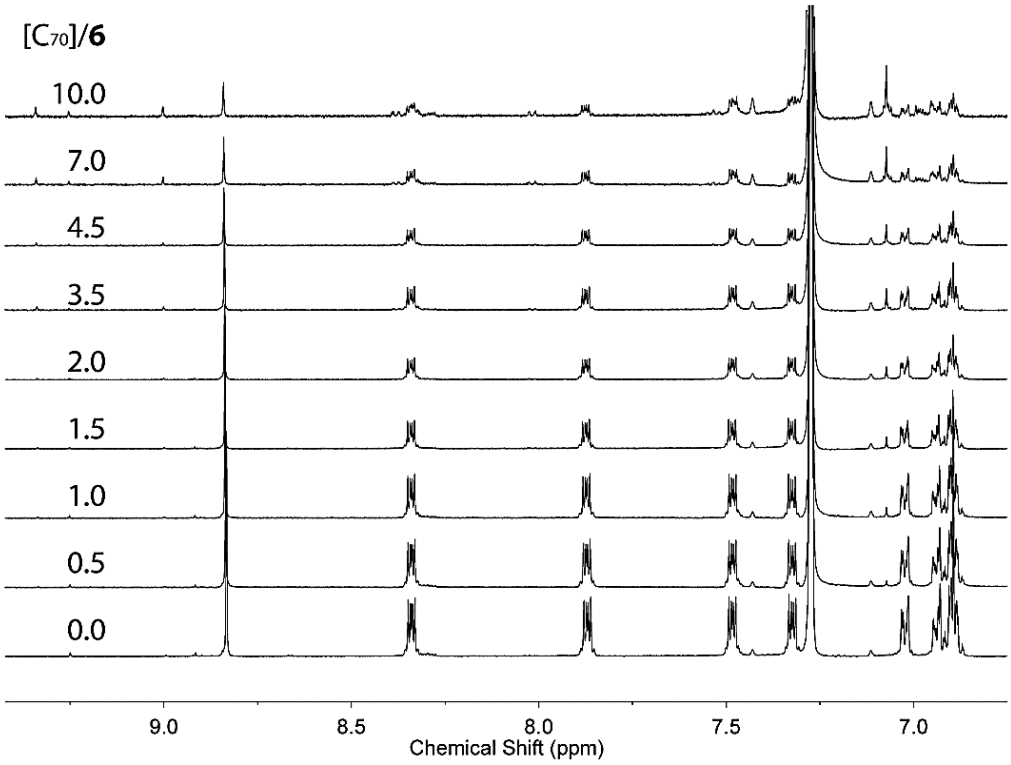

Fig. S-9 ^{1}H NMR spectra of **6** (8.04×10^{-3} M in benzene-*d6* and CS_2, 1:1 v/v) in response to the addition of C_{70} fullerene from 0 to 10.0 molar equivalents.

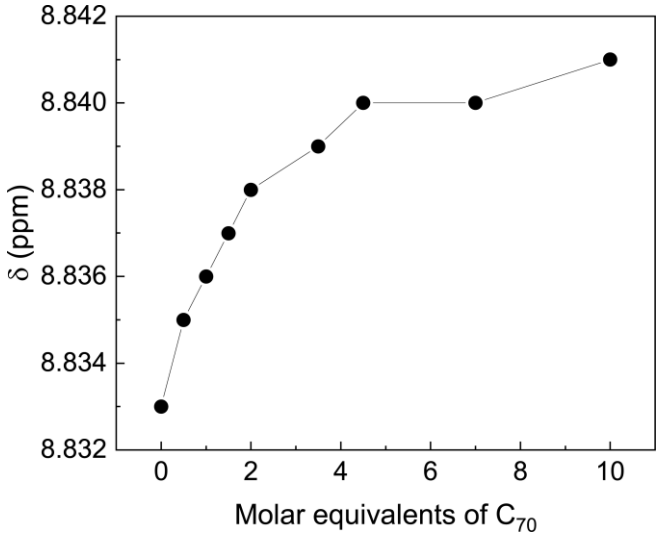

Figure S-10 Correlation of the chemical shift of the ^{1}H NMR signal of **6** at 8.83 ppm with the molar equivalence of C_{70} fullerene titrated.

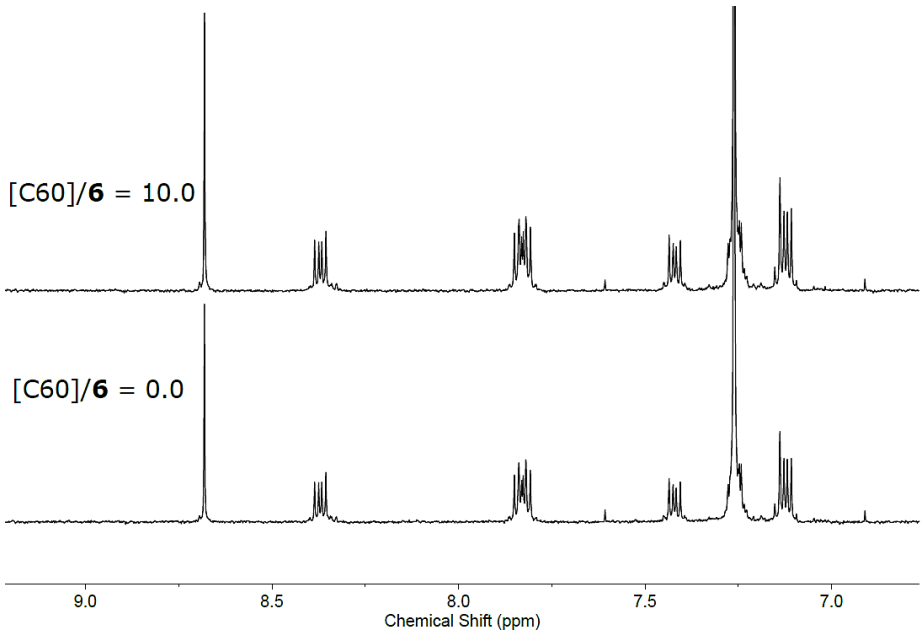

Fig. S-11 ^{1}H NMR spectra of **6** (8.04×10^{-3} M in $CDCl_3$ and CS_2, 1:1 v/v) before and after addition of 10.0 molar equivalents of C_{60} fullerene.

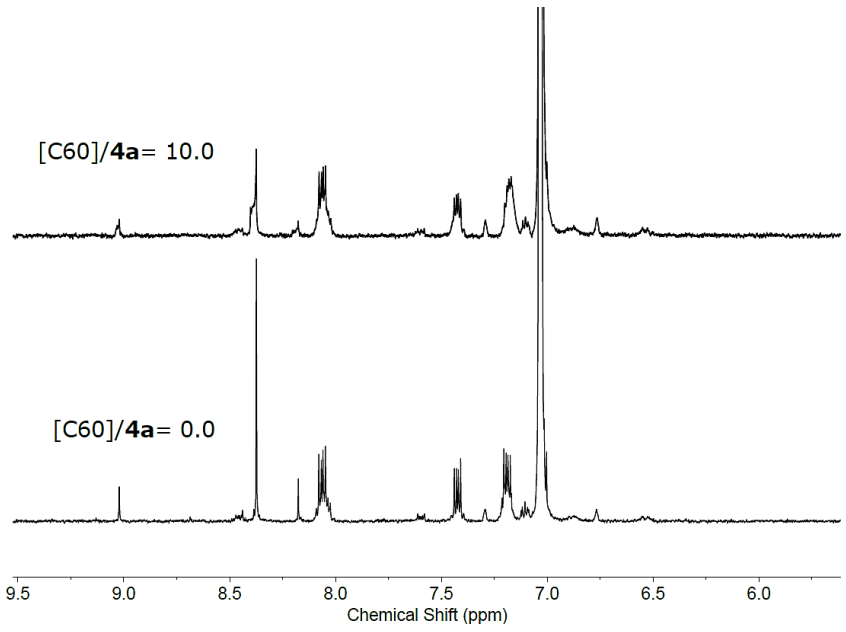

Fig. S-12 ^{1}H NMR spectra of **4a** (2.05×10^{-3} M in in benzene-*d6* and CS_2, 1:1 v/v) before and after addition of 10.0 molar equivalents of C_{60} fullerene.

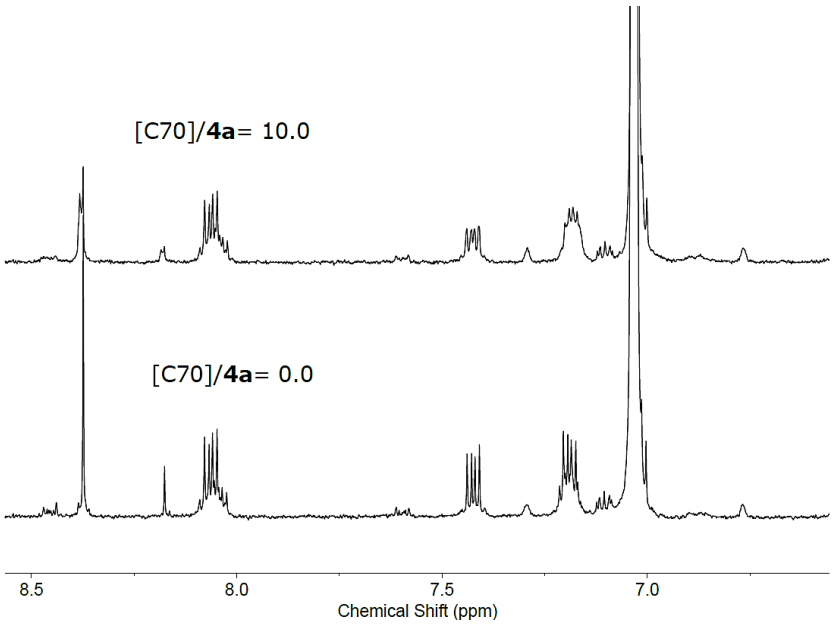

Fig. S-13 ^{1}H NMR spectra of **4a** (2.05×10^{-3} M in in benzene-*d6* and CS_2, 1:1 v/v) before and after addition of 10.0 molar equivalents of C_{70} fullerene.

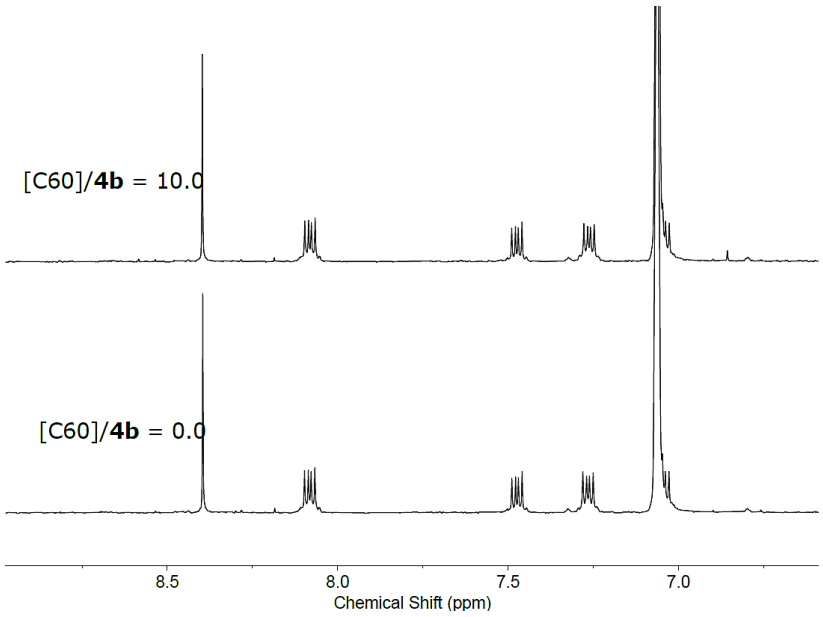

Fig. S-14 ^{1}H NMR spectra of **4b** (5.2×10^{-3} M in in benzene-*d6* and CS_2, 1:1 v/v) before and after addition of 10.0 molar equivalents of C_{60} fullerene.

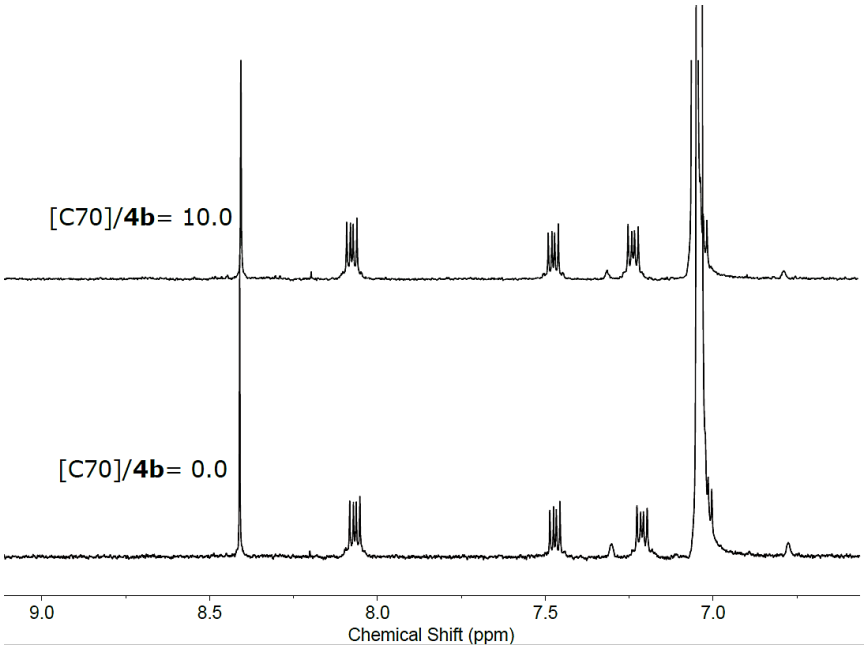

Fig. S-15 ^{1}H NMR spectra of **4b** (5.2×10^{-3} M in in benzene-*d6* and CS_2, 1:1 v/v) before and after addition of 10.0 molar equivalents of C_{70} fullerene.

3. UV-Vis Titrations of 4a, 4b, and 6 with C_{70} and C_{60} Fullerenes

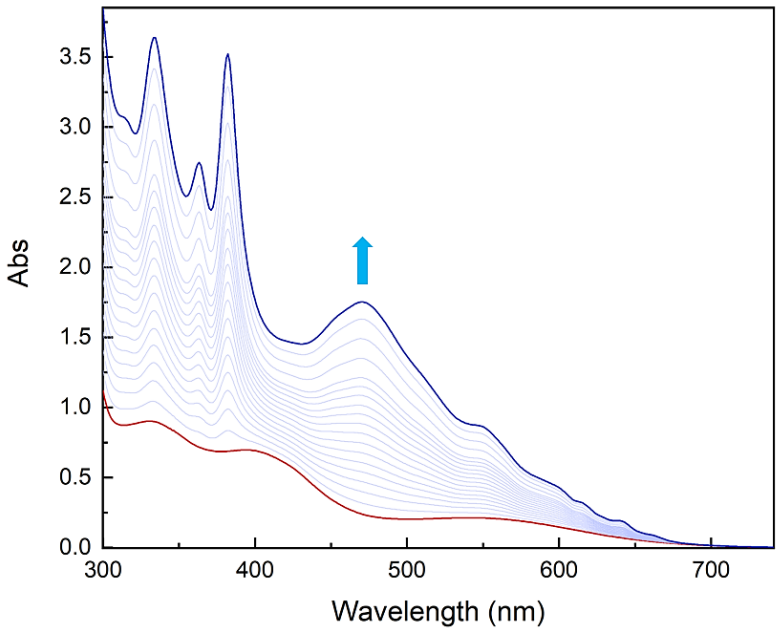

Fig. S-16 UV-Vis absorption spectra of **4a** (16.5 μM in chlorobenzene) in response to the addition of C_{70} fullerene from 0.0 to 5.3 molar equivalents. The arrow indicates the trend of spectral variations.

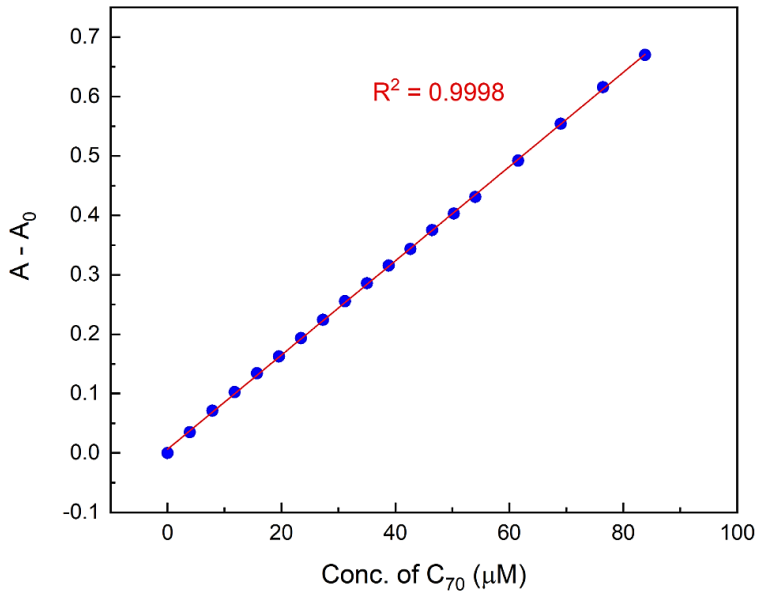

Fig. S-17 Linear correlation of the absorbance change ($A - A_0$) of **4a** (16.5 μM in chlorobenzene) with the concentration of C_{70} fullerene in the solution. A: observed absorbance at 540 nm; A_0: initial absorbance at 540 nm.

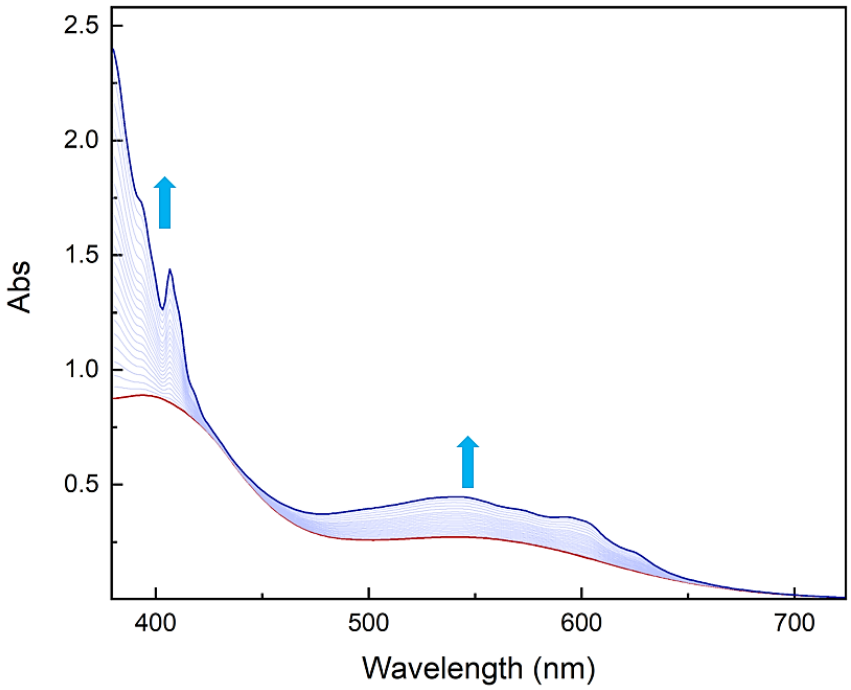

Fig. S-18 UV-Vis absorption spectra of **4a** (16.5 μM in chlorobenzene) in response to the addition of C_{60} fullerene from 0.0 to 12 molar equivalents. The arrow indicates the trend of spectral variations.

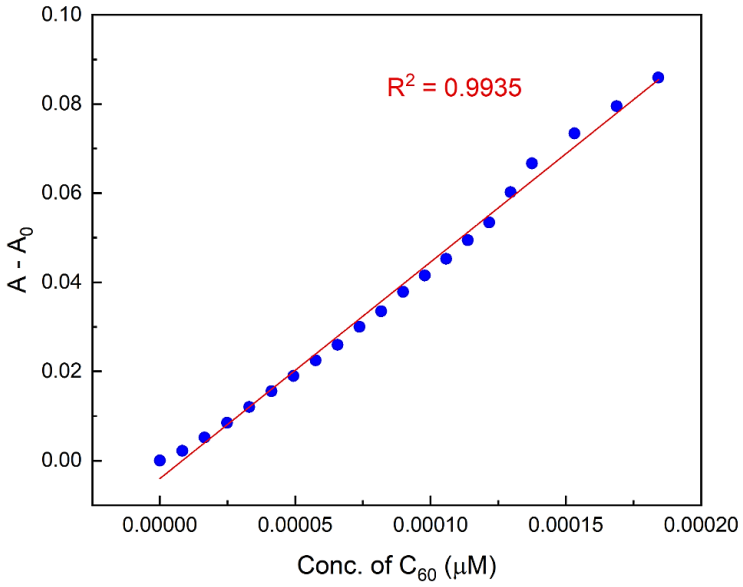

Fig. S-19 Linear correlation of the absorbance change ($A - A_0$) of **4a** (16.5 μM in chlorobenzene) with the concentration of C_{60} fullerene in the solution. A: observed absorbance at 475 nm; A_0: initial absorbance at 475 nm.

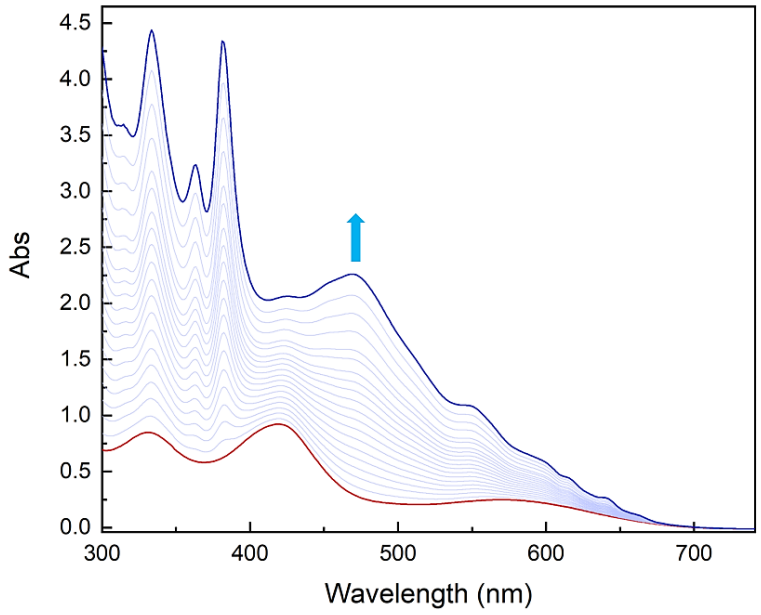

Fig. S-20 UV-Vis absorption spectra of **4b** (18 μM in chlorobenzene) in response to the addition of C_{70} fullerene from 0.0 to 5.0 molar equivalents. The arrow indicates the trend of spectral variations.

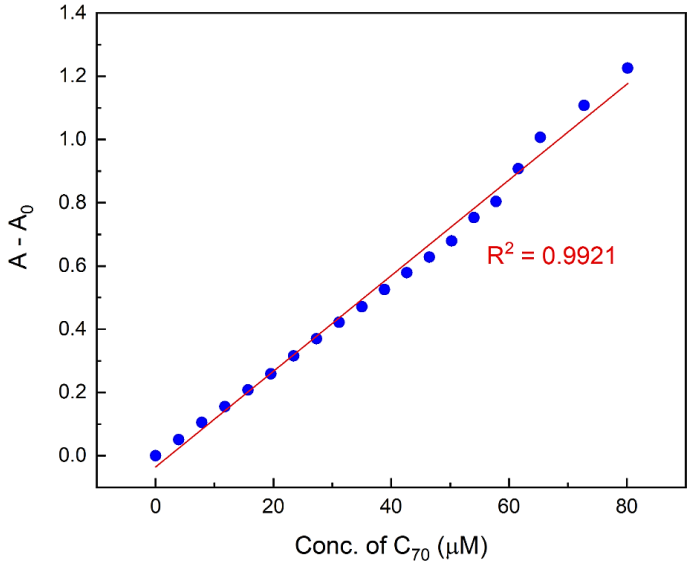

Fig. S-21 Linear correlation of the absorbance change ($A - A_0$) of **4b** (18 μM in chlorobenzene) with the concentration of C_{70} fullerene in the solution. A: observed absorbance at 515 nm; A_0: initial absorbance at 515 nm.

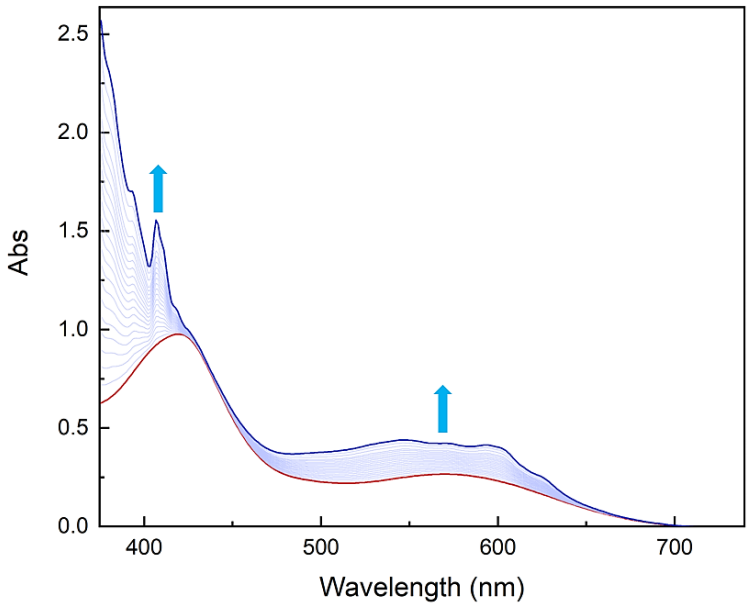

Fig. S-22 UV-Vis absorption spectra of **4b** (18.0 μM in chlorobenzene) in response to the addition of C_{60} fullerene from 0.0 to 10.2 molar equivalents. The arrows indicate the trend of spectral variations.

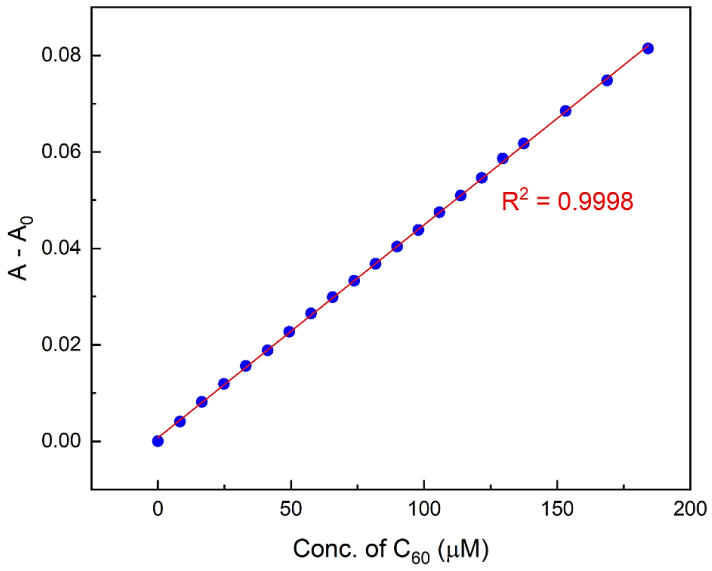

Fig. S-23 Linear correlation of the absorbance change ($A - A_0$) of **4b** (18 μM in chlorobenzene) with the concentration of C_{60} fullerene in the solution. A: observed absorbance at 470 nm; A_0: initial absorbance at 470 nm.

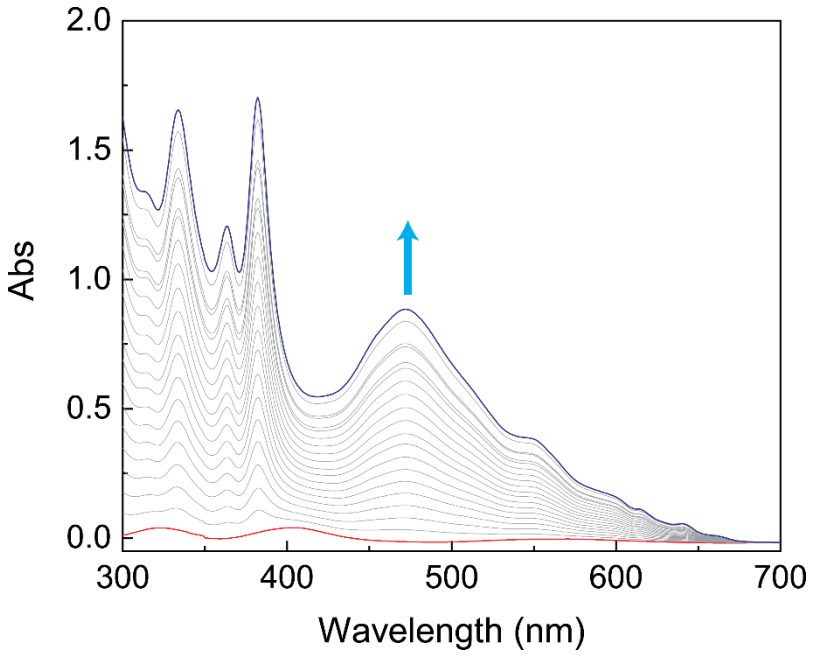

Fig. S-24 UV-Vis absorption spectra of **6** (5.2 μM in chlorobenzene) in response to the addition of C_{70} fullerene from 0.0 to 8.5 molar equivalents. The arrow indicates the trend of spectral variations.

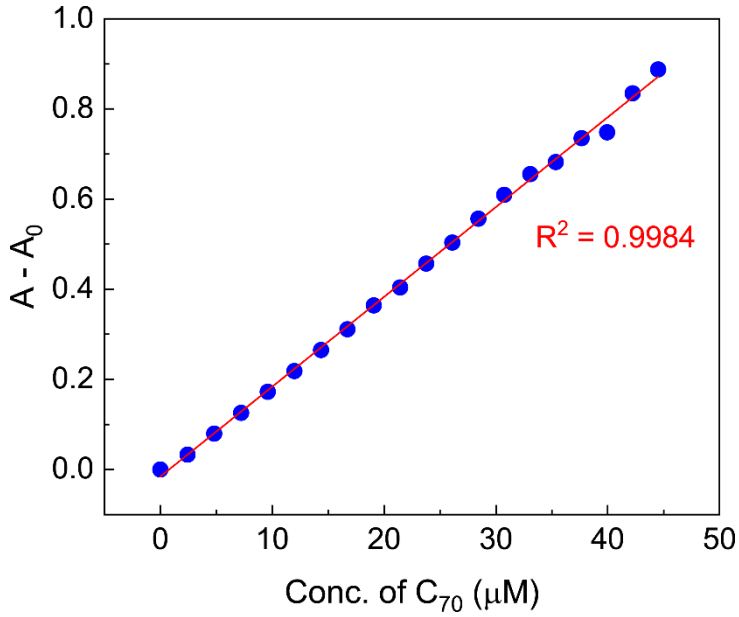

Fig. S-25 Linear correlation of the absorbance change ($A - A_0$) of **6** (5.2 μM in chlorobenzene) with the concentration of C_{70} fullerene in the solution. A: observed absorbance at 471 nm; A_0: initial absorbance at 471 nm.

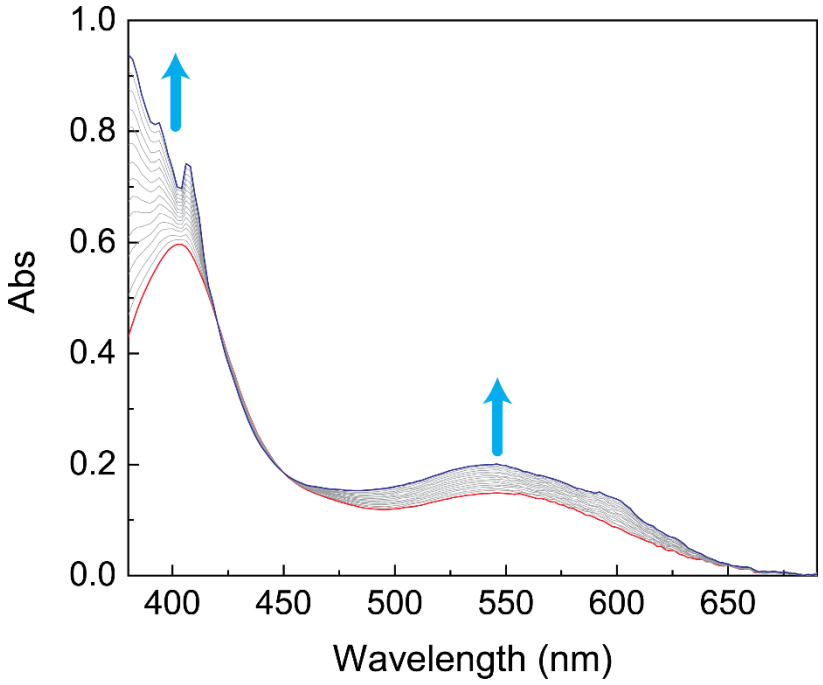

Fig. S-26 UV-Vis absorption spectra of **6** (12.0 μM in chlorobenzene) in response to the addition of C_{60} fullerene from 0.0 to 6.0 molar equivalents. The arrows indicate the trend of spectral variations.

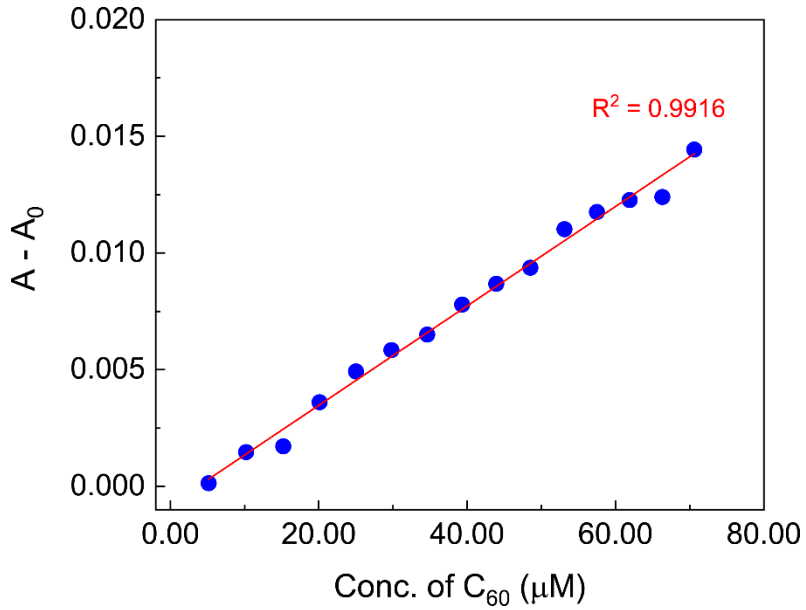

Fig. S-27 Linear correlation of the absorbance change ($A - A_0$) of **6** (5.2 μM in chlorobenzene) with the concentration of C_{60} fullerene in the solution. A: observed absorbance at 430 nm; A_0: initial absorbance at 430 nm.

4. UV-Vis Absorption Spectra of 4a, 4b, and 6 in Various Organic Solvents

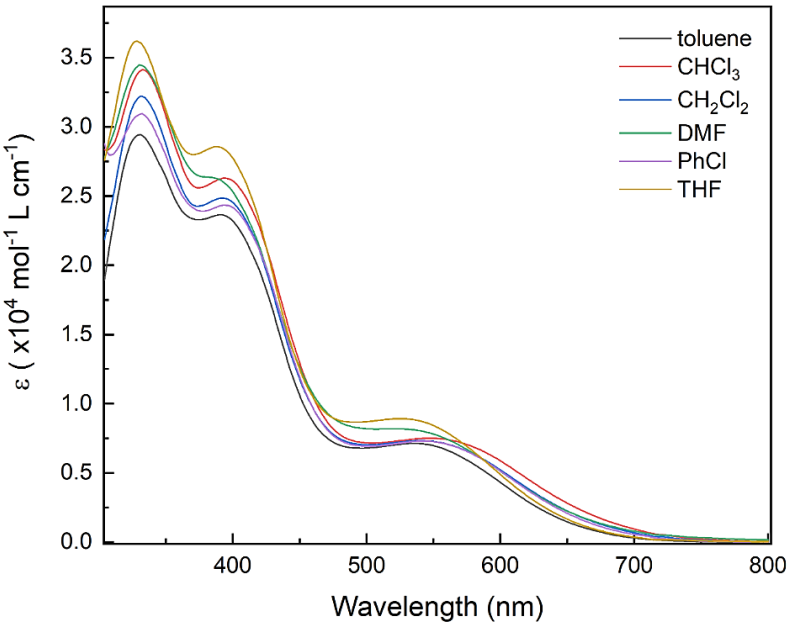

Fig. S-28 UV-Vis absorption spectra of **4a** measured in various organic solvents at room temperature.

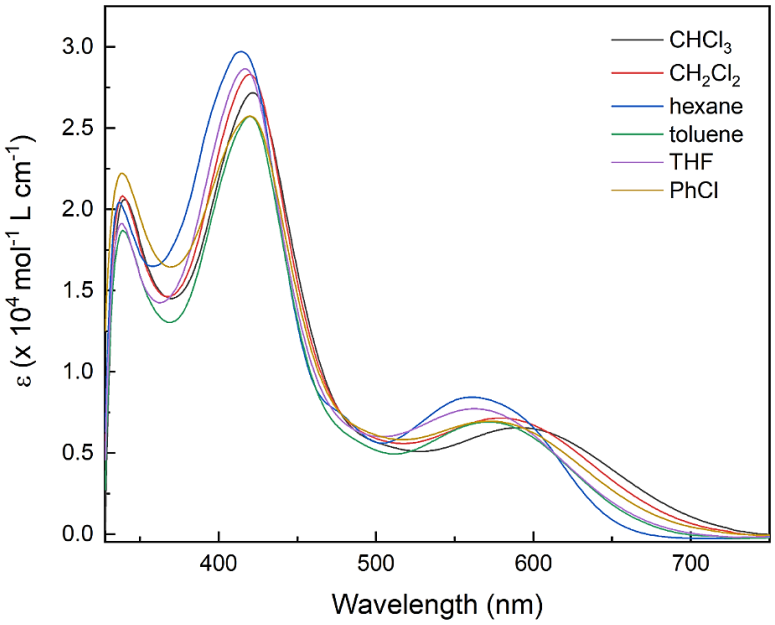

Fig. S-29 UV-Vis absorption spectra of **4b** measured in various organic solvents at room temperature.

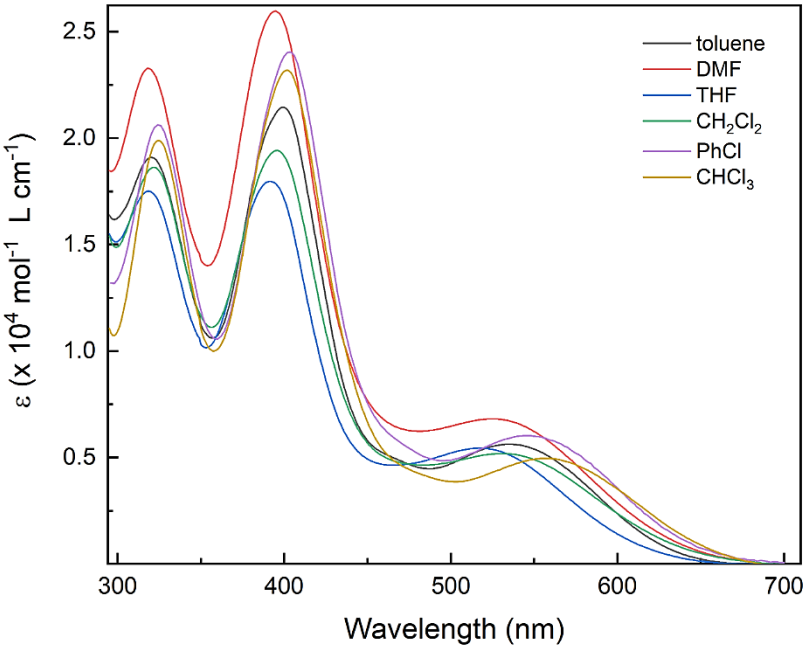

Fig. S-30 UV-Vis absorption spectra of **6** measured in various organic solvents at room temperature.

Table S-1 Summary of UV-Vis absorption data of compound **4a**.

Solvent	**UV-Vis absorption λ_{max}/nm (ε/mol^{-1} L cm^{-1})**
toluene	542 (7.06 × 10^3), 392 (2.36 × 10^4), 330 (2.94 × 10^4)
$CHCl_3$	560 (7.50 × 10^3), 395 (2.64 × 10^4), 333 (3.42 × 10^4)
CH_2Cl_2	551 (7.30 ×10^3), 393 (2.48 × 10^4), 332 (3.22 × 10^4)
DMF	545 (7.94 × 10^3), 389 (2.62 × 10^4), 331 (3.45 × 10^4)
PhCl	551 (7.30 ×10^3), 396 (2.44 × 10^4), 331 (3.08 × 10^4)
THF	532 (8.89 × 10^3), 389 (2.85 × 10^4), 328 (3.62 × 10^4)

Table S-2 Summary of UV-Vis absorption data of compound **4b**.

Solvent	**UV-Vis absorption λ_{max}/nm (ε/mol^{-1} L cm^{-1})**
toluene	571 (7.04×10^3), 419 (2.58×10^4), 339 (1.87×10^4)
$CHCl_3$	596 (6.66×10^3), 421 (2.71×10^4), 340 (2.06×10^4)
CH_2Cl_2	584 (7.18×10^3), 418 (2.82×10^4), 339 (2.08×10^4)
hexane	561 (8.42×10^3), 414 (2.97×10^4), 336 (2.04×10^4)
PhCl	575 (6.96×10^3), 420 (2.57×10^4), 338 (2.22×10^4)
THF	564 (7.74×10^3), 417 (2.86×10^4), 338 (1.91×10^4)

Table S-3 Summary of UV-Vis absorption data of compound **6**.

Solvent	**UV-Vis absorption λ_{max}/nm (ε/mol^{-1} L cm^{-1})**
toluene	537 (5.68×10^3), 399 (2.15×10^4), 320 (1.91×10^4)
$CHCl_3$	564 (4.94×10^3), 401 (2.31×10^4), 324 (1.98×10^4)
CH_2Cl_2	538 (5.17×10^3), 396 (1.94×10^4), 322 (1.86×10^4)
DMF	529 (6.83×10^3), 394 (2.59×10^4), 318 (2.33×10^4)
PhCl	550 (6.06×10^3), 403 (2.40×10^4), 324 (2.06×10^4)
THF	516 (5.47×10^3), 391 (1.79×10^4), 319 (1.75×10^4)

5. X-ray Single Crystallographic Data

Table S-4 Crystallographic data and structure refinement of compound **2**

formula	$C_{24}H_{10}Br_4O_2$
formula weight	649.96
crystal dimensions (mm)	0.28 × 0.14 × 0.11
crystal system	monoclinic
space group	$P2_1/c$ (No. 14)
unit cell parameters[a]	
a (Å)	17.6409(6)
b (Å)	7.1377(3)
c (Å)	16.5136(6)
β (deg)	98.2956(11)
V (Å^3)	2057.56(13)
Z	4
ρ_{calcd} (g cm^{-3})	2.098
μ (mm^{-1})	9.715
diffractometer	Bruker D8/APEX II CCD[b]
radiation (λ [Å])	Cu $K\alpha$ (1.54178) (microfocus source)
temperature (°C)	–100
scan type	ω and ϕ scans (1.0°) (5 s exposures)
data collection 2θ limit (deg)	145.29
total data collected	13722 ($-21 \le h \le 21$, $-8 \le k \le 8$, $-20 \le l \le 20$)
independent reflections	4080 (R_{int} = 0.0193)
number of observed reflections (*NO*)	4071 [$F_o^2 \ge 2\sigma(F_o^2)$]
structure solution method	intrinsic phasing (*SHELXT-2014*)
refinement method	full-matrix least-squares on F^2 (*SHELXL–2017*)
absorption correction method	Gaussian integration (face-indexed)
range of transmission factors	0.1756–0.0369
data/restraints/parameters	4080 / 0 / 272
extinction coefficient (x)[c]	0.00464(9)
goodness-of-fit (S)[d] [all data]	1.130
final R indices[e]	
R_1 [$F_o^2 \ge 2\sigma(F_o^2)$]	0.0217
wR_2 [all data]	0.0572
largest difference peak and hole	0.461 and –0.550 e Å^{-3}

[a] Obtained from least-squares refinement of 9562 reflections with $5.06° < 2\theta < 145.12°$.

[b] Programs for diffractometer operation, data collection, data reduction and absorption correction were those supplied by Bruker.

[c] $F_c^* = kF_c[1 + x\{0.001F_c^2\lambda^3/\sin(2\theta)\}]^{-1/4}$ where k is the overall scale factor.

[d] $S = [\Sigma w(F_o^2 - F_c^2)^2/(n - p)]^{1/2}$ (n = number of data; p = number of parameters varied; w =

$[\sigma^2(F_o^2) + (0.0280P)^2 + 1.8203P]^{-1}$ where $P = [\mathrm{Max}(F_o^2, 0) + 2F_c^2]/3)$.

[e] $R_1 = \Sigma||F_o| - |F_c||/\Sigma|F_o|$; $wR_2 = [\Sigma w(F_o^2 - F_c^2)^2/\Sigma w(F_o^4)]^{1/2}$.

Table S-5 Crystallographic data and structure refinement of compound **6**.

formula	$C_{37}H_{20}Cl_2O_2S_4$
formula weight	695.67
temperature/K	100(2)
crystal system	monoclinic
space group	$P2_1/c$
a/Å	17.0760(2)
b/Å	12.61038(12)
c/Å	14.39284(18)
β/°	103.7162(12)
volume/Å^3	3010.90(6)
Z	4
ρ_{calc}g/cm^3	1.535
μ/mm^{-1}	4.823
F(000)	1424.0
crystal size/mm^3	0.18 × 0.13 × 0.1
radiation	Cu $K\alpha$ (λ = 1.54184)
2θ range for data collection/°	5.328 to 154.494
index ranges	$-21 \le h \le 21$, $-13 \le k \le 15$, $-17 \le l \le 18$
reflections collected	38574
independent reflections	6317 [R_{int} = 0.0561, R_{sigma} = 0.0359]
data/restraints/parameters	6317/0/406
goodness-of-fit on F^2	1.067
final R indexes [I>=2σ (I)]	R_1 = 0.0498, wR_2 = 0.1391
final R indexes [all data]	R_1 = 0.0535, wR_2 = 0.1426
largest diff. peak/hole / e Å^{-3}	0.70/-0.94

Table S-6 Crystallographic data and structure refinement of co-crystal **6** and C_{70} fullerene

formula	$C_{118}H_{32.5}Cl_{1.5}O_2S_4$
formula weight	1663.35
temperature/K	100(2)
crystal system	monoclinic
space group	*I*2
a/Å	15.42301(8)
b/Å	21.19184(11)
c/Å	23.06291(13)
β/°	105.9958(6)
volume/Å^3	7246.07(7)
Z	4
ρ_{calc}mg/mm^3	1.525
μ/mm^{-1}	2.234
F(000)	3384.0
crystal size/mm^3	0.137 × 0.068 × 0.046
2*θ* range for data collection	5.77 to 154.622°
index ranges	$-19 \le h \le 18$, $-26 \le k \le 26$, $-28 \le l \le 29$
reflections collected	90447
independent reflections	15178[*R*(int) = 0.0385]
data/restraints/parameters	15178/2025/1160
goodness-of-fit on F^2	1.647
final *R* indexes [$I>=2\sigma$ (I)]	R_1 = 0.1126, wR_2 = 0.3316
final *R* indexes [all data]	R_1 = 0.1172, wR_2 = 0.3416
largest diff. peak/hole / e Å^{-3}	1.05/-1.07
flack parameter	0.09(4)

Table S-7 Crystallographic data and structure refinement of compound **4a**.

Formula	$C_{35}H_{29}O_2S_8$
Formula weight	738.06
Temperature/K	100(2)
Crystal system	monoclinic
Space group	$P2_1/n$
a/Å	8.70740(10)
b/Å	19.8437(4)
c/Å	20.9601(4)
β/°	91.536(2)
Volume/Å^3	3620.33(11)
Z	4
ρ_{calc}g/cm^3	1.354
μ/mm^{-1}	4.810
F(000)	1532.0
Crystal size/mm^3	0.343 × 0.07 × 0.038
Radiation	Cu $K\alpha$ (λ = 1.54184)
2θ range for data collection/°	6.134 to 159.444
Index ranges	$-10 \leq h \leq 7$, $-23 \leq k \leq 25$, $-26 \leq l \leq 26$
Reflections collected	45547
Independent reflections	7742 [R_{int} = 0.0482, R_{sigma} = 0.0370]
Data/restraints/parameters	7742/0/432
Goodness-of-fit on F^2	1.044
Final R indexes [I>=2σ (I)]	R_1 = 0.1000, wR_2 = 0.2809
Final R indexes [all data]	R_1 = 0.1113, wR_2 = 0.2939
Largest diff. peak/hole / e Å^{-3}	1.18/-0.88

6. DFT Computational Results

6.1 TD-DFT Results for Compounds 4a, 4b, and 6.

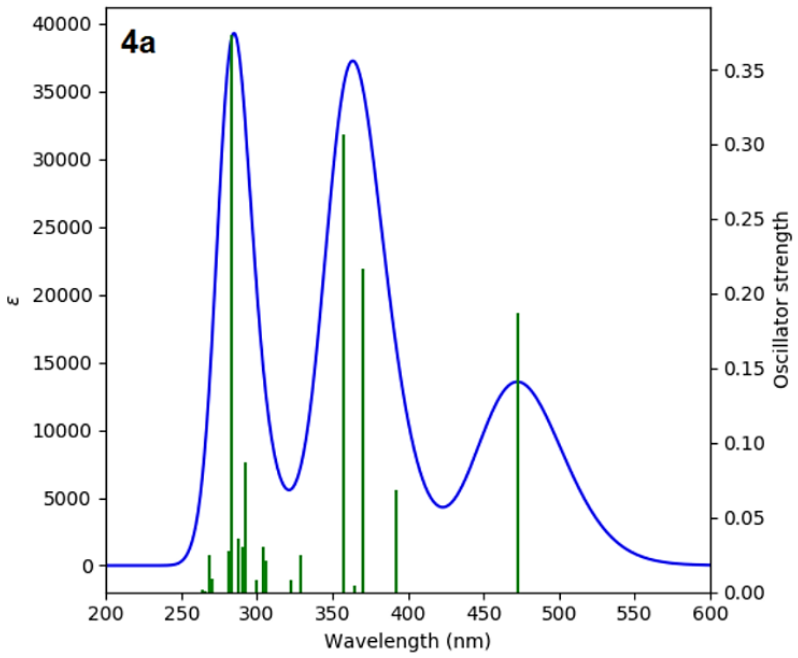

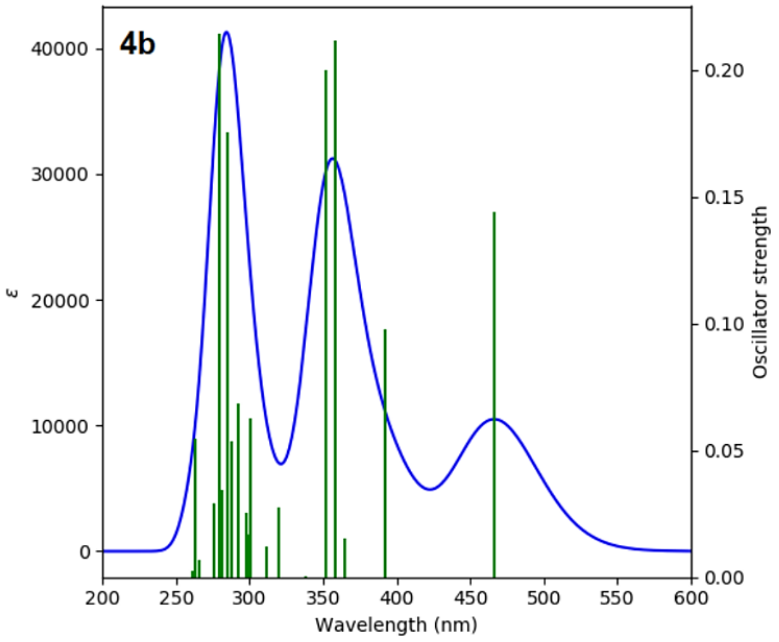

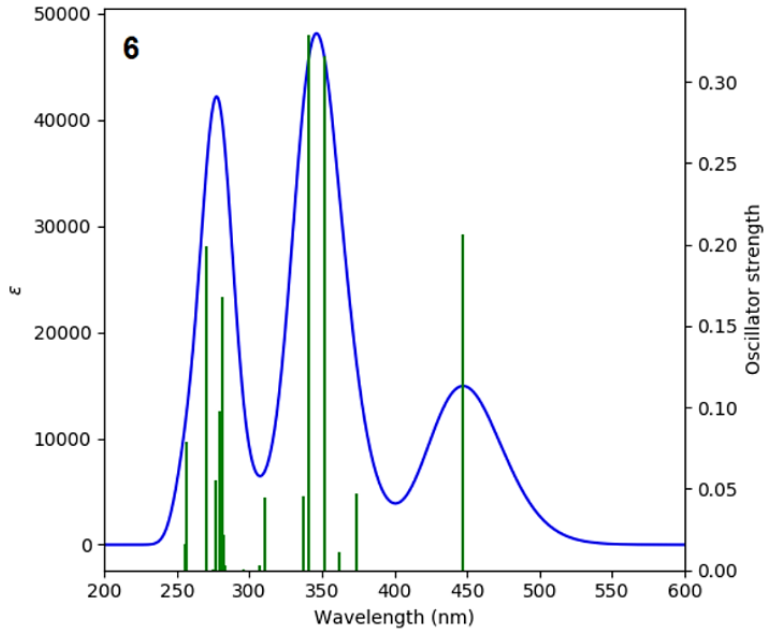

Fig. S-31 Simulated UV-Vis spectrum of compounds **4a**, **4b**, and **6** calculated at the CAM-B3LYP/6-311+G(2d,p) level of theory.

Table S-8 Summary of TD-DFT calculated electronic transitions of **4a** at the CAM-B3LYP/6-311+G(2d,p) level of theory.

λ (nm)	***f***	**Major MO Contributions**
472.5	0.187	H→L (91%)
392.2	0.068	H-1→L (77%)
370.1	0.216	H→L+1 (73%)
364.6	0.004	H-9→L (77%)
357.4	0.306	H→L+2 (79%)
357.4	0.306	H→L+2 (79%)
337.8	0.000	H-13→L (72%), H-9→L+1 (13%)
329.3	0.025	H-1→L+1 (27%), H-1→L+3 (12%), H→L+9 (17%)
322.3	0.008	H-1→L+2 (12%), H→L+3 (15%), H→L+10
306.2	0.021	H-1→L+5 (14%), H→L+5 (34%)
304.5	0.029	H-1→L+4 (17%), H→L+4 (55%)
299.9	0.007	H-6→L (31%), H-1→L+1 (14%)

292.3	0.086	H-1→L+2 (43%)
290.8	0.030	H-6→L (10%), H-1→L+1 (23%), H-1→L+2 (11%)
287.2	0.035	H-7→L (18%), H→L+3 (13%), H→L+11 (11%)
282.9	0.373	H-11→L (11%), H-7→L (13%), H-3→L (15%), H→L+3 (17%), H→L+11 (12%)
281.3	0.028	H-8→L (72%)
270.0	0.008	H-2→L (12%), H→L+6 (32%), H→L+7 (16%)
268.1	0.025	H-2→L (40%), H→L+6 (17%)
265.6	0.000	H-1→L+6 (12%), H→L+7 (21%), H→L+8 (18%)

Table S-9 Summary of TD-DFT calculated electronic transitions of **4b** at the CAM-B3LYP/6-311+G(2d,p) level of theory.

λ (nm)	***f***	**Major MO Contributions**
466.7	0.144	H→L (90%)
392.5	0.097	H-1→L (81%)
364.6	0.015	H-10→L (77%)
358.2	0.211	H→L+1 (70%)
352.2	0.199	H→L+2 (69%)
337.8	0.000	H-14→L (74%), H-10→L+1 (13%)
319.9	0.027	H-1→L+1 (21%)
312.0	0.012	H-1→L+1 (20%), H-1→L+2 (17%)
300.8	0.062	H→L+4 (15%), H→L+6 (29%)
299.7	0.016	H-6→L (17%), H-1→L+4 (11%), H→L+4 (21%)
298.0	0.025	H-6→L (26%)
291.9	0.068	H-1→L+1 (12%), H-1→L+2 (23%)
287.7	0.053	H-7→L (20%), H-1→L+1 (12%)
285.3	0.175	H-7→L (17%), H-1→L+2 (15%)
281.2	0.034	H-9→L (70%)
279.8	0.214	H→L+3 (28%), H→L+11 (16%)
275.8	0.029	H-2→L (68%)
265.5	0.006	H-3→L (11%), H→L+5 (28%)

263.3	0.054	H-5→L (12%), H-3→L (40%)
261.3	0.002	H→L+7 (26%), H→L+8 (12%)

Table S-10 Summary of TD-DFT calculated electronic transitions of **6** at the CAM-B3LYP/6-311+G(2d,p) level of theory.

λ (nm)	***f***	**Major MO Contributions**
447.4	0.206	H→L (92%)
374.3	0.047	H-9→L (24%), H-1→L (56%)
362.0	0.011	H-9→L (56%), H-1→L (16%)
351.9	0.316	H-1→L (14%), H→L+1 (68%)
341.2	0.329	H-11→L (12%), H→L+2 (69%)
337.3	0.046	H-11→L (62%), H-9→L+1 (11%), H→L+2 (12%)
310.3	0.045	H-1→L+1 (34%), H-1→L+3 (13%), H→L+9 (22%)
306.7	0.003	H-1→L+2 (14%), H-1→L+9 (11%), H→L+3 (22%), H→L+8 (15%)
295.8	0.001	H-6→L (20%), H-4→L (26%), H-2→L (14%)
283.1	0.003	H-1→L+1 (38%), H→L+6 (10%), H→L+9 (11%)
282.5	0.022	H-8→L (13%), H-1→L+2 (10%), H→L+3 (13%), H→L+4 (12%), H→L+7 (13%)
281.7	0.168	H-8→L (30%), H-1→L+2 (19%)
280.9	0.027	H-8→L (27%), H-7→L (22%), H-1→L+2 (13%)
280.3	0.072	H-1→L+4 (27%), H→L+5 (53%)
279.6	0.098	H-1→L+5 (16%), H→L+4 (32%)
277.1	0.055	H-7→L (25%), H-3→L (10%), H-1→L+2 (15%), H→L+7 (11%)
274.9	0.000	H-1→L+7 (21%), H→L+6 (50%)
270.5	0.199	H-1→L+6 (13%), H→L+3 (10%), H→L+7 (28%), H→L+8 (13%)
257.1	0.079	H-10→L (34%), H-2→L (19%), H→L+10 (12%)
255.7	0.016	H-2→L (14%), H→L+10 (41%)

6.2 Binding Energies, Noncovalent Interactions, and AIM Molecular Graphs of π-Dimers of 4a and 6

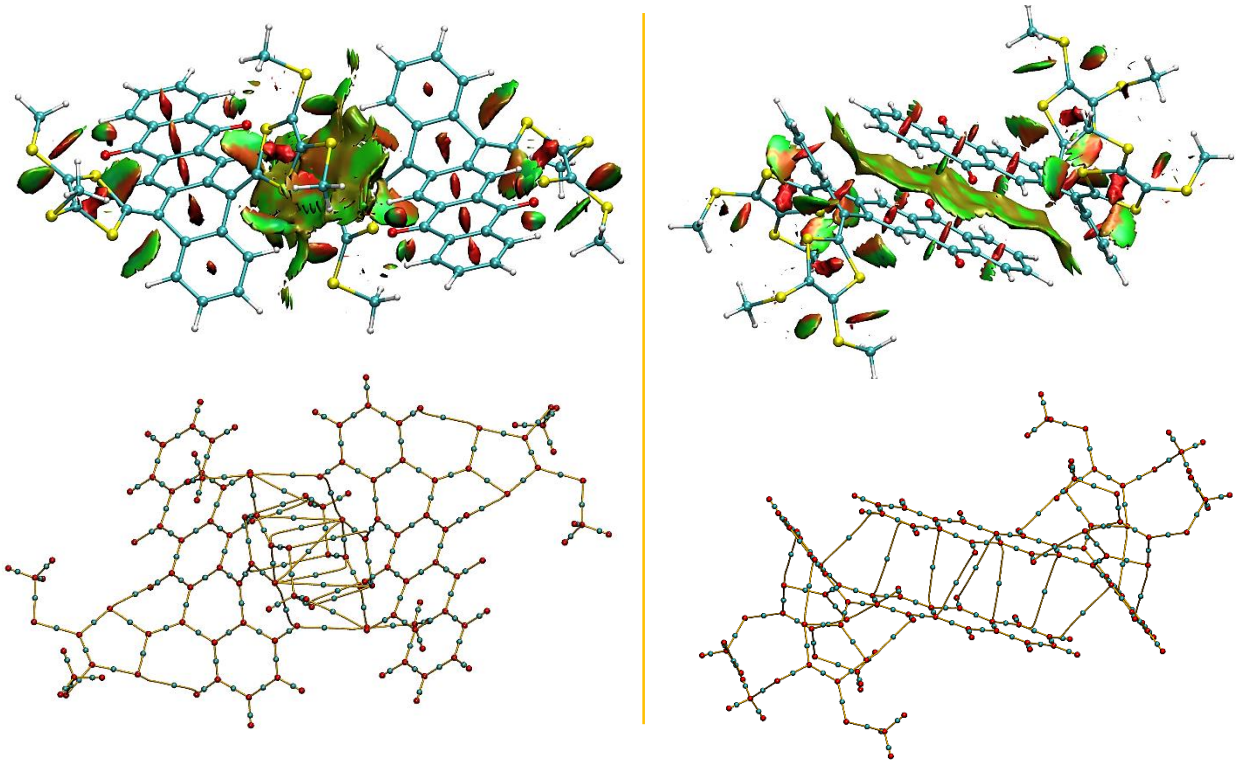

Fig. S-32 Top row: Optimized geometries and RDG isosurfaces (0.7 a.u) of dimers of **4a**. Left: dimer of **4a** interacting via dithiole···dithiole face-to-face stacking (ΔE_{int} = -20.8 kcal/mol, ΔH_{int} = -20.5 kcal/mol, ΔG_{int} = -5.18 kcal/mol). Right: dimer of **4a** interacting via anthraquinone···anthraquinone face-to-face stacking (ΔE_{int} = -21.5 kcal/mol, ΔH_{int} = -21.1 kcal/mol, ΔG_{int} = -5.79 kcal/mol). Bottom row: molecular graphs with bond paths (orange-color lines) and (3, -1) bond critical points (cyan-color dots). Calculations were performed at the M06-2X/Def2SVP level of theory.

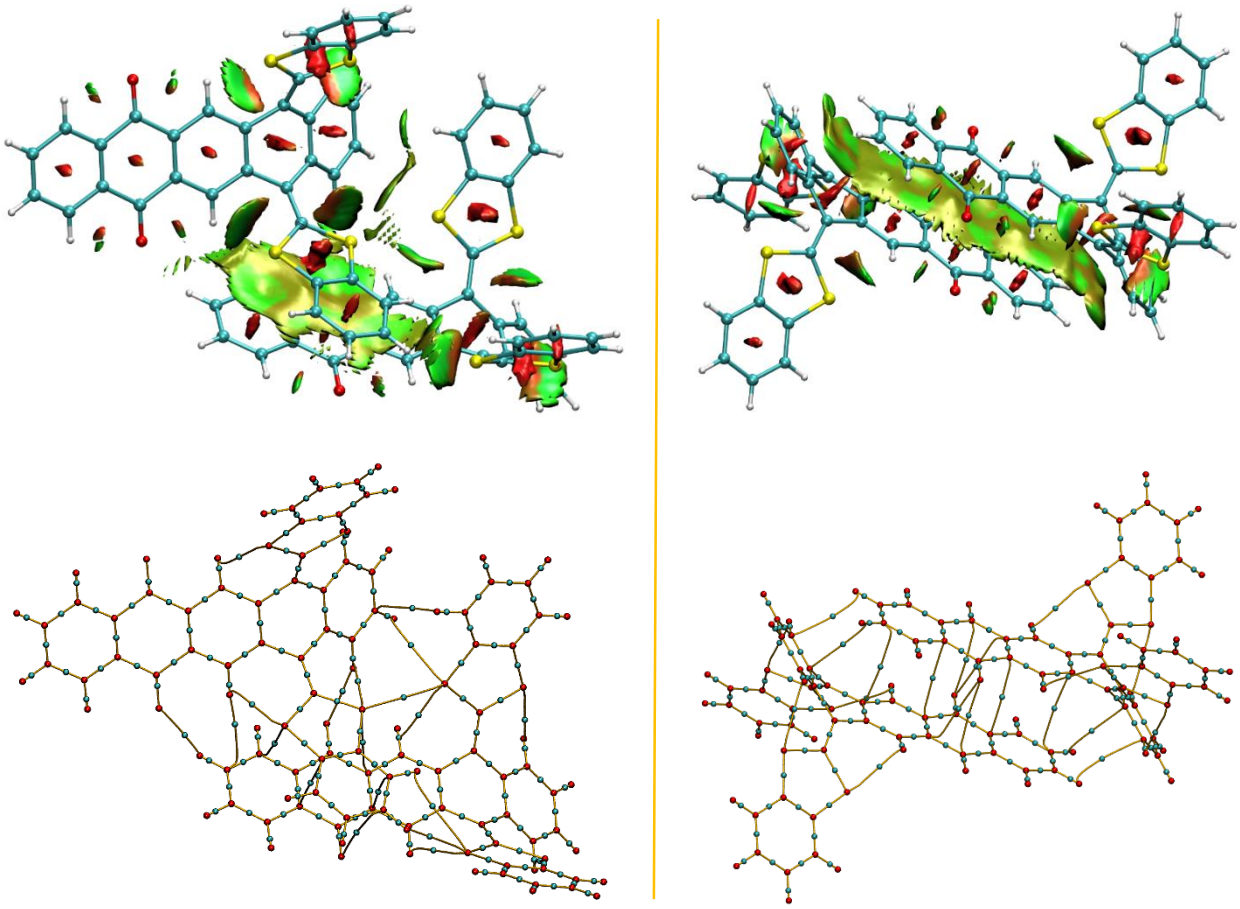

Fig. S-33 Top row: Optimized geometries and RDG isosurfaces (0.7 a.u) of dimers of **6**. Left: dimer of **6** interacting via dithiole···anthraquinone face-to-face stacking (ΔE_{int} = -22.3 kcal/mol, ΔH_{int} = -21.9 kcal/mol, ΔG_{int} = -6.78 kcal/mol). Right: dimer of **6** interacting via anthraquinone···anthraquinone face-to-face stacking (ΔE_{int} = -20.5 kcal/mol, ΔH_{int} = -19.9 kcal/mol, ΔG_{int} = -5.92 kcal/mol). Bottom row: molecular graphs with bond paths (orange-color lines) and (3, -1) bond critical points (cyan-color dots). Calculations were performed at the M06-2X/Def2SVP level of theory.

Appendix III

Supplementary Information for Chapter 4

Donor–Acceptor Fluorophores and Macrocycles Built Upon Wedge-Shaped π−Extended Phenanthroimidazoles

https://doi.org/10.1021/acs.joc.2c02511

Table of Contents

1. NMR Spectra of New Compounds

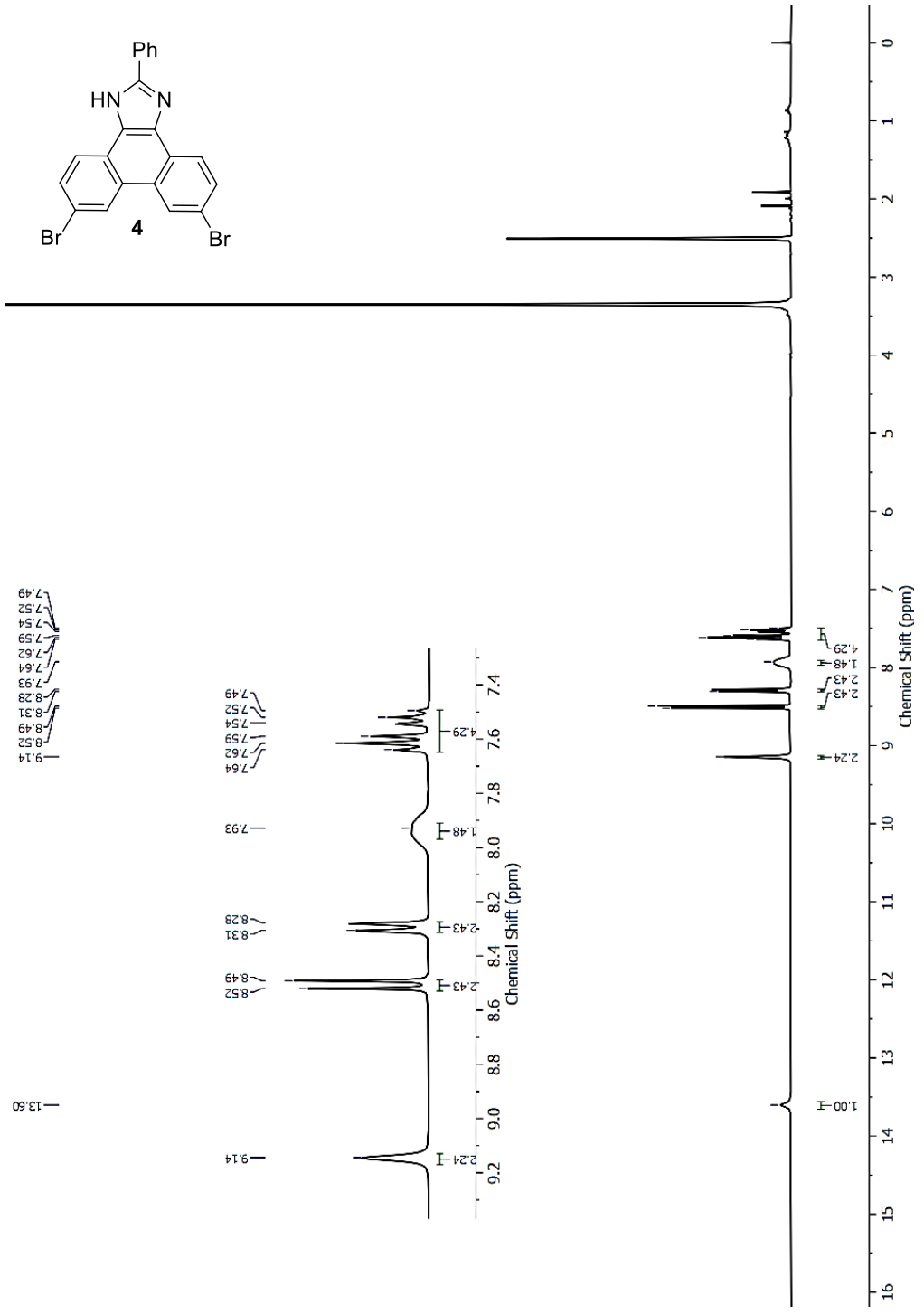

Fig. S-1 ^{1}H NMR (300 MHz, DMSO-*d6*) of compound **4**.

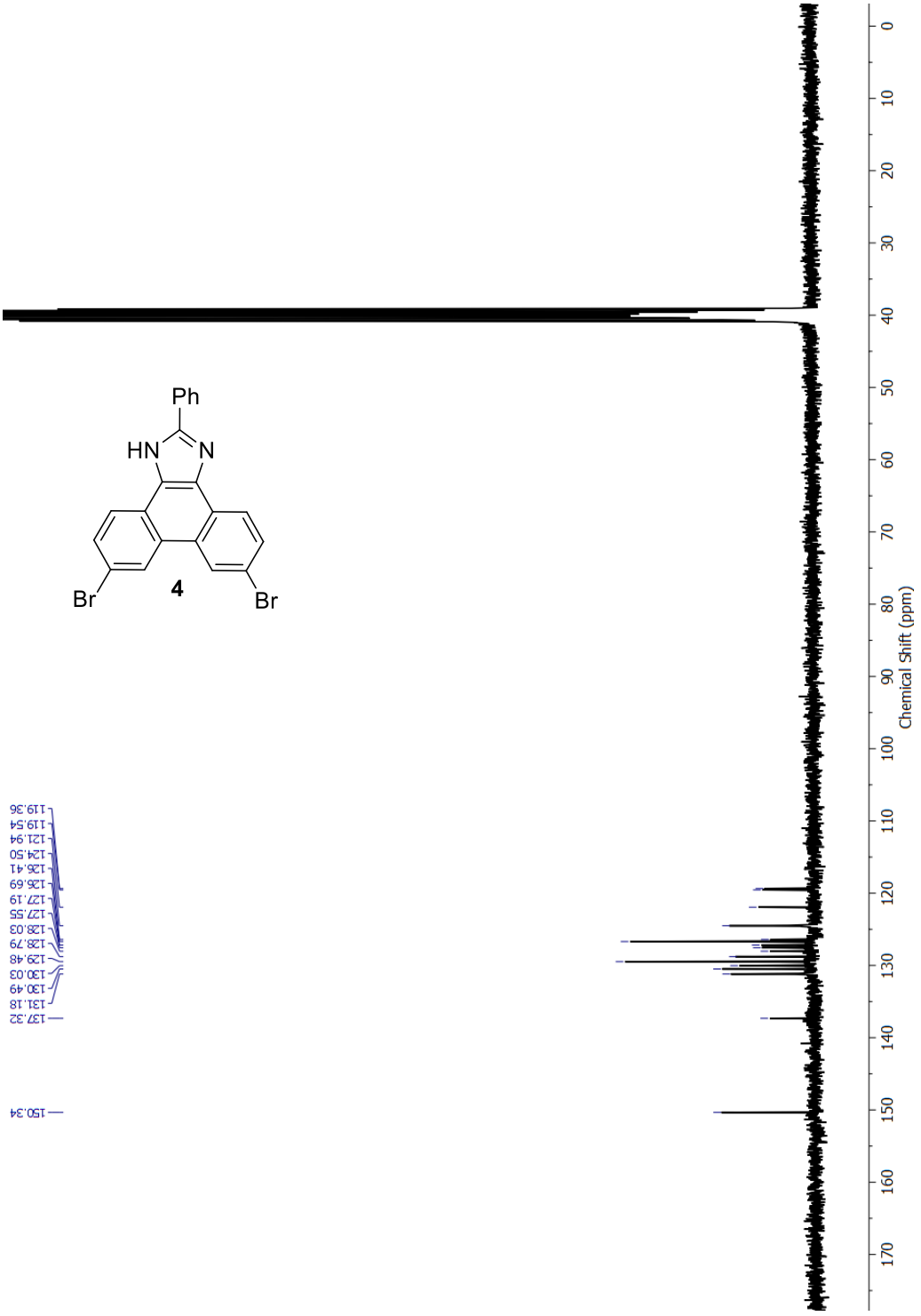

Fig. S-2 $^{13}C\{^{1}H\}$ NMR (75 MHz, DMSO-*d6*) of compound **4.**

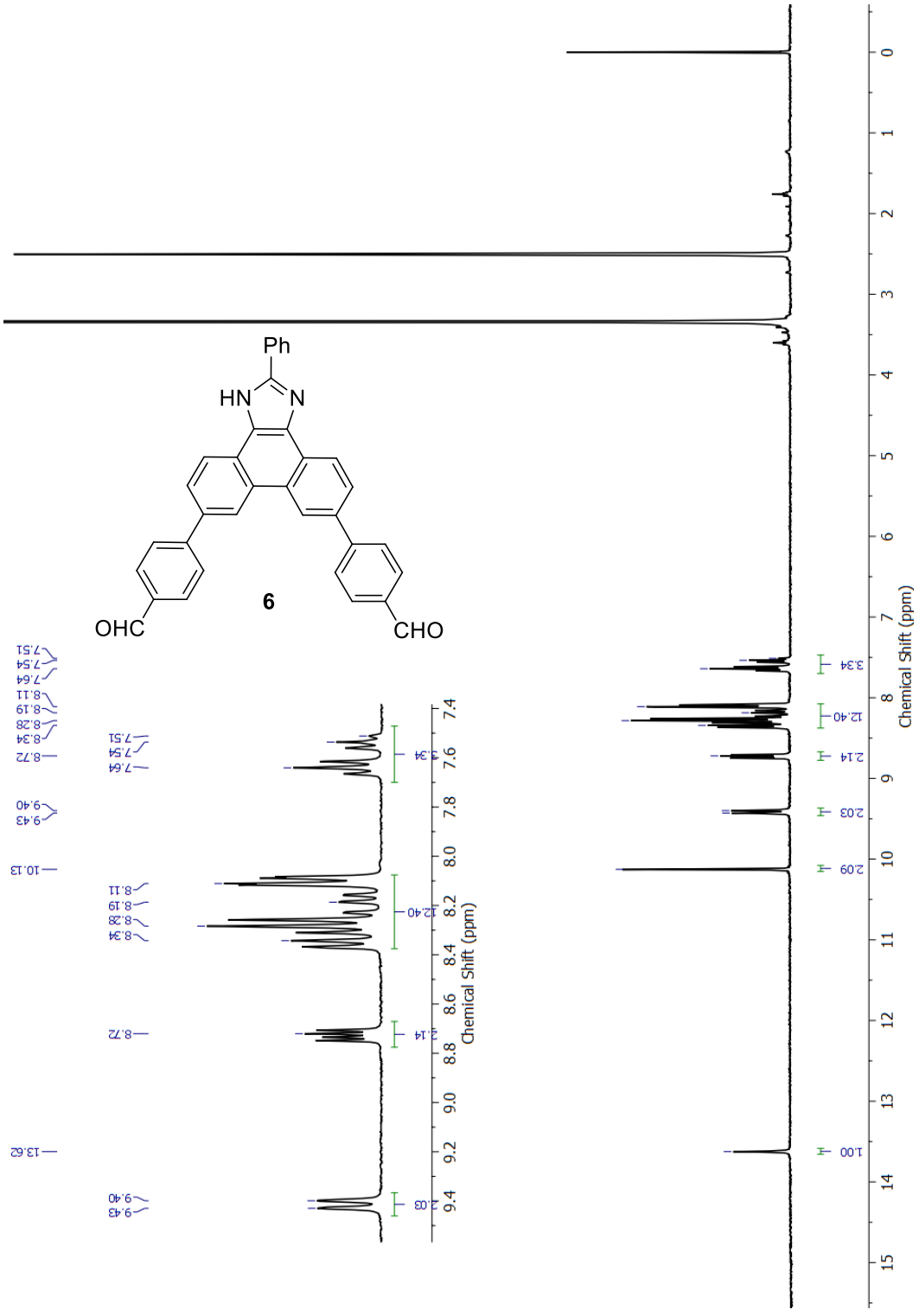

Fig. S-3 ^{1}H NMR (300 MHz, DMSO-*d6*) of compound **6**.

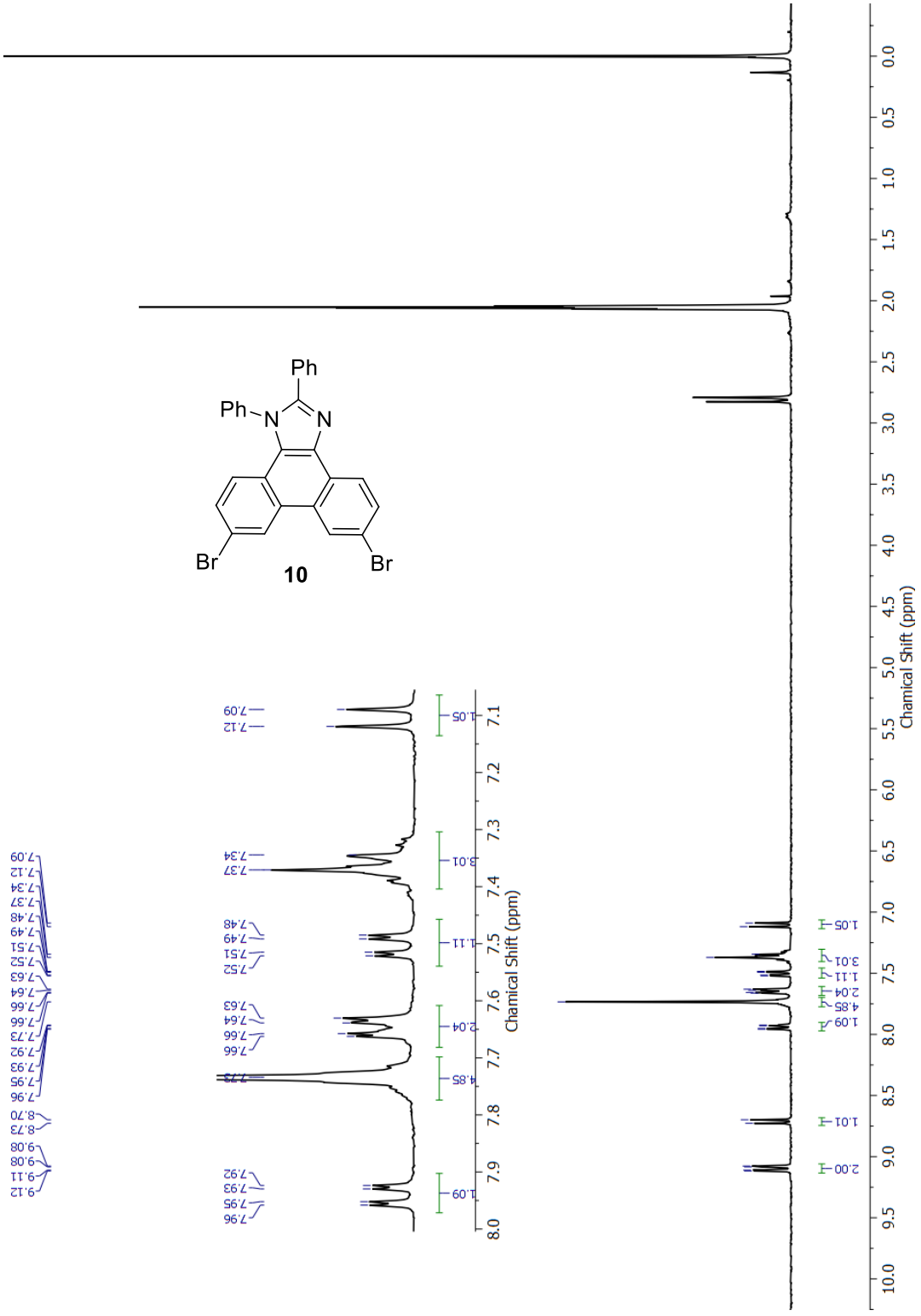

Fig. S-4 ^{1}H NMR (300 MHz, acetone-*d6*) of compound **10**.

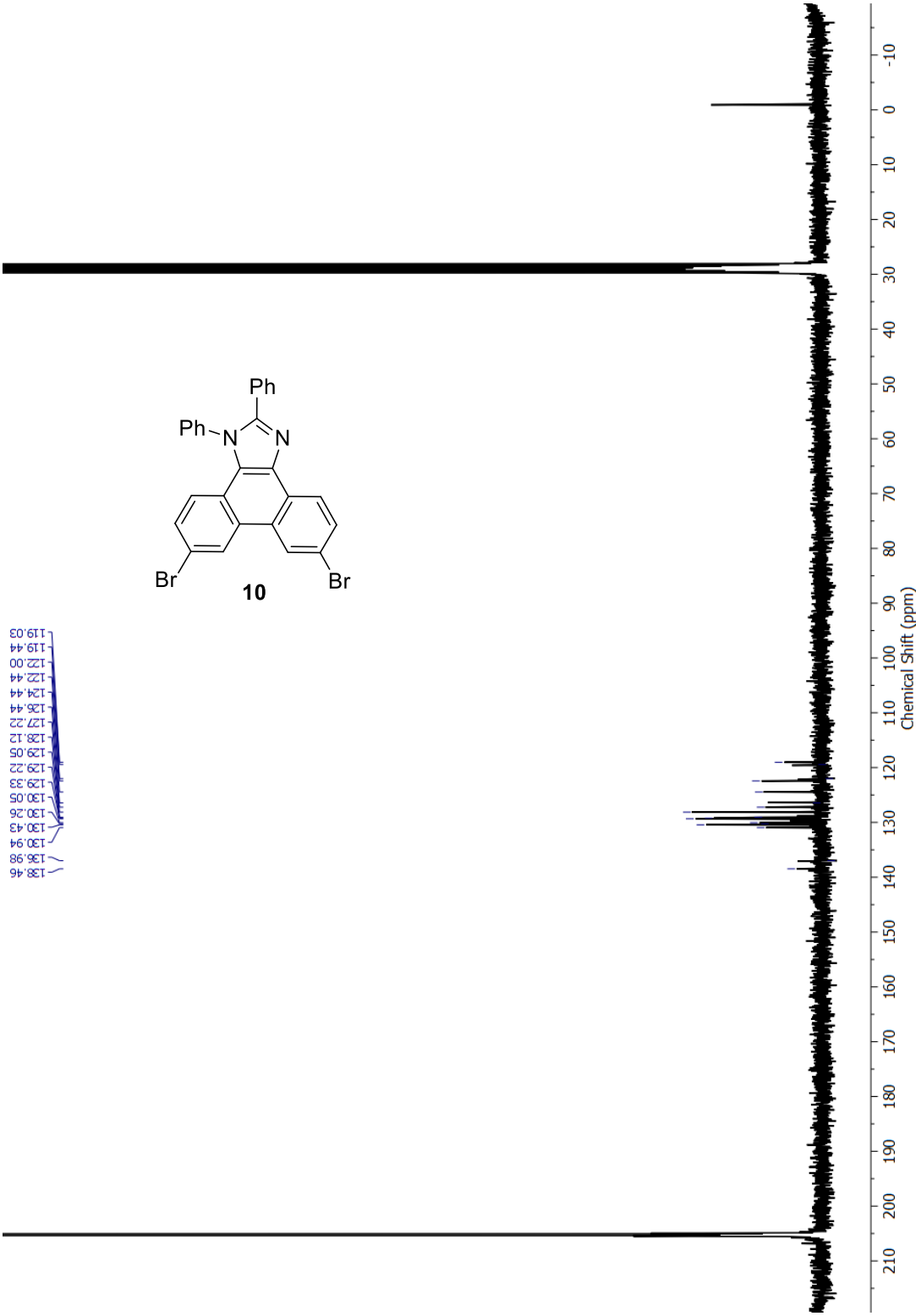

Fig. S-5 $^{13}C\{^{1}H\}$ NMR (75 MHz, acetone-*d6*) of compound **10.**

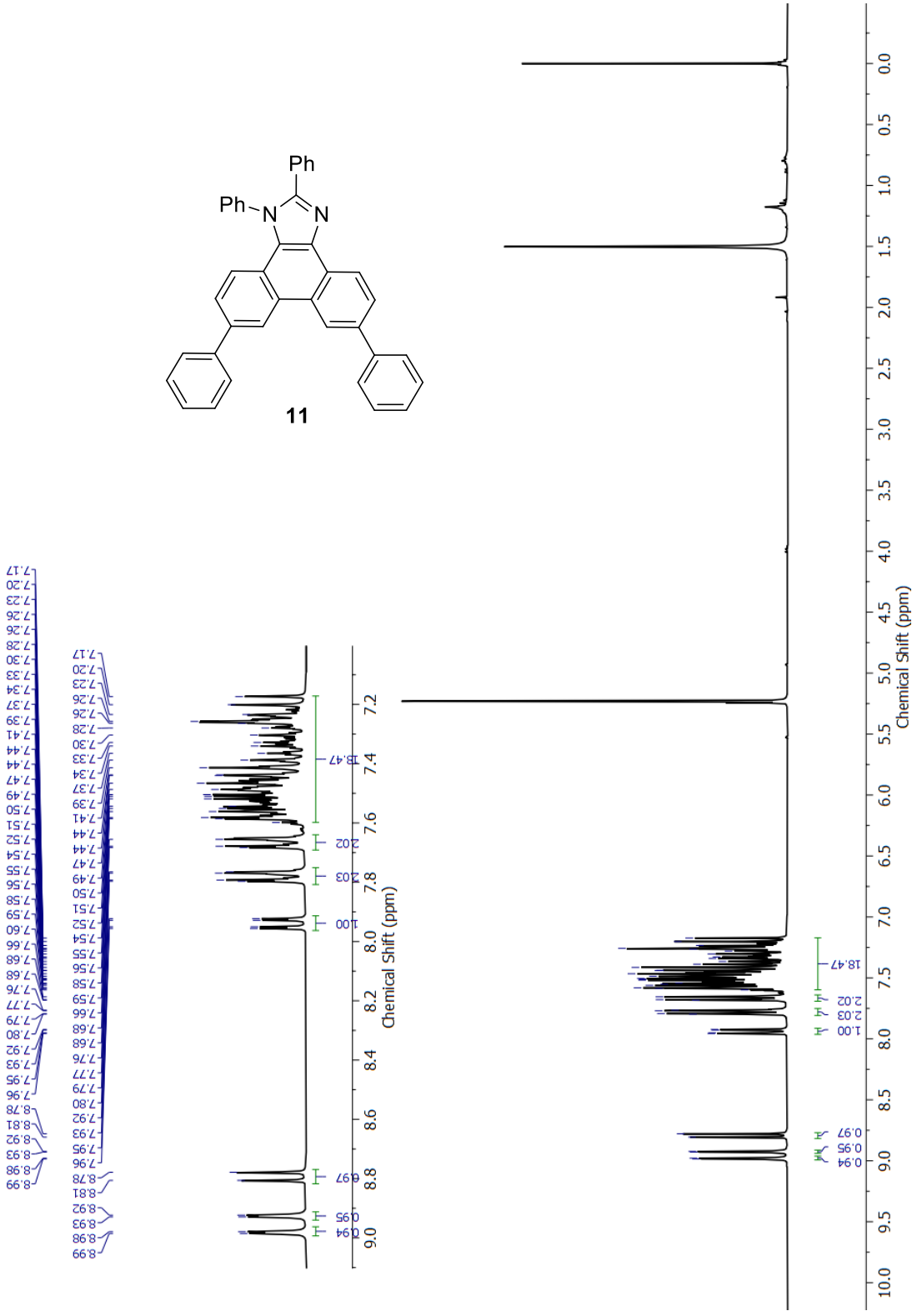

Fig. S-6 ^{1}H NMR (300 MHz, CD_2Cl_2) of compound **11**.

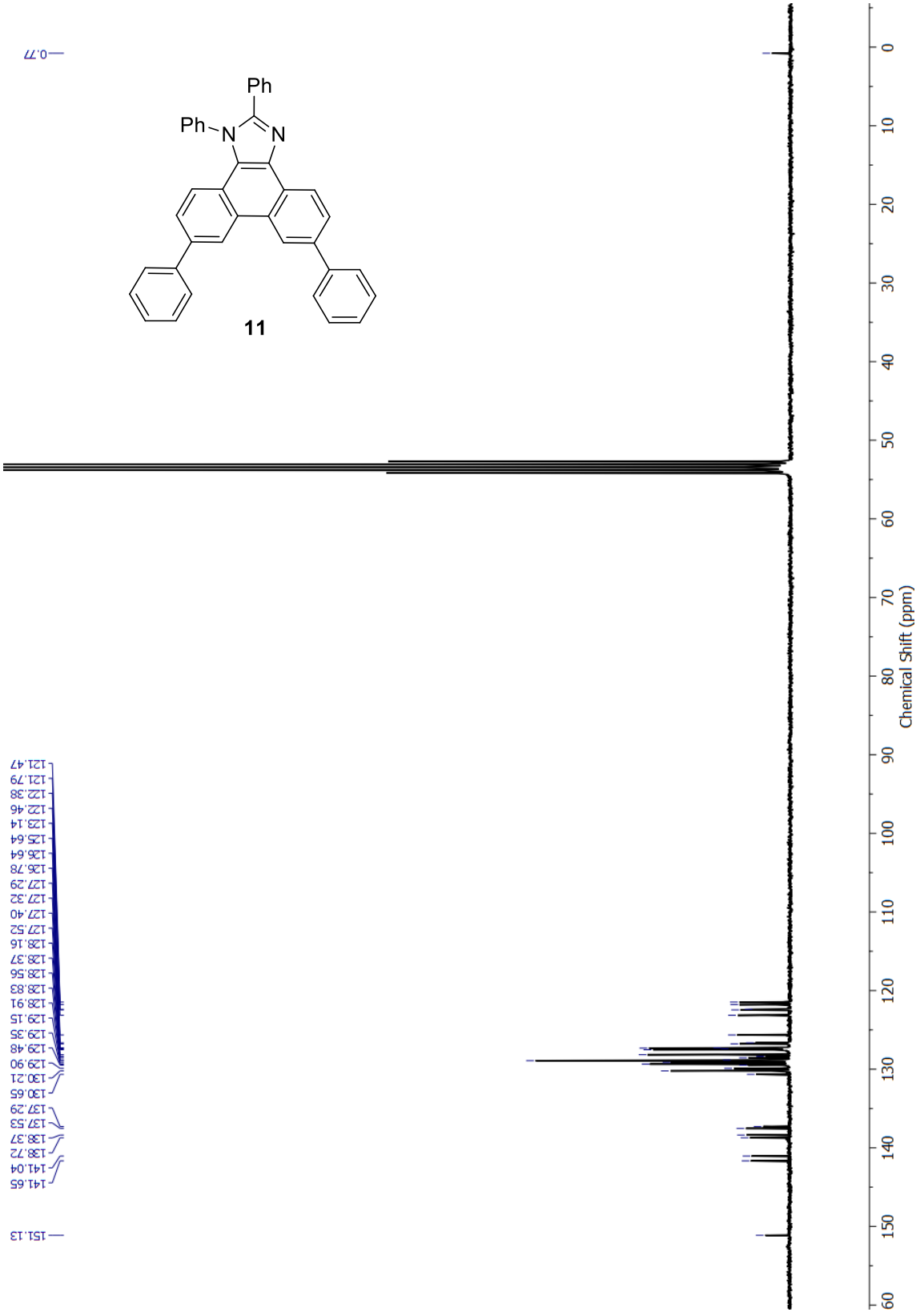

Fig. S-7 $^{13}C\{^{1}H\}$ NMR (75 MHz, CD_2Cl_2) of compound **11.**

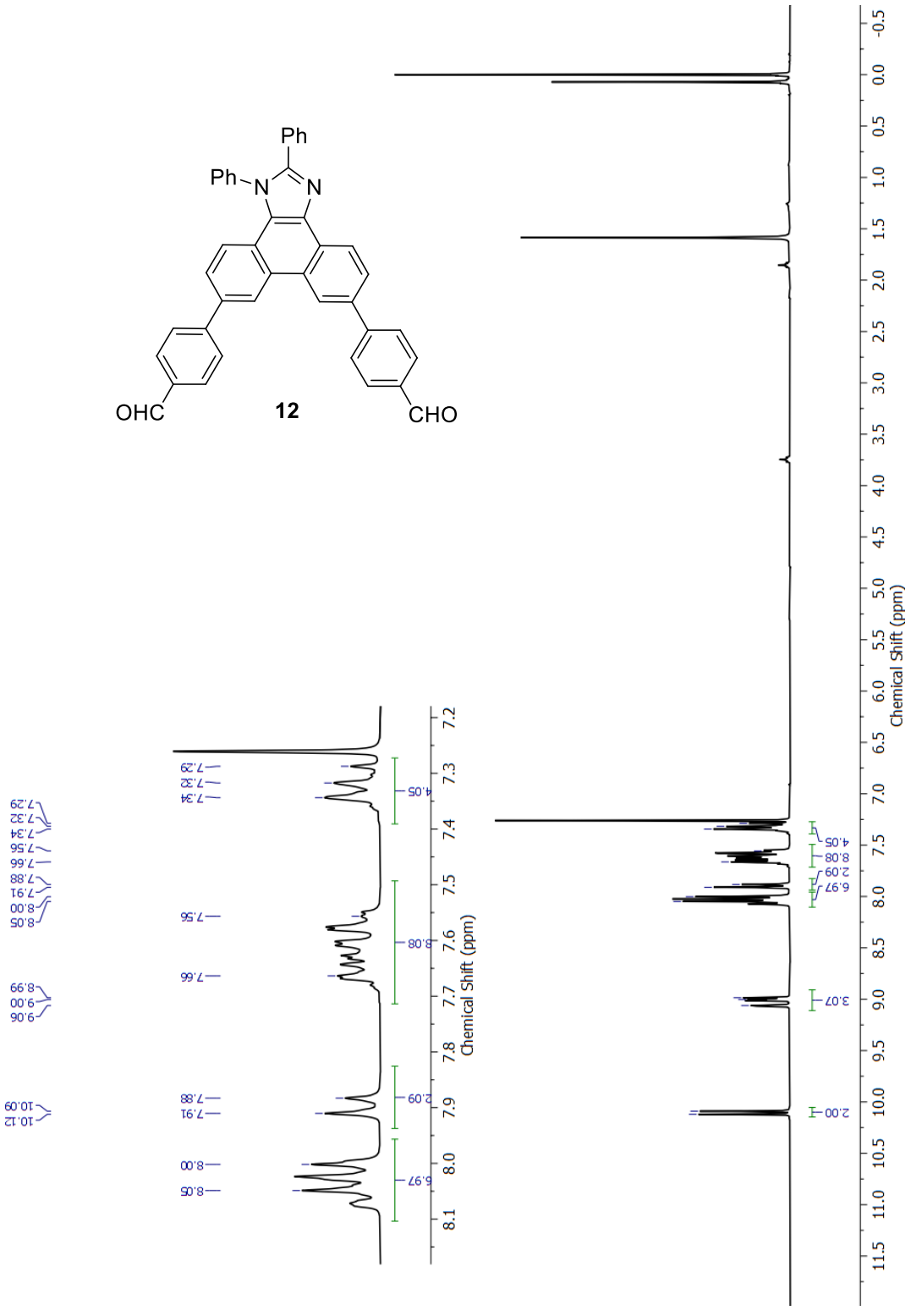

Fig. S-8 ^{1}H NMR (300 MHz, $CDCl_3$) of compound **12**.

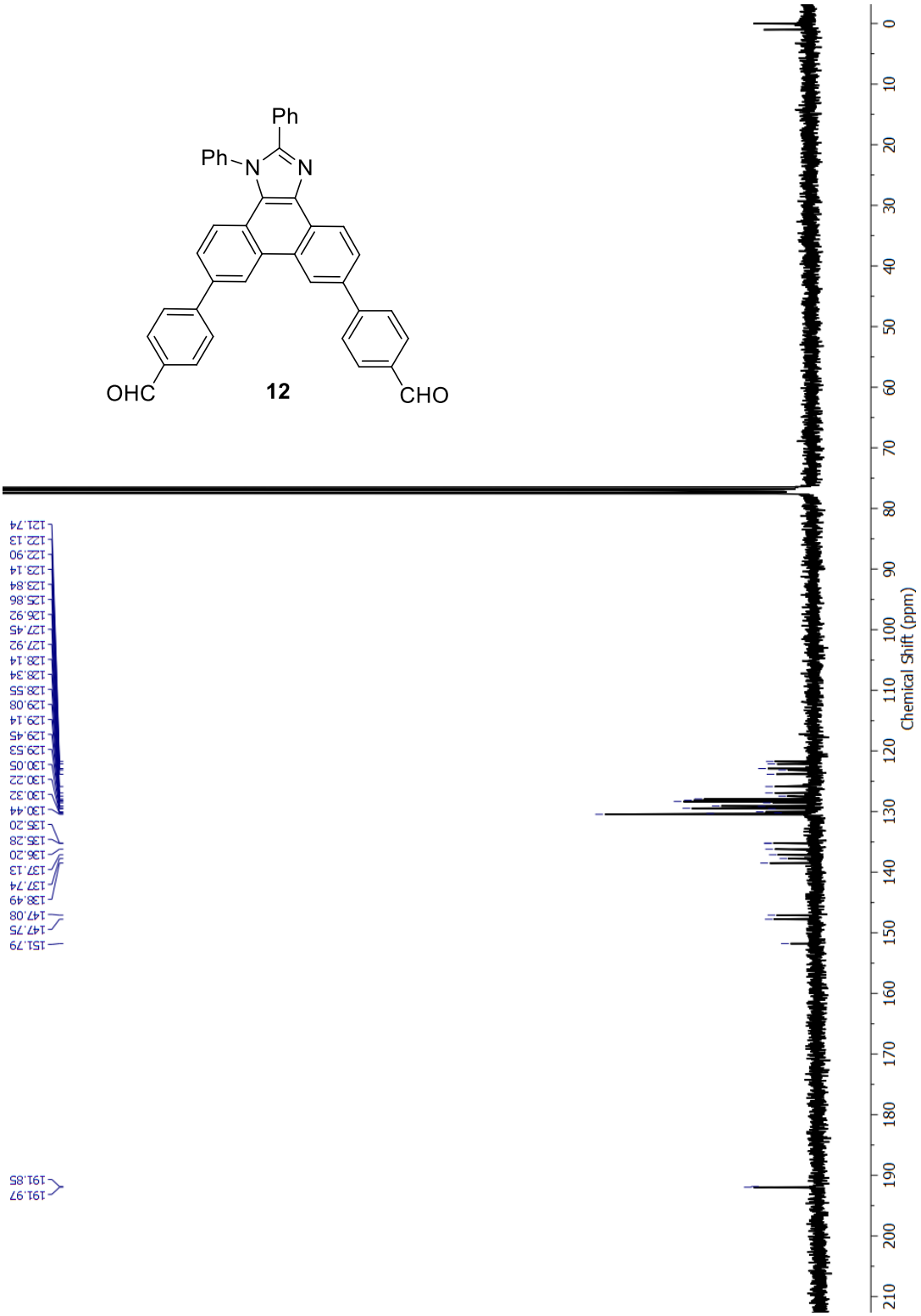

Fig. S-9 $^{13}C\{^{1}H\}$ NMR (75 MHz, $CDCl_3$) of compound **12.**

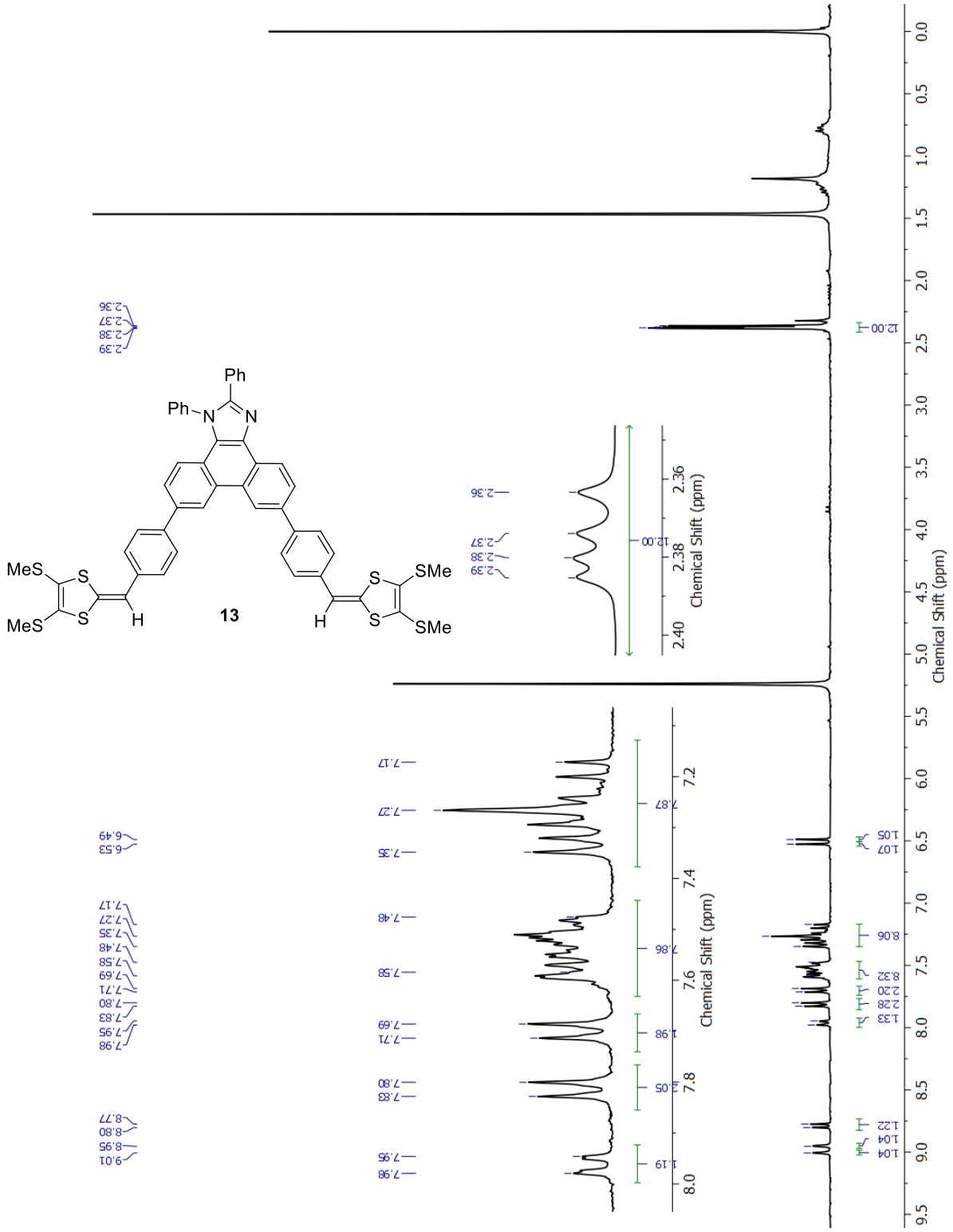

Fig. S-10 ^{1}H NMR (300 MHz, CD_2Cl_2) of compound **13**.

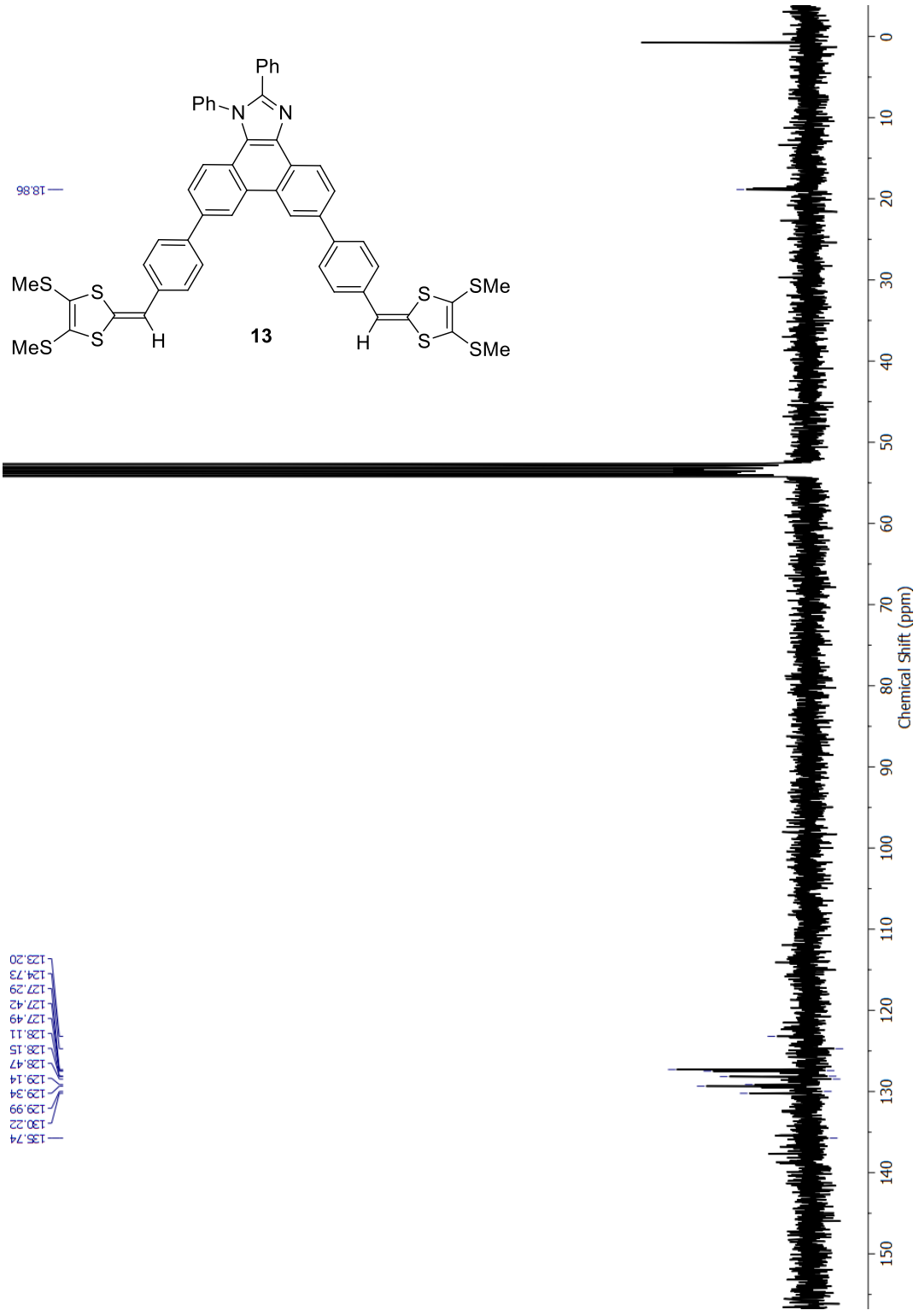

Fig. S-11 $^{13}C\{^{1}H\}$ NMR (75 MHz, CD_2Cl_2) of compound **13.**

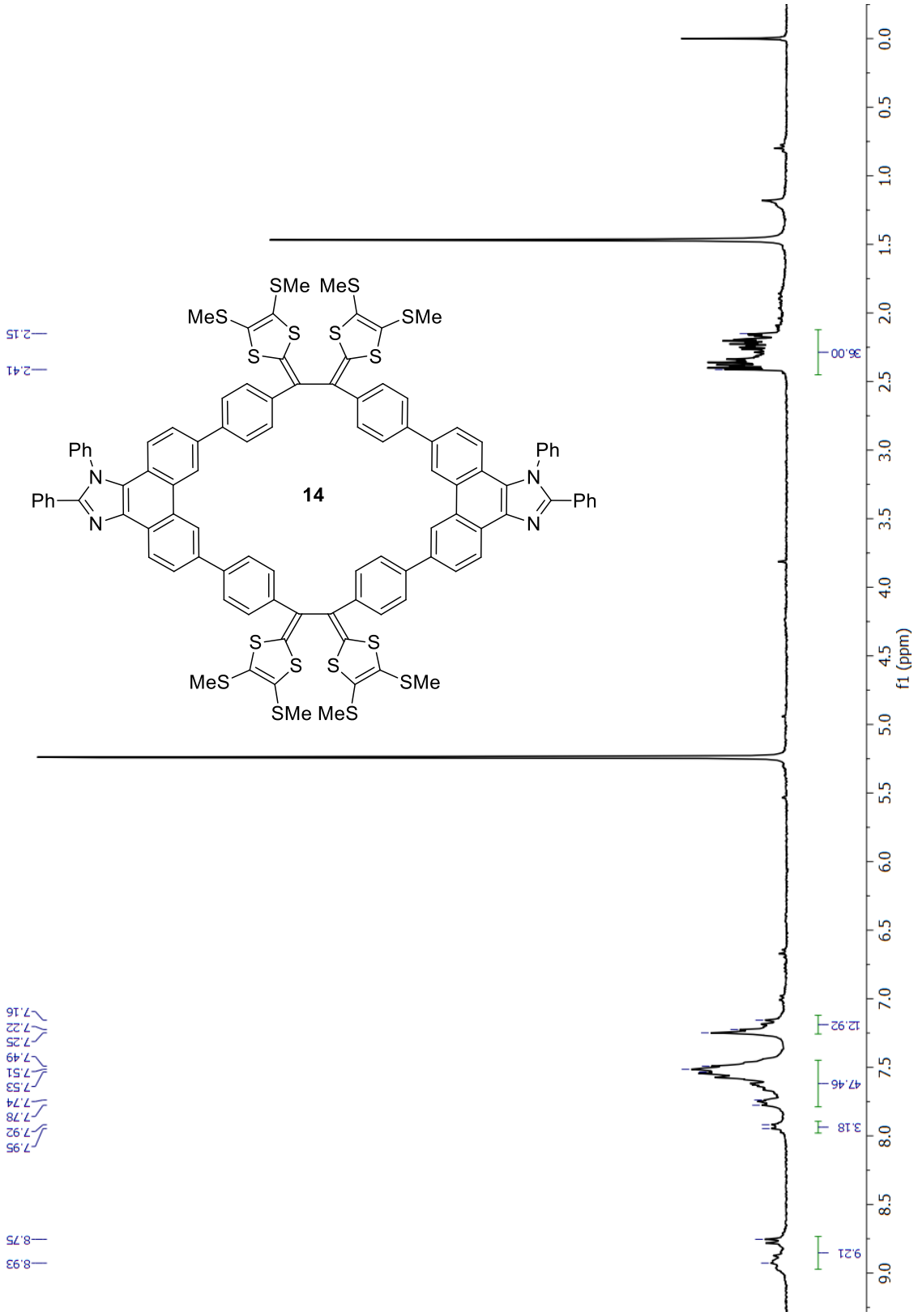

Fig. S-12 ^{1}H NMR (300 MHz, CD_2Cl_2) of compound **14**.

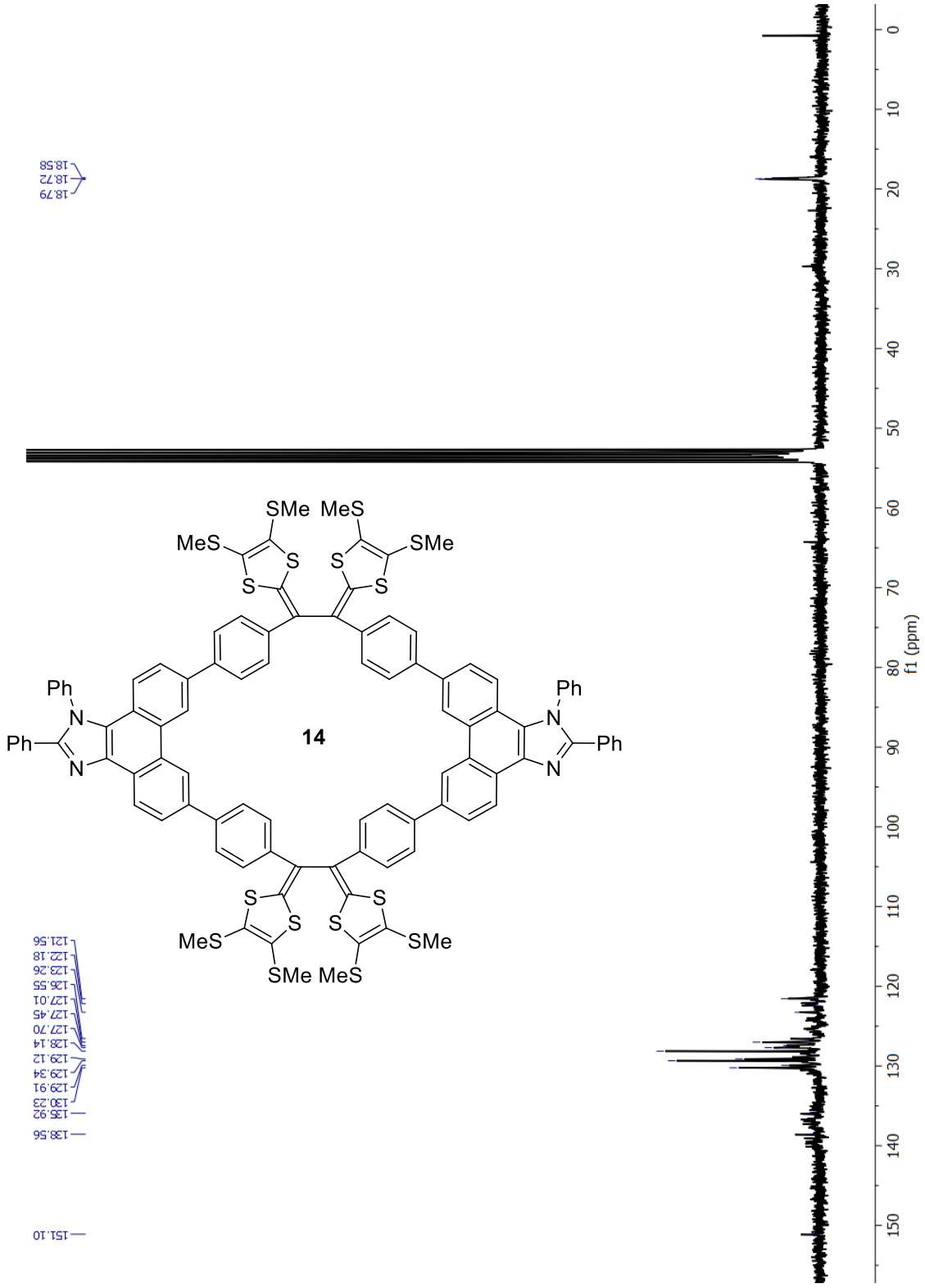

Fig. S-13 $^{13}C\{^{1}H\}$ NMR (75 MHz, CD_2Cl_2) of compound **14.**

2. ^{1}H NMR titration of 14 with C_{60} and C_{70}

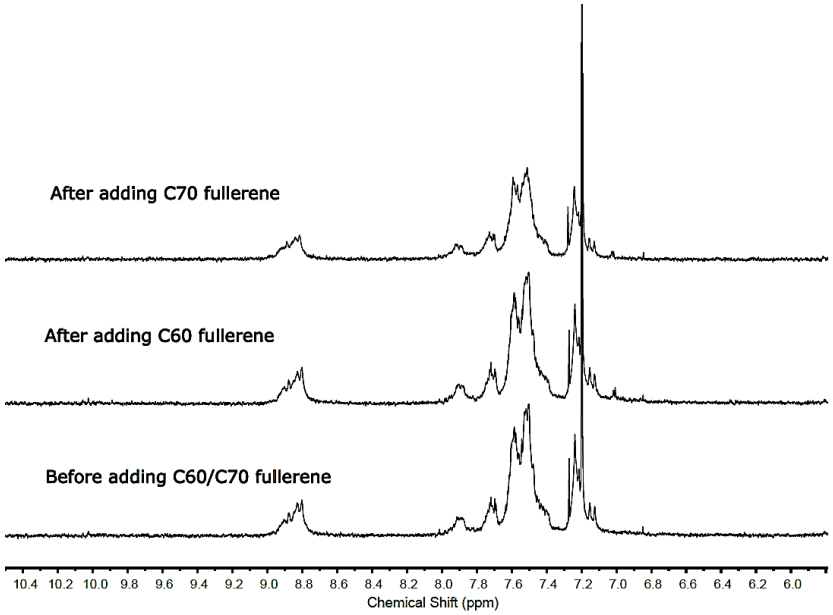

Fig. S-14 ^{1}H NMR (300MHz, C_6D_6) spectra of TTFV-**PI** macrocycles **14** before and after addition of C_{60} and C_{70} fullerene for 24 h.

3. UV-Vis Spectroscopic Data

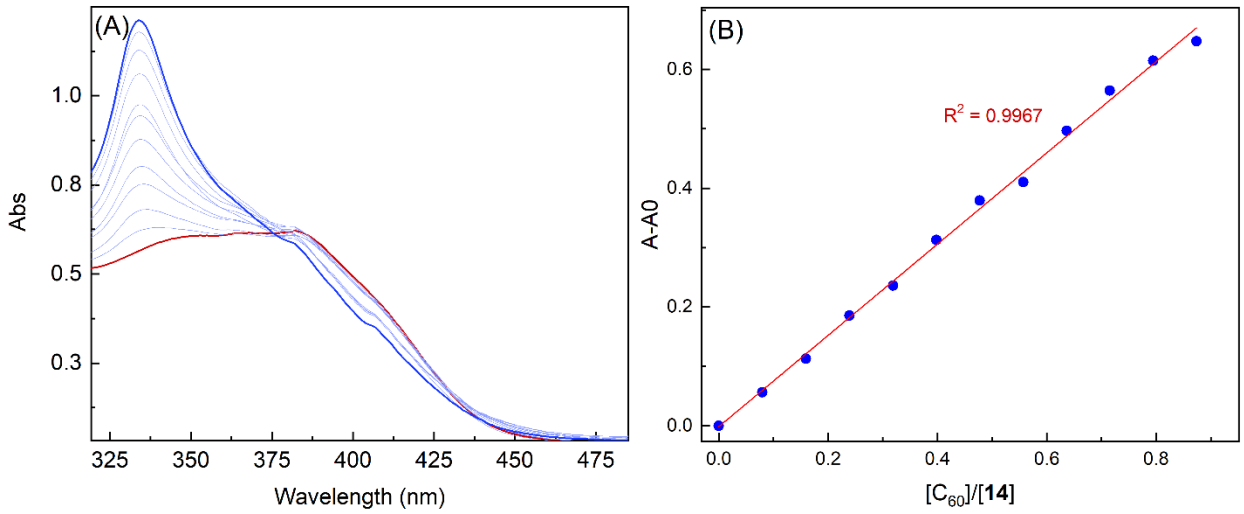

Fig. S-15 (A) UV-Vis absorption spectra of **14** (5.25×10^{-6} M in chlorobenzene) in response to the addition of C_{60} fullerene from 0.00 to 0.87 molar equivalents. (B) Plot of absorbance change ($A-A_0$) as a function of the mole ratio of C_{60} and **14**. A_0 and A are absorbance observed at 381 nm before and during the titration of **14** with C_{60} fullerene.

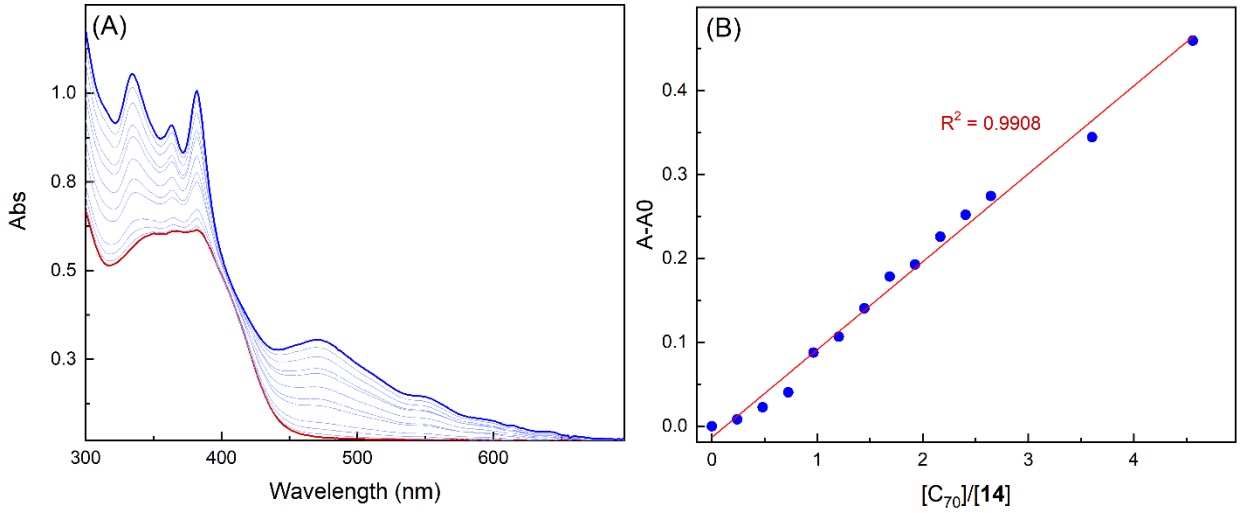

Fig. S-16 (A) UV-Vis absorption spectra of **14** (5.09×10^{-6} M in chlorobenzene) in response to the addition of C_{70} fullerene from 0.00 to 4.56 molar equivalents. (B) Plot of absorbance change ($A-A_0$) as a function of the mole ratio of C_{70} and **14**. A_0 and A are absorbance observed at 418 nm before and during the titration of **14** with C_{70} fullerene.

4. Fluorescence Spectroscopic Data

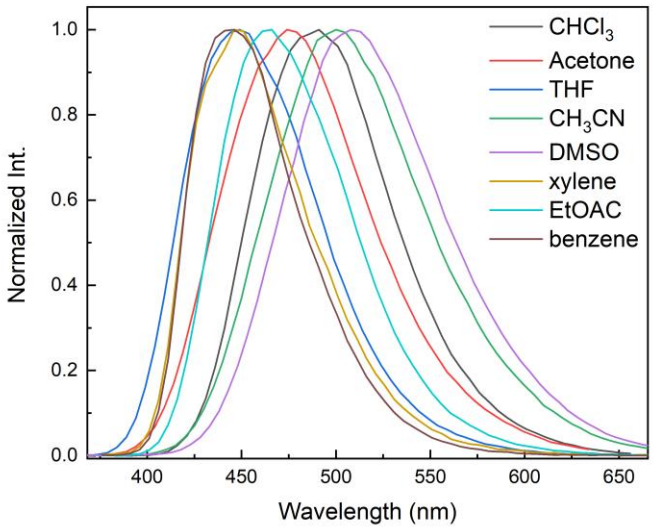

Fig. S-17 Normalized fluorescence spectra of compound **6** measured in various organic solvents at room temperature.

4.1 Job Plots

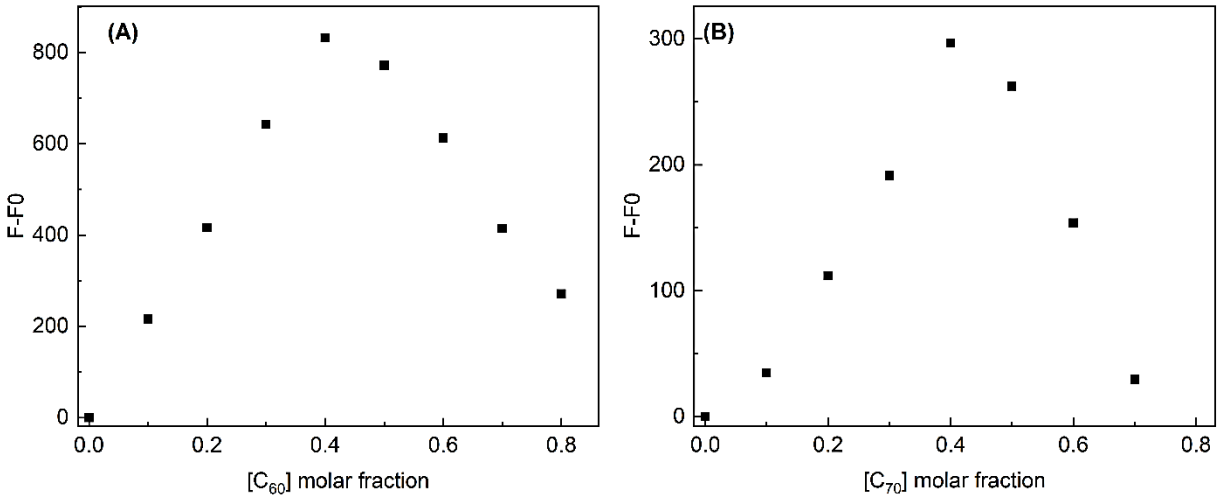

Fig. S-18 Job plots of (A) **14:C$_{60}$** and (B) **14:C$_{70}$** complex formation.

5. Dynamic Light Scattering (DLS) Data

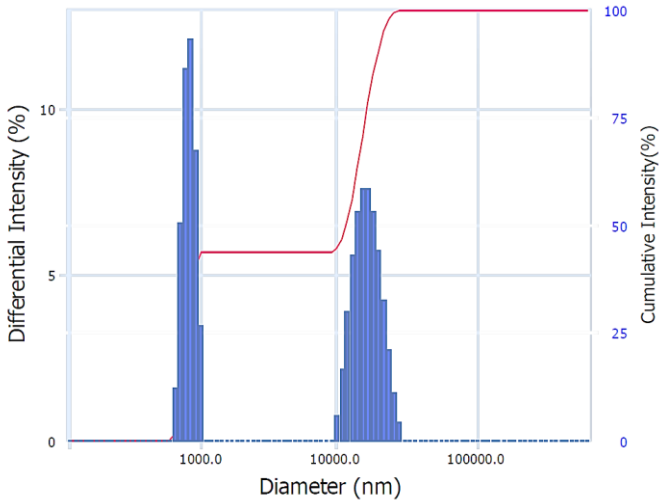

Fig. S-19 Particle size distribution of **12** (1.0×10^{-5} M) in hexanes.

6. X-ray Single Crystallographic Data

Table S-1 Crystallographic data and structure refinement of compound 12.

Empirical formula	$C_{41}H_{26}N_2O_2$
Formula weight	578.64
Temperature/K	100(2)
Crystal system	Triclinic
Space group	*P*-1
a/Å	8.7331(3)
b/Å	12.7004(3)
c/Å	14.3830(6)
α/°	69.147(3)
β/°	74.254(4)
γ/°	88.705(2)
Volume/Å^3	1429.97(9)
Z	2
ρ_{calc}g/cm^3	1.344
μ/mm^{-1}	0.651
F(000)	604.0
Crystal size/mm^3	0.13 × 0.094 × 0.067
Radiation	Cu *K*α (λ = 1.54184)
2θ range for data collection/°	6.854 to 155.086
Index ranges	$-11 \le h \le 10$, $-16 \le k \le 14$, $-18 \le l \le 18$
Reflections collected	35968
Independent reflections	5969 [R_{int} = 0.0482, R_{sigma} = 0.0305]
Data/restraints/parameters	5969/0/406
Goodness-of-fit on F^2	1.034
Final *R* indexes [*I*>=2σ (I)]	R_1 = 0.0481, wR_2 = 0.1255
Final *R* indexes [all data]	R_1 = 0.0603, wR_2 = 0.1333
Largest diff. peak/hole / e Å^{-3}	0.22/-0.25

Table S-2 Crystallographic data and structure refinement of co-crystal 12 and oxalic acid.

Empirical formula	$C_{46}H_{31}N_2O_{12}$
Formula weight	803.73
Temperature/K	100(2)
Crystal system	triclinic
Space group	*P*-1
a/Å	10.3878(2)
b/Å	12.9862(2)
c/Å	14.0980(2)
α/°	95.0150(10)
β/°	100.329(2)
γ/°	100.9620(10)
Volume/Å^3	1822.24(5)
Z	2
ρ_{calc}g/cm^3	1.465
μ/mm^{-1}	0.894
F(000)	834.0
Crystal size/mm^3	0.143 × 0.107 × 0.066
Radiation	Cu *K*α (λ = 1.54184)
2θ range for data collection/°	6.424 to 154.792
Index ranges	$-11 \le h \le 13$, $-16 \le k \le 16$, $-17 \le l \le 17$
Reflections collected	45346
Independent reflections	7605 [R_{int} = 0.0450, R_{sigma} = 0.0292]
Data/restraints/parameters	7605/5/559
Goodness-of-fit on F^2	1.036
Final *R* indexes [*I*>=2σ (I)]	R_1 = 0.0652, wR_2 = 0.1902
Final *R* indexes [all data]	R_1 = 0.0755, wR_2 = 0.1999
Largest diff. peak/hole / e Å^{-3}	0.51/-0.56

7. DFT and TD-DFT Computational Results

7.1 Frontier Molecular Orbitals of Compounds 11, 12, and 13

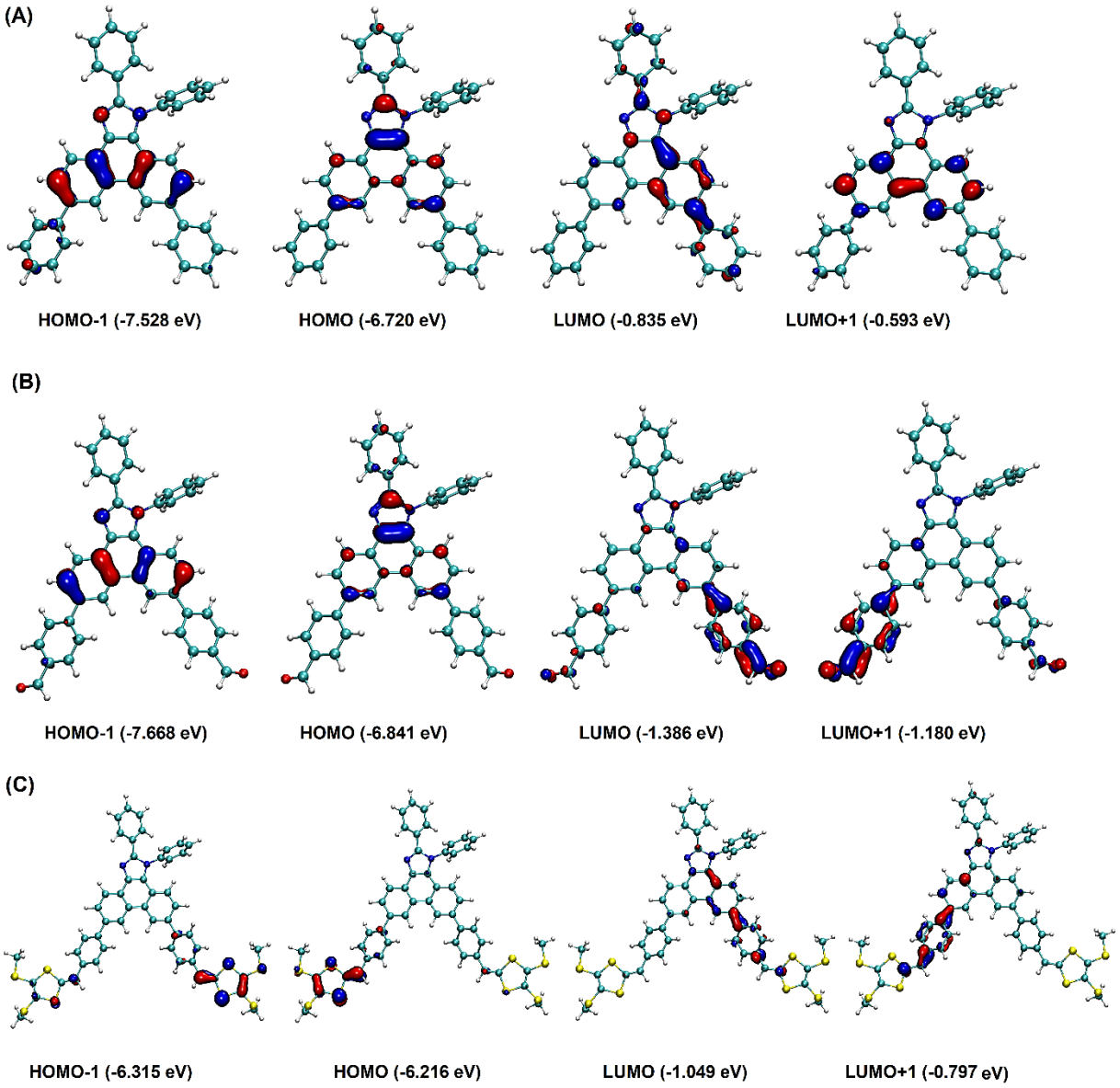

Fig. S-20 Frontier molecular orbital (FMO) distribution of (A) **11**, (B) **12**, and (C) **13**, using PCM(CH_2Cl_2)//M06-2X/Def2-SVP optimized geometries.

7.2 TD-DFT results for compounds 11, 12, and 13

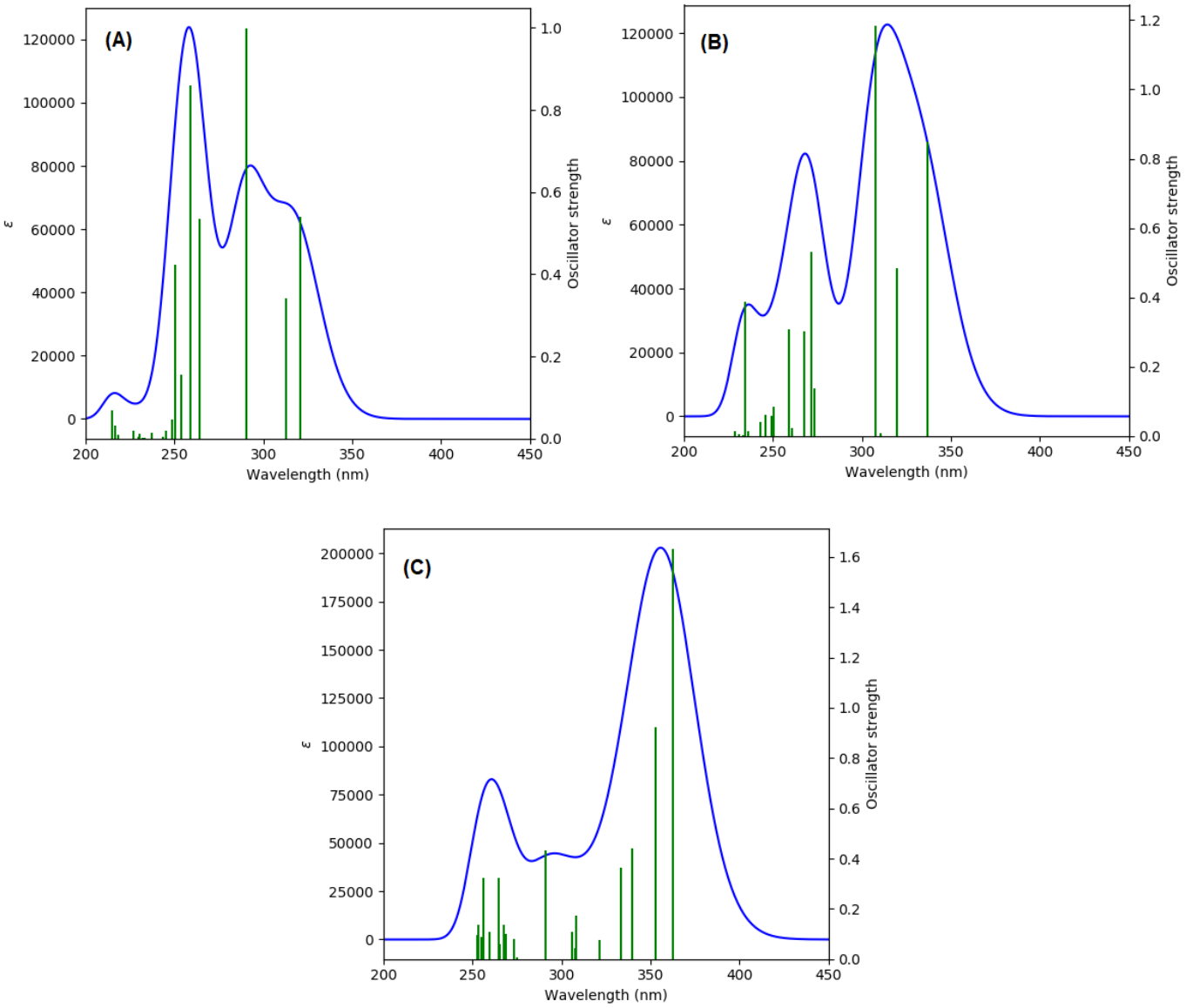

Fig. S-21 Simulated UV-Vis spectrum of compounds (A) **11**, (B) **12**, and (C) **13** calculated at the PCM(CH_2Cl_2)//TD-M06-2X/6-311+G(2d,p) level of theory. Spectral simulations were done using the GaussSum software package.[Δ]

[Δ]O'Boyle, N. M.; Tenderholt, A. L.; Langner, K. M. *J. Comp. Chem*. **2008**, *29*, 839-845.

Table S-3 Summary of TD-DFT calculated electronic transitions of **11** at the PCM(CH_2Cl_2)//TD-M06-2X/6-311+G(2d,p) level of theory.

λ (nm)	***f***	**Major MO Contributions**
320.5	0.473	HOMO→LUMO (53%), HOMO→L+1 (33%)
311.4	0.453	HOMO→LUMO (38%), HOMO→L+1 (49%)
291.0	0.959	HOMO→L+2 (87%)
264.06	0.483	H-1→L+1 (45%), H-1→→L+2 (29%)
259.7	0.853	H-1→LUMO (52%), H-1→L+1 (11%), HOMO→L+1 (10%)
255.4	0.083	HOMO→L+3 (70%)
250.3	0.180	H-2→L+1 (16%), HOMO→L+4 (34%), HOMO→L+5 (18%)
249.1	0.351	H-2→LUMO (12%), H-2→L+1 (15%), H-1→L+1 (10%), HOMO→L+5 (21%)
246.7	0.069	HOMO→L+4 (39%), HOMO→L+5 (31%)
243.0	0.001	HOMO→L+6 (22%), HOMO→L+8 (12%)
241.8	0.002	HOMO→L+8 (14%), HOMO→L+9 (11%)
238.5	0.000	HOMO→L+6 (18%)
237.6	0.012	HOMO→L+4 (11%), HOMO→L+6 (24%), HOMO→L+10 (20%)
234.4	0.000	H-2→LUMO(30%), H-1→LUMO (11%), H-1→L+2 (24%),
231.2	0.038	H-2→LUMO (19%), H-2→L+1 (31%)
229.3	0.001	H-9→L+3 (18%), H-7→L+4 (21%)
227.1	0.023	H-3→LUMO (17%), H-2→L+1 (10%), H-2→L+2 (33%),
222.0	0.004	HOMO→L+7 (62%)
219.5	0.013	H-3→LUMO (16%), H-2→L+2 (15%), H-1→L+3 (11%)
218.1	0.009	HOMO→L+11 (19%)

Table S-4 Summary of TD-DFT calculated electronic transitions of **12** at the PCM(CH_2Cl_2)//TD-M06-2X/6-311+G(2d,p) level of theory.

λ (nm)	***f***	**Major MO Contributions**
336.4	0.843	HOMO→LUMO (81%)
328.4	0.004	H-12→LUMO (44%), H-12→L+1 (16%), H-12→L+3 (11%)

328.0	0.006	H-11→LUMO (18%), H-11→L+1 (49%)
319.8	0.491	HOMO→L+1 (23%), HOMO→L+2 (56%)
308.8	1.056	H-1→LUMO (10%), HOMO→L+1 (52%), HOMO→L+2 (16%)
272.7	0.280	H-1→LUMO (34%), HOMO→L+3 (44%)
271.7	0.520	H-1→LUMO (14%), H-1→L+1 (12%), H-1→L+2 (29%), HOMO→L+2 (10%), HOMO→L+3 (10%)
268.0	0.246	H-1→LUMO (16%), H-1→L+1 (18%), H-1→L+2 (15%), HOMO→L+3 (16%)
258.1	0.338	H-2→L+1 (14%), H-2→L+2 (12%), H-1→L+1 (15%), H-1→L+2 (10%), HOMO→L+4 (14%)
256.7	0.0175	H-7→LUMO (46%), H-7→L+1 (14%)
256.3	0.006	H-6→LUMO (19%), H-6→L+1 (44%)
251.7	0.032	HOMO→L+4 (19%), HOMO→L+5 (42%)
249.0	0.055	H-2→L+1 (12%), H-1→L+1 (18%), H-1→L+2 (23%), HOMO→L+5 (13%)
246.7	0.074	H-2→LUMO (49%)
245.6	0.052	H-2→LUMO (11%), HOMO→L+4 (31%), HOMO→L+6 (32%)
237.7	0.202	HOMO→L+6 (28%)
236.7	0.027	H-2→L+2 (13%), HOMO→L+5 (14%), HOMO→L+11 (13%)
235.6	0.221	H-2→L+1 (11%), HOMO→L+7 (22%), HOMO→L+8 (10%)
233.3	0.016	H-2→L+2 (38%), HOMO→L+7 (10%)
229.1	0.009	H-8→L+5 (7%)

Table S-5 Summary of TD-DFT calculated electronic transitions of **13** at the PCM(CH_2Cl_2)//TD-M06-2X/6-311+G(2d,p) level of theory.

λ (nm)	***f***	**Major MO Contributions**
371.3	1.444	H-1→LUMO (15%), H-1→L+1 (12%), HOMO→LUMO (35%)
363.7	0.676	H-1→LUMO (23%), HOMO→L+1 (26%)
349.5	0.574	HOMO→L+1 (15%), HOMO→L+4 (12%)
343.2	0.502	H-1→LUMO (10%), H-1→L+8 (27%)
324.6	0.097	H-2→L+2 (29%), HOMO→L+2 (30%)
311.7	0.145	H-1→L+4 (15%), HOMO→L+4 (40%)

310.7	0.092	H-2→LUMO (40%)
309.4	0.091	H-1→L+5 (49%), HOMO→L+5 (16%)
295.3	0.386	H-2→L+1 (39%), H-1→L+1 (10%)
281.8	0.025	H-1→L+2 (26%), HOMO→L+15 (10%)
279.6	0.135	HOMO→L+11 (14%)
275.9	0.117	HOMO→L+11 (17%)
275.8	0.041	HOMO→LUMO (11%)
273.4	0.035	H-1→L+9 (11%), H-1→L+13 (10%)
272.3	0.055	H-1→L+16 (10%)
265.7	0.084	H-2→LUMO (17%), H-1→L+1 (23%), HOMO→LUMO (16%)
263.8	0.245	H-3→LUMO (20%), H-2→L+3 (19%), HOMO→L+3 (10%)
262.3	0.018	H-1→L+21 (11%)
260.7	0.203	H-3→LUMO (14%), HOMO→L+2 (14%)
259.6	0.071	H-1→L+1 (22%)

Appendix IV

Supplementary Information for Chapter 5

On the Photocyclization of R-DHA Derivatives

Table of Content

1. NMR Spectra for New Compounds

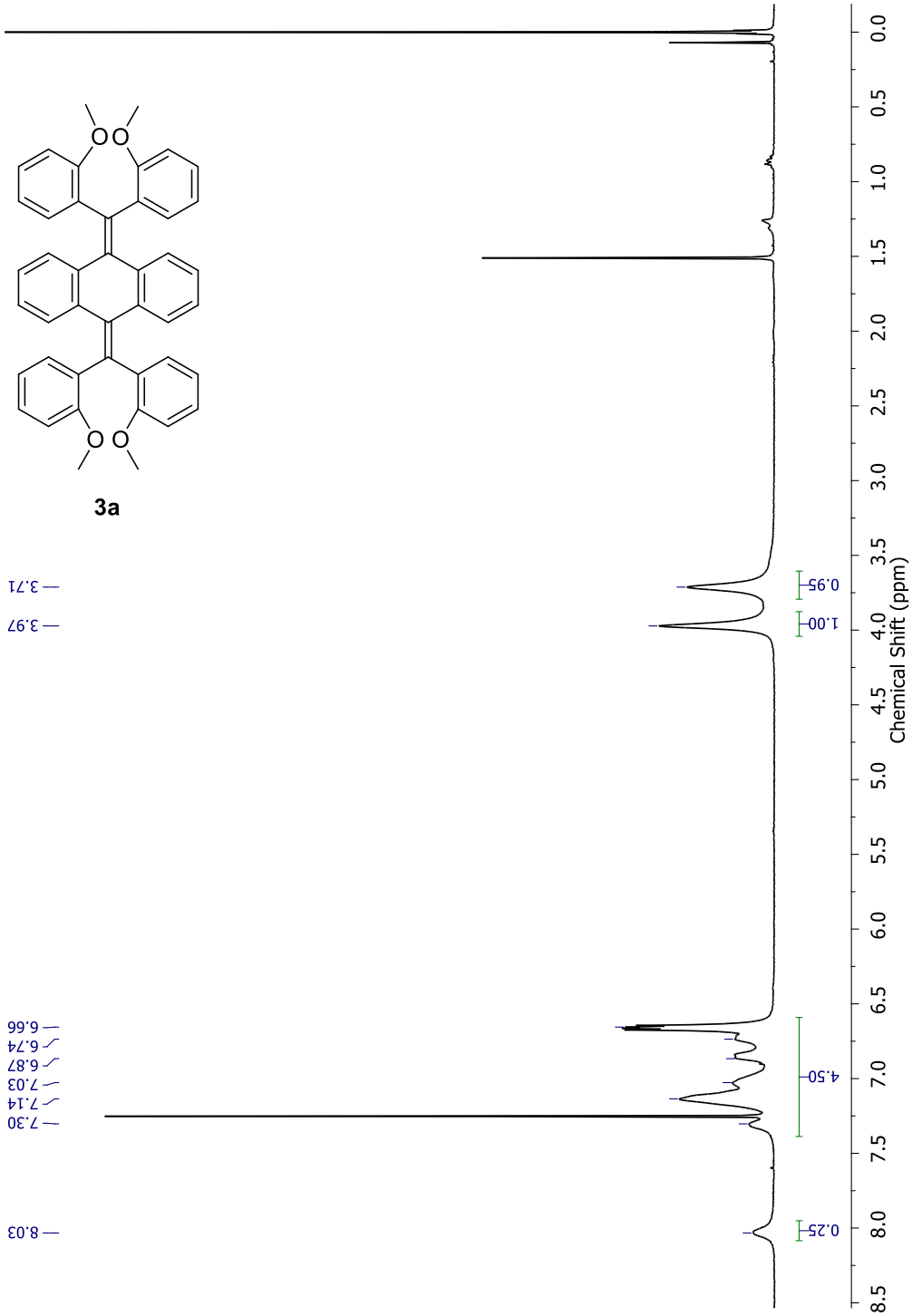

Figure S-1 ^{1}H NMR (300 MHz, $CDCl_3$) of compound **3a**

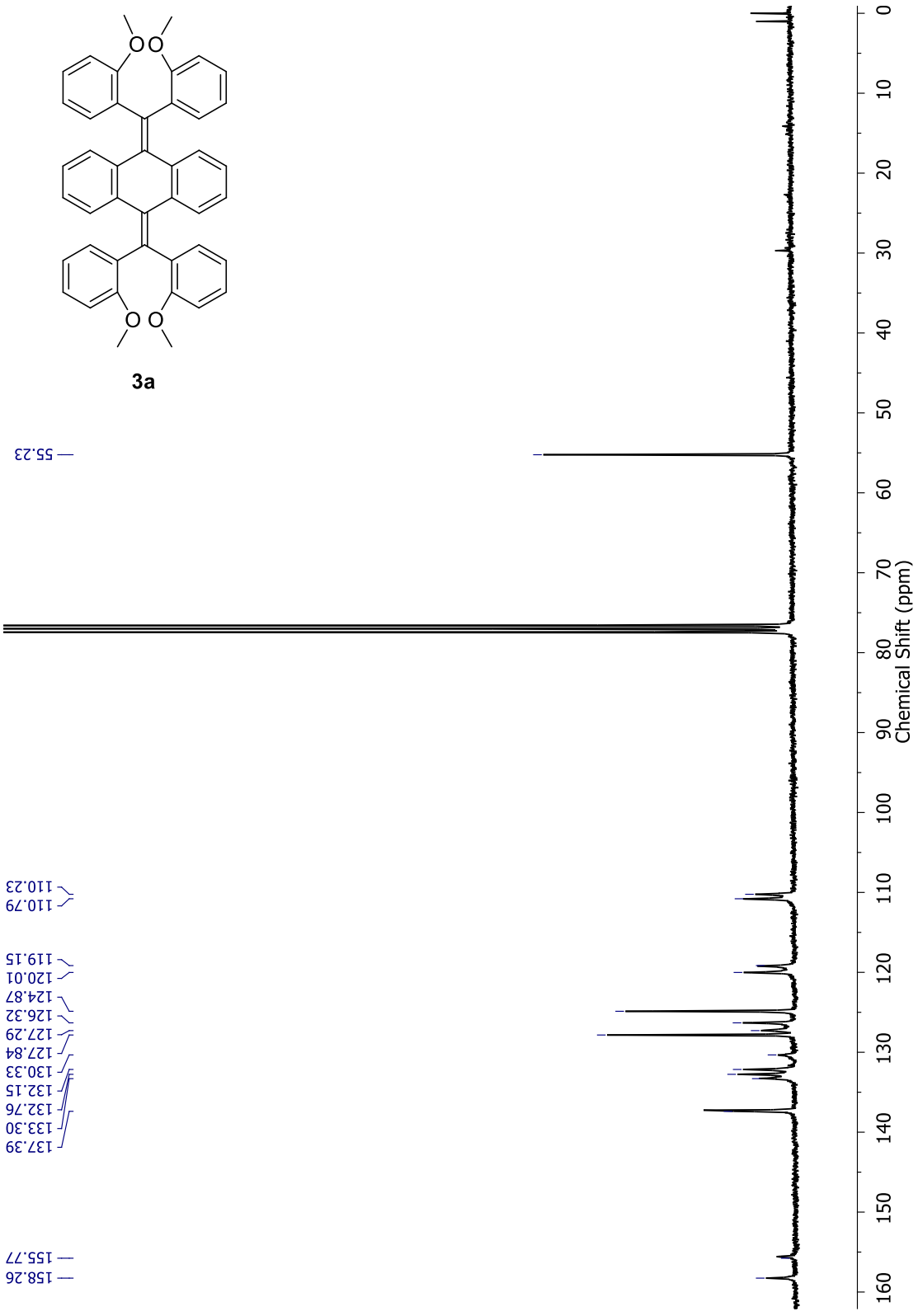

Figure S-2 ^{13}C NMR (75 MHz, $CDCl_3$) of compound **3a**.

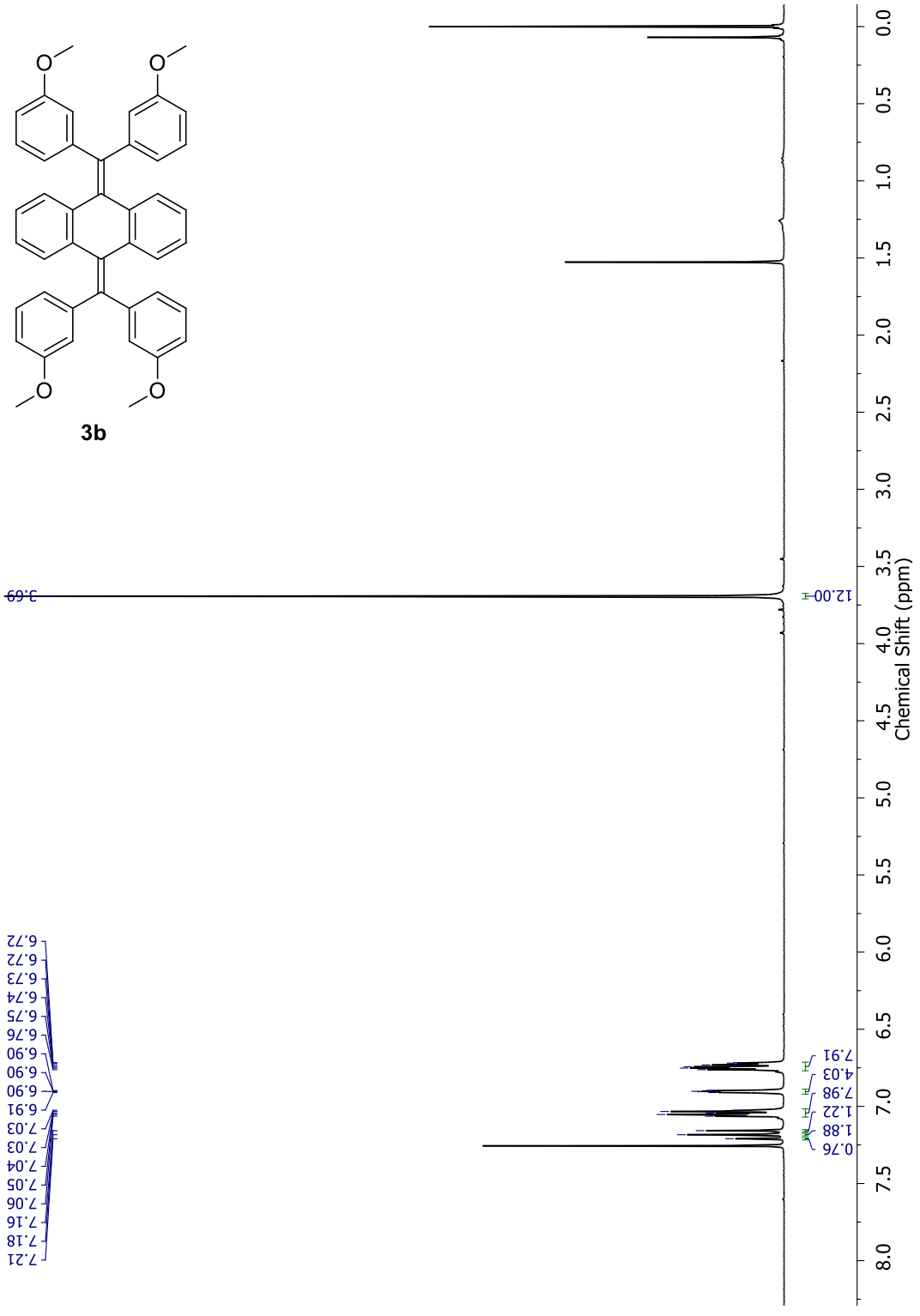

Figure S-3 ^{1}H NMR (300 MHz, $CDCl_3$) of compound **3b**.

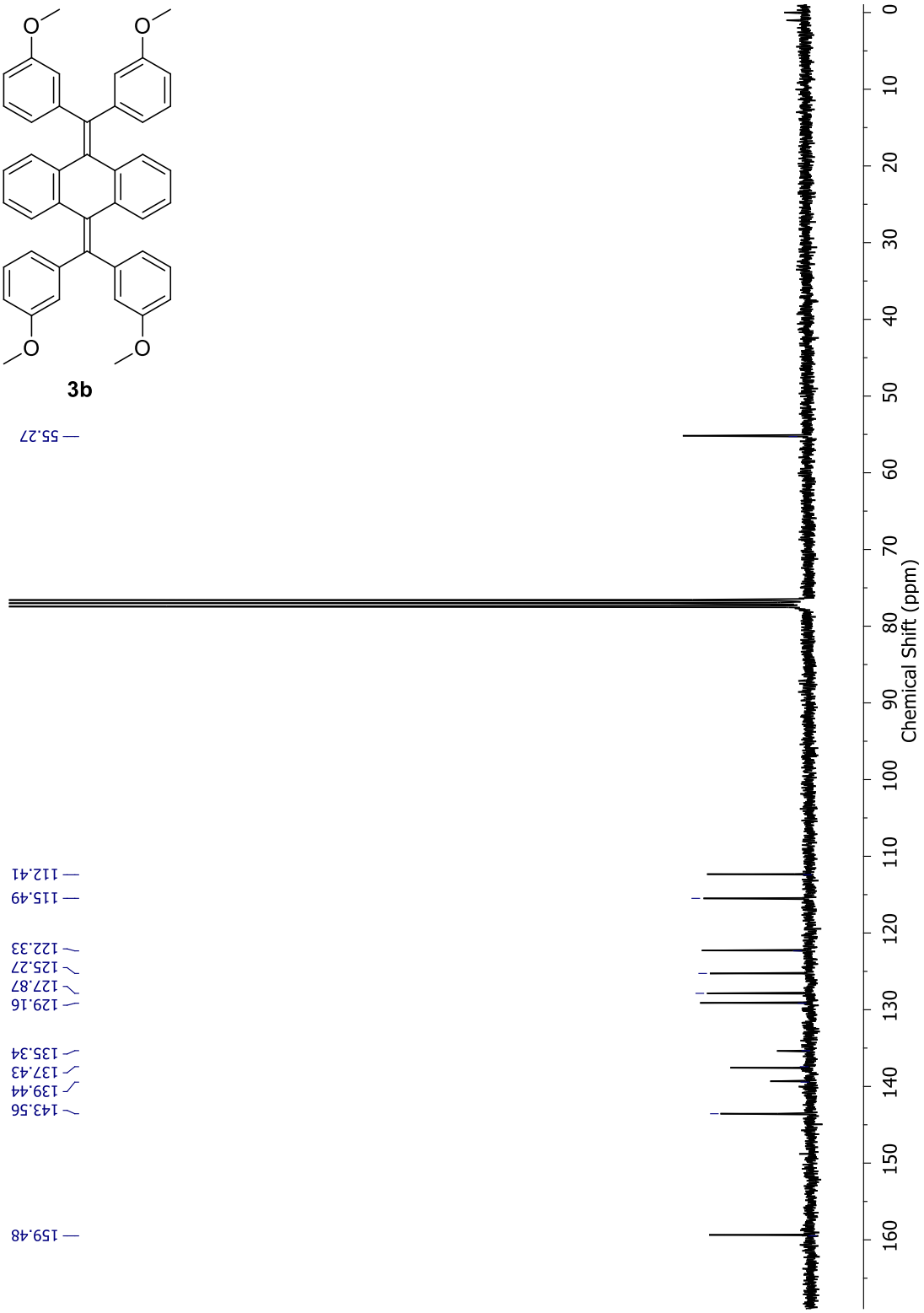

Figure S-4 ^{13}C NMR (75 MHz, $CDCl_3$) of compound **3b**.

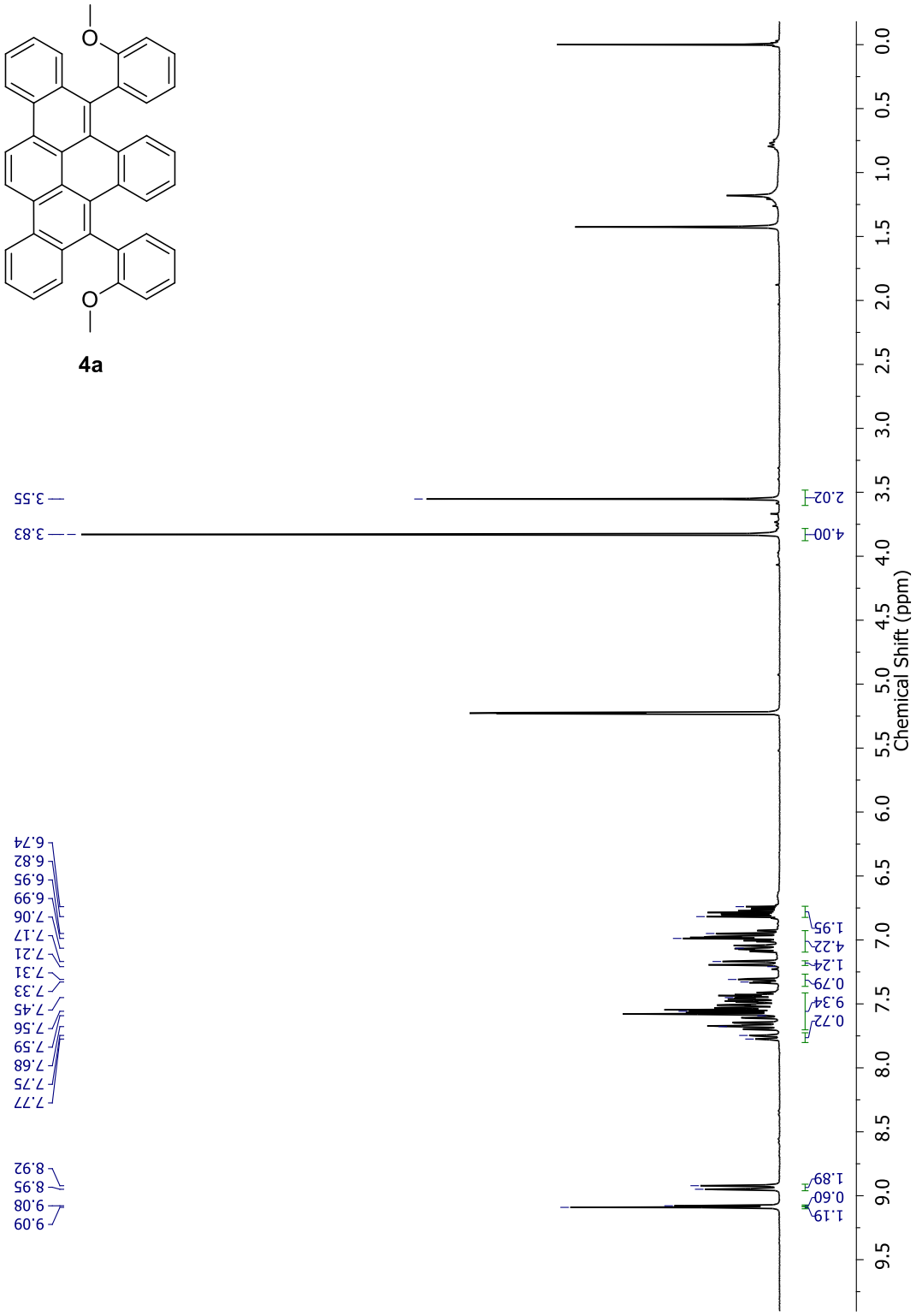

Figure S-5 ^{1}H NMR (300 MHz, CD_2Cl_2) of compound **4a**

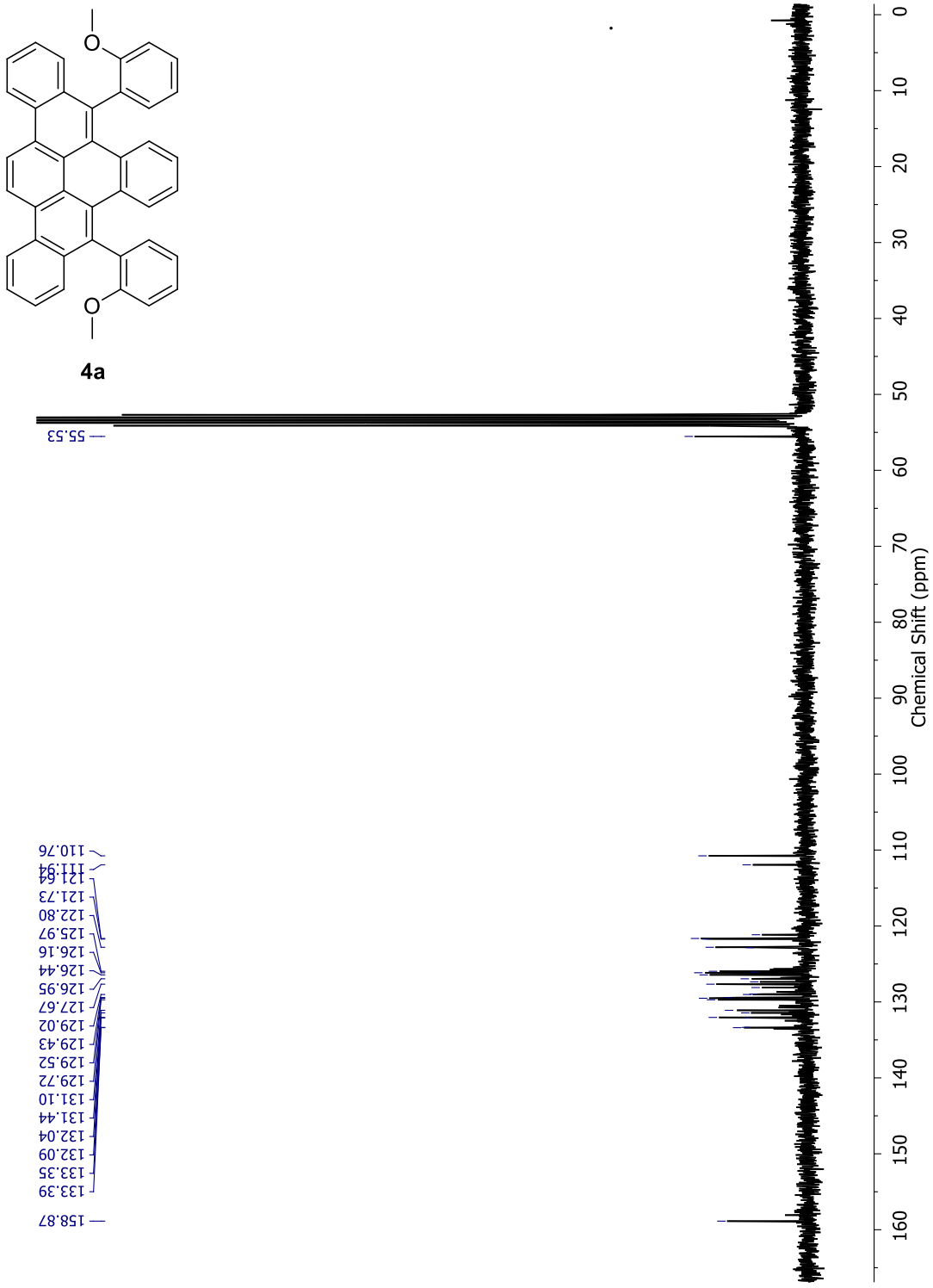

Figure S-6 ^{13}C NMR (75 MHz, CD_2Cl_2) of compound **4a**.

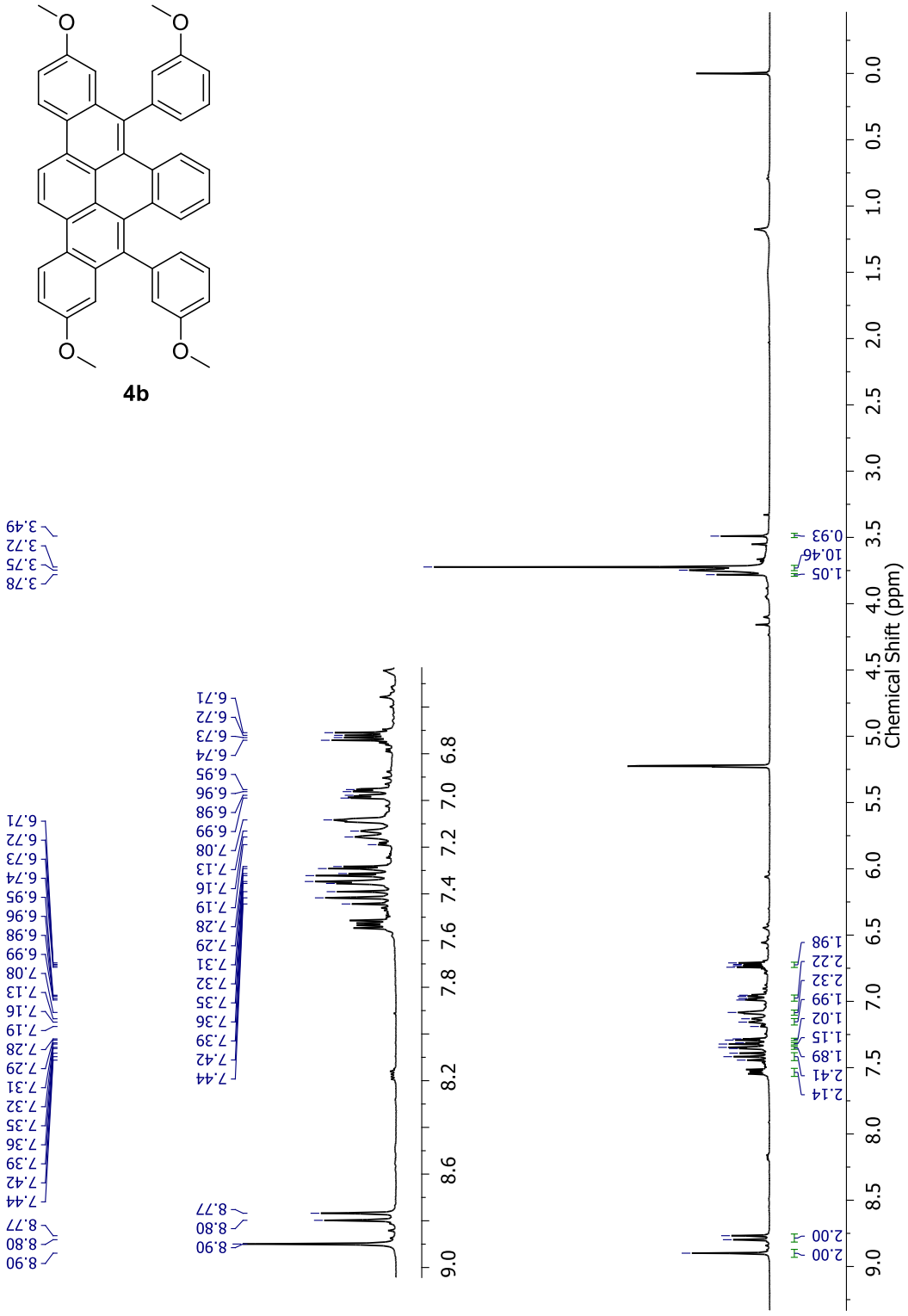

Figure S-7 ^{1}H NMR (300 MHz, CD_2Cl_2) of compound **4b**.

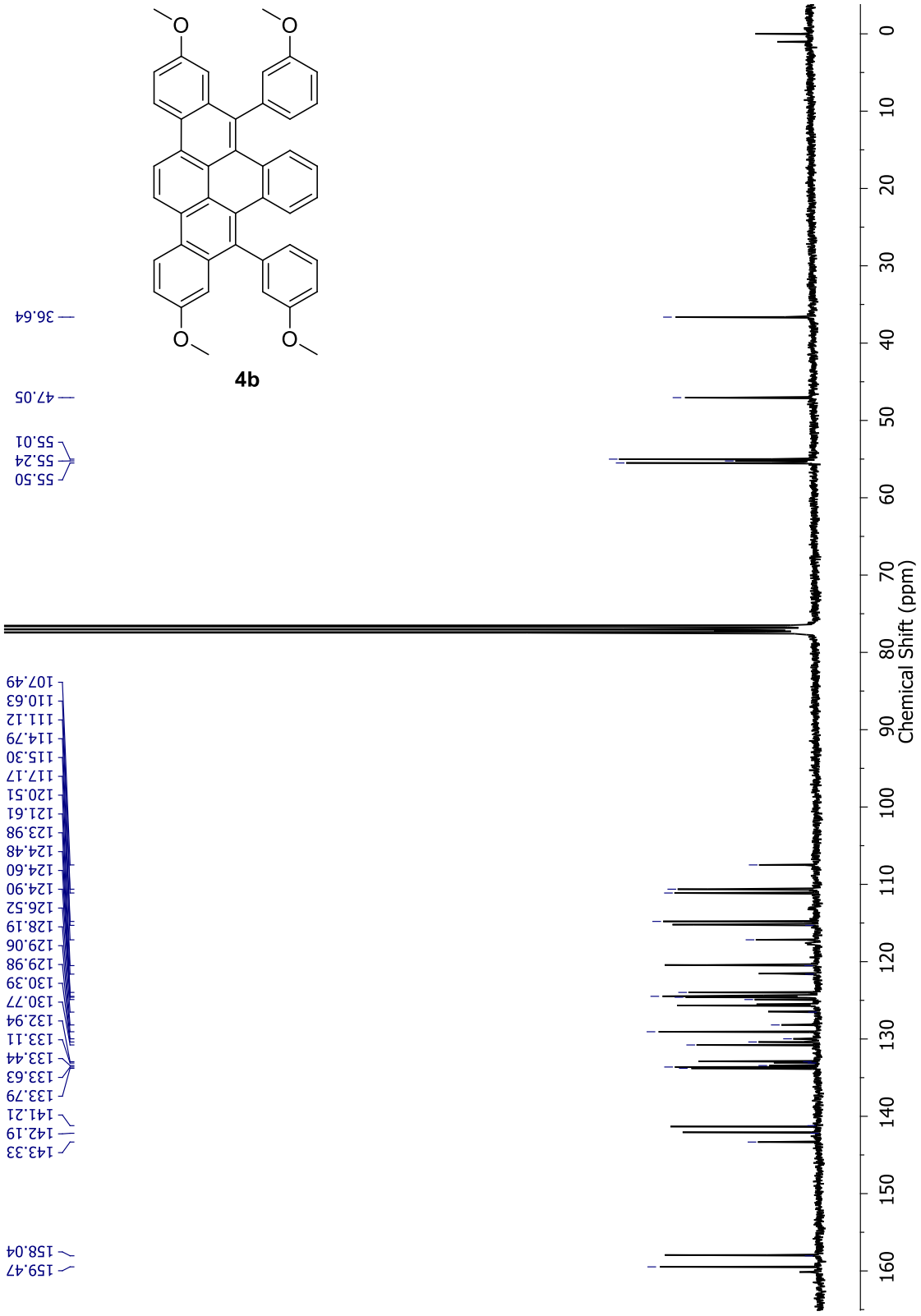

Figure S-8 ^{13}C NMR (75 MHz, $CDCl_3$) of compound **4b**.

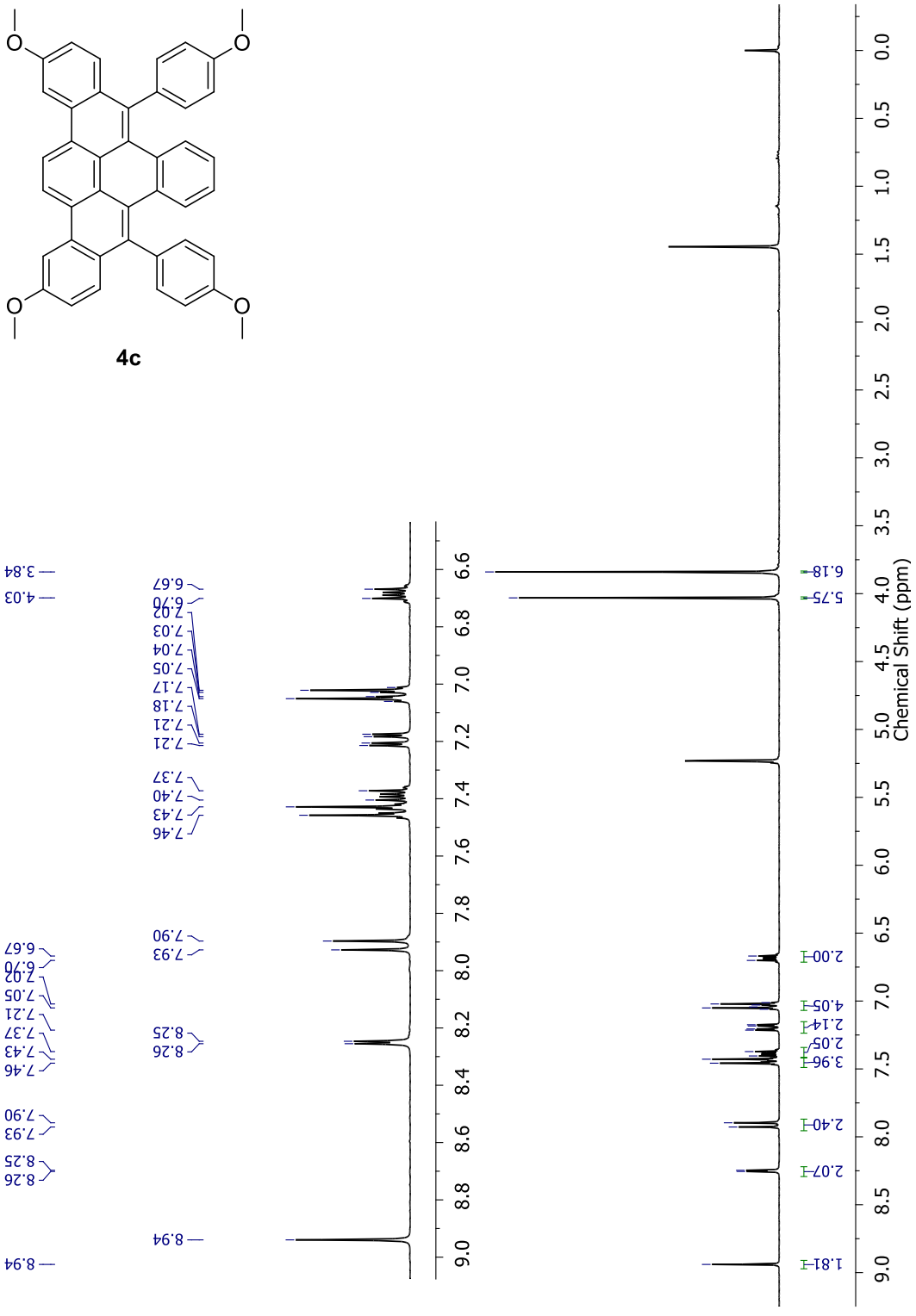

Figure S-9 ^{1}H NMR (300 MHz, CD_2Cl_2) of compound **4c**.

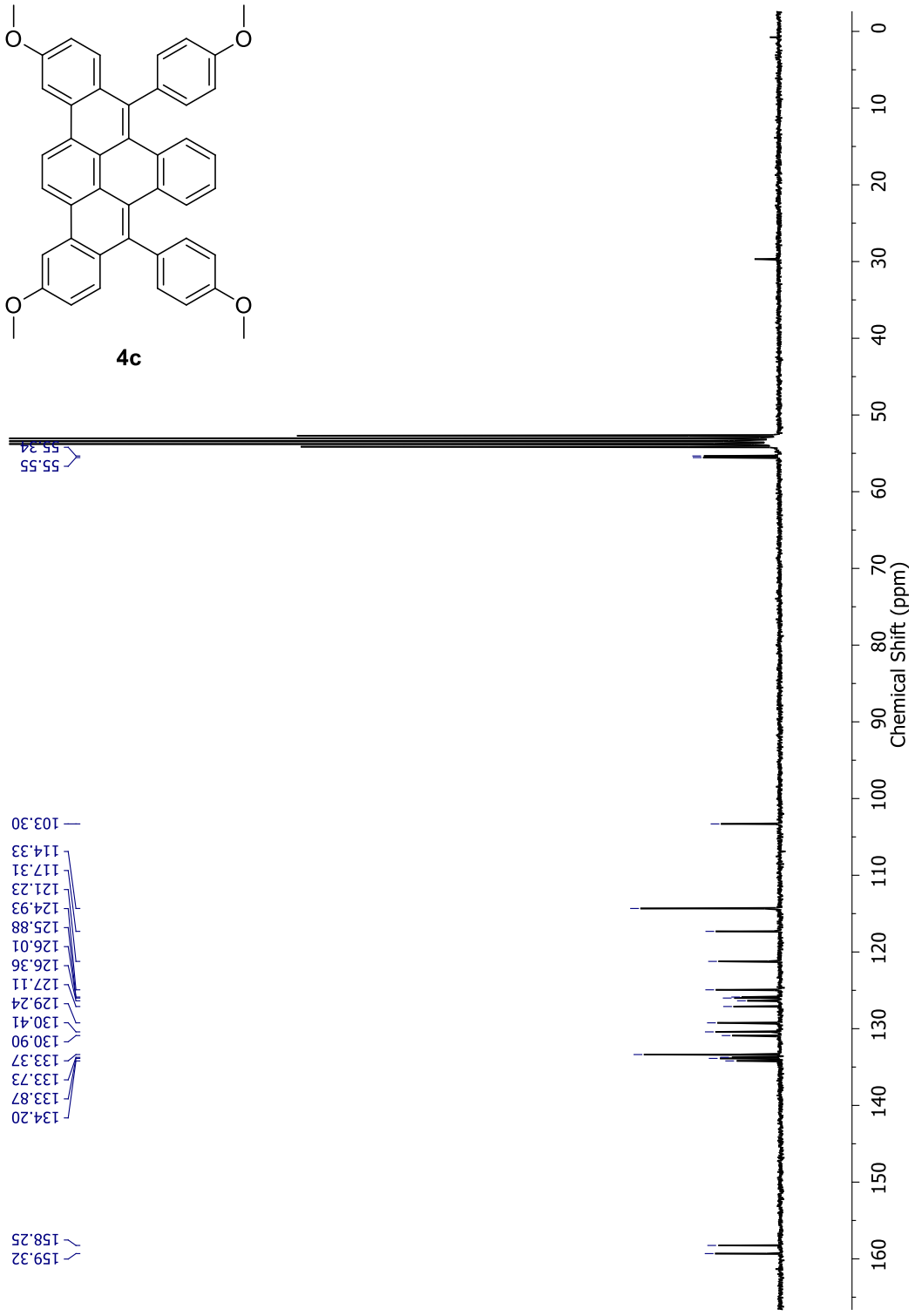

Figure S-10 ^{13}C NMR (75 MHz, CD_2Cl_2) of compound **4c**.

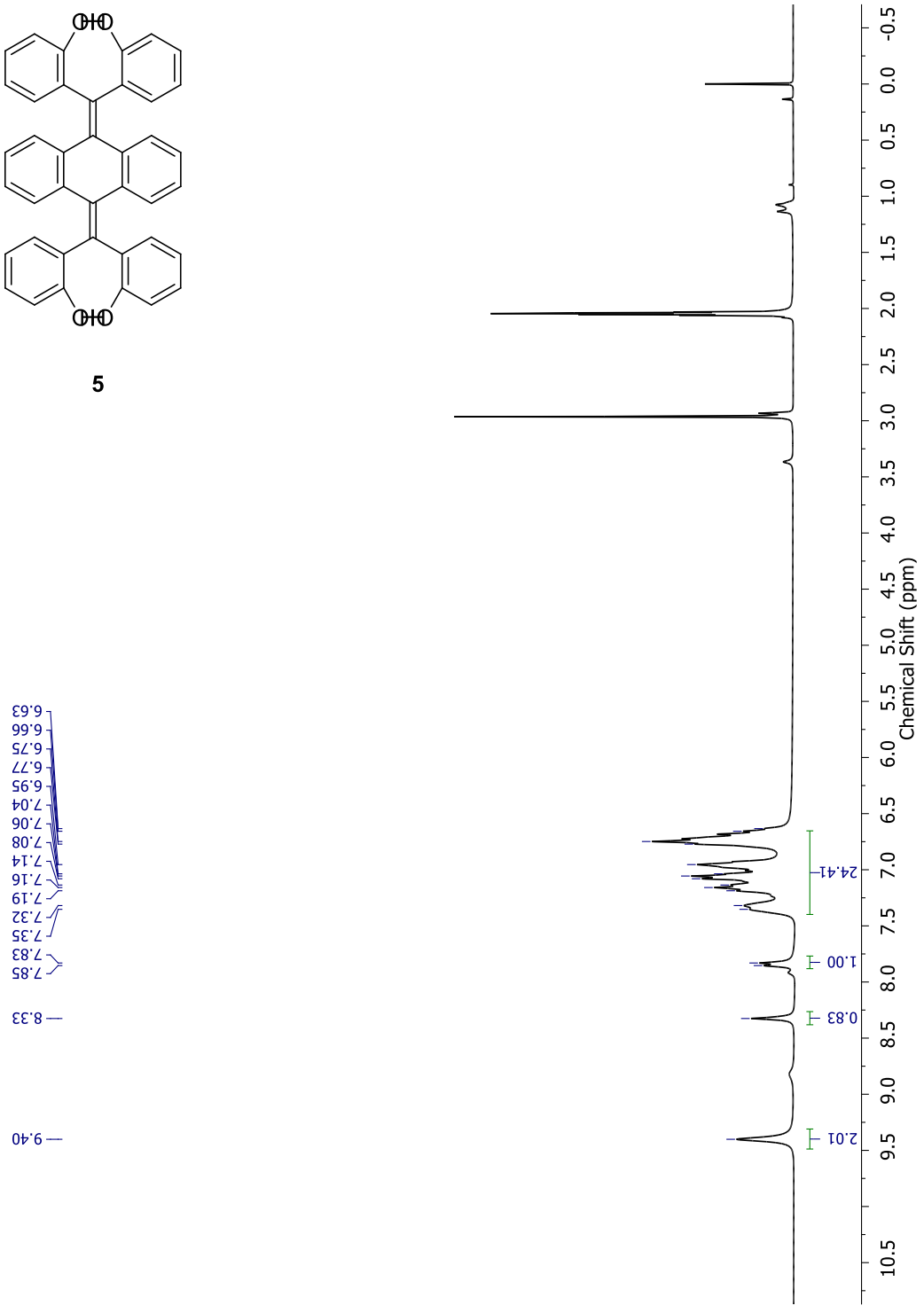

Figure S-11 ^{1}H NMR (300 MHz, Acetone, d_6) of compound **5**.

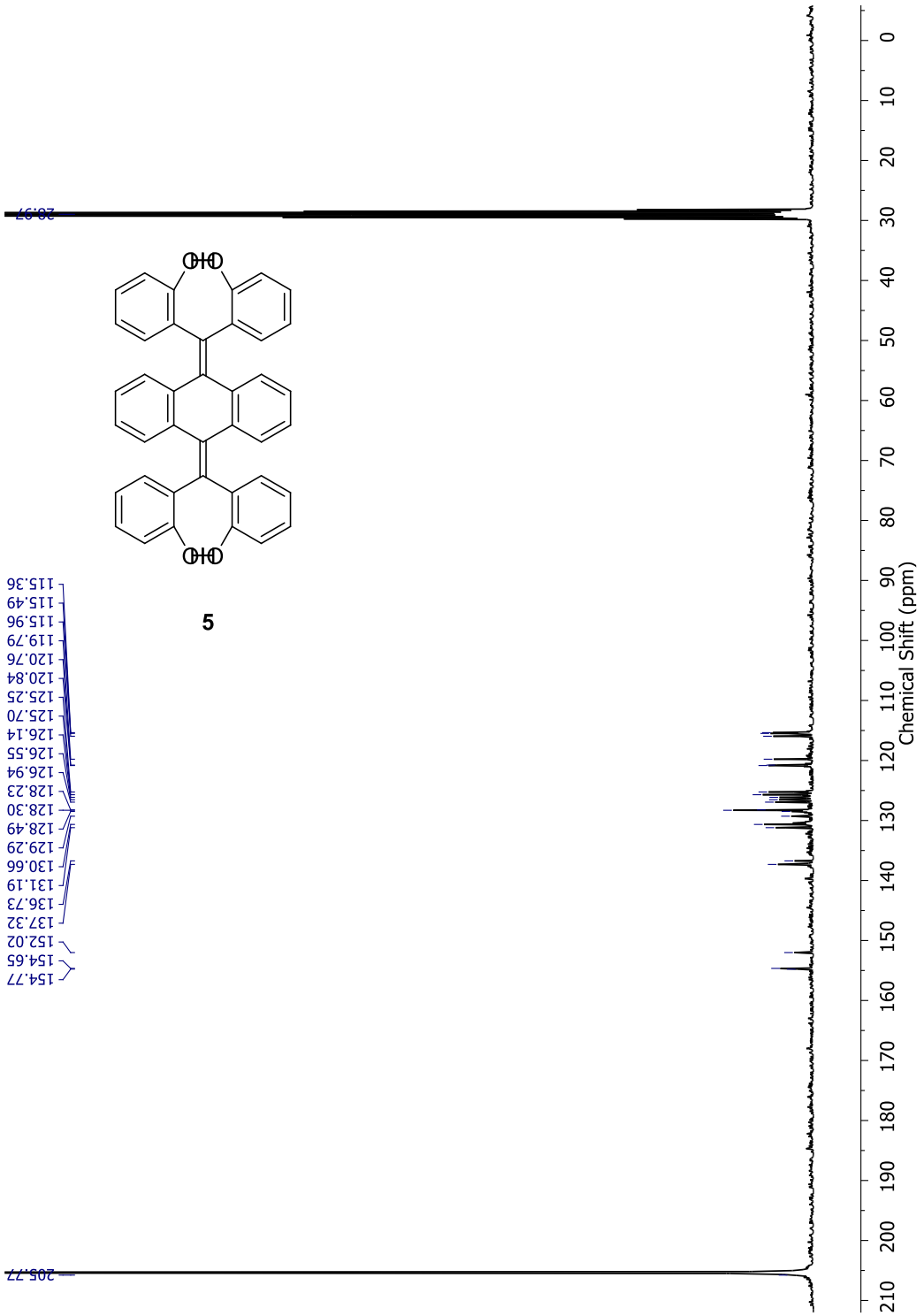

Figure S-12 ^{13}C NMR (75 MHz, Acetone, d_6) of compound **5**.

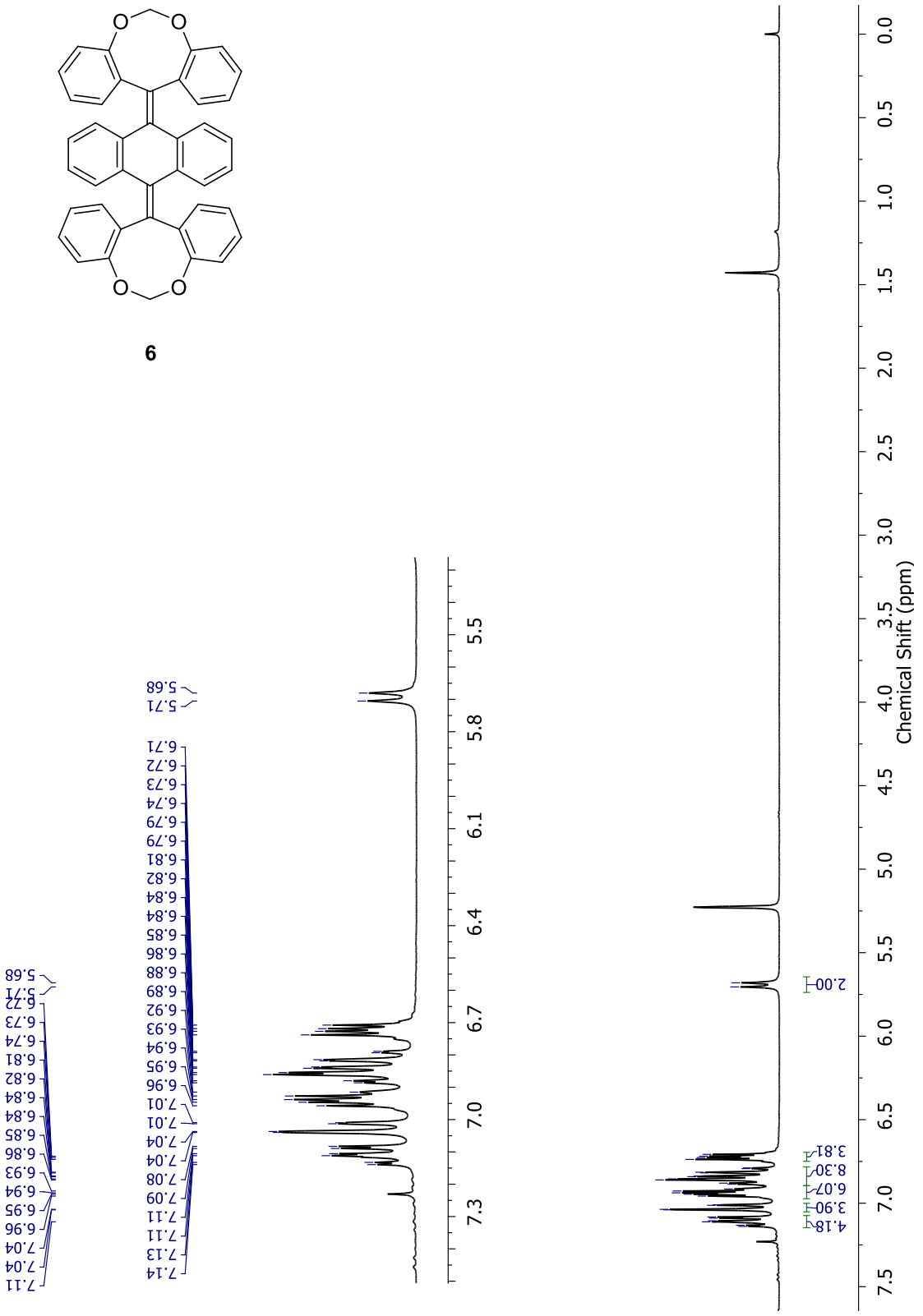

Figure S-13 ^{1}H NMR (300 MHz, CD_2Cl_2) of compound **6**.

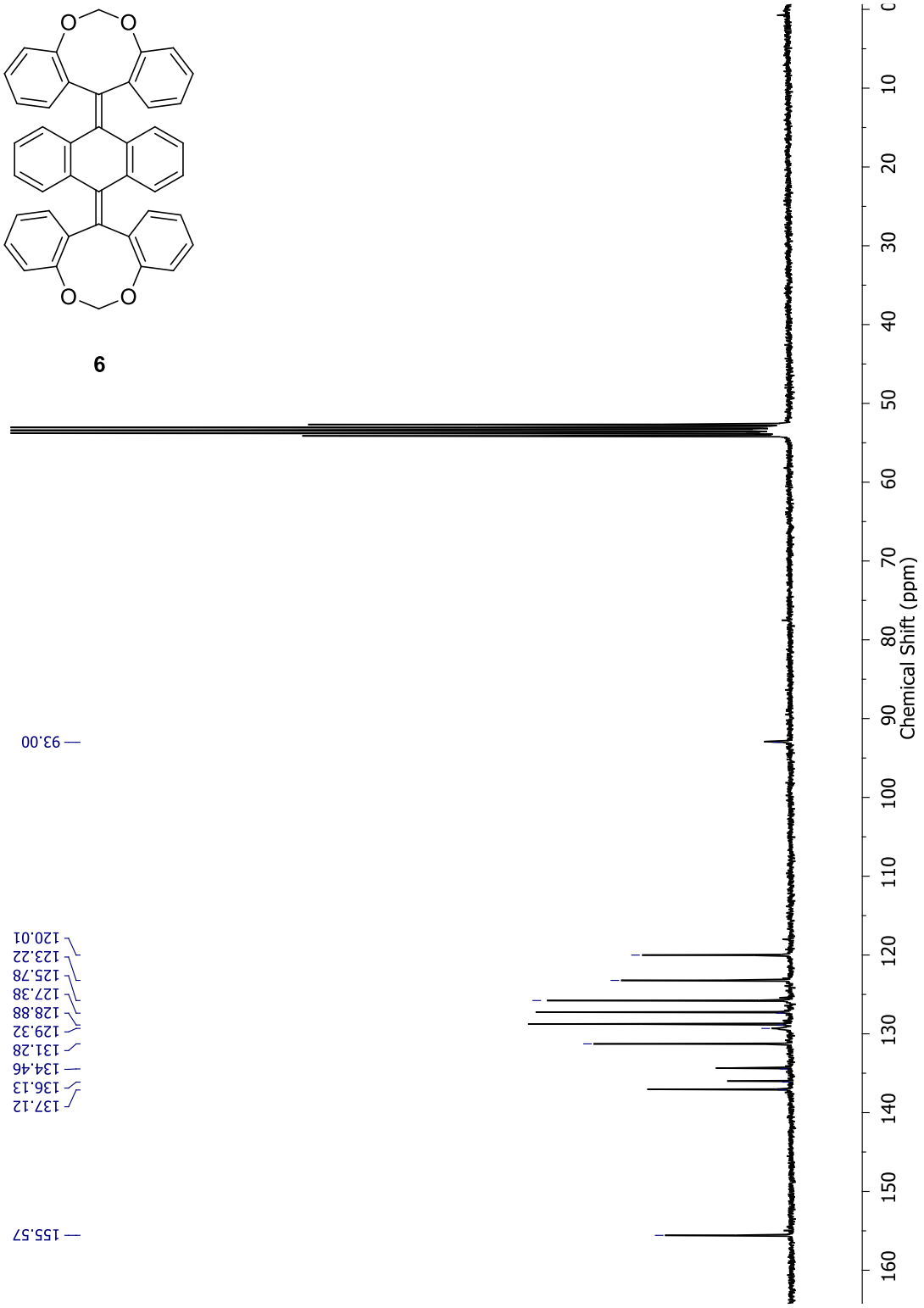

Figure S-14 ^{13}C NMR (75 MHz, CD_2Cl_2) of compound **6**.

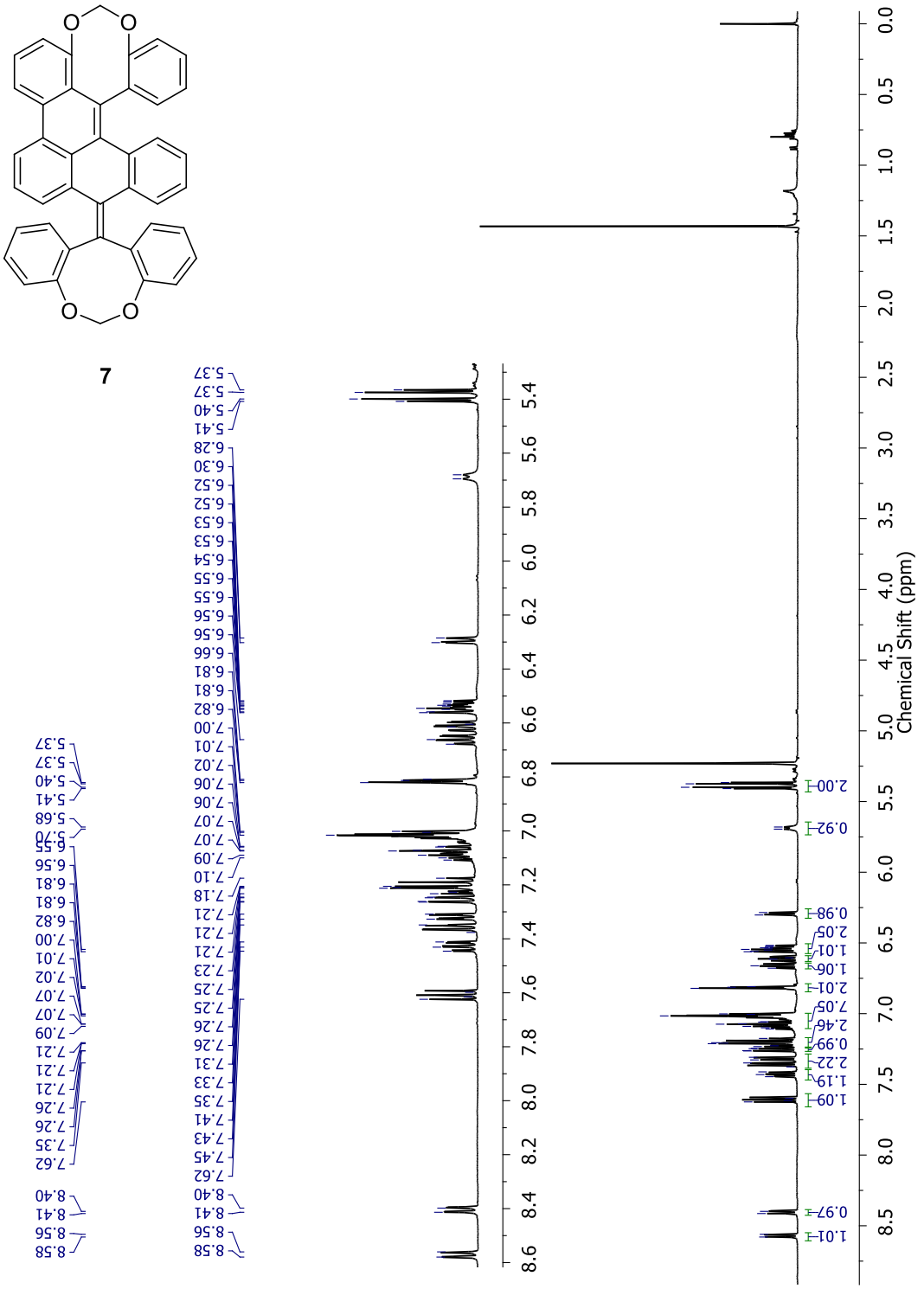

Figure S-15 ^{1}H NMR (300 MHz, CD_2Cl_2) of compound **7**.

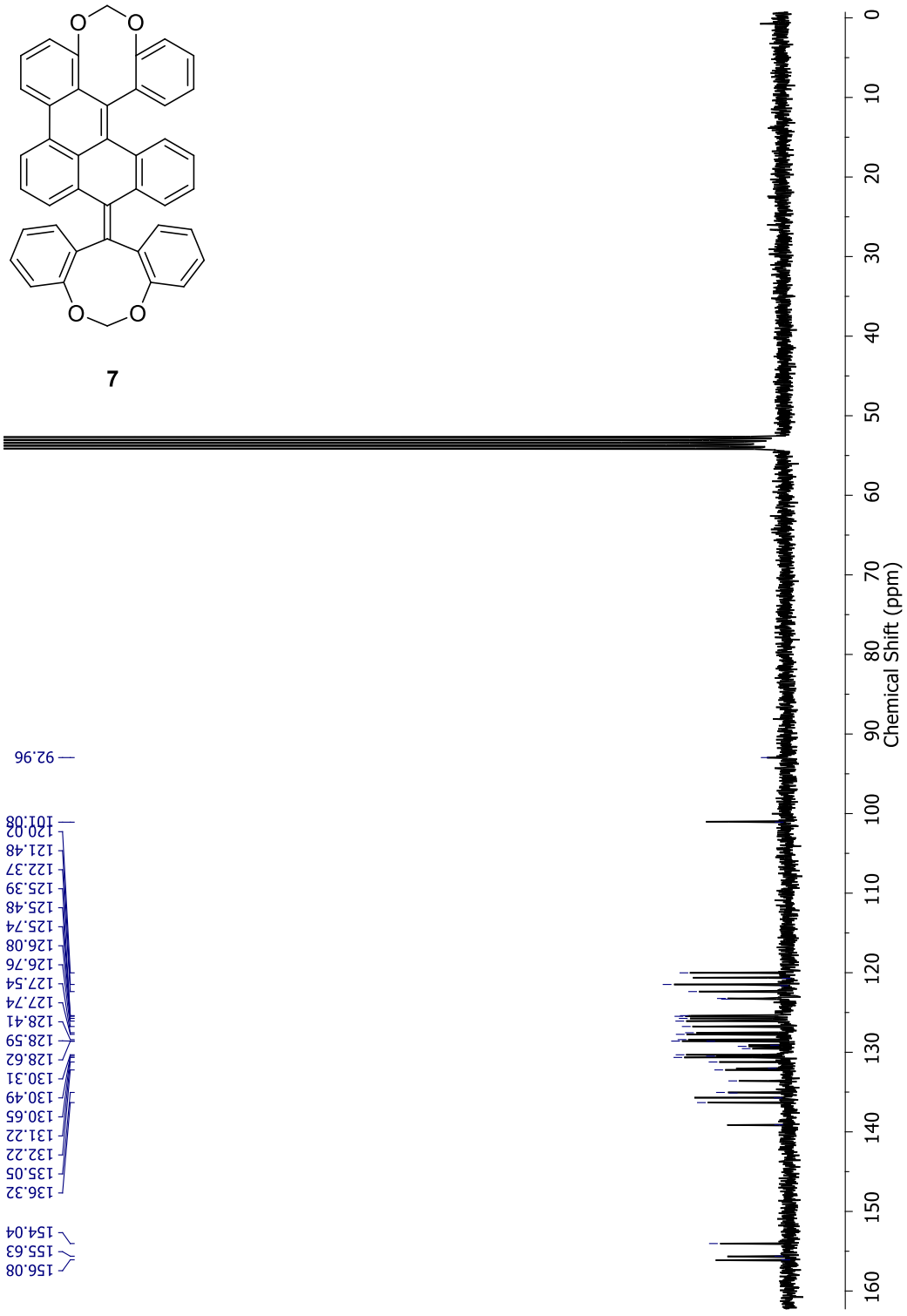

Figure S-16 ^{13}C NMR (75 MHz, CD_2Cl_2) of compound **7**.

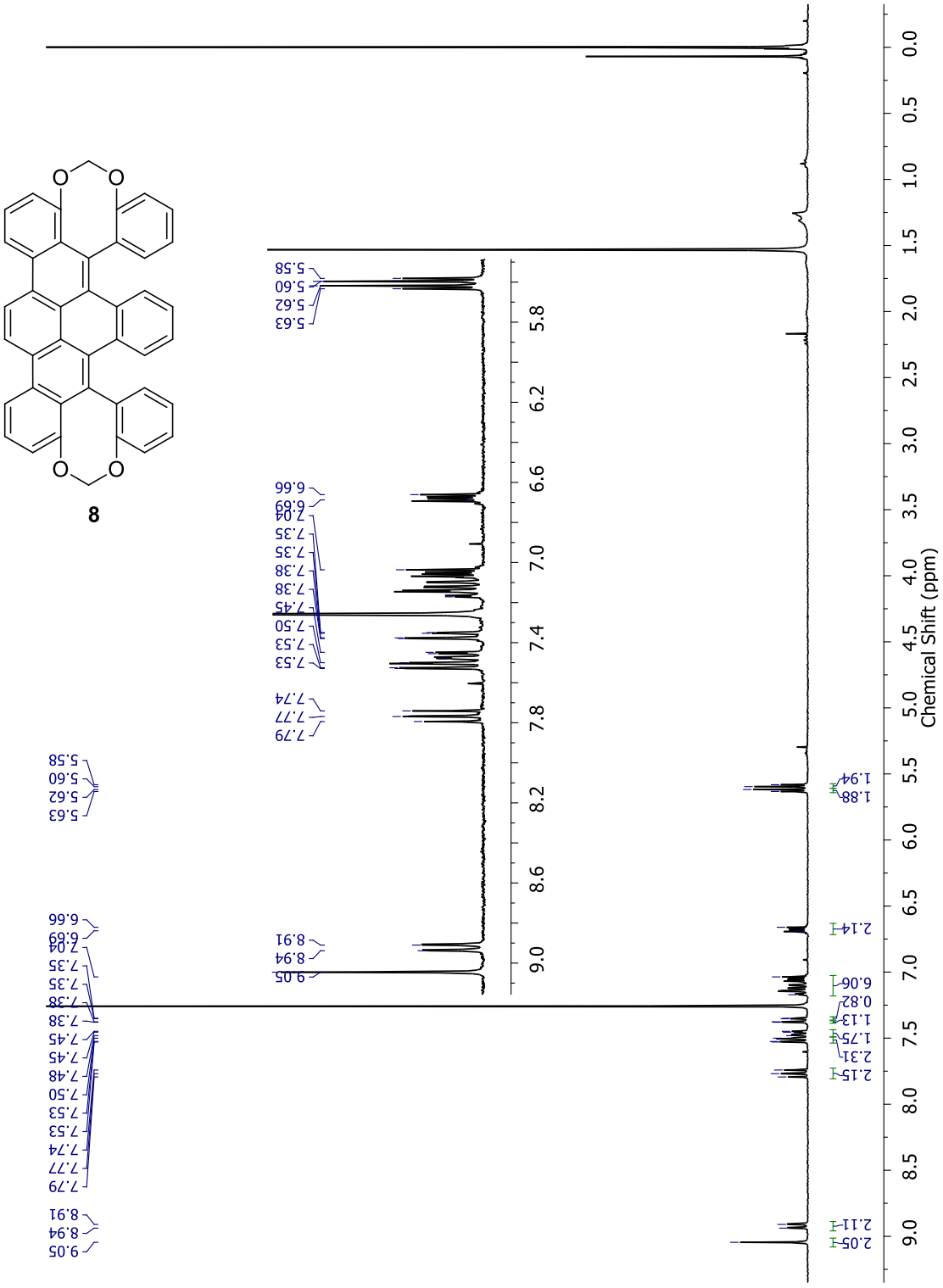

Figure S-17 ^{1}H NMR (300 MHz, $CDCl_3$) of compound **8**.

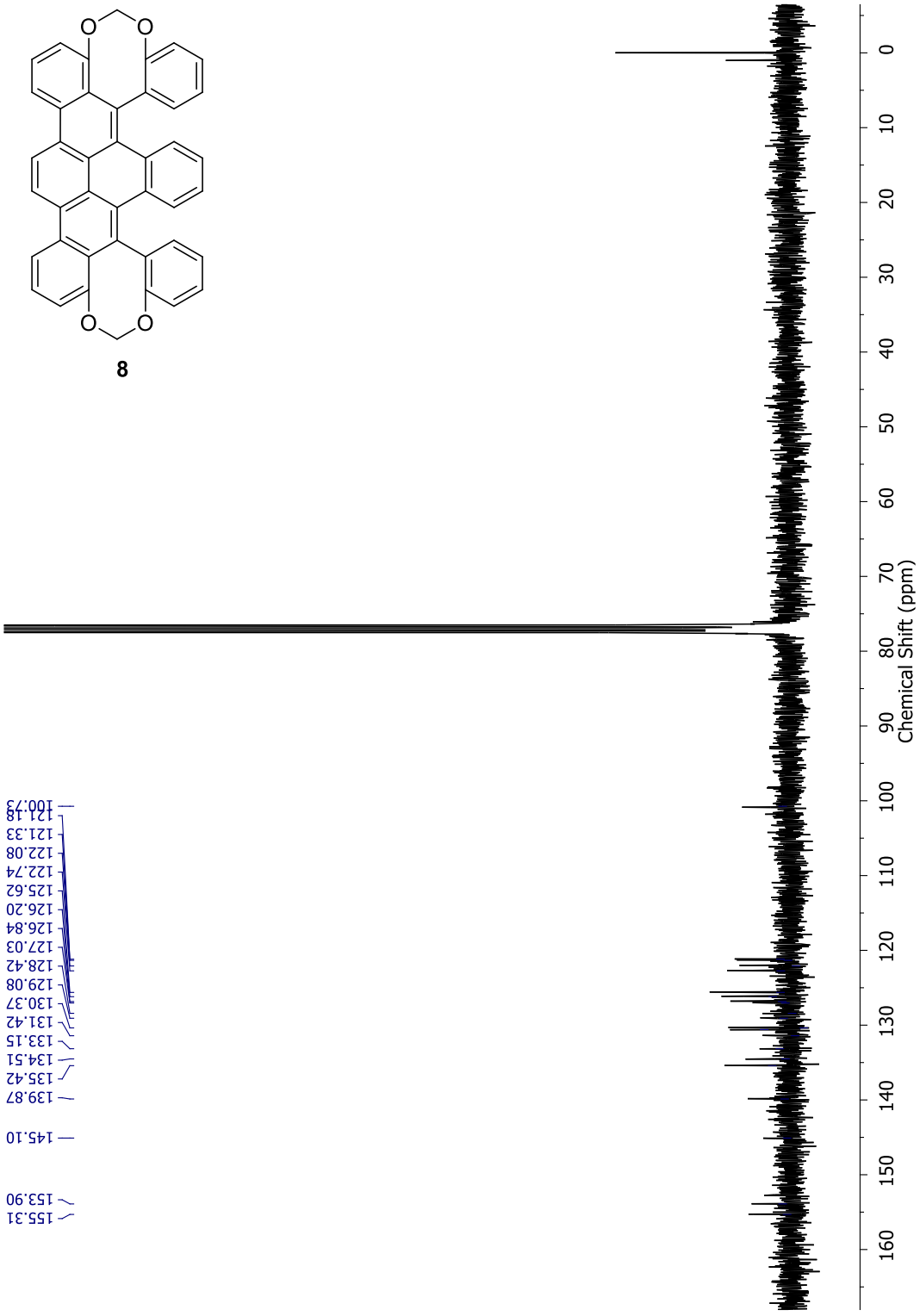

Figure S-18 ^{13}C NMR (75 MHz, $CDCl_3$) of compound **8**.

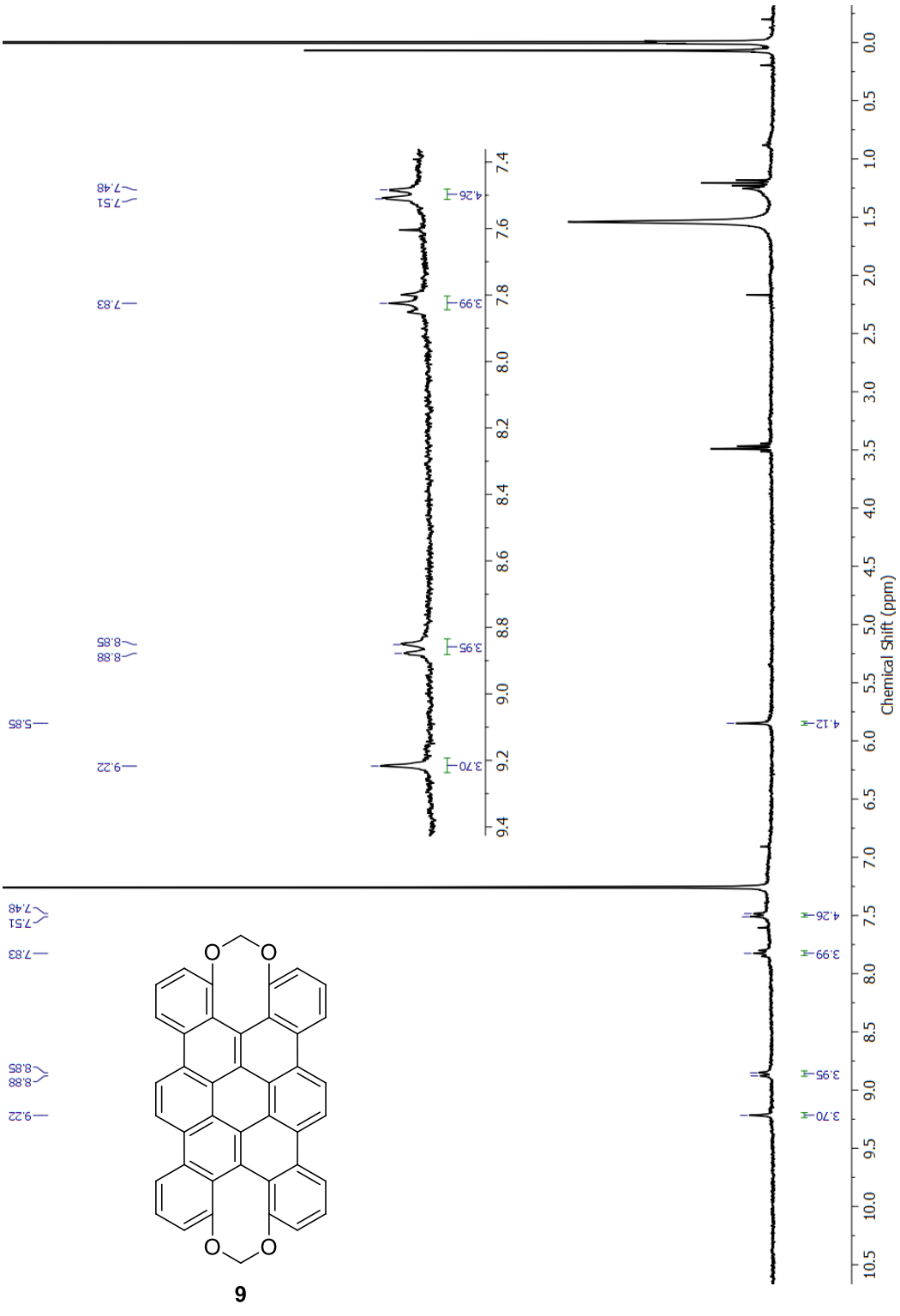

9

Figure S-19 ^{13}C NMR (75 MHz, $CDCl_3$) of compound **9**.

2. UV-Vis Spectroscopic Data

Table S-1 Summary of UV-Vis absorption and fluorescence data of compounds **3a-c**, **4a-c**, **6, 8,** and **9.**

	UV-Vis absorption λ_{max}**/nm (ε/mol^{-1} L cm^{-1})**	**Fluorescence** λ_{em}**/nm**	**Quantum Yield**
3a	284 (2.61×10^4), 300 (sh, 2.93×10^4)	-	-
3b	285 (2.05×10^4), 313 (sh, 1.66×10^4)	-	-
3c	307 (2.09×10^4)	-	-
4a	278 (2.73×10^4), 303 (4.18×10^4), 331 (1.05×10^4), 377 (1.74×10^4), 394 (1.88×10^4)	444	0.42
4b	313 (3.90×10^4), 382 (1.21×10^4), 399 (1.38×10^4)	444	0.13
4c	277 (2.89×10^4), 308 (4.17×10^4), 395 (1.87×10^4), 410 (1.90×10^4)	481	0.09
6	276 (1.67×10^4), 313 (1.59×10^4)	440	0.11
8	286 (2.98×10^4), 298 (2.96×10^4), 309 (3.06×10^4), 346 (1.36×10^4), 399 (2.50×10^4), 417 (2.62×10^4)	455	0.44
9	332 (2.37×10^4), 345 (2.04×10^4), 364 (1.86×10^4), 421 (5.61×10^4), 444 (6.61×10^4)	-	-

3. X-ray Single Crystallographic Data

Table S-2 Crystallographic data and structure refinement of compound **3a**.

formula	$C_{46}H_{38}Cl_6O_4$
formula weight	867.46
crystal dimensions (mm)	0.31 × 0.21 × 0.18
crystal system	monoclinic
space group	$P2_1/c$ (No. 14)
unit cell parameters[a]	
a (Å)	20.2505(4)
b (Å)	42.7164(9)
c (Å)	24.4130(5)
β (deg)	98.8638(10)
V (Å^3)	20865.7(7)
Z	20
ρ_{calcd} (g cm^{-3})	1.381
μ (mm^{-1})	4.104
B. Data Collection and Refinement Conditions	
diffractometer	Bruker D8/APEX II CCD[b]
radiation (λ [Å])	Cu Kα (1.54178) (microfocus source)
temperature (°C)	–100
scan type	ω and ϕ scans (1.0°) (5-10-15 s exposures)[c]
data collection 2θ limit (deg)	148.95
total data collected	425903 (-25 ≤ h ≤ 25, -53 ≤ k ≤ 52, -30 ≤ l ≤ 30)
independent reflections	42297 (R_{int} = 0.0794)
number of observed reflections (*NO*)	25759 [$F_o^2 \geq 2\sigma(F_o^2)$]
structure solution method	intrinsic phasing (*SHELXT-2014*[d])
refinement method	full-matrix least-squares on F^2 (*SHELXL–2017*[e])
absorption correction method	multi-scan (*SADABS*)
range of transmission factors	0.9963–0.7333
data/restraints/parameters	42297 / 0 / 2530
goodness-of-fit (S)[f] [all data]	1.020
final R indices[g]	
R_1 [$F_o^2 \geq 2\sigma(F_o^2)$]	0.0847
wR_2 [all data]	0.2673
largest difference peak and hole	1.412 and –0.907 e Å^{-3}

[a]Obtained from least-squares refinement of 9617 reflections with 6.16° < 2θ < 148.00°.

[b]Programs for diffractometer operation, data collection, data reduction and absorption correction were those supplied by Bruker.

[c]Data were collected with the detector set at three different positions. Low-angle (detector 2θ = –33º) data

frames were collected using a scan time of 5 s, medium-angle (detector $2\theta = 75^{\circ}$) frames using a scan time of 10 s, and high-angle (detector $2\theta = 117^{\circ}$) frames using a scan time of 15 s.

[d]Sheldrick, G. M. *Acta Crystallogr.* **2015**, *A71*, 3–8. (*SHELXT-2014*)

[e]Sheldrick, G. M. *Acta Crystallogr.* **2015**, *C71*, 3–8. (*SHELXL-2017*)

[f]$S = [\Sigma w(F_o^2 - F_c^2)^2/(n - p)]^{1/2}$ (n = number of data; p = number of parameters varied; $w = [\sigma^2(F_o^2) + (0.0885P)^2 + 42.3041P]^{-1}$ where $P = [\mathrm{Max}(F_o^2, 0) + 2F_c^2]/3$).

[g]$R_1 = \Sigma||F_o| - |F_c||/\Sigma|F_o|$; $wR_2 = [\Sigma w(F_o^2 - F_c^2)^2/\Sigma w(F_o^4)]^{1/2}$.

Table S-3 Crystallographic data and structure refinement of compound **3b**.

formula	$C_{44}H_{36}O_4$
formula weight	628.73
crystal dimensions (mm)	0.13 × 0.09 × 0.06
crystal system	triclinic
space group	$P\bar{1}$ (No. 2)
unit cell parameters[a]	
a (Å)	10.1507(2)
b (Å)	12.9997(2)
c (Å)	13.1977(2)
α (deg)	70.9130(10)
β (deg)	86.3570(10)
γ (deg)	86.0130(10)
V (Å^3)	1640.25(5)
Z	2
ρ_{calcd} (g cm^{-3})	1.273
μ (mm^{-1})	0.633
B. Data Collection and Refinement Conditions	
diffractometer	Bruker D8/APEX II CCD[b]
radiation (λ [Å])	Cu Kα (1.54178) (microfocus source)
temperature (°C)	–100
scan type	ω and ϕ scans (1.0°) (5-15-30 s exposures)[c]
data collection 2θ limit (deg)	148.18
total data collected	36527 (-12 ≤ h ≤ 12, -16 ≤ k ≤ 16, -16 ≤ l ≤ 16)
independent reflections	6343 (R_{int} = 0.0478)
number of observed reflections (*NO*)	5036 [$F_o^2 \geq 2\sigma(F_o^2)$]
structure solution method	intrinsic phasing (*SHELXT-2014*[d])
refinement method	full-matrix least-squares on F^2 (*SHELXL–2017*[e])
absorption correction method	Gaussian integration (face-indexed)
range of transmission factors	0.9894–0.9015
data/restraints/parameters	6343 / 0 / 437
goodness-of-fit (*S*)[f] [all data]	1.034
final R indices[g]	
R_1 [$F_o^2 \geq 2\sigma(F_o^2)$]	0.0404
wR_2 [all data]	0.1083
largest difference peak and hole	0.260 and –0.249 e Å^{-3}

[a]Obtained from least-squares refinement of 7302 reflections with 7.10° < 2θ < 147.84°.

[b]Programs for diffractometer operation, data collection, data reduction and absorption correction were those supplied by Bruker.

[c]Data were collected with the detector set at three different positions. Low-angle (detector 2θ = –33º) data

frames were collected using a scan time of 5 s, medium-angle (detector $2\theta = 75^{\circ}$) frames using a scan time of 15 s, and high-angle (detector $2\theta = 117^{\circ}$) frames using a scan time of 30 s.

[d]Sheldrick, G. M. *Acta Crystallogr.* **2015**, *A71*, 3–8. (*SHELXT-2014*)

[e]Sheldrick, G. M. *Acta Crystallogr.* **2015**, *C71*, 3–8. (*SHELXL-2017*)

[f]$S = [\Sigma w(F_o^2 - F_c^2)^2/(n - p)]^{1/2}$ (n = number of data; p = number of parameters varied; $w = [\sigma^2(F_o^2) + (0.0499P)^2 + 0.3535P]^{-1}$ where $P = [\text{Max}(F_o^2, 0) + 2F_c^2]/3$).

[g]$R_1 = \Sigma||F_o| - |F_c||/\Sigma|F_o|$; $wR_2 = [\Sigma w(F_o^2 - F_c^2)^2/\Sigma w(F_o^4)]^{1/2}$.

Table S-4 Crystallographic data and structure refinement of compound **3c**.

formula	$C_{44}H_{36}O_4$
formula weight	628.73
crystal dimensions (mm)	0.31 × 0.29 × 0.25
crystal system	triclinic
space group	$P\bar{1}$ (No. 2)
unit cell parameters[a]	
a (Å)	10.8188(4)
b (Å)	10.8894(4)
c (Å)	15.4163(5)
α (deg)	103.7157(4)
β (deg)	93.9199(5)
γ (deg)	107.0912(4)
V (Å^3)	1667.75(10)
Z	2
ρ_{calcd} (g cm^{-3})	1.252
μ (mm^{-1})	0.079
B. Data Collection and Refinement Conditions	
diffractometer	Bruker PLATFORM/APEX II CCD[b]
radiation (λ [Å])	graphite-monochromated Mo Kα (0.71073)
temperature (°C)	–80
scan type	ω scans (0.3°) (20 s exposures)
data collection 2θ limit (deg)	55.01
total data collected	14901 ($-14 \le h \le 14$, $-14 \le k \le 14$, $-20 \le l \le 20$)
independent reflections	7646 (R_{int} = 0.0145)
number of observed reflections (*NO*)	6144 [$F_o^2 \ge 2\sigma(F_o^2)$]
structure solution method	intrinsic phasing (*SHELXT-2014*[c])
refinement method	full-matrix least-squares on F^2 (*SHELXL–2016*[d])
absorption correction method	Gaussian integration (face-indexed)
range of transmission factors	1.0000–0.9612
data/restraints/parameters	7646 / 0 / 437
goodness-of-fit (S)[e] [all data]	1.061
final R indices[f]	
R_1 [$F_o^2 \ge 2\sigma(F_o^2)$]	0.0395
wR_2 [all data]	0.1074
largest difference peak and hole	0.221 and –0.186 e Å^{-3}

[a]Obtained from least-squares refinement of 9983 reflections with $4.50° < 2\theta < 54.92°$.

[b]Programs for diffractometer operation, data collection, data reduction and absorption correction were those supplied by Bruker.

[c]Sheldrick, G. M. *Acta Crystallogr.* **2015**, *A71*, 3–8. (*SHELXT-2014*)

[d]Sheldrick, G. M. *Acta Crystallogr.* **2015**, *C71*, 3–8. (*SHELXL-2016*)

[e]$S = [\Sigma w(F_o^2 - F_c^2)^2/(n - p)]^{1/2}$ (n = number of data; p = number of parameters varied; $w = [\sigma^2(F_o^2) + (0.0510P)^2 + 0.2864P]^{-1}$ where $P = [\text{Max}(F_o^2, 0) + 2F_c^2]/3$).

[f]$R_1 = \Sigma||F_o| - |F_c||/\Sigma|F_o|$; $wR_2 = [\Sigma w(F_o^2 - F_c^2)^2/\Sigma w(F_o^4)]^{1/2}$.

Table S-5 Crystallographic data and structure refinement of compound **4a**.

formula	$C_{42}H_{28}O_2$
formula weight	564.64
crystal dimensions (mm)	0.19 × 0.17 × 0.04
crystal system	triclinic
space group	$P\bar{1}$ (No. 2)
unit cell parameters[a]	
a (Å)	13.7290(3)
b (Å)	13.7521(3)
c (Å)	17.3063(4)
α (deg)	71.8654(11)
β (deg)	69.0351(12)
γ (deg)	78.4806(11)
V (Å^3)	2885.21(12)
Z	4
ρ_{calcd} (g cm^{-3})	1.300
μ (mm^{-1})	0.610
B. Data Collection and Refinement Conditions	
diffractometer	Bruker D8/APEX II CCD[b]
radiation (λ [Å])	Cu Kα (1.54178) (microfocus source)
temperature (°C)	–100
scan type	ω and ϕ scans (1.0°) (5 s exposures)
data collection 2θ limit (deg)	144.64
total data collected	20463 (-16 ≤ h ≤ 16, -16 ≤ k ≤ 16, -21 ≤ l ≤ 20)
independent reflections	10966 (R_{int} = 0.0234)
number of observed reflections (*NO*)	8732 [$F_o^2 \geq 2\sigma(F_o^2)$]
structure solution method	intrinsic phasing (*SHELXT-2014*[c])
refinement method	full-matrix least-squares on F^2 (*SHELXL–2017*[d])
absorption correction method	Gaussian integration (face-indexed)
range of transmission factors	0.9921–0.8804
data/restraints/parameters	10966 / 51[e] / 868
extinction coefficient (x)[f]	0.0017(2)
goodness-of-fit (S)[g] [all data]	1.026
final R indices[h]	
R_1 [$F_o^2 \geq 2\sigma(F_o^2)$]	0.0606
wR_2 [all data]	0.1768
largest difference peak and hole	0.500 and –0.315 e Å^{-3}

[a]Obtained from least-squares refinement of 7851 reflections with 5.66° < 2θ < 143.74°.

[b]Programs for diffractometer operation, data collection, data reduction and absorption correction were those supplied by Bruker.

[c]Sheldrick, G. M. *Acta Crystallogr.* **2015**, *A71*, 3–8. (*SHELXT-2014*)

[d]Sheldrick, G. M. *Acta Crystallogr.* **2015**, *C71*, 3–8. (*SHELXL-2017*)

[e]The disordered anisotropic placement parameters for the oxygen and carbon atoms of the methoxyphenyl group of molecule B were restrained by use of the *SHELXL* **RIGU** instruction (the rigid-bond restraint).

[f]$F_c^* = kF_c[1 + x\{0.001F_c^2\lambda^3/\sin(2\theta)\}]^{-1/4}$ where k is the overall scale factor.

[g]$S = [\Sigma w(F_o^2 - F_c^2)^2/(n - p)]^{1/2}$ (n = number of data; p = number of parameters varied; $w = [\sigma^2(F_o^2) + (0.0720P)^2 + 0.8613P]^{-1}$ where $P = [\text{Max}(F_o^2, 0) + 2F_c^2]/3$).

[h]$R_1 = \Sigma||F_o| - |F_c||/\Sigma|F_o|$; $wR_2 = [\Sigma w(F_o^2 - F_c^2)^2/\Sigma w(F_o^4)]^{1/2}$.

Table S-6 Crystallographic data and structure refinement of compound **7**.

Empirical formula	$C_{42}H_{26}O_4$
Formula weight	594.63
Temperature/K	100(2)
Crystal system	monoclinic
Space group	$P2_1/n$
a/Å	11.31760(10)
b/Å	18.03190(10)
c/Å	14.10490(10)
β/°	97.0440(10)
Volume/Å^3	2856.77(4)
Z	4
ρ_{calc}g/cm^3	1.383
μ/mm^{-1}	0.701
F(000)	1240.0
Crystal size/mm^3	0.191 × 0.07 × 0.065
Radiation	Cu Kα (λ = 1.54184)
2Θ range for data collection/°	7.996 to 154.982
Index ranges	$-14 \le h \le 14$, $-22 \le k \le 22$, $-17 \le l \le 17$
Reflections collected	57382
Independent reflections	6036 [R_{int} = 0.0434, R_{sigma} = 0.0217]
Data/restraints/parameters	6036/0/519
Goodness-of-fit on F^2	1.091
Final R indexes [I>=2σ (I)]	R_1 = 0.0405, wR_2 = 0.1007
Final R indexes [all data]	R_1 = 0.0430, wR_2 = 0.1024
Largest diff. peak/hole / e Å^{-3}	0.21/-0.20

4. DFT Computational Results

DFT computational modeling were performed using the Gaussian 16 software package.[6] Molecular geometries of compound **4c** and **7** were optimized in the gas phase at the M06-2X/Def2SVP level of theory. The optimized geometries were subjected to frequency calculations at the same level to validate they are energy minima (without imaginary frequencies) as well as to obtain thermodynamic energies. TD-DFT calculations of **4c** was performed on its optimized geometries at the M06-2X/Def2SVP level of theory. Molecular structures and frontier molecular orbitals of **7** were visualized by the VMD software package.[7]

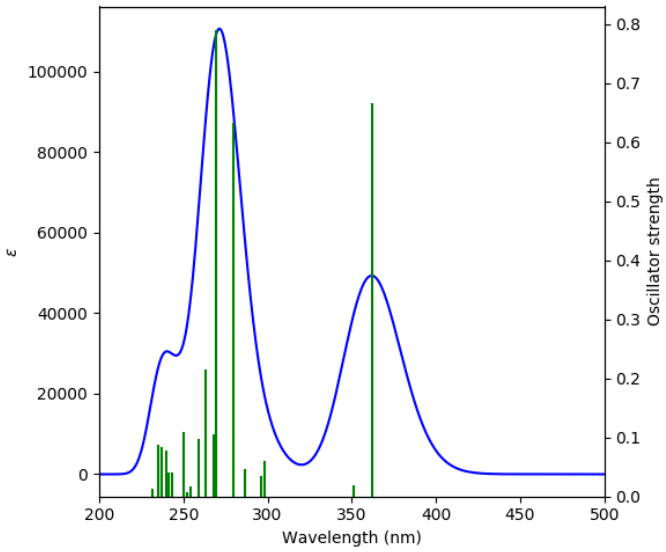

Figure S-20 Simulated UV-Vis spectrum of compound 4c calculated at the M06-2X/Def2SVP level of theory.

6 Gaussian 16, Revision C.01, M. J. Frisch, G. W. Trucks, H. B. Schlegel, G. E. Scuseria, M. A. Robb, J. R. Cheeseman, G. Scalmani, V. Barone, G. A. Petersson, H. Nakatsuji, X. Li, M. Caricato, A. V. Marenich, J. Bloino, B. G. Janesko, R. Gomperts, B. Mennucci, H. P. Hratchian, J. V. Ortiz, A. F. Izmaylov, J. L. Sonnenberg, D. Williams-Young, F. Ding, F. Lipparini, F. Egidi, J. Goings, B. Peng, A. Petrone, T. Henderson, D. Ranasinghe, V. G. Zakrzewski, J. Gao, N. Rega, G. Zheng, W. Liang, M. Hada, M. Ehara, K. Toyota, R. Fukuda, J. Hasegawa, M. Ishida, T. Nakajima, Y. Honda, O. Kitao, H. Nakai, T. Vreven, K. Throssell, J. A. Montgomery, Jr., J. E. Peralta, F. Ogliaro, M. J. Bearpark, J. J. Heyd, E. N. Brothers, K. N. Kudin, V. N. Staroverov, T. A. Keith, R. Kobayashi, J. Normand, K. Raghavachari, A. P. Rendell, J. C. Burant, S. S. Iyengar, J. Tomasi, M. Cossi, J. M. Millam, M. Klene, C. Adamo, R. Cammi, J. W. Ochterski, R. L. Martin, K. Morokuma, O. Farkas, J. B. Foresman, and D. J. Fox, Gaussian, Inc., Wallingford CT, 2016.

7 Humphrey, W., Dalke, A. and Schulten, K., "VMD - Visual Molecular Dynamics", J. Molec. Graphics, 1996, vol. 14, pp. 33-38.

Table S-7 Summary of TD-DFT calculated electronic transitions of 4c at the M06-2X/Def2SVP level of theory.

λ (nm)	***f***	**Major MO Contributions**
362.1	0.666	HOMO→LUMO (94%)
351.4	0.019	HOMO→L+1 (72%)
298.5	0.059	H-2→LUMO (10%), H-1→LUMO (20%), HOMO→L+2 (57%)
296.0	0.034	H-1→LUMO (71%), HOMO→L+2 (12%)
286.5	0.046	H-1→L+1 (46%), HOMO→L+3 (12%)
279.4	0.632	H-2→LUMO (62%), HOMO→L+1 (13%), HOMO→L+2 (21%)
269.4	0.790	H-3→LUMO (18%), H-2→L+1 (54%)
268.1	0.106	H-5→LUMO (10%), HOMO→L+3 (12%), HOMO→L+4 (50%)
262.9	0.214	H-3→LUMO (50%), H-2→L+1 (19%), H-1→L+1 (12%)
259.4	0.097	H-4→LUMO (77%)
254.5	0.017	HOMO→L+3 (29%), HOMO→L+4 (14%)
252.4	0.007	HOMO→L+5 (39%)
250.1	0.0109	H-5→LUMO (61%), HOMO→L+4 (10%)
243.0	0.039	H-1→L+1 (21%), H-1→L+2 (20%), HOMO→L+3 (10%)
241.3	0.040	H-5→L+1 (13%), H-3→L+1 (19%), H-2→L+4 (14%)
239.7	0.078	H-6→LUMO (25%), H-1→L+4 (13%), HOMO→L+9 (21%)
237.2	0.083	H-1→L+2 (12%), HOMO→L+6 (40%)
237.0	0.58	H-1→L+2 (43%), HOMO→L+6 (19%)
234.8	0.087	H-5→LUMO (13%), H-2→L+2 (42%)
231.7	0.013	HOMO→L+7 (14%), HOMO→L+8 (37%)